



VNIVERSITAT  
DE VALÈNCIA

Instituto de Ciencia Molecular - Departamento de Química

Inorgánica

Facultad de Química - Universitat de València

**Multiproperty complexes of 4d and 4f metal  
ions based on biomolecules: From fundamental  
research to potential applications**

Programa de Doctorado en Nanociencia y Nanotecnología (RD  
99/2011)

Tesis Doctoral

Marta Orts Arroyo

Mayo 2023

Dirigida por el Doctor F. José Martínez Lillo





**Dr. F. José Martínez Lillo**, Profesor Titular de Química Inorgánica de la Universitat de València,

**CERTIFICA:**

Que el trabajo titulado “*Multiproperty complexes of 4d and 4f metal ions based on biomolecules: From fundamental research to potential applications*”, presentado por MARTA ORTS ARROYO en el marco del Programa de Doctorado de Nanociencia y Nanotecnología, ha sido realizado bajo mi dirección en el Instituto de Ciencia Molecular de la Universitat de València para optar al título de Doctora en Nanociencia y Nanotecnología.

Para que así conste, firmo el presente certificado.

Paterna, Junio de 2023

Fdo.: F. José Martínez Lillo



---

# *Table of Contents*

<b>Acknowledgements</b>	<b>v</b>
<b>Acronyms</b>	<b>x</b>
<b>Abbreviations</b>	<b>xii</b>
<b>Resumen</b>	<b>xv</b>
<b>Abstract</b>	<b>xxxiii</b>
<b>Chapter 1: Introduction and background</b>	<b>1</b>
1.1 Coordination Chemistry in Molecular Magnetism . . . . .	3
1.2 Other applications of coordination compounds: from biology to nanomedicine and nanotechnology . . . . .	9
1.3 Biomolecules as ligands . . . . .	13
1.4 General Objectives . . . . .	17
References . . . . .	20
<b>Chapter 2: Mono- and dinuclear ruthenium(III)/(IV)-chloride complexes based on nucleobases, polyazines and polyazoles: From SIMs to biosensors and antitumour drugs</b>	<b>25</b>
2.1 Prologue . . . . .	27
2.2 Contents . . . . .	34
References . . . . .	37

---

Article 1. <i>Magnetochemistry</i> <b>2022</b> , <i>8</i> , 93 . . . . .	43
Article 2. <i>Crystals</i> <b>2022</b> , <i>12</i> , 448 . . . . .	57
Article 3. <i>Biosensors</i> <b>2021</b> , <i>11</i> , 19 . . . . .	69
Article 4. <i>J. Inorg. Biochem.</i> <b>2022</b> , <i>232</i> , 111812 . . . . .	81
Article 5. <i>Cancers</i> <b>2023</b> , <i>15</i> , 69 . . . . .	91
Article 6. <i>Cryst. Growth Des.</i> <b>2020</b> , <i>20</i> , 3 . . . . .	109
<b>Chapter 3: Gadolinium(III) and dysprosium(III) complexes based on nucleobases, amino acids and oxalic acid: From SMMs to MRI contrast agents and magnetic coolers</b>	<b>125</b>
3.1 Prologue . . . . .	127
3.2 Contents . . . . .	134
References . . . . .	136
Article 7. <i>Int. J. Mol. Sci.</i> <b>2021</b> , <i>22</i> , 4586 . . . . .	143
Article 8. <i>Dalton Trans.</i> <b>2020</b> , <i>49</i> , 9155 . . . . .	157
Article 9. <i>Inorganics</i> <b>2022</b> , <i>10</i> , 32 . . . . .	169
Article 10. <i>Dalton Trans.</i> <b>2021</b> , <i>50</i> , 3801 . . . . .	183
<b>Chapter 4: Conclusions and Perspectives</b>	<b>191</b>
<b>Appendix A: Supporting Information Chapter 2</b>	<b>199</b>
SI <i>Magnetochemistry</i> <b>2022</b> , <i>8</i> , 93 . . . . .	201
SI <i>J. Inorg. Biochem.</i> <b>2022</b> , <i>232</i> , 111812 . . . . .	205
SI <i>Cancers</i> <b>2023</b> , <i>15</i> , 69 . . . . .	211
SI <i>Cryst. Growth Des.</i> <b>2020</b> , <i>20</i> , 3 . . . . .	221
<b>Appendix B: Supporting Information Chapter 3</b>	<b>235</b>
SI <i>Int. J. Mol. Sci.</i> <b>2021</b> , <i>22</i> , 4586 . . . . .	237
SI <i>Dalton Trans.</i> <b>2020</b> , <i>49</i> , 9155 . . . . .	247
SI <i>Dalton Trans.</i> <b>2021</b> , <i>50</i> , 3801 . . . . .	261

---

## *Acknowledgements*

Disfruto poco escribiendo para lo mucho que hablo (irónico, ¿verdad?). Pero, dadas las circunstancias, haré un último esfuerzo, ya que sí me gustaría expresar de forma breve el agradecimiento que siento hacia quienes han contribuido de una forma u otra a la culminación de esta tesis.

En primer lugar me gustaría dar las gracias a Francisco Lloret Pastor y Miguel Julve Olcina, por la confianza depositada al darme la oportunidad de formar parte del grupo de Química de Coordinación a través de la financiación obtenida mediante la ayuda para contratos predoctorales para la formación de doctores/as (FPI).

En la misma línea, quiero dar las gracias a mi tutor, Jose Martínez Lillo, que ha estado acompañándome durante todo este proceso. Jose ha sido, sin duda, una de las bases más importantes para que esta tesis se haya podido realizar con éxito. Siempre he creído que un trabajo exitoso es fruto de personas que tienen ambición y se rodean de otras que aportan, tanto académica como personalmente. En este escenario, no podría haber sido más afortunada de tenerte como mentor académico. A lo largo de estos años has sabido expresar tus pensamientos con respeto y aportar tus conocimientos con rigor, dejando siempre espacio para el desacuerdo, lo que me ha dado la confianza necesaria para tomar las riendas de mi trabajo con iniciativa.

---

Has sabido sobrellevar mis vaivenes emocionales con empatía, dándome el espacio y tiempo necesarios para seguir adelante con esta tarea que, aunque aparentemente sencilla, conlleva demasiados altibajos. Gracias por la comprensión cuando no podía ofrecer más y por animarme a continuar cuando yo creía que no podía (no ha sobrado ninguna vez que has terminado tu disertación con un: ¡Ánimo!). Has puesto el listón muy alto como tutor. Ojalá tener la mitad de suerte de aquí en adelante.

Isabel Castro, nos conocemos desde mis primeros pasos en la investigación. Siempre has mostrado implicación en mi trabajo y te has preocupado por mi futuro académico. Agradezco tu opinión y punto de vista. Ambos han sido de gran utilidad en esta tesis.

Asimismo, me gustaría expresar mi gratitud a Rafa Ruiz García. Te conozco desde el primer día que aparecí en el ICMol. Me ofreciste un vaso de agua cuando entré en el laboratorio un asfixiante día de agosto y en ese momento pensé: estoy en buen lugar. Desde entonces, mi gratitud hacia ti no ha hecho más que crecer. Has ofrecido tus conocimientos de manera altruista, siempre con respeto y humildad, dando valor al trabajo que hacía en el laboratorio. Cuando no sabía por dónde seguir, abriste nuevos caminos interesantes por los que continuar. Esta tesis también tiene una parte de ti de la que me siento orgullosa.

Nicolas Moliner, soy consciente de que apareces en todas las tesis. Lo más probable es que seas la persona que más agradecimientos ha recibido, entre otras cosas porque nos has rescatado de las medidas magnéticas (lo que, para mí, es motivo suficiente para construirte un pedestal). Pero no sólo eso, sino también porque, al menos en mi caso, he tenido la oportunidad de compartir contigo innumerables comidas al sol, luchando contra mosquitos, hormigas y avispas. Creo que eso nos ha unido más que las tantas conversaciones que hemos tenido

sobre la vida y el futuro. Tu opinión y tus consejos siempre han sido muy útiles, aunque la señorita Orts no siempre te haya hecho caso.

Me gustaría agradecer al Grupo de Investigación en Imagen Biomédica y al Departamento de Radiología, dirigido por el Dr. Luis Martí Bonmatí, por colaborar en este proyecto y realizar el estudio con fantomas de resonancia magnética de nuestros compuestos. Del mismo modo, deseo expresar mi gratitud al instituto INCLIVA, bajo la dirección de Gloria Ribas, por el estudio *in vitro* de nuestros compuestos para evaluar su respuesta antitumoral, ayudando así a completar esta tesis.

A lo largo de estos años he conocido a muchas personas. Personas que vienen y van y gente que siempre ha permanecido. Si tengo que empezar por alguien, ese es Carlos R. Marcaste un punto de inflexión en mi vida y fuiste el primero en confiar en mí, antes incluso que yo misma. Gracias a tu ímpetu decidí empezar el camino de la investigación. Me enseñaste a luchar por lo que uno quiere, cueste lo que cueste y aunque a veces no se gane.

A todas esas personas que fueron de paso, TFGs, TFGMs, PhDs, gracias. Absolutamente todos me habéis enseñado algo, ya sea en lo académico o en lo personal. Sois tantos que sería imposible no olvidarme de alguno al mencionaros.

Sin duda alguna, mi mayor descubrimiento han sido mis queridas Marta A., Mireia R. y Raquel R. Lo que empezó en Santiago de Compostela que no termine nunca. Este último año ha sido difícil coincidir, pero gracias por esas llamadas, comidas, visitas, etc. Todo ello me hace creer que sigue habiendo buenas personas y buenos compañeros de trabajo.

Cristian Z., has aparecido en mi vida en los últimos años de esta aventura, así que se puede decir que te ha tocado la parte más dura, pues convivir con un/a doctorando/a no es tarea sencilla. Gracias por tu paciencia y por no aban-

---

donarme, aún cuando yo quería huir. Eres un gran apoyo para mí. Gracias por abrirme las puertas de tu casa y hacerla sentir, de algún modo, mía también.

Algo que durante muchos años me ha perseguido (y sigue, pero a paso más ligero) es el miedo. Para muchas personas, irse de estancia a otro país puede ser el único motivo por el que empezar una carrera de investigación. En mi caso, siempre fue todo lo contrario. Es por ello que me gustaría agradecer a Euan K. Brechin y a todo su grupo de investigación por la cálida acogida que me brindaron en Edimburgo (y mira que calor, precisamente, no hacía). En especial, me gustaría agradecer a Álvaro E., quien ha estado pendiente de mí desde el primer hasta el último día. Has contribuido en gran medida a hacer mi estancia agradable, preocupándote siempre por mi bienestar. No solo eso, también me has enseñado Química desde otro punto de vista, abriéndome la mente. No obstante, eso ha supuesto conocer de primera mano las temidas columnas, aunque han sido menos duras de lo esperado gracias a tu optimismo y pasión por la Química Orgánica. Gracias a ello he aprendido a valorar más mi trabajo y, por supuesto, mis ligandos.

Por otro lado, aunque no hayan participado implícitamente en mi tesis, siento que debo agradecer a dos personas que, durante todos los años de tesis, e incluso antes de ello, han sido un apoyo incondicional para mí. Ellos son Hector C. y Ruben S. (sí Rubén, tú también). Voy a estar eternamente agradecida por las mil y una charlas que habéis tenido que aguantar (os admiro). Sois la definición de amistad más exacta que conozco y ojalá nunca se separen nuestros caminos.

Del mismo modo puedo hablar de Paula G. y Luis B. Nos conocemos desde hace aproximadamente unos diez años, pero el destino quiso unirnos más adelante, y qué agradecida me siento por ello. Vuestra amistad ha sido, y es, fundamental para mí.



Vosotros cuatro habéis sido mis ojos cuando yo no podía ver. Gracias por la empatía, la inteligencia emocional y el sentido común. Son valores que escasean hoy en día y contar con todos ellos os convierte en un regalo para mí.

Gracias también a mi familia, a los que están y a los que se fueron, a aquellos que me han apoyado, aunque sigan sin entender qué estoy haciendo y me pregunten constantemente: ¿pero tú estás estudiando o trabajando? Os quiero.

Por último, y no por ello menos importante, me gustaría ser fiel a mí misma. Eso implica agradecer a la Marta que durante estos años de investigación ha sabido siempre seguir, aún cuando temía lo que había al otro lado del puente y debajo de él. Suena fácil pero, siendo honesta, ha sido un camino complejo. Algunas veces conté con ayuda que me impulsó hacia delante y otras veces con dificultades que me intentaban arrastrar al inicio. Sin embargo, siento que lo he conseguido. Porque la clave del éxito, bajo mi punto de vista, es tener miedo pero seguir hacia delante.

Así que, como me preguntaría alguien a quien ya he mencionado y quiero mucho: ¿Ya te has desahogado?

Por primera vez le voy a contestar que sí.

---

# *Acronyms*

**ac** alternating current

**bpy** 2,2'-bipyridine

**bpym** 2,2'-bipyrimidine

**CMR** Cryogenic Magnetic Refrigeration

**CP** Coordination Polymer

**dc** direct current

**dien** diethylenetriamine

**DMF** N, N'-Dimethylformamide

**dmpy** 4,4'-dimethyl-2,2'-bipyridine

**DMSO** Dimethyl sulfoxide

**DOTA** 1,4,7,10-tetraazacyclododecane-N,N',N'',N'''-tetraacetic acid

**DTPA** Diethylenetriaminepentaacetic acid

**EPR** Electron Paramagnetic Resonance

**GBCAs** Gadolinium-based contrast agents

**hpp** 1,3,4,6,7,8-hexahydro-2H-pyrimido[1,2-a]pyrimidinate

**KP1019** *trans*-[tetrachlorobis(indazole)ruthenate(III)]

**MCE** Magnetocaloric Effect

**MCU** Mitochondrial Calcium Uniporter

**MOFs** Metal-Organic Frameworks

**MRI** Magnetic Resonance Imaging

**NAMI-A** *trans*-[tetrachloro(DMSO)(imidazole)ruthenate(III)]

**NMR** Nuclear Magnetic Resonance

**NP** Nanoparticle

**phen** 1,10-phenanthroline

**QTM** Quantum Tunneling of the Magnetisation

**SCM** Single-Chain Magnet

**SIM** Single-Ion Magnet

**SMM** Single-Molecule Magnet

**ZFS** Zero-Field Splitting

---

## *Abbreviations*

$\beta$	Bohr Magneton ( $9.27401 \times 10^{-24} \text{ JT}^{-1}$ )
$\chi_M$	Molar magnetic susceptibility ( $\text{cm}^3 \text{ mol}^{-1}$ )
$\chi'_M$ and $\chi''_M$	In phase and out-of-phase ac-magnetic signals ( $\text{cm}^3 \text{ mol}^{-1}$ )
$\lambda$	Spin-orbit coupling constant
$\nu$	Frequency
$\tau$	Relaxation time
$k_B$	Boltzman constant ( $1.38066 \times 10^{-23} \text{ JK}^{-1}$ )
$N_A$	Avogadro's number ( $6.02214 \times 10^{23} \text{ mol}^{-1}$ )
$T_B$	Blocking temperature (K)
$T_{ad}$	Adiabatic temperature (K)
$U_{eff}$	Effective energy barrier
$g$	Landé factor
$h$	Plank's constant ( $6.62607 \times 10^{-34} \text{ J}\cdot\text{s}$ )
$J$	Magnetic exchange coupling constant ( $\text{cm}^{-1}$ )

$M$  Magnetisation

$S$  Total spin



---

# *Resumen*

El trabajo desarrollado en esta Tesis se enmarca en el campo de la Química de Coordinación y el Magnetismo Molecular, vectores base para el desarrollo de múltiples aplicaciones en Nanomedicina y Nanotecnología. El estudio de los compuestos de coordinación tiene una larga historia que se remonta a principios del siglo XIX, con notables contribuciones de químicos como Berzelius y Jørgensen. Esta rama de la química se centra en la comprensión de las propiedades de unión de los ligandos (moléculas o aniones donadores de electrones) a los iones metálicos. Las teorías de Alfred Werner sobre la coordinación de iones metálicos a principios del siglo XX marcaron un hito importante en este campo. El Magnetismo Molecular, un área de investigación multidisciplinar, se originó hace aproximadamente tres décadas con el objetivo principal de sintetizar y estudiar los compuestos metálicos de coordinación. Este campo ha experimentado un crecimiento significativo gracias a los esfuerzos de colaboración de científicos de diversas disciplinas, como la Química, la Física y la Biología. La complementariedad de las técnicas experimentales y los conocimientos generados por distintas ramas de la ciencia han contribuido al rápido progreso del Magnetismo Molecular. La Química Inorgánica, en particular la Química de Coordinación, ha desempeñado un papel fundamental en el diseño y la síntesis de complejos con estructuras y propiedades magnéticas predecibles. El estudio del magnetismo

---

molecular se centró inicialmente en los complejos mononucleares, que aportaron valiosos conocimientos sobre la estructura y el enlace de los compuestos de coordinación. El campo empezó a florecer a finales de la década de 1970, cuando los investigadores trataron de crear imanes basados en moléculas que imitaran las propiedades de los imanes inorgánicos. Estas investigaciones se centraron principalmente en los iones metálicos 3d, mientras que los iones metálicos 4d y 5d permanecieron relativamente inexplorados debido a su química desafiante y su complejo comportamiento magnético. Sin embargo, las propiedades únicas de los iones metálicos más pesados, como una mayor anisotropía magnética y una difusividad más larga, han llamado la atención, lo que ha llevado a la exploración del Magnetismo Molecular basado en iones 4d y 5d.

“Single-Molecule Magnet” (SMM) es un fenómeno fascinante que se descubrió a principios de la década de 1990 y revolucionó este campo al demostrar que determinados complejos polinucleares poseen la capacidad de mostrar magnetización sin interacciones cooperativas de largo alcance. Los orígenes de SMM se remontan a los trabajos realizados en el grupo de Christou durante la década de 1980, centrados en la síntesis de compuestos modelo del complejo de evolución del oxígeno en el Fotosistema II. Aunque esta investigación produjo varios complejos polinucleares de manganeso de valencia mixta, aún faltaba un modelo para el estado de oxidación más alto del ciclo biológico. Durante la búsqueda para desarrollar tal modelo, se aisló un intrigante compuesto con la fórmula  $[\text{Mn}_{12}\text{O}_{12}(\text{O}_2\text{CPh})_{16}(\text{H}_2\text{O})_4]$  mediante la oxidación de acetato de manganeso con permanganato. La propuesta de un complejo dodecanuclear de manganeso a partir de este tipo de reacción fue realizada por primera vez en 1921 por Weinland y Fischer. Sin embargo, no fue hasta la llegada de los experimentos con rayos X monocristalinos cuando se pudo confirmar la estructura del compuesto como



$[\text{Mn}_{12}\text{O}_{12}(\text{O}_2\text{CCH}_3)_{16}(\text{H}_2\text{O})_4] \cdot 4 \text{H}_2\text{O} \cdot 2 \text{CH}_3\text{COOH}$  o  $[\text{Mn}_{12}]$ , tal y como publicó Lis en 1980. Lis incluyó datos preliminares de susceptibilidad magnética en su publicación, pero no proporcionó ninguna interpretación.

Un estudio posterior de Boyd y colaboradores examinó las propiedades magnéticas del derivado benzoato del  $[\text{Mn}_{12}\text{O}_{12}(\text{O}_2\text{CPh})_{16}(\text{H}_2\text{O})_4]$  y dedujo erróneamente un estado básico de espín de  $S = 14$ . En aquel momento, el espín más alto conocido para una molécula era  $S = 12$ , como informó el grupo de Gatteschi. En respuesta al artículo de Boyd y colaboradores, el grupo de Gatteschi reexaminó el compuesto de Lis utilizando diferentes técnicas, como la magnetización de alto campo y la espectroscopia de Resonancia Paramagnética de Electrones (EPR) de alta frecuencia. Los resultados, publicados por Caneschi y colaboradores en 1991, describían la congelación de la magnetización a campos bajos y demostraban la existencia de un estado fundamental  $S = 10$  para el compuesto  $[\text{Mn}_{12}\text{O}_{12}(\text{O}_2\text{CPh})_{16}(\text{H}_2\text{O})_4]$ . El descubrimiento pionero de una anisotropía magnética significativa en el complejo dodecanuclear de manganeso  $[\text{Mn}_{12}]$  por Lis y los estudios posteriores condujeron a la identificación de la histéresis magnética molecular y supusieron un avance significativo en el campo de los SMM, que se manifiesta como una relajación lenta de la magnetización del compuesto cuando se apaga el campo magnético aplicado. En 1996, Thomas y colaboradores demostraron que este fenómeno era de naturaleza molecular y describieron la relajación cuántica, logrando así un avance significativo. Esta observación de un comportamiento superparamagnético en moléculas discretas marcó el comienzo de la era de la SMM, aunque Caneschi y colaboradores aún no utilizaban el término SMM. Por lo tanto, el estudio de los SMMs ha hecho avanzar significativamente nuestra comprensión del comportamiento magnético a nivel molecular. El descubrimiento y la caracterización del  $[\text{Mn}_{12}]$  y sus propiedades

---

únicas han allanado el camino para seguir explorando y utilizando los SMMs en diversos campos, como la electrónica molecular, el almacenamiento de datos y la computación cuántica. La investigación de los SMMs sigue cautivando a los investigadores, ya que ofrece un rico campo de estudio con un inmenso potencial para los avances tecnológicos.

En un principio, la atención se centró en las moléculas polimetálicas basadas en iones 3d, incluidas familias como  $[\text{Mn}_{12}]$ ,  $[\text{V}_4]$ ,  $[\text{Fe}_8]$ ,  $[\text{Co}_4]$  y  $[\text{Ni}_{12}]$ . Posteriormente, la atención se centró en explorar el potencial de los iones metálicos 4d y 5d para mostrar un comportamiento SMM. Entre los iones metálicos 4d y 5d, se han estudiado ampliamente los sistemas basados en Mo(III), Ru(III), Re(IV) y Os(V). La elevada anisotropía magnética y los valores de espín favorables de los complejos de Re(IV) los han hecho especialmente interesantes para investigar la relajación magnética lenta. Por otro lado, los lantánidos que inicialmente se pasaron por alto en Magnetismo Molecular debido a sus débiles interacciones magnéticas y a las dificultades técnicas, se han convertido en un tema de interés en los últimos años. Los complejos basados en lantánidos han mostrado una relajación magnética lenta similar a la de los SMMs, pero tienen propiedades intrínsecas inherentes a los iones metálicos aislados dentro de estructuras moleculares. La utilización de los lantánidos en espintrónica molecular ha realzado aún más su importancia.

Los compuestos de coordinación pueden utilizarse en biomedicina para tratar enfermedades mediante el uso de fármacos basados en metales; para tratar disfunciones metabólicas o eliminar el envenenamiento por metales pesados en el cuerpo humano mediante el uso de agentes quelantes o complejantes; y para transportar metales a lugares específicos del cuerpo como ayuda en la obtención de imágenes, mediante el uso de complejos de coordinación paramagnéticos. La bioquímica

inorgánica, también conocida como química de la biocoordinación, es un campo en rápida evolución centrado en la investigación de la reactividad química de los iones metálicos en entornos biológicos. La interacción entre iones metálicos y biomoléculas ha despertado gran interés en la investigación bioquímica de las últimas décadas. La química de coordinación ofrece valiosas herramientas para desarrollar moléculas y nanomateriales biológicamente activos. Seleccionando cuidadosamente los centros metálicos, modulando los números de coordinación e incorporando ligandos bioactivos o auxiliares, pueden crearse nanomateriales con discretos modos de acción biológica para el diagnóstico de enfermedades, la detección y la terapia. La exploración continua de las interacciones entre iones metálicos y biomoléculas en el marco de la bioquímica inorgánica encierra un inmenso potencial para avanzar en diversos campos y abordar importantes retos biológicos. Las características de la química de coordinación resultan atractivas para sintetizar compuestos fisiológicamente activos y nanomateriales. Eligiendo cuidadosamente los centros metálicos, modificando el número de coordinación, sus grupos lábiles y los ligandos bioactivos o accesorios, se podrían desarrollar y explotar nanomateriales con modos de acción biológica discretos para detectar, diagnosticar y tratar enfermedades. Investigadores de diversas disciplinas se han sentido atraídos por este amplio tema, impulsados por el creciente interés en comprender las interacciones entre los iones metálicos y las biomoléculas, en particular las nucleobases. Estas investigaciones han dado lugar a avances significativos en este campo, allanando el camino para el desarrollo de polímeros de coordinación (PC) mediante el autoensamblaje de nucleobases, nucleósidos y nucleótidos con iones metálicos. La reactividad de las nucleobases frente a los iones metálicos varía en función del ion metálico específico y de la nucleobase implicada. Las nucleobases poseen pares solitarios de nitrógeno y oxígeno

---

accesibles, lo que les permite actuar como ligandos. La exploración de las interacciones entre iones metálicos y nucleobases reviste gran importancia debido al papel crucial que desempeñan los iones metálicos en la estructura y función de los ácidos nucleicos, incluida la transferencia de información genética. Las posiciones donante y aceptora de enlaces de hidrógeno dentro de las nucleobases generan compuestos con propiedades únicas, posibilitadas por su capacidad complementaria de enlace de hidrógeno. Este enlace específico, observado en los pares de bases del ADN, constituye la base química de la genética. El aprovechamiento de este potente sistema de reconocimiento molecular en nanotecnología permite el ensamblaje dirigido de materiales altamente estructurados con características específicas a nanoescala. Del mismo modo, en la computación del ADN, facilita el procesamiento de información compleja. Mediante un diseño racional, se pueden adaptar las propiedades de estos materiales, incluyendo aplicaciones en luminiscencia, magnetismo, conductividad eléctrica y actividad catalítica, capitalizando su naturaleza híbrida metal-orgánica. Sin embargo, el estudio de las propiedades magnéticas en sistemas inorgánicos basados en biomoléculas sigue siendo escaso.

Otra importante área de investigación dentro de las interacciones ion metálico-biomolécula surgió con el descubrimiento de la actividad antitumoral del cisplatino. Aunque el mecanismo exacto de acción *in vivo* sigue siendo objeto de debate, los compuestos de platino(II), incluido el cisplatino, han demostrado su eficacia en el tratamiento de diversas formas de cáncer. No obstante, la resistencia a los fármacos y los importantes efectos secundarios han limitado su utilidad clínica. En consecuencia, los investigadores se han visto motivados a explorar otros complejos de metales de transición como posibles alternativas a los fármacos basados en el platino. Los complejos de rutenio, como los complejos amínicos de Ru(II) y Ru(III), se unen selectivamente a los sitios imínicos de las

biomoléculas, dejando sus pares solitarios de nitrógeno disponibles para la coordinación de los iones metálicos. Esta selectividad permite a los complejos de rutenio dirigirse a tejidos específicos coordinándose con los nitrógenos histidilo imidazol de las proteínas y con el sitio  $N^7$  del anillo imidazol de los nucleótidos de purina. Por tanto, estos complejos pueden utilizar las propiedades de las proteínas, los oligonucleótidos y los ácidos nucleicos para diseñar agentes terapéuticos dirigidos. Los aminoácidos, componentes fundamentales de proteínas y enzimas, también sirven como precursores de biomoléculas esenciales como hormonas y neurotransmisores. Con una inmunogenicidad mínima, baja toxicidad y afinidad por receptores corporales específicos, los aminoácidos son excelentes candidatos para crear nanomateriales en aplicaciones biológicas. Su diversidad estructural, quiralidad y grupos funcionales los convierten en bloques versátiles para la síntesis de nanomateriales. Por otro lado, cabe decir que es crucial la selección de ligandos de tipo carboxilato apropiados de naturaleza biológica para obtener nuevos complejos multifuncionales y polímeros de coordinación que presenten biocompatibilidad. El uso de ligandos carboxilato en el diseño de complejos metálicos ha suscitado una gran atención debido a sus versátiles modos de coordinación y a su capacidad para servir como ligandos puente, permitiendo la formación de diversas arquitecturas metal-ligando. Entre los ligandos carboxilato, el oxalato, el dianión dicarboxilato más simple, ha sido elegido como ligando clave en esta investigación. El oxalato está omnipresente en la naturaleza, se encuentra en diversas plantas y minerales, y puede tener orígenes biológicos. La producción endógena primaria de oxalato se produce a través de la conversión metabólica de glioxalato en oxalato por la enzima lactato deshidrogenasa (LDH) del hígado. Los peroxisomas de las células hepáticas desempeñan un papel crucial en el metabolismo intermedio de la glicina, la hidroxiprolina y el glicolato, que conduce a la generación de

---

glioxalato y oxalato. Esta vía metabólica pone en relieve la relevancia biológica del oxalato y motiva su investigación como ligando en la síntesis de complejos multifuncionales. La elección del oxalato como ligando se justifica por su versatilidad, derivada de su capacidad para adoptar numerosos modos de coordinación al formar complejos metálicos con otros coligandos. Esta flexibilidad permite la construcción de diversos marcos metal-ligando, ofreciendo oportunidades para diseñar materiales novedosos con propiedades a medida. Además, el oxalato es un excelente mediador de las interacciones magnéticas entre iones metálicos cuando se utiliza como ligando puente. La fuerza y la naturaleza de estas interacciones contribuyen a las propiedades magnéticas exhibidas por los complejos y polímeros de coordinación resultantes.

El objetivo de esta Tesis Doctoral es investigar la química de coordinación y la magnetoquímica de varios iones metálicos paramagnéticos utilizando biomoléculas y ligandos biocompatibles. En general, esta Tesis Doctoral presenta una exploración exhaustiva de los complejos de rutenio y lantánidos, sus propiedades únicas y sus aplicaciones potenciales en diversos campos. El estudio de estos complejos metálicos proporciona información valiosa para el diseño y desarrollo de materiales funcionales con propiedades ópticas, espectroscópicas y magnéticas a medida, abriendo vías para futuras investigaciones y avances tecnológicos en diferentes áreas como la electrónica molecular, el almacenamiento de datos, la terapia molecular, la detección molecular, la imagen médica y la refrigeración magnética criogénica.

La investigación realizada en esta tesis consiste en la síntesis de varios complejos metálicos que incorporan ligandos oxalato y otros coligandos complementarios. Los complejos resultantes se caracterizan mediante diversas técnicas analíticas, como cristalografía de rayos X, métodos espectroscópicos y medidas magnéticas.

Los conocimientos estructurales obtenidos a partir de estas caracterizaciones proporcionan información valiosa sobre los modos de coordinación, las interacciones de enlace y la arquitectura general de los complejos.

La investigación realizada en esta Tesis Doctoral se ha centrado en la caracterización estructural, estudio de propiedades magnéticas y posibles aplicaciones de sistemas basados en iones metálicos Ru(III)/(IV) [4d] y Gd(III)/Dy(III) [4f].

El presente trabajo de Tesis Doctoral se recoge en formato de “compendio de artículos”, de acuerdo con la normativa para el depósito, evaluación y defensa de Tesis Doctorales de la Universitat de València (ACCUV 266/2011) y se divide en dos capítulos principales: capítulo 2 y capítulo 3.

El capítulo 2 se centra en la Química de Coordinación y las propiedades de los complejos de rutenio, con especial énfasis en dos estados de oxidación: rutenio(III) y rutenio(IV). El rutenio (Ru), un metal de la serie 4d, presenta una amplia gama de estados de oxidación formales (-2 a +8) y es conocido por su estabilidad en los estados de oxidación +2, +3 y +4 en condiciones fisiológicas. Esta característica, combinada con su coordinación octaédrica dominante y su fuerte estabilización ligando-campo, ha despertado un gran interés en el estudio de la coordinación del rutenio y la química organometálica. Los complejos de rutenio han encontrado aplicaciones en diversos campos, como la biomedicina, la catálisis, la nanociencia, los sistemas redox y los materiales fotoactivos. Los complejos de rutenio(III) presentan una amplia química de coordinación, formando complejos mononucleares neutros, catiónicos y aniónicos estables con propiedades cinéticamente inertes. Estos complejos suelen poseer una estructura octaédrica de bajo espín con características paramagnéticas. Por otra parte, los complejos de rutenio(IV) presentan una química acuosa compleja, principalmente en forma de especies dinucleares, mientras que los aductos mononucleares están relativa-

---

mente menos estudiados. La configuración electrónica del rutenio(IV) suele dar lugar a sistemas mononucleares paramagnéticos de bajo espín o a sistemas dinucleares diamagnéticos fuertemente acoplados antiferromagnéticamente. Aquí se exploran más a fondo las intrigantes propiedades de los complejos de dirutenio oxobridados, que se han estudiado ampliamente debido a su actividad catalítica molecular en reacciones de oxidación del agua y a su potencial como modelos artificiales del centro del Fotosistema II. Estos complejos, como el Ru360, también han demostrado efectos inhibidores sobre el uniportador de calcio mitocondrial (MCU), lo que los hace útiles para la investigación biológica. Aunque los complejos de rutenio han mostrado un potencial prometedor en aplicaciones biomédicas, sobre todo como metalodrogas, su comportamiento magnético y su magnetismo molecular han recibido relativamente menos atención en comparación con sus homólogos de la serie 3d. Las propiedades únicas de los iones de la serie 4d, incluido su alto grado de anisotropía magnética, los convierten en candidatos interesantes para investigar la relajación de la red de espín y explorar su potencial en Magnetismo Molecular.

El capítulo también profundiza en las diversas aplicaciones de los complejos de rutenio en la investigación antitumoral, destacando las propiedades favorables de los complejos de rutenio(III), como su capacidad para imitar al hierro, presentar estados de oxidación accesibles desde el punto de vista redox, su baja toxicidad y su interacción con el ADN y las proteínas. En particular, los complejos de rutenio(III) con ligandos de imidazol y benzopirazol, como NAMI-A y KP1019, se han sometido a ensayos clínicos y han mostrado notables propiedades antimetastásicas. Además, la formación de enlaces metal-metal, incluidos los enlaces múltiples, es un rasgo característico de los metales de transición 4d como el rutenio, que los distingue de sus homólogos de la serie 3d. Se han estudiado



ampliamente complejos dinucleares de rutenio con estructuras “paddle-wheel”, bioctaédricas con caras compartidas y planares biscuadradas. Estos complejos presentan diversos estados de oxidación y sus propiedades electroquímicas pueden adaptarse seleccionando los ligandos puente adecuados. Estos complejos de dirutenio han encontrado aplicaciones en electrónica molecular, materiales magnéticos, bioquímica y química medicinal.

En resumen, el capítulo 2 ofrece una visión global de la química de coordinación, las propiedades magnéticas y las aplicaciones biomédicas de los complejos de rutenio. Destaca el potencial de los compuestos basados en el rutenio en diversos campos y subraya la necesidad de seguir explorando y desarrollando estas fascinantes moléculas.

El capítulo 3 se centra en la química de coordinación y las propiedades de los complejos de lantánidos, con especial énfasis en el gadolinio (III) y el disprosio (III). A principios del siglo XXI, los lantánidos, inicialmente poco explorados en Magnetismo Molecular, cobraron importancia. Los informes sobre complejos que contienen lantánidos y presentan una relajación magnética lenta similar a la de los SMM dieron lugar a la aparición de los “Single-Ion Magnets” (SIMs). Los lantánidos, con su alto espín y su anisotropía magnética intrínseca, se convirtieron en componentes esenciales en el desarrollo de los SIMs. Los compuestos de coordinación se utilizan en aplicaciones en diversos campos, como la biomedicina, la nanomedicina y la nanotecnología. Los fármacos basados en metales, como el *cis*-diclorodiaminoplatino (CISPLATINO), han demostrado su eficacia en el tratamiento del cáncer. Los agentes quelantes se han empleado para tratar disfunciones metabólicas y eliminar del organismo venenos de metales pesados. Los complejos de coordinación también se han utilizado para transportar metales con fines de imagen, mejorando técnicas de diagnóstico como la Resonancia Magnética

---

(RM). Una de las principales aplicaciones de los imanes permanentes en la medicina moderna es la IRM. La utilización de compuestos de coordinación en la IRM, especialmente los complejos de gadolinio(III), ha revolucionado el diagnóstico médico por imagen. Los tiempos de relajación, así como el tiempo de relajación longitudinal  $T_1$  y el tiempo de relajación transversal  $T_2$ , desempeñan un papel crucial en la IRM.

El desarrollo de agentes de contraste ha mejorado el contraste y la resolución de las imágenes clínicas, abriendo nuevas vías de investigación. La RMN está directamente relacionada con el fenómeno de la IRM, en la que la técnica de imagen se centra en un núcleo atómico específico para generar imágenes de distribución espacial, a menudo centradas en los protones del agua. A diferencia de otras técnicas espectroscópicas, la escasa diferencia de energía entre los estados excitado y básico requiere una relajación estimulada. El tiempo de relajación longitudinal,  $T_1$ , representa el retorno al equilibrio de magnetización a lo largo del eje z y está influido por la interacción entálpica del núcleo excitado con los agentes magnéticos activos del entorno. En consecuencia,  $T_1$  depende de la movilidad y viscosidad del entorno. El tiempo de relajación transversal,  $T_2$ , caracteriza el decaimiento de la señal en el plano xy. En IRM, se suele utilizar el parámetro  $T_2^*$ , que engloba  $T_2$  y las contribuciones de la falta de homogeneidad del campo magnético dentro de la muestra.  $T_2^*$  proporciona información valiosa sobre las propiedades de los tejidos y tiene una amplia aplicación en la IRM médica. La RM, en su forma básica, no requiere el uso de agentes de contraste, ya que éstos no contribuyen directamente al contraste visible. En su lugar, los agentes de contraste de la RM interactúan con los protones del agua ( $H_2O$ ) y modifican sus tiempos de relajación o participan en la magnetización de estos protones. No obstante, para mejorar la calidad de la imagen, cada vez se utilizan más agentes de

contraste de RM. La clase más extendida se basa en el mecanismo de relajación longitudinal, en el que el movimiento de los protones  $^1H$  cercanos crea un campo magnético oscilante que favorece la vuelta al equilibrio de los protones  $H_2O$ . La introducción de moléculas que contienen electrones no apareados en el entorno del  $H_2O$  acelera eficazmente el proceso de relajación debido al momento magnético más fuerte de los electrones en comparación con los protones. Los complejos que contienen iones de gadolinio(III), que poseen siete electrones no apareados, se emplean habitualmente como agentes de contraste de RMN. Estos complejos reducen la constante de tiempo de relajación  $T_1$ , lo que aumenta el brillo de las imágenes de RM. Durante la adquisición de datos, los agentes de contraste de gadolinio reducen el tiempo de retorno de la magnetización al equilibrio.

Por otra parte, en las últimas décadas, los complejos de gadolinio(III) también han despertado un gran interés debido a sus posibles aplicaciones tecnológicas en entornos de baja y ultrabaja temperatura, así como en la refrigeración magnetocalórica (RMC). La RMC es una tecnología criogénica estándar capaz de alcanzar temperaturas extremadamente bajas, incluso en el rango sub-Kelvin. Las aplicaciones de la RMC abarcan los imanes superconductores y los licuadores de helio, entre otros, proporcionando una alternativa a las costosas tecnologías de refrigeración basadas en diluciones de  $^3He/^4He$ . Las raíces de la RMC se remontan a finales de la década de 1920, con los trabajos de Debye y Giauque sobre la desmagnetización adiabática del octahidrato de sulfato de gadolinio(III), que permitieron alcanzar temperaturas ultrabajas. El fenómeno responsable de las variaciones de temperatura que se producen en un material magnético al conectar/desconectar un campo magnético externo en condiciones adiabáticas se conoce como efecto magnetocalórico (EMC). En consecuencia, el equilibrio entre los cambios en la entropía de la red y la entropía magnética isotérmica durante el ciclo de magne-

---

tización/desmagnetización determina los cambios de temperatura. Atendiendo a esto, el capítulo 3 se centra en el estudio de los complejos de lantánidos, en particular los lantánidos en química de coordinación y supramolecular, así como sus propiedades ópticas, espectroscópicas y magnéticas únicas. La investigación explora las aplicaciones potenciales de los complejos de lantánido(III) con ligandos quelantes en diversos campos, como los dispositivos orgánicos emisores de luz, los materiales cristalinos líquidos, los sensores y los agentes de contraste en resonancia magnética. Las propiedades de luminiscencia de estos complejos, resultantes del llenado de los orbitales 4f, pueden ajustarse desde la región visible a la infrarroja seleccionando el ion lantánido(III) apropiado. En esta tesis también se analizan las propiedades magnéticas de los lantánidos debido a su naturaleza altamente electropositiva y reactiva, que conduce a un comportamiento magnético peculiar y notable. Asimismo, en el capítulo 3 se profundiza en los SMMs basados en iones de lantánido(III), que han suscitado gran interés debido a sus posibles aplicaciones en el almacenamiento de datos cuánticos y de alta densidad, el procesamiento cuántico de la información, la refrigeración molecular y la espintrónica. En concreto, nos centramos en los SMMs que contienen iones disprosio(III) y gadolinio(III). Los complejos de disprosio(III), especialmente los dinucleares, se han estudiado ampliamente por sus propiedades magnéticas, mientras que los complejos mononucleares de disprosio(III) han recibido menos atención a pesar de mostrar un comportamiento SMM prometedor. Por otra parte, los complejos de gadolinio(III), aunque altamente paramagnéticos, pueden mostrar una lenta relajación magnética en determinadas condiciones, lo que los hace interesantes para aplicaciones específicas. La tesis aborda el diseño y la síntesis de complejos mononucleares de gadolinio(III) y disprosio(III) con diversos ligandos y explora sus propiedades magnéticas y su comportamiento de relajación.

El capítulo 2 se centró en la investigación de las propiedades magnéticas de complejos mono- y dinucleares de rutenio(III) basados en nucleobases. Estos complejos demostraron propiedades biológicas y bioquímicas, lo que los hace atractivos para aplicaciones en catálisis redox y otras áreas de investigación. Sin embargo, se necesitan más estudios teóricos y experimentales para comprender plenamente la dinámica de relajación de estos intriganes imanes de un solo ion basados en rutenio(III).

Se demuestra el potencial de los complejos de rutenio(III) basados en purinas como dispositivos sensores. La sensibilidad, reproducibilidad y estabilidad de los sistemas de dirutenio los convierten en candidatos prometedores para detectar biomoléculas como la hipoxantina. Además, un complejo dinuclear de rutenio(III) basado en adenina muestra potencial como agente quimioterapéutico contra líneas celulares cancerosas, lo que justifica nuevas investigaciones. Por otro lado, se exploraron las propiedades multifuncionales de los complejos sintetizados, haciendo especial hincapié en su biocompatibilidad.

La biocompatibilidad es un aspecto crucial en el desarrollo de materiales para aplicaciones biomédicas. Se ha investigado la capacidad de los complejos basados en oxalato para interactuar con los sistemas biológicos y su potencial de uso en aplicaciones terapéuticas y de diagnóstico. Los estudios de biocompatibilidad incluyen evaluaciones *in vitro* e *in vivo* de la citotoxicidad, la absorción celular y la eficacia terapéutica de los complejos. Inspirados por el éxito inicial del complejo dinuclear de rutenio(III) basado en adenina frente a líneas celulares cancerosas, la investigación avanzó hacia el desarrollo de una familia de compuestos con propiedades similares. Uno de estos compuestos, Runat-BI, resulta ser más eficaz contra varios tipos de cáncer y posee un perfil de toxicidad mejor que el complejo de rutenio(III) basado en la adenina. Runat-BI presenta un mecan-

---

ismo de acción multiobjetivo que lo convierte en una prometedora alternativa a los actuales fármacos quimioterapéuticos. Asimismo, el análisis de la estructura cristalina de los complejos de dirutenio(IV) revela su potencial como bloques de construcción para ensamblar nuevas estructuras supramoleculares. Utilizando enlaces orgánicos adecuados, estos compuestos podrían encontrar aplicaciones en dispositivos eléctricos basados en sus propiedades redox. Se están llevando a cabo nuevas investigaciones en este campo.

En el capítulo 3, se exploran complejos basados en lantánidos de diferente dimensionalidad, descubriendo sus interesantes propiedades magnéticas, incluidos los comportamientos SIM y SMM en MOFs unidimensionales y bidimensionales, respectivamente. Estos complejos presentan temperaturas de bloqueo moderadamente altas y efectos magnetocalóricos significativos, lo que los convierte en candidatos potenciales para materiales refrigerantes magnéticos moleculares de baja temperatura y relajación lenta. La investigación también se centra en la preparación de películas delgadas de estos MOF para estudiar sus efectos SIM y magnetocalóricos en dispositivos prácticos. El trabajo pone en relieve las limitaciones de los agentes de contraste actuales y subraya la necesidad de agentes de contraste basados en gadolinio (GBCA) con mayor estabilidad y resistencia a largo plazo a la transmetalación/transquelación. Se anima a los químicos de coordinación a emplear enfoques innovadores para construir GBCA más estables y mejorar el diseño de los agentes de contraste. Este trabajo presenta el potencial de los compuestos de gadolinio(III) basados en la nucleobase timina como candidatos prometedores para futuras investigaciones en RMN.

La combinación de las propiedades inherentes del gadolinio como agente de contraste y la incorporación de biomoléculas como ligandos abre vías para el desarrollo de agentes de contraste versátiles, así como la incorporación de difer-

entes biomoléculas, como antibióticos y vitaminas en nuevos compuestos puede dar lugar a agentes de contraste con múltiples propiedades.

Los resultados de esta tesis doctoral contribuyen al creciente campo de la química bioinorgánica y la ciencia de materiales, ofreciendo nuevos conocimientos sobre el diseño y la síntesis de complejos multifuncionales y polímeros de coordinación con ligandos biocompatibles. En otras palabras, se ha profundizado en la química de coordinación y la magnetoquímica de iones metálicos paramagnéticos. La investigación explora las aplicaciones potenciales de los compuestos moleculares magnéticos en diversos campos y destaca la importancia de los enfoques innovadores en el desarrollo de agentes de contraste y técnicas de imagen molecular. Los hallazgos contribuyen al avance de las herramientas terapéuticas y de diagnóstico en campos como la terapia molecular, la bioimagen molecular, la refrigeración molecular y la detección molecular.





---

# *Abstract*

The work developed in this Thesis falls within the field of Coordination Chemistry and Molecular Magnetism, which are the basis vectors for the development of multiple applications in Nanomedicine and Nanotechnology. The study of coordination compounds has a long history dating back to the early 19th century, with notable contributions from chemists such as Berzelius and Jørgensen. This branch of chemistry focuses on understanding the binding properties of ligands (electron-donating molecules or anions) to metal ions. Alfred Werner's theories on metal ion coordination in the early 20th century marked a significant milestone in the field.

Molecular Magnetism, a multidisciplinary area of research, originated approximately three decades ago with a primary focus on synthesising and studying metal coordination compounds. This field has experienced significant growth due to the collaborative efforts of scientists from various disciplines, such as Chemistry, Physics, and Biology. The complementary nature of experimental techniques and the knowledge generated by different branches of science have contributed to the rapid progress of Molecular Magnetism. Inorganic Chemistry, particularly Coordination Chemistry, has played a vital role in designing and synthesising complexes with predictable structures and magnetic properties. The study of Molecular Magnetism initially concentrated on mononuclear complexes, which

---

provided valuable insights into the structure and bonding of coordination compounds. The field started to flourish in the late 1970s when researchers sought to create molecule-based magnets mimicking the properties of inorganic magnets. These investigations were primarily centred around 3d metal ions, while the 4d and 5d metal ions remained relatively unexplored due to their challenging chemistry and complex magnetic behaviour. However, the unique properties of the heavier metal ions, such as higher magnetic anisotropy and longer diffusivity, have garnered attention, leading to the exploration of 4d and 5d-based Molecular Magnetism.

Single-Molecule Magnetism (SMM), is a fascinating phenomenon that was discovered in the early 1990s, revolutionised the field by demonstrating that specific polynuclear complexes possess the ability to exhibit magnetisation without long-range cooperative interactions. The origins of SMM can be traced back to the work conducted in the Christou group during the 1980s, which focused on synthesising model compounds of the oxygen-evolving complex in Photosystem II. Although this research produced several polynuclear mixed-valence manganese complexes, a model for the highest oxidation state of the biological cycle was still lacking. During the quest to develop such a model, an intriguing compound with the formula  $[\text{Mn}_{12}\text{O}_{12}(\text{O}_2\text{CPh})_{16}(\text{H}_2\text{O})_4]$  was isolated through the oxidation of manganese acetate with permanganate. The proposal of a dodecanuclear manganese complex from this type of reaction was first made in 1921 by Weinland and Fischer. However, it was not until the advent of monocrystal X-ray experiments that the structure of the compound could be confirmed as  $[\text{Mn}_{12}\text{O}_{12}(\text{O}_2\text{CCH}_3)_{16}(\text{H}_2\text{O})_4] \cdot 4 \text{H}_2\text{O} \cdot 2 \text{CH}_3\text{COOH}$  or  $[\text{Mn}_{12}]$ , as published by Lis in 1980. Lis included preliminary magnetic susceptibility data in his publication, but no interpretation was provided. A subsequent study by Boyd *et al.* examined

the magnetic properties of the benzoate derivative of  $[\text{Mn}_{12}\text{O}_{12}(\text{O}_2\text{CPh})_{16}(\text{H}_2\text{O})_4]$  and erroneously deduced a spin ground state of  $S = 14$ . At that time, the highest spin known for a molecule was  $S = 12$ , as reported by Gatteschi's group. In response to Boyd *et al.*'s paper, the Gatteschi group reexamined the Lis compound using different techniques, including high-field magnetisation and high-frequency Electron Paramagnetic Resonance (EPR) spectroscopy. The results, published by Caneschi *et al.* in 1991, described the freezing of magnetisation at low fields and provided evidence of a  $S = 10$  ground state for  $[\text{Mn}_{12}\text{O}_{12}(\text{O}_2\text{CPh})_{16}(\text{H}_2\text{O})_4]$ . The pioneering discovery of significant magnetic anisotropy on the dodecanuclear manganese complex  $[\text{Mn}_{12}]$  by Lis, and subsequent studies led to the identification of molecular magnetic hysteresis and marked a significant advancement in the field of SMMs, which manifests as a slow relaxation of the compound's magnetisation when the applied magnetic field is turned off. This phenomenon was demonstrated to be of a molecular nature in 1996 by Thomas *et al.*, who reported quantum relaxation, thereby achieving a significant breakthrough. This observation of superparamagnetic-like behaviour in discrete molecules marked the advent of the SMM era, even though the term SMM was not yet in use by Caneschi *et al.* Therefore, the study of SMM has significantly advanced our understanding of magnetic behaviour at the molecular level. The discovery and characterisation of  $[\text{Mn}_{12}]$  and its unique properties have paved the way for further exploration and utilisation of SMM in various fields, including molecular electronics, data storage, and quantum computing. The investigation of Single-Molecule Magnets continues to captivate researchers, offering a rich area of study with immense potential for technological advancements.

The initial focus was on 3d-based polymetallic molecules, including families such as  $[\text{Mn}_{12}]$ ,  $[\text{V}_4]$ ,  $[\text{Fe}_8]$ ,  $[\text{Co}_4]$ , and  $[\text{Ni}_{12}]$ . Subsequently, attention shifted

---

towards exploring the potential of 4d and 5d metal ions in exhibiting SMM behaviour. Among the 4d and 5d metal ions, systems based on Mo(III), Ru(III), Re(IV), and Os(V) have been extensively studied. The high magnetic anisotropy and favourable spin values of Re(IV) complexes have made them particularly intriguing for investigating slow magnetic relaxation. Lanthanides, initially overlooked in Molecular Magnetism due to weak magnetic interactions and technical challenges, have emerged as a focal point in recent years. Lanthanide-based complexes have exhibited slow magnetic relaxation similar to Single-Molecule Magnets but have intrinsic properties inherent to isolated metal ions within molecular structures. The utilisation of lanthanides in molecular spintronics has further enhanced their significance.

Coordination compounds can be used in biomedicine to treat diseases through the use of metal-based drugs; to treat metabolic dysfunction or to remove heavy metal poisoning in the human body through the use of chelating or complexing agents; and to transport metals to specific sites in the body to aid in imaging, through the use of paramagnetic coordination complexes. Inorganic biochemistry, also known as biocoordination chemistry, is a rapidly evolving field focused on investigating the chemical reactivity of metal ions within biological environments. The interaction between metal ions and biomolecules has attracted much interest in biochemical research over the past decades.

Coordination Chemistry offers valuable tools for developing biologically active molecules and nanomaterials. By carefully selecting metal centres, modulating coordination numbers, and incorporating bioactive or ancillary ligands, nanomaterials with discrete biological modes of action can be created for disease diagnostics, sensing, and therapy. The continuous exploration of metal ion-biomolecule interactions within the framework of inorganic biochemistry holds immense po-

tential for advancing various fields and addressing important biological challenges. Coordination Chemistry's characteristics are enticing for synthesising physiologically active compounds and nanomaterials. By carefully choosing metal centres, modifying the coordination number, their labile groups and bioactive or accessory ligands, nanomaterials with discrete biological modes of action could be developed and exploited for detecting, diagnosing and treating diseases. Researchers from diverse disciplines have been attracted to this broad subject, driven by a growing interest in understanding the interactions between metal ions and biomolecules, particularly nucleobases. These investigations have led to significant advancements in the field, paving the way for developing coordination polymers (CPs) through the self-assembly of nucleobases, nucleosides, and nucleotides with metal ions. The reactivity of nucleobases towards metal ions varies depending on the specific metal ion and the nucleobase involved. Nucleobases possess accessible nitrogen and oxygen lone pairs, allowing them to act as ligands. Exploring the interactions between metal ions and nucleobases holds great significance due to the crucial role metal ions play in the structure and function of nucleic acids, including the transfer of genetic information. The hydrogen bond donor and acceptor positions within nucleobases generate compounds with unique properties, enabled by their complementary hydrogen bonding capability. This specific bonding, observed in DNA base pairs, forms the chemical foundation for genetics. Leveraging this powerful molecular recognition system in nanotechnology enables the directed assembly of highly structured materials with specific nanoscale features.

Similarly, in DNA computation, it facilitates the processing of complex information. Through rational design, the properties of these materials can be tailored, including applications in luminescence, Magnetism, electrical conductivity,

---

and catalytic activity, capitalising on their hybrid metal-organic nature. However, studying magnetic properties in inorganic systems based on biomolecules remains scarce. Another significant area of research within the metal ion-biomolecule interactions emerged with the discovery of the antitumor activity of cisplatin. Although the exact *in vivo* mechanism of action remains a topic of debate, platinum(II) compounds, including cisplatin, have shown effectiveness in treating various forms of cancer. Nonetheless, drug resistance and significant side effects have limited their clinical utility. Consequently, researchers have been motivated to explore other transition metal complexes as potential alternatives to platinum-based drugs. Ruthenium complexes, such as amine complexes of Ru(II) and Ru(III), exhibit selective binding to imine sites in biomolecules, leaving their nitrogen lone pairs available for metal ion coordination. This selectivity allows ruthenium complexes to target specific tissues by coordinating with histidyl imidazole nitrogens on proteins and the  $N^7$  site on the imidazole ring of purine nucleotides. Therefore, these complexes can use the properties of proteins, oligonucleotides, and nucleic acids to design targeted therapeutic agents. Amino acids, the fundamental building blocks of proteins and enzymes, also serve as precursors for essential biomolecules such as hormones and neurotransmitters. With minimal immunogenicity, low toxicity, and affinity for specific body receptors, amino acids are excellent candidates for creating nanomaterials in biological applications. Their structural diversity, chirality, and functional groups make them versatile building blocks for nanomaterial synthesis.

On the other hand, it is worth saying that the selection of appropriate carboxylate-type ligands of biological nature to obtain new multifunctional complexes and coordination polymers that exhibit biocompatibility is crucial. The use of carboxylate ligands in the design of metal complexes has gained significant at-

tention due to their versatile coordination modes and ability to serve as bridging ligands, enabling the formation of diverse metal-ligand architectures. Among the carboxylate ligands, oxalate, the simplest dicarboxylate dianion, has been chosen as a key ligand in this research. Oxalate is ubiquitously present in nature, found in various plants and minerals, and it may have biological origins. The primary endogenous production of oxalate occurs through the metabolic conversion of glyoxalate to oxalate by the liver's lactate dehydrogenase (LDH) enzyme. The peroxisomes of hepatic cells play a crucial role in the intermediate metabolism of glycine, hydroxyproline, and glycolate, leading to the generation of glyoxalate and oxalate. This metabolic pathway highlights the biological relevance of oxalate and motivates its investigation as a ligand in the synthesis of multifunctional complexes. The choice of oxalate as a ligand is justified by its versatility, which stems from its ability to adopt numerous coordination modes when forming metal complexes with other coligands. This flexibility enables the construction of diverse metal-ligand frameworks, offering opportunities to design novel materials with tailored properties. Moreover, oxalate serves as an excellent mediator of magnetic interactions between metal ions when used as a bridging ligand. The strength and nature of these interactions contribute to the magnetic properties exhibited by the resulting complexes and coordination polymers.

The aim of this doctoral Thesis is to investigate the coordination chemistry and magnetochemistry of various paramagnetic metal ions using biomolecules and biocompatible ligands. Overall, this PhD thesis presents a comprehensive exploration of ruthenium and lanthanide complexes, their unique properties, and potential applications in various fields. The study of these metal-based complexes provides valuable insights into the design and development of functional materials with tailored optical, spectroscopic, and magnetic properties, open-

---

ing avenues for future research and technological advancements in different areas such as molecular electronics, data storage, molecular therapy, Molecular Sensing, medical imaging, and cryogenic magnetic cooling. The research performed in this thesis involves the synthesis of various metal complexes incorporating oxalate ligands and other complementary coligands. The resulting complexes are characterised using various analytical techniques, including X-ray crystallography, spectroscopic methods, and magnetic measurements. The structural insights obtained from these characterisations provide valuable information about the complexes coordination modes, bonding interactions, and overall architecture.

The research carried out in this Doctoral Thesis has focused on the structural characterisation, study of magnetic properties and possible applications of systems based on Ru(III)/(IV) [4d] and Gd(III)/Dy(III) [4f] metal ions.

The present Doctoral Thesis work is collected in the format of a “compendium of articles”, in accordance with the regulations for the deposit, evaluation and defence of Doctoral Thesis of the Universitat de València (ACCUV 266/2011) and is divided into two main chapters: chapter 2 and chapter 3.

Chapter 2 focuses on the Coordination Chemistry and properties of ruthenium complexes with specific emphasis on two oxidation states: ruthenium(III) and ruthenium(IV). Ruthenium (Ru), a 4d-series metal, exhibits a wide range of formal oxidation states (-2 to +8) and is known for its stability in oxidation states +2, +3, and +4 under physiological conditions. This characteristic, combined with its dominant octahedral coordination and strong ligand-field stabilisation, has attracted significant research interest in the study of ruthenium coordination and organometallic chemistry. Ruthenium complexes have found applications in diverse fields, such as biomedicine, catalysis, nanoscience, redox systems, and photoactive materials. Ruthenium(III) complexes exhibit extensive



coordination chemistry, forming stable neutral, cationic, and anionic mononuclear complexes with kinetically inert properties. These complexes commonly possess a low-spin six-coordinate structure with paramagnetic characteristics. On the other hand, ruthenium(IV) complexes display complex aqueous chemistry, primarily in the form of dinuclear species, while mononuclear adducts are relatively less studied. The electronic configuration of ruthenium(IV) often gives rise to paramagnetic low-spin mononuclear or strong antiferromagnetically coupled diamagnetic dinuclear systems. Here, it is further explored the intriguing properties of oxo-bridged diruthenium complexes, have been studied extensively due to their molecular catalytic activity in water oxidation reactions and their potential as artificial models of the Photosystem II centre. These complexes, such as Ru360, have also demonstrated inhibitory effects on the mitochondrial calcium uniporter (MCU), making them useful for biological research. While ruthenium complexes have shown promising potential in biomedical applications, particularly as metallodrugs, their magnetic behaviour and Molecular Magnetism have received relatively less attention compared to their 3d-series counterparts. The unique properties of 4d-series ions, including their high degree of magnetic anisotropy, make them interesting candidates for investigating spin-lattice relaxation and exploring their potential in Molecular Magnetism. The chapter also delves into the various applications of ruthenium complexes in antitumor research, highlighting the favourable properties of ruthenium(III) complexes, such as their ability to mimic iron, exhibit redox-accessible oxidation states, low toxicity, and interaction with DNA and proteins. Notably, ruthenium(III) complexes with imidazole and benzopyrazole ligands, such as NAMI-A and KP1019, have entered clinical trials and displayed remarkable antimetastatic properties. Moreover, the formation of metal-metal bonds, including multiple bonds, is a

---

characteristic feature of 4d transition metals like ruthenium, distinguishing them from their 3d-series counterparts. Dinuclear ruthenium complexes with paddle-wheel structures, face-sharing bioctahedral, and bisquare planar structures have been extensively studied. These complexes exhibit diverse oxidation states, and their electrochemical properties can be tailored by selecting appropriate bridging ligands. Such diruthenium complexes have found applications in molecular electronics, magnetic materials, biochemistry, and medicinal chemistry.

In sum, chapter 2 provides a comprehensive overview of the coordination chemistry, magnetic properties, and biomedical applications of ruthenium complexes. It highlights the potential of ruthenium-based compounds in various fields and underscores the need for further exploration and development of these fascinating molecules.

Chapter 3 focuses on the coordination chemistry and properties of lanthanide complexes with specific emphasis on Gadolinium(III) and Dysprosium(III). In the early 21st century, lanthanides, initially underexplored in Molecular Magnetism, gained significance. Reports on lanthanide-containing complexes exhibiting slow magnetic relaxation similar to SMMs led to the emergence of Single-Ion Magnetism (SIM). Lanthanides, with their high spin and intrinsic magnetic anisotropy, became essential components in the development of SIMs. Coordination compounds have found applications in various fields, including biomedicine, nanomedicine, and nanotechnology. Metal-based drugs, such as *cis*-dichlorodiammineplatinum (CISPLATIN), have shown efficacy in cancer treatment. Chelating agents have been employed to treat metabolic dysfunction and remove heavy metal poisons from the body. Coordination complexes have also been used to transport metals for imaging purposes, enhancing diagnostic techniques like Magnetic Resonance Imaging (MRI). One of the prominent applications of permanent

magnets in modern medicine is MRI. The utilisation of coordination compounds in magnetic resonance imaging, especially gadolinium(III) complexes, has revolutionised medical imaging. Relaxation times, such as longitudinal relaxation time  $T_1$  and transversal relaxation time  $T_2$ , play crucial roles in MRI. The development of contrast agents has improved the contrast and resolution of clinical images, opening new avenues for research. NMR is directly related to the MRI phenomenon, wherein the imaging technique focuses on a specific atomic nucleus to generate spatial distribution images, often centered on water protons. Unlike other spectroscopic techniques, the low energy difference between the excited and ground states necessitates stimulated relaxation. The longitudinal relaxation time,  $T_1$ , represents the return to magnetisation equilibrium along the z-axis and is influenced by the enthalpic interaction of the excited nucleus with magnetic active agents in the environment. Consequently,  $T_1$  depends on the environment's mobility and viscosity. The transversal relaxation time,  $T_2$ , characterises the signal decay in the xy-plane. In MRI, the parameter  $T_2^*$  is commonly used, encompassing  $T_2$  and contributions from magnetic field inhomogeneity within the sample.  $T_2^*$  provides valuable information about tissue properties and finds extensive application in medical MRI. MRI, in its basic form, does not require the use of contrast agents, as they do not directly contribute to the visible contrast. Instead, MRI contrast agents interact with water protons ( $\text{H}_2\text{O}$ ) and modify their relaxation times or participate in the magnetisation of these protons. Nevertheless, to improve image quality, there is a growing utilisation of MRI contrast agents. The most prevalent class relies on the mechanism of longitudinal relaxation, where the motion of the nearby  $^1\text{H}$  protons creates an oscillating magnetic field that promotes the return to equilibrium of the  $\text{H}_2\text{O}$  protons. The introduction of molecules containing unpaired electrons into the  $\text{H}_2\text{O}$  environment effec-

---

tively accelerates the relaxation process due to the stronger magnetic moment of electrons compared to protons. Gadolinium(III) ion-containing complexes, possessing seven unpaired electrons, are commonly employed as MRI contrast agents. These complexes decrease the relaxation time constant  $T_1$ , resulting in enhanced brightness in molecular resonance images. During data acquisition, gadolinium contrast agents reduce the magnetisation's return to equilibrium time. In recent decades, on the other hand, gadolinium(III) complexes have also garnered significant interest due to their potential technological applications in low and ultra-low temperature settings, as well as magnetocaloric refrigeration (CMR). CMR serves as a standard cryogenics technology capable of achieving extremely low temperatures, even in the sub-Kelvin range. The applications of CMR encompass superconducting magnets and helium liquefiers, among others, providing an alternative to expensive cooling technologies reliant on  $^3\text{He}/^4\text{He}$  dilutions. The roots of CMR trace back to the late 1920s, initiated by Debye and Giauque's work involving the adiabatic demagnetisation of gadolinium(III) sulfate octahydrate, which enabled the attainment of ultra-low temperatures. The phenomenon is responsible for temperature variations occurring in a magnetic material upon connection/disconnection of an external magnetic field under adiabatic conditions is known as the magnetocaloric effect (MCE). Consequently, the balance between changes in lattice entropy and isothermal magnetic entropy during the magnetisation/demagnetisation cycle determines the temperature changes. Attending to that, chapter 3 focuses on the study of lanthanide complexes, particularly the lanthanides in coordination and supramolecular chemistry, as well as their unique optical, spectroscopic, and magnetic properties. The research explores the potential applications of lanthanide(III) complexes with chelating ligands in various fields such as organic light-emitting devices, liquid crystalline materials, sensors, and

contrast agents in MRI. The luminescence properties of these complexes, resulting from the filling of the 4f orbitals, can be adjusted from the visible to the infrared region by selecting the appropriate lanthanide(III) ion. The dissertation also discusses the magnetic properties of lanthanides due to their highly electropositive and reactive nature, leading to peculiar and remarkable magnetic behaviour. Also in chapter 3, there is a further investigation in Single Molecule Magnets (SMMs) based on lanthanide(III) ions, which have gained significant attention due to their potential applications in quantum and high-density data storage, quantum information processing, molecular refrigeration, and spintronics. Specifically, the focus is on SMMs containing dysprosium(III) and gadolinium(III) ions. Dysprosium(III) complexes, especially dinuclear ones, have been extensively studied for their magnetism properties, while mononuclear dysprosium(III) complexes have received less attention despite showing promising SMM behaviour. On the other hand, gadolinium(III) complexes, although highly paramagnetic, can exhibit slow magnetic relaxation under certain conditions, making them interesting for specific applications. The dissertation discusses the design and synthesis of mononuclear gadolinium(III) and dysprosium(III) complexes with various ligands and explores their magnetic properties and relaxation behaviour. Chapter 2 focused on the investigation of the magnetic properties of mono- and dinuclear complexes of ruthenium(III) based on nucleobases. These complexes demonstrated biological and biochemical properties, making them appealing for applications in redox catalysis and other research areas. However, further theoretical and experimental studies are needed to fully comprehend the relaxation dynamics of these intriguing ruthenium(III)-based Single-Ion Magnets. Additionally, the Thesis demonstrated the potential of purine-based ruthenium(III) complexes as sensor devices. The sensitivity, reproducibility, and stability of diruthenium systems

---

make them promising candidates for detecting biomolecules like hypoxanthine. Moreover, a dinuclear ruthenium(III) complex based on adenine shows potential as a chemotherapeutic agent against cancer cell lines, warranting further investigations. Furthermore, the multifunctional properties of the synthesised complexes were explored, with a particular emphasis on their biocompatibility. Biocompatibility is a crucial aspect in the development of materials for biomedical applications. The ability of the oxalate-based complexes to interact with biological systems and their potential for use in therapeutic and diagnostic applications are investigated. The biocompatibility studies involve *in vitro* and *in vivo* assessments, evaluating the complexes' cytotoxicity, cellular uptake, and therapeutic efficacy. Inspired by the initial success of the dinuclear ruthenium(III) complex based on adenine against cancer cell lines, the research progressed towards the development of a family of compounds with similar properties. One such compound, Runat-BI, proves to be more effective against various cancers and possesses a better toxicity profile than the adenine-based ruthenium(III) complex. Runat-BI exhibits a multitargeted mechanism of action, making it a promising alternative to current chemotherapy drugs. Also, the crystal structure analysis of diruthenium(IV) complexes reveals their potential as building blocks for assembling new supramolecular structures. By utilising appropriate organic linkers, these compounds could find applications in electrical devices based on their redox properties. Further investigations in this area are ongoing. In Chapter 3, lanthanide-based complexes of different dimensionality, uncovering their interesting magnetic properties, including SIM and SMM behaviours in one- and two-dimensional metal-organic frameworks (MOFs), respectively, were explored. These complexes exhibit moderately high blocking temperatures and significant magnetocaloric effects, making them potential candidates for low-temperature,

slow-relaxing molecular magnetic refrigerant materials. The research also focuses on the preparation of thin films of these MOFs for studying their SIM and magnetocaloric effects in practical devices. The Thesis highlights the limitations of current contrast agents and emphasises the need for gadolinium-based contrast agents (GBCAs) with enhanced stability and long-term resistance to transmetalation/transchelation. Coordination chemists are encouraged to employ innovative approaches to build more stable GBCAs and improve contrast agent design. This work presents the potential of gadolinium(III) compounds based on thymine nucleobase as promising candidates for further MRI research. The combination of inherent gadolinium properties as a contrast agent and the incorporation of biomolecules as ligands open avenues for the development of versatile contrast agents. The incorporation of different biomolecules, such as antibiotics and vitamins, in new compounds can lead to multi-property contrast agents.

The findings from this PhD thesis contribute to the growing field of bioinorganic chemistry and materials science, offering new insights into the design and synthesis of multifunctional complexes and coordination polymers with biocompatible ligands. In other words, comprehensive insights into the Coordination Chemistry and Magnetochemistry of paramagnetic metal ions were done. The research explores the potential applications of magnetic molecular compounds in various fields and highlights the significance of innovative approaches in developing contrast agents and molecular imaging techniques. The findings contribute to the advancement of therapeutic and diagnostic tools in fields such as Molecular Therapy, Molecular Bioimaging, Molecular Refrigeration, and Molecular Sensing.





# *CHAPTER 1*

---

*Introduction and background*



## 1.1 Coordination Chemistry in Molecular Magnetism

Since the appearance of water on the Earth, metal-aqua complexes must have existed. The subsequent appearance of life depended on the interaction of metal ions with organic molecules. Coordination Chemistry is, quite simply, the chemistry of coordination compounds. Attempts to understand the metal-binding properties of what are now recognised as electron-donating molecules or anions (ligands) date from the development of analytical procedures for metals by Berzelius and his contemporaries (*Lärboki Kemien*, vol. 1, 1808), establishing that the elements in inorganic substances are bound together in definite proportions by weight. The synthesis of the great variety of metal complexes that could be isolated and crystallised was being rapidly developed by chemists such as S. M. Jørgensen in Copenhagen. Subsequently, by the late XIX century, there were numerous examples of the complexing metal ions. Studies on the ‘residual affinity’ of metal ions for other molecules and anions culminated in the theories of Alfred Werner, although they were universally accepted in the mid 1920s. Molecular Magnetism is a wide ranging area of research that began only 30 years ago, primarily involving the synthesis and study of mainly metal based compounds.

The pioneering research on the magnetic properties of mononuclear complexes has largely contributed to the basic knowledge of the structure and bonding in coordination compounds. In fact, Molecular Magnetism appears intimately related to Coordination Chemistry. The flexibility thus provided, regarding the different nature and oxidation degree of the metal ions and the plasticity of their coordination environment, the variety of the blocking and bridging ligands with

---

potential optical, redox, and photochemical properties, or the different stability and solubility of the corresponding metal complexes in solution, constitute invaluable tools when aiming at preparing tailor-made, discrete polynuclear complexes and extended coordination polymers under mild conditions. In this respect, the history of the Coordination Chemistry-based approach to Molecular Magnetism flows back and forth between the two limiting cases of lower to higher nuclearity and dimensionality, creating a plethora of multimetallic coordination compounds with unique structures and magnetic or physical properties through this perpetual pendular movement.

Molecular Magnetism is a wide-ranging area of research that began focusing mainly on the synthesis and the study of metal coordination compounds, which has experienced an increase in the attention of scientists from different specialties, such as Chemistry, Physics or Biology. This convergence of disciplines has led to the rapid development of this area due to the complementarity of both the experimental techniques used and the knowledge generated. The knowledge provided by Inorganic Chemistry (specifically Coordination Chemistry) is of great help since it is intended to prepare complexes with predictable structures and magnetic properties from chemical reactions in solution.

Molecular Magnetism targets the design, synthesis and investigation of the magnetic properties of molecular materials. The start of Molecular Magnetism can be dated from the attempts made in the late 1970s of the last century to obtain molecule-based magnets. Molecule-based magnets can mimic the unique magnetic properties exhibited by conventional inorganic magnets (metal alloys and oxides), while incorporating additional properties to the magnetic ones (optical, electronic, conducting, sensing or adsorbing). These coexisting properties would lead to new magnetic phenomena resulting from the synergy between them.

For a few years, researchers in this field made efforts to design coordination compounds ordering ferromagnetically. Finally, it was in 1987 when Kahn *et al.* reported the first molecule-based ferromagnet of formula  $[\text{MnCu}(\text{pba})(\text{H}_2\text{O})_3] \cdot 2\text{H}_2\text{O}$  (pba = 1,3-propylene-bis(oxamato)), a heterobimetallic 1D coordination polymer built up from the regular alternation of Mn(II) and Cu(II) ions across the oxamato bridges, which exhibits a long-range ferromagnetic order at a very low critical temperature of  $T_c = 4.6\text{ K}$  (Figure 1.1) [1].

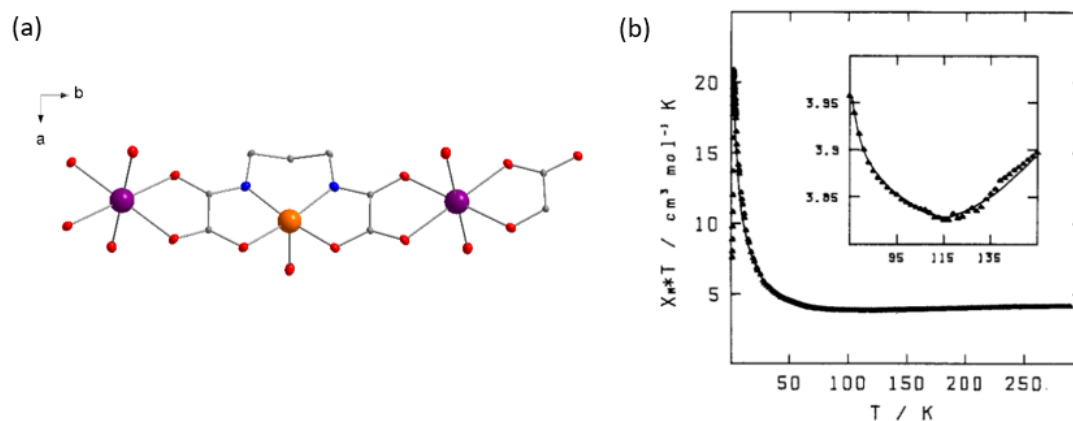


Figure 1.1: (a) View along the  $c$  axis of a fragment of the chain structure of  $[\text{MnCu}(\text{pba})(\text{H}_2\text{O})_3] \cdot 2\text{H}_2\text{O}$ . Colour code: purple, Mn; orange, Cu; red, O; blue, N; grey, C. Hydrogen atoms have been omitted for clarity. (b) Experimental ( $\bullet$ ) and theoretical (—) temperature dependence of  $\chi_M T$ .

The study of the magnetic properties of the molecular compounds was centered mainly on 3d (and 4f) ions, remaining the 4d and 5d ions almost unexplored. The possible reason for that could be the more difficult chemistry that 4d and 5d ions present as well as the complication to model and interpret their magnetic data. Besides, these heavier metal ions tend to lead to low-spin complexes, which, in most cases, present all paired electrons, losing the interest in this field. In contrast, when having unpaired electrons, these ions remain attractive as they show longer diffusivity and anisotropy, which can increase the intensity of the

---

magnetic exchange compared to the 3d ions.

Magnets are widely used for a large number of applications. Among all of them, information storage is certainly one of the future applications for magnets. Like in all information technologies, there is a tendency to reduce the size of the magnetic memory elements.

The phenomenon of Single-Molecule Magnetism was established in the early 1990s, when it was discovered that specific polynuclear complexes, so-called molecular metal compounds, possessed the ability to be magnetised without the necessity of long-range cooperative magnetic interactions. In some ways, Single-Molecule Magnet (SMM) story starts with the work performed in the Christou group during the 1980s [2]. The research was dedicated to the synthesis of model compounds of the oxygen-evolving complex in Photosystem II. The work resulted in many polynuclear mixed-valence manganese complexes being made, but lacked a model for the highest oxidation state of the biological cycle.

In attempting to make such a model by oxidation of manganese acetate with permanganate, a compound of formula  $[\text{Mn}_{12}\text{O}_{12}(\text{O}_2\text{CPh})_{16}(\text{H}_2\text{O})_4]$  was isolated. The first proposal of a dodecanuclear manganese complex from this type of reaction was made in 1921 by Weinland and Fischer [3]. Nevertheless, only when monocrystal X-ray experiments were commonly used it was possible to confirm the structure of the compound as  $[\text{Mn}_{12}\text{O}_{12}(\text{O}_2\text{CCH}_3)_{16}(\text{H}_2\text{O})_4] \cdot 4\text{H}_2\text{O} \cdot 2\text{CH}_3\text{COOH}$  or  $[\text{Mn}_{12}]$ , published in 1980 by Lis [4], who included the preliminary magnetic susceptibility data from 4-300 K, but did not interpret them.

Boyd *et al.* measured the magnetic properties of the benzoate derivative of formula  $[\text{Mn}_{12}\text{O}_{12}(\text{O}_2\text{CPh})_{16}(\text{H}_2\text{O})_4]$  and deduced an incorrect spin ground state of  $S = 14$ . At that time, the highest spin known for a molecule was  $S = 12$ , as reported by Gatteschi's group [5]. As a result of the paper by Boyd *et al.*, the

Gatteschi group reinvestigated the Lis compound by different techniques, such as high-field magnetisation and high-frequency Electron Paramagnetic Resonance (EPR) spectroscopy. The results were published by Caneschi *et al.* in 1991 [6], describing the freezing of the magnetisation at low fields. The use of these techniques provided evidence of a  $S = 10$  ground state and later, measurements confirmed that  $[\text{Mn}_{12}\text{O}_{12}(\text{O}_2\text{CPh})_{16}(\text{H}_2\text{O})_4]$  also had a  $S = 10$  ground state [7, 8].

The identification of a large magnetic anisotropy in  $[\text{Mn}_{12}]$  led to the first observation of molecular magnetic hysteresis (Figure 1.2) [7]. This hysteresis appears due to a slow relaxation of the magnetisation of the compound when switched off the applied magnetic field. The phenomenon was molecular, and in 1996, the quantum relaxation was reported by Thomas *et al.* reaching a total success [9]. In this manner, superparamagnetic-like behaviour was shown unambiguously in discrete molecules. Caneschi *et al.* did not use the term SMM at that moment. However, these molecules are now universally known, forming the basis for the SMM era.

The initial area of interest for the development of SMMs was 3d-based poly-metallic molecules in the vein of  $[\text{Mn}_{12}]$ , where exchange interactions were harnessed to construct molecules with giant total spin [10]. These studies were also performed on systems like  $[\text{V}_4]$ ,  $[\text{Fe}_8]$ ,  $[\text{Co}_4]$ ,  $[\text{Ni}_{12}]$  and other  $[\text{Mn}_n]$  families, among others.

Finally, the less explored 4d and 5d metal ions started to draw attention since, as mentioned before, the 4d and 5d metal ions possess higher magnetic anisotropy and longer diffusivity than the systems proceeding from 3d ions. After approximately a decade of the finding of the pioneering SMM, the first SMMs based on 4d and 5d metal ions were reported [11].

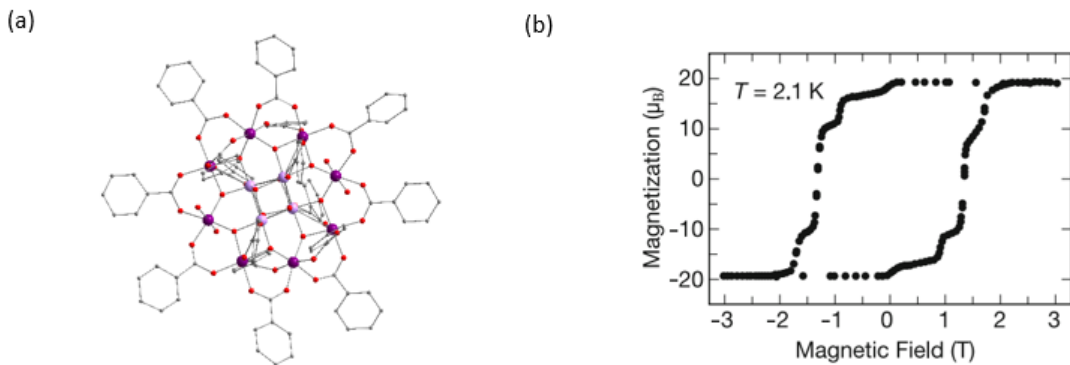


Figure 1.2: (a) Molecular structure of  $[\text{Mn}_{12}\text{O}_{12}(\text{O}_2\text{CPh})_{16}(\text{H}_2\text{O})_4]$ . Colour code: purple, Mn(III); lavender, Mn(IV); red, O; grey, C. Hydrogen atoms have been omitted for clarity. (b) Magnetisation versus magnetic field hysteresis loop for  $\text{Mn}_{12}$ -acetate complex on a single crystal with the magnetic field applied along the tetragonal axis of each  $[\text{Mn}_{12}]$  molecule. The vertical parts of the “steps” correspond to critical values of the field where resonant magnetisation tunnelling is allowed.

From the Molecular Magnetism point of view, the most explored and studied systems are those based on Mo(III), Ru(III), Re(IV) and Os(V). Among them, Re(IV) systems have been the most studied due to its high magnetic anisotropy and spin value ( $S = 3/2$ ) of the ground state. On the contrary, the strong quantum signatures of the 4d metal ions, such as Ru(III), make their compounds less likely to exhibit typical SMM behaviour. As a result, the motivation to investigate the slow magnetic relaxation in such molecules diminished for an extended period of time.

On the other hand, lanthanides were fairly unexplored in Molecular Magnetism till the beginning of this century. The main reasons for the lack of interest were (i) the weak magnetic interactions, (ii) the difficulties associated with a large unquenched orbital contribution, which demands high doses of quantum mechanics and (iii) the need for routine magnetic measurements below 4K, which were not available in chemistry labs.



The very weak interaction between f orbitals and ligand orbitals led to a less rich variety of coordination compounds. Later, compared to transition metal ions, lanthanides became one of the focal points of molecular spintronics, where they provided the advantages of their unquenched orbital momentum.

The change in attitude towards all the issues presented above came at the beginning of this century when two reports on completely different materials showed that isolated lanthanide ions could give rise to slow magnetic relaxation, not due to cooperative phenomena but to intrinsic properties of the metal ions that are present in a molecular structure, analogous to what was observed in SMMs. The first example of a mononuclear complex that showed Single-Ion Magnet (SIM) behaviour was reported in 2003 by N. Ishikawa *et al.* [12]. This compound of formula  $(\text{NBu}_4)[\text{TbPc}_2]$  ( $\text{H}_2\text{Pc}$  = phthalocyanine) presents an energy barrier of 331 K, which is higher than those observed for the most representative SMMs of the manganese family until that moment (Figure 1.3). Therefore, lanthanides have constituted the foundation for the development of the first families of SIMs due to their high spin and intrinsic magnetic anisotropy values. So, many of these lanthanide-containing complexes have been reported during the last decades.

## **1.2 Other applications of coordination compounds: from biology to nanomedicine and nanotechnology**

Coordination compounds can be employed in the treatment, management or diagnosis of diseases. Metal complexes can be formed in the body to handle dysfunction due to metal poisoning. There are four main areas of the use of

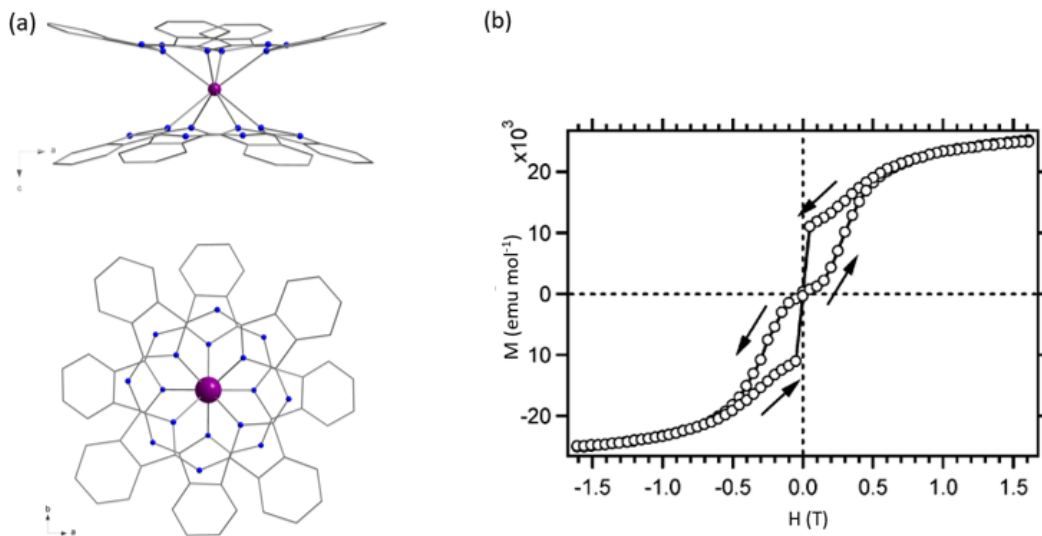


Figure 1.3: (a) Molecular structure of  $[\text{Tb}^{\text{III}}\text{Pc}_2]^-$  complex viewed along the  $b$  and  $c$  axes. Colour code: purple, Tb; blue, N; grey, C. Hydrogen atoms and  $\text{NBu}_4^+$  cations are omitted for clarity. (b) Magnetisation vs field plot measured at 1.7 K for the  $[\text{TbPc}_2]^-$  complex.

transition metal compounds in biomedicine: (i) The application of coordination compounds, or metal-based drugs, to treat diseases. An example can be the effectiveness of *cis*-dichlorodiammineplatinum (CISPLATIN) in the treatment of certain types of cancer [13] or the use (for 50 years) of complexes of gold in the treatment of rheumatoid arthritis [14]; (ii) The employment of chelating or complexing agents to treat metabolic dysfunction. The classic example is the use of D-penicillamine to treat Wilson's disease [15], which is caused by an inability of the body to metabolise copper in the normal way; (iii) The utilisation of complexing, chelating or sequestering agents to remove heavy metal poisons from the body (Chelation therapy may be the only acceptable treatment); (iv) The use of complexes to transport metals to specific sites in the body to aid in imaging. The classic example is the applicability of these complexes in radioimaging. Recently, with the advent of Nuclear Magnetic Resonance (NMR) imaging of the human

body, there has been much interest in using paramagnetic complexes, which go to specific sites in the body to improve the contrast of clinical images [16]. Thus, there is a growing area of research on the design of ligands that will go to a specific organ in the body and can be used to take any metal as needed to that site.

One of the most recent and popular applications of permanent magnets in modern-day medicine is Magnetic Resonance Imaging (MRI). The discovery of gadolinium(III) complexes inducing shifts in the NMR spectra and increasing resolution was an important step towards this research field. NMR is directly related to the MRI phenomenon. In most cases, MRI focuses on one type of atomic nucleus and can generate an image showing the spatial distribution of spin density of a specific type of atom, usually the water protons [17]. Unlike other spectroscopic techniques, the difference between the excited and the ground states is too low to allow spontaneous relaxation, so relaxation needs to be stimulated. The longitudinal relaxation time  $T_1$  is characteristic of the return to equilibrium of the magnetisation along  $z$  axis, corresponding this phenomenon to the enthalpic interaction of the excited nucleus with the magnetic active agents of the environment. Therefore,  $T_1$  will depend on the mobility and, in consequence, on the viscosity of the environment. The transversal relaxation time  $T_2$  is characteristic of the disappearance of the signal in the  $xy$  plane. In MRI, the parameter of the relaxation time  $T_2^*$  is often used and contains both  $T_2$  and the contribution of all magnetic field lack of homogeneity characteristic of the sample.  $T_2^*$  is, thus, linked to specific properties of the tissue under study and is very useful in medical MRI.

MRI does not require the use of contrast agents, and it is not the contrast agent itself that is visible. Indeed, the MRI contrast agents interact with  $H_2O$

---

protons and either modify their relaxation times or are directly involved in the H<sub>2</sub>O proton magnetisation level. Nevertheless, with the aim of improving the quality of MRI images, there is a continuous increase in the use of the so-called MRI contrast agents [18]. The most widely used class of MRI contrast agents is based on the mechanism of longitudinal relaxation. It is usually the motion of the <sup>1</sup>H protons from the neighbourhood which creates an oscillating magnetic field that stimulates a return to equilibrium of the H<sub>2</sub>O protons. Suppose we introduce molecules that contain unpaired electrons into the H<sub>2</sub>O molecule environment. In that case, they will activate the return to equilibrium of the H<sub>2</sub>O protons more effectively due to the strength of the magnetic moment of the electron, which is 658 times stronger than that of the proton. Based on that, gadolinium(III) ion-containing seven unpaired electrons is commonly used as an MRI contrast agent. Therefore, the activity of gadolinium(III) complexes will cause a decrease in the  $T_1$  relaxation time constant, resulting in a brightening of the MR image [19]. When acquiring data, the gadolinium contrast agent will reduce the time of return to equilibrium of the magnetisation.

Gadolinium(III) complexes have also attracted much attention in the last two decades because of their potential technological applications in low and ultra-low temperatures or Cryogenic Magnetic Refrigeration (CMR). Magnetic refrigeration is a standard cryogenics technology proven effective in cooling temperatures as low as a few Kelvin degrees. The applications of CMR include superconducting magnets and helium liquefiers, among others, and serve as a viable alternative to the costly cooling technologies based on <sup>3</sup>He/<sup>4</sup>He dilutions [20, 21]. The origins of CMR may be traced back to the late 1920s, starting with the work of Debye and Giauque, who achieved ultra-low temperatures in the sub-Kelvin realm by adiabatic demagnetisation of gadolinium(III) sulphate octahydrate [22, 23].

The increase or decrease in temperature that occurs in a magnetic material when an external magnetic field is connected to/disconnected from it under adiabatic conditions ( $T_{ad}$ ) is known as the Magnetocaloric Effect (MCE). As a result, the lattice entropy changes balance out the isothermal magnetic entropy ones ( $S = S_M + S_L = 0$ ) during the magnetisation/demagnetisation cycle [24, 25].

### 1.3 Biomolecules as ligands

Inorganic biochemistry (or biocoordination chemistry) may be described as the study of the chemical reactivity of metal ions in biological environments. It is a broad and emerging subject that has attracted researchers from various unrelated disciplines [26].

The interest in the interactions of metal ions with nucleobases and other biomolecules during the past few decades has led to considerable advances in inorganic biochemistry [27, 28]. With multiple metal binding sites, nucleobases, nucleosides and nucleotides form coordination polymers (CPs) with metal ions (Figure 1.4). These self-assembled materials are especially appealing due to their ease of preparation, highly tunable structure and properties and outstanding biocompatibility. The reactivity of nucleobases towards metal ions varies, depending on the nature of the metal ions and the selected nucleobases.

The presence of accessible nitrogen and oxygen lone pairs in the nucleobases allows these molecules to act as ligands [29]. Studies on the metal ion–nucleobase interactions are of great interest since metal ions play a crucial role in the structure and function of nucleic acids and genetic information transfer. The capacity of the compounds generated with these biomolecules comes from the rich and diverse combination of hydrogen bond donor and acceptor positions, in many cases

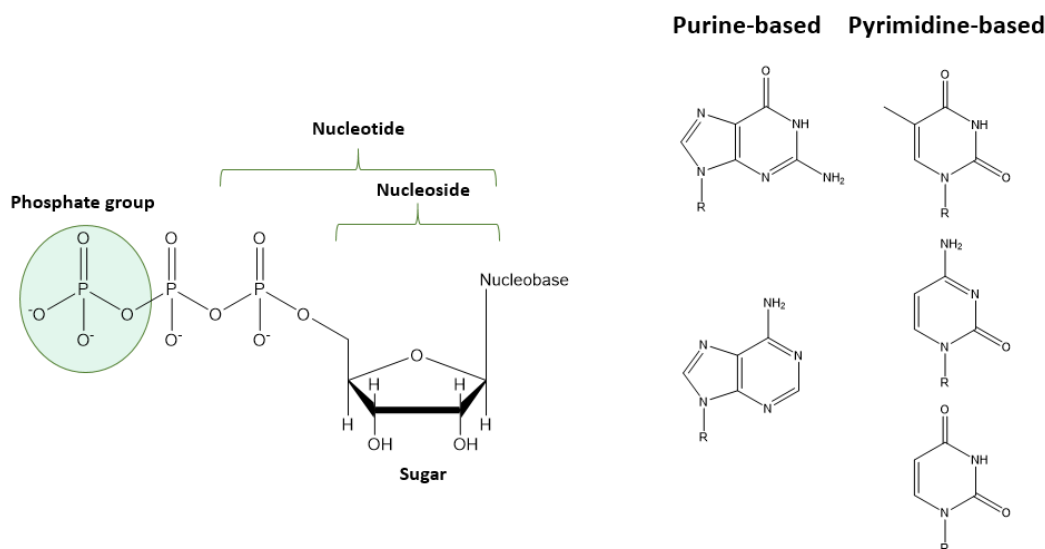


Figure 1.4: Structure of natural nucleobases, nucleosides and nucleotides with deoxyribose.

close enough to provide complementary hydrogen bonding capability [30]. This specific bonding of DNA base pairs provides the chemical foundation for genetics. This powerful molecular recognition system can be used in nanotechnology to direct the assembly of highly structured materials with specific nanoscale features [31] and in DNA computation to process complex information. A rational design of this type of material leads to different properties that can be tuned at will, providing in this way materials with applications in areas such as luminescence [32], magnetism [33–35], electrical conductivity [36] or catalytic activity [37], since they benefit from their hybrid metal–organic nature. Despite all these features, there are scarce examples of inorganic systems based on biomolecules to study the magnetic properties in this field [30, 34, 35].

On the other hand, the research on metal ion-nucleic acid complexes was advanced when antitumour activity of CISPLATIN was discovered [13]. The exact mechanism of the *in vivo* action is still a matter of debate [38], but platinum(II)

compounds have been tested in treating several forms of cancer. Despite its success in the treatment of tumours, the clinical effectiveness of this compound has been greatly limited by drug resistance and significant side effects [39]. As a consequence of these limitations, researchers found an incentive to research other transition metal complexes further to develop new drugs that would overcome the disadvantages of the platinum ones. Many amine complexes of Ru(II) and Ru(III) tend to selectively bind to imine sites in biomolecules (which do not protonate at neutral pH), leaving their nitrogen lone pairs available for metal ion coordination. For this reason, ruthenium complexes often selectively coordinate histidyl imidazole nitrogens on proteins [40, 41] and the N<sup>7</sup> site on the imidazole ring of purine nucleotides. Thus, it can take advantage of the properties of proteins, oligonucleotides and nucleic acids to target specific tissues.

Amino acids, additionally, are the basic building blocks of proteins and enzymes, and also serve as precursors for the creation of other significant biomolecules, including hormones and neurotransmitters (Figure 1.5). Amino acids have a strong affinity for some body receptors and minimal immunogenicity and toxicity. Because of their structural variety, chirality, and various functional groups, are excellent building blocks for creating nanomaterials for their use in biological applications [42].

In the framework of this PhD Thesis, selecting appropriate carboxylate-type ligands of biological nature is crucial to obtain new multifunctional complexes and coordination polymers, which are biocompatible.

Oxalate is the simplest dicarboxylate dianion. Oxalic acid and oxalate salts are present in a variety of plants, and oxalate found in minerals may be of biological origin [43]. Oxalate is primarily produced by endogenous metabolism (Figure 1.6), with just a minor contribution from food. Glyoxalate is converted

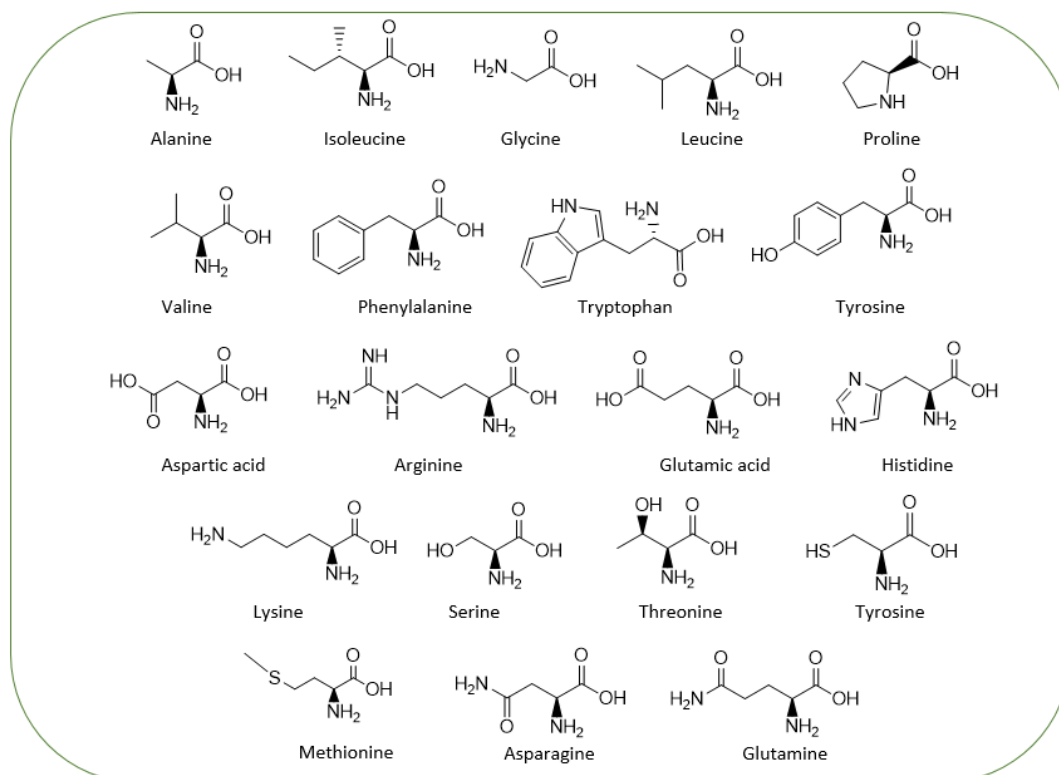


Figure 1.5: Structure of natural amino acids.

into oxalate by the liver's lactate dehydrogenase (LDH) enzyme. This molecule is formed during the intermediate metabolism of glycine, hydroxyproline, and glycolate in the peroxisomes of hepatic cells [44].

The choice of oxalate as ligand relies on its versatility due to the significant number of coordination modes that can adopt in its metal complexes with other coligands (Figure 1.7). Furthermore, while serving as a bridge, it is an excellent mediator of magnetic interactions between metal ions, with the strength and nature of these interactions.

Coordination Chemistry has appealing tools for the development of biologically active molecules and nanomaterials. Nanomaterials displaying discrete biological modes of action might be created and used for disease diagnostics, sensing,



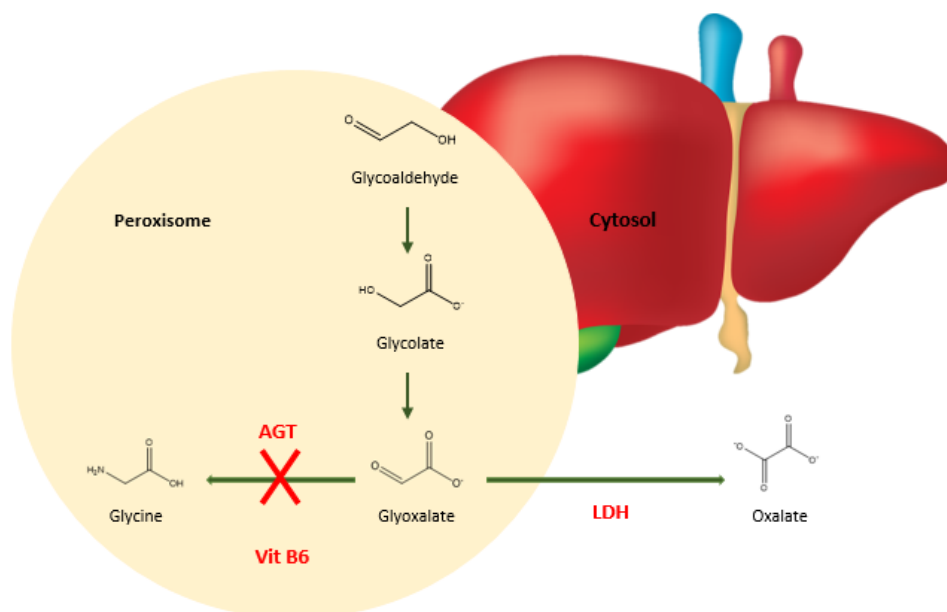


Figure 1.6: Oxalic acid metabolism diagram.

and therapy by carefully selecting metal centres, modulating coordination number, their labile groups and bioactive or ancillary ligands [45].

## 1.4 General Objectives

The current PhD Thesis is centred on Coordination Chemistry, aiming to explore and research novel classes of molecules that combine chemical and physical features that are fundamentally important for commercial and technological applications. As a result, the focus of this effort will be on the design, synthesis, and structural characterisation of new metal complexes that can provide a link between Molecular Magnetism and the next step in nanoscience and nanotechnology, using biomolecules and biocompatible ligands as a common thread. Along this line, we have undertaken a research project in this PhD Thesis to develop further the 4d and 4f Coordination Chemistry and magnetochemistry, dividing

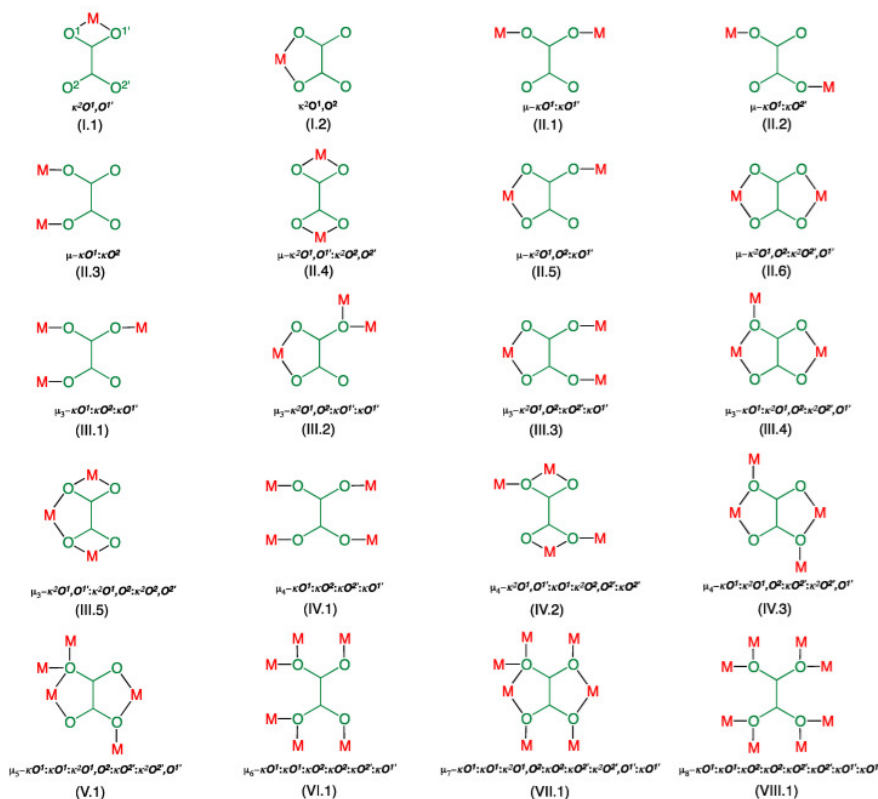


Figure 1.7: Different coordination modes in oxalato complexes.

the content of this Thesis into two main Chapters, each of which focuses on a different metal type.

In Chapter 2, it is shown that metal complexes based on biomolecules can be a very useful tool in the diagnosis and treatment of some diseases as well as in other biomedical applications. Some ruthenium(III) complexes such as *trans*-[tetrachloro(DMSO)(imidazole)ruthenate(III)] (NAMI-A), *trans*-[tetrachlorobis-(indazole)ruthenate(III)](KP1019) and others, as we mentioned before, show a clinically proven biological activity against diseases and pathologies of different type. Nevertheless, the study of their magnetic properties has not been performed yet. This Chapter, presents a more complete analysis of this kind of complexes, where the biological applications, other interesting properties and their magnetic

behaviour are studied.

Finally, since most of the commercial contrast agents (Magnevist, Dotarem, Omniscan, etc.) have been developed for their use in 1T MRI scanners, and the current equipment in hospitals are based on 3T devices, new lanthanide-based contrast agents must be developed. In this sense, in Chapter 3, the choice of biocompatible ligands such as amino acids, vitamins or nucleobases towards gadolinium(III) and dysprosium(III) ions will let us to prepare and investigate novel and stable compounds, which would minimise the toxicity (due to its intrinsic composition) and will be tested in the current equipment placed in hospitals.

On the other hand, compounds showing a significant MCE often include atoms with a large number of unpaired electrons, each of which creates its own small magnetic moment. An external magnetic field forces these atomic magnetic moments to line up in the same direction during magnetic refrigeration. The temperature of the material rises as the magnetism of the atoms becomes more organised (reducing the entropy of the system). The reason why gadolinium(III) is a frequent component of magnetic refrigerant materials is because its ground state has the highest entropy per single ion. Additionally, the quenched orbital momentum indicates that the effects of the crystal field are negligibly minor. In this regard, gadolinium(III) can be combined with bridging ligands like oxalate to create Gd-MOFs, whose MCE effectiveness will be higher than its gadolinium(III) SIMs equivalents.

---

## *References*

- (1) Pei, Y.; Verdaguer, M.; Kahn, O.; Sletten, J.; Renard, J.-P. *ChemInform* **1987**, *18*, 7428–7430.
- (2) Christou, G. *Acc. Chem. Res.* **1989**, *22*, 328–335.
- (3) Weinland, R.; Fischer, G. *Z. Anorg. Allg. Chem.* **1921**, *120*, 161–180.
- (4) Baikie, A. R.; Hursthouse, M. B.; New, D. B.; Thornton, P. J. *J. Chem. Soc., Chem. Commun.* **1978**, 62–63.
- (5) Caneschi, A.; Gatteschi, D.; Laugier, J.; Rey, P.; Sessoli, R.; Zanchini, C. *J. Am. Chem. Soc.* **1988**, *110*, 2795–2799.
- (6) Caneschi, A.; Gatteschi, D.; Sessoli, R.; Barra, A. L.; Brunel, L. C.; Guillot, M. *J. Am. Chem. Soc.* **1991**, *113*, 5873–5874.
- (7) Sessoli, R.; Gatteschi, D.; Caneschi, A.; Novak, M. *Nature* **1993**, *365*, 141–143.
- (8) Sessoli, R.; Tsai, H. L.; Schake, A. R.; Wang, S.; Vincent, J. B.; Folting, K.; Gatteschi, D.; Christou, G.; Hendrickson, D. N. *J. Am. Chem. Soc.* **1993**, *115*, 1804–1816.
- (9) Thomas, L.; Lioni, F.; Ballou, R.; Gatteschi, D.; Sessoli, R.; Barbara, B. *Nature* **1996**, *383*, 145–147.

- 
- (10) Chilton, N. F. *Annu. Rev. Mater. Res.* **2022**, *52*, 79–101.
- (11) Wang, X.-Y.; Avendaño, C.; Dunbar, K. R. *Chem. Soc. Rev.* **2011**, *40*, 3213–3238.
- (12) Ishikawa, N.; Sugita, M.; Ishikawa, T.; Koshihara, S.; Kaizu, Y. *J. Am. Chem. Soc.* **2003**, *125*, 8694–8695.
- (13) Rosenberg, B.; Vancamp, L.; Trosko, J. E.; Mansour, V. H. *Nature* **1969**, *222*, 385–386.
- (14) Messori, L.; Marcon, G. *Met. Ions Biol. Syst.* **2004**, *41*, 279–304.
- (15) Van Caillie-Bertrand, M.; Degenhart, H.; Luijendijk, I.; Bouquet, J.; Sinaasappel, M. *Arch. Dis. Child.* **1985**, *60*, 652–655.
- (16) Köhler, F. H. *eMagRes* **2007**.
- (17) Merbach, A. S.; Helm, L.; Toth, E., *The chemistry of contrast agents in medical magnetic resonance imaging*; John Wiley & Sons: 2013.
- (18) Benelli, C.; Gatteschi, D., *Introduction to molecular magnetism: From transition metals to lanthanides*; John Wiley & Sons: 2015.
- (19) Hingorani, D. V.; Bernstein, A. S.; Pagel, M. D. *Contrast Media Mol. Imaging* **2015**, *10*, 245–265.
- (20) Evangelisti, M. *Molecular Magnets: Physics and Applications* **2014**, 365–387.
- (21) Konieczny, P.; Sas, W.; Czernia, D.; Pacanowska, A.; Fitta, M.; Pełka, R. *Dalton Trans.* **2022**, *51*, 12762–12780.
- (22) Debye, P. *Ann. Phys.* **1926**, *386*, 1154–1160.
- (23) Giaque, W. *J. Am. Chem. Soc.* **1927**, *49*, 1864–1870.

- 
- (24) Pecharsky, V. K.; Gschneidner Jr, K. A. *J. Magn. Magn. Mater.* **1999**, *200*, 44–56.
- (25) Franco, V.; Blázquez, J.; Ipus, J.; Law, J.; Moreno-Ramirez, L.; Conde, A. *Prog. Mater. Sci.* **2018**, *93*, 112–232.
- (26) Cowan, J. A., *Inorganic biochemistry: an introduction*; John Wiley & Sons: 1997.
- (27) Lopez, A.; Liu, J. *ChemNanoMat* **2017**, *3*, 670–684.
- (28) Constable, E., *Comprehensive coordination chemistry II: from biology to nanotechnology*; Newnes: 2003.
- (29) Sivakova, S.; Rowan, S. J. *Chem. Soc. Rev.* **2005**, *34*, 9–21.
- (30) Pascual-Colino, J.; Beobide, G.; Castillo, O.; Lodewyckx, P.; Luque, A.; Pérez-Yáñez, S.; Roman, P.; Velasco, L. F. *J. Inorg. Biochem.* **2020**, *202*, 110865.
- (31) Seeman, N. C. *Nature* **2003**, *421*, 427–431.
- (32) Heine, J.; Müller-Buschbaum, K. *Chem. Soc. Rev.* **2013**, *42*, 9232–9242.
- (33) Kurmoo, M. *Chem. Soc. Rev.* **2009**, *38*, 1353–1379.
- (34) Armentano, D.; Mastropietro, T. F.; Julve, M.; Rossi, R.; Rossi, P.; De Munno, G. *J. Am. Chem. Soc.* **2007**, *129*, 2740–2741.
- (35) Pérez-Yáñez, S.; Beobide, G.; Castillo, O.; Cepeda, J.; Luque, A.; Román, P. *Cryst. Growth Des.* **2012**, *12*, 3324–3334.
- (36) Givaja, G.; Amo-Ochoa, P.; Gómez-García, C. J.; Zamora, F. *Chem. Soc. Rev.* **2012**, *41*, 115–147.
- (37) Lee, J.; Farha, O. K.; Roberts, J.; Scheidt, K. A.; Nguyen, S. T.; Hupp, J. T. *Chem. Soc. Rev.* **2009**, *38*, 1450–1459.

- 
- (38) Lee, J.; Farha, O. K.; Roberts, J.; Scheidt, K. A.; Nguyen, S. T.; Hupp, J. T. *Chem. Soc. Rev.* **2009**, *38*, 1450–1459.
- (39) Motswainyana, W. M.; Ajibade, P. A. *Adv. Chem* **2015**, *2015*, 1–21.
- (40) Gray, H. B.; Winkler, J. R. *Annu. Rev. Biochem.* **1996**, *65*, 537–561.
- (41) Messori, L.; Orioli, P.; Vullo, D.; Alessio, E.; Iengo, E. *Eur. J. Biochem.* **2000**, *267*, 1206–1213.
- (42) Wang, S.; Zhao, Y.; Zhang, Z.; Zhang, Y.; Li, L. *Chin. J. Chem. Eng.* **2021**, *38*, 30–42.
- (43) Christensen, A. N.; Lebech, B.; Andersen, N. H.; Grivel, J.-C. *Dalton Trans.* **2014**, *43*, 16754–16768.
- (44) Lorenzo, V.; Torres, A.; Salido, E. *Nefrologia (Madrid)* **2014**, *34*, 398–412.
- (45) Bruijninx, P. C.; Sadler, P. J. *Curr. Opin. Chem. Biol.* **2008**, *12*, 197–206.





## *CHAPTER 2*

---

*Mono- and dinuclear  
ruthenium(III)/(IV)-chloride  
complexes based on nucleobases,  
polyazines and polyazoles: From  
SIMs to biosensors and  
antitumour drugs*



## 2.1 Prologue

Ruthenium (Ru), with an atomic number of 44, is one of the 4d-series metals. It is known to be stable in oxidation states +2, +3, and +4 under physiological conditions, but forms complexes in a wide range of formal oxidation states (from -2 to +8) [1]. It is characterised by dominant octahedral coordination, due to strong ligand-field stabilisation. Only ruthenium complexes with high oxidation states show tetragonal pyramidal, trigonal bipyramidal, or tetrahedral geometries that deviate from the octahedral environment [2].

As ruthenium can exist in multiple oxidation states, there has been remarkable growth in the study of its coordination and organometallic chemistry during the last decades [3]. As a result, there are many publications on the formation of Ru-based complexes and their applications in areas such as biomedicine [4], catalysis [5, 6], nanoscience [7], redox systems [8] and photoactive materials [9].

In particular, ruthenium(III) displays extensive Coordination Chemistry, forming many stable neutral, cationic and anionic mononuclear complexes, which are kinetically inert. In addition, the electronic configuration of ruthenium(III) commonly gives rise to paramagnetic ( $S = 1/2$ ) low-spin six-coordinate mononuclear complexes [10].

On the contrary, ruthenium(IV) shows a complex aqueous chemistry, dominated mainly by dinuclear species. Very few mononuclear adducts have been well characterised. The electronic configuration of ruthenium(IV) frequently gives rise to paramagnetic low-spin ( $S = 1$ ) six-coordinate mononuclear or very strong antiferromagnetically coupled diamagnetic dinuclear systems [11]. In recent years, an insight has been gained into the bonding in the diamagnetic oxo- and nitrido-bridged diruthenium(IV) complexes.

---

In fact, oxo-bridged diruthenium complexes have attracted the interest of researchers due to their properties as molecular catalysts in water oxidation reactions and, thus, as artificial models of the Photosystem II centre (PSII) [12]. It has been discovered that oxo-bridged diruthenium complexes containing the Ru-O-Ru core, such as Ru<sub>360</sub> (Figure 2.1), have potent inhibitory effects on the mitochondrial calcium uniporter (MCU), that regulates the mitochondrial calcium uptake and modulates physiological functions like metabolism and cell death [13, 14]. As a result, the chemical properties of these ruthenium complexes also make them useful for this kind of biological research.

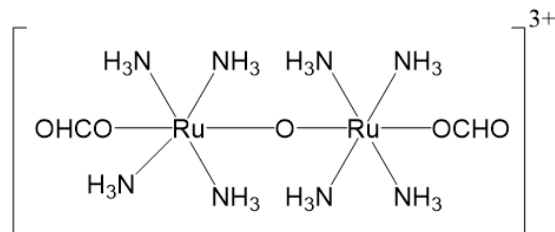


Figure 2.1: Molecular structure of Ru<sub>360</sub>.

Very little work has been done on the magnetic behaviour of paramagnetic complexes belonging to the 4d-series. The complexes containing 4d-series ions differ from those of the first transition (3d) elements, mainly because of four factors: (i) the stronger crystal field; (ii) the stronger spin-orbit coupling; (iii) an interelectronic repulsion comparable to spin-orbit coupling and (iv) a larger overlap of the 4d magnetic orbitals with those of the ligands [15].

One of the most important features of the 4d metal ions is their high degree of magnetic anisotropy, which can arise from both the local and global origins. The Landé factors ( $g$ ) for the 4d metal centres are often highly anisotropic, and the magnetic anisotropy ( $D$ ) values are significantly higher than those found for 3d metal ions. The spin-orbit coupling is proportional to  $Z_{eff}^4$  ( $Z_{eff}$  is the effective

atomic number) and the spin-orbit coupling constant ( $\lambda$ ) value of the 4d ions is close to  $1000 \text{ cm}^{-1}$  [16].

However, their strong quantum signatures make ruthenium(III) less possible to exhibit typical SMM behaviour. As a result, the enthusiasm to investigate the spin-lattice relaxation in such molecules diminished for a long period of time. This fact may partly explain why the mononuclear complexes incorporating 4d-block ions are less studied in Molecular Magnetism when compared with the 3d-based species, although 4d-based building blocks have been adopted for constructing various intriguing magnetic polynuclear molecules [17]. Figure 2.2 shows the first mononuclear ruthenium(III) complex, without second-order anisotropy, displaying slow magnetic relaxation, namely, the octahedral ruthenium(III)-chloride complex of formula  $[\text{RuCl}_3(\text{PPh}_3)_2(\text{MeCN})]$  ( $\text{PPh}_3$  = triphenylphosphine,  $\text{MeCN}$  = acetonitrile).

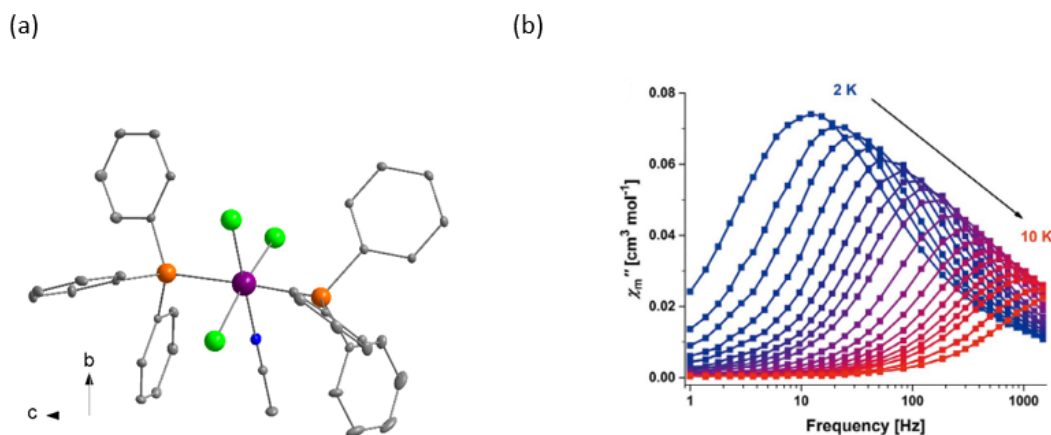


Figure 2.2: (a) Molecular structure of the  $[\text{RuCl}_3(\text{PPh}_3)_2(\text{MeCN})]$  complex. Colour code: purple, Ru; blue, N; orange, P; green, Cl; grey, C. Hydrogen atoms have been omitted for clarity. (b) Temperature dependent out-of-phase  $ac$  magnetic susceptibility ( $\chi''$ ) as a function of the frequency.

Ruthenium systems can also have applications as metallodrugs. Complexes containing this metal in their core present several advantages, such as mimick-

---

ing iron, redox accessible oxidation states, low toxicity compared to other metals, smooth interaction and binding with DNA and proteins. These properties highlight their ability to act as metallodrugs and make them attractive in this research area [18]. Ruthenium(III) complexes have demonstrated similar favorable ligand exchange kinetics to those of platinum(II) antitumour drugs, already used in the clinic. Although they have very little in common with the existing platinum-based drugs, like the well-known CISPLATIN, the ruthenium(III) complexes display lower toxicity, as previously reported [3].

Due to the octahedral geometry of ruthenium(III) complexes, as opposed to the square-planar geometry of platinum(II)-based ones, their antitumour mechanisms should be different, even though the initial DNA binding site of many ruthenium complexes is the same as that of CISPLATIN [19]. Nevertheless, ruthenium compounds appear to penetrate tumours well and bind to cellular DNA by crosslinking adjacent N<sup>7</sup> of guanine, thereby causing a type of DNA binding proteins to adhere to the target [20].

The slow ligand exchange rates of ruthenium-based complexes, which are close to those of cellular processes, make ruthenium compounds suitable for their use in biological applications [21].

Among the numerous ruthenium complexes extensively studied, the antitumour efficiency is reflected in the discovery of the promising ruthenium(III) complexes with *N*-donor imidazole and benzopyrazole ligands: NAMI-A and KP1019 (Figure 2.3) [3], NAMI-A being the most widely studied because of its remarkable antimetastatic properties [22]. These complexes have entered clinical trials. They adopt octahedral coordination geometry with respect to the ruthenium(III) metal center, but they exhibit different biological activities despite their structural and chemical similarities.

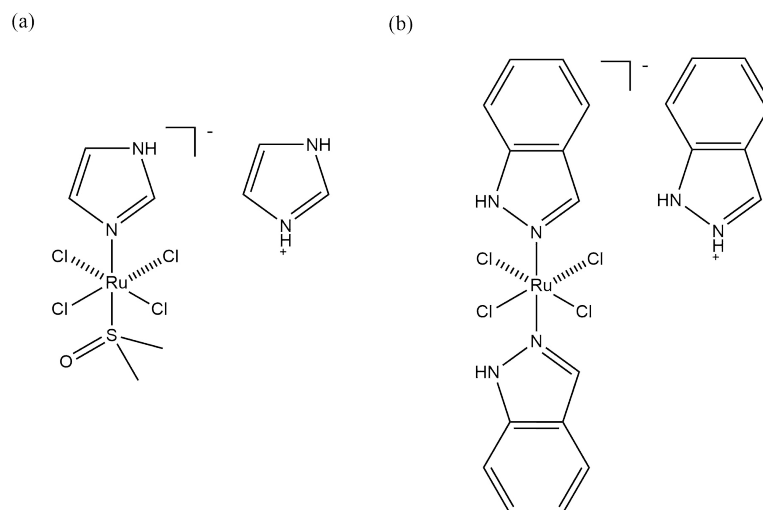


Figure 2.3: Molecular structure of (a) NAMI-A and (b) KP1019.

The versatile synthetic chemistry of ruthenium opens the door to get a great family of complexes based on a variety of ligands that could provide interesting compounds for clinical uses. The interactions of various ruthenium compounds with purine base derivatives have attracted attention to study its binding to DNA [23]. In 2004, the first mononuclear ruthenium(III)-chloride complex containing monoprotonated guanine (Hgua) of formula  $trans-[Ru^{III}Cl_4(Hgua)(DMSO)] \cdot 2H_2O$  was reported, showing a weak activity against tumour cell proliferation, but an interesting pro-adhesive effect that suggests possible activity against tumour malignancy [24].

Apart from that, the 4d transition metals tend to form stable metal-metal bonds, including multiple bonds, which is not common for the 3d metals. In 1982, the first edition of the book *“Multiple Bonds between Metal Atoms”* was published by Cotton *et al.*; then, in 2005, the third edition appeared [25]. More recently, one more book on metal-metal bond complexes has been published [26]. From the reading of these references, it is extracted that the majority of dinuclear  $Ru_2$  complexes adopt the paddlewheel structure, in which four bidentate bridging

---

ligands are arranged symmetrically around the two multiply-bonded Ru atoms, or the face-sharing bioctahedral and bisquare planar structures (Figure 2.4) [16]. Typical examples of bridging ligands are carboxylates, amidates or hydroxypyridinates and aminopyridinates, triazenates, benzamidinates or formamidinates [27].

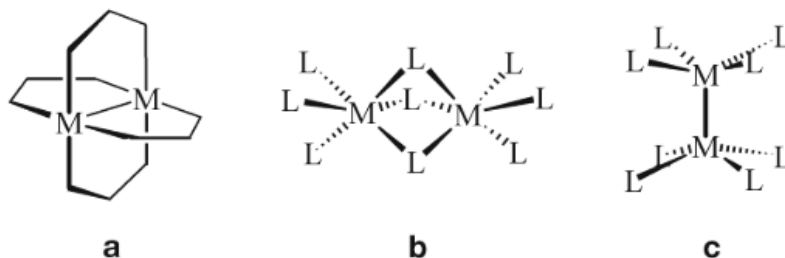


Figure 2.4: (a) Paddlewheel and (b, c) face-sharing bioctahedral and bisquare planar structures.

In these dinuclear systems, the metal atoms can be in the same oxidation state, usually +2 or +3. However, the mixed-valence complexes with formal oxidation state +2 and +3 are also known, in which the odd electron is delocalised between the metals [28–30].

Diruthenium complexes of the paddlewheel framework have been isolated in three different formal oxidation states:  $\text{Ru}_2^{4+}$ ,  $\text{Ru}_2^{5+}$  and  $\text{Ru}_2^{6+}$ . Those with the  $\text{Ru}_2^{5+}$  core are the most common [31]. In 1966, the first synthesis of these paddlewheel-type compounds, in which ruthenium form dinuclear carboxylate-bridged species with metal–metal bonds, was reported by Stephenson and Wilkinson [32]. Applications of these bimetallic compounds have also been described in the areas of biochemistry [33–35] and medicinal chemistry [36–38].

Diruthenium complexes coordinated by ligands containing different  $\sigma$  and  $\pi$  donor/acceptor groups have been synthesised and characterised, attending to their spectroscopic and electrochemical properties [39–43]. For example, higher



oxidation states of the diruthenium unit are electrochemically accessed by replacing the tetracarboxylate O,O'- bridging ligands with mono-anionic O,N- or N,N'- bridging ligands. In fact, the use of electron-rich N,N'- donor ligands, like aminopyridinates, formamidinates, benzamidinates and pyrimidinate (hpp), with or without the assistance of axial coligands, are known to stabilise the dimetal units in high oxidation states (Figure 2.5), exhibiting rich redox activities [44].

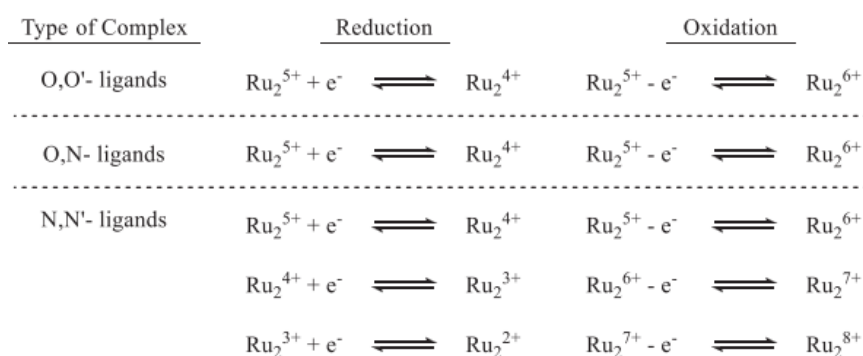


Figure 2.5: Various oxidation states reported for complexes containing O,O'-, O,N- and N,N'- bridging ligands.

Attending to this, it is clear that the four different diruthenium core oxidation states ( $\text{Ru}_2^{2+}$ ,  $\text{Ru}_2^{3+}$ ,  $\text{Ru}_2^{7+}$  or  $\text{Ru}_2^{8+}$ ) could be electrogenerated depending in large part on the bridging ligands. Recent advances in  $\text{Ru}_2$  paddlewheels focus on their applications as building blocks in molecular electronic wires and devices, as well as in magnetic materials. Magnetic materials composed of metal-metal bonded compounds within paddlewheel  $\text{Ru}_2$  cores are relatively rare, but they have been recognised and highlighted because of their unique ferrimagnetic properties [45–47].

Besides, the  $\text{Ru}_2^{5+}$  tetracarboxylate complexes have been used in antitumour activity studies. In attempts to understand the mechanism of antitumour activity, the binding of the guanidinate derivative 1,3,4,6,7,8-hexahydro-2H-pyrimido[1,2-

a]pyrimidinate (hpp) and guanine bases to  $\text{Ru}_2^{5+}$  tetracarboxylate complexes has also been studied [31]. In 1996, Dunbar and coworkers investigated the binding of guanine derivatives to various dimetal carboxylates,  $\text{Ru}_2^{5+}$  species included (Figure 2.6a) [48]. On the other hand, adenine and adenosine derivatives of  $[\text{Ru}_2(\text{O}_2\text{CCH}_3)_4]^+$  cation were synthesised and characterised from a magnetic point of view by S. Gangopadhyay *et al.* However, no crystal structures for these systems were reported (Figure 2.6b) [49].

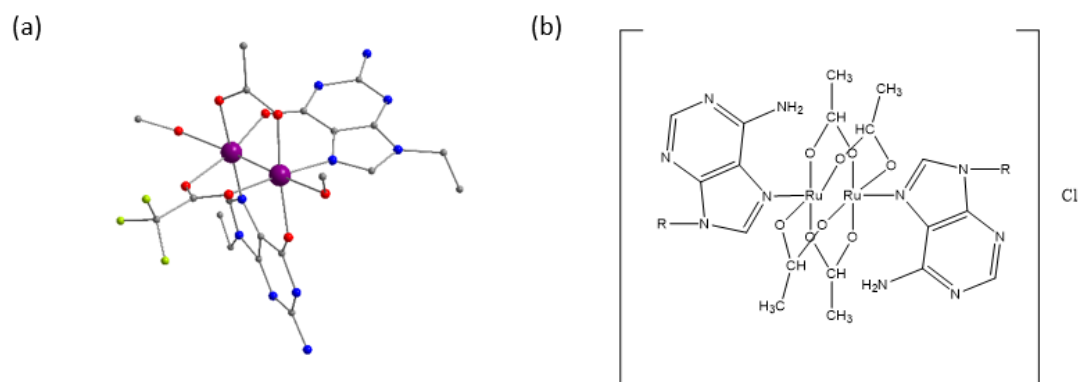


Figure 2.6: (a) Molecular structure of the  $[\text{Ru}_2(\text{O}_2\text{CMe})_{2-x}(\text{O}_2\text{CCF}_3)_x(9\text{-EtHgua})_2]$  complex. Colour code: purple, Ru; blue, N; red, O; pale green, F; grey, C. Hydrogen atoms have been omitted for clarity. (b) Proposed chemical structure of adenosine derivative of tetraacetatodiruthenium (II,III) chloride ( $\text{R} = \beta\text{-D-Ribofuronosyl}$  group).

Besides the binding of biologically relevant ligands, the importance of these complexes relies on their lesser toxicity than other diruthenium complexes. This property allows the use of increased concentrations in antitumour activity tests.

## 2.2 Contents

In this Chapter 2, six works have been included. In the first one, titled “*Ferromagnetic Coupling and Single-Ion Magnet Phenomenon in Mononu-*

**clear Ruthenium(III) Complexes Based on Guanine Nucleobase**", two  $\text{Ru}^{\text{III}}$  complexes of formula *trans*- $[\text{RuCl}_4(\text{Hgua})(\text{DMSO})] \cdot 2 \text{H}_2\text{O}$  and *trans*- $[\text{RuCl}_4(\text{Hgua})(\text{gua})] \cdot 3 \text{H}_2\text{O}$  are reported, along with their synthesis and magnetostructural characterisation.

In the second work, titled "**Molecular Self-Assembly of an Unusual Dinuclear Ruthenium(III) Complex Based on the Nucleobase Guanine**", a novel dinuclear ruthenium(III) complex based on guanine, of formula  $[\{\text{Ru}(\mu\text{-Cl})(\mu\text{-gua})\}_2\text{Cl}_4]\text{Cl}_2 \cdot 2 \text{H}_2\text{O}$ , has been synthesised and characterised by FT-IR, SEM-EDX, single-crystal X-ray diffraction (XRD), Hirshfeld surface analysis and cyclic voltammetry (CV).

In the third work, titled "**Detection of Hypoxanthine from Inosine and Unusual Hydrolysis of Immunosuppressive Drug Azathioprine through the Formation of a Diruthenium(III) System**", it is reported the synthesis and characterisation of a stable diruthenium(III) compound in its hydrated and dehydrated form with formula  $[\{\text{Ru}(\mu\text{-Cl})(\mu\text{-hpx})\}_2\text{Cl}_4]$  and  $[\{\text{Ru}(\mu\text{-Cl})(\mu\text{-hpx})\}_2\text{Cl}_4] \cdot 2 \text{H}_2\text{O}$ , respectively. Electrochemical studies have been performed to demonstrate the ability of this type of complex to be employed as a possible sensor device to detect hypoxanthine.

The fourth work, titled "**A novel adenine-based diruthenium(III) complex: Synthesis, crystal structure, electrochemical properties and evaluation of the anticancer activity**", reports the synthesis and characterisation, through different techniques, of a dinuclear ruthenium(III) complex based on the adenine nucleobase, with formula  $[\{\text{Ru}(\mu\text{-Cl})(\mu\text{-Hade})\}_2\text{Cl}_4]\text{Cl}_2 \cdot 2 \text{H}_2\text{O}$ . The anticancer activity of this compound has been evaluated in different cancer cell lines.

The fifth work, titled "**RUNAT-BI: A Ruthenium(III) Complex as**

---

*a Selective Anti-Tumor Drug Candidate against Highly Aggressive Cancer Cell Lines*”, describes the analysis of the activity of Runat-BI, a racemic Ru(III) mixture, and of one of its isomers, against eight tumour cell lines of breast, colon and gastric cancer as well as on a non-tumoural control. These results led the obtaining of an international patent with certificate PCT/ES2022/070415.

The sixth work, titled “*Molecular Self-Assembly in a Family of Oxo-Bridged Dinuclear Ruthenium(IV) Systems*”, describes a series of six novel Ru(IV) compounds of formula  $(\text{H}_2\text{bpy})_2[\{\text{RuCl}_5\}_2(\mu\text{-O})]$ ,  $(\text{PPh}_4)_2[\{\text{RuCl}_4(\text{H}_2\text{O})\}_2(\mu\text{-O})] \cdot 4 \text{H}_2\text{O}$ ,  $(\text{PPh}_4)_2[\{\text{RuCl}_4(\text{MeCN})\}_2(\mu\text{-O})]$ ,  $(\text{PPh}_4)_2[\{\text{RuCl}_4(\text{dmf})\}_2(\mu\text{-O})]$ ,  $(\text{PPh}_4)_2[\{\text{RuCl}_4(\text{py})\}_2(\mu\text{-O})]$  and  $[\{\text{RuCl}_3(\text{bpym})\}_2(\mu\text{-O})] \cdot 6 \text{H}_2\text{O}$ , which have been spectroscopically, electrochemically and magnetically characterised.

---

## References

- (1) Higgins, S. *Nat. Chem.* **2010**, *2*, 1100–1100.
- (2) Sahu, A. K.; Dash, D. K.; Mishra, K.; Mishra, S. P.; Yadav, R.; Kashyap, P. In *Noble and Precious Metals-Properties, Nanoscale Effects and Applications*; IntechOpen: 2018.
- (3) Motswainyana, W. M.; Ajibade, P. A. *Advances in Chemistry* **2015**, *2015*, 1–21.
- (4) Adhireksan, Z.; Davey, G. E.; Campomanes, P.; Groessel, M.; Clavel, C. M.; Yu, H.; Nazarov, A. A.; Yeo, C. H. F.; Ang, W. H.; Dröge, P.; Rothlisberger, U.; Dyson, P. J.; Davey, C. A. *Nat. Commun.* **2014**, *5*, 1–13.
- (5) Bruneau, C.; Achard, M. *Coord. Chem. Rev.* **2012**, *256*, 525–536.
- (6) Friedberger, T.; Ziller, J. W.; Guan, Z. *Organometallics* **2014**, *33*, 1913–1916.
- (7) Ferrando-Soria, J.; Vallejo, J.; Castellano, M.; Martínez-Lillo, J.; Pardo, E.; Cano, J.; Castro, I.; Lloret, F.; Ruiz-García, R.; Julve, M. *Coord. Chem. Rev.* **2017**, *339*, 17–103.
- (8) Duan, L.; Bozoglian, F.; Mandal, S.; Stewart, B.; Privalov, T.; Llobet, A.; Sun, L. *Nat. Chem.* **2012**, *4*, 418–423.

- 
- (9) Yamamoto, Y.; Tamaki, Y.; Yui, T.; Koike, K.; Ishitani, O. *J. Am. Chem. Soc.* **2010**, *132*, 11743–11752.
- (10) Seddon, E.; Seddon, K. *Topics in Inorganic and General Chemistry, Chemistry on Ruthenium* **1984**, *19*, 43–55.
- (11) Seddon, E. A.; Seddon, K. R., *The chemistry of ruthenium*; Elsevier: 2013.
- (12) Liu, F.; Concepcion, J. J.; Jurss, J. W.; Cardolaccia, T.; Templeton, J. L.; Meyer, T. J. *Inorg. Chem.* **2008**, *47*, 1727–1752.
- (13) García-Rivas, G.; Carvajal, K.; Correa, F.; Zazueta, C. *Br. J. Pharmacol.* **2006**, *149*, 829–837.
- (14) Nathan, S. R.; Pino, N. W.; Arduino, D. M.; Perocchi, F.; MacMillan, S. N.; Wilson, J. J. *Inorg. Chem.* **2017**, *56*, 3123–3126.
- (15) Saha, M. *Indian J. Phys.* **1969**, *43*, 646–653.
- (16) Wang, X.-Y.; Avendaño, C.; Dunbar, K. R. *Chem. Soc. Rev.* **2011**, *40*, 3213–3238.
- (17) Wu, S.-Q.; Miyazaki, Y.; Nakano, M.; Su, S.-Q.; Yao, Z.-S.; Kou, H.-Z.; Sato, O. *Chem. Eur. J.* **2017**, *23*, 10028–10033.
- (18) Li, F.; Collins, J. G.; Keene, F. R. *Chem. Soc. Rev.* **2015**, *44*, 2529–2542.
- (19) Brabec, V.; Nováková, O. *Drug Resist. Updat.* **2006**, *9*, 111–122.
- (20) Clarke, M. J. *Coord. Chem. Rev.* **2002**, *232*, 69–93.
- (21) Reedijk, B. J. *Platinum Met. Rev.* **2008**, *52*, 2–11.
- (22) Alessio, E.; Messori, L. *Molecules* **2019**, *24*, 1995.

- 
- (23) Hotze, A. C.; Velders, A. H.; Ugozzoli, F.; Biagini-Cingi, M.; Manotti-Lanfredi, A. M.; Haasnoot, J. G.; Reedijk, J. *Inorg. Chem.* **2000**, *39*, 3838–3844.
- (24) Turel, I.; Pečanac, M.; Golobič, A.; Alessio, E.; Serli, B.; Bergamo, A.; Sava, G. *J. Inorg. Biochem.* **2004**, *98*, 393–401.
- (25) Cotton, F. A.; Murillo, C. A.; Walton, R. A., *Multiple bonds between metal atoms*; Springer Science & Business Media: 2005.
- (26) Liddle, S. T., *Molecular metal-metal bonds: compounds, synthesis, properties*; John Wiley & Sons: 2015.
- (27) Cortijo, M.; Gonzalez-Prieto, R.; Herrero, S.; Priego, J. L.; Jimenez-Aparicio, R. *Coord. Chem. Rev.* **2019**, *400*, 213040.
- (28) Aquino, M.; Lee, F.; Gabe, E.; Bensimon, C.; Greedan, J.; Crutchley, R. *J. Am. Chem. Soc.* **1992**, *114*, 5130–5140.
- (29) Creutz, C.; Taube, H. *J. Am. Chem. Soc.* **1973**, *95*, 1086–1094.
- (30) Creutz, C.; Newton, M. D.; Sutin, N. *J. Photochem. Photobiol. A Chem.* **1994**, *82*, 47–59.
- (31) Angaridis, P. In *Multiple bonds between metal atoms*; Springer: 2005, pp 377–430.
- (32) Stephenson, T.; Wilkinson, G. *J. Inorg. Nucl. Chem.* **1966**, *28*, 2285–2291.
- (33) Santos, R. L. S. R.; van Eldik, R.; de Oliveira Silva, D. *Dalton Trans.* **2013**, *42*, 16796–16805.
- (34) Boer, D. R.; Wu, L.; Lincoln, P.; Coll, M. *Angew. Chem. Int. Ed.* **2014**, *126*, 1980–1983.

- 
- (35) Santos, R. L.; van Eldik, R.; de Oliveira Silva, D. *Inorg. Chem.* **2012**, *51*, 6615–6625.
- (36) Santos, R. L.; Bergamo, A.; Sava, G.; de Oliveira Silva, D. *Polyhedron* **2012**, *42*, 175–181.
- (37) Ribeiro, G.; Benadiba, M.; Colquhoun, A.; de Oliveira Silva, D. *Polyhedron* **2008**, *27*, 1131–1137.
- (38) Freitas, T. E.; Gomes, R. N.; Colquhoun, A.; de Oliveira Silva, D. *J. Inorg. Biochem.* **2016**, *165*, 181–191.
- (39) Bear, J. L.; Chen, W.-Z.; Han, B.; Huang, S.; Wang, L.-L.; Thuriere, A.; Van Caemelbecke, E.; Kadish, K. M.; Ren, T. *Inorg. Chem.* **2003**, *42*, 6230–6240.
- (40) Malinski, T.; Chang, D.; Feldmann, F.; Bear, J.; Kadish, K. *Inorg. Chem.* **1983**, *22*, 3225–3233.
- (41) Bear, J. L.; Li, Y.; Han, B.; Van Caemelbecke, E.; Kadish, K. M. *Inorg. Chem.* **2001**, *40*, 182–186.
- (42) Valente, E.; Zubkowski, J., et al. *J. Chem. Soc., Dalton Trans.* **1998**, 571–576.
- (43) Xu, G.-L.; DeRosa, M. C.; Crutchley, R. J.; Ren, T. *J. Am. Chem. Soc.* **2004**, *126*, 3728–3729.
- (44) Van Caemelbecke, E.; Phan, T.; Osterloh, W. R.; Kadish, K. M. *Coord. Chem. Rev.* **2021**, *434*, 213706.
- (45) Mikuriya, M.; Yoshioka, D.; Handa, M. *Coord. Chem. Rev.* **2006**, *250*, 2194–2211.



- (46) Liao, Y.; Shum, W. W.; Miller, J. S. *J. Am. Chem. Soc.* **2002**, *124*, 9336–9337.
- (47) Vos, T. E.; Liao, Y.; Shum, W. W.; Her, J.-H.; Stephens, P. W.; Reiff, W. M.; Miller, J. S. *J. Am. Chem. Soc.* **2004**, *126*, 11630–11639.
- (48) Crawford, C. A.; Day, E. F.; Saharan, V. P.; Folting, K.; Huffman, J. C.; Dunbar, K. R.; Christou, G. *Chem. Commun.* **1996**, 1113–1114.
- (49) Gangopadhyay, S.; Gangopadhyay, P. *J. Inorg. Biochem.* **1997**, *66*, 175–178.



---

*ARTICLE 1*

*Ferromagnetic Coupling and  
Single-Ion Magnet Phenomenon  
in Mononuclear Ruthenium(III)  
Complexes Based on Guanine  
Nucleobase*



## Article

# Ferromagnetic Coupling and Single-Ion Magnet Phenomenon in Mononuclear Ruthenium(III) Complexes Based on Guanine Nucleobase

Marta Orts-Arroyo, Nicolás Moliner, Francesc Lloret and José Martínez-Lillo \* 

Instituto de Ciencia Molecular (ICMol), Departament de Química Inorgànica, Universitat de València, c/Catedrático José Beltrán 2, Paterna, 46980 València, Spain

\* Correspondence: f.jose.martinez@uv.es; Tel.: +34-9635-44460

**Abstract:** Two mononuclear Ru<sup>III</sup> complexes of formula *trans*-[RuCl<sub>4</sub>(Hgua)(dmsO)]·2H<sub>2</sub>O (**1**) and *trans*-[RuCl<sub>4</sub>(Hgua)(gua)]·3H<sub>2</sub>O (**2**) [Hgua = protonated guanine (gua), dmsO = dimethyl sulfoxide] have been synthesized and characterized magnetostructurally. **1** and **2** crystallize in the monoclinic system with space groups *P*2<sub>1</sub>/*n* and *P**c*, respectively. Each Ru<sup>III</sup> ion in **1** and **2** is bonded to four chloride ions and one (**1**) or two (**2**) nitrogen atoms from guanine molecules and one sulfur atom (**1**) of a dmsO solvent molecule, generating axially compressed octahedral geometries in both cases. In their crystal packing, the Ru<sup>III</sup> complexes are connected through an extended network of N-H···Cl hydrogen bonds and π···Cl intermolecular interactions, forming novel supramolecular structures of this paramagnetic 4d ion. Variable-temperature dc magnetic susceptibility data were obtained from polycrystalline samples of **1** and **2** and their plots show a different magnetic behavior. While **1** is a ferromagnetic compound at low temperature, **2** exhibits a behavior of magnetically isolated mononuclear Ru<sup>III</sup> complexes with *S* = 1/2. The study on ac magnetic susceptibility data reveal slow relaxation of the magnetization, when external dc fields are applied, only for **2**. These results highlight the presence of field-induced single-ion magnet (SIM) behavior for this mononuclear guanine-based Ru<sup>III</sup> complex.

**Keywords:** ruthenium; crystal structures; ferromagnetic coupling; molecular magnetism; single-ion magnet



**Citation:** Orts-Arroyo, M.; Moliner, N.; Lloret, F.; Martínez-Lillo, J. Ferromagnetic Coupling and Single-Ion Magnet Phenomenon in Mononuclear Ruthenium(III) Complexes Based on Guanine Nucleobase. *Magnetochemistry* **2022**, *8*, 93. <https://doi.org/10.3390/magnetochemistry8080093>

Academic Editor: Redha Taiar

Received: 22 July 2022

Accepted: 13 August 2022

Published: 17 August 2022

**Publisher's Note:** MDPI stays neutral with regard to jurisdictional claims in published maps and institutional affiliations.



**Copyright:** © 2022 by the authors. Licensee MDPI, Basel, Switzerland. This article is an open access article distributed under the terms and conditions of the Creative Commons Attribution (CC BY) license (<https://creativecommons.org/licenses/by/4.0/>).

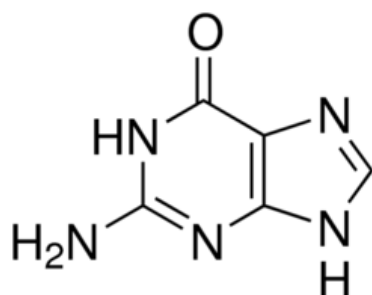
## 1. Introduction

Heteroleptic mononuclear Ru(III) complexes are especially relevant for the study of molecular systems with very appealing biological and biochemical properties [1]. The most successful examples of Ru(III) complexes are prepared with imidazole and indazole ligands, namely the anionic complexes *trans*-[tetrachloro(dimethyl sulfoxide)(imidazole)ruthenate(III)] (NAMI-A) and *trans*-[tetrachlorobis(indazole)ruthenate(III)] (KP1019), which are effective anticancer and antimetastatic compounds that have been investigated in clinical trials [2,3]. Most metal-based anti-tumor compounds interact strongly with DNA, however, NAMI-A acts as an inhibitor of the metastatic potential of tumor and its activity is not related with DNA binding in cancer cells [4].

Similar studies have been performed on ruthenium complexes based on nitrogenous bases [5–8]. In 2004, the first guanine-based Ru(III) compound of formula *trans*-[RuCl<sub>4</sub>(Hgua)(dmsO)]·2H<sub>2</sub>O (Hgua = monoprotonated guanine) was investigated [5]. It was prepared by refluxing a mixture of *trans*-[RuCl<sub>4</sub>(dmsO)<sub>2</sub>]<sup>−</sup> complex and acyclovir in ethanol and HCl. It was characterized by single-crystal X-ray diffraction and the in vitro antitumor activity was also evaluated [5], but the study of its magnetic properties, as for the most of these mononuclear Ru<sup>III</sup> complexes, remain largely unexplored. Indeed, in the literature there exists only one mononuclear Ru<sup>III</sup> complex exhibiting Single-Ion Magnet (SIM) behavior reported up to date, the Ru<sup>III</sup> system of formula [RuCl<sub>3</sub>(PPh<sub>3</sub>)<sub>2</sub>(MeCN)]

(PPh<sub>3</sub> = triphenylphosphine) [9]. This low number of works dealing with Ru(III)-based SIMs could be due to the complexity of the treatment of the experimental magnetic data of this 4d ion with a <sup>2</sup>T<sub>g</sub> ground term and orbital contribution.

In this work, we report the synthesis, crystal structure and the study of the magnetic properties of two Ru<sup>III</sup> complexes of formula *trans*-[RuCl<sub>4</sub>(Hgua)(dmsu)]·2H<sub>2</sub>O (**1**) and *trans*-[RuCl<sub>4</sub>(Hgua)(gua)]·3H<sub>2</sub>O (**2**) [Hgua = protonated guanine (gua), dmsu = dimethyl sulfoxide], which are based on the guanine ligand (Scheme 1). While **1** is a novel ferromagnetic complex, **2** is the second reported example of SIM based on Ru<sup>III</sup> metal ion.



**Scheme 1.** Molecular structure of guanine.

## 2. Results and Discussion

### 2.1. Description of the Crystal Structures

The crystal structure of compound **1** was previously reported elsewhere, and was deposited with identifier ARAMUB [5]. Nevertheless, we include here some structural data and details, which are useful to discuss and understand its magnetic properties (Table 1). Compounds **1** and **2** crystallize in monoclinic space groups (*P*<sub>2</sub><sub>1</sub>/*n* and *Pc* for **1** and **2**, respectively). The crystal structure of **1** is made up of neutral [RuCl<sub>4</sub>(Hgua)(dmsu)] units, whereas that of **2** is made up of neutral [RuCl<sub>4</sub>(Hgua)(gua)] units. In both crystal structures, hydration H<sub>2</sub>O molecules are also present (Figure 1).

**Table 1.** Crystal data along with structure refinement values for compounds **1** and **2**.

Compound	1	2
Formula	C <sub>7</sub> H <sub>16</sub> N <sub>5</sub> O <sub>4</sub> SCl <sub>4</sub> Ru	C <sub>10</sub> H <sub>11</sub> N <sub>10</sub> O <sub>5</sub> Cl <sub>4</sub> Ru
<i>M</i> <sub>r</sub> /g mol <sup>-1</sup>	509.18	594.16
Crystal system	monoclinic	monoclinic
Space group	<i>P</i> <sub>2</sub> <sub>1</sub> / <i>n</i>	<i>Pc</i>
<i>a</i> /Å	9.836(1)	7.319(1)
<i>b</i> /Å	13.326(1)	11.433(1)
<i>c</i> /Å	12.886(1)	11.402(1)
α/°	90(1)	90(1)
β/°	93.04(1)	91.64(1)
γ/°	90(1)	90(1)
<i>V</i> /Å <sup>3</sup>	1686.6(1)	953.7(1)
<i>Z</i>	4	2
<i>D</i> <sub>c</sub> /g cm <sup>-3</sup>	2.005	2.069
μ(Mo-Kα)/mm <sup>-1</sup>	1.708	1.433
<i>F</i> (000)	1012	586
Goodness-of-fit on <i>F</i> <sup>2</sup>	1.435	1.073
<i>R</i> <sub>1</sub> [ <i>I</i> > 2σ( <i>I</i> )]	0.0340	0.0591
<i>wR</i> <sub>2</sub> [ <i>I</i> > 2σ( <i>I</i> )]	0.0350	0.1552

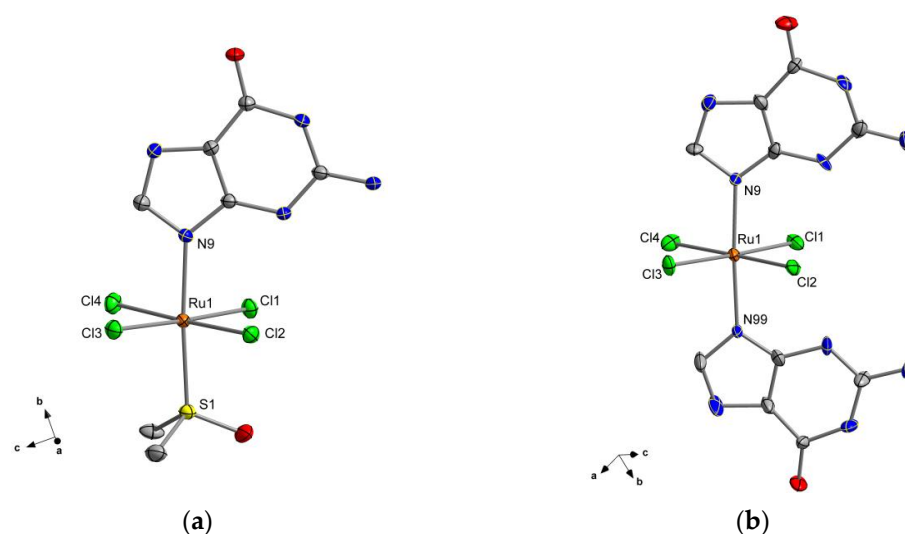


**Figure 1.** View of the  $[\text{RuCl}_4(\text{Hgua})(\text{dmsu})]$  and  $[\text{RuCl}_4(\text{Hgua})(\text{gua})]$  complexes showing the atom numbering of the Ru(III) metal ions together with those of their chromophores in **1** (a) and **2** (b). Water molecules and H atoms have been omitted for clarity. Thermal ellipsoids are shown at the 50% of probability.

In **1**, the Ru(III) ion is six-coordinate and bonded to four chloride ions, one sulfur atom from a dimethyl sulfoxide molecule and one nitrogen atom from one protonated guanine molecule. In **2**, the Ru(III) ion is bonded to four chloride ions and two nitrogen atoms from two guanine ligands (Figure 1). The average values of the Ru-Cl bond lengths are 2.353(1) and 2.350(1) Å for **1** and **2**, respectively. The Ru-N bond length in **1** [2.107(4) Å] is somewhat longer than the average value of the Ru-N bond lengths in **2** [2.081(1) Å]. In both cases, the central metal ion exhibits two axial bonds [Ru-S (**1**) and Ru-N (**1** and **2**)] which are shorter than those of the equatorial bonds [Ru-Cl (**1** and **2**)], generating axially compressed octahedral geometries. In **2**, the two guanine molecules are pretty much planar and form an intramolecular angle between them of approximately  $2.0(1)^\circ$ . In **1** and **2**, the C-C, C-N and C-O bond lengths of the guanine ligands are as previously reported for this molecule when coordinated through N9 to 4d/5d metal centers [10–13].

In the crystal lattice of compound **1**, adjacent  $[\text{RuCl}_4(\text{Hgua})(\text{dmsu})]$  units are connected through H-bonding interactions between carbonyl and amino groups of protonated guanine and dmsu ligands, which generate one-dimensional motifs growing offshore the *b* crystallographic axis [O $\cdots$ N distances covering the range ca. 2.72(1)–2.81(1) Å; (a) =  $-x + 3/2, y + 1/2, -z + 5/2$ ]. These chains are also linked through additional H bonds involving water molecules and forming a 2D framework (Figure 2) [Ow $\cdots$ N and Ow $\cdots$ Cl distances of ca. 2.734(1) and 3.367(1) Å, respectively; (b) =  $x + 3/2, y + 1/2, -z + 3/2$ ]. In **1**, Cl $\cdots$  $\pi$  contacts covering the range 3.24(1)–3.53(1) Å occur and lead to the formation of Ru-Cl $\cdots$  $\pi$  $\cdots$ Cl-Ru interactions between neighboring  $[\text{RuCl}_4(\text{Hgua})(\text{dmsu})]$  units (Figure 2), this being a motif which have been observed previously in systems displaying intermolecular ferromagnetic coupling [14,15].

In the crystal packing of **2**, N–H $\cdots$ (Cl)<sub>2</sub> type hydrogen bonds between amino groups and chloride ions of adjacent  $[\text{RuCl}_4(\text{Hgua})(\text{gua})]$  units form zig-zag 1D motifs, that grow along the crystallographic *c* axis [Cl1 $\cdots$ N22a distance = 3.273 Å and Cl4b $\cdots$ N22 distance = 3.285 Å; being (a) =  $x, -y + 2, z - 1/2$  and (b) =  $x, -y + 2, z + 1/2$ , respectively] (Figure 3). Longer H-bonded N–H $\cdots$ Cl interactions of ca. 3.377 Å connect these chains forming a 2D framework [Cl3 $\cdots$ N2c distance = 3.377 Å; (c) =  $x + 1, -y + 1, z - 1/2$ ] in **2** (Figure 3). The shortest intermolecular Cl $\cdots$ Cl distance is ca. 4.073 Å [Cl1 $\cdots$ Cl3d; (d) =  $x - 1, y, z$ ], whereas the shortest Ru $\cdots$ Ru separation is approximately 6.996 Å [Ru(1) $\cdots$ Ru(1e); (e) =  $x, -y + 1, z - 1/2$ ]. Finally,  $\pi$  $\cdots$ Cl contacts, which cover the range ca. 3.18(1)–3.47(1) Å, stabilize the crystal structure of **2**.

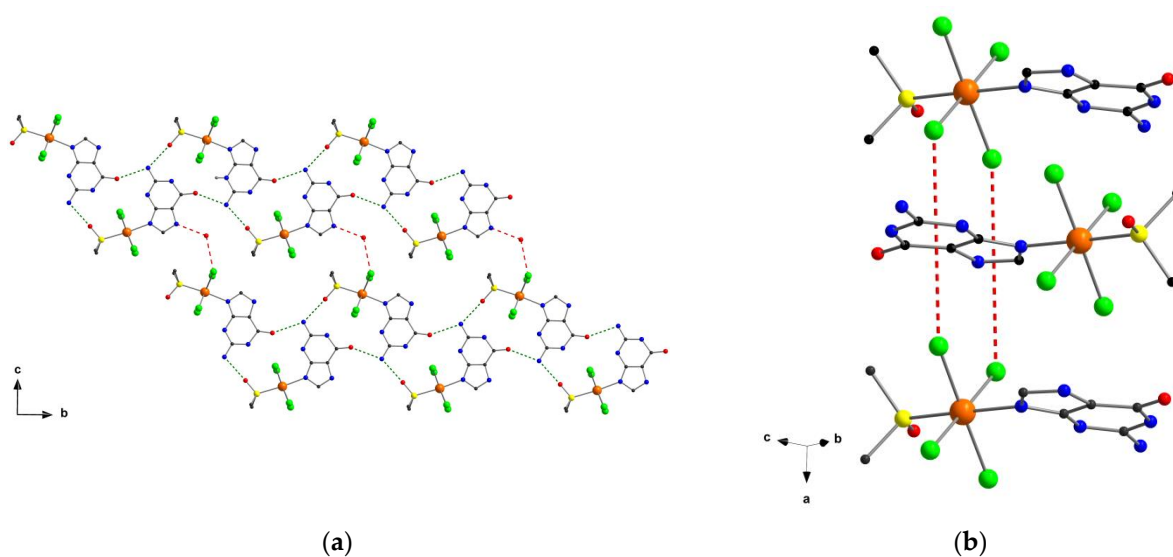


**Figure 2.** (a) A fragment of the crystal of **1** showing hydrogen bonds involving [RuCl<sub>4</sub>(Hgua)(dmsu)] units (dashed green lines), and [RuCl<sub>4</sub>(Hgua)(dmsu)] complexes and water molecules (dashed red lines), along the crystallographic *a* axis; (b) Detail of the Ru–Cl...π...Cl–Ru interaction (dashed red lines) generated by alternate [RuCl<sub>4</sub>(Hgua)(dmsu)] complexes in **1**.

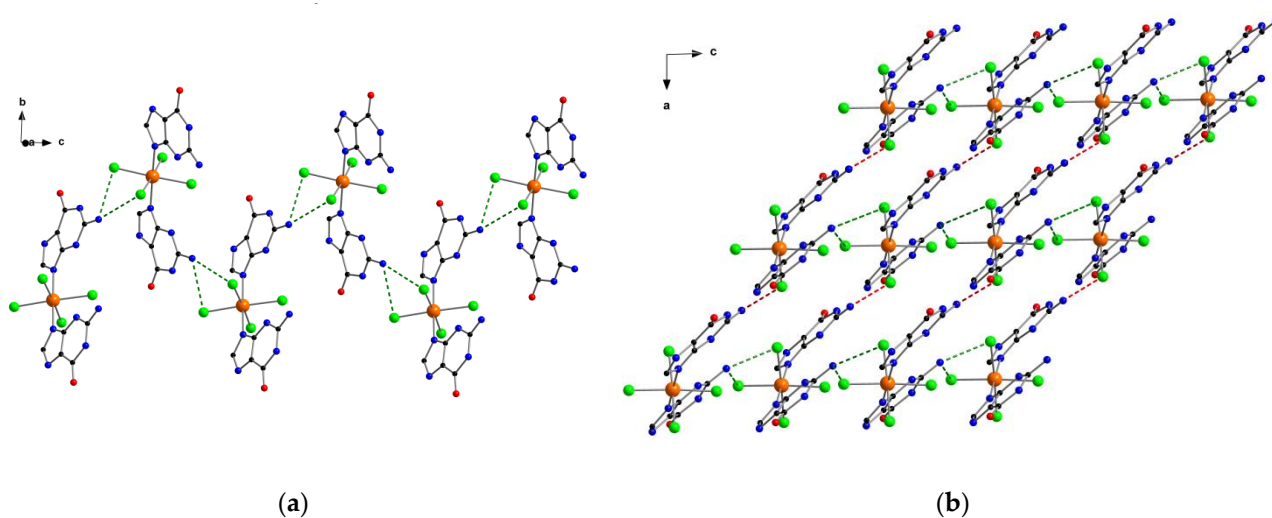


**Figure 3.** (a) Detail of the zig-zag chain formed through bifurcated three-centered hydrogen bonds (dashed green lines) between mononuclear [RuCl<sub>4</sub>(Hgua)(gua)] units in **2**; (b) 2D arrangement of [RuCl<sub>4</sub>(Hgua)(gua)] complexes in **2** connected through additional hydrogen bonds (dashed red lines) and viewed along the crystallographic *b* axis.

## 2.2. Computed Hirshfeld Surfaces

The Hirshfeld surfaces, along with their fingerprint maps, for complexes **1** and **2** are given in Figures 4 and 5, respectively. Shorter contacts are displayed by using red color, whereas white color is assigned to interactions around the van der Waals distance [16,17]. In **1**, the most relevant contacts are H...O interactions involving water molecules and also interactions between carbonyl and amino groups of neighboring guanine molecules. These contacts gave ca. 26.4% of the fingerprint plot (Figure 4). Moreover, intermolecular Cl...H interactions, which are mainly generated by chloride ions and water molecules, cover approximately 21.8% of the full fingerprint plot of **1** (Figure 4). In compound **2**, the Cl...H interactions, with a value of 17.5% of the full fingerprint plot, represent a percentage lower than that found in **1**, whereas the H-bonding H...O interactions cover pretty much the same



value in both compounds, this value being approximately 26.5% of the complete fingerprint plot of **2** (Figure 5).

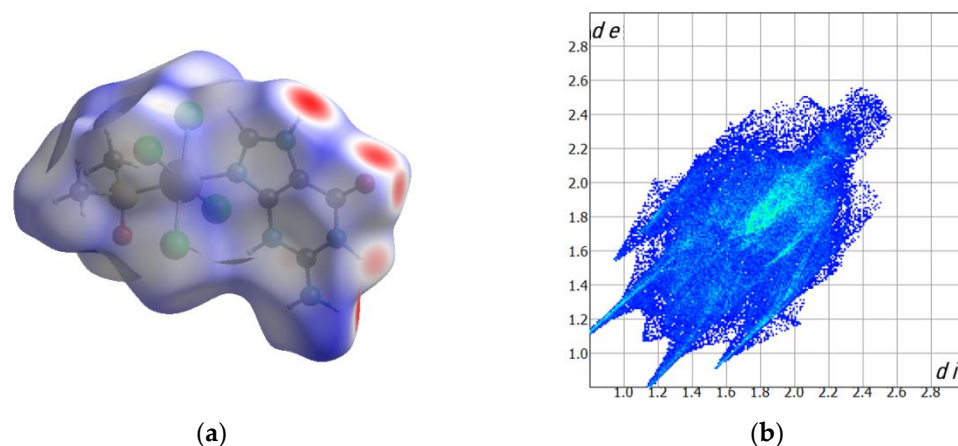


**Figure 4.** (a) Hirshfeld surface of **1** calculated through  $d_{\text{norm}}$  function; (b) Fingerprint maps for compound **1** (see text).

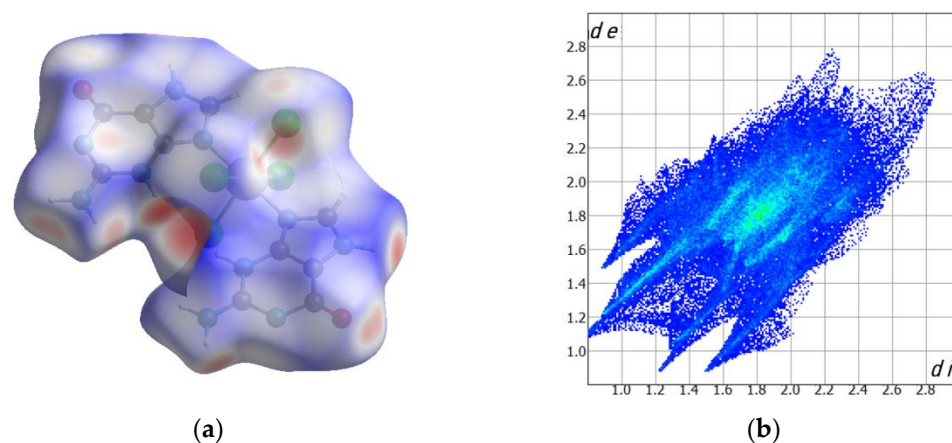


**Figure 5.** (a) Hirshfeld surface of **2** calculated through  $d_{\text{norm}}$  function; (b) Fingerprint maps for compound **2** (see text).

Hirshfeld surfaces of the neutral  $[\text{RuCl}_4(\text{Hgua})(\text{dms})]$  and  $[\text{RuCl}_4(\text{Hgua})(\text{gua})]$  complexes were thus obtained and their intermolecular contacts were studied by means of CrystalExplorer [16,17]. The surfaces were drawn considering the distances from a point on the surface to the nearest atom outside ( $d_e$ ) and inside ( $d_i$ ) their surfaces. Any restriction associated to the size of the involved atoms was corrected through a normalized distance, named  $d_{\text{norm}}$ , which was analyzed as previously done [18–20].

### 2.3. Magnetic Properties

#### 2.3.1. Dc Magnetic Susceptibility

The magnetic properties of **1** and **2** were investigated through direct current (dc) magnetic susceptibility measurements on polycrystalline samples in the range of temperature 300–2 K and along with an external dc magnetic field ( $H_{\text{dc}} = 0.5$  T).  $\chi_{\text{M}}T$  vs.  $T$  plots for compounds **1** and **2** [ $\chi_{\text{M}}$  being the molar magnetic susceptibility per Ru(III) ion] are given in Figure 6. At  $T = 300$  K,  $\chi_{\text{M}}T$  values are approximately 0.58 (**1**) and 0.54  $\text{cm}^3 \text{mol}^{-1} \text{K}$  (**2**), which are very close to those earlier published for mononuclear Ru(III) compounds with low-spin configuration ( $t_{2g}^5$ ) and  $S = 1/2$  for this  $4d^5$  metal ion [21–24]. Upon cooling,  $\chi_{\text{M}}T$  for **1** decreases constantly to ca. 70 K and then more slowly with decreasing temperature, reaching a minimum value of 0.49  $\text{cm}^3 \text{mol}^{-1} \text{K}$  at 30 K. Then, it increases gradually to a maximum value of ca. 0.66  $\text{cm}^3 \text{mol}^{-1} \text{K}$  at 2.0 K (Figure 6). In contrast,  $\chi_{\text{M}}T$  for **2** continuously

decreases with decreasing temperature, showing a linear dependence and reaching a final value of approximately  $0.46 \text{ cm}^3 \text{ mol}^{-1} \text{ K}$  at 2.0 K (Figure 6). The decrease observed for the  $\chi_{\text{M}}T$  value of both compounds at medium-high temperature would occur as a result of the spin-orbit coupling (SOC) of the  $^2T_{2g}$  ground term and its orbital contribution [21,22]. The increase of the  $\chi_{\text{M}}T$  value observed at low T values for **1** would indicate the phenomenon of an unprecedented intermolecular ferromagnetic exchange in a mononuclear Ru(III) complex. This magnetic behavior has been previously studied in complexes containing a magnetically-active 5d ion, but never before on a paramagnetic 4d metal ion [14,15].

$$\hat{H} = -\kappa L\hat{S} + \Delta[L_Z^2 - (1/3)L(L + 1)] + \beta H(-\kappa L + 2\hat{S}) \quad (1)$$

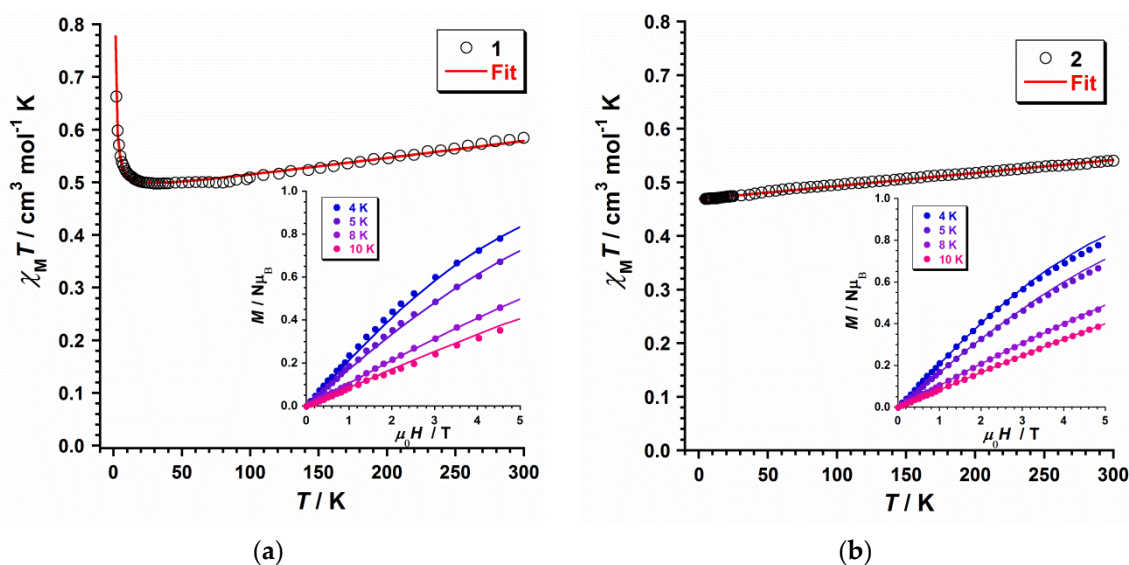


**Figure 6.** (a) Plot of  $\chi_{\text{M}}T$  vs.  $T$  obtained for compound **1**, the solid red line being the best fit. The inset displays the  $M$  vs.  $H$  plot for **1**; (b) Plot of  $\chi_{\text{M}}T$  vs.  $T$  obtained for compound **2**, the solid red line being the best fit. The inset displays the  $M$  vs.  $H$  plot for **2**.

To investigate the magnetic properties of **1** and **2**, the Hamiltonian of equation (1) and its theoretical expression for the magnetic susceptibility, adding a  $\theta$  parameter to explain any intermolecular interaction, was used as previously done for similar complexes with  $S = 1/2$  [25,26]. Besides, the PHI program was employed for comparing the results of some of the fitted values [27]. The three sections in equation (1) can be assigned to the SOC, the field-ligand axial distortion and the Zeeman effect, respectively. It deserves to be mentioned that the three main parameters in Equation (1) [considering  $L = 1$ ,  $S = 1/2$  and  $g_{\parallel} = g_{\perp} = g$  for both **1** and **2**], namely, energy gap ( $\Delta$ ), orbital reduction factor ( $\kappa$ ) and the spin-orbit coupling constant ( $\lambda$ ), are strongly correlated [25,26]. The experimental data of the  $\chi_{\text{M}}T$  vs.  $T$  curves of **1** and **2** can be reproduced with the following parameters:  $\Delta = 913 \text{ cm}^{-1}$ ,  $\kappa = 0.86$ ,  $\lambda = -865 \text{ cm}^{-1}$  and  $\theta = +0.57 \text{ cm}^{-1}$  for **1** and  $\Delta = 1140 \text{ cm}^{-1}$ ,  $\kappa = 0.81$  and  $\lambda = -885 \text{ cm}^{-1}$  for **2**. Besides, the  $g$  and  $\theta$  values were in good agreement with the simulation obtained through PHI program [ $g = 2.26$ ,  $\theta = +0.57 \text{ cm}^{-1}$  and  $\chi_{\text{TIP}} = 326 \times 10^{-6} \text{ cm}^3 \text{ mol}^{-1}$  for **1** and  $g = 2.23$ , and  $\chi_{\text{TIP}} = 244 \times 10^{-6} \text{ cm}^3 \text{ mol}^{-1}$  for **2**] and were used to simultaneously fit the field dependence of the molar magnetization ( $M$ ) plots at several temperatures for **1** and **2** [9], which are given in the respective insets of Figure 6. In general, the computed curves fit well the experimental data at the studied temperatures. The parameters thus obtained are very close to those of earlier published Ru(III) compounds [21–24]. The positive  $\theta$  value obtained for **1** would indicate the presence of a ferromagnetic exchange coupling for this compound. It is well-known that short halogen...halogen intermolecular contacts can transmit antiferromagnetic couplings between neighboring paramagnetic metal ions [28–34], but ferromagnetic exchange

couplings thus obtained are uncommon [14,15]. A suitable spatial arrangement of the mononuclear  $[\text{RuCl}_4(\text{Hgua})(\text{gua})]$  units with  $\text{Ru}-\text{Cl}\cdots\pi\cdots\text{Cl}-\text{Ru}$  interactions, as shown in Figure 2b, would generate a spin polarization by means of guanine rings between close  $[\text{RuCl}_4(\text{Hgua})(\text{gua})]$  units, and would explain the unprecedented ferromagnetic behavior observed only for 1.

### 2.3.2. Ac Magnetic Susceptibility

Alternating current (ac) magnetic susceptibility studies on polycrystalline samples of 1 and 2 were carried out, and it was observed that none of them showed out-of-phase ac signals ( $\chi''_M$ ) at  $H_{\text{dc}} = 0$  G. Nonetheless, compound 2 displays ac signals at low temperatures when an external dc magnetic field is utilized ( $H_{\text{dc}} = 2500$  and 5000 G). In the case of compound 1, structural factors and/or a strong quantum tunneling of the magnetization (QTM), would cancel any slow relaxation of the magnetization for this other mononuclear Ru(III) complex. The features observed for 2 are characteristic of compounds displaying slow relaxation of magnetization, what is called Single-Ion Magnet (SIM) behavior when they are mononuclear systems [19,35]. These out-of-phase ac signals obtained at 2500 and 5000 G are given as  $\chi''_M$  vs.  $\nu$  plots in Figure 7. As one can observe, the number of  $\chi''_M$  maxima, as well as their intensity, increase with increasing the utilized dc magnetic field. Besides, these  $\chi''_M$  maxima shift to higher frequencies with increasing the external magnetic field (Figure 7).

$$\tau^{-1} = \tau^{-1}_{\text{ORBACH}} + \tau^{-1}_{\text{DIRECT}} + \tau^{-1}_{\text{RAMAN}} + \tau^{-1}_{\text{QTM}} \quad (2)$$

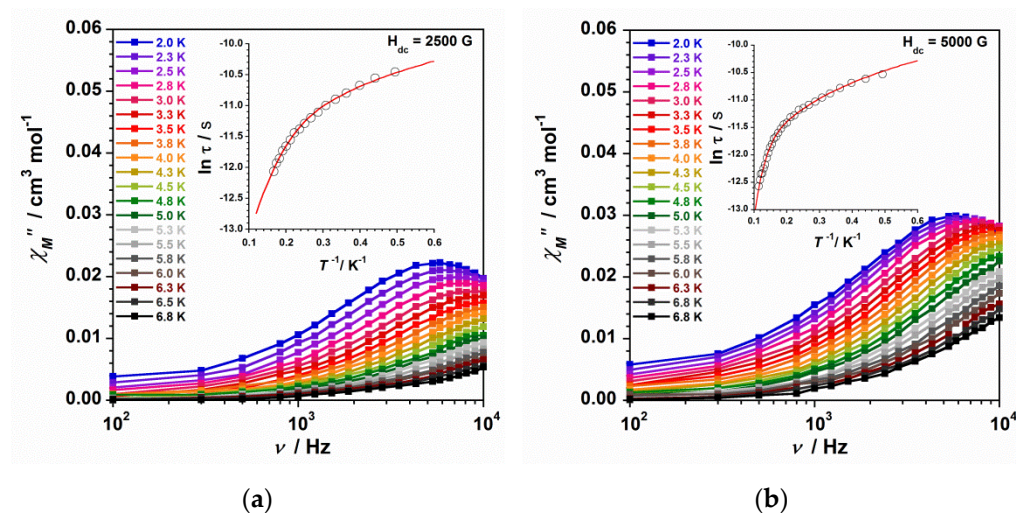


**Figure 7.** (a) Out-of-phase ac susceptibility vs. frequency plot under an external dc field of 2500 G for 2. The inset is the  $\ln(\tau)$  vs.  $1/T$  plot with the fit considering the contribution of two relaxation mechanisms (direct + Raman); (b) Out-of-phase ac susceptibility vs. frequency plot under an external dc field of 5000 G for 2. The inset is the  $\ln(\tau)$  vs.  $1/T$  plot with the fit considering the contribution of two relaxation mechanisms (direct + Raman).

Through the data of the out-of-phase ac susceptibility, the  $\ln(\tau)$  vs.  $1/T$  plots at 2500 and 5000 G were obtained for complex 2 (insets in Figure 7). These data draw curved lines which would account for the occurrence of at least two relaxation processes in compound 2. As a result, the whole  $\ln(\tau)$  vs.  $1/T$  curve could be fitted through equation (2), where several mechanisms for spin-lattice relaxation of magnetization could be examined, that is, Orbach [ $\tau_0^{-1} \exp(-U_{\text{eff}}/k_{\text{B}}T)$ ; with  $\tau_0$  being the preexponential factor,  $\tau$  is the relaxation time,  $U_{\text{eff}}$  is the anisotropy energy barrier to the magnetization reorientation, and  $k_{\text{B}}$  is the Boltzmann constant], direct ( $AT$ ), Raman ( $CT^n$ ), and Quantum Tunneling (QTM). All these relaxation processes were analyzed during the fitting method of the  $\ln(\tau)$  vs.  $1/T$  curves for 2, even though the best fits were obtained when considering the Orbach and



direct mechanisms and the direct + Raman mechanisms. Thus, taking into account only Orbach and direct processes, the best least-squares fit of the experimental data of **2** gave as result:  $\tau_o = 2.6 \times 10^{-7}$  s,  $U_{\text{eff}} = 17.1 \text{ cm}^{-1}$  and  $A = 17,464 \text{ s}^{-1} \text{ K}^{-1}$  for data obtained at 2500 G and  $\tau_o = 1.7 \times 10^{-8}$  s,  $U_{\text{eff}} = 36.6 \text{ cm}^{-1}$  and  $A = 17,454 \text{ s}^{-1} \text{ K}^{-1}$  for data obtained at 5000 G. If we consider only direct and Raman processes, the best least-squares fit of the experimental data of **2** give the following values:  $A = 16,914 \text{ s}^{-1} \text{ K}^{-1}$ ,  $C = 18.52 \text{ s}^{-1} \text{ K}^{-n}$  and  $n = 4.4$  for data obtained at 2500 G and  $A = 17,330 \text{ s}^{-1} \text{ K}^{-1}$ ,  $C = 0.04 \text{ s}^{-1} \text{ K}^{-n}$  and  $n = 7.0$  for data obtained at 5000 G. From these results, which are somewhat unsimilar to those of other SIMs of metal ions with  $S = 1/2$  [36,37], it is worthy to point out that the energy barrier value ( $U_{\text{eff}}$ ) increases with increasing field, the external dc magnetic field of 5000 G being optimal for **2**. Indeed, the values of the  $U_{\text{eff}}$  parameter computed for **2** are higher than that reported for the first Ru(III)-based SIM, the  $[\text{RuCl}_3(\text{PPh}_3)_2(\text{MeCN})]$  complex, with  $\tau_o = 9.8 \times 10^{-6}$  s and  $U_{\text{eff}} = 15.3 \text{ cm}^{-1}$ , these values being obtained through the Arrhenius equation [9]. Nevertheless, for this other Ru(III)-based SIM, it was suggested a phonon-bottlenecked direct relaxation for temperatures up to 10 K [9]. The  $n > 4$  values obtained for **2** fall into the range typical of metal ions with relaxation through optical and acoustic Raman-like process, this fact suggesting that only a phonon-bottlenecked direct process could not be expected in the relaxation dynamics of compound **2**.

In any case, this comparison shows that both Ru(III) SIMs display relaxation dynamics with distinct relaxation pathways and further detailed magnetic and theoretical studies performed on different Ru(III) complexes will be necessary to correctly understand the relaxation dynamics of Ru(III)-based SIMs.

### 3. Materials and Methods

#### 3.1. Reagents and Instruments

All the synthesis were carried out under aerobic conditions, by using reagents as received. The ruthenium precursor  $(\text{PPh}_4)_2[\{\text{RuCl}_4(\text{H}_2\text{O})\}_2(\mu\text{-O})]\cdot 4\text{H}_2\text{O}$  was obtained following the synthetic method previously described in the literature [18]. SEM-EDX analyses were obtained through a Hitachi S-4800 field emission scanning electron microscope, and elemental analyses (C, H, N) were performed by the Central Service for the Support to Experimental Research (SCSIE) at the University of Valencia (Hitachi High-Tech, GLOBAL). Infrared spectra of **1** and **2** were recorded with a PerkinElmer Spectrum 65 FT-IR spectrometer (4000–400  $\text{cm}^{-1}$  region, PerkinElmer, Inc., Waltham, MA, USA) (Figure S1). Variable-temperature, solid-state (dc and ac) magnetic susceptibility data down to 2.0 K were collected on a Quantum Design MPMS-XL SQUID magnetometer equipped with a 5 T dc magnet (Quantum Design, San Diego, CA, USA). Experimental magnetic data were corrected for the diamagnetic contributions of the involved atoms by using Pascal's constants [38].

#### 3.2. Preparation of the Compounds

##### 3.2.1. Synthesis of $[\text{RuCl}_4(\text{Hgua})(\text{dmsO})]\cdot 2\text{H}_2\text{O}$ (**1**)

Guanine (0.06g, 0.40 mmol) was dissolved in a dmsO:HCl mixture (20 mL, 1.0 M, 5:1, *v/v*) and added drop by drop to a refluxing solution of  $(\text{PPh}_4)_2[\{\text{RuCl}_4(\text{H}_2\text{O})\}_2(\mu\text{-O})]\cdot 4\text{H}_2\text{O}$  (0.198 g, 0.15 mmol) in dmsO (30 mL). Then, the reflux was kept for 24 h. The resulting reddish-brown solution was filtered and then heated at 60 °C until the solvent was left to evaporate. The solid residue was collected with HCl (10 mL, 1.0 M) and the generated solution was filtered. EtOH (10 mL) was poured to the final solution that was left to evaporate at room temperature. Red crystals of **1** were obtained in 2 weeks. Yield: ca. 45%. Anal. Calcd. for  $\text{C}_7\text{H}_{16}\text{Cl}_4\text{N}_5\text{O}_4\text{SRu}$  (**1**): C, 16.5; H, 3.2; N, 13.8%. Found: C, 16.7; H, 3.4; N, 13.7%. SEM-EDX analysis gave 1:1 (Ru/S) and 1:4 (Ru/Cl) molar ratios for **1**. IR (KBr pellets/ $\text{cm}^{-1}$ ): the absorption associated to  $\text{H}_2\text{O}$  molecule occurs at 3423br and bands assigned to the coordinated/protonated guanine and dmsO appear at 3240(m), 3194(s), 3117(w), 3005(w), 1718(s), 1669(vs), 1635(m), 1578(m), 1457(m), 1457(m), 1406(m), 1385(m), 1158(m), 1099(s), 765(m), 667(m), 545(m), and 497(m).

### 3.2.2. Synthesis of $[\text{RuCl}_4(\text{Hgua})(\text{gua})]\cdot 3\text{H}_2\text{O}$ (**2**)

$\text{K}_2[\text{RuCl}_5(\text{H}_2\text{O})]$  (11.2 mg, 0.03 mmol) and guanine (6.80 mg, 0.03 mmol) were reacted by means of a solvothermal synthesis in HCl (2.5 mL, 6.0 M) at 90 °C for two days, then a 48 h cooling process took place to room temperature. Orange cubes of **2** were thus obtained. Yield: ca. 35%. Anal. Calcd. for  $\text{C}_{10}\text{H}_{17}\text{Cl}_4\text{N}_{10}\text{O}_5\text{Ru}$  (**2**): C, 20.0; H, 2.9; N, 23.3%. Found: C, 20.3; H, 2.9; N, 23.6%. SEM-EDX analysis gave a 1:4 (Ru/Cl) molar ratio for **2**. IR peaks (KBr pellets,  $\nu/\text{cm}^{-1}$ ): 3402(m), 3330(sh), 3220(m), 3123(m), 2568(w), 2924(w), 1732(s), 1669(vs), 1635(s), 1559(m), 1473(m), 1456(m), 1370(m), 1300(w), 1258(w), 1204(m), 1149(s), 1052(m), 976(m), 760(s), 709(m), and 668(m).

### 3.3. X-ray Data Collection and Structure Refinement

X-ray diffraction data from a single crystal of dimensions  $0.13 \times 0.10 \times 0.09 \text{ mm}^3$  (**2**) were collected on a Bruker D8 Venture diffractometer with graphite-monochromated Mo- $\text{K}\alpha$  radiation ( $\lambda = 0.71073 \text{ \AA}$ ). The resulting crystal and refinement parameters for **1** and **2** are given in Table 1. The structure of **2** was solved by standard direct methods and in turn completed by Fourier recycling by using the SHELXTL software packages (Shelxtl-2018/1, Bruker Analytical X-ray Instruments, Madison, WI, USA). The model thus obtained was refined through version 2018/1 of SHELXL against  $F^2$  on all data by full-matrix least squares [39]. All non-hydrogen atoms were refined anisotropically. The hydrogen atoms of the guanine molecules were set in calculated positions and refined isotropically by using the riding model. The H atoms of the disordered  $\text{H}_2\text{O}$  molecules in **2** were neither detected nor included in the model. Graphical manipulations were carried out through DIAMOND [40]. CCDC code for **2**: 2191993.

## 4. Conclusions

In summary, we have characterized magnetostructurally two novel mononuclear guanine-based Ru(III) compounds of formula *trans*- $[\text{RuCl}_4(\text{Hgua})(\text{dmsO})]\cdot 2\text{H}_2\text{O}$  (**1**) and *trans*- $[\text{RuCl}_4(\text{Hgua})(\text{gua})]\cdot 3\text{H}_2\text{O}$  (**2**) [Hgua = protonated guanine (gua), dmsO = dimethyl sulfoxide]. The two  $\text{Ru}^{\text{III}}$  complexes are self-assembled through an extended network of N-H $\cdots$ Cl hydrogen bonds and  $\pi\cdots\text{Cl}$  intermolecular contacts, which generates novel supramolecular structures based on this 4d metal ion. The investigation of the magnetic properties of **1** and **2** by means of dc magnetic susceptibility data reveals a different magnetic behavior. While **1** is a ferromagnetic compound at low temperatures, **2** exhibits a behavior characteristic of magnetically isolated mononuclear Ru(III) complexes with  $S = 1/2$ . In addition, the ac magnetic susceptibility experimental data reveal slow relaxation of the magnetization in the presence of external dc fields only for **2**, hence indicating the occurrence of field-induced single-ion magnet (SIM) behavior in this mononuclear guanine-based Ru(III) complex. In fact, the  $U_{\text{eff}}$  value for **1** is higher than that of an earlier published Ru(III)-based SIM. Anyway, more theoretical and experimental studies will need to fully understand the relaxation dynamics of the very interesting Ru(III)-based SIMs.

**Supplementary Materials:** The following supporting information can be downloaded at: <https://www.mdpi.com/article/10.3390/magnetochemistry8080093/s1>. Figure S1 and X-ray crystallographic data in CIF format for compound **2**.

**Author Contributions:** Conceptualization, F.L. and J.M.-L.; funding acquisition, F.L. and J.M.-L.; methodology, M.O.-A., N.M. and J.M.-L.; investigation, M.O.-A., N.M., F.L. and J.M.-L.; formal analysis, M.O.-A., N.M. and J.M.-L.; writing—original draft preparation, J.M.-L.; writing—review and editing, J.M.-L. All authors have read and agreed to the published version of the manuscript.

**Funding:** This research was funded by the VLC-BIOCLINIC Program of the University of Valencia [Project PI-2021-007-DIRUGEN] and the Spanish Ministry of Science and Innovation [Projects PID2019-109735GB-I00 and CEX2019-000919-M (Excellence Unit “María de Maeztu”)].

**Institutional Review Board Statement:** Not applicable.

**Informed Consent Statement:** Not applicable.

**Data Availability Statement:** The raw data that support the findings of this study are available from the corresponding author upon reasonable request.

**Acknowledgments:** M.O.A. thanks the Spanish “FPI fellowships” Program.

**Conflicts of Interest:** The authors declare no conflict of interest.

## References

1. Li, F.; Collins, J.G.; Keene, F.R. Ruthenium complexes as antimicrobial agents. *Chem. Soc. Rev.* **2015**, *44*, 2529–2542. [[CrossRef](#)]
2. Hartinger, C.G.; Zorbas-Seifried, S.; Jakupec, M.A.; Kynast, B.; Zorbas, H.; Keppler, B.K. From bench to bedside—preclinical and early clinical development of the anticancer agent indazolium trans-[tetrachlorobis(1H-indazole)ruthenate(III)] (KP1019 or FFC14A). *J. Inorg. Biochem.* **2006**, *100*, 891–904. [[CrossRef](#)]
3. Hartinger, C.G.; Jakupec, M.A.; Zorbas-Seifried, S.; Groessl, M.; Egger, A.; Berger, W.; Zorbas, H.; Dyson, P.J.; Keppler, B.K. KP1019, A New Redox-Active Anticancer Agent—Preclinical Development and Results of a Clinical Phase I Study in Tumor Patients. *Chem. Biodivers.* **2008**, *5*, 2140–2155. [[CrossRef](#)]
4. Ang, W.H.; Casini, A.; Sava, G.; Dyson, P.J. Organometallic ruthenium-based antitumor compounds with novel modes of action. *J. Organomet. Chem.* **2011**, *696*, 989–998. [[CrossRef](#)]
5. Turel, I.; Pečanac, M.; Golobič, A.; Alessio, E.; Serli, B.; Bergamo, A.; Sava, G. Solution, solid state and biological characterization of ruthenium(III)-DMSO complexes with purine base derivatives. *J. Inorg. Biochem.* **2004**, *98*, 393–401. [[CrossRef](#)]
6. Correa, R.S.; Freire, V.; Barbosa, M.I.F.; Bezerra, D.P.; Bomfim, L.M.; Moreira, D.R.M.; Soares, M.B.P.; Ellena, J.; Batista, A.A. Ru(II)-thymine complexes: New metallodrug candidates against tumor cells. *N. J. Chem.* **2018**, *42*, 6794–6802. [[CrossRef](#)]
7. Silva, S.L.R.; Baliza, I.R.S.; Dias, R.B.; Sales, C.B.S.; Rocha, C.A.G.; Soares, M.B.P.; Correa, R.S.; Batista, A.A.; Bezerra, D.P. Ru(II)-thymine complex causes DNA damage and apoptotic cell death in human colon carcinoma HCT116 cells mediated by JNK/p38/ERK1/2 via a p53-independent signaling. *Sci. Rep.* **2019**, *9*, 11094. [[CrossRef](#)] [[PubMed](#)]
8. Orts-Arroyo, M.; Gutiérrez, F.; Gil-Tebar, A.; Ibarrola-Villava, M.; Jiménez-Martí, E.; Silvestre-Llora, A.; Castro, I.; Ribas, G.; Martínez-Lillo, J. A novel adenine-based diruthenium(III) complex: Synthesis, crystal structure, electrochemical properties and evaluation of the anticancer activity. *J. Inorg. Biochem.* **2022**, *232*, 111812. [[CrossRef](#)]
9. Wu, S.-Q.; Miyazaki, Y.; Nakano, M.; Su, S.-Q.; Yao, Z.S.; Kou, H.-Z.; Sato, O. Slow Magnetic Relaxation in a Mononuclear Ruthenium(III) Complex. *Chem. Eur. J.* **2017**, *23*, 10028–10033. [[CrossRef](#)]
10. Colacio, E.; Crespo, O.; Cuesta, R.; Kivekas, R.; Laguna, A.  $[\text{Au}_2(\mu\text{-G})(\mu\text{-dmpe})]\cdot(\text{KBr})_{0.75}\cdot 2\text{H}_2\text{O}$ , a cyclic dinuclear gold(I) complex with an N3,N9-bridging coordination mode of guanine and aurophilic interactions: Synthesis, X-ray crystal structure and luminescence properties (dmpe=1,2-bis(dimethylphosphino)ethane and G=guaninato dianion). *J. Inorg. Biochem.* **2004**, *98*, 595–600.
11. Gaballa, A.S.; Schmidt, H.; Wagner, C.; Steinborn, D. Structure and characterization of platinum(II) and platinum(IV) complexes with protonated nucleobase ligands. *Inorg. Chim. Acta* **2008**, *361*, 2070–2080. [[CrossRef](#)]
12. Gupta, D.; Nowak, R.; Lippert, B. Pt(II) complexes of unsubstituted guanine and 7-methylguanine. *Dalton Trans.* **2010**, *39*, 73–84. [[CrossRef](#)] [[PubMed](#)]
13. Orts-Arroyo, M.; Silvestre-Llora, A.; Castro, I.; Martínez-Lillo, J. Molecular Self-Assembly of an Unusual Dinuclear Ruthenium(III) Complex Based on the Nucleobase Guanine. *Crystals* **2022**, *12*, 448. [[CrossRef](#)]
14. Martínez-Lillo, J.; Armentano, D.; De Munno, G.; Marino, N.; Lloret, F.; Julve, M.; Faus, J. A self-assembled tetrameric water cluster stabilized by the hexachlororhenate(IV) anion and diprotonated 2,2'-biimidazole: X-ray structure and magnetic properties. *Cryst. Eng. Comm.* **2008**, *10*, 1284–1287. [[CrossRef](#)]
15. Martínez-Lillo, J.; Pedersen, A.H.; Faus, J.; Julve, M.; Brechin, E.K. Effect of Protonated Organic Cations and Anion- $\pi$  Interactions on the Magnetic Behavior of Hexabromorhenate(IV) Salts. *Cryst. Growth Des.* **2015**, *15*, 2598–2601. [[CrossRef](#)]
16. Spackman, M.A.; Jayatilaka, D. Hirshfeld surface analysis. *Cryst. Eng. Comm.* **2009**, *11*, 19–32. [[CrossRef](#)]
17. Turner, M.J.; McKinnon, J.J.; Wolff, S.K.; Grimwood, D.J.; Spackman, P.R.; Jayatilaka, D.; Spackman, M.A. *Crystal Explorer 17*; University of Western Australia: Perth, Australia, 2017.
18. Orts-Arroyo, M.; Castro, I.; Lloret, F.; Martínez-Lillo, J. Molecular Self-Assembly in a Family of Oxo-Bridged Dinuclear Ruthenium(IV) Systems. *Cryst. Growth Des.* **2020**, *20*, 2044–2056. [[CrossRef](#)]
19. Sanchis-Perucho, A.; Orts-Arroyo, M.; Camús-Hernández, J.; Rojas-Dotti, C.; Escrivà, E.; Lloret, F.; Martínez-Lillo, J. Hexahalorhenate(IV) salts of protonated ciprofloxacin: Antibiotic-based single-ion magnets. *Cryst. Eng. Comm.* **2021**, *23*, 8579–8587. [[CrossRef](#)]
20. Orts-Arroyo, M.; Ten-Esteve, A.; Ginés-Cárdenas, S.; Castro, I.; Martí-Bonmatí, L.; Martínez-Lillo, J. A gadolinium(III) complex based on the thymine nucleobase with properties suitable for magnetic resonance imaging. *Int. J. Mol. Sci.* **2021**, *22*, 4586. [[CrossRef](#)]
21. Yeung, W.F.; Man, W.-L.; Wong, W.-T.; Lau, T.-C.; Gao, S. Ferromagnetic Ordering in a Diamond-Like Cyano-Bridged  $\text{Mn}^{\text{II}}\text{Ru}^{\text{III}}$  Bimetallic Coordination Polymer. *Angew. Chem. Int. Ed.* **2001**, *40*, 3031–3033. [[CrossRef](#)]
22. Toma, L.M.; Toma, L.D.; Delgado, F.S.; Ruiz-Pérez, C.; Sletten, J.; Cano, J.; Clemente-Juan, J.M.; Lloret, F.; Julve, M. Trans-dicyanobis(acetylacetonato)ruthenate(III) as a precursor to build novel cyanide-bridged  $\text{Ru}^{\text{III}}\text{-M}^{\text{II}}$  bimetallic compounds [M = Co and Ni]. *Coord. Chem. Rev.* **2006**, *250*, 2176–2193. [[CrossRef](#)]

23. Armentano, D.; Martínez-Lillo, J. Hexachlororhenate(IV) salts of ruthenium(III) cations: X-ray structure and magnetic properties. *Inorg. Chim. Acta* **2012**, *380*, 118–124. [[CrossRef](#)]
24. Palacios, M.A.; Mota, A.J.; Ruiz, J.; Hänninen, M.M.; Sillanpää, R.; Colacio, E. Diphenoxo-Bridged Ni<sup>II</sup>Ln<sup>III</sup> Dinuclear Complexes as Platforms for Heterotrimetallic (Ln<sup>III</sup>Ni<sup>II</sup>)<sub>2</sub>Ru<sup>III</sup> Systems with a High-Magnetic-Moment Ground State: Synthesis, Structure, and Magnetic Properties. *Inorg. Chem.* **2012**, *51*, 7010–7012. [[CrossRef](#)] [[PubMed](#)]
25. Pacheco, M.; Cuevas, A.; González-Platas, J.; Faccio, R.; Lloret, F.; Julve, M.; Kremer, C. Synthesis, crystal structure and magnetic properties of the Re(II) complexes NBU<sub>4</sub>[Re(NO)Br<sub>4</sub>(L)] (L = pyridine and diazine type ligands). *Dalton Trans.* **2013**, *42*, 15361–15371. [[CrossRef](#)] [[PubMed](#)]
26. Pacheco, M.; Cuevas, A.; González-Platas, J.; Lloret, F.; Julve, M.; Kremer, C. The crystal structure and magnetic properties of 3-pyridinecarboxylate-bridged Re(II)M(II) complexes (M = Cu, Ni, Co and Mn). *Dalton Trans.* **2015**, *44*, 11636–11648. [[CrossRef](#)]
27. Chilton, N.F.; Anderson, R.P.; Turner, L.D.; Soncini, A.; Murray, K.S. PHI: A powerful new program for the analysis of anisotropic monomeric and exchange-coupled polynuclear d- and f-block complexes. *J. Comput. Chem.* **2013**, *34*, 1164–1175. [[CrossRef](#)]
28. González, R.; Chiozzone, R.; Kremer, C.; Guerra, F.; De Munno, G.; Lloret, F.; Julve, M.; Faus, J. Magnetic Studies on Hexaiodorhenate(IV) Salts of Univalent Cations. Spin Canting and Magnetic Ordering in K<sub>2</sub>[ReI<sub>6</sub>] with T<sub>c</sub> = 24 K. *Inorg. Chem.* **2004**, *43*, 3013–3019. [[CrossRef](#)]
29. Martínez-Lillo, J.; Armentano, D.; De Munno, G.; Lloret, F.; Julve, M.; Faus, J. A Two-Dimensional Re<sup>IV</sup>Ag<sup>I</sup> Compound: X-ray Structure and Magnetic Properties. *Cryst. Growth Des.* **2006**, *6*, 2204–2206. [[CrossRef](#)]
30. Martínez-Lillo, J.; Armentano, D.; De Munno, G.; Faus, J. Magneto-structural study on a series of rhenium(IV) complexes containing biimH<sub>2</sub>, pyim and bipy ligands. *Polyhedron* **2008**, *27*, 1447–1454. [[CrossRef](#)]
31. Martínez-Lillo, J.; Faus, J.; Lloret, F.; Julve, M. Towards multifunctional magnetic systems through molecular-programmed self assembly of Re(IV) metalloligands. *Coord. Chem. Rev.* **2015**, *289–290*, 215–237. [[CrossRef](#)]
32. Martínez-Lillo, J.; Kong, J.; Julve, M.; Brechin, E.K. Self-Assembly of the Hexabromorhenate(IV) Anion with Protonated Benzotriazoles: X-ray Structure and Magnetic Properties. *Cryst. Growth Des.* **2014**, *14*, 5985–5990. [[CrossRef](#)]
33. Armentano, D.; Barquero, M.A.; Rojas-Dotti, C.; Moliner, N.; De Munno, G.; Brechin, E.K.; Martínez-Lillo, J. Enhancement of Intermolecular Magnetic Exchange through Halogen···Halogen Interactions in Bisadeninium Rhenium(IV) Salts. *Cryst. Growth Des.* **2017**, *17*, 5342–5348. [[CrossRef](#)]
34. Armentano, D.; Sanchis-Perucho, A.; Rojas-Dotti, C.; Martínez-Lillo, J. Halogen···halogen interactions in the self-assembly of one-dimensional 2,2'-bipyrimidine-based Cu<sup>II</sup>Re<sup>IV</sup> systems. *Cryst. Eng. Comm.* **2018**, *20*, 4575–4581. [[CrossRef](#)]
35. Rojas-Dotti, C.; Sanchis-Perucho, A.; Orts-Arroyo, M.; Moliner, N.; González, R.; Lloret, F.; Martínez-Lillo, J. Field-Induced Single-Ion Magnet Phenomenon in Hexabromo- and Hexaiodorhenate(IV) Complexes. *Magnetochemistry* **2020**, *6*, 20. [[CrossRef](#)]
36. Sanchis-Perucho, A.; Martínez-Lillo, J.J. Ferromagnetic exchange interaction in a new Ir(IV)–Cu(II) chain based on the hexachloroiridate(IV) anion. *Dalton Trans.* **2019**, *48*, 13925–13930. [[CrossRef](#)]
37. Sanchis-Perucho, A.; Martínez-Lillo, J.J. A new family of one-dimensional bromo-bridged Ir(IV)–Cu(II) complexes based on the hexabromoiridate(IV) metalloligand. *Dalton Trans.* **2022**, *51*, 3323–3330. [[CrossRef](#)]
38. Bain, G.A.; Berry, J.F. Diamagnetic Corrections and Pascal's Constants. *J. Chem. Educ.* **2008**, *85*, 532–536. [[CrossRef](#)]
39. *SHELXTL-2018/1*; Bruker Analytical X-ray Instruments. Bruker: Madison, WI, USA, 2018.
40. *DIAMOND 4.5.0*; Crystal Impact GbR. Crystal Impact: Bonn, Germany, 2018.





---



*ARTICLE 2*

*Molecular Self-Assembly of an  
Unusual Dinuclear  
Ruthenium(III) Complex Based  
on the Nucleobase Guanine*



## Article

# Molecular Self-Assembly of an Unusual Dinuclear Ruthenium(III) Complex Based on the Nucleobase Guanine

Marta Orts-Arroyo, Adriana Silvestre-Llora, Isabel Castro  and José Martínez-Lillo \* 

Instituto de Ciencia Molecular (ICMol), Universitat de València, c/Catedrático José Beltrán 2, Paterna, 46980 València, Spain; marta.orts-arroyo@uv.es (M.O.-A.); asillo@alumni.uv.es (A.S.-L.); isabel.castro@uv.es (I.C.)

\* Correspondence: f.jose.martinez@uv.es; Tel.: +34-9635-44460

**Abstract:** The study of crystal structures based on complexes containing purine nucleobases is a significant research subject, mainly regarding the diagnosis and treatment of some diseases and the investigation of genetic mutations and biochemical structures in life sciences. We have obtained and characterized a new dinuclear ruthenium(III) complex based on guanine with the formula  $[\{\text{Ru}(\mu\text{-Cl})(\mu\text{-gua})\}_2\text{Cl}_4]\cdot 2\text{H}_2\text{O}$  (**1**) (gua = guanine). **1** was characterized by means of Fourier transform infrared spectroscopy (FT-IR), scanning electron microscopy and energy dispersive X-ray analysis (SEM-EDX), single-crystal X-ray diffraction (XRD), Hirshfeld surface analysis and cyclic voltammetry (CV). The study of its electrochemical properties allowed us to investigate the presence of guanine molecules when linked to the ruthenium(III) ion in **1**. The well-resolved voltammetric response together with the reliability and stability achieved through **1** could provide a step forward to developing new ruthenium-based platforms, devices and modified electrodes adequate to study this purine nucleobase.

**Keywords:** guanine; ruthenium; FT-IR spectroscopy; Hirshfeld surface; SEM-EDX; cyclic voltammetry



**Citation:** Orts-Arroyo, M.; Silvestre-Llora, A.; Castro, I.; Martínez-Lillo, J. Molecular Self-Assembly of an Unusual Dinuclear Ruthenium(III) Complex Based on the Nucleobase Guanine. *Crystals* **2022**, *12*, 448. <https://doi.org/10.3390/cryst12040448>

Academic Editors: Ana M. Garcia-Deibe and Jesús Sanmartín-Matalobos

Received: 7 March 2022

Accepted: 18 March 2022

Published: 23 March 2022

**Publisher's Note:** MDPI stays neutral with regard to jurisdictional claims in published maps and institutional affiliations.

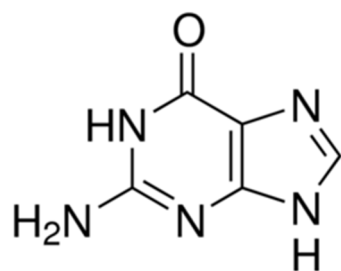


**Copyright:** © 2022 by the authors. Licensee MDPI, Basel, Switzerland. This article is an open access article distributed under the terms and conditions of the Creative Commons Attribution (CC BY) license (<https://creativecommons.org/licenses/by/4.0/>).

## 1. Introduction

Guanine is one of the main nitrogenous bases found in the nucleotides of the nucleic acids (DNA and RNA) present in the cells of living organisms and viruses. Besides being involved in the storage and the expression of genetic information, it participates in many other cellular biochemical processes and structures [1–3]. Given that this purine nucleobase can be present in the fluids of human beings, their levels have been proposed as direct and indirect biomarkers for a variety of diseases and pathologies, such as Alzheimer's disease [4], epilepsy [5] and human immunodeficiency virus (HIV) infection [6,7]. Hence, sensitive and selective methods for determining both this and other purine nucleobases are being investigated in several research areas [8,9].

Ruthenium complexes have undergone significant development in different research areas for the last 20 years [10], displaying a wide variety of technological applications, and ranging from catalysis to anticancer drugs [11–18]. Following our ongoing investigation into biomolecule-based complexes [19–27], we have focused also on the purine nucleobase guanine (Scheme 1). There exists only one guanine-containing Ru(III) complex, of the formula *trans*- $[\text{RuCl}_4(\text{Hgua})(\text{DMSO})]\cdot 2\text{H}_2\text{O}$  (Hgua = protonated guanine), which was reported in 2004 [28]. This compound was characterized by single-crystal X-ray diffraction and its *in vitro* antitumor activity was also evaluated, showing a mild antiproliferative effect but an interesting proadhesive effect [28]. Herein, we report the synthesis and characterization of a new guanine-bridged diruthenium(III) complex, of formula  $[\{\text{Ru}(\mu\text{-Cl})(\mu\text{-gua})\}_2\text{Cl}_4]\cdot 2\text{H}_2\text{O}$  (**1**) (gua = guanine). To our knowledge, **1** is the first dinuclear ruthenium(III) compound based on guanine which has been reported so far.



**Scheme 1.** Molecular structure of guanine.

## 2. Materials and Methods

### 2.1. Reagents and Instruments

Guanine (99.90%) was purchased from Acros Organics and the ruthenium precursor  $K_2[RuCl_5(H_2O)]$  (99.95%) was acquired from Alfa Aesar. The elemental analyses (C, H, N) and X-ray microanalysis were performed through Central Service for the Support to Experimental Research (SCSIE) at the University of Valencia. Images and results of scanning electron microscopy (SEM-EDX) were obtained through a Hitachi S-4800 field emission scanning electron microscope, with 20 kV and 9.0 mm of accelerating voltage and working distance, respectively. Each infrared spectrum (FT-IR) was performed on KBr pellets and was obtained through a PerkinElmer Spectrum 65 FT-IR spectrometer in the 4000–500  $cm^{-1}$  with 25 scans and a spectral resolution of 4  $cm^{-1}$ . The study of the electrochemical properties was carried out on **1** by means of an Autolab/PGSTAT 204 scanning potentiostat at a scan rate working in the 10–250 range ( $mVs^{-1}$ ) and with Metrohm electrodes. CV curves were obtained with a 0.1 M  $(NBu_4)[PF_6]$  solution, as supporting electrolyte, and a  $10^{-3}$  M solution of **1** in dry *N,N'*-dimethylformamide (DMF). A glassy carbon disk of 0.32  $cm^2$  was used as working electrode, polished with 1.0  $\mu m$  diamond powder, which was sonicated and then washed with absolute ethanol and acetone, and air-dried. The AgCl/Ag reference electrode was separated from the test solution through a salt bridge with the solvent and supporting electrolyte. The platinum electrode was auxiliary. The study was performed in a standard electrochemical cell at 20 °C with flowing argon. The studied potential range was from  $-1.5$  to  $+1.5$  V vs. AgCl/Ag. Ferrocene (Fc) was added as an internal standard at the end of the measurements.

### 2.2. Preparation

#### Synthesis of $[Ru(\mu-Cl)(\mu-gua)_2Cl_4] \cdot 2H_2O$ (**1**)

$K_2[RuCl_5(H_2O)]$  (11.2 mg, 0.03 mmol) and guanine (6.80 mg, 0.03 mmol) were reacted through a solvothermal synthesis in HCl (4 mL, 3.0 M) at 90 °C for three days, then a 12 h cooling process took place to room temperature. Dark brown parallelepipeds of **1** were obtained. Yield: ca. 53%. Anal. Calcd. for  $C_{10}H_{10}Cl_6N_{10}O_2Ru_2$  (**1**): C, 16.8; H, 1.4; N, 19.5. Found: C, 16.7; H, 1.7; N, 19.2. SEM-EDX: a molar ratio of 1:3 for Ru/Cl was found for **1**. IR peaks (KBr pellets): 3419(s), 3325(m), 3208(m), 3114(m), 3062(m), 3012(m), 2922(m), 2853(m), 1708(vs), 1635(vs), 1594(m), 1559(m), 1540(s), 1506(w), 1457(m), 1394(s), 1270(w), 1210(m), 1124(w), 1095(w), 983(w), 873(m), 768(m), 704(w), 612(w), 573(w), 474(w)  $cm^{-1}$ .

### 2.3. X-ray Diffraction Data Collection and Structure Refinement

Data collection from a single crystal of **1** (with dimensions of  $0.46 \times 0.13 \times 0.09$   $mm^3$ ) was performed on a Bruker D8 Venture diffractometer with graphite-monochromated  $Mo-K_{\alpha}$  radiation ( $\lambda = 0.71073$  Å). Table 1 summarizes the crystal parameters and refinement results for **1**. The structure of **1** was solved by standard direct methods and then completed by Fourier recycling through the SHELXTL program. The model was refined with version 2018/1 of SHELXL against  $F^2$  on all data by full-matrix least-squares [29]. The non-hydrogen atoms were anisotropically refined, and the H atoms of the guanine molecules were set in calculated positions and refined isotropically. The H atoms of the water molecules in **1** were neither detected nor included in the model, this fact being due

to the thermal disorder observed on the water molecules, which increases the  $R_1$  and  $wR_2$  parameters in this system (Table 1). The graphic manipulations were performed with the DIAMOND program [30] of CCDC 2081706.

**Table 1.** Summary of the crystal data and structure refinement parameters for **1** (see Supplementary Material).

Compound	1
CIF	2081706
Formula	$C_{10}H_{10}Cl_6N_{10}O_4Ru_2$
$M_r/g\ mol^{-1}$	749.12
Crystal system	Monoclinic
Space group	$C2/c$
$a/\text{\AA}$	22.462(4)
$b/\text{\AA}$	11.330(2)
$c/\text{\AA}$	12.446(2)
$\alpha/^\circ$	90
$\beta/^\circ$	122.42(1)
$\gamma/^\circ$	90
$V/\text{\AA}^3$	2673.6(9)
Z	4
$D_c/g\ cm^{-3}$	1.861
$\mu(\text{Mo-K}\alpha)/\text{mm}^{-1}$	1.765
$F(000)$	1448
Goodness-of-fit on $F^2$	1.080
$R_1 [I > 2\sigma(I)]/(\text{all})$	0.0616/0.0745
$wR_2 [I > 2\sigma(I)]/(\text{all})$	0.1775/0.1896

### 3. Results and Discussion

#### 3.1. Synthetic Procedure

The ruthenium(III) precursor  $K_2[\text{RuCl}_5(\text{H}_2\text{O})]$  was made to react with guanine in hydrochloric acid (3.0 M) solutions, thus we prepared a new purine-based ruthenium(III) complex of the formula  $[\{\text{Ru}(\mu\text{-Cl})(\mu\text{-gua})_2\text{Cl}_4\} \cdot 2\text{H}_2\text{O}$  (**1**) (Figure 1). The synthetic procedure was carried out by means of heating this mixture at 90 °C in a solvothermal reaction and, in order to crystallize, the process continued for a further 12 h cooling step to room temperature. In this way, dark brown crystals of **1** were obtained with a satisfactory yield (53%). It is worth mentioning that compound **1** was also obtained by replacing hydrochloric acid with acetic acid, but the yield was too low (less than 10%). These results support the fact that this is an adequate synthesis to prepare purine-based dinuclear ruthenium(III) complexes.

#### 3.2. Infrared Spectroscopy

The infrared (IR) spectra of **1** and that of the free guanine ligand are given in Figure 2. The IR spectrum of guanine has been previously studied [31,32], so that it has been added in this work only for comparison. In general, the vibrational bands mainly associated with N-H symmetric ( $\nu_s$ ) and asymmetric ( $\nu_{as}$ ) stretching for the free guanine molecule were more intense and complex than those of **1** in the ca. 3800–2000  $\text{cm}^{-1}$  region (Figure 2), which would be due to a more ordered hydrogen-bonding network in the crystalline solid for the free nucleobase [31,32]. In the case of the IR spectrum of **1**, the values associated to the vibrational  $\nu_{as}(\text{NH}_2)$  (3325  $\text{cm}^{-1}$ ) and  $\nu_s(\text{NH}_2)$  (3114 and 3062  $\text{cm}^{-1}$ ) bands were very similar to those obtained for the free guanine [31,32] (Figure 2). In the 1800–500  $\text{cm}^{-1}$  region, the most interesting features were the two strong vibrational bands associated to the stretching  $\nu(\text{C}=\text{N})$  and  $\nu(\text{C}=\text{C})$  and bending  $\delta(\text{NH}_2)$ , mainly scissoring, which were found at 1695 and 1672  $\text{cm}^{-1}$  for the guanine molecule [31,32]. In the IR spectrum of **1**, these two vibrational bands were shifted to 1708 and 1635  $\text{cm}^{-1}$ , respectively, with this fact indicating the coordination of the Ru(III) metal ions to guanine molecules in compound **1** (Figure 2).

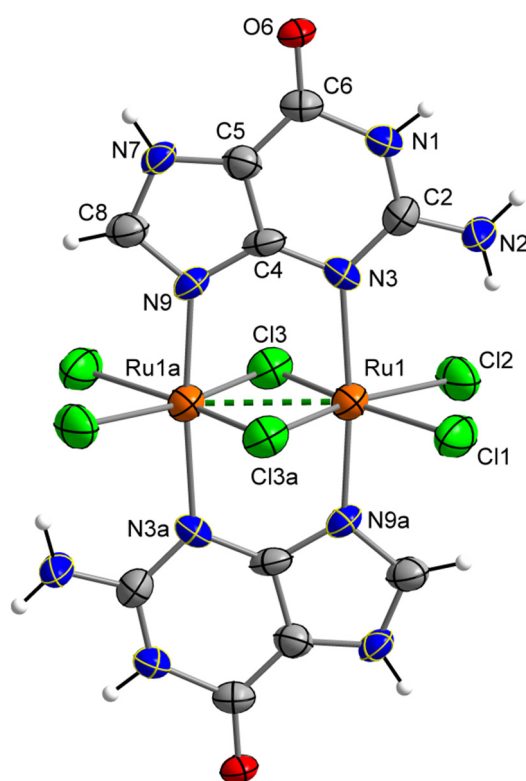


**Figure 1.** Molecular structure of the neutral  $[\{\text{Ru}(\mu\text{-Cl})(\mu\text{-gua})_2\text{Cl}_4\}]$  complex in **1** along with the atom labels scheme, the green-dashed line indicating a metal–metal bond. Water molecules have been omitted for clarity.

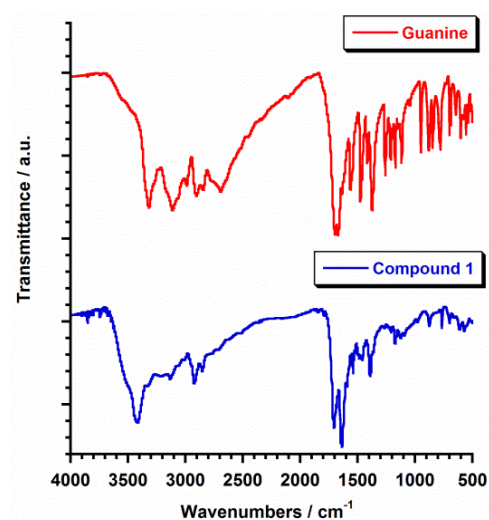


**Figure 2.** FT-IR spectra for guanine (red) and compound **1** (blue).

### 3.3. Description of the Crystal Structure

The crystal structure of **1** was obtained by single-crystal X-ray diffraction. A CSD survey revealed that **1** displays the first reported crystal structure based on a dinuclear Ru(III) compound containing guanine. Compound **1** crystallizes in the monoclinic system with space group  $C2/c$  (Table 1). The crystal structure of **1** is made up of neutral  $[\{\text{Ru}(\mu\text{-Cl})(\mu\text{-gua})_2\text{Cl}_4\}]$  units and  $\text{H}_2\text{O}$  molecules. The asymmetric unit of **1** consists of half a  $[\{\text{Ru}(\mu\text{-Cl})(\mu\text{-gua})_2\text{Cl}_4\}]$  complex and one  $\text{H}_2\text{O}$  molecule (Figure 1).

In this dinuclear complex, each Ru(III) ion is linked to four chloride ions and two nitrogen atoms (these are N3 and N9) from two guanine molecules in an almost regular Oh geometry. The two Ru(III) ions are connected to each other through two guanine molecules and two chloro-bridges (Figure 1). A very short intramolecular Ru $\cdots$ Ru distance [Ru(1) $\cdots$ Ru(1a) = 2.644 Å, (a) =  $-x-1/2, -y+1/2, -z-2$ ] indicates the formation of a metal–metal bond (dashed line in Figure 1). The average values of the Ru–Cl [2.318(1) Å] and Ru–N [2.103(1) Å] bond lengths are in agreement with those values published for previously reported Ru(III) systems with a similar metal environment [17,25].

In the crystal of **1**, H-bonding interactions between neighboring guanine molecules [O(6) $\cdots$ N(7b) distance of ca. 2.745(1) Å, (b) =  $-x, -y, -z-1$ ] afford chains of neutral  $[\{\text{Ru}(\mu\text{-Cl})(\mu\text{-gua})_2\text{Cl}_4\}]$  units (Figure 3). These chains are linked by additional H-bonds involving Cl $^-$  anions and NH $_2$  groups of adjacent guanine molecules [Cl(3) $\cdots$ N(2c) distance of ca. 3.345(1) Å, (c) =  $-x-1/2, y-1/2, -z-3/2$ ], which set up a two-dimensional network. The cohesiveness of the structure is further strengthened by the presence of intermolecular Cl $\cdots$  $\pi$  interactions among  $[\{\text{Ru}(\mu\text{-Cl})(\mu\text{-gua})_2\text{Cl}_4\}]$  units [Cl $\cdots$  $\pi$  interactions ranging with 3.52–3.81 Å values]. The thus packed  $[\{\text{Ru}(\mu\text{-Cl})(\mu\text{-gua})_2\text{Cl}_4\}]$  units generate cavities with a diameter of ca. 13 Å, where most of the water molecules are located in **1** (Figure 4). The supramolecular network is supported by additional H-bonding interactions, which stabilize the crystal structure in compound **1**.

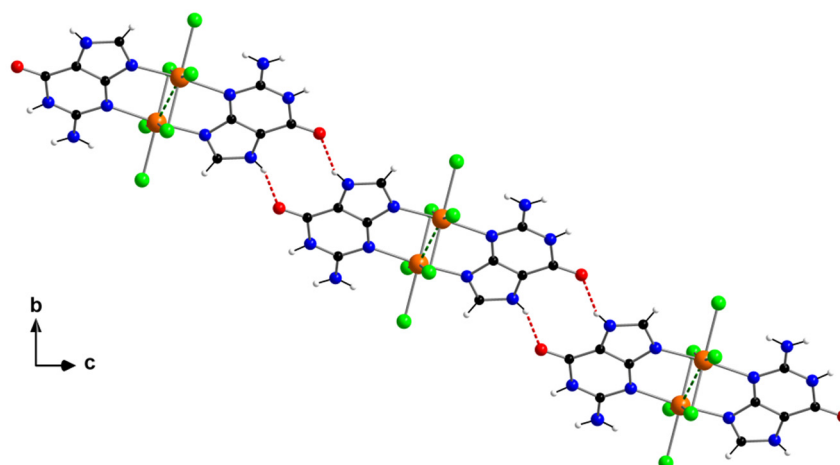


**Figure 3.** View along the crystallographic  $a$  axis of a fragment of the crystal packing of **1**. H-bonding interactions between O atoms and N-H groups of adjacent  $[\{\text{Ru}(\mu\text{-Cl})(\mu\text{-gua})_2\text{Cl}_4\}]$  units are shown as red-dashed lines. Water molecules have been omitted for clarity.

### 3.4. Hirshfeld Surface Analysis

The intermolecular interactions of the neutral  $[\{\text{Ru}(\mu\text{-Cl})(\mu\text{-gua})_2\text{Cl}_4\}]$  complex were further studied through the CrystalExplorer program [33,34]. This program calculated the surfaces which allowed us the qualitative and quantitative investigation as well as the visualization of the main intermolecular contacts in **1** by mapping the distances from the surface to the nearest atom outside ( $d_e$ ) and inside ( $d_i$ ) this surface. Besides, a normalized contact distance called  $d_{\text{norm}}$  was also taken into account to overcome some limitations generated by the atom size [33,34]. The Hirshfeld surfaces for complex **1** are given in Figure 5, the shorter contacts being shown with red color [34]. The intermolecular H $\cdots$ O contacts generated among the N-H and carbonyl groups of adjacent guanine molecules are approximately 16% of the complete fingerprint plot (Figure 5). The Cl $\cdots$ H contacts involving Cl $^-$  anions and N-H groups of neighboring dinuclear  $[\{\text{Ru}(\mu\text{-Cl})(\mu\text{-gua})_2\text{Cl}_4\}]$  units are the main interactions observed on the Hirshfeld surface, which covers ca. 24% (Figure 5). Finally, further O $\cdots$ H contacts involving solvent water molecules and N-H groups of the guanine molecules are close to the 6% of the fingerprint plot (Figure 5).



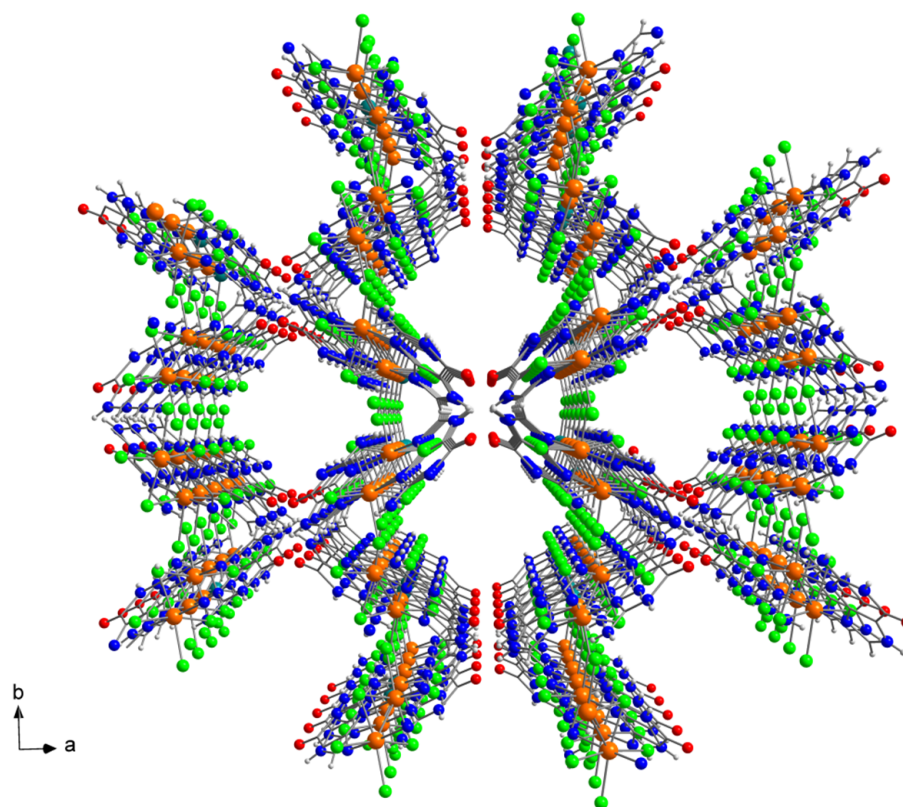


**Figure 4.** View along the crystallographic  $c$  axis of a fragment of the crystal packing of **1**. Water molecules have been omitted for clarity.

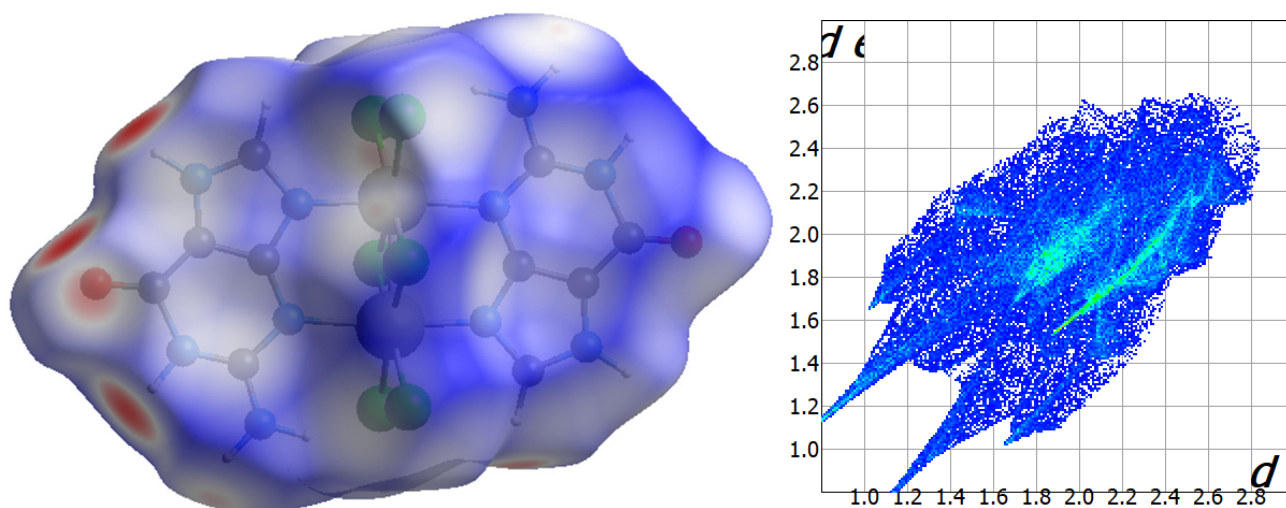
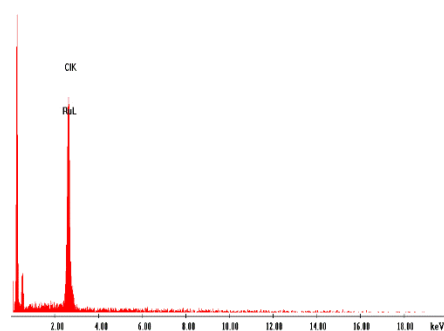


**Figure 5.** Hirshfeld surface mapped with  $d_{\text{norm}}$  function for **1** (left); Full fingerprint plot for the dinuclear Ru(III) complex of **1** (right).

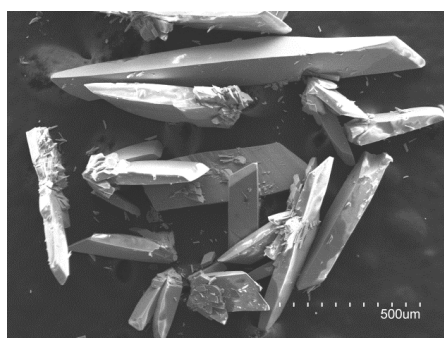
### 3.5. Scanning Electron Microscopy–Energy Dispersive X-ray Analysis

Compound **1** was studied by means of scanning electron microscopy and energy dispersive X-ray analysis (SEM-EDX), these analyses being carried out as previously performed for other ruthenium systems [35,36]. The results of the microanalysis gave a Ru/Cl molar ratio of 1:3 for **1**. A recorded image of **1** is given in Figure 6. Crystals of **1** are shown as crystallized parallelepipeds in Figure 6.





(a)



(b)

**Figure 6.** Energy dispersive X-ray analysis (EDX) spectrum for **1** (a); scanning electron microscopy (SEM) image of crystals of **1** (b).

### 3.6. Cyclic Voltammetry (CV)

The study of the electrochemical properties of compound **1** was performed employing cyclic voltammetry (CV) in *N,N'*-dimethylformamide (DMF), containing 0.1 M [NBu<sub>4</sub>][PF<sub>6</sub>], in the range of potential values of +1.5 and −1.5 V and at 20 °C. The CV curve for **1** is shown in Figure 7.

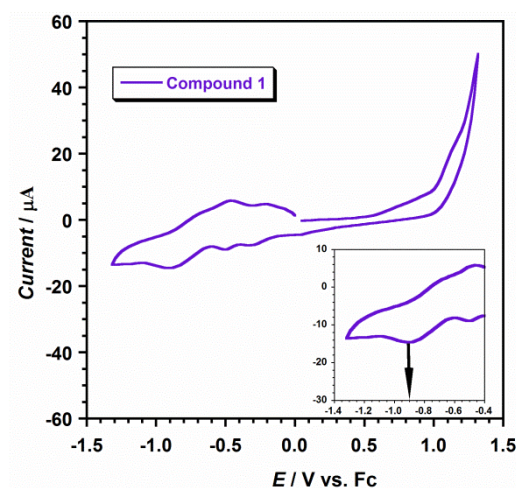


**Figure 7.** Cyclic voltammogram of **1** in a dry DMF 10<sup>−3</sup> M solution (with 0.1 M [NBu<sub>4</sub>][PF<sub>6</sub>]) at 20 °C and scan rate 200 mV/s. The area of the working electrode is 0.32 cm<sup>2</sup>.

Dinuclear ruthenium compounds containing metal–metal bonds have been studied for many years [37]. They show redox properties that are strongly dependent upon the solvent and the supporting electrolyte and are generally well known [38–40]. So, this type of Ru–Ru compound could be an acceptable reference in electrochemical studies [38–40].

In the CV curve of **1**, three reduction processes can be observed (Figure 7). The first two reduction peaks were found between 0.0 V and −0.50 V, which would be associated with the formation of the mixed-valent Ru(II)-Ru(III) species (at −0.30 V) and also to that of the Ru(II)-Ru(II) system (at −0.50 V). These reduction potential values are close to those published for other dinuclear ruthenium complexes [38–40]. Nevertheless, much more interesting would be the third detected reduction peak at −0.89 V, which would be generated by the influence of the guanine molecule, see inset in Figure 7. It is worth mentioning that this value assigned to guanine is in agreement with those previously reported for this purine nucleobase in electrochemistry research works performed through modified electrodes based on polyaniline-MnO<sub>2</sub> [41] and graphite-WS<sub>2</sub> [42], which have shown high accuracy and promising redox activity toward purine nucleobases [41,42]. In order to analyze the repeatability of the CV curve, it was measured five times. Indeed, a relative standard deviation value of ca. 1.2% for the current response was obtained for **1**. In any case, these results could establish a first step to develop new sensor devices suitable for the detection of purine nucleobases as guanine [25]. Nevertheless, this is an early stage of the research and, therefore, this type of diruthenium(III) systems must be further investigated. The comparison with other methods together with the study of the nature of the samples to be measured will be addressed subsequently in future works [25].

#### 4. Conclusions

An unusual guanine-based dinuclear ruthenium(III) complex, of the formula  $[\{\text{Ru}(\mu\text{-Cl})(\mu\text{-gua})\}_2\text{Cl}_4] \cdot 2\text{H}_2\text{O}$  (**1**) (gua = guanine), was prepared and characterized. Compound **1** is the first dinuclear ruthenium(III) compound based on guanine reported so far. Compound **1** was characterized by FT-IR, SEM-EDX, single-crystal X-ray diffraction (XRD), Hirshfeld surface analysis and cyclic voltammetry (CV). The study of its electrochemical properties revealed well-resolved, potentially useful, current peaks, which allowed us to investigate the guanine when linked to the ruthenium ion in **1**.

**Supplementary Materials:** The following supporting information can be downloaded at: <https://www.mdpi.com/article/10.3390/cryst12040448/s1>, X-ray crystallographic data in CIF format for compound **1**.

**Author Contributions:** Conceptualization, I.C. and J.M.-L.; funding acquisition, I.C. and J.M.-L.; methodology, M.O.-A., A.S.-L., I.C. and J.M.-L.; investigation, M.O.-A., A.S.-L., I.C. and J.M.-L.; formal analysis, M.O.-A., A.S.-L., I.C. and J.M.-L.; writing—original draft preparation, J.M.-L.; writing—review and editing, J.M.-L. All authors have read and agreed to the published version of the manuscript.

**Funding:** This research was funded by Spanish Ministry of Science and Innovation (Grant number PID2019-109735GB-I00) and also by VLC-BIOCLINIC Program of the University of Valencia (Grant number PI-2021-007-DIRUGEN).

**Institutional Review Board Statement:** Not applicable.

**Informed Consent Statement:** Not applicable.

**Data Availability Statement:** The raw data that support the findings of this study are available from the corresponding author upon reasonable request.

**Acknowledgments:** M.O.-A. thanks the Spanish “FPI” PhD funding action plan.

**Conflicts of Interest:** The authors declare no conflict of interest.

#### References

1. An, S.; Kumar, R.; Sheets, E.D.; Benkovic, S.J. Reversible Compartmentalization of de Novo Purine Biosynthetic Complexes in Living Cells. *Science* **2008**, *320*, 103–106. [[CrossRef](#)] [[PubMed](#)]
2. Pedley, A.M.; Benkovic, S.J. A New View into the Regulation of Purine Metabolism—The Purinosome. *Trends Biochem. Sci.* **2017**, *42*, 141–154. [[CrossRef](#)] [[PubMed](#)]
3. Rhodes, D.; Lipps, H.J. G-quadruplexes and their regulatory roles in biology. *Nucleic Acids Res.* **2015**, *43*, 8627–8637. [[CrossRef](#)]

4. Huynh, R.A.; Mohan, C. Alzheimer's Disease: Biomarkers in the Genome, Blood, and Cerebrospinal Fluid. *Front. Neurol.* **2017**, *8*, 102. [[CrossRef](#)] [[PubMed](#)]
5. Beamer, E.; Lacey, A.; Alves, M.; Conte, G.; Tian, F.; de Diego-García, L.; Khalil, M.; Rosenow, F.; Delanty, N.; Dale, N.; et al. Elevated blood purine levels as a biomarker of seizures and epilepsy. *Epilepsia* **2021**, *62*, 817–828. [[CrossRef](#)]
6. Kolgiri, V.; Patil, V.W. Protein carbonyl content: A novel biomarker for aging in HIV/AIDS patients. *Braz. J. Infect. Dis.* **2017**, *21*, 35–41. [[CrossRef](#)]
7. Ellis, R.J.; Moore, D.J.; Sundermann, E.E.; Heaton, R.K.; Mehta, S.; Hulgán, T.; Samuels, D.; Fields, J.A.; Letendre, S.L. Nucleic acid oxidation is associated with biomarkers of neurodegeneration in CSF in people with HIV. *Neurol. Neuroimmunol. Neuroinflamm.* **2020**, *7*, e902. [[CrossRef](#)]
8. Klampfl, C.W.; Himmelsbach, M.; Buchberger, W.; Klein, H. Determination of purines and pyrimidines in beer samples by capillary zone electrophoresis. *Anal. Chim. Acta* **2002**, *454*, 185–191. [[CrossRef](#)]
9. Inazawa, K.; Sato, A.; Kato, Y.; Yamaoka, N.; Fukuuchi, T.; Yasuda, M.; Mawatari, K.; Nakagomi, K.; Kaneko, K. Determination and profiling of purines in foods by using HPLC and LC-MS. *Nucleosides Nucleotides Nucleic Acids* **2014**, *33*, 439–444. [[CrossRef](#)]
10. Higgins, S. Regarding ruthenium. *Nat. Chem.* **2010**, *2*, 1100. [[CrossRef](#)]
11. Bruneau, C.; Achard, M. Allylic ruthenium(IV) complexes in catalysis. *Coord. Chem. Rev.* **2012**, *256*, 525–536. [[CrossRef](#)]
12. Furrer, J.; Süß-Fink, G. Thiolato-bridged dinuclear arene ruthenium complexes and their potential as anticancer drugs. *Coord. Chem. Rev.* **2016**, *309*, 36–50. [[CrossRef](#)]
13. Zeng, L.; Gupta, P.; Chen, Y.; Wang, E.; Ji, L.; Chao, H.; Chen, Z.-S. The development of anticancer ruthenium(II) complexes: From single molecule compounds to nanomaterials. *Chem. Soc. Rev.* **2017**, *46*, 5771–5804. [[CrossRef](#)]
14. Alessio, E. Thirty Years of the Drug Candidate NAMI-A and the Myths in the Field of Ruthenium Anticancer Compounds: A Personal Perspective. *Eur. J. Inorg. Chem.* **2017**, 1549–1560. [[CrossRef](#)]
15. Alessio, E.; Messori, L. NAMI-A and KP1019/1339, Two Iconic Ruthenium Anticancer Drug Candidates Face-to-Face: A Case Story in Medicinal Inorganic Chemistry. *Molecules* **2019**, *24*, 1995. [[CrossRef](#)]
16. Chen, H.; Parkinson, J.A.; Parsons, S.; Coxall, R.A.; Gould, R.O.; Sadler, P.J. Organometallic Ruthenium(II) Diamine Anticancer Complexes: Arene-Nucleobase Stacking and Stereospecific Hydrogen-Bonding in Guanine Adducts. *J. Am. Chem. Soc.* **2002**, *124*, 3064–3082. [[CrossRef](#)]
17. Armentano, D.; Martínez-Lillo, J. Hexachlororhenate(IV) salts of ruthenium(III) cations: X-ray structure and magnetic properties. *Inorg. Chim. Acta* **2012**, *380*, 118–124. [[CrossRef](#)]
18. Orts-Arroyo, M.; Castro, I.; Lloret, F.; Martínez-Lillo, J. Molecular Self-Assembly in a Family of Oxo-Bridged Dinuclear Ruthenium(IV) Systems. *Cryst. Growth Des.* **2020**, *20*, 2044–2056. [[CrossRef](#)]
19. Escrivà, E.; García-Lozano, J.; Martínez-Lillo, J.; Nuñez, H.; Server-Carrió, J.; Soto, L.; Carrasco, R.; Cano, J. Synthesis, Crystal Structure, Magnetic Properties, and Theoretical Studies of  $[\{\text{Cu}(\text{mepirizole})\text{Br}\}_2(\mu\text{-OH})(\mu\text{-pz})]$  (Mepirizole = 4-Methoxy-2-(5-methoxy-3-methyl-1H-pyrazol-1-yl)-6-methylpyrimidine; pz = Pyrazolate), a Novel  $\mu$ -Pyrazolato- $\mu$ -Hydroxo-Dibridged Copper(II) Complex. *Inorg. Chem.* **2003**, *42*, 8328–8336.
20. Armentano, D.; Marino, N.; Mastropietro, T.F.; Martínez-Lillo, J.; Cano, J.; Julve, M.; Lloret, F.; De Munno, G. Self-Assembly of a Chiral Carbonate- and Cytidine-Containing Dodecanuclear Copper(II) Complex: A Multiarm-Supplied Globular Capsule. *Inorg. Chem.* **2008**, *47*, 10229–10231. [[CrossRef](#)]
21. Marino, N.; Armentano, D.; Mastropietro, T.F.; Julve, M.; De Munno, G.; Martínez-Lillo, J. Cubane-Type  $\text{Cu}^{\text{II}}_4$  and  $\text{Mn}^{\text{II}}_2\text{Mn}^{\text{III}}_2$  Complexes Based on Pyridoxine: A Versatile Ligand for Metal Assembling. *Inorg. Chem.* **2013**, *52*, 11934–11943. [[CrossRef](#)] [[PubMed](#)]
22. Armentano, D.; Barquero, M.A.; Rojas-Dotti, C.; Moliner, N.; De Munno, G.; Brechin, E.K.; Martínez-Lillo, J. Enhancement of Intermolecular Magnetic Exchange through Halogen...Halogen Interactions in Bisadeninium Rhenium(IV) Salts. *Cryst. Growth Des.* **2017**, *17*, 5342–5348. [[CrossRef](#)]
23. Orts-Arroyo, M.; Castro, I.; Lloret, F.; Martínez-Lillo, J. Field-induced slow relaxation of magnetisation in two one-dimensional homometallic dysprosium(III) complexes based on alpha- and beta-amino acids. *Dalton Trans.* **2020**, *49*, 9155–9163. [[CrossRef](#)] [[PubMed](#)]
24. Orts-Arroyo, M.; Ten-Esteve, A.; Ginés-Cárdenas, S.; Castro, I.; Martí-Bonmatí, L.; Martínez-Lillo, J. A gadolinium(III) complex based on the thymine nucleobase with properties suitable for magnetic resonance imaging. *Int. J. Mol. Sci.* **2021**, *22*, 4586. [[CrossRef](#)] [[PubMed](#)]
25. Orts-Arroyo, M.; Castro, I.; Martínez-Lillo, J. Detection of Hypoxanthine from Inosine and Unusual Hydrolysis of Immunosuppressive Drug Azathioprine through the Formation of a Diruthenium(III) System. *Biosensors* **2021**, *11*, 19. [[CrossRef](#)] [[PubMed](#)]
26. Sanchis-Perucho, A.; Orts-Arroyo, M.; Camús-Hernández, J.; Rojas-Dotti, C.; Escrivà, E.; Lloret, F.; Martínez-Lillo, J. Hexahalorhenate(IV) salts of protonated ciprofloxacin: Antibiotic-based single-ion magnets. *CrystEngComm* **2021**, *23*, 8579–8587. [[CrossRef](#)]
27. Orts-Arroyo, M.; Sanchis-Perucho, A.; Moliner, N.; Castro, I.; Lloret, F.; Martínez-Lillo, J. One-Dimensional Gadolinium (III) Complexes Based on Alpha- and Beta-Amino Acids Exhibiting Field-Induced Slow Relaxation of Magnetization. *Inorganics* **2022**, *10*, 32. [[CrossRef](#)]
28. Turel, I.; Pecanac, M.; Golobic, A.; Alessio, E.; Serli, B.; Bergamo, A.; Sava, G. Solution, solid state and biological characterization of ruthenium(III)-DMSO complexes with purine base derivatives. *J. Inorg. Biochem.* **2004**, *98*, 393–401. [[CrossRef](#)]
29. SHELXTL-2017/1, Bruker Analytical X-ray Instruments; Bruker: Madison, WI, USA, 2017.

30. DIAMOND 4.5.0, *Crystal Impact GbR.*; Crystal Impact: Bonn, Germany, 2018.
31. Sheina, G.G.; Stepanian, S.G.; Radchenko, E.D.; Blagoi, Y.P. IR spectra of guanine and hypoxanthine isolated molecules. *J. Mol. Struct.* **1987**, *158*, 275–292. [[CrossRef](#)]
32. Beć, K.B.; Grabska, J.; Czarnecki, M.A.; Huck, C.W.; Wójcik, M.J.; Nakajima, T.; Ozaki, Y. IR Spectra of Crystalline Nucleobases: Combination of Periodic Harmonic Calculations with Anharmonic Corrections Based on Finite Models. *J. Phys. Chem. B* **2019**, *123*, 10001–10013. [[CrossRef](#)]
33. Spackman, M.A.; Jayatilaka, D. Hirshfeld surface analysis. *CrystEngComm* **2009**, *11*, 19–32. [[CrossRef](#)]
34. Turner, M.J.; McKinnon, J.J.; Wolff, S.K.; Grimwood, D.J.; Spackman, P.R.; Jayatilaka, D.; Spackman, M.A. *Crystal Explorer 17*; University of Western Australia: Perth, Australia, 2017.
35. Mohite, S.S.; Patil-Deshmukh, A.B.; Chavan, S.S. Synthesis and characterization of Ru(III) complexes with 2-((E)-((4-(4-bromophenyl)ethynyl)phenyl)imino)methyl-4-((E)-phenyldiazenyl)phenol and their use as a precursor for RuO<sub>2</sub> nanoparticles. *J. Mol. Struct.* **2019**, *1176*, 386–393. [[CrossRef](#)]
36. Sur, V.P.; Mazumdar, A.; Kopel, P.; Mukherjee, S.; Vitek, P.; Michalkova, H.; Vaculovičová, M.; Moulick, A. A Novel Ruthenium Based Coordination Compound Against Pathogenic Bacteria. *Int. J. Mol. Sci.* **2020**, *21*, 2656. [[CrossRef](#)] [[PubMed](#)]
37. Cotton, F.A.; Pedersen, E. Magnetic and electrochemical properties of transition metal complexes with multiple metal-to-metal bonds. II. Tetrabutyratodiruthenium(n+) with n = 0 and 1. *Inorg. Chem.* **1975**, *14*, 388–391. [[CrossRef](#)]
38. Malinski, T.; Chang, D.; Feldmann, F.N.; Bear, J.L.; Kadish, K.M. Electrochemical studies of a novel ruthenium(II,III) dimer, trifluoroacetamidatoruthenium chloride (Ru<sub>2</sub>(HNOCCF<sub>3</sub>)<sub>4</sub>Cl). *Inorg. Chem.* **1983**, *22*, 3225–3233. [[CrossRef](#)]
39. Hiraoka, Y.; Ikeue, T.; Sakiyama, H.; Guégan, F.; Luneau, D.; Gillon, B.; Hiromitsu, I.; Yoshioka, D.; Mikuriya, M.; Kataoka, Y.; et al. An unprecedented up-field shift in the <sup>13</sup>C NMR spectrum of the carboxyl carbons of the lantern-type dinuclear complex TBA[Ru<sub>2</sub>(O<sub>2</sub>CCH<sub>3</sub>)<sub>4</sub>Cl<sub>2</sub>] (TBA<sup>+</sup> = tetra(n-butyl)ammonium cation). *Dalton Trans.* **2015**, *44*, 13439–13443. [[CrossRef](#)]
40. Kataoka, Y.; Mikami, S.; Sakiyama, H.; Mitsumi, M.; Kawamoto, T.; Handa, M. A neutral paddlewheel-type diruthenium(III) complex with benzamidinato ligands: Synthesis, crystal structure, magnetism, and electrochemical and absorption properties. *Polyhedron* **2017**, *136*, 87–92. [[CrossRef](#)]
41. Prathap, M.U.A.; Srivastava, R.; Satpati, B. Simultaneous detection of guanine, adenine, thymine, and cytosine at polyaniline/MnO<sub>2</sub> modified electrode. *Electrochim. Acta* **2013**, *114*, 285–295. [[CrossRef](#)]
42. Zhang, J.; Han, D.; Wang, S.; Zhang, X.; Yang, R.; Ji, Y.; Yu, X. Electrochemical detection of adenine and guanine using a three-dimensional WS<sub>2</sub> nanosheet/graphite microfiber hybrid electrode. *Electrochem. Commun.* **2019**, *99*, 75–80. [[CrossRef](#)]

---

*ARTICLE 3*

*Detection of Hypoxanthine from  
Inosine and Unusual Hydrolysis  
of Immunosuppressive Drug  
Azathioprine through the  
Formation of a  
Diruthenium(III) System*



## Article

# Detection of Hypoxanthine from Inosine and Unusual Hydrolysis of Immunosuppressive Drug Azathioprine through the Formation of a Diruthenium(III) System

Marta Orts-Arroyo, Isabel Castro  and José Martínez-Lillo \* 

Instituto de Ciencia Molecular (ICMol), Universitat de València, c/ Catedrático José Beltrán 2, Paterna, 46980 València, Spain; marta.orts-arroyo@uv.es (M.O.-A.); isabel.castro@uv.es (I.C.)

\* Correspondence: f.jose.martinez@uv.es; Tel.: +34-9635-44460

**Abstract:** Hypoxanthine (hpx) is an important molecule for both biochemistry research and biomedical applications. It is involved in several biological processes associated to energy and purine metabolism and has been proposed as a biomarker for a variety of disease states. Consequently, the discovery and development of systems suitable for the detection of hypoxanthine is pretty appealing in this research field. Thus, we have obtained a stable diruthenium (III) compound in its dehydrated and hydrated forms with formula  $[\{\text{Ru}(\mu\text{-Cl})(\mu\text{-hpx})\}_2\text{Cl}_4]$  (**1a**) and  $[\{\text{Ru}(\mu\text{-Cl})(\mu\text{-hpx})\}_2\text{Cl}_4]\cdot 2\text{H}_2\text{O}$  (**1b**), respectively. This purine-based diruthenium(III) system was prepared from two very different starting materials, namely, inosine and azathioprine, the latter being an immunosuppressive drug. Remarkably, it was observed that an unusual azathioprine hydrolysis occurs in the presence of ruthenium, thus generating hypoxanthine instead of the expected 6-mercaptopurine antimetabolite, so that the hpx molecule is linked to two ruthenium(III) ions. **1a** and **1b** were characterized through IR, SEM, powder and single-crystal X-ray Diffraction and Cyclic Voltammetry (CV). The electrochemical studies allowed us to detect the hpx molecule when coordinated to ruthenium in the reported compound. The grade of sensitivity, repeatability and stability reached by this diruthenium system make it potentially useful and could provide a first step to develop new sensor devices suitable to detect hypoxanthine.

**Keywords:** hypoxanthine; inosine; azathioprine; 6-mercaptopurine; biomarker; ruthenium



**Citation:** Orts-Arroyo, M.; Castro, I.; Martínez-Lillo, J. Detection of Hypoxanthine from Inosine and Unusual Hydrolysis of Immunosuppressive Drug Azathioprine through the Formation of a Diruthenium(III) System. *Biosensors* **2021**, *11*, 19. <https://doi.org/10.3390/bios11010019>

Received: 24 November 2020

Accepted: 6 January 2021

Published: 11 January 2021

**Publisher's Note:** MDPI stays neutral with regard to jurisdictional claims in published maps and institutional affiliations.



**Copyright:** © 2021 by the authors. Licensee MDPI, Basel, Switzerland. This article is an open access article distributed under the terms and conditions of the Creative Commons Attribution (CC BY) license (<https://creativecommons.org/licenses/by/4.0/>).

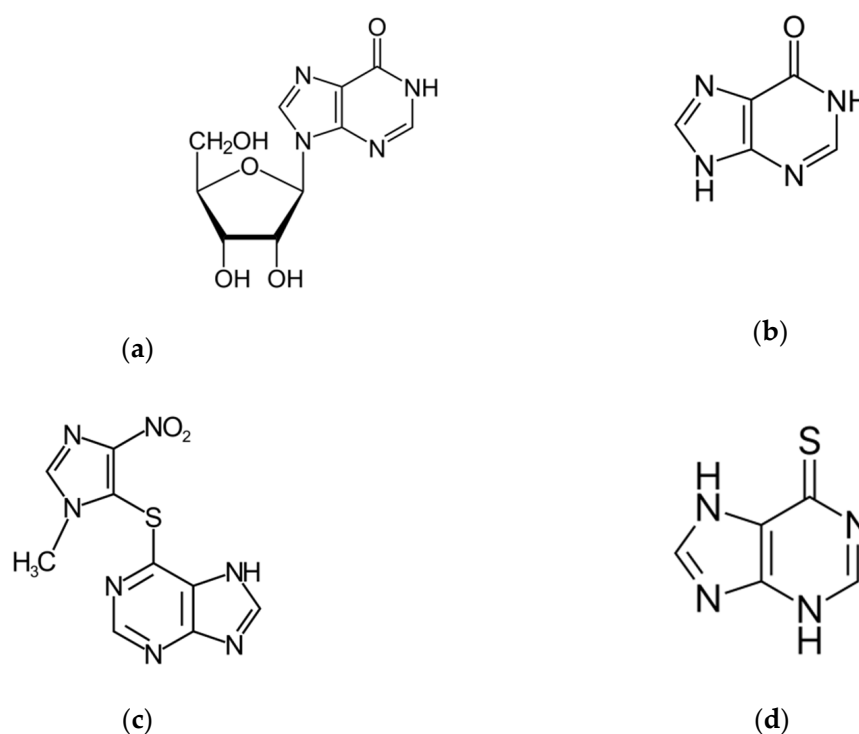
## 1. Introduction

Hypoxanthine (6-hydroxypurine) is a deaminated form of adenine and a constituent of the nucleoside inosine (Scheme 1). It is formed during purine metabolism and is found in both tissues and body fluids of human beings and animals. The identification of hypoxanthine (hpx) as a biomarker for hypoxia has long been known [1,2]. More recently, hpx has also been proposed as a biomarker for colorectal cancer [3], Alzheimer's disease [4], multiple sclerosis [5] and cardiac ischemia [6] and as checkpoint metabolite for other inflammatory processes [7] and toxicity levels [8]. In addition, hpx has been studied as a strong predictor of performance in highly trained athletes in sports and physical exertion, the hpx concentration indicating the training status and adaptation in consecutive phases of long training cycles [9,10]. Moreover, the determination of levels of hpx in meat and fish products has been established to be an important and convenient indicator of freshness and quality control in the food industry [11,12].

As a continuation of our interest in investigating biomolecule-based complexes of several metal ions [13–17] and their implementation in devices [18,19], we have studied the synthesis of ruthenium with some purine-based compounds that either contain hypoxanthine or could generate this analyte. Thus, we have investigated the products of the hydrolysis reactions with inosine and azathioprine (Scheme 1).



The nucleoside inosine is formed by a hpx molecule that is connected to a ribose ring through N(9)-glycosidic bond. It belongs to a group of purine antimetabolites recommended for treatment of measles and herpes infections, among others [20]. Studies on the inosine hydrolysis have been previously reported [21,22]. Azathioprine is a slow-release prodrug of the antimetabolite 6-mercaptopurine (Scheme 1), which is used as an anticancer and immunosuppressive drug [23,24]. It is used as an established clinical agent for the treatment of several pathologies, such as rheumatoid arthritis, ulcerative colitis, systemic lupus and Crohn's disease, and also as an anti-rejection medication in human organ transplantation [23,24]. The N-methylnitroimidazolyl group of the azathioprine molecule protects the active form 6-mercaptopurine. Azathioprine undergoes hydrolysis *in vivo* to alter the metabolism and distribution of the drug toward its target [23,24].



**Scheme 1.** Molecular structure of: (a) Inosine, (b) Hypoxanthine, (c) Azathioprine and (d) 6-Mercaptopurine.

Previously reported methods of determination of hpx include high-performance liquid chromatography [25–28], capillary electrophoresis [29,30], spectrophotometry [31,32] and electrochemiluminescence [33,34], which are usually costly and laborious and require a long analysis time. On the other hand, electrochemical methods offer several advantages, such as relatively simple and cheap instrumentation, high selectivity and sensitivity, high stability and rapid response time [35–37]. Nevertheless, given the wide range of potentially interfering purine-based compounds that can affect the detection of hpx generated in biological processes, more selective methods of analysis are needed.

Herein, we report the preparation, characterization and electrochemical properties of a new diruthenium system (Figure 1), which shows great stability and also selectivity for the hypoxanthine molecule, and therefore, could establish a first step to develop new sensor devices suitable for hypoxanthine detection.



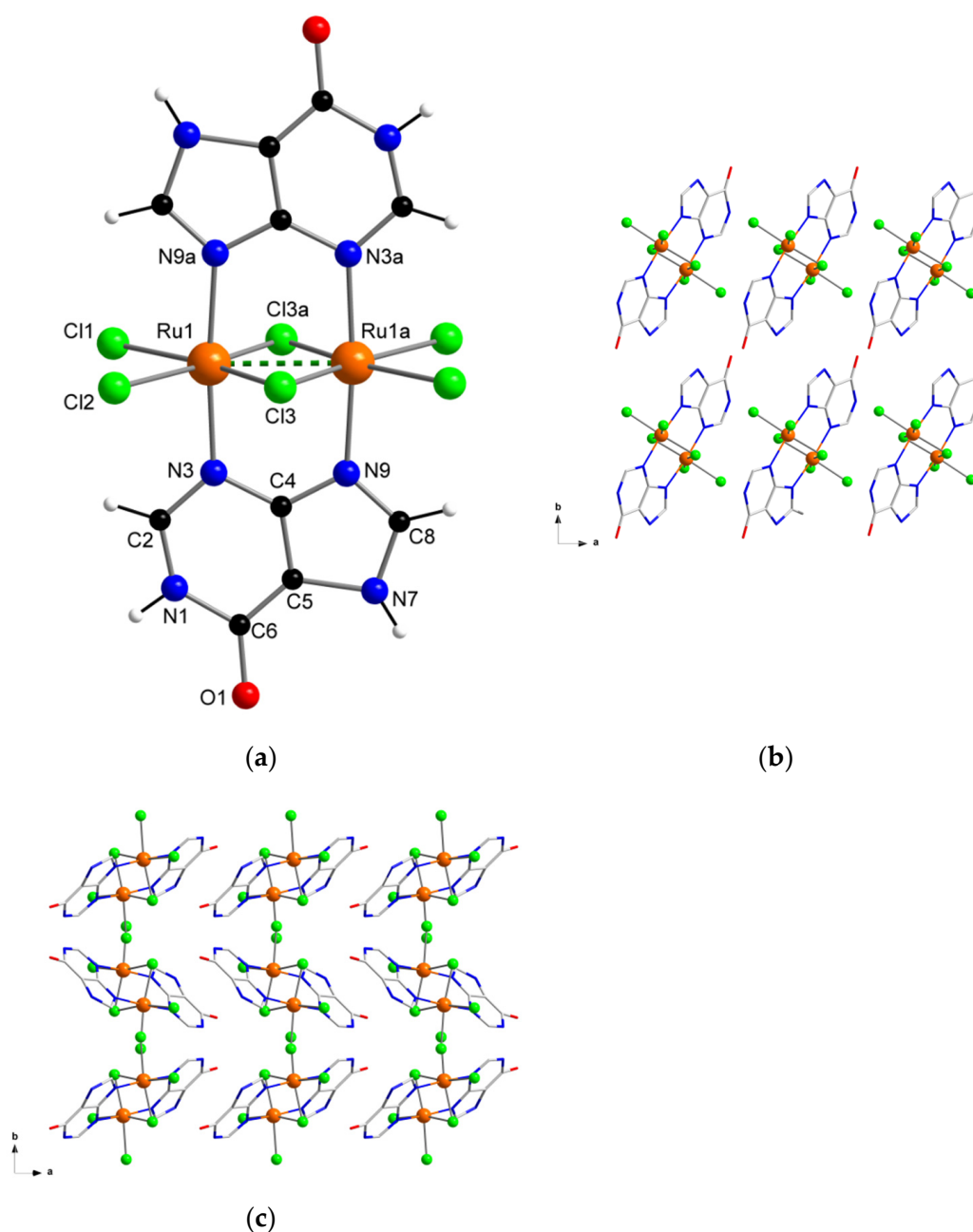


**Figure 1.** (a) Molecular structure of the  $[\{\text{Ru}(\mu\text{-Cl})(\mu\text{-hpx})\}_2\text{Cl}_4]$  complex in **1a** and **1b**; (b) view along the crystallographic  $c$  axis of a fragment of the crystal packing of **1a**; (c) view along the crystallographic  $c$  axis of a fragment of the crystal packing of **1b**.

## 2. Materials and Methods

### 2.1. Reagents and Instruments

All of the manipulations were performed under aerobic conditions. Azathioprine and inosine were purchased from Alfa Aesar and Sigma Aldrich, respectively. Ruthenium precursors,  $\text{RuCl}_3 \cdot \text{H}_2\text{O}$  and  $\text{K}_2[\text{RuCl}_5(\text{H}_2\text{O})]$ , and the rest of materials were used as-received and were of reagent grade. Elemental analyses (C, H, N) and X-ray microanalysis were performed by the Central Service for the Support to Experimental Research (SCSIE) at the University of Valencia. Scanning electron microscopy (SEM) images and results were obtained from a Hitachi S-4800 field emission scanning electron microscope. Infrared spec-

tra (IR) of **1a** and **1b** (in the Supplementary Materials) were recorded with a PerkinElmer Spectrum 65 FT-IR spectrometer in the range of 400 to 4000  $\text{cm}^{-1}$  (Figure 2).

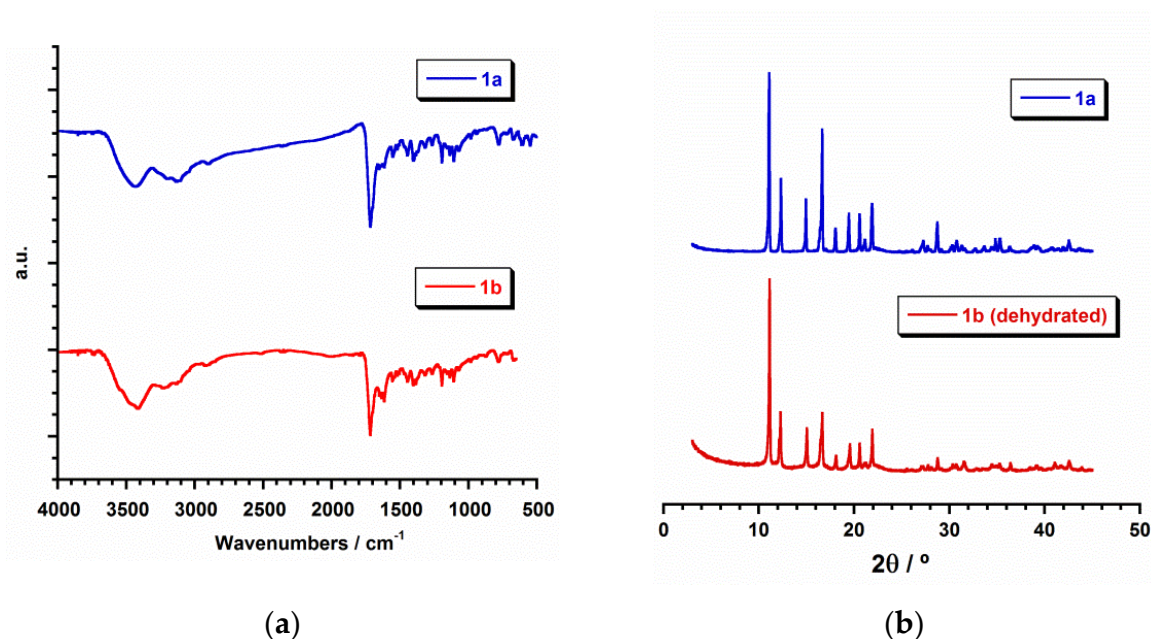


**Figure 2.** (a) IR spectra (Transmission mode) for **1a** (blue) and **1b** (red); (b) plot of the experimental powder X-ray diffraction (PXRD) patterns profile ( $2\theta/^\circ$ ) in the range 0–50° for **1a** (blue) and dehydrated **1b** (red).

Electrochemical studies were performed by using an Autolab/PGSTAT 204 scanning potentiostat operating at a scan rate range of 10–250  $\text{mV s}^{-1}$ . Cyclic voltammograms were carried out by using 0.1 M  $\text{NBU}_4\text{PF}_6$  as supporting electrolyte and 0.001 M solutions of **1a**, inosine and azathioprine in dry dimethylformamide (dmf). The working electrode was a glassy carbon disk (0.32  $\text{cm}^2$ ) that was polished with 1.0  $\mu\text{m}$  of diamond powder, sonicated, washed with absolute ethanol and acetone and air dried. The reference electrode was  $\text{AgCl}/\text{Ag}$ , separated from the test solution by a salt bridge containing the solvent/supporting electrolyte, with platinum as an auxiliary electrode. All experiments were performed in standard electrochemical cells at 25  $^\circ\text{C}$  under argon. The investigated potential range was in the range of  $-2.0$  to  $+2.0$  V vs.  $\text{AgCl}/\text{Ag}$ . Ferrocene ( $\text{F}_c$ ) was added as internal standard at the end of all the measurements. The formal potentials were measured at a scan rate of 200  $\text{mV s}^{-1}$  and were referred to the ferrocenium/ferrocene ( $\text{F}_c^+/\text{F}_c$ ) redox couple.

## 2.2. Preparation of the Compounds

### 2.2.1. Synthesis of $[\{\text{Ru}(\mu\text{-Cl})(\mu\text{-hpx})\}_2\text{Cl}_4]$ (**1a**)

A solvothermal reaction of  $\text{K}_2[\text{RuCl}_5(\text{H}_2\text{O})]$  (3.52 mg, 0.01 mmol) and inosine (2.66 mg, 0.01 mmol) was performed in  $\text{HCl}$  (4 mL, 3 M) at 90  $^\circ\text{C}$  for 3 days, followed by a 12-h cooling process to room temperature. Dark brown crystals of **1a** were obtained and were suitable for X-ray data collection. Yield: ca. 55%. Anal. Calcd. for  $\text{C}_{10}\text{H}_8\text{Cl}_6\text{N}_8\text{O}_2\text{Ru}_2$  (**1a**): C, 17.5; H, 1.2; N, 16.3. Found: C, 17.7; H, 1.3; N, 16.5. IR peaks (KBr pellets,  $\nu/\text{cm}^{-1}$ ): 3202(m), 3132(m), 3110(m), 3046(m), 2905(m), 1718(vs), 1653(m), 1555(m), 1522(w), 1447(m), 1407(m), 1318(m), 1267(m), 1196(s), 1160(w), 1137(m), 1118(s), 984(w), 779(m), 723(w), 674(m), 610(m), 550(m), 478(w) and 412(w).

### 2.2.2. Synthesis of $[\{\text{Ru}(\mu\text{-Cl})(\mu\text{-hpx})\}_2\text{Cl}_4]\cdot 2\text{H}_2\text{O}$ (**1b**)

$\text{RuCl}_3\cdot\text{H}_2\text{O}$  (6.60 mg, 0.03 mmol) and azathioprine (6.80 mg, 0.03 mmol) reacted through a solvothermal reaction in  $\text{HCl}$  (4 mL, 3 M) at 90  $^\circ\text{C}$  for 3 days, followed by a 12-h cooling process to room temperature. Dark brown crystals of **1b** were thus obtained, which

were suitable for X-ray data collection. Yield: *ca.* 72%. Anal. Calcd. for  $C_{10}H_{12}Cl_6N_8O_4Ru_2$  (**1b**): C, 16.6; H, 1.7; N, 15.5. Found: C, 16.7; H, 1.9; N, 15.2. IR peaks (KBr pellets,  $\nu/cm^{-1}$ ): 3433(br), 3202(m), 3133(m), 3110(m), 3047(m), 2905(m), 1718(vs), 1653(m), 1615(m), 1554(m), 1522(w), 1447(m), 1407(m), 1318(m), 1267(m), 1196(s), 1160(w), 1137(m), 1118(s), 984(w), 779(m), 723(w), 674(m), 610(m), 550(m), 478(w) and 412(w).

### 2.3. X-ray Data Collection and Structure Refinement

X-ray diffraction data from single crystals of dimensions  $0.18 \times 0.06 \times 0.04$  (**1a**) and  $0.27 \times 0.14 \times 0.11$  mm<sup>3</sup> (**1b**) were collected on a Bruker D8 Venture diffractometer with graphite-monochromated Mo-K $\alpha$  radiation ( $\lambda = 0.71073$  Å). Crystal parameters and refinement results for **1a** and **1b** are summarized in Table 1. The structures were solved by standard direct methods and subsequently completed by Fourier recycling by using the SHELXTL software packages. The obtained models were refined with version 2017/1 of SHELXL against  $F^2$  on all data by full-matrix least squares [38]. In the two samples, all non-hydrogen atoms were anisotropically refined, whereas the hydrogen atoms of the hpx molecules were set in calculated positions and refined isotropically by using the riding model. The graphical manipulations were performed with the DIAMOND program [39]. The CCDC codes for **1a** and **1b** are 2046049 and 2046050, respectively. In addition, X-ray powder diffraction (PXRD) measurements were performed through a capillary sample holder in a PANalytical Empyrean diffractometer containing a hybrid monochromator (Cu-K $\alpha_1$  radiation) and a PIXcel detector.

**Table 1.** Summary of the crystal data and structure refinement parameters for **1a** and **1b**.

Compound	<b>1a</b>	<b>1b</b>
CCDC	2046049	2046050
Formula	$C_{10}H_8Cl_6N_8O_2Ru_2$	$C_{10}H_{12}Cl_6N_8O_4Ru_2$
$M_r/g\ mol^{-1}$	687.08	723.12
Crystal system	monoclinic	monoclinic
Space group	$P2_1/c$	$P2_1/c$
$a/\text{Å}$	7.161(1)	8.714(1)
$b/\text{Å}$	10.720(1)	11.865(1)
$c/\text{Å}$	11.666(1)	10.286(1)
$\alpha/^\circ$	90	90
$\beta/^\circ$	90.81(1)	112.32(1)
$\gamma/^\circ$	90	90
$V/\text{Å}^3$	895.52(9)	983.81(3)
Z	2	2
$D_c/g\ cm^{-3}$	2.548	2.441
$\mu(\text{Mo-K}\alpha)/mm^{-1}$	2.611	2.390
$F(000)$	660.0	700.0
Goodness-of-fit on $F^2$	1.170	1.066
$R_1 [I > 2\sigma(I)]$	0.0726	0.0844
$wR_2 [I > 2\sigma(I)]$	0.1811	0.2014

## 3. Results and Discussion

### 3.1. Synthetic Procedure

By reacting  $K_2[RuCl_5(H_2O)]$  with inosine (for **1a**) and  $RuCl_3 \cdot H_2O$  with azathioprine (for **1b**) in hydrochloric acid (3 M) solutions, we obtained the same diruthenium(III) complex, but in its dehydrated and hydrated forms  $\{[Ru(\mu-Cl)(\mu-hpx)]_2Cl_4\}$  (**1a**) and  $\{[Ru(\mu-Cl)(\mu-hpx)]_2Cl_4\} \cdot 2H_2O$  (**1b**), respectively. In both cases, the synthesis process was performed by heating the reaction mixture at 90 °C through a solvothermal method, followed by a 12-h cooling process to room temperature as the crystallization technique. Thus, dark brown crystals of **1a** and **1b** were obtained in satisfactory yields. Inosine was chosen in this work as starting material because it is a suitable source of hypoxanthine (Scheme 1), and given the synthetic conditions, this purine nucleoside can easily undergo hydrolysis

through a N(9)-glycosidic bond with a rapid release of hypoxanthine along with the ribose sugar [21]. The released hypoxanthine molecule acts as a ligand towards the ruthenium metal ions, generating the stable complex **1a**. In the case of the synthesis with azathioprine, **1b** was obtained as an unexpected product in a reaction which was intended to replace some of the Cl groups linked to the ruthenium(III) ions by the potentially chelating 6-mercaptopurine antimetabolite (Scheme 1). Instead, the species **1b** was formed. The hydrolytic reaction that azathioprine undergoes during its mechanism of drug action, that is, the cleavage of the N-methylnitroimidazolyl group from the sulfur atom, and therefore, the release of 6-mercaptopurine [23,24], in the presence of ruthenium(III) ions and in an acid medium, would be modified. After releasing the 6-mercaptopurine molecule, water attacks it, generating hypoxanthine, which in turn would lead to the formation of the species **1b**, so that the reported syntheses constitute new preparative methods to obtain purine-based Ru(III) compounds.

### 3.2. Description of the Crystal Structure

The crystal structure and exact chemical composition of **1a** and **1b** were established by single-crystal X-ray diffraction. **1a** and **1b** crystallize in the monoclinic system with space group  $P2_1/c$  (Table 1). Their structures are made up of the neutral dinuclear  $[\{\text{Ru}(\mu\text{-Cl})(\mu\text{-hpx})\}_2\text{Cl}_4]$  units. Only in **1b** there are solvent molecules of crystallization, which are  $\text{H}_2\text{O}$  molecules. In their asymmetric units, half a  $[\{\text{Ru}(\mu\text{-Cl})(\mu\text{-hpx})\}_2\text{Cl}_4]$  complex is in both **1a** and **1b**, and one  $\text{H}_2\text{O}$  molecule of crystallization is also present in **1b** (Figure 1).

In the dinuclear complex of **1a** and **1b**, each six-coordinate  $\text{Ru}^{\text{III}}$  ion is bonded to four chloride ions and two nitrogen atoms (N3 and N9) from two hpx molecules in a distorted octahedral environment. No significant differences are found in the Ru–Cl [average value, 2.329(1) Å in **1a** and 2.310(1) Å in **1b**] and Ru–N [2.066(1) Å in **1a** and 2.061(1) Å in **1b**] bond lengths, which are similar in both compounds and are in agreement with those values found in previously reported  $\text{Ru}^{\text{III}}$  systems [40,41]. The two  $\text{Ru}^{\text{III}}$  ions are linked each other through two hpx molecules and a double Ru–Cl–Ru bridge and the short intramolecular Ru···Ru distance that is generated (ca. 2.6 Å) indicates the formation of a metal-metal bond (dashed line in Figure 1a). The hpx molecule in **1a** and **1b** is planar and its bond lengths and angles agree with those found in the literature for similar dinuclear complexes [42,43].

In the crystal lattice of **1a** and **1b** the dinuclear  $[\{\text{Ru}(\mu\text{-Cl})(\mu\text{-hpx})\}_2\text{Cl}_4]$  units pack in different ways (Figure 1b,c), because of their pseudopolymorphism. Thus,  $\pi\cdots\pi$  stacking interactions between neighboring rings of coordinated hpx molecules occur in **1b** [with the shortest intercentroid distance being ca. 3.85 Å], whereas no  $\pi\cdots\pi$  type interactions are observed in **1a**.  $\text{Cl}\cdots\pi$  interactions between adjacent  $[\{\text{Ru}(\mu\text{-Cl})(\mu\text{-hpx})\}_2\text{Cl}_4]$  units take place in both  $\text{Ru}^{\text{III}}$  compounds [ $\text{Cl}\cdots\pi$  distances varying in the ranges 3.16–3.37 and 3.46–3.73 Å for **1a** and **1b**, respectively]. In addition, H-bonding interactions contribute to stabilizing the crystal structure in both systems. Finally, the powder X-ray diffraction (PXRD) patterns of **1a** and **1b**, which are quite different to that of the hpx molecule [44], confirmed the homogeneity of their bulk samples (Figure 2).

### 3.3. Scanning Electron Microscopy (SEM)

The study of X-ray microanalysis through of scanning electron microscopy (SEM) gave an Ru/Cl molar ratio of 1:3 for both studied samples (**1a** and **1b**) and was performed as previously done for other ruthenium systems [45,46]. Sulfur was not detected in **1a** nor **1b**. The pseudopolymorphism of **1a** and **1b** was evident in the recorded images that are given in Figure 3, where crystals of **1a** are shown as needles, whereas crystals of **1b** are displayed as crystallized plates.

### 3.4. Cyclic Voltammetry (CV)

The electrochemical properties of the diruthenium(III) complex were investigated through cyclic voltammetry (CV) in dry dmf and at room temperature. Figure 4 shows a comparison of CV curves obtained in the same conditions for **1a**, inosine and azathio-

prine. The electrochemical behavior of azathioprine has been studied in detail in previous works [47–50]; nevertheless, we have included it for the purpose of our investigation. The most characteristic feature observed during the electrochemical reduction of azathioprine is the peak detected at a potential of about  $-1.30$  V, which can be assigned to the reduction of the nitro group ( $-\text{NO}_2$ ) to the corresponding hydroxylamine ( $-\text{NHOH}$ ) that the N-methylnitroimidazolyl moiety of the molecule contains [47–50]. The CV curve obtained for inosine is very similar to that of hypoxanthine, which makes the detection of hypoxanthine in the presence of inosine quite difficult [51,52].

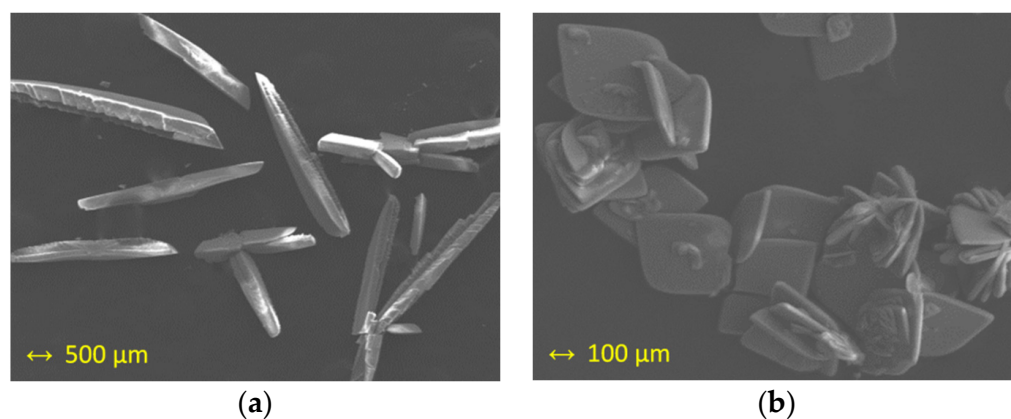


**Figure 3.** Scanning electron microscopy (SEM) images of: (a) crystals of **1a**; (b) crystals of **1b**.

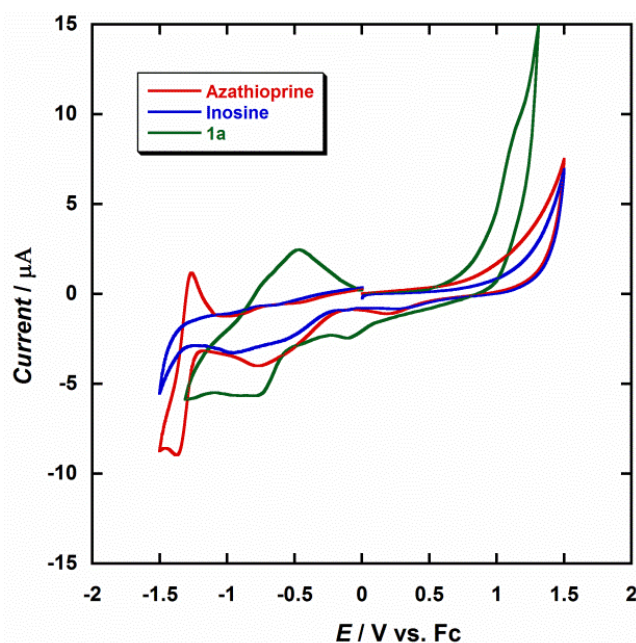


**Figure 4.** Cyclic voltammograms of **1a** (green), inosine (blue) and azathioprine (red) in dry dmf (0.1 M  $\text{NBu}_4\text{PF}_6$ ) at  $25^\circ\text{C}$  and scan rate  $200\text{ mV/s}$ .

Diruthenium complexes exhibiting metal–metal bonding have been extensively investigated for decades [53]. In general, this type of  $\text{Ru}_2$  compounds show electronic structures and redox properties that are unique [54–56]. Only one or up to three redox processes can be observed in the CV curves of these systems, depending on the solvent and the supporting electrolyte [54–56]. In dimethylformamide (dmf), only a single reduction would be expected, which would occur between  $0.0$  V and  $-0.30$  V, so that the first reduction peak observed at  $-0.11$  V for **1a** would be associated to the  $\text{Ru}^{\text{III}}/\text{Ru}^{\text{II}}$  reduction process, which is very close to that reported for similar  $\text{Ru}_2^{\text{III}}$  systems [54]. A second peak at  $-0.82$  V



would be generated by the influence of the analyte, in this case the hpx molecule (Figure 4). For testing repeatability of the CV curve of the studied  $\text{Ru}_2^{\text{III}}$  system (**1a**), it was measured five times. Thus, a relative standard deviation of approximately 1.5% of the current response was obtained. It is evident from Figure 4 that there is a marked difference between the reported reductions waves for these three compounds, their current peaks being found to be well-resolved at the employed conditions, and the coordination of the hpx molecule being responsible of the CV curve observed for **1a**. Therefore, given the possibility of coexistence of hypoxanthine and inosine, or azathioprine, in singular biological processes or biomedical studies, our results can be used for the designing and development of new ruthenium-based devices that act as sensors for the detection of hypoxanthine.

#### 4. Conclusions

In summary, a new purine-based diruthenium(III) system of formula  $[\{\text{Ru}(\mu\text{-Cl})(\mu\text{-hpx})\}_2\text{Cl}_4]$  (hpx = hypoxanthine) has been prepared from two different starting materials, namely, inosine and azathioprine, the latter being an immunosuppressant drug. Remarkably, it was observed that during the synthetic process azathioprine undergoes hydrolytic reaction that in the presence of ruthenium generates hpx, instead of the expected 6-mercaptapurine antimetabolite, which in turn was detected through the formation of the diruthenium(III) system. The diruthenium(III) system was obtained in its dehydrated and hydrated forms and characterized by IR, SEM, powder and single-crystal X-ray diffraction and cyclic voltammetry (CV). The study on the CV curves allowed us to detect hpx when coordinated to ruthenium in the reported compound. The grade of sensitivity, repeatability and stability reached by this diruthenium system make it potentially useful and could provide a first step to develop sensor devices suitable to detect the hpx molecule. Further investigations on the synthesis and characterization of this type of ruthenium systems is now in progress for similar target molecules in our group.

**Supplementary Materials:** X-ray crystallographic data in CIF format for compounds **1a** and **1b** are available online at <https://www.mdpi.com/2079-6374/11/1/19/s1>.

**Author Contributions:** I.C. and J.M.-L. conceived the idea and obtained funding for the project. M.O.-A. performed the synthesis, the X-ray data collection and the rest of the physical measurements. J.M.-L. analyzed the data associated with all the experiments and wrote the manuscript, which all authors discussed and commented on. All authors have read and agreed to the published version of the manuscript.

**Funding:** This research was funded by the VLC-BIOCLINIC Program (2017) of the University of Valencia [Subprogram A “Acciones Exploratorias”, Project 02-2017-A] and the Spanish Ministry of Science, Innovation and Universities [Project PID2019-109735GB-I00].

**Institutional Review Board Statement:** Not applicable.

**Informed Consent Statement:** Not applicable.

**Data Availability Statement:** Not applicable.

**Acknowledgments:** The authors M.O.-A. and J.M.-L. thank the Spanish “FPI fellowships” and “Ramón y Cajal” programs, respectively.

**Conflicts of Interest:** The authors declare no conflict of interest.

#### References

1. Saugstad, O.D. Hypoxanthine as a Measurement of Hypoxia. *Pediatr. Res.* **1975**, *9*, 158–161. [[CrossRef](#)] [[PubMed](#)]
2. Nagao, H.; Nishizawa, H.; Tanaka, Y.; Fukata, T.; Mizushima, T.; Furuno, M.; Bamba, T.; Tsushima, Y.; Fujishima, Y.; Kita, S.; et al. Hypoxanthine Secretion from Human Adipose Tissue and its Increase in Hypoxia. *Obesity* **2018**, *26*, 1168–1178. [[CrossRef](#)] [[PubMed](#)]
3. Long, Y.; Sánchez-Espiridion, B.; Lin, M.; White, L.; Mishra, L.; Raju, G.S.; Kopetz, S.; Eng, C.; Hildebrandt, M.A.T.; Chang, D.W.; et al. Global and targeted serum metabolic profiling of colorectal cancer progression. *Cancer* **2017**, *123*, 4066–4074. [[CrossRef](#)] [[PubMed](#)]
4. Chouraki, V.; Preis, S.R.; Yang, Q.; Beiser, A.; Li, S.; Larson, M.G.; Weinstein, G.; Wang, T.J.; Gerszten, R.E.; Vasan, R.S.; et al. Association of amine biomarkers with incident dementia and Alzheimer’s disease in the Framingham Study. *Alzheimer’s Dement.* **2017**, *13*, 1327–1336. [[CrossRef](#)] [[PubMed](#)]

5. Lazzarino, G.; Amorini, A.M.; Petzold, A.; Gasperini, C.; Ruggieri, S.; Quartuccio, M.E.; Lazzarino, G.; Di Stasio, E.; Tavazzi, B. Serum Compounds of Energy Metabolism Impairment Are Related to Disability, Disease Course and Neuroimaging in Multiple Sclerosis. *Mol. Neurobiol.* **2017**, *54*, 7520–7533. [[CrossRef](#)] [[PubMed](#)]
6. Farthing, D.E.; Farthing, C.A.; Xi, L. Inosine and hypoxanthine as novel biomarkers for cardiac ischemia: From bench to point-of-care. *Exp. Biol. Med.* **2015**, *240*, 821–831. [[CrossRef](#)]
7. Lee, J.S.; Wang, R.X.; Alexeev, E.E.; Lanis, J.M.; Battista, K.D.; Glover, L.E.; Colgan, S.P. Hypoxanthine is a checkpoint stress metabolite in colonic epithelial energy modulation and barrier function. *J. Biol. Chem.* **2018**, *293*, 6039–6051. [[CrossRef](#)] [[PubMed](#)]
8. Casali, E.; Berni, P.; Spisni, A.; Baricchi, R.; Pertinhez, T.A. Hypoxanthine: A new paradigm to interpret the origin of transfusion toxicity. *Blood Transfus.* **2016**, *14*, 555–556.
9. Zieliński, J.; Krasieńska, B.; Kusy, K. Hypoxanthine as a Predictor of Performance in Highly Trained Athletes. *Int. J. Sports Med.* **2013**, *34*, 1079–1086. [[CrossRef](#)]
10. Zieliński, J.; Kusy, K. Hypoxanthine: A Universal Metabolic Indicator of Training Status in Competitive Sports. *Exerc. Sport Sci. Rev.* **2015**, *43*, 214–221. [[CrossRef](#)]
11. Lawal, A.T.; Adeloju, S.B. Polypyrrole-Based Xanthine Oxidase Potentiometric Biosensor for Hypoxanthine. *J. Appl. Sci.* **2008**, *8*, 2599–2605. [[CrossRef](#)]
12. Hernández-Cázares, A.S.; Aristoy, M.C.; Toldrá, F. Hypoxanthine-based enzymatic sensor for determination of pork meat freshness. *Food Chem.* **2010**, *123*, 949–954. [[CrossRef](#)]
13. Escrivà, E.; García-Lozano, J.; Martínez-Lillo, J.; Nuñez, H.; Server-Carrió, J.; Soto, L.; Carrasco, R.; Cano, J. Synthesis, Crystal Structure, Magnetic Properties, and Theoretical Studies of  $[\{\text{Cu}(\text{mepirizole})\text{Br}\}_2(\mu\text{-OH})(\mu\text{-pz})]$  (Mepirizole = 4-Methoxy-2-(5-methoxy-3-methyl-1H-pyrazol-1-yl)-6-methylpyrimidine; pz = Pyrazolate), a Novel  $\mu$ -Pyrazolato– $\mu$ -Hydroxo-Dibridged Copper(II) Complex. *Inorg. Chem.* **2003**, *42*, 8328–8336. [[PubMed](#)]
14. Armentano, D.; Marino, N.; Mastropietro, T.F.; Martínez-Lillo, J.; Cano, J.; Julve, M.; Lloret, F.; De Munno, G. Self-Assembly of a Chiral Carbonate- and Cytidine-Containing Dodecanuclear Copper(II) Complex: A Multiarm-Supplied Globular Capsule. *Inorg. Chem.* **2008**, *47*, 10229–10231. [[CrossRef](#)] [[PubMed](#)]
15. Marino, N.; Armentano, D.; Mastropietro, T.F.; Julve, M.; De Munno, G.; Martínez-Lillo, J. Cubane-Type  $\text{Cu}^{\text{II}}_4$  and  $\text{Mn}^{\text{II}}_2\text{Mn}^{\text{III}}_2$  Complexes Based on Pyridoxine: A Versatile Ligand for Metal Assembling. *Inorg. Chem.* **2013**, *52*, 11934–11943. [[CrossRef](#)] [[PubMed](#)]
16. Armentano, D.; Barquero, M.A.; Rojas-Dotti, C.; Moliner, N.; De Munno, G.; Brechin, E.K.; Martínez-Lillo, J. Enhancement of Inter-molecular Magnetic Exchange through Halogen...Halogen Interactions in Bisadeninium Rhenium(IV) Salts. *Cryst. Growth Des.* **2017**, *17*, 5342–5348. [[CrossRef](#)]
17. Orts-Arroyo, M.; Castro, I.; Lloret, F.; Martínez-Lillo, J. Field-induced slow relaxation of magnetisation in two one-dimensional homometallic dysprosium(III) complexes based on alpha- and beta-amino acids. *Dalton Trans.* **2020**, *49*, 9155–9163. [[CrossRef](#)] [[PubMed](#)]
18. Rojas-Dotti, C.; Martínez-Lillo, J. Thioester-functionalised and oxime-based hexametallc manganese(III) single-molecule magnets. *RSC Adv.* **2017**, *7*, 48841–48847. [[CrossRef](#)]
19. Tyagi, P.; Riso, C.; Amir, U.; Rojas-Dotti, C.; Martínez-Lillo, J. Exploring room-temperature transport of single-molecule magnet-based molecular spintronics devices using the magnetic tunnel junction as a device platform. *RSC Adv.* **2020**, *10*, 13006–13015. [[CrossRef](#)]
20. Chen, P.; Goldberg, D.E.; Kolb, B.; Lanser, M.; Benowitz, L.I. Inosine induces axonal rewiring and improves behavioral outcome after stroke. *Proc. Natl. Acad. Sci. USA* **2002**, *99*, 9031–9036. [[CrossRef](#)]
21. Kline, P.C.; Schramm, V.L. Purine Nucleoside Phosphorylase. Inosine Hydrolysis, Tight Binding of the Hypoxanthine Intermediate, and Third-the-Sites Reactivity. *Biochemistry* **1992**, *31*, 5964–5973. [[CrossRef](#)] [[PubMed](#)]
22. Jelińska, A. Kinetics of hydrolysis of inosine in aqueous solutions. *React. Kinet. Catal. Lett.* **2001**, *72*, 93–100. [[CrossRef](#)]
23. Chifotides, H.T.; Dunbar, K.R.; Matonic, J.H.; Katsaros, N. Unusual structural features of tetrakis( $\mu$ -carboxylato)dirhodium(II), an antitumor agent, bound to azathioprine, a biologically active mercaptopurine derivative. *Inorg. Chem.* **1992**, *31*, 4628–4634. [[CrossRef](#)]
24. Karran, P.; Attard, N. Thiopurines in current medical practice: Molecular mechanisms and contributions to therapy-related cancer. *Nat. Rev. Cancer* **2008**, *8*, 24–36. [[CrossRef](#)]
25. Jones, N.R.; Murray, J.; Livingston, E.I.; Murray, C.K. Rapid estimations of hypoxanthine concentrations as indices of the freshness of chill-stored fish. *J. Sci. Food Agric.* **1964**, *15*, 763–774. [[CrossRef](#)]
26. Cooper, N.; Khosravan, R.; Erdmann, C.; Fiene, J.; Lee, J.W. Quantification of uric acid, xanthine and hypoxanthine in human serum by HPLC for pharmacodynamic studies. *J. Chromatogr. B* **2006**, *837*, 1–10. [[CrossRef](#)]
27. Farthing, D.; Sica, D.; Gehr, T.; Wilson, B.; Fakhry, I.; Larus, T.; Farthing, C.; Karnes, H.T. An HPLC method for determination of inosine and hypoxanthine in human plasma from healthy volunteers and patients presenting with potential acute cardiac ischemia. *J. Chromatogr. B* **2007**, *854*, 158–164. [[CrossRef](#)]
28. Xiang, L.W.; Li, J.; Lin, J.M.; Li, H.F. Determination of gouty arthritis' biomarkers in human urine using reversed-phase high-performance liquid chromatography. *J. Pharm. Anal.* **2014**, *4*, 153–158. [[CrossRef](#)]
29. Bory, C.; Chantoin, C.; Bouliou, R. Comparison of capillary electrophoretic and liquid chromatographic determination of hypoxanthine and xanthine for the diagnosis of xanthinuria. *J. Chromatogr. A* **1996**, *730*, 329–331. [[CrossRef](#)]

30. Bory, C.; Chantin, C.; Boulieu, R. Capillary Electrophoretic Analysis of Hypoxanthine and Xanthine for the Diagnosis of Xanthinuria. In *Purine and Pyrimidine Metabolism in Man IX*; Griesmacher, A., Müller, M.M., Chiba, P., Eds.; Advances in Experimental Medicine and Biology; Springer: Boston, MA, USA, 1998; Volume 431.
31. Klinenberg, J.R.; Goldfinger, S.; Bradley, K.H.; Seegmiller, J.E. An enzymatic spectrophotometric method for the determination of xanthine and hypoxanthine. *Clin. Chem.* **1967**, *10*, 834–846. [[CrossRef](#)]
32. Khajehsharifi, H.; Pourbasheer, E. Simultaneous spectrophotometric determination of xanthine, hypoxanthine and uric acid in real matrix by orthogonal signal correction-partial least squares. *J. Iran. Chem. Soc.* **2011**, *8*, 1113–1119. [[CrossRef](#)]
33. Zhang, Y.; Deng, S.; Lei, J.; Xu, Q.; Ju, H. Carbon nanospheres enhanced electrochemiluminescence of CdS quantum dots for biosensing of hypoxanthine. *Talanta* **2011**, *85*, 2154–2158. [[CrossRef](#)] [[PubMed](#)]
34. Zuo, F.; Zhang, H.; Xie, J.; Chen, S.; Yuan, R. A sensitive ratiometric electrochemiluminescence biosensor for hypoxanthine detection by in situ generation and consumption of coreactants. *Electrochim. Acta* **2018**, *271*, 173–179. [[CrossRef](#)]
35. Dou, Z.-Y.; Cui, L.-L.; He, X.Q. Electrochemical determination of uric acid, xanthine and hypoxanthine by poly(xylitol) modified glassy carbon electrode. *J. Cent. South Univ.* **2014**, *21*, 870–876. [[CrossRef](#)]
36. Mardini-Farias, P.A.; Castro, A.A. Determination of Xanthine in the Presence of Hypoxanthine by Adsorptive Stripping Voltammetry at the Mercury Film Electrode. *Anal. Chem. Insights* **2014**, *9*, 49–55. [[CrossRef](#)]
37. Juban, K.B.B.; Billones, J.B. Simultaneous Electrochemical Determination of Hypoxanthine and Xanthine by Poly(Threonine) Film-Modified Electrode. *Anal. Bioanal. Electrochem.* **2015**, *7*, 149–160.
38. *SHELXTL-2017/1, Bruker Analytical X-ray Instruments*; Bruker: Madison, WI, USA, 2017.
39. *DIAMOND 4.5.0, Crystal Impact GbR*; Crystal Impact: Bonn, Germany, 2018.
40. Armentano, D.; Martínez-Lillo, J. Hexachlororhenate(IV) salts of ruthenium(III) cations: X-ray structure and magnetic properties. *Inorg. Chim. Acta* **2012**, *380*, 118–124. [[CrossRef](#)]
41. Orts-Arroyo, M.; Castro, I.; Lloret, F.; Martínez-Lillo, J. Molecular Self-Assembly in a Family of Oxo-Bridged Dinuclear Ruthenium(IV) Systems. *Cryst. Growth Des.* **2020**, *20*, 2044–2056. [[CrossRef](#)]
42. Dubler, E.; Hänggi, G.; Schmalte, H. Synthesis and structure of dimeric metal complexes with N(3)/N(9)-chelating hypoxanthine ligands and with bridging water molecules:  $[M_2(\mu\text{-hyxan})_2(\text{SO}_4)_2(\mu\text{-H}_2\text{O})_2(\text{H}_2\text{O})_2]$  (M = copper, cadmium, zinc; hyxan = hypoxanthine). *Inorg. Chem.* **1990**, *29*, 2518–2523. [[CrossRef](#)]
43. Hänggi, G.; Schmalte, H.; Dubler, E. Structure of  $[\text{Co}_2(\mu\text{-hypoxanthine})_2(\text{SO}_4)_2(\mu\text{-H}_2\text{O})_2(\text{H}_2\text{O})_2]$ . *Acta Cryst.* **1992**, *C48*, 1008–1012.
44. Reid, J.; Bond, T.; Wang, S.; Zhou, J.; Hu, A. Synchrotron powder diffraction, X-ray absorption and  $^1\text{H}$  nuclear magnetic resonance data for hypoxanthine. *Powder Diffr.* **2015**, *30*, 278–285. [[CrossRef](#)]
45. Mohite, S.S.; Patil-Deshmukh, A.B.; Chavan, S.S. Synthesis and characterization of Ru(III) complexes with 2-((E)-((4-(4-bromophenyl)ethynyl)phenyl)imino)methyl-4-((E)-phenyldiazenyl)phenol and their use as a precursor for RuO<sub>2</sub> nanoparticles. *J. Mol. Struct.* **2019**, *1176*, 386–393. [[CrossRef](#)]
46. Sur, V.P.; Mazumdar, A.; Kopel, P.; Mukherjee, S.; Vitek, P.; Michalkova, H.; Vaculovičová, M.; Moulick, A. A Novel Ruthenium Based Coordination Compound Against Pathogenic Bacteria. *Int. J. Mol. Sci.* **2020**, *21*, 2656. [[CrossRef](#)] [[PubMed](#)]
47. Shahrokhian, S.; Ghalkhani, M. Electrochemical study of Azathioprine at thin carbon nanoparticle composite film electrode. *Electrochem. Commun.* **2009**, *11*, 1425–1428. [[CrossRef](#)]
48. Rao, C.N.; Balaji, K.; Venkateswarlu, P. Determination of azathioprine and rocuronium in biological fluid samples by voltammetry. *Biomed. Pharmacol. J.* **2009**, *2*, 117–121.
49. Jalali, F.; Rasaee, G. Electrochemical, spectroscopic, and theoretical studies on the interaction between azathioprine and DNA. *Int. J. Biol. Macromol.* **2015**, *81*, 427–434. [[CrossRef](#)]
50. Asadian, E.; Iraj Zad, A.; Shahrokhian, S. Voltammetric studies of Azathioprine on the surface of graphite electrode modified with graphene nanosheets decorated with Ag nanoparticles. *Mater. Sci. Eng. C* **2016**, *58*, 1098–1104. [[CrossRef](#)]
51. Oliveira-Brett, A.M.; Silva, L.A.; Farace, G.; Vadgama, P.; Brett, C.M.A. Voltammetric and impedance studies of inosine-5'-monophosphate and hypoxanthine. *Bioelectrochemistry* **2003**, *59*, 49–56. [[CrossRef](#)]
52. Revin, S.B.; John, S.A. Selective determination of inosine in the presence of uric acid and hypoxanthine using modified electrode. *Anal. Biochem.* **2012**, *421*, 278–284. [[CrossRef](#)]
53. Cotton, F.A.; Pedersen, E. Magnetic and electrochemical properties of transition metal complexes with multiple metal-to-metal bonds. II. Tetrabutyratodiruthenium(n+) with n = 0 and 1. *Inorg. Chem.* **1975**, *14*, 388–391. [[CrossRef](#)]
54. Malinski, T.; Chang, D.; Feldmann, F.N.; Bear, J.L.; Kadish, K.M. Electrochemical studies of a novel ruthenium(II, III) dimer, trifluoroacetamidatoruthenium chloride (Ru<sub>2</sub>(HNOCCF<sub>3</sub>)<sub>4</sub>Cl). *Inorg. Chem.* **1983**, *22*, 3225–3233. [[CrossRef](#)]
55. Hiraoka, Y.; Ikeue, T.; Sakiyama, H.; Guégan, F.; Luneau, D.; Gillon, B.; Hiromitsu, I.; Yoshioka, D.; Mikuriya, M.; Kataoka, Y.; et al. An unprecedented up-field shift in the <sup>13</sup>C NMR spectrum of the carboxyl carbons of the lantern-type dinuclear complex TBA[Ru<sub>2</sub>(O<sub>2</sub>CCH<sub>3</sub>)<sub>4</sub>Cl<sub>2</sub>] (TBA<sup>+</sup> = tetra(n-butyl)ammonium cation). *Dalton Trans.* **2015**, *44*, 13439–13443. [[CrossRef](#)] [[PubMed](#)]
56. Kataoka, Y.; Mikami, S.; Sakiyama, H.; Mitsumi, M.; Kawamoto, T.; Handa, M. A neutral paddlewheel-type diruthenium(III) complex with benzamidinato ligands: Synthesis, crystal structure, magnetism, and electrochemical and absorption properties. *Polyhedron* **2017**, *136*, 87–92. [[CrossRef](#)]



---

## *ARTICLE 4*

*A novel adenine-based  
diruthenium(III) complex:  
Synthesis, crystal structure,  
electrochemical properties and  
evaluation of the anticancer  
activity*





## A novel adenine-based diruthenium(III) complex: Synthesis, crystal structure, electrochemical properties and evaluation of the anticancer activity

Marta Orts-Arroyo<sup>a</sup>, Fernanda Gutiérrez<sup>b,c</sup>, Anabel Gil-Tebar<sup>b,c</sup>, Maider Ibarrola-Villava<sup>b,c</sup>, Elena Jiménez-Martí<sup>b,c,d</sup>, Adriana Silvestre-Llora<sup>a</sup>, Isabel Castro<sup>a</sup>, Gloria Ribas<sup>b,\*</sup>, José Martínez-Lillo<sup>a,\*</sup>

<sup>a</sup> Departament de Química Inorgànica, Institut de Ciència Molecular (ICMol), Universitat de València, 46980 Paterna, València, Spain

<sup>b</sup> Department of Medical Oncology, INCLIVA Biomedical Research Institute, Universitat de València, 46010 Valencia, Spain

<sup>c</sup> CIBERONC, Centro de Investigación Biomédica en Red Cáncer, Instituto de Salud Carlos III, Spain

<sup>d</sup> Departament de Bioquímica i Biologia Molecular, Facultat de Medicina, Universitat de València, Spain

### ARTICLE INFO

#### Keywords:

Ruthenium(III)  
Adenine  
Crystal structure  
Cyclic voltammetry  
Cancer cell lines  
Cell viability

### ABSTRACT

Metal complexes based on purine nucleobases can be a very useful tool in the diagnosis and treatment of some diseases as well as in other biomedical applications. We have prepared and characterized a novel dinuclear ruthenium(III) complex based on the nucleobase adenine of formula  $[\{\text{Ru}(\mu\text{-Cl})(\mu\text{-Hade})\}_2\text{Cl}_4]\text{Cl}_2 \cdot 2\text{H}_2\text{O}$  (**1**) [Hade = protonated adenine]. Complex **1** was characterized through Fourier transform infrared spectroscopy (FT-IR), scanning electron microscopy and energy dispersive X-ray analysis (SEM-EDX), magnetometer (SQUID) and cyclic voltammetry (CV) techniques. The crystal structure of **1** was determined by single-crystal X-ray diffraction. **1** crystallizes in the monoclinic system with space group  $P2_1/n$ . Each ruthenium(III) ion is six-coordinate and bonded to four Cl atoms [the average value of the  $\text{Ru}^{\text{III}}\text{-Cl}$  bonds lengths is ca. 2.329(1) Å] and two N atoms (N3 and N9) from two adenine molecules, the N1 atom being protonated in both of them. The anticancer activity was evaluated through cell viability assays performed on a colon cancer (HCT116) and a gastric cancer cell lines (AGS), **1** showing an incipient anticancer effect on the AGS cell line at the highest concentration used in the study.

### 1. Introduction

Ruthenium coordination chemistry has undergone a considerable development in different research fields during the last two decades [1], including promising systems for current and future investigations that involve several oxidation states, which display a wide variety of technological applications covering from catalysis to anticancer drugs [2–11].

Heteroleptic mononuclear  $\text{Ru}^{\text{III}}$  complexes have proven to be

particularly important for the design of metallic systems with exciting biological properties [12]. Some examples are the  $\text{Ru}^{\text{III}}$  complexes based on imidazole and indazole ligands [13,14], namely, the anionic complexes *trans*-[tetrachloro(dimethyl sulfoxide)(imidazole)ruthenate(III)] (NAMI-A) and *trans*-[tetrachlorobis(indazole)ruthenate(III)] (KP1019), which behave as anticancer and antimetastatic agents that have entered clinical trials [15–17].

In the literature, there exist a few ruthenium complexes based on nucleobases with tested antitumor activity [18–21], as for instance, the

**Abbreviations:** FT-IR, fourier transform infrared spectroscopy; SEM-EDX, scanning electron microscopy and energy dispersive X-ray analysis; CV, cyclic voltammetry; HCT116, colon cancer cell line; AGS, gastric cancer cell line; NAMI-A, *trans*-[tetrachloro(dimethyl sulfoxide)(imidazole)ruthenate(III)]; KP1019, *trans*-[tetrachlorobis(indazole)ruthenate(III)]; DMSO, dimethyl sulfoxide; PTA, 1,3,5-triaza-7-phosphaadamantane; 5'-AMP, adenosine 5'-monophosphate; MPMS, magnetic properties measurement system; SQUID, superconducting quantum interference device; DMF, N,N'-dimethylformamide; Fc, ferrocene; CCDC, cambridge crystallographic data centre; MTT, 3-(4,5-dimethylthiazolyl)-2,5-diphenyltetrazolium bromide; PI, propidium iodide; PBS, phosphate buffered saline; FITC, fluorescein isothiocyanate; PXRD, powder X-ray diffraction.

\* Corresponding authors.

E-mail address: [f.jose.martinez@uv.es](mailto:f.jose.martinez@uv.es) (J. Martínez-Lillo).

<https://doi.org/10.1016/j.jinorgbio.2022.111812>

Received 11 January 2022; Received in revised form 10 March 2022; Accepted 31 March 2022

Available online 6 April 2022

0162-0134/© 2022 The Authors. Published by Elsevier Inc. This is an open access article under the CC BY license (<http://creativecommons.org/licenses/by/4.0/>).

thymine-based Ru<sup>II</sup> complex [Ru(PPh<sub>3</sub>)<sub>2</sub>(thy)(bpy)]PF<sub>6</sub> [where PPh<sub>3</sub> = triphenylphosphine, thy = thymine and bpy = 2,2'-bipyridine], which is a potent cytotoxic agent that by DNA-binding induces apoptotic cell death in human colon carcinoma [18,19]. The first guanine-containing Ru<sup>III</sup> complex of formula trans-[Ru<sup>III</sup>Cl<sub>4</sub>(Hgua)(DMSO)]·2H<sub>2</sub>O (Hgua = monoprotonated guanine) was reported in 2004 [20]. This compound was characterized by single-crystal X-ray diffraction and its in vitro antitumor activity was also evaluated, showing a mild antiproliferative effect but an interesting proadhesive effect [20]. With deprotonated adenine, the Ru(II)-arene complex [RuCp(adeninate-κN7)(PPh<sub>3</sub>)(PTA)] (PTA = 1,3,5-triaza-7-phosphaadamantane) was obtained and its antiproliferative activity was also analyzed. This complex displayed results comparable to those of cisplatin, and better than those of the deprotonated guanine derivative [21].

Herein we report a novel dinuclear Ru<sup>III</sup> complex of formula [{Ru(μ-Cl)(μ-Hade)}<sub>2</sub>Cl<sub>4</sub>]Cl<sub>2</sub>·2H<sub>2</sub>O (**1**) (Hade = protonated adenine). **1** is the first dinuclear ruthenium(III) system based on adenine. In this work, we discuss its preparation, crystal structure, electrochemical properties and anticancer activity.

## 2. Experimental

### 2.1. Materials

All starting chemicals and solvents used in the synthesis of **1** were purchased from commercial sources and used without further purification. Adenosine 5'-monophosphate (5'-AMP) (99.00%) was purchased from Acros Organics and the ruthenium precursor K<sub>2</sub>[RuCl<sub>5</sub>(H<sub>2</sub>O)] (99.95%) was acquired from Alfa Aesar.

### 2.2. Synthesis

#### 2.2.1. Synthesis of [{Ru(μ-Cl)(μ-Hade)}<sub>2</sub>Cl<sub>4</sub>]Cl<sub>2</sub>·2H<sub>2</sub>O (**1**)

A solvothermal reaction of K<sub>2</sub>[RuCl<sub>5</sub>(H<sub>2</sub>O)] (11.2 mg, 0.03 mmol) and adenosine 5'-monophosphate monohydrate (11.0 mg, 0.03 mmol) was carried out in HCl (4 mL, 3.0 M) at 90 °C for 3 days, followed by a 12 h cooling process to room temperature. Dark brown plates of **1** were thus grown and were suitable for X-ray diffraction studies. Yield: ca. 65%. Anal. Calcd. for C<sub>10</sub>H<sub>16</sub>Cl<sub>8</sub>N<sub>8</sub>O<sub>2</sub>Ru<sub>2</sub>: C, 15.1; H, 2.0; N, 17.6. Found: C, 15.2; H, 1.9; N, 17.7. SEM-EDX: a molar ratio of 1:4 for Ru/Cl was found for **1**. IR peaks (KBr pellets, ν/cm<sup>-1</sup>): 3405(m), 3327(m), 3116(m), 3056(m), 2955(m), 2923(m), 2853(m), 1706(vs), 1653(m), 1616(m), 1559(m), 1521(w), 1466(s), 1404(m), 1320(m), 1234(s), 1180(m), 1135(m), 940(w), 800(w), 669(w), 608(m), 562(m), 414(w).

### 2.3. Physical measurements

Elemental analyses (C, H, N) and X-ray microanalysis were performed by the Central Service for the Support to Experimental Research (SCSIE) at the University of Valencia. The images and results of scanning electron microscopy (SEM-EDX) were obtained from a Hitachi S-4800 field emission scanning electron microscope, with 20 kV and 9.0 mm of accelerating voltage and working distance, respectively. Infrared spectrum (FT-IR) of **1** was recorded as a KBr pellet with a PerkinElmer Spectrum 65 FT-IR spectrometer in the range of 400 to 4000 cm<sup>-1</sup> with 25 scans and a spectral resolution of 4 cm<sup>-1</sup> (OMNIC 7.1a spectra software). Direct current (dc) magnetic susceptibility data were collected on a Quantum Design MPMS-XL SQUID magnetometer. The experimental magnetic data were corrected for the diamagnetic contributions of the constituent atoms as well as for the sample holder. Electrochemical studies were carried out on **1** by means of an Autolab/PGSTAT 204 scanning potentiostat operating at a scan rate range of 10–250 mV/s with Metrohm electrodes (NOVA 2.0 software). Cyclic voltammograms were performed by using 0.1 M (NBu<sub>4</sub>)[PF<sub>6</sub>] as supporting electrolyte and a 10<sup>-3</sup> M solution of **1** in dry *N,N'*-dimethylformamide (DMF). A glassy carbon disk of 0.32 cm<sup>2</sup> was used as

**Table 1**  
Crystal data and structure refinement for **1**.

Formula	C <sub>10</sub> H <sub>12</sub> Cl <sub>8</sub> N <sub>10</sub> O <sub>2</sub> Ru <sub>2</sub>
Formula weight	790.04
Crystal system	monoclinic
Space group	<i>P</i> 2 <sub>1</sub> / <i>n</i>
Z	2
<i>a</i> (Å)	6.961(1)
<i>b</i> (Å)	19.042(2)
<i>c</i> (Å)	9.197(1)
α (°)	90
β (°)	101.20(1)
γ (°)	90
<i>V</i> (Å <sup>3</sup> )	1195.9(2)
<i>D<sub>c</sub></i> (g cm <sup>-3</sup> )	2.194
<i>F</i> (000)	764.0
μ (mm <sup>-1</sup> )	2.189
Goodness-of-fit on <i>F</i> <sup>2</sup>	1.175
<i>R</i> <sub>1</sub> [ <i>I</i> > 2σ( <i>I</i> )] <sup>a</sup> / all	0.0589 / 0.0719
<i>wR</i> <sub>2</sub> <sup>b,c</sup> / all	0.1630 / 0.1780

$$^a R_1 = \sum ||F_o| - |F_c|| / \sum |F_o|.$$

$$^b wR_2 = \{ \sum [w(F_o^2 - F_c^2)^2] / [\sum w(F_o^2)^2] \}^{1/2}.$$

$$^c w = 1 / [\sigma^2(F_o^2) + (aP)^2 + bP] \text{ with } P = [F_o^2 + 2F_c^2] / 3.$$

working electrode, which was polished with 1.0 μm diamond powder, sonicated, washed with absolute ethanol and acetone, and air-dried. The AgCl/Ag reference electrode was separated from the test solution by a salt bridge containing the solvent/supporting electrolyte, with platinum as auxiliary electrode. All experiments were performed in standard electrochemical cells at 25 °C under argon. The investigated potential range was in the range of -1.5 to +1.5 V vs. AgCl/Ag. Ferrocene (Fc) was added as internal standard at the end of all the measurements.

### 2.4. Crystallographic data collection and structure determination

X-ray diffraction data collection from a single crystal of dimensions 0.16 × 0.06 × 0.02 mm<sup>3</sup> was performed on a Bruker D8 Venture diffractometer with graphite-monochromated Mo-K<sub>α</sub> radiation (λ = 0.71073 Å). Crystal parameters and refinement results for **1** are summarized in Table 1. The structure of **1** was solved by standard direct methods and subsequently completed by Fourier recycling by using the SHELXTL software packages. The obtained model was refined with version 2017/1 of SHELXL against *F*<sup>2</sup> on all data by full-matrix least squares [22]. All non-hydrogen atoms were anisotropically refined, whereas the hydrogen atoms of the adenine molecule were set in calculated positions and refined isotropically by using the riding model. The hydrogen atoms of the water molecules were neither detected nor included into the model. The graphical manipulations were performed with DIAMOND program [23]. The CCDC code for **1** is 2.081.705.

### 2.5. Cancer cell line cultures

Two cancer cell lines from American Type Culture Collection (ATCC Rockville, MD) were used to test compound **1**: AGS (gastric cancer) and HCT116 (colon cancer). Cell lines were cultured following the conditions recommended by the supplier. The culture medium used in all cases was RPMI 1640 (Roswell Park Memorial Institute), supplemented with 10% Fetal Bovine Serum (GIBCO, New York, NY) and 1% Penicillin, under conditions of 37 °C at 5% CO<sub>2</sub>.

### 2.6. Cell proliferation assays: MTT

Three thousand cells were cultured in 96-well plates during 24 h. After that, the cells were treated with 1, 10, 20 and 31 μM concentrations of **1** (the solvent being Polyethylene glycol 3350) in triplicate and the effect was measured at 48 and 72 h after treatment.

A 3-(4,5-dimethylthiazolyl-2)-2,5-diphenyltetrazolium bromide (MTT) assay was used to evaluate cell proliferation. MTT is a

colorimetric assay indicating cell survival and proliferation, which is based on the metabolic reduction of the MTT by the mitochondrial enzyme succinate dehydrogenase, under defined conditions, to a purple-coloured compound (formazan), thus allowing the determination of the mitochondrial function of the treated cells. MTT, a yellow tetrazole, is reduced to purple in living cells. A dimethyl sulfoxide (DMSO) solution is added to solubilize the compound and convert the insoluble purple formazan into a coloured solution, the absorbance of which is measured at 560 nm in the spectrophotometer. An increase in absorbance corresponds to an increase in cell proliferation, while a decrease in absorbance means a decrease in cell proliferation. Each value is repeated in triplicate and the mean is calculated. Each absorbance of the tested compound is checked with its respective untreated control. Viability is calculated according to the following equation: % Viability = (Optical Density treated cells x 100) / Optical Density control cells.

### 2.7. Apoptosis evaluation by cytometry

Three thousand cells were cultured in 96-well plates during 24 h. After that, the cells were treated with 1, 10, 20 and 31  $\mu\text{M}$  of compound **1** in triplicate, and the effect was measured at 48 and 72 h after treatment.

Cells were washed with cold phosphate buffered saline (PBS) and trypsinized with 0.05% trypsin and the collected cells were then centrifuged at 1500 rpm at 4 °C for 5 min.

The pellet collection was staining for Annexin V-FITC and phycoerythrin-Cyanine7 (PE-Cy7)-A using an apoptosis detection kit II (Pharmingen, San Diego, CA, USA) based on the binding properties of annexin A5 to phosphatidylserine with a vital dye such as propidium iodide (PI). Samples were diluted in binding buffer. From this solution and aliquot of 100  $\mu\text{L}$  was stained with 5  $\mu\text{L}$  Protein A conjugated with fluorescein isothiocyanate (A-FITC) solution and 10  $\mu\text{L}$  PI solution. Samples were incubated for 15 min, and 400  $\mu\text{L}$  of binding buffer was added. Samples were analyzed within 1 h. The samples were analyzed using a BD FACSVESSE Cell Analyzer (BD Bioscience) equipped with standard optics. An Ar-ion laser (INNOVA 90, Coherent, Santa Clara, CA, USA) tuned at 488 nm and running at 200 mW was used as light source. From each cell, forward light scatter (FSC), orthogonal light scatter (SSC), A-FITC fluorescence, and PI fluorescence were evaluated using Cellquest version 3.3 (Becton Dickinson, San Jose, CA, USA). The percentages of Annexin-V negative or positive, and PI negative or positive as well as double positive cells were evaluated, based on quadrants determined from single-stained and unstained control samples.

## 3. Results and discussion

### 3.1. Synthetic procedure

By reacting the ruthenium(III) precursor  $\text{K}_2[\text{RuCl}_5(\text{H}_2\text{O})]$  with adenine 5'-monophosphate (5'-AMP) in a hydrochloric acid (3.0 M) solution, we prepared a novel purine-based ruthenium(III) complex of formula  $[\{\text{Ru}(\mu\text{-Cl})(\mu\text{-Hade})\}_2\text{Cl}_4]\text{Cl}_2 \cdot 2\text{H}_2\text{O}$  (**1**). The synthetic procedure was performed by heating the reaction mixture at 90 °C through a solvothermal method. As crystallization technique, the process continued during a further 12 h cooling step to room temperature. In this way, dark brown crystals of **1** were obtained in satisfactory yield (65%). The nucleotide 5'-AMP was used here as starting material of **1** because it is a suitable source of adenine. Besides, a better yield was obtained when 5'-AMP was employed instead of just adenine. To obtain compound **1** the combination of the solvothermal method and strong acid medium is mandatory, leading to the hydrolysis of the nucleotide precursor and the protonation of the adenine moiety at N1 atom. These results support the fact that this is an adequate synthetic method to obtain purine-based diruthenium(III) compounds [24].

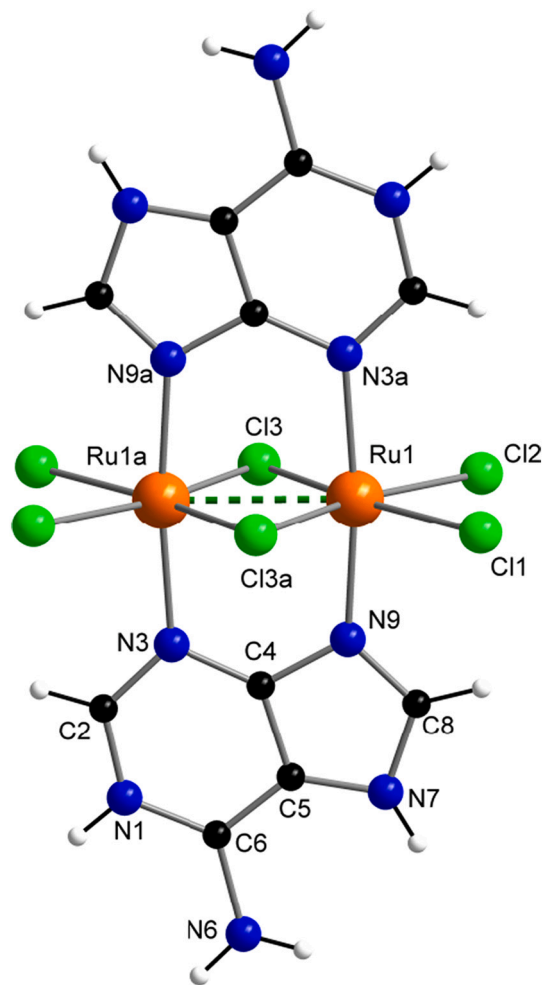


Fig. 1. Molecular structure of the  $[\{\text{Ru}(\mu\text{-Cl})(\mu\text{-Hade})\}_2\text{Cl}_4]^{2+}$  complex in **1** along with the atom labels scheme.

### 3.2. Crystal structure of $[\{\text{Ru}(\mu\text{-Cl})(\mu\text{-Hade})\}_2\text{Cl}_4]\text{Cl}_2 \cdot 2\text{H}_2\text{O}$ (**1**)

The crystal structure of **1** was obtained by single-crystal X-ray diffraction. A Cambridge Structural Database (CSD) survey revealed that **1** is the first reported compound with a crystal structure based on a dinuclear Ru(III) compound containing adenine. **1** crystallizes in the monoclinic system, with space group  $P2_1/n$  (Table 1), and its core is very similar to that of the previously reported neutral  $[\{\text{Ru}(\mu\text{-Cl})(\mu\text{-hpx})\}_2\text{Cl}_4]$  (hpx = hypoxanthine molecule) complex, which crystallizes in the monoclinic system with space group  $P2_1/c$  [24]. The crystal structure of **1** is made up of dinuclear cationic  $[\{\text{Ru}(\mu\text{-Cl})(\mu\text{-Hade})\}_2\text{Cl}_4]^{2+}$  complexes, chloride anions and  $\text{H}_2\text{O}$  molecules. The asymmetric unit of **1** consists of half a  $[\{\text{Ru}(\mu\text{-Cl})(\mu\text{-Hade})\}_2\text{Cl}_4]^{2+}$  complex, one chloride and one water molecule (Fig. 1).

Each Ru(III) ion is bonded to four chloride ions and two nitrogen atoms (N3 and N9) from two purine bases in a distorted octahedral environment, the N1 being protonated in both adenine molecules. The two Ru(III) ions are connected each other through two adenine molecules and two chloro-bridges (Fig. 1). In **1**, a very short intramolecular Ru...Ru distance  $[\text{Ru}(1)\cdots\text{Ru}(1a)] = 2.713 \text{ \AA}$ ,  $(a) = -x + 1, -y + 1, -z + 2]$  indicates the formation of a metal-metal bond (dashed lines in Fig. 1). The average values of the Ru—Cl [ $2.329(1) \text{ \AA}$ ] and Ru—N [ $2.067(1) \text{ \AA}$ ] bond lengths are in agreement with those values found in the literature for previously reported Ru(III) complexes with a similar environment [24,25]. The adenine molecules in **1** show C—C and C—N bond lengths with values which are in agreement with those previously reported for



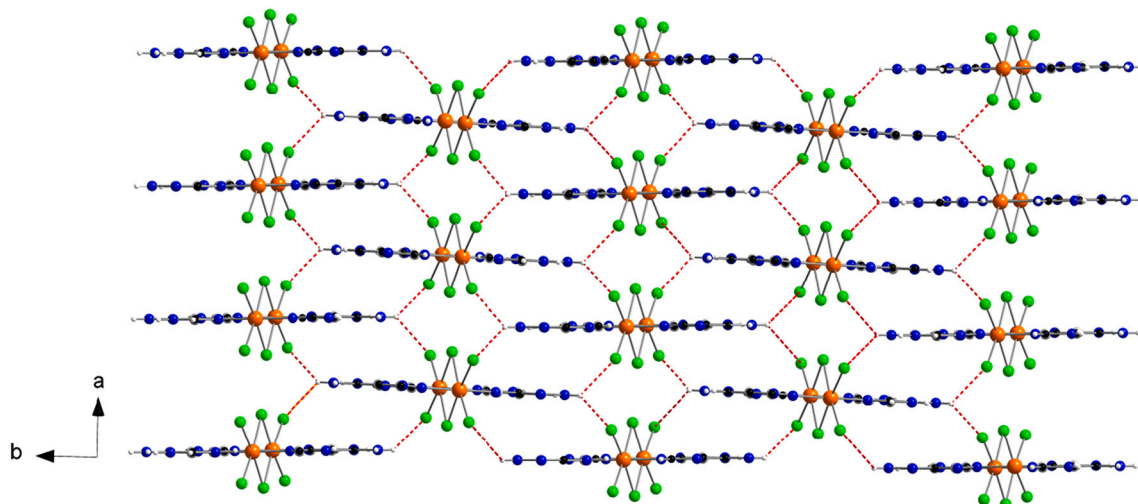


**Fig. 2.** View along the crystallographic *c* axis of a fragment of the crystal packing of **1**. H-bonding interactions between  $\text{Cl}^-$  anions and N–H groups of adjacent  $[\{\text{Ru}(\mu\text{-Cl})(\mu\text{-Hade})\}_2\text{Cl}_4]^{2+}$  units are shown as red-dashed lines. Non-coordinating  $\text{Cl}^-$  anions and water molecules have been omitted for clarity. (For interpretation of the references to colour in this figure legend, the reader is referred to the web version of this article.)

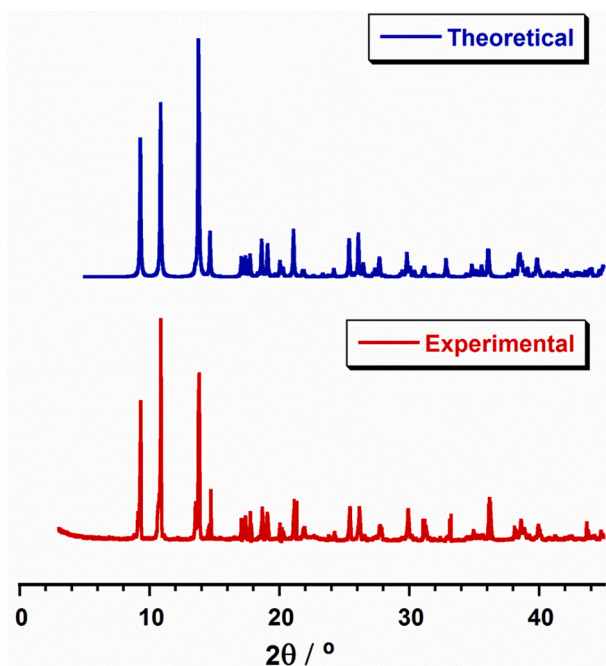


**Fig. 3.** Plot of the experimental (red) and theoretical (blue) powder X-ray diffraction (PXRD) patterns profile ( $2\theta/^\circ$ ) in the range  $0\text{--}45^\circ$  for **1**. (For interpretation of the references to colour in this figure legend, the reader is referred to the web version of this article.)

compounds containing this nucleobase [26–33].

In the crystal packing of **1**, the  $[\{\text{Ru}(\mu\text{-Cl})(\mu\text{-Hade})\}_2\text{Cl}_4]^{2+}$  cations and  $\text{Cl}^-$  anions are arranged in an alternate way. The shortest intermolecular Cl–Cl interaction of ca.  $3.373(2)$  Å connects the  $[\{\text{Ru}(\mu\text{-Cl})(\mu\text{-Hade})\}_2\text{Cl}_4]^{2+}$  units each other generating chains that grow along the crystallographic *a* axis  $[\text{Cl}(3)\cdots\text{Cl}(3b)$ ,  $(b) = -x, -y + 2, -z + 2]$  (Fig. 2). H-bonding interactions between  $\text{Cl}^-$  anions and N–H groups of adjacent  $[\{\text{Ru}(\mu\text{-Cl})(\mu\text{-Hade})\}_2\text{Cl}_4]^{2+}$  units [with  $\text{Cl}\cdots\text{N}$  separations of ca.  $3.193(3)$  Å] lead these chains to the formation of a two-dimensional network, which is extended along the *ab* plane (Fig. 2). The shortest intermolecular Ru $\cdots$ Ru distance is ca.  $6.76$  Å  $[\text{Ru}(1)\cdots\text{Ru}(1c)$ ,  $(c) = -x + 1, -y + 2, -z + 1]$ . Although no  $\pi\cdots\pi$  interactions are observed in **1** [the shortest centroid $\cdots$ centroid distance being approximately  $5.701(1)$

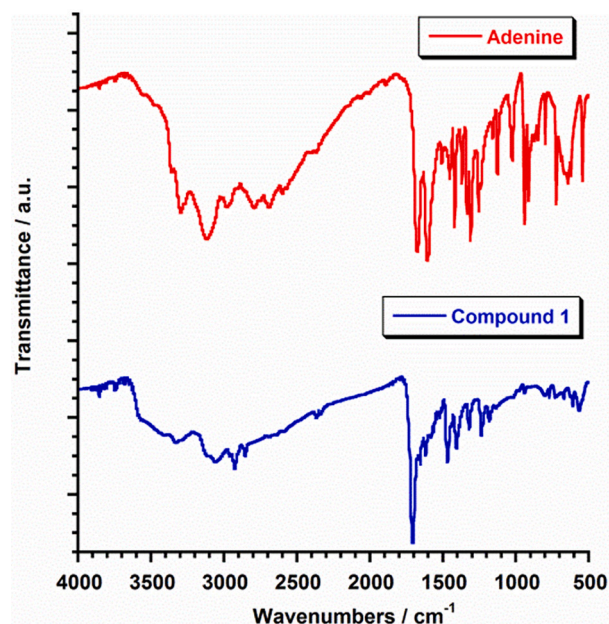


**Fig. 4.** FT-IR spectra for adenine (red) and compound **1** (blue), see text. (For interpretation of the references to colour in this figure legend, the reader is referred to the web version of this article.)

Å],  $\text{Cl}\cdots\pi$  interactions of approximately  $3.501(1)$  Å take place between intercalated  $\text{Cl}^-$  anions and the pyrimidine ring of adenine molecules. The supramolecular network is supported by additional H-bonding interactions, which stabilize the crystal structure in **1**. The powder X-ray diffraction (PXRD) pattern of **1** confirmed the homogeneity of the bulk sample (Fig. 3).

### 3.3. Infrared spectroscopy

The infrared (IR) spectrum of **1** along with that of the free adenine ligand are given in Fig. 4. The IR spectrum of adenine has been previously studied [34,35], so that it has been added in this work only for comparison. In general, the vibrational bands mainly associated to the N–H symmetric ( $\nu_s$ ) and asymmetric ( $\nu_{as}$ ) stretching for the free adenine molecule were more intense and complex than those of **1** in the ca.

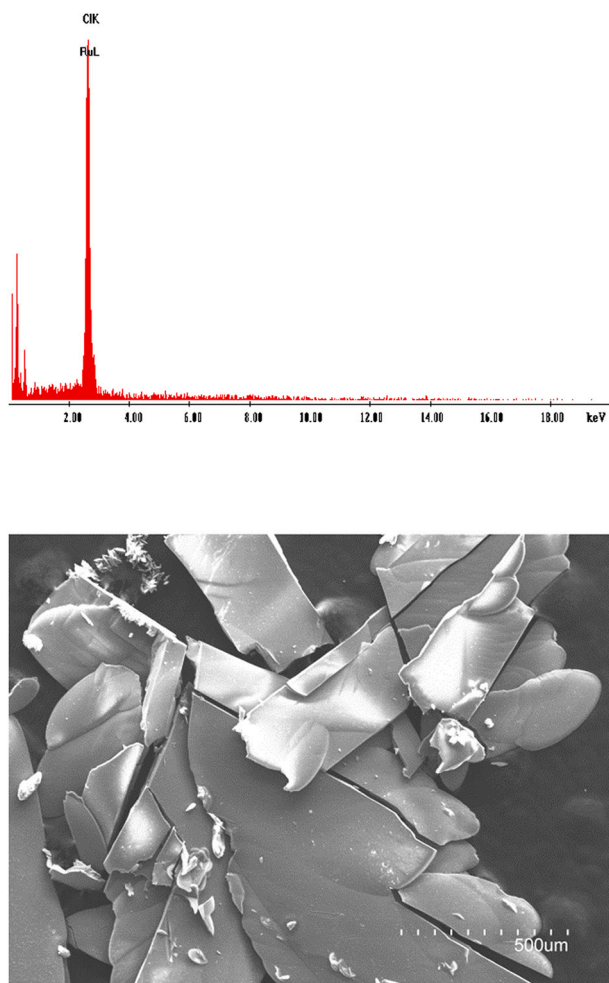


Fig. 5. (Top) Energy dispersive X-ray analysis (EDX) spectrum for **1**. (Bottom) Scanning electron microscopy (SEM) image of crystals of **1**.

3800–2000  $\text{cm}^{-1}$  region (Fig. 4), which would be due to a more ordered hydrogen-bonding network in the crystalline solid for the free ligand [34,35]. The experimental  $\nu_{\text{as}}(\text{NH}_2)$  value of the adenine molecule observed at 3296  $\text{cm}^{-1}$  was slightly shifted to higher wavenumbers when compared with that detected for **1** [3327  $\text{cm}^{-1}$ ], whereas the experimental  $\nu_{\text{s}}(\text{NH}_2)$  value remained pretty much unaltered in the IR spectrum of **1** [3116  $\text{cm}^{-1}$ ] (Fig. 4). In the 1800–500  $\text{cm}^{-1}$  region, the most interesting features were the two strong vibrational bands associated to the stretching  $\nu(\text{C}=\text{N})$  and  $\nu(\text{C}=\text{C})$  and bending  $\delta(\text{NH}_2)$ , mainly scissoring, which were found at 1680 and 1600  $\text{cm}^{-1}$  for the adenine molecule [34,35]. These vibrational bands were transformed into only one band, which was observed at 1706  $\text{cm}^{-1}$  for **1**, with this fact indicating the coordination of the  $\text{Ru}^{\text{III}}$  metal ions to adenine molecules in compound **1** (Fig. 4). The  $\text{Ru}-\text{Cl}$  band is expected to be found around 310–330  $\text{cm}^{-1}$ . Unfortunately, we cannot report this value for compound **1** given that our IR device works in the 4000–400  $\text{cm}^{-1}$  range.

### 3.4. Scanning electron microscopy - energy dispersive X-ray analysis

A sample of compound **1** was measured through of scanning electron microscopy and energy dispersive X-ray analysis (SEM-EDX), these analyses being carried out as previously performed for other ruthenium systems [36,37]. The results of the microanalysis gave a  $\text{Ru}/\text{Cl}$  molar ratio of 1:4. An example of the recorded images of **1** is given in Fig. 5, where crystals of **1** are shown as plates.

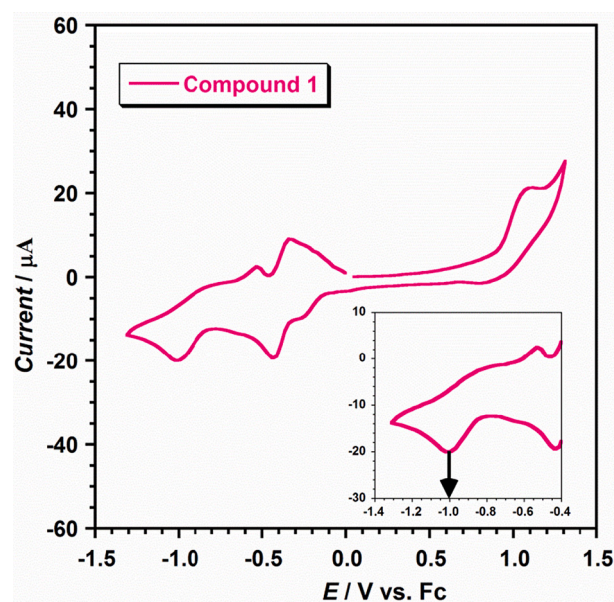


Fig. 6. Cyclic voltammogram of **1** in a dry DMF  $10^{-3}$  M solution with 0.1 M  $(\text{NBu}_4)[\text{PF}_6]$  at 25 °C and scan rate 200 mV/s. The area of the working electrode is 0.32  $\text{cm}^2$ . The inset shows a detail of reduction peak assigned to adenine.

### 3.5. Magnetic properties

Direct current (dc) magnetic susceptibility measurements were carried out on a microcrystalline sample of compound **1** and under an external magnetic field of 1000 G. These measurements revealed that **1** is diamagnetic at room temperature. The value of its molar magnetic susceptibility ( $\chi_{\text{M}}$ ) was calculated to be  $-0.0296 \text{ cm}^3 \text{ mol}^{-1}$  at 300 K. The diamagnetic nature observed for **1** is mainly due to a very strong anti-ferromagnetic coupling between the involved ruthenium ions ( $4d^5$  configuration and  $S = 1/2$  each), that are connected through two adenine ligands and two chloro bridges, which lead to the formation of a metal-metal bond and hence generating a ruthenium system with  $S = 0$ .

### 3.6. Electrochemical properties

The electrochemical properties of **1** were investigated by means of cyclic voltammetry (CV) in dry  $N,N'$ -dimethylformamide (DMF), containing 0.1 M  $(\text{NBu}_4)[\text{PF}_6]$ , in the range of potential between +1.5 and  $-1.5$  V and at room temperature. The CV plot obtained is shown in Fig. 6.

Dinuclear ruthenium compounds containing metal-metal bonds have been studied for several decades [38]. They show electronic structures and redox properties which are strongly depending on the solvent and the supporting electrolyte and, in general, are well-known [39–41]. Therefore, this type of  $\text{Ru}-\text{Ru}$  compounds could be an acceptable reference in electrochemical studies applied in several areas of investigation [39–41]. In the CV curves of **1**, three reduction processes can be observed (Fig. 6). The first two reduction peaks were found between 0.0 V and  $-0.50$  V, which would be associated to the formation of the mixed-valent  $\text{Ru}(\text{II})-\text{Ru}(\text{III})$  species [at  $-0.27$  V] and also to that of the  $\text{Ru}(\text{II})-\text{Ru}(\text{II})$  system [at  $-0.43$  V]. These reduction potential values are very close to those reported for similar diruthenium compounds [39–41]. Nevertheless, much more interesting would be the third detected reduction peak, which would be generated by the influence of the adenine ligand and would be observed at  $-1.00$  V, see inset in Fig. 6. It is worth mention that this value assigned to adenine is in agreement with those previously reported for this purine nucleobase in electrochemistry studies performed through modified electrodes based on different polyaniline- $\text{MnO}_2$  [42] and graphite- $\text{WS}_2$  composite materials



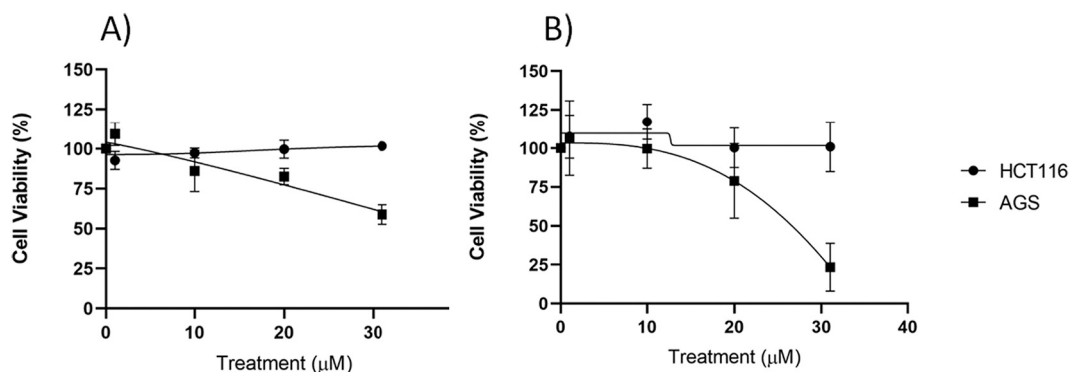


**Fig. 7.** Cell viability obtained by MTT assay. Cells were seeded in 12-well plates at a density of  $3 \times 10^3$  cells/mL and allowed to grow for 24 h before treatments. Concentrations: 1, 10, 20 and 31  $\mu$ M. Treatment duration was performed at 48 (A) and 72 h (B). Cell viability was determined by MTT assay at each time point, including the baseline and the DMSO (1:1000), and for each treatment. The method was carried out at least three times in triplicate.

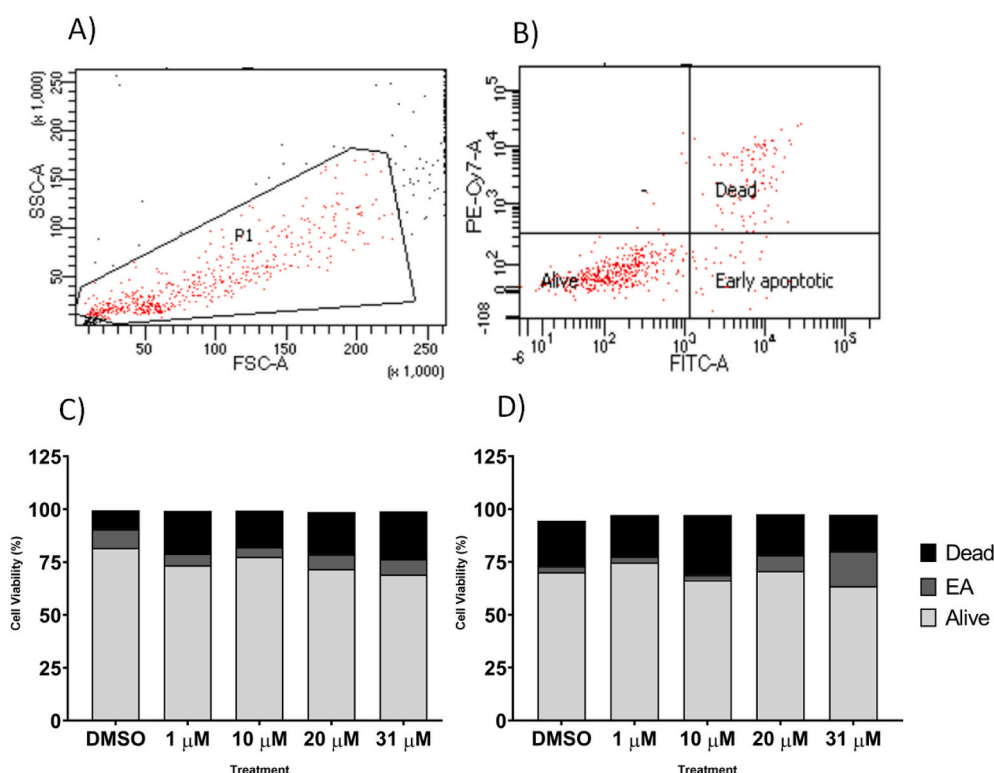


**Fig. 8.** (A) Cells events were selected from debris against forward (FSC-A) and side (SSC-A) scatter parameters. (B) Dot plot of gated cells staining with Annexin-V (FITC-A) and iodine propidium (PE-Cy7-A) in AGS cell lines. The upper right quadrant represents necrotic cells binding Annexin-V and PI, the lower right quadrant shows early apoptotic cells which bind Annexin-V but exclude PI, alive cells are represented in the lower left quadrant with no signal from Annexin-V neither from PI. Piled histogram representing the proportion of alive (light grey), necrotic cells (black) and early apoptotic (EA) cells (dark grey) in (C) HCT116 cells and (D) AGS cells at 48 h and at different concentrations of **1**.

[43], which shown high accuracy and promising redox activity toward purine nucleobases [42,43]. In addition, a similar electrochemical behavior was observed in the case of the hypoxanthine molecule when linked to this type of diruthenium compound, with a reduction peak for this other purine found at  $-0.82$  V [24]. In order to analyze the repeatability of the CV curves they were measured for five times. Indeed, a relative standard deviation value of approximately 1.4% for the current response was obtained for **1**. This latter fact shows the reliability and stability achieved by this type of diruthenium compounds [44].

### 3.7. Viability of AGS and HCT116 cells treated with **1**

Cytotoxicity of **1** was analyzed in HCT116 and AGS cell lines by MTT assay and cell cytometry. The cell lines were subjected to increasing concentrations of **1** (1, 10, 20 and 31  $\mu$ M) for 48 and 72 h. As shown in Fig. 7A, it is observed a small dose-time-dependent reduction in cell proliferation when **1** is tested in the AGS cell lines and 48 h incubation at

10 and 20  $\mu$ M concentrations. However, MTT assay showed 42% viability reduction at 31  $\mu$ M (Fig. 7A). Again, when MTT assay was performed at 72 h incubation a strong reduction of more than 90% viability can be detected at 31  $\mu$ M (Fig. 7B). Therefore,  $IC_{50}$  for **1** was detected at 23.25  $\mu$ M when 72 h incubation were tested. In addition, our results showed that compound **1** displays low to none activity against HCT116 cells. In Fig. 8, a small increase of early apoptotic cells can be seen at the highest concentration (31  $\mu$ M) of **1**.

## 4. Conclusions

A novel dinuclear ruthenium(III) complex of formula  $[\{Ru(\mu-Cl)(\mu-Hade)\}_2Cl_4]Cl_2 \cdot 2H_2O$  (**1**) was synthesized by reacting the precursor  $K_2[RuCl_5(H_2O)]$  with adenine 5'-monophosphate (5'-AMP) in a hydrochloric acid solution. **1** is the first dinuclear ruthenium(III) system based on adenine. This adenine-based diruthenium complex was characterized through Fourier transform infrared spectroscopy (FT-IR), scanning



electron microscopy, energy dispersive X-ray analysis (SEM–EDX), magnetometer (SQUID) and single-crystal X-ray diffraction. The study of its electrochemical properties by means of cyclic voltammetry (CV) technique revealed a behavior typical of dinuclear Ru(III) compounds containing a metal–metal bond, displaying a well-resolved reduction peak assignable to the adenine molecule.

Compound **1** has only shown anticancer activity on gastric cancer cells (AGS), by inducing apoptosis at the highest concentration. Cisplatin is one of the most active drugs for cancer treatment, but also a high toxicity inducer. In comparison, cisplatin has been tested in AGS cell lines of gastric origin detecting anticancer activities at IC<sub>50</sub> of 4.84 μM and 16.6 μM [45,46]. Our results obtained with **1** show higher IC<sub>50</sub> (but in a similar range of molarity) than those previously published with the same cell line being treated with cisplatin. In our study, the drug activity was not tested on normal cell lines for comparison. Nevertheless, we have used a negative control group using the cell lines treated with the vehicle compound without the chemotherapy drug in each experiment. In any case, this is the first time that a dinuclear ruthenium (III) complex based on adenine has been tested toward cancer cell lines, and further studies will be performed to get new insights into its potential chemotherapeutic action.

### Ethical approval

Not required.

### Data availability statement

The raw data that support the findings of this study are available from the corresponding author upon reasonable request.

### Declaration of Competing Interest

The authors declare that they have no known competing financial interests or personal relationships that could have appeared to influence the work reported in this paper.

### Acknowledgements

This research was funded by the VLC-BIOCLINIC Program of the University of Valencia [Projects 02-RUN-AT-MARTINEZ-RIBAS-2017-A and PI-2021-007-DIRUGEN] and the Spanish Ministry of Science and Innovation [Projects PID2019-109735GB-I00 and CEX2019-000919-M (Excellence Unit “María de Maeztu”)].

### Appendix A. Supplementary data

Supplementary data to this article can be found online at <https://doi.org/10.1016/j.jinorgbio.2022.111812>.

### References

- [1] S. Higgins, Regarding ruthenium, *Nature Chem.* 2 (2010) 1100.
- [2] C. Bruneau, M. Achard, Allylic ruthenium(IV) complexes in catalysis, *Coord. Chem. Rev.* 256 (2012) 525–536.
- [3] L. Duan, F. Bozoglian, S. Mandal, B. Stewart, T. Privalov, A. Llobet, L. Sun, A molecular ruthenium catalyst with water-oxidation activity comparable to that of photosystem II, *Nature Chem.* 4 (2012) 418–423.
- [4] T. Friedberger, J.W. Ziller, Z. Guan, Ruthenium(IV) complexes for ethylene insertion polymerization, *Organometallics* 33 (2014) 1913–1916.
- [5] Z. Adhikaran, G.E. Davey, P. Campomanes, M. Groessl, C.M. Clavel, H. Yu, A. A. Nazarov, C.H.F. Yeo, W.H. Ang, P. Dröge, U. Rothlisberger, P.J. Dyson, C. A. Davey, Ligand substitutions between ruthenium–cymene compounds can control protein versus DNA targeting and anticancer activity, *Nat. Commun.* 5 (2014) 3462.
- [6] Y. Yamamoto, Y. Tamaki, T. Yui, K. Koike, O. Ishitani, New Light-Harvesting Molecular Systems Constructed with a Ru(II) Complex and a Linear-Shaped Re(I) Oligomer, *J. Am. Chem. Soc.* 132 (2010) 11743–11752.
- [7] J. Ferrando-Soria, J. Vallejo, M. Castellano, J. Martínez-Lillo, E. Pardo, J. Cano, I. Castro, F. Lloret, R. Ruiz-García, M. Julve, Molecular magnetism, quo vadis? A historical perspective from a coordination chemist viewpoint, *Coord. Chem. Rev.* 339 (2017) 17–103.
- [8] M.J. Clarke, Ruthenium metallopharmaceuticals, *Coord. Chem. Rev.* 236 (2003) 209–233.
- [9] C. Mari, V. Pierroz, S. Ferrari, G. Gasser, Combination of Ru(II) complexes and light: new frontiers in cancer therapy, *Chem. Sci.* 6 (2015) 2660–2686.
- [10] S.P. Mulcahy, K. Gründler, C. Frias, L. Wagner, A. Prokop, E. Meggers, Discovery of a strongly apoptotic ruthenium complex through combinatorial coordination chemistry, *Dalton Trans.* 39 (2010) 8177–8182.
- [11] L. Zeng, P. Gupta, Y. Chen, E. Wang, L. Ji, H. Chao, Z.-S. Chen, The development of anticancer ruthenium(II) complexes: from single molecule compounds to nanomaterials, *Chem. Soc. Rev.* 46 (2017) 5771–5804.
- [12] F. Li, J.G. Collins, F.R. Keene, Ruthenium complexes as antimicrobial agents, *Chem. Soc. Rev.* 44 (2015) 2529–2542.
- [13] D. Musumeci, L. Rozza, A. Merlino, L. Paduano, T. Marzo, L. Massai, L. Messori, D. Montesarchio, Interaction of anticancer Ru(III) complexes with single stranded and duplex DNA model systems, *Dalton Trans.* 44 (2015) 13914–13925.
- [14] J. Furrer, G. Süß-Fink, Thiolato-bridged dinuclear arene ruthenium complexes and their potential as anticancer drugs, *Coord. Chem. Rev.* 309 (2016) 36–50.
- [15] C.G. Hartinger, S. Zorbas-Seifried, M.A. Jakupec, B. Kynast, H. Zorbas, B. K. Keppler, From bench to bedside – preclinical and early clinical development of the anticancer agent indazolium trans-[tetrachlorobis(1H-indazole)ruthenate(III)] (KP1019 or FFC14A), *J. Inorg. Biochem.* 100 (2006) 891–904.
- [16] C.G. Hartinger, M.A. Jakupec, S. Zorbas-Seifried, M. Groessl, A. Egger, W. Berger, H. Zorbas, P.J. Dyson, B.K. Keppler, KP1019, a new redox-active anticancer agent – preclinical development and results of a clinical phase I study in tumor patients, *Chem. Biodivers.* 5 (2008) 2140–2155.
- [17] W.H. Ang, A. Casini, G. Sava, P.J. Dyson, Organometallic ruthenium-based antitumor compounds with novel modes of action, *J. Organomet. Chem.* 696 (2011) 989–998.
- [18] R.S. Correa, V. Freire, M.I.F. Barbosa, D.P. Bezerra, L.M. Bomfim, D.R.M. Moreira, M.B.P. Soares, J. Ellena, A.A. Batista, Ru(II)-thymine complexes: New metaldrug candidates against tumor cells, *New J. Chem.* 42 (2018) 6794–6802.
- [19] S.L.R. Silva, I.R.S. Baliza, R.B. Dias, C.B.S. Sales, C.A.G. Rocha, M.B.P. Soares, R. S. Correa, A.A. Batista, D.P. Bezerra, Ru(II)-thymine complex causes DNA damage and apoptotic cell death in human colon carcinoma HCT116 cells mediated by JNK/p38/ERK1/2 via a p53-independent signaling, *Sci. Rep.* 9 (2019) 11094.
- [20] I. Turel, M. Pečanac, A. Golobič, E. Alessio, B. Serli, A. Bergamo, G. Sava, Solution, solid state and biological characterization of ruthenium(III)-DMSO complexes with purine base derivatives, *J. Inorg. Biochem.* 98 (2004) 393–401.
- [21] L. Hajji, C. Saraiba-Bello, G. Segovia-Torrente, F. Scalambra, A. Romerosa, CpRu complexes containing water soluble phosphane PTA and natural purines adenine, guanine and theophylline: synthesis, characterization, and antiproliferative properties, *Eur. J. Inorg. Chem.* 38 (2019) 4078–4086.
- [22] Bruker Analytical X-ray Instruments. SHELXL-2017/1; Bruker Analytical X-ray Instruments: Madison, WI, USA, 2017.
- [23] DIAMOND 4.5.0. Crystal Impact GbR: Bonn, Germany, 2018.
- [24] M. Orts-Arroyo, I. Castro, J. Martínez-Lillo, Detection of Hypoxanthine from inosine and unusual hydrolysis of immunosuppressive drug azathioprine through the formation of a diruthenium(III) system, *Biosensors* 11 (2021) 19.
- [25] D. Armentano, J. Martínez-Lillo, Hexachlororhenate(IV) salts of ruthenium(III) cations: X-ray structure and magnetic properties, *Inorg. Chim. Acta* 380 (2012) 118–124.
- [26] C. Gagnon, J. Hubert, R. Rivest, A.L. Beauchamp, Crystal structure of di-μ-adeninium-disilver(I) perchlorate monohydrate, *Inorg. Chem.* 16 (1977) 2469–2473.
- [27] C.H. Wei, K.B. Jacobson, X-ray crystallographic characterization of an adenine-cadmium(II) complex, di-μ-adeninium-di-μ-aquo-tetrakis(nitrate-O,O')dicadmium (II) dinitrate, containing a cationic nucleic acid base as a bidentate ligand, *Inorg. Chem.* 20 (1981) 356–363.
- [28] A.K. Mishra, R.K. Prajapati, S. Verma, Probing structural consequences of N9-alkylation in silver-adenine frameworks, *Dalton Trans.* 39 (2010) 10034–10037.
- [29] Y. Song, X. Yin, B. Tu, Q. Pang, H. Li, X. Ren, B. Wang, Q. Li, Metal–organic frameworks constructed from mixed infinite inorganic units and adenine, *CrystEngComm* 16 (2014) 3082–3085.
- [30] D. Armentano, M.A. Barquero, C. Rojas-Dotti, N. Moliner, G. De Munno, E. K. Brechin, J. Martínez-Lillo, Enhancement of Intermolecular Magnetic Exchange through Halogen–Halogen Interactions in Bisadeninium Rhenium(IV) Salts, *Cryst. Growth Des.* 17 (2017) 5342–5348.
- [31] Hui-Fang Ma, Li-Wen Ding, Lin Chen, Yu-Ling Wang, Qing-Yan Liu, Two cadmium compounds with adenine and carboxylate ligands: syntheses, structures and photoluminescence, *J. Coord. Chem.* 70 (2017) 145–155.
- [32] A. Valentín-Pérez, J. Perles, S. Herrero, R. Jiménez-Aparicio, Coordination capacity of cytosine, adenine and derivatives towards open-paddlewheel diruthenium compounds, *J. Inorg. Biochem.* 187 (2018) 109–115.
- [33] J. Pascual-Colino, G. Beobide, O. Castillo, P. Lodewyckx, A. Luque, S. Pérez-Yáñez, P. Román, L.F. Velasco, Adenine nucleobase directed supramolecular architectures based on ferromagnetic heptanuclear copper(II) entities and benzenecarboxylate anions, *J. Inorg. Biochem.* 202 (2020) 110865.
- [34] G.C.P. Van Zundert, S. Jæqx, G. Berden, J.M. Bakker, K. Kleinermanns, J. Oomens, A.M. Rijs, IR spectroscopy of isolated neutral and protonated adenine and 9-methyladenine, *ChemPhysChem* 12 (2011) 1921–1927.
- [35] K.B. Beč, J. Grabska, M.A. Czarniecki, W. Huck, M.J. Wójcik, T. Nakajima, Y. Ozaki, IR spectra of crystalline nucleobases: combination of periodic harmonic calculations with anharmonic corrections based on finite models, *J. Phys. Chem. B* 123 (2019) 10001–10013.

- [36] S.S. Mohite, A.B. Patil-Deshmukh, S.S. Chavan, Synthesis and characterization of Ru(III) complexes with 2-(E)-((4-(4-bromophenyl)ethynyl)phenyl)imino)methyl-4-((E)-phenyldiazenyl)phenol and their use as a precursor for RuO<sub>2</sub> nanoparticles, *J. Mol. Struct.* 1176 (2019) 386–393.
- [37] V.P. Sur, A. Mazumdar, P. Kopel, S. Mukherjee, P. Vřtek, H. Michalkova, M. Vaculovičová, A. Moulick, A novel ruthenium based coordination compound against pathogenic bacteria, *Int. J. Mol. Sci.* 21 (2020) 2656.
- [38] F.A. Cotton, E. Pedersen, Magnetic and electrochemical properties of transition metal complexes with multiple metal-to-metal bonds. II. Tetrabutyratodiruthenium (n+) with n = 0 and 1, *Inorg. Chem.* 14 (1975) 388–391.
- [39] T. Malinski, D. Chang, F.N. Feldmann, J.L. Bear, K.M. Kadish, Electrochemical studies of a novel ruthenium(II,III) dimer, trifluoroacetamidatoruthenium chloride (Ru<sub>2</sub>(HNOCCF<sub>3</sub>)<sub>4</sub>Cl), *Inorg. Chem.* 22 (1983) 3225–3233.
- [40] Y. Hiraoka, T. Ikeue, H. Sakiyama, F. Guégan, D. Luneau, B. Gillon, I. Hiromitsu, D. Yoshioka, M. Mikuriya, Y. Kataoka, M. Handa, An unprecedented up-field shift in the <sup>13</sup>C NMR spectrum of the carboxyl carbons of the lantern-type dinuclear complex TBA[Ru<sub>2</sub>(O<sub>2</sub>CCH<sub>3</sub>)<sub>4</sub>Cl<sub>2</sub>] (TBA<sup>+</sup> = tetra(n-butyl)ammonium cation), *Dalton Trans.* 44 (2015) 13439–13443.
- [41] Y. Kataoka, S. Mikami, H. Sakiyama, M. Mitsumi, T. Kawamoto, M. Handa, A neutral paddlewheel-type diruthenium(III) complex with benzamidinato ligands: Synthesis, crystal structure, magnetism, and electrochemical and absorption properties, *Polyhedron* 136 (2017) 87–92.
- [42] M.U.A. Prathap, R. Srivastava, B. Satpati, Simultaneous detection of guanine, adenine, thymine, and cytosine at polyaniline/MnO<sub>2</sub> modified electrode, *Electrochim. Acta* 114 (2013) 285–295.
- [43] J. Zhang, D. Han, S. Wang, X. Zhang, R. Yang, Y. Ji, X. Yu, Electrochemical detection of adenine and guanine using a three-dimensional WS<sub>2</sub> nanosheet/graphite microfiber hybrid electrode, *Electrochem. Commun.* 99 (2019) 75–80.
- [44] M. Orts-Arroyo, I. Castro, F. Lloret, J. Martínez-Lillo, Molecular self-assembly in a family of oxo-bridged dinuclear ruthenium(IV) systems, *Cryst. Growth Des.* 20 (2020) 2044–2056.
- [45] S.A. Suttie, K.G.M. Park, T.A.D. Smith, [<sup>18</sup>F]2-Fluoro-2-deoxy-D-glucose incorporation by AGS gastric adenocarcinoma cells in vitro during response to epirubicin, cisplatin and 5-fluorouracil, *Br. J. Cancer* 97 (2007) 902–909.
- [46] B. Mora-Lagos, I. Cartas-Espinel, I. Riquelme, A.C. Parker, S.R. Piccolo, T. Viscarra, Functional and transcriptomic characterization of cisplatin-resistant AGS and MKN-28 gastric cancer cell lines, *PLOS ONE* 15 (1) (2020) e0228331.

---

*ARTICLE 5*

*RUNAT-BI: A Ruthenium(III)*

*Complex as a Selective*

*Anti-Tumor Drug Candidate*

*against Highly Aggressive*

*Cancer Cell Lines*



F. José Martínez Lillo, Profesor Titular de Química Inorgánica de la Universitat de València, miembro del Instituto de Ciencia Molecular (ICMol) y del Departamento de Química Inorgánica de la Facultad de Química,

CERTIFICA:

Que Marta Orts Arroyo ha tenido una participación relevante en el trabajo en coautoría que presenta en esta Memoria, titulado ***“RUNAT-BI: A Ruthenium(III) Complex as a Selective Anti-Tumor Drug Candidate against Highly Aggressive Cancer Cell Lines”*** y publicado en la revista *Cancers*. La contribución de la doctoranda en este trabajo ha sido la síntesis y caracterización del compuesto, que ha sido investigado en colaboración con el INCLIVA para la obtención de los resultados que aparecen en la publicación.

Se firma esta publicación científica como segundo autor puesto que, en este caso, el primer y segundo firmante contribuyen por igual y son los responsables de los análisis publicados.

Por último, se deja constancia de que los resultados reportados en esta publicación no han sido ni serán utilizados implícita ni explícitamente por ninguno de los coautores para la realización de una Tesis Doctoral.

Y para que así conste, firmo el presente certificado.

Paterna, Junio de 2023

Fdo.: F. José Martínez Lillo



## Article

# RUNAT-BI: A Ruthenium(III) Complex as a Selective Anti-Tumor Drug Candidate against Highly Aggressive Cancer Cell Lines

Marta Albanell-Fernández <sup>1,†</sup> , Sara S. Oltra <sup>1,†</sup> , Marta Orts-Arroyo <sup>2</sup>, Maider Ibarrola-Villava <sup>1,3</sup>, Fany Carrasco <sup>1,3</sup>, Elena Jiménez-Martí <sup>1,3,4</sup> , Andrés Cervantes <sup>1,3</sup> , Isabel Castro <sup>2</sup> , José Martínez-Lillo <sup>2,\*</sup>  and Gloria Ribas <sup>1,3,\*</sup>

<sup>1</sup> INCLIVA Biomedical Research Institute, Hospital Clínico Universitario Valencia, University of Valencia, 46010 Valencia, Spain

<sup>2</sup> Instituto de Ciencia Molecular (ICMol)/Departament de Química Inorgànica, University of Valencia, 46980 Valencia, Spain

<sup>3</sup> Center for Biomedical Network Research on Cancer (CIBERONC), 28029 Madrid, Spain

<sup>4</sup> Departament de Bioquímica i Biologia Molecular, Facultat de Medicina, University of Valencia, 46010 Valencia, Spain

\* Correspondence: f.jose.martinez@uv.es (J.M.-L.); gribasdespuig@gmail.com (G.R.); Tel.: +34-9635-44460 (J.M.-L.)

† These authors contributed equally to this work.

**Simple Summary:** To overcome some limitations of platinum-based chemotherapy agents, new active metallodrugs based on other transition metals are being researched. Runat-BI is a ruthenium-based compound which was synthesized and characterized at the University of Valencia. We investigated the *in vitro* effect of this compound on eight cell lines of different cancer types. Runat-BI reduced tumor growth and migration significantly in three cancer cell lines, showing selectivity for tumoral cells and little effect on non-tumoral ones. Its mechanism of action is still unknown but seems related to DNA synthesis as the cells with higher growth rates are the most affected by this chemotherapy agent. However, additional mechanism(s) likely play a role in its selectivity for several cancer cell lines. Moreover, Runat-BI slightly increases expression of the proapoptotic genes *BAX* and *CASPASE-3*. All these findings support its study as a potential anticancer therapy.



**Citation:** Albanell-Fernández, M.; Oltra, S.S.; Orts-Arroyo, M.; Ibarrola-Villava, M.; Carrasco, F.; Jiménez-Martí, E.; Cervantes, A.; Castro, I.; Martínez-Lillo, J.; Ribas, G. RUNAT-BI: A Ruthenium(III) Complex as a Selective Anti-Tumor Drug Candidate against Highly Aggressive Cancer Cell Lines. *Cancers* **2023**, *15*, 69. <https://doi.org/10.3390/cancers15010069>

Academic Editor: Alexander Shtil

Received: 8 November 2022

Revised: 19 December 2022

Accepted: 20 December 2022

Published: 22 December 2022



**Copyright:** © 2022 by the authors. Licensee MDPI, Basel, Switzerland. This article is an open access article distributed under the terms and conditions of the Creative Commons Attribution (CC BY) license (<https://creativecommons.org/licenses/by/4.0/>).

**Abstract:** Ruthenium compounds have demonstrated promising activity in different cancer types, overcoming several limitations of platinum-based drugs, yet their global structure–activity is still under debate. We analyzed the activity of Runat-BI, a racemic Ru(III) compound, and of one of its isomers in eight tumor cell lines of breast, colon and gastric cancer as well as in a non-tumoral control. Runat-BI was prepared with 2,2′-biimidazole and dissolved in polyethylene glycol. We performed assays of time- and dose-dependent viability, migration, proliferation, and expression of pro- and antiapoptotic genes. Moreover, we studied the growth rate and cell doubling time to correlate it with the apoptotic effect of Runat-BI. As a racemic mixture, Runat-BI caused a significant reduction in the viability and migration of three cancer cell lines from colon, gastric and breast cancer, all of which displayed fast proliferation rates. This compound also demonstrated selectivity between tumor and non-tumor lines and increased proapoptotic gene expression. However, the isolated isomer did not show any effect. Racemic Runat-BI is a potential drug candidate for treatment of highly aggressive tumors. Further studies should be addressed at evaluating the role of the other isomer, for a more precise understanding of its antitumoral potential and mechanism of action.

**Keywords:** antitumoral agent; ruthenium compound; 2,2′-biimidazole; cancer cell lines; apoptosis

## 1. Introduction

Cancer represents a major public health problem. With an estimated 19.3 million new cases worldwide in 2020, it remains among the main causes of death (10.0 million deaths) [1,2]. By percentage of new cases, the most frequent cancer types are female breast cancer with 11.7% (2.3 million), colon with 6% (1.1 million) and gastric with 5.6% (1.1 million) [2]. Cancer is defined as uncontrolled growth of abnormal cells anywhere in the body. It has traditionally been treated with surgery, chemotherapy, and radiation therapy; however, increasing studies in cancer research have extended new approaches such as immunotherapy, hormone therapy, gene therapy, and targeted therapy [3]. Nevertheless, treatment fails in certain tumors, predominantly due to metastasis, recurrence, heterogeneity, resistance to chemotherapy and radiotherapy and avoidance of immunological surveillance [4–6]. Current chemotherapy agents are greatly limited by their side effects and intrinsic or acquired drug resistance [7], prompting renewed research effort within the scientific community to obtain new highly effective agents for cancer treatment.

The most widely used drugs in conventional chemotherapy are platinum-based, among which cisplatin is one of the most commonly utilized to treat various solid cancers, either as a single agent or in combination. Cisplatin exerts anticancer activity via multiple mechanisms, mainly by generating DNA damage followed by activation of several signal transduction pathways which finally lead to apoptosis [8]. Despite the success of these compounds, drug resistance and several undesirable side effects have been reported, especially due to their lack of selectivity for cancerous over normal tissues. It is therefore of interest to seek out alternative therapeutic metal-based compounds that could overcome the limitations of these platinum-based drugs [9–11].

Ruthenium species have demonstrated promise in different cancer types, opening the door to the design of novel metal-based chemotherapeutic agents [9]. Those agents are most typically multitargeted, with specific activities against different cancers, a favorable toxicity profile and clearance properties, as they are eliminated from the kidneys, liver and bloodstream [7,12,13]. Ruthenium complexes such as RAPTA-C, NAMI-A and KP1019 have undergone preclinical or clinical trials for the treatment of different cancers [11,13]. KP1019 is a cytotoxic agent for the treatment of platinum-resistant colorectal cancers, whereas the non-cytotoxic NAMI-A is considered a very effective antimetastatic drug [14]. NAMI-A was the first ruthenium-based agent to enter phase I clinical trials, showing disease stabilization in patients with non-small-cell lung cancer. In a clinical phase-I/II study, however, the combination of NAMI-A with gemcitabine was less active than gemcitabine alone [12,15].

Global structure–activity relationships are still under debate for ruthenium metallo-drugs as regards *in vitro* antiproliferative/cytotoxic activity and *in vivo* tumor-inhibiting properties as well as pharmacokinetics [12]. The mechanism of action of many of these complexes remains unclear. DNA was considered the main target of action [16]; however, RAPTA-C was found to bind exclusively on the histone proteins, unlike platinum metallo-drugs [12,17]. KP1019 and KP1339, which are under clinical investigation, induced apoptosis predominantly by the intrinsic mitochondrial pathway [18]. The chaperone protein GRP78 (glucose regulatory protein 78) was its main target [19].

The increasing focus on and promising results shown by ruthenium-based antitumor agents led to our study and synthesis of new Ru(III)-based anticancer compounds. Among these, we selected Runat-BI to study antitumor activity, with the aim of analyzing its effect on viability, migration, cell doubling time (CDT) and expression of pro- and antiapoptotic genes in six breast cancer (BC) cell lines (HCC1937, HCC1500, HCC1806, MCF-7, MDA-MB-231, BT474), a colon cancer cell line (HCT116), and a gastric cancer cell line (AGS). The MCF10A cell line from a human mammary gland was used as the non-tumoral cell line control.



## 2. Materials and Methods

### 2.1. Reagents and Instruments

All starting chemicals and solvents used in the synthesis of Runat-BI were purchased from commercial sources and used without further purification. The elemental analyses (C, H, N) and X-ray microanalysis were performed through Central Support Service for Experimental Research (SCSIE) at the University of Valencia. The results of scanning electron microscopy (SEM-EDX) were obtained through a Hitachi S-4800 field emission scanning electron microscope with 20 kV of accelerating voltage and 9.0 mm of working distance. Electrospray Ionization Mass (ESI-MS) spectrum of Runat-BI was performed on a SCIEX TripleTOF 6600+ mass spectrometer by using a direct infusion electrospray ionization source (Figure S1). The infrared spectra (FT-IR) data for Runat-BI and 2,2'-biimidazole molecules were obtained through a Perkin Elmer Spectrum 65 FT-IR spectrometer in the 4000–500 range ( $\text{cm}^{-1}$ ) with 25 scans and a spectral resolution of  $4 \text{ cm}^{-1}$  (Figure S2). X-ray diffraction data collection was performed on a Bruker D8 Venture diffractometer with graphite-monochromated Mo- $K_{\alpha}$  radiation ( $\lambda = 0.71073 \text{ \AA}$ ). Crystal parameters and refinement data, along with selected bond lengths and angles, for Runat-BI are summarized in Tables S1 and S2.

### 2.2. Cell Line Culture and Treatment

Breast, gastric and colon cancer cell lines were obtained from the American Type Culture Collection (ATCC, Rockville, MD, USA). Cell lines were cultured in RPMI 1640 or DMEM medium supplemented with 1% L-glutamine and 10% fetal bovine serum (GIBCO, New York, NY, USA). The culture conditions were identical in all cell lines:  $37 \text{ }^{\circ}\text{C}$  and 5%  $\text{CO}_2$ . Cells were seeded for 24 h before treatment with Runat-BI or PEG (control) for MTT, wound healing and CDT (Table S3).

### 2.3. Cell Proliferation Assay

Cell proliferation was analyzed by colorimetric MTT [3-(4,5-dimethylthiazol-2-yl)-2,5-diphenyltetrazolium bromide] assay. We seeded and cultured 3000 cells in 96-well plates. Next, cells were treated with a specific drug dose and the MTT assay was performed 24, 48 and 72 h after treatment. DMSO was used as a dissolvent to solubilize the compound and convert the formazan into a colored solution. Absorbance of this colored solution was quantified by measuring through a spectrophotometer at 590 nm. Each experiment was performed in triplicate and repeated at least twice. Average values for triplicates were calculated. Absorbance observed at different drug concentrations was compared with the respective non-treated controls and cell viability was calculated. The  $\text{IC}_{50}$  was calculated using GraphPad Prism, with the R indicating the goodness of fit.

### 2.4. Scratch/Wound Healing Assay

Cells were seeded in 6-well plates at a density of  $4 \times 10^5$  cells/well and incubated overnight until they reached 70% confluence. A pipette tip was used to create a wound in the cell layer. Cells were then treated with Runat-BI ( $21 \mu\text{M}$ ). Each experiment was performed in triplicate and repeated at least twice. Images were obtained at 0, 24, 48 and 72 h at the same position and closure area of migrating cells was measured using Image J software, and the percentage of wound closure was calculated and compared with time zero. The assay is particularly suitable for studying the effects of cell–matrix and cell–cell interactions on cell migration.

### 2.5. Cell Doubling Time (CDT)

We investigated the growth rate and CDT of the nine cell lines used in this study. On day 0, cells were plated in 6-well plates with an initial concentration of  $1 \times 10^5$  cells. Duplicate counts were made in a Neubauer chamber using Automated Cell Counter TC10TM (BioRad) every 24 h for 10 days after staining cells with trypan blue. Each cell line was cultured in duplicate. From the cell count data, the cell growth curve was

constructed during the time studied and the CDT was calculated using the online tool <http://www.doubling-time.com/compute.php> (accessed on 20 March 2020).

### 2.6. RNA Extraction and Gene Expression by Real Time PCR (RT-qPCR)

Total RNA from all cell lines was isolated using High Pure RNA Isolation Kit from Roche following the manufacturer's protocol. RNA was extracted from cellular pellet from around  $1 \times 10^6$  total cells. RNA concentration was measured using a NanoDrop ND 2000-UV-vis Spectrophotometer (Thermo Fisher Scientific Inc., Wilmington, DE, USA). cDNA synthesis was performed using the High-Capacity cDNA Reverse Transcription kit (Applied Biosystems™ by Life Technologies™, Carlsbad, CA, USA). We used TaqMan® Gene Expression Assays (Applied Biosystems™ by Life Technologies™, Carlsbad, CA, USA). Primers used in the assay were *BAX* and *CASPASA-3* (proapoptotic genes); *BCL-2* (antiapoptotic gene) and *GAPDH* as endogenous control, carried out by quantitative real time-PCR (qRT-PCR) in RNA extracted from cell lines. Normalization was performed with *GAPDH*. The data were managed using the QuantStudio™ Design & Analysis Software v1.4 (Applied Biosystems™ by Life Technologies™, Carlsbad, California, USA). Relative expression was calculated using the comparative Ct method and obtaining the fold-change value ( $\Delta\Delta Ct$ ).

### 2.7. Statistical Analysis

All statistical analyses were performed using R Bioconductor. Results were considered significant when  $p$ -value  $< 0.05$ . The  $IC_{50}$  analysis and graph representations were performed using GraphPad Prism.

## 3. Results

### 3.1. Preparation of Runat-BI

$RuCl_3 \cdot H_2O$  (6.6 mg, 0.03 mmol) and 2,2'-biimidazole (12.1 mg, 0.09 mmol) were reacted by means of a solvothermal synthesis in HCl (2.5 mL, 3.0 M) at 90 °C for 20.5 h, followed by a 20.5 h cooling process to room temperature. Dark blue crystals of Runat-BI were thus obtained and were suitable for X-ray diffraction data collection (Figure 1). Yield: ca. 30%. The same synthesis was performed in a concentrated solution and in a 1:1 ratio of the reactants, thus allowing us to isolate the isomer 1 (Figure 1). Anal. Calcd. for  $C_{12}H_{16}N_8O_2Cl_3Ru$ : C, 28.2; H, 3.2; N, 21.9%. Found: C, 28.5; H, 3.3; N, 22.2%. SEM-EDX analysis gave a Ru:Cl molar ratio of 1:3 for Runat-BI. ESI-MS ( $m/z$ ): 445.90 (4.8%), 444.93 (5.4%), 442.89 (16.4%), 441.82 (94.6%), 440.94 (41.9%), 439.97 (100%), 438.90 (62.0%), 437.93 (36.5%), 436.86 (30.6%), 435.98 (12.7%), 434.90 (3.1%), these  $m/z$  values support the stability of Runat-BI in solution (Figure S1). Infrared (IR) peaks (sample prepared as KBr pellets): 3278 (m), 3147 (m), 3129 (m), 3010 (m), 2923 (w), 2924 (m), 2765 (m), 1638 (s), 1526 (s), 1417 (m), 1394 (m), 1319 (w), 1252 (w), 1177 (m), 1129 (m), 1078 (m), 1008 (w), 922 (m), 870 (w), 811 (w), 754 (s) and 682 (m)  $cm^{-1}$  (Figure S2).

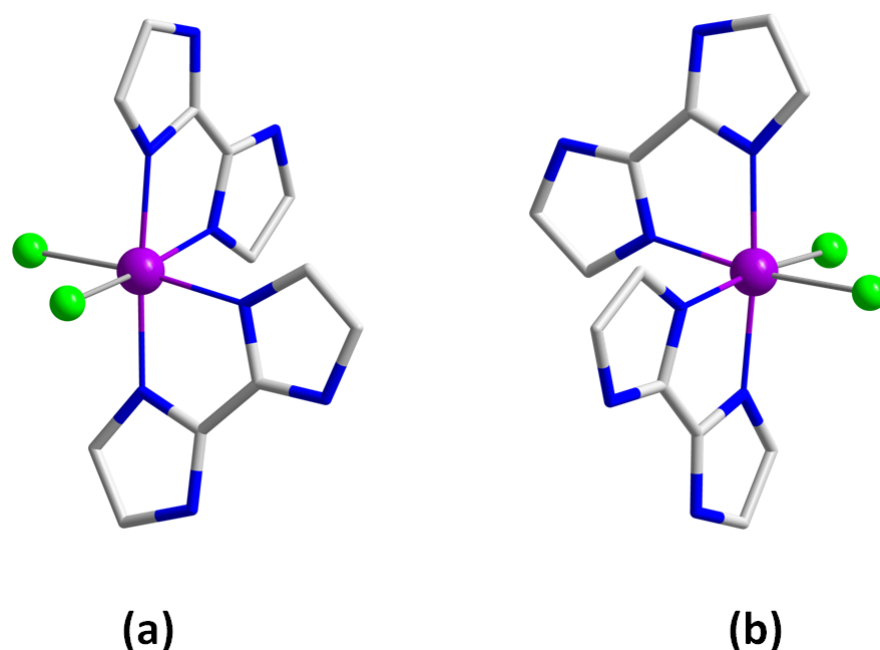


**Figure 1.** (a) Molecular structure of the mononuclear (inactive) isomer 1 of the {cis-[RuCl<sub>2</sub>(H<sub>2</sub>biim)<sub>2</sub>]Cl}<sub>2</sub>·4H<sub>2</sub>O racemic mixture in Runat-BI. (b) Molecular structure of the mononuclear isomer 2 of the {cis-[RuCl<sub>2</sub>(H<sub>2</sub>biim)<sub>2</sub>]Cl}<sub>2</sub>·4H<sub>2</sub>O racemic mixture in Runat-BI. Water molecules, hydrogen atoms and chloride counter anions were omitted for clarity.

### 3.2. Runat-BI Reduces Proliferation in Cancer Cell Lines

Cytotoxicity of Runat-BI was analyzed in HCC1937, HCC1500, HCC1806, MCF-7, MDA-MB-231, BT474, HCT116, AGS and MCF10A cell lines by MTT assay. The nine cell lines used were subjected to increasing concentrations of Runat-BI (0, 5.25, 10.5, 21 and 42  $\mu$ M in PEG) for 24, 48 and 72 h. As shown in Figure 2A–C, a dose- and time-dependent reduction in cell proliferation was observed for some cell lines. MTT assay showed significant viability reduction at 48 h for HCT116 and HCC1806 cell lines, reaching 41% and 36% viability, respectively, which presented the lowest IC<sub>50</sub> (<25  $\mu$ M) [Table S4]. At 72 h after treatment, we detected an around 50% reduction in BT474 and AGS cell line viability. The three lines (HCT116, HCC1806 and AGS) remained highly aggressive tumors with rapid growth and proliferation. In contrast, the MDA-MB-231 cell line displayed a moderate viability reduction (61%) after 72 h of treatment. Our results showed that Runat-BI compound is not active against HCC1937 (IC<sub>50</sub> 94.23  $\mu$ M), HCC1500 (IC<sub>50</sub> 76.03  $\mu$ M) or MCF-7 (IC<sub>50</sub> > 200  $\mu$ M), all belonging to BC cell lines; these were not significantly affected in terms of viability, which remained above 80% at 72 h. Table S4 displays the IC<sub>50</sub> after 48 and 72 h of Runat-BI treatment. Nonetheless, viability of the non-tumor mammary gland cell line MCF10A was not reduced at any time or at any concentration (Figure 2D). The Runat-BI compound is not active against this cell line despite its rapid growth rate. These results support the specificity of the Ru(III) compound to affect tumor cells but not normal cell lines like MCF10A.

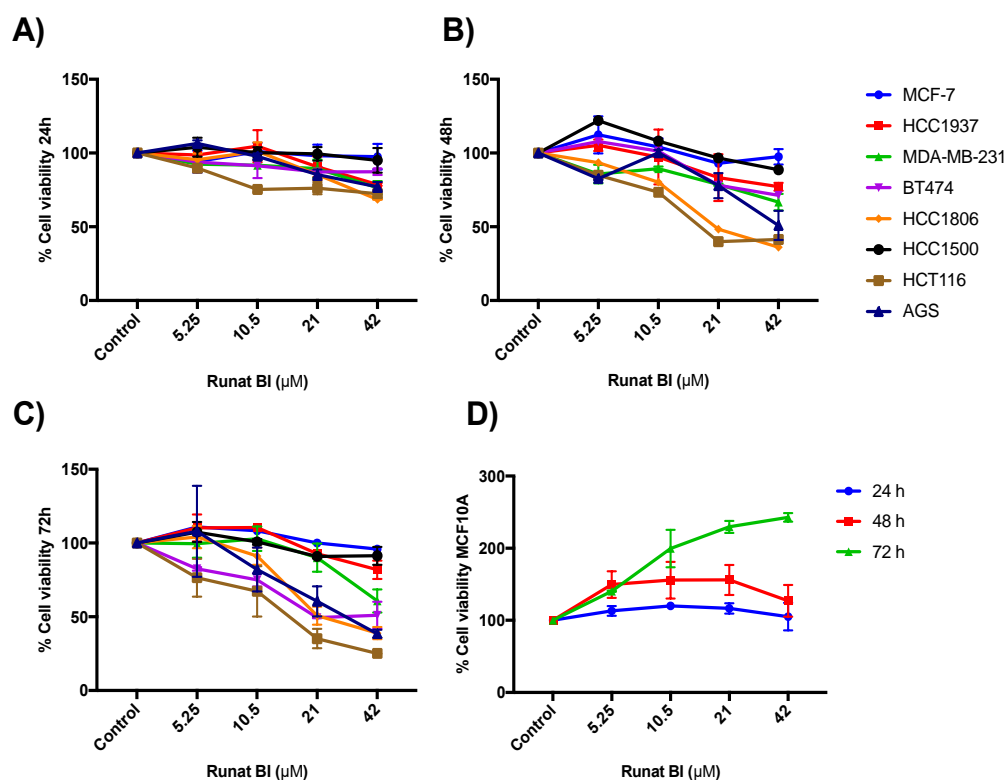


**Figure 2.** Viability percentages of the nine cell lines treated with Runat-BI at 24, 48 and 72 h. The breast cancer cell lines (MCF-7, HCC1937, MDA-MB-231, BT474, HCC1806, HCC1500), gastric cancer cell line (AGS) and colon cancer cell line (HCT116) were treated with Runat-BI at different concentrations (0 to 42 μM) for 24 h (A), 48 h (B), and 72 h (C). The mammary gland cell line MCF10A was used as a non-tumor cell line and was treated with Runat-BI at the same concentrations and time: 24 h (blue), 48 h (red) and 72 h (green) (D). Cell proliferation was determined with the MTT assay. Dots indicate the mean of three independent experiments.

### 3.3. Isomer 1 of Runat-BI Showed No Effect on Viability in the Cell Lines Studied

We selected the two cell lines AGS and MDA-MB-231, with different responses against Runat-BI compound, to test the isolated isomer 1 of Runat-BI. The concentrations tested for isomer 1 were slightly higher (0, 6.25, 12.5, 25 and 50 μM). Results showed no reduction in cell viability at any concentration or at any time (24, 48 and 72 h) [Figure S3]. In contrast to the viability reduction observed with Runat-BI, cells treated with isomer 1 showed increased viability at low concentrations of the compound after 48 and 72 h of treatment (Figure S3B,C). These findings showed no effect on isomer 1 from Runat-BI in the cell lines tested. These results open two potential hypotheses that could explain the Runat-BI effect in cancer cell lines: (1) The cytotoxic effect of the Runat-BI compound requires the presence of both isomers 1 and 2, or (2) the cytotoxic effect of Runat-BI is mainly attributed to isomer 2, which has not been isolated as yet.

### 3.4. Migration Reduction in Cell Lines Treated with Runat-BI Measured by Wound Healing Assay

All cell lines were treated with 21 μM of Runat-BI. The concentration was established according to the results observed in the viability assays, which showed a block in viability reduction for doses higher than 21 μM. A scratch was performed at 0 h and the percentage of wound closure was measured using images from 0 to 72 h (Figures 3A and S4).

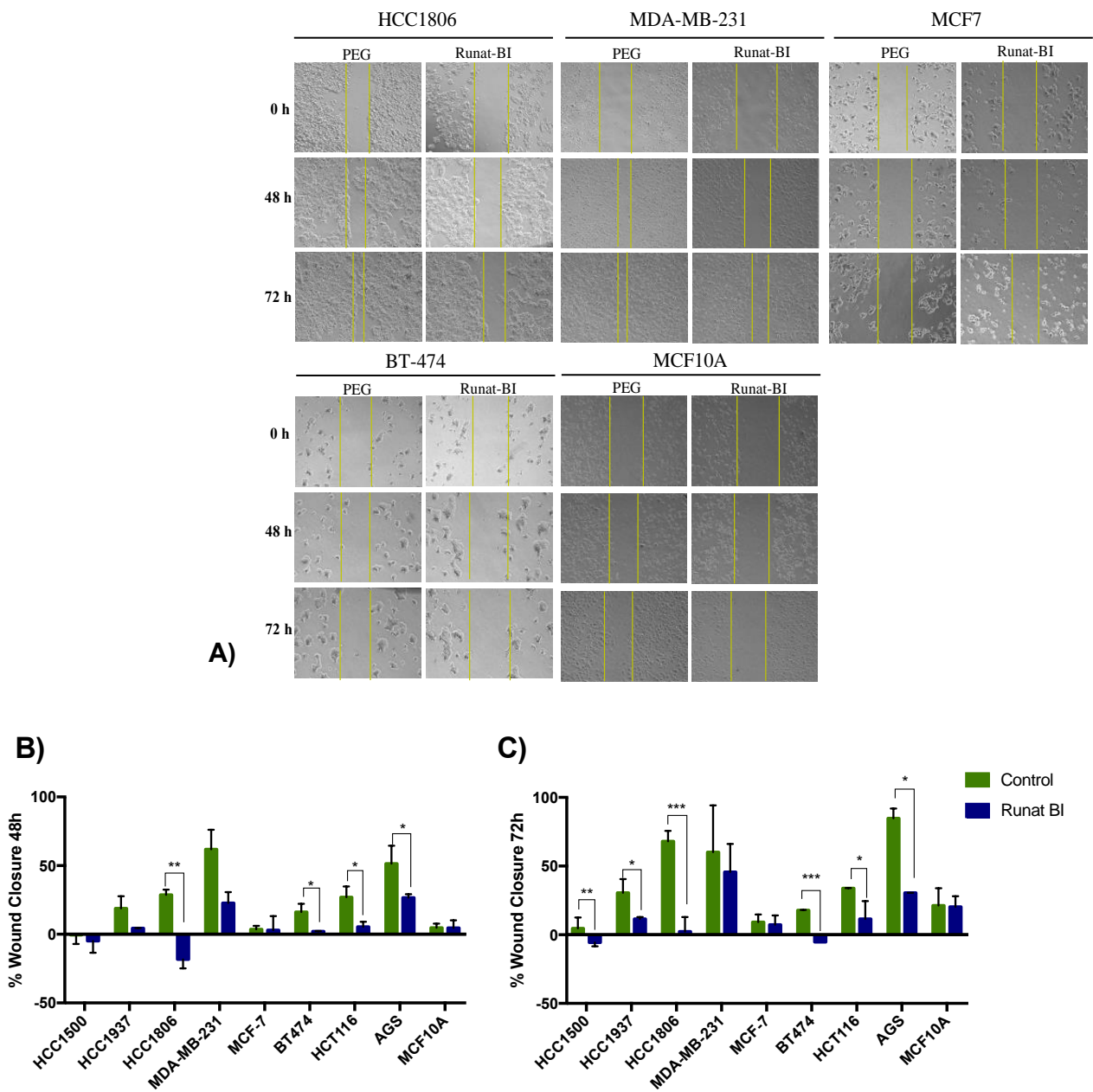


**Figure 3.** Effect of Runat-BI treatment on cell migration. Cell migration of HCC1806, MDA-MB-231, AGS, HCT116 and MCF10A lines was measured by scratch/wound-healing assay after treatment with Runat-BI (21  $\mu$ M) or PEG/control for 48 and 72 h. (A): Images of cell migration at 0, 48 and 72 h after Runat-BI (21  $\mu$ M) treatment or PEG (control). Three separate experiments were performed, and the most representative results are presented (5 $\times$  amplification). Columns express the mean  $\pm$  SD of the percentage of closure in three independent experiments for 48 h (B) and 72 h (C). Green bars represent control/PEG and dark blue bars represent Runat-BI-treated cells. \*  $p \leq 0.1$ , \*\*  $p \leq 0.05$ , \*\*\*  $p \leq 0.01$  were considered statistically significant.

Wound healing assays demonstrated that Runat-BI significantly reduced cell migration in the HCC1806, AGS, HCT116 and MDA-MB-231 cell lines. More specifically, the HCC1806 cell line showed a reduction in migration of ~47.1% at 48 h and ~65.7% at 72 h. AGS also exhibited a significant decrease, mainly at 72 h, reaching approximately 54.3%. This cell line maintained its high growth rate and CDT but showed a substantial reduction in cell migration. No significant differences in cell migration were found in HCT116 between 48 h and 72 h, and the wound remained between 21 and 22% from closure in both cases.

However, a significant reduction in cell growth rate was observed in the sample treated with Runat-BI compared to PEG. These results agree with those previously observed in MTT assays, where these three lines showed a significant drop in cell viability with Runat-BI treatment. MDA-MB-231 exhibited greater reduction in cell viability at 48 h than at 72 h (approximately 39.1% and 14.5%, respectively). Given the fast growth of this line, the wound was almost closed with both treatments, as observed in Figure 3A. The 21  $\mu$ M concentration of Runat-BI at 72 h was probably not sufficient for this cell line, as indicated by the MTT results. BT474 showed hardly any reduction in cell migration, although it experienced prominent cell death. MCF-7, HCC1937 and HCC1500 showed both less viability reduction and low impact on cell migration when treated with Runat-BI (Figure S4). In MCF10A no differences in cell migration were found between Runat-BI treatment and control (Figure 3A).

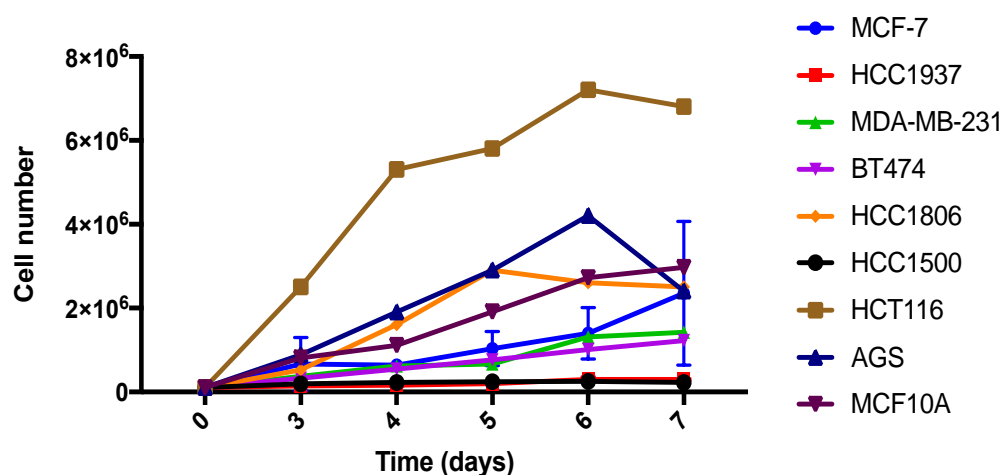
The results obtained in cell migration assay support those obtained in viability assays, with the HCT116, AGS and HCC1806 cell lines clearly showing the most important cytotoxic effect from Runat-BI. The selective action against tumor lines compared with the non-tumor cell line (MCF10A) is again demonstrated by the results obtained in the wound healing assay, which showed no migration differences between treatment and control condition (Figure 3B,C).

Figure S5 shows the comparison of cell migration at 48 h and 72 h in the five lines showing statistical significance in either PEG or Runat-BI, or in both. Generally, the fastest growing lines were more successful in closing the scratch in the control samples at 48 and/or 72 h. However, none of the tumoral cell samples treated with Runat-BI were able to completely close the scratch, demonstrating a clear reduction in cell invasiveness, and in some cell lines, such as BT474, HCC1806 and HCT116, pronounced cell death.

### 3.5. Relationship between Runat-BI Effect and Cell Growth Rate

Ru-based compounds target various DNA conformations and affect DNA processing enzymes. Runat-BI may intercalate in DNA, with the ability to cause DNA condensation and cleavage, inducing cell cycle arrest and/or apoptosis [20]. Cancer cells present higher division rates and are consequently more exposed to the effect of anticancer drugs that act on DNA. Due to the faster growth rates of cancer cell lines, we sought to analyze the possible relationship between CDT and Runat-BI effectiveness.

HCT116, HCC1806 and AGS cell lines showed lower CDT rates (Figure 4). Interestingly, these three cell lines displayed higher viability and migration reduction when they were exposed to Runat-BI, indicating that the compound has higher effectiveness against cell lines with higher growth rates. An intermedia effect of Runat-BI was observed for cell lines with intermedia growth rates, such as BT474 and MDA-MB-231. Consequently, cell lines with slow growth rates (higher number of CDT days), such as HCC1500 and HCC1937, exhibited low or absent treatment effect with Runat-BI. However, the relationship is not completely clear since MCF-7 is relatively fast dividing yet Runat-BI displays no significant effect on this cell line. A similar situation is observed with MCF10A, which despite undergoing fast division, is resistant to Runat-BI. These findings partially support that Runat-BI acts against cells with higher growth rates due to their mechanism of biological action. However, we hypothesize the existence of some additional mechanism(s) leading to the selectivity displayed in some cancer cell lines, and which would explain the lack of effectiveness against luminal A subtype MCF-7 and non-tumoral cell line MCF10A.



**Figure 4.** Cell growth over 7 days in cell lines treated with Runat-BI. Cell growth was measured with the Neubauer chamber using “Automated Cell Counter TC10™”. Dots indicate the mean of two independent experiments.

### 3.6. Apoptosis Induced by Runat-BI Treatment

Ruthenium-based complexes may induce apoptosis in cancer cells, acting as potential cancer treatments [21]. Given that most ruthenium-based agents are multitarget, we investigated whether Runat-BI had a different target apart from binding to nuclear DNA and subsequently interference with the transcription. We studied the apoptotic induction of Runat-BI in the nine cell lines, analyzing the expression of the proapoptotic genes *BAX* and *CASPASE-3* and the antiapoptotic gene *BCL-2*. Our results indicated an increase in *BAX* and *CASPASE-3* in most cell lines treated with Runat-BI compared with control samples (Figure 5A,B), although this did not reach statistical significance as analyzed by *t*-test (*p*-value 0.2 for *BAX* and 0.19 for *CASPASE-3*). However, the non-tumoral cell line MCF-10A did not present gene expression deregulation between the two conditions. Slight downregulation of *BCL-2* was observed in some cell lines treated with Runat-BI, but these results were not significant (*p*-value 0.84) [Figure 5C]. Therefore, Runat-BI slightly increases expression of the proapoptotic genes *BAX* and *CASPASE-3* but seemingly fails to affect expression of the antiapoptotic gene *BCL-2*.



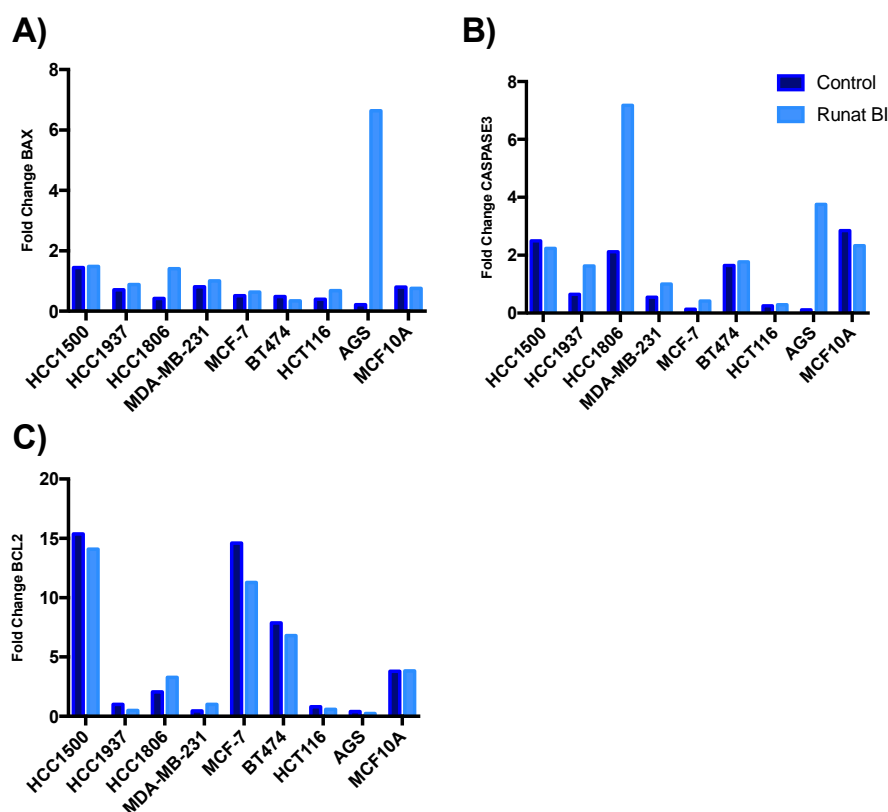


**Figure 5.** Expression of proapoptotic genes *BAX* (A), *CASPASE-3* (B) and the antiapoptotic gene *BCL-2* (C) in cancer cell lines after Runat-BI treatment. Fold-change (FC) results were obtained by quantitative RT-PCR for the BC lines HCC1500, HCC1937, HCC1806, MDA-MB-231, MCF-7, BT474; colon cancer line HCT116, gastric cancer line AGS and non-tumor line MCF10A. Dark blue represents control/PEG-treated samples and light blue represents Runat-BI-treated samples.

#### 4. Discussion

In the search for more effective metal-based antitumor agents with fewer adverse effects, those based on ruthenium have attracted particular research interest [22–25]. Ruthenium complexes have emerged as potential pro-oxidant and multitarget chemotherapeutics to replace platinum-based drugs [26]. We have synthesized a novel compound: Runat-BI, a ruthenium(III) and 2,2'-biimidazole racemic compound, a mixture of two isomers (1:1), of which one (isomer 1) has been isolated. Among the advantages of complexes based on ruthenium(III) with 2,2'-biimidazole are the interactions between nucleobase pairs, which further facilitate the mechanism of action with cancer cell DNA. Furthermore, the ruthenium(III) structure allows them to be more robust and inert when reacting in redox processes or ligand substitution reactions, thus increasing stability and extending the shelf-life of the compound in the physiological environment [27,28]. Ruthenium compounds can carry a high number of potential accessory molecules and show the possibility to exist in biological fluids in almost all the most important oxidation states, from II to IV [29,30].

The results of our experiments with Runat-BI showed a considerable reduction of viability and migration in three cell lines, from three different cancer types: HCT116, from colon cancer, AGS from gastric cancer and HCC1806 from BC. These three cell lines had the lowest CDT rates, proving that Runat-BI is especially active against highly aggressive tumors. Moreover, the reduction in cell migration might prevent tumor expansion to other tissues and thus inhibit metastasis. The  $IC_{50}$  results obtained with Runat-BI showed to be similar to those of cisplatin; the cell lines that displayed lower values for cisplatin also display them for Runat-BI, which seems to indicate that both compounds share some mechanism of action. 104



The compound did not show great effectiveness against HCC1500, HCC1937 and MCF-7, all belonging to BC. Furthermore, BC cell lines belonging to the TNBC subtype (HCC1806 and MDA-MB-231) and luminal B (BT474) exhibited a greater response to Runat-BI treatment than those belonging to the luminal A subtype, such as MCF-7, which showed less remarkable results in both viability and migration assays. Despite the lack of specificity of Runat-BI for a particular cancer type, a selective effect has been observed between non-tumorigenic cell lines such as MCF10A and tumorigenic cell lines. The MCF10A cell line was not affected by the agent, showing no reduction in viability or migration. Similar results in the selectivity of action in non-tumor cell lines have already been demonstrated with other ruthenium agents [16,22,25,31]. Popolin et al. studied four ruthenium-based antitumor complexes with different ligands, among which  $[\text{Ru}(\text{CH}_3\text{CO}_2)(\text{dppb})(\text{bipy})]\text{PF}_6$  [where dppb = 1,4-bis(diphenylphosphino)butane and bipy = 2,2'-bipyridine] showed the best results and was selected to be studied in three BC cell lines: MDA-MB-231, MCF-7 and MCF-10A. This complex was more efficient in inhibiting proliferation, adhesion, migration and invasion in MDA-MB-231 cells than non-tumor cells (MCF10A). Nevertheless, the Ru(III) complex showed inconsistent results in MCF-7 [29]. Similarly, Naves et al. reported a selective effect of a ruthenium-biphosphine complex containing gallic acid as a ligand, with selective cytotoxicity against the TNBC cell line (MDA-MB-231) over non-tumor cells (MCF10A), inhibiting its migration and invasion and inducing apoptosis [16,25]. Our in vitro studies support the use of Runat-BI as a potent drug candidate for highly aggressive and proliferative cancers.

Despite the anticancer properties found in Runat-BI, no significant results were obtained for isolated isomer 1 from this complex, which is therefore not solely responsible for its antitumor action. Work is currently underway on the isolation and purification of the second isomer to verify whether Runat-BI agent requires both isomers to exert its action or if only one is responsible for the activity.

There seems to be a relationship between Runat-BI effectiveness and the growth rate of cell lines, since the fastest growing ones generally show the greatest response, probably due to the binding to DNA, which has been considered the main target of action of the agent. However, the relationship is still unclear, as Ru-based drugs seem to exert their anticancer effects through a multitarget mechanism [26], which makes these agents less prone to drug resistance [32,33]. Several studies have revealed that DNA is not necessarily the primary target of ruthenium compounds but rather that these compounds have shown a higher affinity for DNA-related proteins [12,17,32]. In our study, MCF-7 and MCF10A were not affected by Runat-BI despite their rapid growth rates, warranting exploration in future studies of other mechanism(s) of action potentially at play.

We further investigated the expression of proapoptotic genes *BAX* and *CASPASE-3* and the antiapoptotic gene *BCL-2*. Our results showed that Runat-BI upregulated the expression of proapoptotic genes *BAX* and *CASPASE-3* (although no statistically significant differences were obtained) but exerted no effect the antiapoptotic gene expression of *BCL-2*. This is in agreement with results obtained in previous studies on BC cell lines [16,29]. However, the cell lines with the highest rise in antiapoptotic gene expression were not the ones with the most compromised viability, thus potentially ruling this out as the main factor underlying this increased gene expression and indicating a need for further studies for a more precise understanding of this possible pathway of action.

Runat-BI has shown very positive in vitro results, better even than other earlier reported ruthenium systems [34]. Nevertheless, in vivo trials are also necessary to confirm its selective action and possible indications. Another interesting focus would be to study Runat-BI in combination with other commercialized therapeutic agents to evaluate the possible benefits of several targets of action and their joint effect. The combination of previously reported ruthenium compounds with standard anticancer agents that target DNA has shown to be a reasonable combination strategy, particularly in TNBC [35].

## 5. Conclusions

Ruthenium-based antitumor agents such as Runat-BI are an interesting alternative to current chemotherapy agents, overcoming many disadvantages of the latter due to their specific activity against different cancers, more favorable toxicity profile and multitargeted mechanism of action. Altogether, our novel complex Runat-BI significantly reduced viability and migration in three cancer cell lines taken from colon, gastric and breast cancer, all of which displayed fast proliferation rates. This supports the effectiveness of the complex in highly proliferative and aggressive cancers that have limited available therapeutic options. Its selective action between tumor and non-tumor lines as well as its potential multitargeted effect on DNA and upregulation of proapoptotic gene expression make it a potential drug candidate for cancer treatment. The effectiveness of the racemic mixture Runat-BI is not due to the isolated isomer 1, and hence further studies should be addressed at evaluating the role of isomer 2 to more precisely elucidate the anticancer potential of Runat-BI and its mechanism of action.

## 6. Patents

Runat-BI has the international patent certificate PCT/ES2022/070415, Universitat de València and Fundación INCLIVA (2021): Ruthenium-biimidazole compound (RUNAT-BI) and its therapeutic use. It has been registered in *Oficina Española de Patentes y Marcas* (OEPM) with No. P202130624. <https://www.uv.es/oferta-cientifico-tecnologica/es/resultados/salud/salud-lo-largo-todo-ciclo-vital-1286222426775/OCTResultats.html?id=1286236582025> (accessed on 15 November 2022).

**Supplementary Materials:** The following supporting information can be downloaded at: <https://www.mdpi.com/article/10.3390/cancers15010069/s1>. Figure S1: Electrospray ionization mass spectrum (ESI-MS) for Runat-BI showing the isotopic distribution for the  $[\text{RuCl}_2(\text{H}_2\text{biim})_2]^+$  cation. Figure S2: FT-IR spectra for 2,2'-biimidazole ( $\text{H}_2\text{biim}$ ) and Runat-BI. Table S1: Crystal data and structure refinement for Runat-BI. Table S2: Selected bond lengths (Å) and angles (°) for Runat-BI. Table S3: Cell line characteristics and culture conditions. BC: breast cancer; EGFR: epidermal growth factor receptor; EGP2: epithelial glycoprotein 2; ER: estrogen receptor; FBS: fetal bovine serum; HER2: hormonal estrogen receptor 2; IDC: invasive ductal carcinoma; IGFBP: insulin growth factor binding protein; L-glu: L-glutamine; PR: progesterone receptor; RPMI: RPMI 1640 medium; TGF- $\beta/\alpha$ : transforming growth factor  $\beta/\alpha$ . \*MCF10A is non-tumorigenic human mammary epithelial cells. Table S4:  $\text{IC}_{50}$  in  $\mu\text{M}$  of the nine cancer cell lines studied after 48 h and 72 h of Runat-BI treatment and of Cisplatin. The R square indicates the goodness of fit.  $\text{IC}_{50}$ : half maximal inhibitory concentration. Figure S3: Percentage of viability for AGS and MDA-MB-231 cell lines treated with isomer 1 of Runat-BI at 24, 48 and 72 h. The gastric cancer cell line: AGS and the BC cell line: MDA-MB-231, were treated with isomer 1 of Runat-BI (from 0 to 50  $\mu\text{M}$ ) for 24 h (A), 48 h (B) and 72 h (C). Cell proliferation was determined with the MTT assay. Dots indicate the mean of two independent experiments. Figure S4: Effect of Runat-BI treatment on cell migration. Cell migration in HCC1500, HCC1937, MCF-7 and BT-474 cell lines was measured via wound-healing assay after treatment with Runat-BI (21  $\mu\text{M}$ ) or control/PEG for 48 and 72 h. Images of cell migration at 0, 48 and 72 h after Runat-BI (21  $\mu\text{M}$ ) treatment or PEG (control). Three separate experiments were performed, and the most representative results are presented (5 $\times$  amplification). Figure S5: Comparison of percentage of wound closure of cell lines treated with Runat-BI (21  $\mu\text{M}$ ) or control/PEG for 48 h (green) and 72 h (blue). Columns express the mean  $\pm$  SD of the percentage of closure in three independent experiments by cell line. \*  $p \leq 0.1$ , \*\*  $p \leq 0.05$ , \*\*\*  $p \leq 0.01$  were considered statistically significant.

**Author Contributions:** Conceptualization, J.M.-L. and G.R.; funding acquisition, A.C., I.C., J.M.-L. and G.R.; methodology and study supervision S.S.O., M.I.-V. and G.R.; formal analysis and investigation, M.A.-F., S.S.O., M.O.-A., M.I.-V., F.C. and E.J.-M.; cell line experiments, M.A.-F. and F.C.; legal aspects, E.J.-M.; preparation and characterization of Runat-BI compound, M.O.-A., I.C. and J.M.-L.; writing—original draft preparation, M.A.-F. and S.S.O.; writing—review and editing, M.A.-F., S.S.O. and J.M.-L. All authors have read and agreed to the published version of the manuscript.

**Funding:** This research was funded by the VLC-BIOCLINIC Program of the University of Valencia [Projects 02-RUN-AT-MARTINEZ-RIBAS-2017-A and PI-2021-007-DIRUGEN]. S.S.O. is funded by the FCAECC (POSTD20028OLTR); G.R. is funded on a Miguel Servet II contract (CPII14-00013) from the Carlos III Health Institute; CIBERONC (CB16/12/00481-CB16/12/00473) is an initiative of the Carlos III Health Institute.

**Institutional Review Board Statement:** Not applicable.

**Informed Consent Statement:** Not applicable.

**Data Availability Statement:** The data provided in this study are available from the corresponding author on reasonable request.

**Acknowledgments:** We thank the Cytometry Unit of the Central Medical Research Unit (UCIM), University of Valencia. The Biomedical Research Centre Network in Cancer (CIBERONC) is a Carlos III Health Institute initiative. We are grateful to the private patients' foundation Fundación Le Cadó and several patients' organizations for their financial support.

**Conflicts of Interest:** The authors declare no conflict of interest.

## References

1. Siegel, R.L.; Miller, K.D.; Jemal, A. Cancer statistics, 2018. *CA Cancer J. Clin.* **2018**, *68*, 7–30. [[CrossRef](#)]
2. Sung, H.; Ferlay, J.; Siegel, R.L.; Laversanne, M.; Soerjomataram, I.; Jemal, A.; Bray, F. Global Cancer Statistics 2020: GLOBOCAN Estimates of Incidence and Mortality Worldwide for 36 Cancers in 185 Countries. *CA Cancer J. Clin.* **2021**, *71*, 209–249. [[CrossRef](#)]
3. Lee, Y.T.; Tan, Y.J.; Oon, C.E. Molecular targeted therapy: Treating cancer with specificity. *Eur. J. Pharmacol.* **2018**, *834*, 188–196. [[CrossRef](#)] [[PubMed](#)]
4. Batlle, E.; Clevers, H. Cancer stem cells revisited. *Nat. Med.* **2017**, *23*, 1124–1134. [[CrossRef](#)] [[PubMed](#)]
5. Zielonke, N.; Kregting, L.M.; Heijnsdijk, E.A.M.; Veerus, P.; Heinävaara, S.; McKee, M.; de Kok, I.M.C.M.; de Koning, H.J.; van Ravesteyn, N.T.; EU-TOPIA Collaborators. The potential of breast cancer screening in Europe. *Int. J. Cancer* **2021**, *148*, 406–418. [[CrossRef](#)] [[PubMed](#)]
6. Suhail, Y.; Cain, M.P.; Vanaja, K.; Kurywchak, P.A.; Levchenko, A.; Kalluri, R. Systems Biology of Cancer Metastasis. *Cell Syst.* **2019**, *9*, 109–127. [[CrossRef](#)] [[PubMed](#)]
7. Montani, M.; Pazmay, G.V.B.; Hysi, A.; Lupidi, G.; Pettinari, R.; Gambini, V.; Tilio, M.; Marchetti, F.; Pettinari, C.; Ferraro, S.; et al. The water soluble ruthenium(II) organometallic compound [Ru(p-cymene)(bis(3,5 dimethylpyrazol-1-yl)methane)Cl]Cl suppresses triple negative breast cancer growth by inhibiting tumor infiltration of regulatory T cells. *Pharmacol. Res.* **2016**, *107*, 282–290. [[CrossRef](#)] [[PubMed](#)]
8. Ghosh, S. Cisplatin: The first metal based anticancer drug. *Bioorg. Chem.* **2019**, *88*, 102925. [[CrossRef](#)]
9. Hongthong, K.; Ratanaphan, A. BRCA1-Associated Triple-Negative Breast Cancer and Potential Treatment for Ruthenium-Based Compounds. *Curr. Cancer Drug Targets* **2016**, *16*, 606–617. [[CrossRef](#)]
10. Dasari, S.; Tchounwou, P.B. Cisplatin in cancer therapy: Molecular mechanisms of action. *Eur. J. Pharmacol.* **2014**, *740*, 364–378. [[CrossRef](#)]
11. Golbaghi, G.; Castonguay, A. Rationally designed ruthenium complexes for breast cancer therapy. *Molecules* **2020**, *25*, 265. [[CrossRef](#)] [[PubMed](#)]
12. Meier-Menches, S.M.; Gerner, C.; Berger, W.; Hartinger, C.G.; Keppler, B.K. Structure-activity relationships for ruthenium and osmium anticancer agents-towards clinical development. *Chem. Soc. Rev.* **2018**, *47*, 909–928. [[CrossRef](#)] [[PubMed](#)]
13. Gałczyńska, K.; Drulis-Kawa, Z.; Arabski, M. Antitumor activity of Pt(II), Ru(III) and Cu(II) complexes. *Molecules* **2020**, *25*, 3492. [[CrossRef](#)] [[PubMed](#)]
14. Alessio, E.; Messori, L. NAMI-A and KP1019/1339, two iconic ruthenium anticancer drug candidates face-to-face: A case story in medicinal inorganic chemistry. *Molecules* **2019**, *24*, 1995. [[CrossRef](#)] [[PubMed](#)]
15. Bergamo, A.; Gaiddon, C.; Schellens, J.H.M.; Beijnen, J.H.; Sava, G. Approaching tumour therapy beyond platinum drugs: Status of the art and perspectives of ruthenium drug candidates. *J. Inorg. Biochem.* **2012**, *106*, 90–99. [[CrossRef](#)] [[PubMed](#)]
16. Naves, M.A.; Graminha, A.E.; Vegas, L.C.; Luna-Dulcey, L.; Honorato, J.; Menezes, A.C.S.; Batista, A.A.; Cominetti, M.R. Transport of the Ruthenium Complex [Ru(GA)(dppe)<sub>2</sub>]PF<sub>6</sub> into Triple-Negative Breast Cancer Cells Is Facilitated by Transferrin Receptors. *Mol. Pharm.* **2019**, *16*, 1167–1183. [[CrossRef](#)]
17. Nowak-Sliwinska, P.; Van Beijnum, J.R.; Casini, A.; Nazarov, A.A.; Wagnieres, G.; van den Bergh, H.; Dyson, P.J.; Griffioen, A.W. Organometallic ruthenium(II) arene compounds with antiangiogenic activity. *J. Med. Chem.* **2011**, *54*, 3895–3902. [[CrossRef](#)]
18. Kapitzka, S.; Pongratz, M.; Jakupiec, M.A.; Heffeter, P.; Berger, W.; Lackinger, L.; Keppler, B.K.; Marian, B. Heterocyclic complexes of ruthenium(III) induce apoptosis in colorectal carcinoma cells. *J. Cancer Res. Clin. Oncol.* **2005**, *131*, 101–110. [[CrossRef](#)]
19. Lizardo, M.M.; Morrow, J.J.; Miller, T.E.; Hong, E.S.; Ren, L.; Mendoza, A.; Halsey, C.H.; Scacheri, P.C.; Helman, L.J.; Khanna, C. Upregulation of Glucose-Regulated Protein 78 in Metastatic Cancer Cells Is Necessary for Lung Metastasis Progression. *Neoplasia* **2016**, *18*, 699–710. [[CrossRef](#)]

20. Brabec, V.; Kasparkova, J. Ruthenium coordination compounds of biological and biomedical significance. DNA binding agents. *Coord. Chem. Rev.* **2018**, *376*, 75–94. [[CrossRef](#)]
21. Wang, H.; Wei, J.; Jiang, H.; Zhang, Y.; Jiang, C.; Ma, X. Design, synthesis and pharmacological evaluation of three novel dehydroabietyl piperazine dithiocarbamate ruthenium (II) polypyridyl complexes as potential antitumor agents: DNA damage, cell cycle arrest and apoptosis induction. *Molecules* **2021**, *26*, 1453. [[CrossRef](#)]
22. Popolin, C.P.; Cominetti, M.R. A Review of Ruthenium Complexes Activities on Breast Cancer Cells. *Mini Rev. Med. Chem.* **2017**, *17*, 1435–1441. [[CrossRef](#)]
23. Ferraro, M.G.; Piccolo, M.; Misso, G.; Misso, G.; Maione, F.; Montesarchio, D.; Caraglia, M.; Paduano, L.; Santamaria, R.; Irace, C. Breast Cancer Chemotherapeutic Options: A General Overview on the Preclinical Validation of a Multi-Target Ruthenium(III) Complex Lodged in Nucleolipid Nanosystems. *Cells* **2020**, *9*, 1412. [[CrossRef](#)] [[PubMed](#)]
24. Hartinger, C.G.; Jakupec, M.A.; Zorbas-Seifried, S.; Groessel, M.; Egger, A.; Berger, W.; Zorbas, H.; Dyson, P.J.; Keppler, B.K. KP1019, a new redox-active anticancer agent—Preclinical development and results of a clinical phase I study in tumor patients. *Chem. Biodivers.* **2008**, *5*, 2140–2155. [[CrossRef](#)] [[PubMed](#)]
25. Nayeem, N.; Contel, M. Exploring the Potential of Metallodrugs as Chemotherapeutics for Triple Negative Breast Cancer. *Chem. A Eur. J.* **2021**, *27*, 8891–8917. [[CrossRef](#)] [[PubMed](#)]
26. Silvestri, S.; Cirilli, I.; Marcheggiani, F.; Dlundla, P.; Lupidi, G.; Pettinari, R.; Marchetti, F.; Di Nicola, C.; Falcioni, G.; Marchini, C.; et al. Evaluation of anticancer role of a novel ruthenium(II)-based compound compared with NAMI-A and cisplatin in impairing mitochondrial functionality and promoting oxidative stress in triple negative breast cancer models. *Mitochondrion* **2021**, *56*, 25–34. [[CrossRef](#)]
27. Gaspari, A.P.S.; da Silva, R.S.; Carneiro, Z.A.; de Carvalho, M.R.; Carvalho, I.; Pernomian, L.; Ferreira, L.P.; Ramos, L.C.B.; de Souza, G.A.; Formiga, A. Improving Cytotoxicity against Breast Cancer Cells by Using Mixed-Ligand Ruthenium(II) Complexes of 2,2'-Bipyridine, Amino Acid, and Nitric Oxide Derivatives as Potential Anticancer Agents. *Anti-Cancer Agents Med. Chem.* **2021**, *21*, 1602–1611. [[CrossRef](#)]
28. Scolaro, C.; Geldbach, T.J.; Rochat, S.; Dorcier, A.; Gossens, C.; Bergamo, A.; Cocchietto, M.; Tavernelli, I.; Sava, G.; Rothlisberger, U.; et al. Influence of hydrogen-bonding substituents on the cytotoxicity of RAPTA compounds. *Organometallics* **2006**, *25*, 756–765. [[CrossRef](#)]
29. Popolin, C.P.; Reis, J.P.B.; Becceneri, A.B.; Graminha, A.E.; Almeida, M.A.P.; Corrêa, R.S.; Colina-Vegas, L.A.; Ellena, J.; Batista, A.A.; Cominetti, M.R. Cytotoxicity and anti-tumor effects of new ruthenium complexes on triple negative breast cancer cells. *PLoS ONE* **2017**, *12*, e0183275. [[CrossRef](#)]
30. Wu, Q.; He, J.; Mei, W.; Zhang, Z.; Wu, X.; Sun, F. Arene ruthenium(II) complex, a potent inhibitor against proliferation, migration and invasion of breast cancer cells, reduces stress fibers, focal adhesions and invadopodia. *Metallomics* **2014**, *6*, 2204–2212. [[CrossRef](#)]
31. Bergamo, A.; Masi, A.; Dyson, P.; Sava, G. Modulation of the metastatic progression of breast cancer with an organometallic ruthenium compound. *Int. J. Oncol.* **2008**, *33*, 1281–1289. [[CrossRef](#)] [[PubMed](#)]
32. Casini, A.; Hartinger, C.G.; Nazarov, A.A.; Dyson, P.J. Organometallic antitumour agents with alternative modes of action. *Med. Organomet. Chem.* **2010**, *32*, 57–80. [[CrossRef](#)]
33. Kladnik, J.; Coverdale, J.P.C.; Kljun, J.; Burmeister, H.; Lippman, P.; Ellis, F.G.; Jones, A.M.; Ott, I.; Romero-Canelón, I.; Turel, I. Organoruthenium complexes with benzo-fused pyridiones overcome platinum resistance in ovarian cancer cells. *Cancers* **2021**, *13*, 2493. [[CrossRef](#)] [[PubMed](#)]
34. Orts-Arroyo, M.; Gutiérrez, F.; Gil-Tebar, A.; Ibarrola-Villava, M.; Jiménez-Martí, E.; Silvestre-Llora, A.; Castro, I.; Ribas, G.; Martínez-Lillo, J. A novel adenine-based diruthenium(III) complex: Synthesis, crystal structure, electrochemical properties and evaluation of the anticancer activity. *J. Inorg. Biochem.* **2022**, *232*, 111812–111819. [[CrossRef](#)] [[PubMed](#)]
35. Bakewell, S.; Conde, I.; Fallah, Y.; McCoy, M.; Jin, L.; Shajahan-Haq, A.N. Inhibition of DNA repair pathways and induction of ROS are potential mechanisms of action of the small molecule inhibitor bold-100 in breast cancer. *Cancers* **2020**, *12*, 2647. [[CrossRef](#)] [[PubMed](#)]

**Disclaimer/Publisher's Note:** The statements, opinions and data contained in all publications are solely those of the individual author(s) and contributor(s) and not of MDPI and/or the editor(s). MDPI and/or the editor(s) disclaim responsibility for any injury to people or property resulting from any ideas, methods, instructions or products referred to in the content.

---

*ARTICLE 6*

*Molecular Self-Assembly in a  
Family of Oxo-Bridged  
Dinuclear Ruthenium(IV)  
Systems*





## Molecular Self-Assembly in a Family of Oxo-Bridged Dinuclear Ruthenium(IV) Systems

Marta Orts-Arroyo, Isabel Castro,\* Francesc Lloret, and José Martínez-Lillo\*

Cite This: *Cryst. Growth Des.* 2020, 20, 2044–2056

Read Online

ACCESS |



Metrics &amp; More

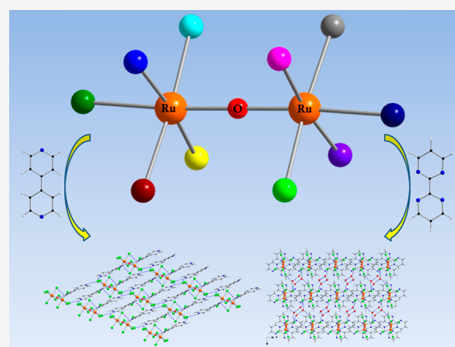


Article Recommendations



Supporting Information

**ABSTRACT:** A series of six novel Ru<sup>IV</sup> compounds of formula (H<sub>2</sub>bpy)<sub>2</sub>-[RuCl<sub>5</sub>]<sub>2</sub>(μ-O) (1), (PPh<sub>4</sub>)<sub>2</sub>[RuCl<sub>4</sub>(H<sub>2</sub>O)]<sub>2</sub>(μ-O)·4H<sub>2</sub>O (2), (PPh<sub>4</sub>)<sub>2</sub>-[RuCl<sub>4</sub>(MeCN)]<sub>2</sub>(μ-O) (3), (PPh<sub>4</sub>)<sub>2</sub>[RuCl<sub>4</sub>(dmf)]<sub>2</sub>(μ-O) (4), (PPh<sub>4</sub>)<sub>2</sub>-[RuCl<sub>4</sub>(py)]<sub>2</sub>(μ-O) (5), and [RuCl<sub>3</sub>(bpym)]<sub>2</sub>(μ-O)·6H<sub>2</sub>O (6) [H<sub>2</sub>bpy<sup>2+</sup> = 4,4'-bipyridine-1,1'-dium cation; PPh<sub>4</sub><sup>+</sup> = tetraphenylphosphonium cation; dmf = N,N'-dimethylformamide; py = pyridine; bpym = 2,2'-bipyrimidine] have been prepared and spectroscopically, electrochemically, and magnetically characterized. Compounds 1, 2, 5, and 6 crystallize in the triclinic system with space group P $\bar{1}$ , whereas 3 and 4 crystallize in the monoclinic system with space group P2<sub>1</sub>/c. While 1–5 are salts based on anionic dinuclear Ru<sup>IV</sup> species, 6 is a neutral diruthenium(IV) complex. The Ru–O–Ru core is present in 1–6 [with values of the Ru–O<sub>oxo</sub> bond length covering the range of 1.774(1)–1.816(1) Å and the values of the Ru–O–Ru angle ( $\theta$ ) varying in the range of 164.3–180.0°]. In their crystal lattice, intermolecular Ru<sup>IV</sup>–Cl⋯Cl–Ru<sup>IV</sup> halogen bonds (1 and 6), Cl⋯ $\pi$  (1 and 3–6), and  $\pi$ ⋯ $\pi$  (5 and 6) type interactions as well as hydrogen bonds (1, 2, and 6) are present. These intermolecular interactions generate novel supramolecular structures based on the self-assembly of ( $\mu$ -oxo)diruthenium(IV) complexes. Magnetic susceptibility measurements performed on microcrystalline samples of 1–6 confirmed the diamagnetic nature for the six compounds, which are strongly antiferromagnetically coupled. The study of the electrochemical properties of 2–6 through cyclic voltammetry (CV) in dmf allowed us to evaluate the effect of the ligand nature on the rich redox features along this series of ( $\mu$ -oxo)diruthenium(IV) complexes.



Ruthenium coordination chemistry has undergone a considerable development in a wide variety of research fields during the last two decades.<sup>1</sup> Promising ruthenium systems for current and future investigations, involving several oxidation states, display a broad array of technological applications that spans from catalysis to chemotherapy.<sup>2–17</sup>

Oxo-bridged diruthenium complexes have attracted great interest for their properties of molecular catalysts in water oxidation reactions and, therefore, as artificial models of the Photosystem II center (PSII).<sup>18–20</sup> In addition, compounds containing the Ru–O–Ru core have been investigated as potent inhibitors of the mitochondrial calcium uniporter (MCU) that regulates the mitochondrial calcium uptake and modulates physiological functions, such as control of metabolism and cell death.<sup>21</sup> The features of this type of ruthenium system make them valuable for biological studies as well.<sup>22</sup> Hence, this wide range of multiproperties motivated us to investigate the crystal structure of oxo-bridged diruthenium complexes.

A current search of the literature and Cambridge Structural Database (CSD) revealed that 24 crystal structures exist containing the (Cl)Ru–O–Ru(Cl) core reported to date. The same search gave 27 hits for systems based on the Ru–O–Ru(H<sub>2</sub>O) core, but found only one example with the (Cl)Ru–O–Ru(MeCN) core,<sup>23</sup> none based on the Ru–O–Ru(dmf)

[dmf = N,N'-dimethylformamide] core, only one crystal structure containing the (Cl)Ru–O–Ru(py) core,<sup>24</sup> and only one system with the Ru–O–Ru(bpym) [bpym = 2,2'-bipyrimidine] core.<sup>25</sup> In all cases, the ruthenium metal ions were oxo-bridged.

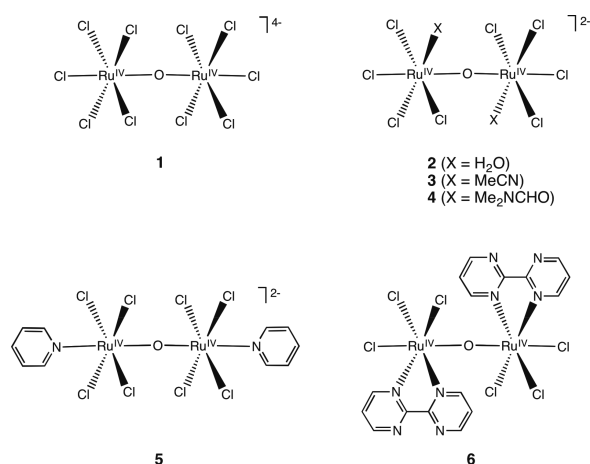
Herein we report the synthesis and characterization of a novel series of six Ru<sup>IV</sup> compounds of formula (H<sub>2</sub>bpy)<sub>2</sub>-[RuCl<sub>5</sub>]<sub>2</sub>(μ-O) (1), (PPh<sub>4</sub>)<sub>2</sub>[RuCl<sub>4</sub>(H<sub>2</sub>O)]<sub>2</sub>(μ-O)·4H<sub>2</sub>O (2), (PPh<sub>4</sub>)<sub>2</sub>[RuCl<sub>4</sub>(MeCN)]<sub>2</sub>(μ-O) (3), (PPh<sub>4</sub>)<sub>2</sub>[RuCl<sub>4</sub>(dmf)]<sub>2</sub>(μ-O) (4), (PPh<sub>4</sub>)<sub>2</sub>[RuCl<sub>4</sub>(py)]<sub>2</sub>(μ-O) (5), and [RuCl<sub>3</sub>(bpym)]<sub>2</sub>(μ-O)·6H<sub>2</sub>O (6) [H<sub>2</sub>bpy<sup>2+</sup> = 4,4'-bipyridine-1,1'-dium cation; PPh<sub>4</sub><sup>+</sup> = tetraphenylphosphonium cation; dmf = N,N'-dimethylformamide; py = pyridine; bpym = 2,2'-bipyrimidine]. From this family, 4 is the first example of a ruthenium system exhibiting the Ru–O–Ru(dmf) core, and 6 is the first reported crystal structure of an oxo-bridged Ru<sup>IV</sup> system containing 2,2'-bipyrimidine.

Received: December 21, 2019

Revised: February 3, 2020

Published: February 11, 2020

Chart 1. Molecular Structure of Compounds 1–6



## RESULTS AND DISCUSSION

**Preparation of 1–6.** Compounds 1, 2, and 6 are synthesized from the Ru<sup>III</sup> salts RuCl<sub>3</sub>·H<sub>2</sub>O (1) and K<sub>2</sub>[RuCl<sub>5</sub>(H<sub>2</sub>O)] (2 and 6) in HCl solutions of different concentration. During the synthesis process the reaction mixture is heated, allowing the oxidation to Ru<sup>IV</sup>. 3 and 5 are synthesized from 2, and compound 4 is obtained from 3. In the case of 1, 5, and 6, they are prepared in the presence of 4,4'-bipyridine, pyridine, and 2,2'-bipyrimidine, respectively (see Experimental Section for full details). With the exception of 1, all of them are barely soluble in water, but highly soluble in dimethylformamide (dmf).

**Structure Description of 1–6.** Compounds 1, 2, 5, and 6 crystallize in the triclinic system with space group *P* $\bar{1}$ , whereas 3 and 4 crystallize in the monoclinic system with space group *P*2<sub>1</sub>/*c* (Table 1). The six compounds are based on oxo-bridged dinuclear Ru<sup>IV</sup> complexes, but each one exhibits singular crystallographic features. 1–5 are made up of dinuclear [{RuCl<sub>5</sub>}<sub>2</sub>(μ-O)]<sup>4-</sup> (1), [{RuCl<sub>4</sub>(H<sub>2</sub>O)}<sub>2</sub>(μ-O)]<sup>2-</sup> (2), [{RuCl<sub>4</sub>(MeCN)}<sub>2</sub>(μ-O)]<sup>2-</sup> (3), [{RuCl<sub>4</sub>(dmf)}<sub>2</sub>(μ-O)]<sup>2-</sup>

(4), and [{RuCl<sub>4</sub>(py)}<sub>2</sub>(μ-O)]<sup>2-</sup> (5) anions together with (H<sub>2</sub>bpy)<sup>2+</sup> (1) and PPh<sub>4</sub><sup>+</sup> (2–5) cations (Figures 1–5). The

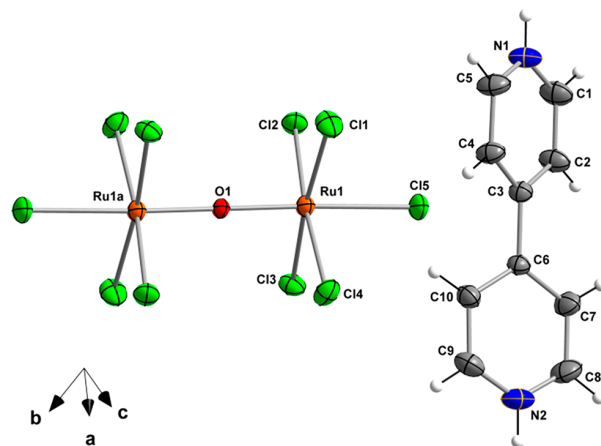


**Figure 1.** Molecular structure of the diprotonated (H<sub>2</sub>bpy)<sup>2+</sup> cation and the dinuclear [RuCl<sub>5</sub>}<sub>2</sub>(μ-O)]<sup>4-</sup> anion in 1. Thermal ellipsoids are depicted at the 50% probability level [symmetry code: (a) =  $-x + 1, -y + 1, -z$ ].

crystal structure of 6 is mainly composed of neutral dinuclear [RuCl<sub>3</sub>(bpy)]<sub>2</sub>(μ-O) complexes (Figure 6). While there are no solvent molecules in 1 and 3–5, water molecules of crystallization are present in 2 and 6. In the lattice of 1–6, a molecular self-assembly occurs through an intricate and extended network of hydrogen bonds (1, 2 and 6), Cl⋯Cl halogen bonds (1 and 6), Cl⋯π (1 and 3–6) and π⋯π type interactions (5 and 6).

The asymmetric unit in 1–6 consists of half a [RuCl<sub>5</sub>}<sub>2</sub>(μ-O)]<sup>4-</sup> anion and a whole molecule of 4,4'-bipyridinium in 1, a [RuCl<sub>4</sub>(H<sub>2</sub>O)}<sub>2</sub>(μ-O)]<sup>2-</sup> anion, two PPh<sub>4</sub><sup>+</sup> cations and four water molecules in 2, half a [RuCl<sub>4</sub>L]}<sub>2</sub>(μ-O)]<sup>2-</sup> anion [L = MeCN (3), dmf (4), py (5)] and one PPh<sub>4</sub><sup>+</sup> cation in 3–5, and half a [RuCl<sub>3</sub>(bpy)]<sub>2</sub>(μ-O) complex along with three

**Table 1.** Summary of the Crystal Data and Structure Refinement Parameters for 1–6

compound	1	2	3	4	5	6
formula	C <sub>20</sub> H <sub>20</sub> Cl <sub>10</sub> N <sub>4</sub> ORu <sub>2</sub>	C <sub>48</sub> H <sub>46</sub> Cl <sub>8</sub> O <sub>7</sub> P <sub>2</sub> Ru <sub>2</sub>	C <sub>52</sub> H <sub>46</sub> Cl <sub>8</sub> N <sub>2</sub> OP <sub>2</sub> Ru <sub>2</sub>	C <sub>54</sub> H <sub>54</sub> Cl <sub>8</sub> N <sub>2</sub> O <sub>3</sub> P <sub>2</sub> Ru <sub>2</sub>	C <sub>58</sub> H <sub>50</sub> Cl <sub>8</sub> N <sub>2</sub> OP <sub>2</sub> Ru <sub>2</sub>	C <sub>16</sub> H <sub>24</sub> Cl <sub>6</sub> N <sub>8</sub> O <sub>7</sub> Ru <sub>2</sub>
<i>M</i> <sub>r</sub> /g mol <sup>-1</sup>	889.04	1282.53	1262.59	1326.67	1338.68	855.27
crystal system	triclinic	triclinic	monoclinic	monoclinic	triclinic	triclinic
space group	<i>P</i> $\bar{1}$	<i>P</i> $\bar{1}$	<i>P</i> 2 <sub>1</sub> / <i>c</i>	<i>P</i> 2 <sub>1</sub> / <i>c</i>	<i>P</i> $\bar{1}$	<i>P</i> $\bar{1}$
<i>a</i> /Å	8.117(1)	10.316(1)	13.034(1)	13.127(1)	11.512(1)	8.174(1)
<i>b</i> /Å	9.661(1)	12.662(1)	12.853(1)	12.792(1)	11.833(1)	9.078(1)
<i>c</i> /Å	10.760(1)	21.402(1)	16.088(1)	16.783(1)	12.078(1)	10.523(2)
$\alpha$ /°	67.87(1)	90.27(1)	90	90	83.85(1)	85.79(1)
$\beta$ /°	74.18(1)	99.96(1)	107.28(1)	105.50(1)	68.69(1)	67.77(1)
$\gamma$ /°	66.18(1)	102.81(1)	90	90	68.69(1)	86.00(1)
<i>V</i> /Å <sup>3</sup>	707.8(1)	2682.2(4)	2573.5(1)	2715.7(1)	1427.27(1)	720.1(2)
<i>Z</i>	1	2	2	2	1	1
<i>D</i> <sub>c</sub> /g cm <sup>-3</sup>	2.086	1.588	1.629	1.622	1.557	1.972
$\mu$ /mm <sup>-1</sup>	2.036	1.069	1.105	1.054	1.001	1.657
<i>F</i> (000)	434	1288	1268	1340	674	422
GOF on <i>F</i> <sup>2</sup>	1.080	1.113	0.952	1.115	0.907	0.944
<i>R</i> <sub>1</sub> [ <i>I</i> > 2σ( <i>I</i> )]	0.0357	0.0280	0.0298	0.0247	0.0281	0.0248
<i>wR</i> <sub>2</sub> [ <i>I</i> > 2σ( <i>I</i> )]	0.0753	0.0761	0.0737	0.0692	0.0801	0.0612
$\Delta\rho_{\max/\min}/e \text{ \AA}^{-3}$	1.944/−1.511	1.103/−0.780	0.590/−0.963	0.503/−0.801	0.821/−0.994	0.934/−0.436



water molecules in **6** (Figures 1–6). In compounds **1** and **3–6**, there a center of symmetry exists on the O(1) atom.

Each six-coordinate Ru<sup>IV</sup> ion in **1** is bonded to five chloride ions and an oxygen atom from an oxo group forming a distorted octahedral environment (Figure 1). The Ru–O bond length is 1.780(1) Å, whereas the average value of the Ru–Cl bond lengths is 2.362(1) Å. These values are in agreement with those previously reported for this anion in its potassium [YAQZIC] and benzamidine [AMEWIA] salts,<sup>22</sup> the latter being reported as a CSD communication. The Ru–O–Ru angle value ( $\theta$ ) subtended by the oxo ligand is 180.0° [Ru(1)–O(1)–Ru(1a); (a) =  $-x + 1, -y + 1, -z$ ]. The intramolecular Ru··Ru distance across the oxo bridge is 3.560(1) Å. The doubly protonated 4,4'-bipyridine molecule acts in **1** as a cation, the two pyridyl rings being non-coplanar (Table 2).

**Table 2. Hydrogen-Bonding Interactions in 1<sup>a</sup>**

D–H··A	D–H/Å	H··A/Å	D··A/Å	(DHA)/°
N(2)–H(2A)··Cl(5c)	0.860	2.515(1)	3.257(1)	144.9(1)
N(1)–H(1B)··Cl(3d)	0.860	2.476(1)	3.171(1)	138.5(1)
N(2)–H(2A)··Cl(5e)	0.860	2.606(1)	3.288(4)	137.1(1)

<sup>a</sup>Symmetry codes: (c) =  $x + 1, y, z$ ; (d) =  $x, y - 1, z$ ; (e) =  $-x + 2, -y, -z + 1$ .

Indeed, the dihedral angle through the inter-ring carbon–carbon bond is approximately 24.3°. The average values of the C–C and C–N bond lengths are in agreement with those found in salts based on this doubly protonated organic cation.<sup>26–33</sup>

Each one of the two Ru<sup>IV</sup> ions in **2** is six-coordinate and bonded to four chloride ions and two oxygen atoms, one from an oxo group and one from a water molecule, in a distorted octahedral geometry (Figure 2). The Ru–Cl and Ru–O<sub>water</sub> bond lengths exhibit average values of 2.339(1) and 2.113(1) Å, respectively. The average value of the Ru–O<sub>oxo</sub> bond length in **2** is 1.781(1) Å.

In complex **2**, two coordinated water molecules are involved in intramolecular H-bonds with chloride ions [average O··Cl distance of ca. 3.12 Å], which induce great distortion in the complex and reduce the Ru–O–Ru angle value [ $\theta$  angle = 164.3°], in comparison with that of complex **1** (Table 3). In **2**, the intramolecular Ru··Ru distance across the oxo group is

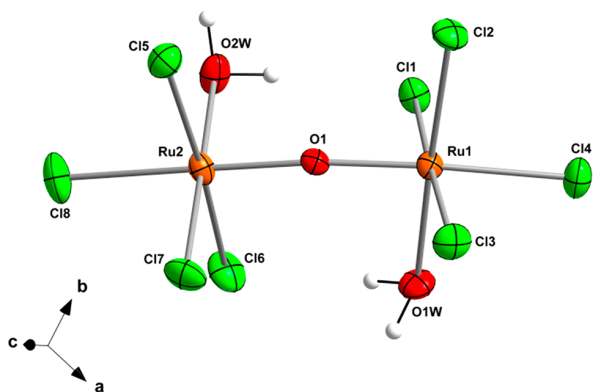


**Figure 2.** Molecular structure of the dinuclear  $[\{RuCl_4(H_2O)\}_2(\mu-O)]^{2-}$  anion in **2**. Thermal ellipsoids are depicted at the 50% probability level. PPh<sub>4</sub><sup>+</sup> cations and noncoordinating water molecules have been omitted for clarity.

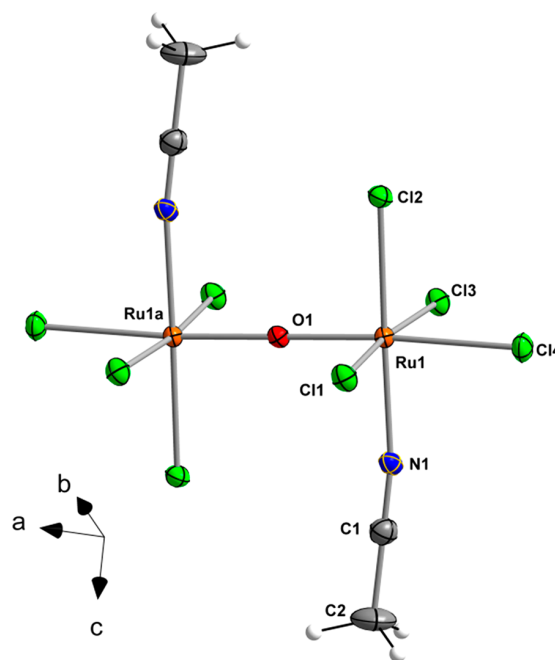


**Figure 3.** Molecular structure of the dinuclear  $[\{RuCl_4(MeCN)\}_2(\mu-O)]^{2-}$  anion in **3**. Thermal ellipsoids are depicted at the 50% probability level. PPh<sub>4</sub><sup>+</sup> cations have been omitted for clarity [symmetry code: (a) =  $-x + 1, -y + 2, -z + 1$ ].

3.529(1) Å, which is somewhat shorter than that of **1**. Two tetraphenylphosphonium cations counterbalance the negative charges in **2**. As expected, they show values of C–C and C–P bond lengths typical of the phenyl groups linked to the central phosphorus atom in this bulky organic cation.

In compounds **3–5**, each Ru<sup>IV</sup> ion is six-coordinate and bonded to four chloride ions, an oxygen atom from an oxo group, and one nitrogen (**3** and **5**)/oxygen (**4**) atom from the MeCN (**3**), dmf (**4**) and py (**5**) ligands, forming a distorted octahedral environment (Figures 3, 4, and 5). As in **2**, PPh<sub>4</sub><sup>+</sup> cations counterbalance the negative charges in the crystal structure of **3–5**.

The Ru<sup>IV</sup> ion in **3** exhibits a Ru–O bond length of 1.785(2) Å. The average value of the Ru–Cl bond lengths is 2.346(2) Å. The Ru–O–Ru angle value ( $\theta$ ) is 180.0° [Ru(1)–O(1)–Ru(1a); (a) =  $-x + 1, -y + 2, -z + 1$ ], and the intramolecular Ru··Ru distance across the oxo bridge is 3.571(1) Å (Figure 3). The MeCN molecule in **3** shows values of the C–C and C–N bond lengths that are in agreement with those found for this ligand when coordinated to other metal ions.<sup>34</sup>

In **4**, the Ru–O bond length involving the oxygen atom of the oxo group is 1.797(1) Å, and the Ru–O bond length of the oxygen atom of the dmf molecule is 2.094(2) Å. The average value of the Ru–Cl bond lengths is 2.349(2) Å. The Ru–O–Ru angle value is 180.0° [Ru(1)–O(1)–Ru(1a); (a) =  $-x + 1, -y, -z + 1$ ], and the intramolecular Ru··Ru distance across the oxo bridge is 3.593(1) Å. The coordinated dmf molecule in **4** is quite planar, and the maximum deviation from planarity is 0.199(1) Å at the C(3) atom. The C–C, C–N, and C–O bond lengths agree with those found in the literature for dmf-based metal complexes.<sup>35</sup> Remarkably, **4** is the first example of a ruthenium system exhibiting the Ru–O–Ru(dmf) core.

In **5**, the Ru<sup>IV</sup> ion shows a Ru–O bond length of 1.774(1) Å, and the value of the Ru–N bond length, involving the N atom

Table 3. Hydrogen-Bonding Interactions in **2**<sup>a</sup>

D–H...A	D–H/Å	H...A/Å	D...A/Å	(DHA)/°
O(1w)–H(1wA)...Cl(6)	0.956	2.27(1)	3.080(1)	142.1(1)
O(1w)–H(1wB)...O(5w)	0.957	1.66(1)	2.612(1)	170.8(1)
O(2w)–H(2wA)...O(3w)	0.943	1.74(1)	2.646(1)	160.0(1)
O(2w)–H(2wB)...Cl(1)	0.945	2.25(1)	3.156(1)	160.1(1)
O(5w)–H(5wA)...O(6w)	0.954	1.78(1)	2.729(1)	175.6(1)
O(5w)–H(5wB)...Cl(7e)	0.955	2.40(1)	3.347(1)	169.9(1)

<sup>a</sup>Symmetry codes: (a) =  $x + 1, y, z$ ; (e) =  $x - 1, y, z$ .

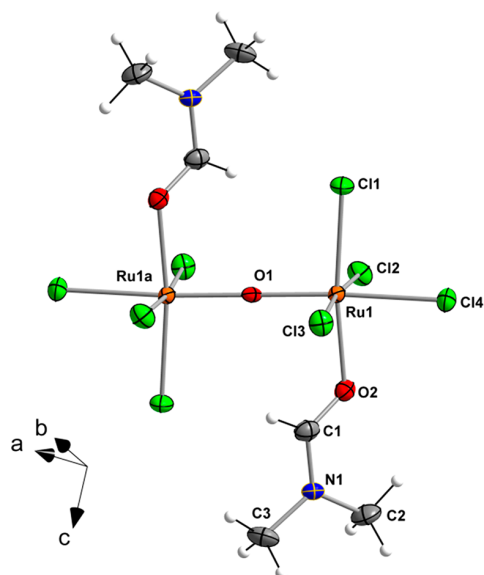


**Figure 4.** Molecular structure of the dinuclear  $[\{\text{RuCl}_4(\text{dmf})\}_2(\mu\text{-O})]^{2-}$  anion in **4**. Thermal ellipsoids are depicted at the 50% probability level.  $\text{PPh}_4^+$  cations have been omitted for clarity [symmetry code: (a) =  $-x + 1, -y, -z + 1$ ].

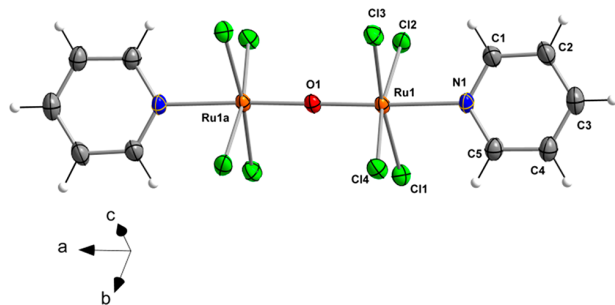


**Figure 5.** Molecular structure of the dinuclear  $[\{\text{RuCl}_4(\text{py})\}_2(\mu\text{-O})]^{2-}$  anion in **5**. Thermal ellipsoids are depicted at the 50% probability level.  $\text{PPh}_4^+$  cations have been omitted for clarity [symmetry code: (a) =  $-x + 2, -y + 2, -z$ ].

of the pyridine molecule, is 2.154(2) Å. The average value of the Ru–Cl bond lengths is 2.356(1) Å. The Ru–O–Ru angle value is 180.0° [Ru(1)–O(1)–Ru(1a); (a) =  $-x + 2, -y + 2, -z$ ], and the intramolecular Ru...Ru distance across the oxo bridge is 3.547(1) Å.

The Ru<sup>IV</sup> ion in **6** is six-coordinate and bonded to three chloride ions, with a *fac* geometry, two nitrogen atoms of a bpy molecule, and an oxygen atom from an oxo ligand in a distorted octahedral environment. The Ru–N and Ru–Cl bond lengths present average values of 2.062(1) and 2.372(1)

Å, respectively. The Ru–O bond length is 1.816(1) Å, and the Ru–O–Ru angle value obtained through the oxo group is 180.0° [Ru(1)–O(1)–Ru(1a); (a) =  $-x + 1, -y + 1, -z + 2$ ]. The intramolecular Ru...Ru distance in **6** is 3.632(1) Å, which is the longest intramolecular Ru...Ru separation in this family of dinuclear Ru<sup>IV</sup> systems, and it could be justified by the presence of the two bpy molecules and the values of the Ru–N bond lengths. The bpy ligand is coordinated to the Ru(1) ion in a bidentate fashion, showing a short bite angle [79.5(1)° for the N(1)–Ru(1)–N(2) atoms set], which is the main distortion of the ideal octahedral geometry in **6**. The C–C and C–N bond lengths of the chelating bpy molecule show expected values. The two pyridyl rings are non-coplanar and exhibit a dihedral angle between them of approximately 6.5°. In the dinuclear complex **6**, intramolecular Cl... $\pi$  interactions take place between the pyridyl rings of the bpy molecule coordinated to one Ru<sup>IV</sup> ion and two chloride ions from the other Ru<sup>IV</sup> center, with Cl...centroid distances of approximately 3.7 and 3.8 Å for the intramolecular Cl(3)... $\pi$  and Cl(2)... $\pi$  separations, respectively.<sup>36</sup> In addition, intramolecular C–H...Cl interactions are also observed in this complex [average C...Cl distance of ca. 3.4 Å] (Figure S1). Remarkably, **6** is the first reported crystal structure of an oxo-bridged Ru<sup>IV</sup> system containing 2,2'-bipyrimidine.

In the crystal packing of compound **1**, the shortest Cl...Cl contact of 3.225(1) Å [Cl(5)...Cl(5b); (b) =  $-x + 1, -y, -z + 1$ ] generates chains of  $[\{\text{RuCl}_5\}_2(\mu\text{-O})]^{4+}$  anions (Figure S2). Thus, the shortest intermolecular Ru...Ru separation in **1** is 7.881(1) Å [Ru(1)...Ru(1b)]. These anionic chains are connected to each other through bifurcated three-centered N–H...Cl<sub>2</sub> hydrogen bonds that are provided by the doubly protonated 4,4'-bipyridine molecule [the average value of the N...Cl distances is ca. 3.24(1) Å] (Table 2),<sup>33,37,38</sup> which act as spacers in **1** (Figure 7). These intermolecular interactions lead to the formation of a two-dimensional supramolecular network in the crystal structure of **1** (Figures 7 and S3). Additional longer Cl...Cl interactions of 3.535(1) Å [Cl(4)...Cl(2c); (c) =  $x + 1, y, z$ ] and weak C–H...Cl contacts (Table S1) tied together the 2D sheets into the overall three-dimensional structure (Figure 8).

In the crystal packing of compound **2**, the  $[\{\text{RuCl}_4(\text{H}_2\text{O})\}_2(\mu\text{-O})]^{2-}$  anions are well separated from each other by means of the bulky  $\text{PPh}_4^+$  cations (Figure 9). The shortest intermolecular Ru–Cl...Cl–Ru separation is 5.298(1) Å [Cl(1)...Cl(1a), (a) =  $x + 1, y, z$ ], and the shortest Ru...Ru distance is 8.165(1) Å [Ru(1)...Ru(2a)]. Nevertheless, crystallization water molecules are H-bonded and linked to coordinate water molecules (O1w and O2w) that connect  $[\{\text{RuCl}_4(\text{H}_2\text{O})\}_2(\mu\text{-O})]^{2-}$  anions through the O2w...O3w...Cl4a and Cl8...O6w...O5w...O1wa pathways (Table 3). A small water aggregate is formed by O1w, O5w, and O6w, resulting in the arrangement of anionic chains that grow along

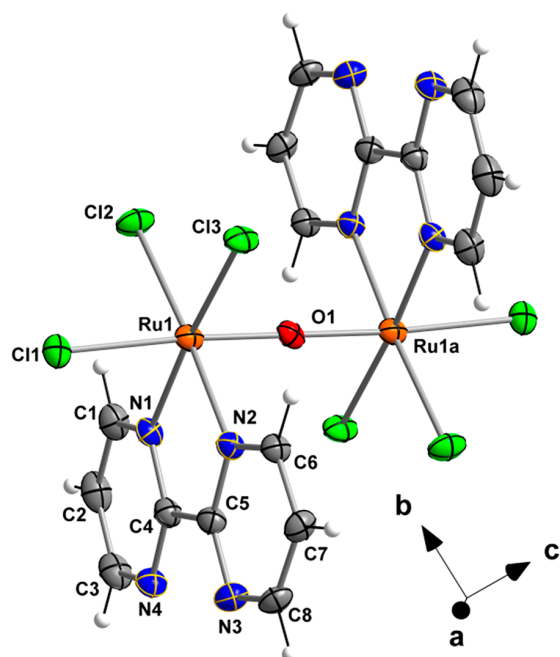


**Figure 6.** Molecular structure of the centrosymmetric dinuclear  $[\{\text{RuCl}_5(\text{bpym})\}_2(\mu\text{-O})]$  complex in **6**. Thermal ellipsoids are depicted at the 50% probability level. Water molecules have been omitted for clarity [symmetry code: (a) =  $-x + 1, -y + 1, -z + 2$ ].

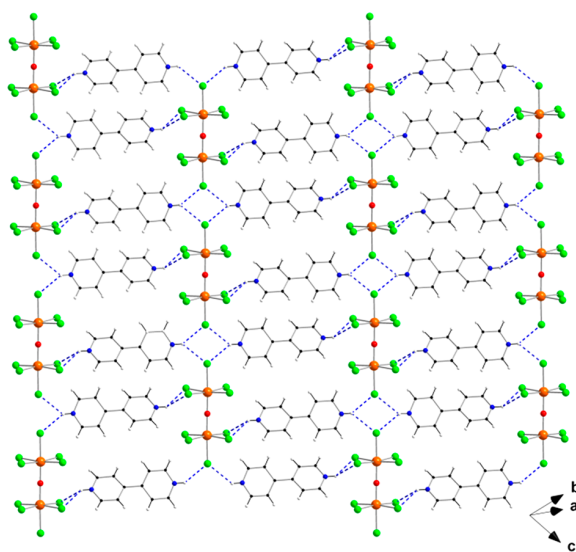


**Figure 7.** Perspective view of the two-dimensional motif generated by bifurcated three-centered hydrogen bonds (dashed blue lines) between  $(\text{H}_2\text{bpy})^{2+}$  organic cations and  $[\{\text{RuCl}_5(\mu\text{-O})\}_4]^{4-}$  anions in the crystal of **1**. Color code: orange, Ru; green, Cl; red, O; blue, N; black, C; white, H.

the *a*-axis direction (Figure 10). The supramolecular network is supported by additional H-bonding interactions that stabilize the crystal structure in **2** (Table 3).

In the crystal packing of compounds **3–5**, the  $[\{\text{RuCl}_4\text{L}\}_2(\mu\text{-O})]^{2-}$  anions [L = MeCN (**3**), dmf (**4**), py (**5**)] are intercalated between the bulky  $\text{PPh}_4^+$  cations. In the case of **3**, intermolecular interactions of the type C–H $\cdots$ Cl [3.408(3) Å; C(2) $\cdots$ Cl(1b); (b) =  $x, -y + 3/2, z + 1/2$ ]

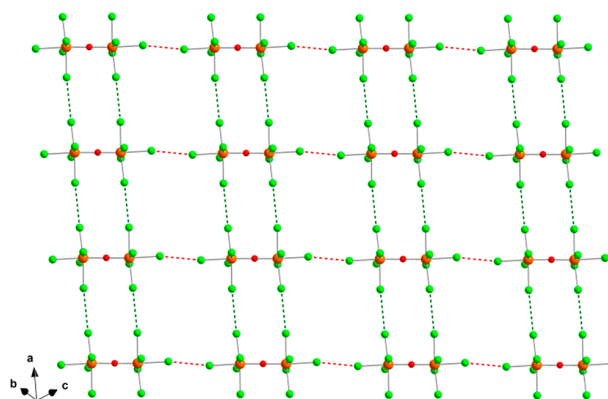


**Figure 8.** View along the crystallographic [011] direction of the anionic grid of  $[\{\text{RuCl}_5(\mu\text{-O})\}_4]^{4-}$  entities connected through intermolecular Cl $\cdots$ Cl interactions in the supramolecular 2D (dashed red lines) and 3D (dashed red and green lines) assemblies of **1**. Color code: orange, Ru; green, Cl; red, O.

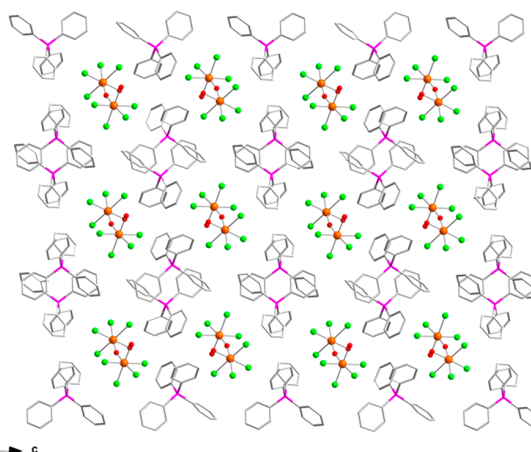


**Figure 9.** View along the *a* axis of the arrangement of  $[\{\text{RuCl}_4(\text{H}_2\text{O})\}_2(\mu\text{-O})]^{2-}$  anions separated from each other by  $\text{PPh}_4^+$  cations (wireframe model) in **2**. H atoms and noncoordinating water molecules have been omitted for clarity. Color code: orange, Ru; green, Cl; pink, P; red, O; gray, C.

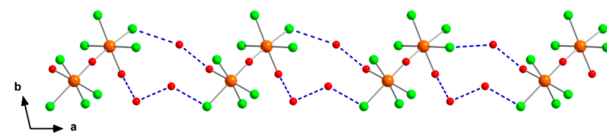


**Figure 10.** Detail of the one-dimensional motif generated by H-bonds (dashed blue lines) connecting  $[\{\text{RuCl}_4(\text{H}_2\text{O})\}_2(\mu\text{-O})]^{2-}$  anions and water molecules in **2**. H atoms and  $\text{PPh}_4^+$  cations have been omitted for clarity. Color code: orange, Ru; green, Cl; red, O.

connect adjacent  $[\{\text{RuCl}_4(\text{MeCN})\}_2(\mu\text{-O})]^{2-}$  anions generating chains that grow along the *b* axis (Figure 11). An anionic two-dimensional layer, growing on the *bc* plane, can be described taking into account additional C–H $\cdots$ Cl interactions between neighboring chains (Figure 11). The C–H $\cdots$ Cl interactions vary in the range 3.33–3.85 Å in **3**. The shortest intermolecular Ru $\cdots$ Ru distance is 9.130(1) Å [Ru(1) $\cdots$ Ru(1c); (c) =  $x, -y + 3/2, z - 1/2$ ].

As in **3**, in the crystal packing of **4** take place intermolecular C–H $\cdots$ Cl interactions, which cover the range 3.23–3.88 Å.

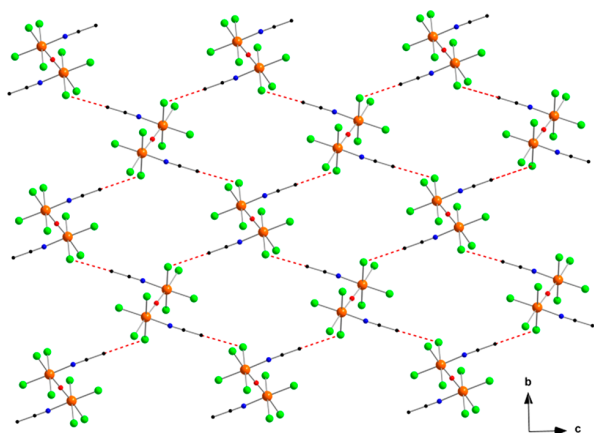


**Figure 11.** View along the *a* axis of the arrangement of  $[\{\text{RuCl}_4(\text{MeCN})\}_2(\mu\text{-O})]^{2-}$  anions connected by means of intermolecular C–H...Cl interactions in **3**.  $\text{PPh}_4^+$  cations and H atoms have been omitted for clarity. Color code: orange, Ru; green, Cl; red, O; blue, N; gray, C.

This type of intermolecular interactions leads to the formation of chains of anionic  $[\{\text{RuCl}_4(\text{dmf})\}_2(\mu\text{-O})]^{2-}$  complexes [3.411(3) Å; C(3)...Cl(3b); (b) =  $x, -y - 1/2, z + 1/2$ ] (Figure 12). Additional C–H...Cl interactions between

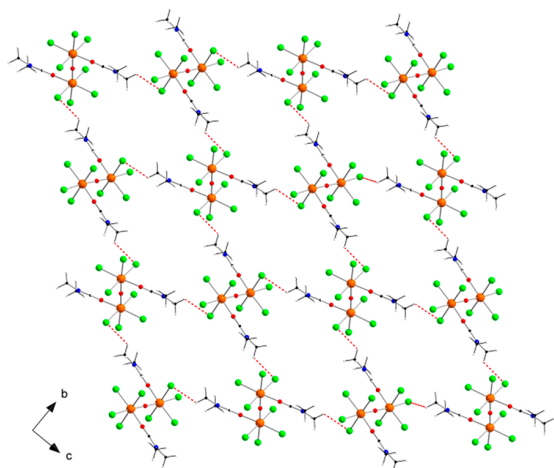


**Figure 12.** View along the *a* axis of the arrangement of  $[\{\text{RuCl}_4(\text{dmf})\}_2(\mu\text{-O})]^{2-}$  anions connected by means of intermolecular C–H...Cl interactions in **4**.  $\text{PPh}_4^+$  cations have been omitted for clarity. Color code: orange, Ru; green, Cl; red, O; blue, N; gray, C; white, H.

neighboring chains generate two-dimensional sheets that grow on the *bc* plane (Figure 12). In **4**, the shortest intermolecular Ru...Ru distance is 9.448(1) Å [Ru(1)...Ru(1b)].

Despite the presence of bulky  $\text{PPh}_4^+$  cations in **5** (Figure 13), face-to-face stacked  $\pi\cdots\pi$  interactions [centroid–centroid distance of ca. 3.76 Å] occur between pyridine rings of  $[\{\text{RuCl}_4(\text{py})\}_2(\mu\text{-O})]^{2-}$  anions, which generate 1D motifs (Figure S4). Besides, in **5** there are C–H...Cl interactions that vary in the range 3.60–3.82 Å (Figure S5). This group of interactions makes the value of the shortest intermolecular Ru...Ru distance to be 8.213(1) Å [Ru(1)...Ru(1b); (b) =  $-x + 1, -y + 2, -z$ ].

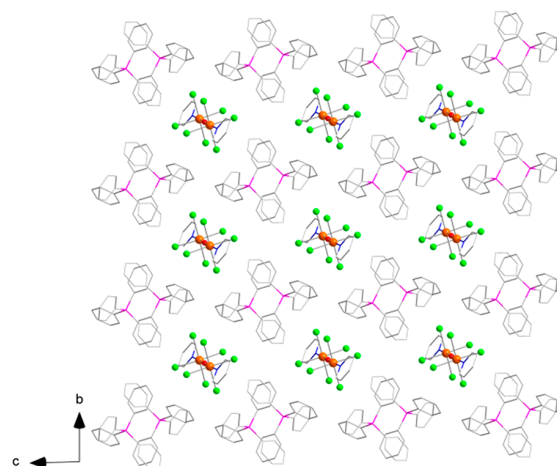


**Figure 13.** View along the *a* axis of the arrangement of  $[\{\text{RuCl}_4(\text{py})\}_2(\mu\text{-O})]^{2-}$  anions separated each other by  $\text{PPh}_4^+$  cations (wireframe model) in **5**. H atoms have been omitted for clarity. Color code: orange, Ru; green, Cl; pink, P; red, O; blue, N; gray, C.

In the crystal packing of compound **6**, the shortest intermolecular Cl...Cl interaction of 3.978(1) Å [Cl(3)...Cl(3b); (b) =  $-x, -y + 1, -z + 2$ ] leads to the formation of neutral chains of  $[\{\text{RuCl}_3(\text{bpym})\}_2(\mu\text{-O})]$  complexes, which grow along the *a*-axis direction (Figure S6). The shortest intermolecular Ru...Ru distance is 7.363(1) Å [Ru(1)...Ru(1c); (c) =  $-x, -y + 1, -z + 1$ ].  $\pi\cdots\pi$  stacking interactions of offset type [centroid–centroid distance of ca. 3.56 Å] take place between pyridyl rings of adjacent bpym molecules (Figure 14). These intermolecular interactions, together with

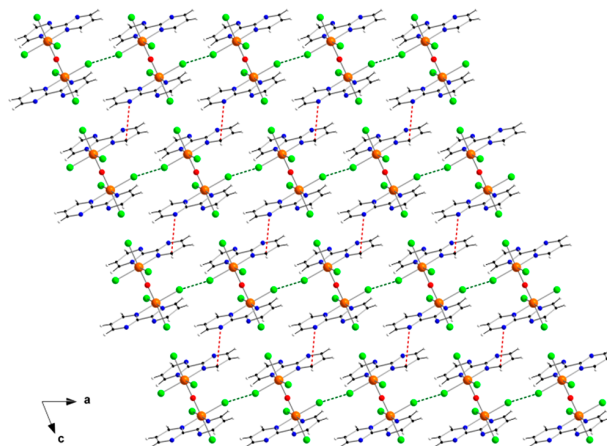


**Figure 14.** Perspective view of the two-dimensional arrangement of neutral  $[\{\text{RuCl}_3(\text{bpym})\}_2(\mu\text{-O})]$  entities linked through  $\pi\cdots\pi$  stacking (dashed red lines) and Cl...Cl (dashed green lines) intermolecular interactions in **6**. Water molecules have been omitted for clarity. Color code: orange, Ru; green, Cl; red, O; blue, N; black, C; white, H.

additional intermolecular Cl... $\pi$  contacts between pyridyl rings and neighboring chloride ions of approximately 3.88 Å, result in a layered structure that grows along the *ac* plane of **6** (Figure 14).

The adjacent layers of  $[\{\text{RuCl}_3(\text{bpym})\}_2(\mu\text{-O})]$  complexes are linked by means of H-bonding interactions, involving water molecules and Cl ions of each plane [3.17(1) Å for the shortest O...Cl distance], which form  $-\text{Cl}(\text{H}_2\text{O})_2(\text{H}_2\text{O})_2\text{-Cl}-$  ring



Table 4. Hydrogen-Bonding Interactions in **6**<sup>a</sup>

D–H...A	D–H/Å	H...A/Å	D...A/Å	(DHA)/°
O(1w)–H(1wA)···Cl(2d)	0.916	2.35(1)	3.201(1)	154.9(1)
O(1w)–H(1wB)···Cl(2e)	0.935	2.84(1)	3.358(1)	116.4(1)
O(1w)–H(1wB)···Cl(3e)	0.935	2.28(1)	3.172(1)	159.3(1)
O(2w)–H(2wB)···Cl(1f)	0.949	2.91(1)	3.411(1)	114.6(1)
O(2w)–H(2wB)···Cl(3f)	0.949	2.30(1)	3.196(1)	158.3(1)
O(3w)–H(3wB)···Cl(3f)	0.904	2.57(1)	3.177(1)	125.1(1)

<sup>a</sup>Symmetry codes: (d) =  $-x + 2, -y + 1, -z + 1$ ; (e) =  $x + 1, y - 1, z - 1$ ; (f) =  $-x + 1, -y + 1, -z + 1$ .

arrangements (Table 4). Thus, these interactions between the neutral oxo-bridged diruthenium complexes and crystallization water molecules, along with weaker intermolecular C–H···Cl contacts [average C···Cl distance of ca. 3.7 Å] (Table S6), support the cohesion of the whole supramolecular network in the crystal structure of **6** (Figure 15).

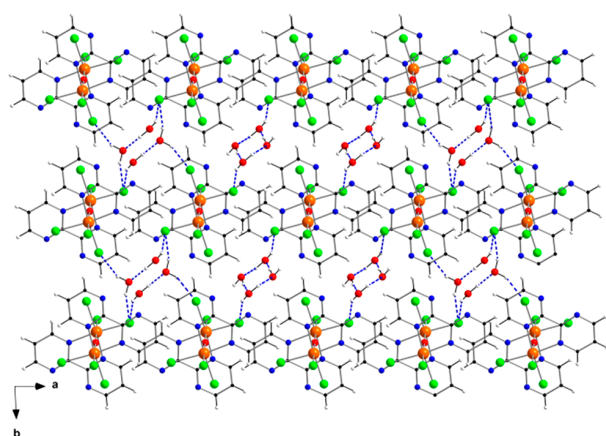


Figure 15. Fragment of the 3D crystal packing of **6** showing adjacent [ $\{\text{RuCl}_3(\text{bpym})\}_2(\mu\text{-O})$ ] layers connected through interlayer H-bonding interactions (dashed blue lines). Color code: orange, Ru; green, Cl; red, O; blue, N; black, C; white, H.

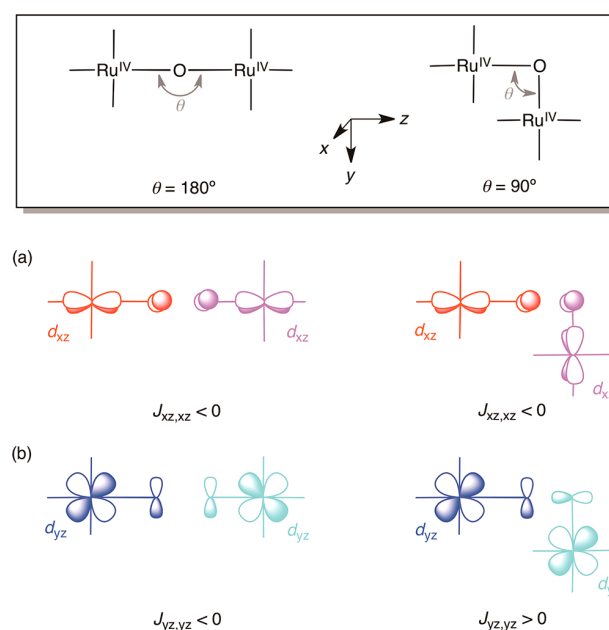
Finally, the  $\text{PPh}_4^+$  cations in **2–5** display different intermolecular phenyl–phenyl interactions, which provide previously reported supramolecular conformations.<sup>39–41</sup> The shortest P···P distance between cations is ca. 6.2 Å, which is found among adjacent  $\text{PPh}_4^+$  dimers exhibiting multiple phenyl embraces (Figure S7). These intermolecular phenyl–phenyl connections generate an example of sextuple phenyl embrace (SPE), which combines both edge-to-face and offset face-to-face type interactions (Figure S7). The six interacting rings in these moieties occur as three parallel pairs of phenyl groups. The rings involved in edge-to-face interactions show intercentroid distances of approximately 5.7 Å and form an angle of ca. 69.5°, these values being in agreement with those previously reported for SPEs.<sup>40</sup> In addition, a parallel quadruple phenyl embrace (PQPE) motif is also observed in these  $\text{Ru}^{\text{IV}}$  compounds, with a P···P distance between cations of ca. 8.9 Å and intercentroid separations of approximately 5.6 Å (Figure S8). According to previous examinations of the Cambridge Structural Database (CSD),<sup>39–41</sup> most of the crystal structures reported with SPE and PQPE pairs are centrosymmetric, as observed in **2–5**.

**Magnetic Properties.** Direct current (dc) magnetic susceptibility measurements were carried out on microcrystalline samples of **1–6** and under an external magnetic field of

1000 G. These measurements revealed that the six studied compounds are diamagnetic at room temperature. The values of their molar magnetic susceptibility ( $\chi_{\text{M}}$ ) were calculated to be  $-0.0127$  (**1**),  $-0.0178$  (**2**),  $-0.0120$  (**3**),  $-0.0085$  (**4**),  $-0.0158$  (**5**), and  $-0.0015 \text{ cm}^3 \text{ mol}^{-1}$  (**6**) at 300 K. The diamagnetic nature observed for **1–6** is mainly due to a very strong antiferromagnetic coupling between the involved ruthenium ions connected through the oxo ligand, which could be affected, at least in part, for the different terminal ligands present in this family of dinuclear  $\text{Ru}^{\text{IV}}$  systems. In Figure S9 is shown a linear trend observed when we plot the  $\chi_{\text{M}}$  values versus the intramolecular Ru–Ru distance. The value of the diamagnetism (negative  $\chi_{\text{M}}$  values) increases when the Ru–Ru separation shortens (Figure S9), compound **6** being the family member that shows the longer intramolecular Ru–Ru distance along with the lower diamagnetic value, which is somewhat close to paramagnetism. Hence, in this family, the shorter the Ru–Ru distance, the stronger the diamagnetism.

The very strong antiferromagnetic coupling between the two low-spin (LS)  $\text{Ru}^{\text{IV}}$  ions ( $S = 1$ ) through the almost linear oxo bridge in **1–6** ( $\theta = 164.3\text{--}180.0^\circ$ ) can be nicely explained within the framework of the orbital model of the electron exchange magnetic interaction developed by Kahn and co-workers, as illustrated in Chart 2.

Chart 2. Illustration of the Magnetic Interaction through  $d_{xz} \cdots d_{xz}$  (a) and  $d_{yz} \cdots d_{yz}$  (b) Orbital Pathways in **1–6**



Within the framework of the Kahn's model, the magnitude of the antiferromagnetic coupling contribution is proportional to the square of the orbital overlap between the involved magnetic orbitals in the bridge region. Hence, a maximum orbital overlap between the  $d_{xz}$ - and  $d_{xz}$ -type magnetic orbitals is expected for a linear Ru–O–Ru bridge ( $\theta = 180^\circ$ , Chart 2a,b, left). When increasing the bending of the Ru–O–Ru bridge, the orbital overlap between the  $d_{xz}$ -type magnetic orbitals remains equal, while that between the  $d_{yz}$ -type magnetic orbitals decreases down to zero ( $\theta = 90^\circ$ , Chart 2a,b, right).

**Electrochemical Properties.** The electrochemical properties of 2–6 have been investigated through cyclic voltammetry (CV) in dry dmf at room temperature, in order to evaluate the influence of the ligand nature on the rich redox features along this series of ( $\mu$ -oxo)diruthenium(IV) complexes. The cyclic voltammograms of 4–6 are depicted in Figure 16, while those of 2 and 3 are shown in Figure S10 for comparison.

2–5 show a qualitatively similar electrochemical behavior with two more or less resolved, almost irreversible reduction waves [ $E_1 = -0.75$  (2),  $-0.77$  (3),  $-0.77$  (4), and  $-0.80$  V vs Fc (5) and  $E_2 = -1.34$  (2),  $-1.60$  (3),  $-1.59$  (4), and  $-1.68$  V vs Fc (5); Table S7]. Interestingly, the reduction through the first irreversible reduction wave gives rise to the appearance of either one (2 and 5) or two (3 and 4) additional pretty much reversible oxidation waves (Figure 16 (top) and (center) and Figure S10). In contrast, the cyclic voltammogram of 6 shows up to four well-resolved, pseudoreversible reduction waves ( $E_1 = -0.61$ ,  $E_2 = -0.78$ ,  $E_3 = -1.05$ , and  $E_4 = -1.26$  V vs Fc; Table S7), together with one reversible oxidation wave ( $E_5 = +0.17$  V vs Fc; Table S7) (Figure 16 (bottom)). In fact, the values of the anodic peak to cathodic peak separation for the reduction waves in 6 are somewhat greater than that of the oxidation wave ( $\Delta E_1 = -0.072$ ,  $\Delta E_2 = -0.097$ ,  $\Delta E_3 = -0.138$ ,  $\Delta E_4 = -0.144$ , and  $\Delta E_5 = -0.075$  V vs Fc; Table S7), which is comparable to that of the ferricinium/ferrocene couple under the same conditions [ $\Delta E_p(\text{Fc}) = 80$  mV]. However, a perfect linear plot of the peak current against the square root of the scan rate is only obtained for the oxidation wave, which is then stated to be completely reversible on the voltammetric time-scale. In this case, an additional oxidation wave also appears after reduction through the two first irreversible reduction waves.

The first pair of well-separated pseudoreversible reduction waves of 6 can be assigned to the stepwise one-electron reduction of the Ru<sup>IV</sup> ions to give the hetero- and homovalent Ru<sup>III/IV</sup><sub>2</sub>O and Ru<sup>III</sup><sub>2</sub>O species, while the second pair of well-separated pseudoreversible reduction waves is likely attributed to the further stepwise one-electron reduction of the Ru<sup>III</sup> ions to give the hetero- and homovalent Ru<sup>II/III</sup><sub>2</sub>O and Ru<sup>II</sup><sub>2</sub>O species. Alternatively, the reversible oxidation wave of 6 corresponds to the one-electron oxidation of the homovalent Ru<sup>IV</sup><sub>2</sub>O compound to afford the heterovalent Ru<sup>V/IV</sup><sub>2</sub>O species. This rich multiredox behavior of the bpm derivative 6, both thermodynamic and kinetic, contrasts with that of 2–5. In all cases, however, the additional oxidation waves past the first reduction waves would correspond to the reversible oxidation of the products, which result from the partial decomposition of the relatively unstable Ru<sup>III</sup><sub>2</sub>O dimer following protonation of the oxo bridge and/or cleavage of the resulting hydroxo bridge in Ru<sup>III</sup><sub>2</sub>OH to give the corresponding Ru<sup>III</sup> monomers, as previously suggested for related oxo-bridged ruthenium(III) dimers.<sup>42–44</sup>

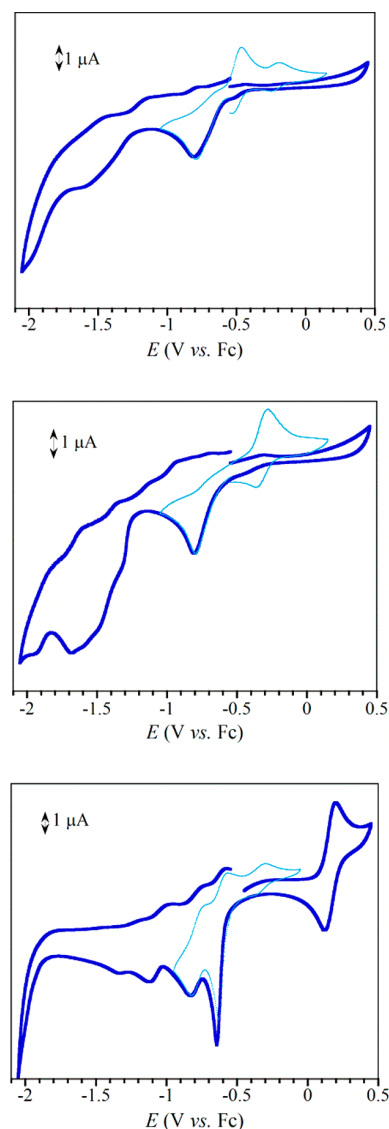


**Figure 16.** Cyclic voltammograms of 4 (top), 5 (center), and 6 (bottom) in dry dmf (0.1 M NBu<sub>4</sub>PF<sub>6</sub>) at 25 °C and 200 mV s<sup>-1</sup>. The pale blue curves show the cyclic voltammograms of the oxidation waves when the potential is scanned through the first reversible reduction waves.

**Electronic Absorption Spectroscopy.** The electronic absorption spectra of 2–6 in dmf are shown in Figure 17. The spectra of 2–4 show a similar pattern consisting of an intense peak in the visible region centered at 398 (2) and 399 nm (3 and 4) together with a distinct shoulder around 493 (2) and 495 nm (3 and 4) (Table S8), which are responsible for their deep yellow color in solution (Figure 17). Interestingly, the spectra of 3 and 4 are pretty much identical, suggesting thus a solvolysis process, with the replacement of the coordinated acetonitrile by dmf molecules in 3 to give 4. On the other hand, the spectra of 5 shows two intense peaks at 437 and 501 nm (Table S8), while that of 6 exhibits one UV peak at 358 nm and two Vis peaks at 397 and 498 nm (Table S8), which accounts for their light and deep red color, respectively. The higher energy UV bands for 2–6 ( $\epsilon = 0.75$ – $2.84 \times 10^3$  M<sup>-1</sup> cm<sup>-1</sup>; Table S8) are likely assigned to ligand-to-metal charge

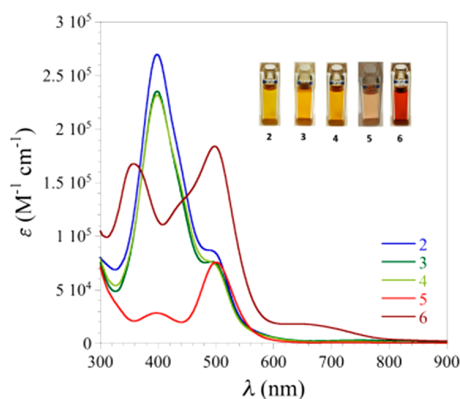


**Figure 17.** Absorption spectra ( $\epsilon$  vs  $\lambda$ ) covering the range of 300–900 nm for compounds 2 (blue), 3 (dark green), 4 (pale green), 5 (red), and 6 (brown).

transfer (LMCT) transitions from the bridging oxo group to the  $\text{Ru}^{\text{IV}}$  ions, whereas the additional lower energy Vis peaks would be assigned to metal-to-ligand charge transfer (MLCT) transitions from the  $\text{Ru}^{\text{IV}}$  ions to the aromatic pyridine and bipyrimidine terminal ligands in 5 and 6, respectively.

**Bond Valence Sum (BVS) Calculations.** The bond valence sum (BVS) method is a very useful tool to predict the oxidation state of metal ions in crystal structures. This model is based on the valence sum rule from the Pauling's electrostatic valence concept, which implies that the amount of valence in each bond is directly correlated with its length,<sup>45,46</sup> and it can be expressed by eq 1,

$$s = \exp[(R_0 - R)/B] \quad (1)$$

where  $s$  is the bond valence and  $R$  is the bond length value, whereas  $R_0$  and  $B$  are empirically determined parameters that have been previously tabulated.<sup>47–51</sup> The sum of bond valences for each atom in the studied compound is equal to the oxidation state of that atom and is frequently used in the analysis and modeling of crystal structures, as for instance, for determining the oxidation state of metal centers in metalloproteins, including those of oxo-bridged diiron enzymes.<sup>49</sup> The method estimates correctly the oxidation state for 3d metal ions,<sup>52–55</sup> but some discrepancies are found for heavier ions.<sup>50,51</sup> Indeed, the  $B$  parameter, which measures the softness of the interaction between the two bonded atoms, in general adopts a fixed value ( $B = 0.37$ ), but larger  $B$  values are also used when one of the involved atoms is much softer.

During our BVS calculations for determining the oxidation state of the ruthenium ions in 1–6,  $B$  was kept constant at 0.37, and the  $R_0$  values were taken from previously reported tables, when available.<sup>47</sup> Nevertheless, some  $R_0$  values for +2 and +4 oxidation states of ruthenium metal ion [Ru–N, Ru–O, and Ru–Cl pairs of atoms] were not found as tabulated data, and their values were satisfactorily computed following the approach previously reported by Brown et al.<sup>48</sup> Our final results are given in Table 5, where the bold value is the one closest to the charge for which it was calculated, the oxidation state being the nearest integer number to the bold value, so that the oxidation state for all the ruthenium ions in 1–6 is +4. As far as we know, this is the first time this method is applied to oxo-bridged ruthenium complexes.

**Computed Hirshfeld Surfaces.** The calculated Hirshfeld surface of a molecule can be a very useful tool to identify

**Table 5. Bond Valence Sum (BVS) Values for the Ruthenium Ions in Compounds 1–6<sup>a</sup>**

ion	$\text{Ru}^{\text{II}}$	$\text{Ru}^{\text{III}}$	$\text{Ru}^{\text{IV}}$
Compound 1			
Ru(1)	4.4	4.8	<b>4.1</b>
Compound 2			
Ru(1)	4.2	4.7	<b>4.3</b>
Ru(2)	4.3	4.7	<b>4.2</b>
Compound 3			
Ru(1)	4.5	4.8	<b>4.3</b>
Compound 4			
Ru(1)	4.3	4.7	<b>4.3</b>
Compound 5			
Ru(1)	4.5	4.8	<b>4.3</b>
Compound 6			
Ru(1)	4.3	4.8	<b>4.1</b>

<sup>a</sup>The oxidation state calculated for each ion is the nearest integer number to the bold value.

strong, directional, reliable noncovalent interactions.<sup>56,57</sup> Hirshfeld surface is defined by the molecule and the proximity of its nearest neighbors, and hence encodes information about intermolecular interactions that can be analyzed through the *CrystalExplorer* program.<sup>57,58</sup> The distances  $d_e$  (distance from a point on the surface to the nearest atom outside the surface) and  $d_i$  (distance from a point on the surface to the nearest atom inside the surface) mapped on the Hirshfeld surface provide a three-dimensional picture of intermolecular close contacts, which are used to generate a fingerprint, that is, a two-dimensional summarized plot of intermolecular interactions (Figures 18 and 19 and Figures S11 and S12).

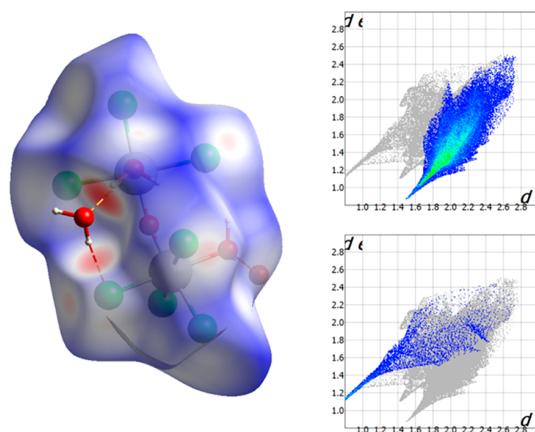


**Figure 18.** Hirshfeld surface mapped with  $d_{\text{norm}}$  function (left) and fingerprint plots (right) for compound 2. Intermolecular Cl...H (right, top) and O...H (right, bottom) contacts are highlighted from the full fingerprint.

Nevertheless, even though  $d_e$  and  $d_i$  are mapped, they do not take into account the relative sizes of atoms, so that closer contacts between heavier atoms (in our case, Ru or Cl atoms) are often not effectively highlighted. To overcome this limitation, it is defined as a normalized contact distance,  $d_{\text{norm}}$  (eq 2),

$$d_{\text{norm}} = [(d_i - r_i^{\text{vdW}})/(r_i^{\text{vdW}})] + [(d_e - r_e^{\text{vdW}})/(r_e^{\text{vdW}})] \quad (2)$$



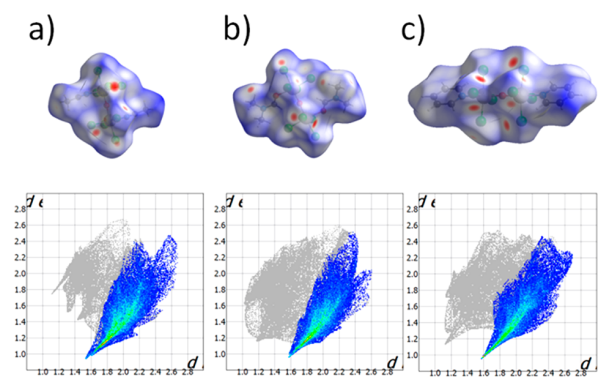


**Figure 19.** Hirshfeld surfaces mapped with  $d_{\text{norm}}$  function and fingerprints plots for the anionic  $[\{\text{RuCl}_4(\text{L})\}_2(\mu\text{-O})]^{2-}$  unit of compounds **3** (a), **4** (b), and **5** (c). Intermolecular  $\text{Cl}\cdots\text{H}$  contacts are highlighted from the full fingerprint.

where  $r^{\text{vdW}}$  is the van der Waals radius of the suitable atom internal or external to the surface.  $d_{\text{norm}}$  is negative when contacts are shorter than van der Waals separations and positive for contacts greater than van der Waals distances. It is displayed using a red–white–blue set of colors, red being used for shorter contacts, white indicates contacts around the van der Waals separation, and blue is for longer contacts.

Hirshfeld surfaces were calculated for compounds **1–6** (Figures 18 and 19 and Figures S11 and S12), which reflect the variety of intermolecular contacts and different levels of importance that take place in their crystal lattice. For compound **1**, the most important intermolecular interactions are  $\text{Cl}\cdots\text{H}$  contacts (Figure S11), involving H-bonds between  $(\text{H}_2\text{bpy})^{2+}$  cations and  $[\{\text{RuCl}_3\}_2(\mu\text{-O})]^{2-}$  anions, which are approximately 90% of the complete fingerprint plot (Figure S11). H-bonding interactions involving water molecules and chlorine atoms are also detected on the Hirshfeld surface of **2**, which have been highlighted from the full fingerprint as intermolecular  $\text{Cl}\cdots\text{H}$  (Figure 18, right, top) and  $\text{O}\cdots\text{H}$  (Figure 18, right, bottom) contacts. The Hirshfeld surfaces of **3–5** are shown in Figure 19, where the shorter contacts are those involving  $\text{Cl}\cdots\text{H}$  interactions between  $[\{\text{RuCl}_4\}_2(\mu\text{-O})]^{2-}$  anions and  $\text{PPh}_4^+$  cations. These contacts cover approximately 40–60% of the fingerprint (Figure 19). Finally, short  $\text{Cl}\cdots\text{H}$  and  $\text{N}\cdots\text{H}$  contacts between water molecules and neutral  $[\{\text{RuCl}_3(\text{bpym})\}_2(\mu\text{-O})]$  entities are detected on the Hirshfeld surface of **6** and have been highlighted separately from the full fingerprint as intermolecular  $\text{Cl}\cdots\text{H}$  (Figure S12, right, top) and  $\text{N}\cdots\text{H}$  (Figure S12, right, bottom) contacts.

## CONCLUSIONS

In summary, we have reported the synthesis and characterization of a family of six oxo-bridged dinuclear  $\text{Ru}^{\text{IV}}$  compounds (**1–6**). Magnetic susceptibility measurements along with BVS calculations support the diamagnetic nature and oxidation state +4 for all the ruthenium metal ions in compounds **1–6**. Remarkably, **4** is the first example of a ruthenium system exhibiting the  $\text{Ru–O–Ru}(\text{dmf})$  core, and **6** is the first reported example of oxo-bridged  $\text{Ru}^{\text{IV}}$  system containing 2,2'-bipyrimidine. Given the diverse type of intermolecular interactions (halogen and hydrogen bonds, as well as halogen $\cdots\pi$  and  $\pi\cdots\pi$  contacts) that **1–6** exhibit in their crystal lattice, they are good candidates to be used as building blocks to synthesize new supramolecular structures based on

the self-assembly of diruthenium(IV) complexes. Besides, because of their redox properties, some of them could exhibit potential applications in different research areas, as for instance in redox catalysis, or, by incorporating suitable organic linkers, they could even be employed in electronic devices. This latter work is in progress.

## EXPERIMENTAL SECTION

**Materials and Physical Measurements.** All manipulations were performed under aerobic conditions, using materials as received (reagent grade). Elemental analyses (C, H, N) and X-ray microanalysis were performed by the Central Service for the Support to Experimental Research (SCSIE) at the University of Valencia. Infrared spectra of **1–6** were recorded (as KBr pellets) with a PerkinElmer Spectrum 65 FT-IR spectrometer in the 4000–400  $\text{cm}^{-1}$  region. Solid-state direct current (dc) magnetic susceptibility data were collected on a Quantum Design MPMS-XL SQUID magnetometer. The experimental magnetic data were corrected for the diamagnetic contributions of the constituent atoms as well as for the sample holder.

The electrochemical studies were performed using an AUTOLAB PGSTAT 204 scanning potentiostat operating at a scan rate range of 10–250  $\text{mV s}^{-1}$ . Cyclic voltammograms were carried out using 0.1 M  $\text{NBu}_4\text{PF}_6$  as supporting electrolyte and 1.0 mM of **2–6** in dry dimethylformamide (dmf). The working electrode was a glassy carbon disk (0.32  $\text{cm}^2$ ) that was polished with 1.0  $\mu\text{m}$  diamond powder, sonicated, washed with absolute ethanol and acetone, and air-dried. The reference electrode was  $\text{AgCl}/\text{Ag}$  separated from the test solution by a salt bridge containing the solvent/supporting electrolyte, with platinum as auxiliary electrode. All experiments were performed in standard electrochemical cells at 25  $^\circ\text{C}$  under argon. The investigated potential range was in the range of  $-2.0$  to  $+0.5$  V vs  $\text{AgCl}/\text{Ag}$ . Ferrocene (Fc) was added as internal standard at the end of the measurements. The formal potentials were measured at a scan rate of 200  $\text{mV s}^{-1}$  and were referred to the ferrocenium/ferrocene ( $\text{Fc}^+/\text{Fc}$ ) redox couple. The values of the measured formal potential and the anodic to cathodic peaks separation of ferrocene under the same conditions are  $E(\text{Fc}) = +0.55$  V vs  $\text{AgCl}/\text{Ag}$  and  $\Delta E_p(\text{Fc}) = 79$  mV (DMF, 0.1 M  $\text{NBu}_4\text{PF}_6$ , 25  $^\circ\text{C}$ ).

**Preparation of Compounds 1–6.** **1.** A solvothermal reaction of  $\text{RuCl}_3\cdot\text{H}_2\text{O}$  (6.6 mg, 0.03 mmol) and 4,4'-bipyridine (4.7 mg, 0.03 mmol) was performed in HCl (4 mL, 6 M) at 90  $^\circ\text{C}$  for 3 days, followed by a 12 h cooling process to room temperature. Dark red crystals of **1** were thus obtained, which were suitable for X-ray data collection. Yield: ca. 70%. Found: C, 27.3; H, 2.2; N, 5.9. Calc. for  $\text{C}_{20}\text{H}_{20}\text{Cl}_{10}\text{ON}_4\text{Ru}_2$  (**1**): C, 27.0; H, 2.3; N, 6.3%. X-ray microanalysis gave a Ru/Cl molar ratio of 1:5. IR (KBr pellets/ $\text{cm}^{-1}$ ): bands assigned to the  $[\text{H}_2\text{bpy}]^{2+}$  cation are found at 3202 (m), 3189 (m), 3124 (m), 3088 (m), 3057 (m), 1635 (s), 1624 (s), 1590 (m), 1474 (m), 1375 (m), 1268 (w), 1232 (m), 1200 (m), 1125 (w), 1098 (w), 874 (m), 824 (m), 770 (s), 710 (w), 672 (m), 509 (m).

**2.**  $\text{K}_2[\text{RuCl}_5(\text{H}_2\text{O})]$  (0.30 g, 0.84 mmol) was dissolved in HCl (10 mL, 1.0 M) at 50  $^\circ\text{C}$  with continuous stirring. A solution of  $\text{PPh}_4\text{Cl}$  (1.00 g, 2.60 mmol) in HCl (10 mL, 1 M) was added, and the heating and stirring were kept for 15 min, generating a dark brown precipitate of **2**. The precipitate was separated by filtration at room temperature, and the mother liquor was left to evaporate. Brown crystals of **2** were grown in 1–2 days and were suitable for X-ray diffraction studies. Yield: ca. 83%. Found: C, 44.8; H, 3.8. Calc. for  $\text{C}_{48}\text{H}_{52}\text{Cl}_8\text{O}_7\text{P}_2\text{Ru}_2$  (**2**): C, 44.7; H, 4.1%. X-ray microanalysis gave Ru/P and Ru/Cl molar ratios of 1:1 and 1:4, respectively. IR (KBr pellets/ $\text{cm}^{-1}$ ): absorption associated to water molecules appears at 3475 (br), and bands assigned to  $\text{PPh}_4^+$  cation appear at 3044(m), 1437 (vs), 1188 (m), 1165 (m), 1107 (vs), 722 (vs), 690 (s), 528 (vs).

**3.** Compound **1** (0.27 g, 0.2 mmol) was dissolved in MeCN (10 mL). The solution was stirred for 10 min and left to evaporate at room temperature. Reddish-brown crystals were formed in 1 day, which were suitable for X-ray data collection. Yield: ca. 88%. Found: C, 50.0; H, 3.5; N, 2.1. Calc. for  $\text{C}_{52}\text{H}_{46}\text{Cl}_8\text{N}_2\text{OP}_2\text{Ru}_2$  (**3**): C, 49.5; H,



3.7; N, 2.2%. X-ray microanalysis gave Ru/P and Ru/Cl molar ratios of 1:1 and 1:4, respectively. IR (KBr pellets/cm<sup>-1</sup>): absorption associated with coordinated MeCN molecules appears at 2920(s), 2318 (s) and 2284 (w), and bands assigned to the PPh<sub>4</sub><sup>+</sup> cation appear at 3044(m), 1436 (vs), 1166 (m), 1109 (vs), 725 (vs), 690 (s), 530 (vs).

4. Compound 3 (0.14 g, 0.1 mmol) was dissolved in dmf (20 mL). The solution was stirred for 30 min at 80 °C. Brown crystals of 4 appeared in 1 week through vapor diffusion with ether. Yield: ca. 40%. Found: C, 49.0; H, 4.2; N, 2.0. Calc. for C<sub>34</sub>H<sub>34</sub>Cl<sub>8</sub>N<sub>2</sub>O<sub>3</sub>P<sub>2</sub>Ru<sub>2</sub> (4): C, 48.9; H, 4.1; N, 2.1%. X-ray microanalysis gave Ru/P and Ru/Cl molar ratios of 1:1 and 1:4, respectively. IR (KBr pellets/cm<sup>-1</sup>): absorption associated to coordinated dmf molecules appears at 2920(s), 1632 (vs) and 713 (w), and bands assigned to the PPh<sub>4</sub><sup>+</sup> cation appear at 3045(m), 1435 (vs), 1165 (m), 1108 (vs), 723 (vs), 691 (s), 527 (vs).

5. Compound 1 (0.11 g, 0.08 mmol) was dissolved in MeCN (20 mL). The solution was stirred for 5 min at 40 °C. Then, pyridine (1 mL, 12.4 mmol) was added, and the mixture was stirred for a further 5 min. A red solution was obtained, cooled at room temperature, and filtered off. Orange parallelepipeds were obtained in 1 week through vapor diffusion with ether. These crystals were suitable for X-ray diffraction studies. Yield: ca. 25%. Found: C, 53.0; H, 3.7; N, 2.0. Calc. for C<sub>58</sub>H<sub>50</sub>Cl<sub>8</sub>N<sub>2</sub>OP<sub>2</sub>Ru<sub>2</sub> (5): C, 52.0; H, 3.8; N, 2.1%. X-ray microanalysis gave Ru/P and Ru/Cl molar ratios of 1:1 and 1:4, respectively. IR (KBr pellets/cm<sup>-1</sup>): absorption associated to coordinated py molecules appears at 1608 (m), 1220 (m) and 643 (m), and bands assigned to the PPh<sub>4</sub><sup>+</sup> cation appear at 1436 (vs), 1163 (m), 1108 (vs), 724 (vs), 690 (s), 531 (vs).

6. A solvothermal reaction of K<sub>2</sub>[RuCl<sub>5</sub>(H<sub>2</sub>O)] (10.9 mg, 0.03 mmol) and 2,2'-bipyrimidine (9.4 mg, 0.06 mmol) was performed in HCl (5 mL, 3 M) at 75 °C for 20.5 h, followed by a 20.5 h cooling process to room temperature. Brown crystals of 6 were obtained and were suitable for X-ray diffraction studies. Yield: ca. 50%. Found: C, 22.0; H, 2.7; N, 12.8. Calc. for C<sub>16</sub>H<sub>24</sub>Cl<sub>6</sub>O<sub>7</sub>N<sub>8</sub>Ru<sub>2</sub> (6): C, 22.5; H, 2.8; N, 13.1%. X-ray microanalysis gave a Ru/Cl molar ratio of 1:3. IR (KBr pellets/cm<sup>-1</sup>): absorption associated to water molecules appears at 3443 (br) and bands assigned to coordinated bpm molecule are found at 3061 (m), 1577 (vs), 1558 (m), 1407 (vs), 1388 (m), 1212 (w), 1026 (m), 826 (m), 748 (s), 693 (w), 672 (s), 510 (m).

**X-ray Data Collection and Structure Refinement.** X-ray diffraction data on single crystals of dimensions 0.21 × 0.19 × 0.18 (1), 0.32 × 0.10 × 0.07 (2), 0.17 × 0.09 × 0.08 (3), 0.32 × 0.23 × 0.18 (4), 0.20 × 0.09 × 0.07 (5), and 0.85 × 0.52 × 0.12 mm<sup>3</sup> (6) were collected on a Bruker D8 Venture diffractometer with PHOTON II detector and by using monochromatized Mo-K<sub>α</sub> radiation (λ = 0.71073 Å). The structures were solved by standard direct methods and completed by Fourier recycling using the SHELXL<sup>59</sup> software packages and refined by the full-matrix least-squares refinements based on F<sup>2</sup> with all observed reflections. All non-hydrogen atoms were refined anisotropically. The hydrogen atoms on the water molecules O1w, O2w, and O5w in 2 and O1w, O2w, and O3w in 6 were located on the ΔF map and refined with restraints, whereas for the rest of water molecules (O3w, O4w, and O6w in 2) the hydrogen atoms were neither found nor calculated. The final graphical manipulations were performed with the DIAMOND program.<sup>60</sup> CCDC 1898600 (1), 1898601 (2), 1972100 (3), 1972101 (4), 1972102 (5), and 1898602 (6).

## ■ ASSOCIATED CONTENT

### Supporting Information

The Supporting Information is available free of charge at <https://pubs.acs.org/doi/10.1021/acs.cgd.9b01702>.

Figures S1–S12 and Tables S1–S8 (PDF)

### Accession Codes

CCDC 1898600–1898602 and 1972100–1972102 contain the supplementary crystallographic data for this paper. These data can be obtained free of charge via [www.ccdc.cam.ac.uk/](http://www.ccdc.cam.ac.uk/)

[data\\_request/cif](https://pubs.acs.org/crystal), or by emailing [data\\_request@ccdc.cam.ac.uk](mailto:data_request@ccdc.cam.ac.uk), or by contacting The Cambridge Crystallographic Data Centre, 12 Union Road, Cambridge CB2 1EZ, UK; fax: +44 1223 336033.

## ■ AUTHOR INFORMATION

### Corresponding Authors

Isabel Castro – Instituto de Ciencia Molecular (ICMol),  
Universitat de València 46980 Paterna, València, Spain;  
Phone: +34 963544439; Email: [isabel.castro@uv.es](mailto:isabel.castro@uv.es)

José Martínez-Lillo – Instituto de Ciencia Molecular (ICMol),  
Universitat de València 46980 Paterna, València, Spain;  
[orcid.org/0000-0003-1107-2344](https://orcid.org/0000-0003-1107-2344); Phone: +34  
963544460; Email: [fjose.martinez@uv.es](mailto:fjose.martinez@uv.es)

### Authors

Marta Orts-Arroyo – Instituto de Ciencia Molecular (ICMol),  
Universitat de València 46980 Paterna, València, Spain

Francesc Lloret – Instituto de Ciencia Molecular (ICMol),  
Universitat de València 46980 Paterna, València, Spain

Complete contact information is available at:  
<https://pubs.acs.org/10.1021/acs.cgd.9b01702>

### Notes

The authors declare no competing financial interest.

## ■ ACKNOWLEDGMENTS

Financial support from the VLC-BIOCLINIC Program (2017) of the University of Valencia [Subprogram A “Acciones Exploratorias”, Project 02-2017-A], the Spanish Ministry of Science, Innovation and Universities [Projects CTQ2016-75068P and MDM-2015-0538 (Excellence Unit “Maria de Maeztu”)], and the “Ramón y Cajal” Program is gratefully acknowledged. The authors wish to thank Dr. Rafael Ruiz-García for very useful remarks and discussions on the reported results.

## ■ REFERENCES

- Higgins, S. Regarding ruthenium. *Nat. Chem.* **2010**, *2*, 1100–1100.
- Bruneau, C.; Achard, M. Allylic ruthenium(IV) complexes in catalysis. *Coord. Chem. Rev.* **2012**, *256*, 525–536.
- Duan, L.; Bozoglian, F.; Mandal, S.; Stewart, B.; Privalov, T.; Llobet, A.; Sun, L. A molecular ruthenium catalyst with water-oxidation activity comparable to that of photosystem II. *Nat. Chem.* **2012**, *4*, 418–423.
- Friedberger, T.; Ziller, J. W.; Guan, Z. Ruthenium(IV) Complexes for Ethylene Insertion Polymerization. *Organometallics* **2014**, *33*, 1913–1916.
- Adhireksan, Z.; Davey, G. E.; Campomanes, P.; Groessl, M.; Clavel, C. M.; Yu, H.; Nazarov, A. A.; Yeo, C. H. F.; Ang, W. H.; Dröge, P.; Rothlisberger, U.; Dyson, P. J.; Davey, C. A. Ligand substitutions between ruthenium–cymene compounds can control protein versus DNA targeting and anticancer activity. *Nat. Commun.* **2014**, *5*, 3462.
- Yamamoto, Y.; Tamaki, Y.; Yui, T.; Koike, K.; Ishitani, O. New Light-Harvesting Molecular Systems Constructed with a Ru(II) Complex and a Linear-Shaped Re(I) Oligomer. *J. Am. Chem. Soc.* **2010**, *132*, 11743–11752.
- Armentano, D.; Martínez-Lillo, J. Hexachlororhenate(IV) salts of ruthenium(III) cations: X-ray structure and magnetic properties. *Inorg. Chim. Acta* **2012**, *380*, 118–124.
- Ferrando-Soria, J.; Vallejo, J.; Castellano, M.; Martínez-Lillo, J.; Pardo, E.; Cano, J.; Castro, I.; Lloret, F.; Ruiz-García, R.; Julve, M. Molecular magnetism, quo vadis? A historical perspective from a

coordination chemist viewpoint. *Coord. Chem. Rev.* **2017**, *339*, 17–103.

(9) Li, F.; Collins, J. G.; Keene, F. R. Ruthenium complexes as antimicrobial agents. *Chem. Soc. Rev.* **2015**, *44*, 2529–2542.

(10) Clarke, M. J. Ruthenium metallopharmaceuticals. *Coord. Chem. Rev.* **2003**, *236*, 209–233.

(11) Hartinger, C. G.; Zorbas-Seifried, S.; Jakupec, M. A.; Kynast, B.; Zorbas, H.; Keppler, B. K. From bench to bedside – preclinical and early clinical development of the anticancer agent indazolium trans-[tetrachlorobis(1H-indazole)ruthenate(III)] (KP1019 or FFC14A). *J. Inorg. Biochem.* **2006**, *100*, 891–904.

(12) Hartinger, C. G.; Jakupec, M. A.; Zorbas-Seifried, S.; Groessl, M.; Egger, A.; Berger, W.; Zorbas, H.; Dyson, P. J.; Keppler, B. K. KP1019, a new redox-active anticancer agent-preclinical development and results of a clinical phase I study in tumor patients. *Chem. Biodiversity* **2008**, *5*, 2140–2155.

(13) Mulcahy, S. P.; Gründler, K.; Frias, C.; Wagner, L.; Prokop, A.; Meggers, E. Discovery of a strongly apoptotic ruthenium complex through combinatorial coordination chemistry. *Dalton Trans.* **2010**, *39*, 8177–8182.

(14) Mari, C.; Pierroz, V.; Ferrari, S.; Gasser, G. Combination of Ru(II) complexes and light: new frontiers in cancer therapy. *Chem. Sci.* **2015**, *6*, 2660–2686.

(15) Musumeci, D.; Rozza, L.; Merlino, A.; Paduano, L.; Marzo, T.; Massai, L.; Messori, L.; Montesarchio, D. Interaction of anticancer Ru(III) complexes with single stranded and duplex DNA model systems. *Dalton Trans.* **2015**, *44*, 13914–13925.

(16) Furrer, J.; Süß-Fink, G. Thiolato-bridged dinuclear arene ruthenium complexes and their potential as anticancer drugs. *Coord. Chem. Rev.* **2016**, *309*, 36–50.

(17) Zeng, L.; Gupta, P.; Chen, Y.; Wang, E.; Ji, L.; Chao, H.; Chen, Z.-S. The development of anticancer ruthenium(II) complexes: from single molecule compounds to nanomaterials. *Chem. Soc. Rev.* **2017**, *46*, 5771–5804.

(18) Liu, F.; Concepcion, J. J.; Jurss, J. W.; Cardolaccia, T.; Templeton, J. L.; Meyer, T. J. Mechanisms of Water Oxidation from the Blue Dimer to Photosystem II. *Inorg. Chem.* **2008**, *47*, 1727–1752.

(19) Hurst, J. K.; Cape, J. L.; Clark, A. E.; Das, S.; Qin, Ch. Mechanisms of Water Oxidation Catalyzed by Ruthenium Diimine Complexes. *Inorg. Chem.* **2008**, *47*, 1753–1764.

(20) Jurss, J. W.; Concepcion, J. J.; Butler, J. M.; Omberg, K. M.; Baraldo, L. M.; Thompson, D. G.; Lebeau, E. L.; Hornstein, B.; Schoonover, J. R.; Jude, H.; Thompson, J. D.; Dattelbaum, D. M.; Rocha, R. C.; Templeton, J. L.; Meyer, T. J. Electronic Structure of the Water Oxidation Catalyst *cis,cis*-[(bpy)<sub>2</sub>(H<sub>2</sub>O)Ru<sup>III</sup>ORu<sup>III</sup>(OH<sub>2</sub>)-(bpy)<sub>2</sub>]<sup>4+</sup>, The Blue Dimer. *Inorg. Chem.* **2012**, *51*, 1345–1358.

(21) Sancak, Y.; Markhard, A. L.; Kitami, T.; Kovács-Bogdán, E.; Kamer, K. J.; Udeshi, N. D.; Carr, S. A.; Chaudhuri, D.; Clapham, D. E.; Li, A. A.; Calvo, S. E.; Goldberger, O.; Mootha, V. K. EMRE Is an Essential Component of the Mitochondrial Calcium Uniporter Complex. *Science* **2013**, *342*, 1379–1382.

(22) Nathan, S. R.; Pino, N. W.; Arduino, D. M.; Perocchi, F.; MacMillan, S. N.; Wilson, J. J. Synthetic Methods for the Preparation of a Functional Analogue of Ru360, a Potent Inhibitor of Mitochondrial Calcium Uptake. *Inorg. Chem.* **2017**, *56*, 3123–3126.

(23) Tyrlik, S. K.; Kisielinska, M.; Huffman, J. C. Searching for transition metal coordination compounds, which complex carbohydrates in water solution; synthesis, X-ray crystal structure and u.v.-vis. spectra of oxo-bis[bis-acetonitriletrichlororuthenium]. *Transition Met. Chem.* **1995**, *20*, 413–414.

(24) Chen, J.-L.; Yin, G.-Q.; Chen, Z.-N. Synthesis, X-Ray Structure and Characterization of a Triruthenium Cluster Complex Ru<sub>3</sub>(μ<sub>3</sub>-O)(μ-CH<sub>3</sub>COO)<sub>6</sub>(py)<sub>2</sub>Cl with Four Steps One-electron Redox Processes. *Chin. Chem. Lett.* **2003**, *14*, 519–522.

(25) Ye, H.-Y.; Zhang, L.-Y.; Chen, J.-L.; Chen, Z.-N. Dimers of delocalized Ru<sub>3</sub>O clusters linked by ortho-metallated 2,2'-bipyrimidine in μ<sub>4</sub>-η<sup>1</sup>(C),η<sup>1</sup>(C),η<sup>2</sup>(N,N),η<sup>2</sup>(N,N) mode. *Chem. Commun.* **2006**, 1971–1973.

(26) Gillon, A. L.; Orpen, A. G.; Starbuck, J.; Wang, X.-M.; Rodríguez-Martín, Y.; Ruiz-Pérez, C. Cation-controlled formation of [MCl<sub>4</sub>]<sub>n</sub><sup>2n-</sup> chains in [4,4'-H<sub>2</sub>bipy][MCl<sub>4</sub>] (M = Mn, Cd): an alternative to the A<sub>2</sub>MCl<sub>4</sub> <100> layer perovskite structure. *Chem. Commun.* **1999**, 2287–2288.

(27) Ruiz-Pérez, C.; Lorenzo-Luis, P.; Hernández-Molina, M.; Laz, M. M.; Gili, P.; Julve, M. Supramolecular Loop-Chain Network of Pillared Layers via 4,4'-Bipyridine. *Cryst. Growth Des.* **2004**, *4*, 57–61.

(28) Fabelo, O.; Cañadillas-Delgado, L.; Delgado, F. S.; Lorenzo-Luis, P.; Laz, M.; Julve, M.; Ruiz-Pérez, C. Hydrogen Bond-Directed Frameworks Based on 1,2,4,5-Benzene-Tetracarboxylate. *Cryst. Growth Des.* **2005**, *5*, 1163–1167.

(29) Willett, R. D.; Butcher, R. E.; Landee, Ch. P.; Twamley, B. Two halide exchange in copper(II) halide dimers: (4,4'-bipyridinium)-Cu<sub>2</sub>Cl<sub>6-x</sub>Br<sub>x</sub>. *Polyhedron* **2006**, *25*, 2093–2100.

(30) Kumagai, H.; Kawata, S. 4,4'-Bipyridine-1,1'-dium 2,3,5,6-tetra-bromo-terephthalate dihydrate. *Acta Crystallogr., Sect. E: Struct. Rep. Online* **2011**, *67*, o2636–o2636.

(31) Lu, H.; Gautier, R.; Donakowski, M. D.; Liu, Z.; Poeppelmeier, K. R. From Solution to the Solid State: Control of Niobium Oxide-Fluoride [NbO<sub>x</sub>F<sub>y</sub>]<sup>n-</sup> Species. *Inorg. Chem.* **2014**, *53*, 537–542.

(32) Dey, S. K.; Saha, R.; Biswas, S.; Layek, A.; Middya, S.; Steele, I. M.; Fleck, M.; Ray, P. P.; Kumar, S. Tetrabromoterephthalic Acid in Designing Co-crystals and Salts: Modification of Optical Properties and Schottky Barrier Effect. *Cryst. Growth Des.* **2014**, *14*, 207–221.

(33) Pedersen, A. H.; Julve, M.; Brechin, E. K.; Martínez-Lillo, J. Self-assembly of the tetrachlorido(oxalato)rhenate(IV) anion with protonated organic cations: X-ray structures and magnetic properties. *CrystEngComm* **2017**, *19*, 503–510.

(34) Woodall, C. H.; Craig, G. A.; Prescimone, A.; Misek, M.; Cano, J.; Faus, J.; Probert, M. R.; Parsons, S.; Moggach, S.; Martínez-Lillo, J.; Murrie, M.; Kamenev, K. V.; Brechin, E. K. Pressure induced enhancement of the magnetic ordering temperature in rhenium(IV) monomers. *Nat. Commun.* **2016**, *7*, 13870.

(35) Martínez-Lillo, J.; Armentano, D.; De Munno, G.; Lloret, F.; Julve, M.; Faus, J. Ligand substitution in hexahalorhenate(IV) complexes: Synthesis, crystal structures and magnetic properties of NBu<sub>4</sub>[ReX<sub>6</sub>(DMF)] (X = Cl and Br). *Inorg. Chim. Acta* **2006**, *359*, 3291–3296.

(36) Martínez-Lillo, J.; Pedersen, A. H.; Faus, J.; Julve, M.; Brechin, E. K. Effect of Protonated Organic Cations and Anion-π Interactions on the Magnetic Behavior of Hexabromorhenate(IV) Salts. *Cryst. Growth Des.* **2015**, *15*, 2598–2601.

(37) Jeffrey, G. A. Hydrogen-Bonding: An Update. *Crystallogr. Rev.* **1995**, *4*, 213–254.

(38) Rozas, I.; Alkorta, I.; Elguero, J. Bifurcated Hydrogen Bonds: Three-Centered Interactions. *J. Phys. Chem. A* **1998**, *102*, 9925–9932.

(39) Armentano, D.; Martínez-Lillo, J. Aquapentachlororhenate(IV): a singular and promising building block for metal assembly. *RSC Adv.* **2015**, *5*, 54936–54940.

(40) Dance, I.; Scudder, M. Supramolecular Motifs: Concerted Multiple Phenyl Embraces between Ph<sub>4</sub>P<sup>+</sup> Cations are Attractive and Ubiquitous. *Chem. - Eur. J.* **1996**, *2*, 481–486.

(41) Dance, I.; Scudder, M. Supramolecular motifs: sextuple aryl embraces in crystalline [M(2,2'-bipy)<sub>3</sub>] and related complexes. *J. Chem. Soc., Dalton Trans.* **1998**, 1341–1350.

(42) Weaver, T. R.; Meyer, T. J.; Adeyemi, S. A.; Brown, G. M.; Eckberg, R. P.; Hatfield, W. E.; Johnson, E. C.; Murray, R. W.; Untereker, D. Chemically significant interactions between ruthenium ions in oxo-bridged complexes of ruthenium(III). *J. Am. Chem. Soc.* **1975**, *97*, 3039–3048.

(43) Gilbert, J. A.; Eggleston, D. S.; Murphy, W. R., Jr.; Geselowitz, D. A.; Gersten, S. W.; Hodgson, D. J.; Meyer, T. J. Structure and redox properties of the water-oxidation catalyst [(bpy)<sub>2</sub>(OH<sub>2</sub>)-RuORu(OH<sub>2</sub>)(bpy)<sub>2</sub>]<sup>4+</sup>. *J. Am. Chem. Soc.* **1985**, *107*, 3855–3864.

(44) Yoshida, M.; Kondo, M.; Nakamura, T.; Sakai, K.; Masaoka, S. Three Distinct Redox States of an Oxo-Bridged Dinuclear Ruthenium Complex. *Angew. Chem., Int. Ed.* **2014**, *53*, 11519–11523.

- (45) Pauling, L. The principles determining the structure of complex ionic crystals. *J. Am. Chem. Soc.* **1929**, *51*, 1010–1026.
- (46) Pauling, L. Atomic Radii and Interatomic Distances in Metals. *J. Am. Chem. Soc.* **1947**, *69*, 542–553.
- (47) <https://www.iucr.org/resources/data/datasets/bond-valence-parameters>.
- (48) Brown, I. D.; Altermatt, D. Bond-Valence Parameters Obtained from a Systematic Analysis of the Inorganic Crystal Structure Database. *Acta Crystallogr., Sect. B: Struct. Sci.* **1985**, *B41*, 244–247.
- (49) Thorp, H. H. Bond Valence Sum Analysis of Metal-Ligand Bond Lengths in Metalloenzymes and Model Complexes. *Inorg. Chem.* **1992**, *31*, 1585–1588.
- (50) Gagné, O. C.; Hawthorne, F. C. Comprehensive derivation of bond-valence parameters for ion pairs involving oxygen. *Acta Crystallogr., Sect. B: Struct. Sci., Cryst. Eng. Mater.* **2015**, *B71*, 562–578.
- (51) Brown, I. D. What is the best way to determine bond-valence parameters? *IUCrJ* **2017**, *4*, 514–515.
- (52) Palenik, G. J. Bond Valence Sums in Coordination Chemistry Using Oxidation State Independent  $R_0$  Values. A Simple Method for Calculating the Oxidation State of Manganese in Complexes Containing Only Mn–O Bonds. *Inorg. Chem.* **1997**, *36*, 4888–4890.
- (53) Moushi, E. E.; Tasiopoulos, A. J.; Manos, M. J. Synthesis and Structural Characterization of a Metal Cluster and a Coordination Polymer Based on the  $[\text{Mn}_6(\mu_4\text{-O})_2]^{10+}$  Unit. *Bioinorg. Chem. Appl.* **2010**, 367128.
- (54) Marino, N.; Armentano, D.; Mastropietro, T. F.; Julve, M.; De Munno, G.; Martínez-Lillo, J. Cubane-Type  $\text{Cu}^{\text{II}}_4$  and  $\text{Mn}^{\text{II}}_2\text{Mn}^{\text{III}}_2$  Complexes Based on Pyridoxine: A Versatile Ligand for Metal Assembling. *Inorg. Chem.* **2013**, *52*, 11934–11943.
- (55) Liu, J.-Y.; Ma, C.-B.; Chen, H.; Chen, C.-N. Synthesis, crystal structures and magnetic properties of a family of manganese phosphonate clusters with diverse structures. *CrystEngComm* **2015**, *17*, 8736–8745.
- (56) McKinnon, J. J.; Jayatilaka, D.; Spackman, M. A. Towards quantitative analysis of intermolecular interactions with Hirshfeld surfaces. *Chem. Commun.* **2007**, 3814–3816.
- (57) Spackman, M. A.; Jayatilaka, D. Hirshfeld surface analysis. *CrystEngComm* **2009**, *11*, 19–32.
- (58) Turner, M. J.; McKinnon, J. J.; Wolff, S. K.; Grimwood, D. J.; Spackman, P. R.; Jayatilaka, D.; Spackman, M. A. *CrystalExplorer 17*; University of Western Australia, 2017, <http://hirshfeldsurface.net>.
- (59) *SHELXTL-2013/4*, Bruker Analytical X-ray Instruments: Madison, WI, 2013.
- (60) *DIAMOND 4.5.0*; Crystal Impact GbR, 2018.



## *CHAPTER 3*

---

*Gadolinium(III) and  
dysprosium(III) complexes based  
on nucleobases, amino acids and  
oxalic acid: From SMMs to  
MRI contrast agents and  
magnetic coolers*



## 3.1 Prologue

Lanthanides are a group of elements with atomic number increasing from 57 (lanthanum) to 71 (lutetium). They are named lanthanides because the lighter elements in the series are chemically similar to lanthanum. They are also known as f-block elements since the 4f shell gets filled progressively. In contrast to transition metal complexes, where the coordination number for a particular combination of metal ion and oxidation state is often limited to a particular value, the coordination number in lanthanide complexes appears to be essentially determined by populating the coordination sphere, while bearing in mind the strength of the positively-charged metal ion and the electron-rich ligand [1]. In any case, high coordination numbers are predicted for the lanthanides, simply on the basis of the large size of the metal ion.

Lanthanide complexes, as well as their simple salts, have attracted increased interest in recent decades because of their unique optical, spectroscopic and magnetic properties, which generate an interesting field of research in coordination and supramolecular chemistry [2–7]. Some of the lanthanide(III) complexes with chelating ligands display several potential applications, such as organic light-emitting devices [8–11], liquid crystalline materials [12], sensors and contrast agents in MRI [13]. The luminescence of these lanthanide(III) complexes having an attached absorbing chromophore is originated from their gradual filling of the 4f orbitals, and can be readily adjusted from visible to the infrared region simply by the selection of the lanthanide(III) ion [14]. As a result, the characteristic luminescence properties of these lanthanide(III) complexes, and their applications, have been recently reviewed [15].

Besides, valence electrons in 4f orbitals make lanthanides highly electroposi-

---

tive and reactive, giving them peculiar and remarkable magnetic properties. Considering this fact, a basic requirement for observing SMM behaviour is the presence of a large total spin angular momentum in a single molecule, as observed in those SMMs containing polynuclear 3d-5d metal ions [16–21]. Special attention has been paid to the elements whose single-ion anisotropy is relatively high in recent years. In this sense, lanthanides have gained special relevance because the ligand effect is almost negligible (the f orbitals are core orbitals, and thus interact poorly with those of the ligand), and because most of them are characterised by a significant spin-orbit coupling and a large unquenched orbital angular momentum. This fact is associated with the nature of the valence f orbitals in the systems containing 4f ions [22]. These features lead to a significant magnetic anisotropy that allows lanthanide(III) complexes to exhibit slow magnetic relaxation [23–26]. In order to increase the spin, the magnetic anisotropy and subsequently, the energy barrier, much of the current SMM research has shifted towards lanthanide-based complexes. Except for gadolinium(III) and europium(II), which have an  $f^7$  electron configuration and an orbitally non-degenerate ground state, all the rare-earth ions exhibit orbitally degenerate ground states, which are split by spin-orbit coupling and crystal-field effects [27].

Although the interactions involving lanthanide(III) ions are weak, magnetic anisotropy can yield novel phenomena. As indicated before, this singular magnetic behaviour allows SMMs to become promising candidates for potential applications in quantum and high-density data storage at the molecular and atomic scale, quantum information processing, molecular refrigeration and spintronic investigations [28].

During the last two decades, SMMs based on heterometallic 3d–4f mixed systems [29–31], radical bridged compounds, mono- and polynuclear lanthanide(III)



complexes containing highly anisotropic 4f ions [32, 33] have been studied. The lanthanide ions most commonly used in SMMs are terbium(III), dysprosium(III), erbium(III) and holmium(III). The electronic structures of terbium(III) and dysprosium(III) ions possess substantial anisotropy because of the strong angular dependence of their 4f orbitals (Figure 3.1) [34, 35].

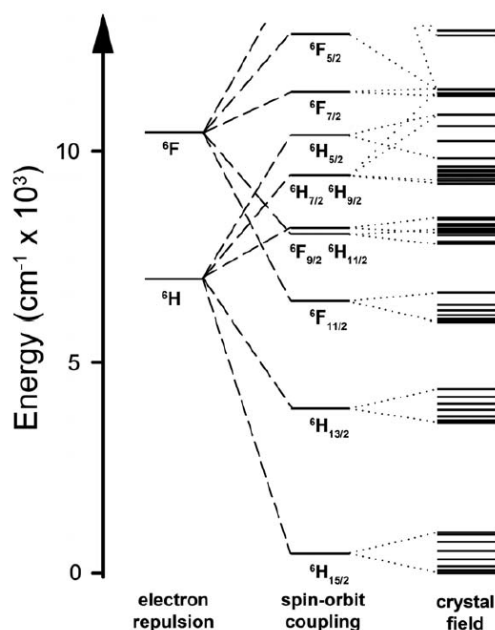


Figure 3.1: Low energy electronic structure of the Dy(III) ion with sequential perturbations of electron-electron repulsion, spin-orbit coupling and the crystal field.

SMMs based on dysprosium(III) are the most numerous in this family of compounds. The ground state of an isolated dysprosium(III) is  ${}^6H_{15/2}$ , which is characterised by a  $g_j=4/3$  value [36]. A low-symmetry environment can generate an isolated Kramer's doublet as the ground state, meaning that the ground state will always be bistable irrespective of the ligand field symmetry.

Many examples of SMMs based on dinuclear dysprosium(III) complexes have been studied from a magnetism point of view [37–42]. The nature of the ligands used to bridge the metals in these dinuclear SMMs are wide and includes ph-

thiocyanates, phenolates, halides, thiolates, and carboxylates. Nevertheless, 1D dysprosium(III) complexes showing slow relaxation of magnetisation have been much less investigated [43–45], despite the fact that SMM behaviour has been observed in complexes that contain only a single lanthanide ion, so-called SIMs.

Since the discovery of the mononuclear Pc-based lanthanide(III) complexes by Ishikawa *et al.* [46, 47], of formula  $[\text{NBu}_4][\text{LnPc}_2]$  ( $\text{Ln}^{\text{III}} = \text{Tb}$  and  $\text{Dy}$ ) displaying unusual relaxation behaviour, many efforts have focused on the synthesis and development of lanthanide(III)-based (see Chapter 1). Recently, a mononuclear dysprosium(III) metallocene of formula  $[(\eta^5\text{-Cp}^*)\text{Dy}(\eta^5\text{-Cp}^{\text{iPr5}})][\text{B}(\text{C}_6\text{F}_5)_4]$  was reported [48]. This dysprocene(III) compound displays a record energy barrier of magnetisation reversal exceeding the  $1500 \text{ cm}^{-1}$  value and a record blocking temperature above the liquid nitrogen ( $> 77\text{K}$ ), presumably being a new benchmark in this research area (Figure 3.2).

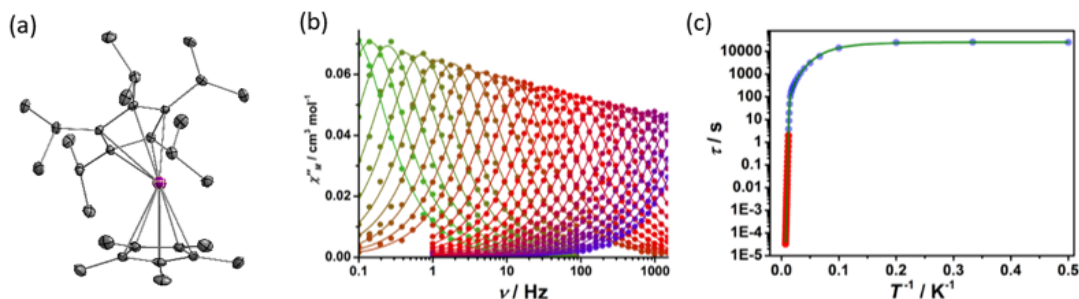


Figure 3.2: (a) Asymmetric unit of the dysprocene(III) compound  $[(\eta^5\text{-Cp}^*)\text{Dy}(\eta^5\text{-Cp}^{\text{iPr5}})][\text{B}(\text{C}_6\text{F}_5)_4]$ . Colour code: purple, Dy; grey, C. Hydrogen atoms and  $[\text{B}(\text{C}_6\text{F}_5)_4]$  cations are omitted for clarity. (b) Frequency dependence of the out-of-phase  $\chi''_M$  molar magnetic susceptibility. (c) Temperature dependence of the relaxation time. The red dots are from the ac susceptibility data and the blue dots are from measurements of the dc magnetic relaxation time. The solid green line is the best fit to the equation  $\tau^{-1} = \tau_0^{-1} e^{-U_{\text{eff}}/k_B T} + CT^n + \tau_{\text{QTM}}^{-1}$ .

In comparison, the gadolinium(III) ion is highly paramagnetic and usually considered as magnetically isotropic because of its half-occupied  $4f^7$  electron con-

figuration, as mentioned above, and the lack of orbital contribution ( $S = 7/2$ ,  $L = 0$ ), with an  ${}^8S_{7/2}$  ground state and a spherical quadrupole moment. As a result, the energy levels are almost degenerated and the magnetic relaxation rates are usually very fast, due to the presence of strong Quantum Tunneling of the Magnetisation (QTM). However, when an external dc magnetic field is applied, the degeneracy can be removed and the QTM suppressed [32].

Indeed, there are some complexes based on gadolinium(III) exhibiting slow magnetic relaxation, which have recently been reported, but most of them are either polynuclear [49–51] or polymeric complexes [31, 52]. These compounds possess non-negligible magnetic interactions between the gadolinium(III) ions, which results in mixed mechanisms of spin–lattice, spin–phonon and spin–spin relaxations. To date, only two works are reported in the literature dealing with mononuclear gadolinium(III) based field-induced magnets. In 2013, Gao *et al.* reported two new mononuclear gadolinium(III) complexes exhibiting field induced magnetic relaxation and MCE [53]. Recently, Yan-Cong *et al.* reported another mononuclear gadolinium(III) complex, that shows slow relaxation of magnetisation when an external field is applied [54]. The reason why gadolinium(III) is selected for some technological applications, among others, is because its symmetric  ${}^8S_{7/2}$  ground state leads to a much slower electronic relaxation rate [55], despite dysprosium(III) or holmium(III) exhibit a larger magnetic moment than that of gadolinium(III). Because of that, it is widely used for applications in technological fields such as neutron capture cancer therapy [56, 57].

In addition, gadolinium(III) complexes are commonly used as contrast agents in MRI, because gadolinium(III) chelates reduce the longitudinal relaxation time ( $T_1$ ) of water molecules [13, 55, 58]. A significant challenge in this area is to balance the need for higher relaxivity with acceptable stability. Unfortunately,

this 4f ion is very toxic in a free state when it is injected into the human body in concentrations necessary for their use as a contrast agent. Therefore, only a few stable and inert mononuclear complexes of this ion with polyaminocarboxylate chelating ligands are employed (Figure 3.3). The successful penetration of gadolinium(III) chelates into radiologic practice and biomedicine started with the study of the complex  $[\text{Gd}(\text{DTPA})(\text{H}_2\text{O})]^{2-}$  (DTPA = Diethylenetriamine pentaacetic acid), reported by D.H Carr *et al.* in 1984 [59]. The off-the-shelf ligands, such as DTPA, form complexes strong enough so that there is no detectable dissociation for the period that the agent is in the body.

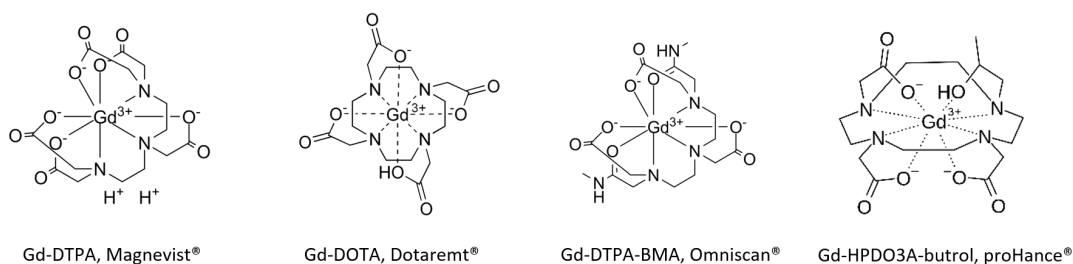


Figure 3.3: Typical commercial gadolinium(III)-based contrast agents.

Besides, some of the reported gadolinium(III)-based complexes can act as magnetic refrigerators due to their low Curie temperature and significant MCE [60–65]. The MCE explains the heating or cooling of a magnetic material under the change of the external magnetic field [63]. To pursue the ideal molecular refrigerant, it is necessary to have a large spin ground state  $S$ , a negligible magnetic anisotropy, the presence of low-lying excited spin states, a dominant ferromagnetic exchange and a relatively low molecular mass (or a large metal/ligand ratio) [66, 67].

Therefore, the trend in this area of molecular cryomagnetic refrigerant materials has been to switch from paramagnetic transition metal ions to lanthanides, and

from discrete zero-dimensional (0D), mono-, di-, and polynuclear complexes to extended one-, two- and three-dimensional (nD, n = 1-3) coordination polymers, respectively. Metal-Organic Frameworks (MOFs) of different dimensionalities and topologies with  $\text{Gd}^{\text{III}}$  ions, and light mono-, di-, and tricarboxylate organic ligands (formate, acetate, iminodiacetate, oxalate, malonate, succinate, fumarate, glutarate, benzene-, aminobenzene-, azobenzene-, furan- or thiophenedicarboxylate, and benzenetricarboxylate) have been investigated as cryogenic magnetic coolers due to their extremely low magnetic ordering temperatures ( $T_N$ ) and large MCE, as well as their inherent chemical stability and high density.

For instance, as seen in Figure 3.4, gadolinium(III) formate has been suggested as a molecular refrigerant in the sub-Kelvin temperature range. The adiabatic temperature ( $-\Delta S_M = 55.9 \text{ J kg}^{-1} \text{ K}^{-1}$  at  $T = 2 \text{ K}$  for  $\Delta H = 7 \text{ T}$  and  $\Delta T_{\text{ad}} = 3 \text{ K}$  for  $\Delta H = 1 \text{ T}$ ) and large isothermal magnetic entropy changes of this 3D Gd-MOF with the formula  $\text{Gd}(\text{form})_3$  are barely above the long-range antiferromagnetic order temperature ( $T_N = 0.8 \text{ K}$ ) [68].

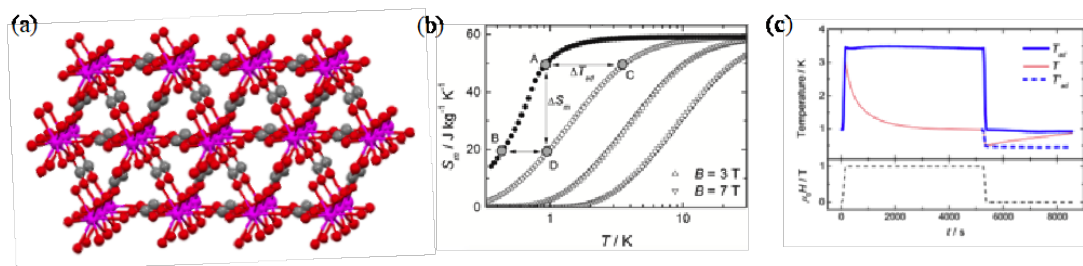


Figure 3.4: Illustration of the magnetocaloric properties of gadolinium(III) formate as an example of Ln MOF proposed as a cryomagnetic refrigerant: (a) Crystal structure of the 3D lattice (Gd, purple; O, red; C, grey). Hydrogen atoms are omitted for clarity. (b) Thermodynamic cycle where isothermal magnetic entropy (AD) and adiabatic temperature (AC or BD) changes accompanying the magnetisation/demagnetisation processes are highlighted. (c) Magnetisation/demagnetisation cycle where the adiabatic temperature change is highlighted.

---

As opposed to conventional oxides like gadolinium gallium garnet (GGG) and its iron-substituted derivatives (GGIG) with general formula  $\text{Gd}_3\text{Ga}_{5-x}\text{Fe}_x\text{O}_{12}$ , which operate in the low-temperature (supra-Kelvin) regime, this type of Ln MOFs are good candidates for multifunctional molecular-based magnetic materials for cryogenic magnetic refrigeration.

## 3.2 Contents

In this Chapter 3, four works are included. The first one, titled ***“A Gadolinium(III) Complex Based on the Thymine Nucleobase with Properties Suitable for Magnetic Resonance Imaging”***, describes the synthesis of a gadolinium(III) complex of formula  $[\text{Gd}(\text{thy})_2(\text{H}_2\text{O})_6](\text{ClO}_4)_3 \cdot 2 \text{H}_2\text{O}$  and its magnetic and relaxometric characteristics are tested.

The second work, titled ***“Field-induced slow relaxation of magnetization in two one-dimensional homometallic dysprosium(III) complexes based on alpha- and beta-amino acids”***, depicts two 1D dysprosium complexes based on the  $\alpha$ -glycine and  $\beta$ -alanine amino acids. The compounds  $\{[\text{Dy}_2(\text{gly})_6(\text{H}_2\text{O})_4](\text{ClO}_4)_6 \cdot 5 \text{H}_2\text{O}\}_n$  and  $\{[\text{Dy}_2(\beta\text{-ala})_6(\text{H}_2\text{O})_4](\text{ClO}_4)_6 \cdot \text{H}_2\text{O}\}_n$  have been structurally and magnetically characterised.

The third work, titled ***“One-Dimensional Gadolinium (III) Complexes Based on Alpha and Beta-Amino Acids Exhibiting Field-Induced Slow Relaxation of Magnetization”***, describes the preparation of two one-dimensional gadolinium(III) complexes based on  $\alpha$ -glycine and  $\beta$ -alanine amino acids, with the formulas  $\{[\text{Gd}_2(\text{gly})_6(\text{H}_2\text{O})_4](\text{ClO}_4)_6 \cdot 5 \text{H}_2\text{O}\}_n$  and  $\{[\text{Gd}_2(\beta\text{-ala})_6(\text{H}_2\text{O})_4](\text{ClO}_4)_6 \cdot \text{H}_2\text{O}\}_n$ . These compounds were magneto-structurally characterised.

The last work in this chapter is titled “*Field-induced slow magnetic relaxation and magnetocaloric effects in an oxalato-bridged gadolinium (III)-based 2D MOF*”, and displays the synthesis and characterisation of a 2D compound with the formula  $[\text{Gd}_2(\text{ox})_3(\text{H}_2\text{O})_6]_n \cdot 4n \text{H}_2\text{O}$ . The observation of field-induced slow magnetic relaxation coexisting with moderately large magnetocaloric efficiency in the supra-Kelvin temperature region can be used as a proof-of-concept design of a new class of slow-relaxing magnetic materials for cryogenic magnetic cooling.

---

## References

- (1) Cotton, S. A. *C. R. Chim.* **2005**, *8*, 129–145.
- (2) Singh, L.; Singh, R. *Chem. Pap.* **2014**, *68*, 223–232.
- (3) Sorace, L.; Benelli, C.; Gatteschi, D. *Chem. Soc. Rev.* **2011**, *40*, 3092–3104.
- (4) Chen, Y.; Ma, S. *Rev. Inorg. Chem.* **2012**, *32*, 81–100.
- (5) Cheng, P.; Bosch, M., *Lanthanide metal-organic frameworks*; Springer: 2015.
- (6) Nguyen, T. N.; Ebrahim, F. M.; Stylianou, K. C. *Coord. Chem. Rev.* **2018**, *377*, 259–306.
- (7) Écija, D.; Urgel, J. I.; Seitsonen, A. P.; Auwärter, W.; Barth, J. V. *Acc. Chem. Res.* **2018**, *51*, 365–375.
- (8) Zhang, L.; Li, B.; Yue, S.; Li, M.; Hong, Z.; Li, W. *J. Lumin.* **2008**, *128*, 620–624.
- (9) Sun, P.-P.; Duan, J.-P.; Shih, H.-T.; Cheng, C.-H. *Appl. Phys. Lett.* **2002**, *81*, 792–794.
- (10) Walzer, K.; Maennig, B.; Pfeiffer, M.; Leo, K. *Chem. Rev.* **2007**, *107*, 1233–1271.



- 
- (11) Zhang, S.; Turnbull, G. A.; Samuel, I. D. *Org. Electron.* **2012**, *13*, 3091–3096.
- (12) Binnemans, K.; Bruce, D. W.; Collinson, S. R.; Deun, R. V.; Galyametdinov, Y. G.; Martin, F. *Philos. Trans. A Math. Phys. Eng. Sci.* **1999**, *357*, 3063–3077.
- (13) Hingorani, D. V.; Bernstein, A. S.; Pagel, M. D. *Contrast Media Mol. Imaging* **2015**, *10*, 245–265.
- (14) Wang, L.; Ni, L., et al. *Solid State Sc.* **2012**, *14*, 1361–1366.
- (15) Afzal, S.; Maitra, U. *Helv. Chim. Acta* **2022**, *105*, e202100194.
- (16) Lecren, L.; Wernsdorfer, W.; Li, Y.-G.; Vindigni, A.; Miyasaka, H.; Clérac, R. *J. Am. Chem. Soc.* **2007**, *129*, 5045–5051.
- (17) Waldmann, O.; Carver, G.; Dobe, C.; Sieber, A.; Güdel, H. U.; Mutka, H. *J. Am. Chem. Soc.* **2007**, *129*, 1526–1527.
- (18) Kanegawa, S.; Karasawa, S.; Maeyama, M.; Nakano, M.; Koga, N. *J. Am. Chem. Soc.* **2008**, *130*, 3079–3094.
- (19) Ruiz, E.; Cirera, J.; Cano, J.; Alvarez, S.; Loose, C.; Kortus, J. *Chem. Commun.* **2008**, 52–54.
- (20) Gómez-Segura, J.; Veciana, J.; Ruiz-Molina, D. *Chem. Commun.* **2007**, 3699–3707.
- (21) Ako, A. M.; Hewitt, I. J.; Mereacre, V.; Clérac, R.; Wernsdorfer, W.; Anson, C. E.; Powell, A. K. *Angew. Chem. Int. Ed.* **2006**, *118*, 5048–5051.
- (22) Habib, F.; Murugesu, M. *Chem. Soc. Rev.* **2013**, *42*, 3278–3288.
- (23) Yamashita, A.; Watanabe, A.; Akine, S.; Nabeshima, T.; Nakano, M.; Yamamura, T.; Kajiwara, T. *Angew. Chem. Int. Ed.* **2011**, *123*, 4102–4105.

- 
- (24) Campbell, V. E.; Guillot, R.; Riviere, E.; Brun, P.-T.; Wernsdorfer, W.; Mallah, T. *Inorg. Chem.* **2013**, *52*, 5194–5200.
- (25) Watanabe, A.; Yamashita, A.; Nakano, M.; Yamamura, T.; Kajiwara, T. *Chem. Eur. J.* **2011**, *17*, 7428–7432.
- (26) AlDamen, M. A.; Clemente-Juan, J. M.; Coronado, E.; Martí-Gastaldo, C.; Gaita-Arino, A. *J. Am. Chem. Soc.* **2008**, *130*, 8874–8875.
- (27) Benelli, C.; Gatteschi, D. *Chem. Rev.* **2002**, *102*, 2369–2388.
- (28) Goodwin, C. A.; Ortu, F.; Reta, D.; Chilton, N. F.; Mills, D. P. *Nature* **2017**, *548*, 439–442.
- (29) Karotsis, G.; Evangelisti, M.; Dalgarno, S. J.; Brechin, E. K. *Angew. Chem. Int. Ed.* **2009**, *121*, 10112–10115.
- (30) Ghosh, T. K.; Maity, S.; Mayans, J.; Ghosh, A. *Inorg. Chem.* **2020**, *60*, 438–448.
- (31) Izuogu, D. C.; Yoshida, T.; Zhang, H.; Cosquer, G.; Katoh, K.; Ogata, S.; Hasegawa, M.; Nojiri, H.; Damjanović, M.; Wernsdorfer, W., et al. *Chem. Eur. J.* **2018**, *24*, 9285–9294.
- (32) Borah, A.; Murugavel, R. *Coord. Chem. Rev.* **2022**, *453*, 214288.
- (33) McAdams, S. G.; Ariciu, A.-M.; Kostopoulos, A. K.; Walsh, J. P.; Tuna, F. *Coord. Chem. Rev.* **2017**, *346*, 216–239.
- (34) Rinehart, J. D.; Long, J. R. *Chem. Sci.* **2011**, *2*, 2078–2085.
- (35) Woodruff, D. N.; Winpenney, R. E.; Layfield, R. A. *Chem. Rev.* **2013**, *113*, 5110–5148.
- (36) Benelli, C.; Caneschi, A.; Gatteschi, D.; Sessoli, R. *Adv. Mater.* **1992**, *4*, 504–505.

- 
- (37) Huang, G.; Yi, X.; Gendron, F.; Le Guennic, B.; Guizouarn, T.; Daiguebonne, C.; Calvez, G.; Suffren, Y.; Guillou, O.; Bernot, K. *Dalton Trans.* **2019**, *48*, 16053–16061.
- (38) Chow, C. Y.; Bolvin, H.; Campbell, V. E.; Guillot, R.; Kampf, J. W.; Wernsdorfer, W.; Gendron, F.; Autschbach, J.; Pecoraro, V. L.; Mallah, T. *Chem. Sci.* **2015**, *6*, 4148–4159.
- (39) Ma, X.; Chen, B.; Zhang, Y.-Q.; Yang, J.; Shi, Q.; Ma, Y.; Liu, X. *Dalton Trans.* **2019**, *48*, 12622–12631.
- (40) Cen, P.; Liu, X.; Zhang, Y.-Q.; Ferrando-Soria, J.; Xie, G.; Chen, S.; Pardo, E. *Dalton Trans.* **2020**, *49*, 808–816.
- (41) Zhang, L.; Zhang, Y.-Q.; Zhang, P.; Zhao, L.; Guo, M.; Tang, J. *Inorg. Chem.* **2017**, *56*, 7882–7889.
- (42) Sran, B. S.; Gonzalez, J. F.; Montigaud, V.; Le Guennic, B.; Pointillart, F.; Cador, O.; Hundal, G. *Dalton Trans.* **2019**, *48*, 3922–3929.
- (43) Pointillart, F.; Klementieva, S.; Kuropatov, V.; Le Gal, Y.; Golhen, S.; Cador, O.; Cherkasov, V.; Ouahab, L. *Chem. Commun.* **2012**, *48*, 714–716.
- (44) Wang, Y.; Li, X.-L.; Wang, T.-W.; Song, Y.; You, X.-Z. *Inorg. Chem.* **2010**, *49*, 969–976.
- (45) Li, D.-P.; Wang, T.-W.; Li, C.-H.; Liu, D.-S.; Li, Y.-Z.; You, X.-Z. *Chem. Commun.* **2010**, *46*, 2929–2931.
- (46) Ishikawa, N.; Sugita, M.; Ishikawa, T.; Koshihara, S.-y.; Kaizu, Y. *J. Am. Chem. Soc.* **2003**, *125*, 8694–8695.

- 
- (47) Ishikawa, N.; Sugita, M.; Ishikawa, T.; Koshihara, S.-y.; Kaizu, Y. *J. Phys. Chem. B* **2004**, *108*, 11265–11271.
- (48) Guo, F.-S.; Day, B. M.; Chen, Y.-C.; Tong, M.-L.; Mansikkamäki, A.; Layfield, R. A. *Science* **2018**, *362*, 1400–1403.
- (49) Liu, B.; Wang, B.; Wang, Z.; Gao, S. *Sci. China Chem.* **2012**, *55*, 926–933.
- (50) Orendáč, M.; Sedláková, L.; Čížmár, E.; Orendáčová, A.; Feher, A.; Zvyagin, S.; Wosnitza, J.; Zhu, W.; Wang, Z.; Gao, S. *Phys. Rev. B* **2010**, *81*, 214410.
- (51) Holmberg, R. J.; Ungur, L.; Korobkov, I.; Chibotaru, L. F.; Murugesu, M., et al. *Dalton Trans.* **2015**, *44*, 20321–20325.
- (52) Yoshida, T.; Cosquer, G.; Izuogu, D. C.; Ohtsu, H.; Kawano, M.; Lan, Y.; Wernsdorfer, W.; Nojiri, H.; Breedlove, B. K.; Yamashita, M. *Chem. Eur. J.* **2017**, *23*, 4551–4556.
- (53) Kang, Q.; Bingwu, W.; Zheming, W.; Gang, S.; Song, G. *Acta Chim. Sinica* **2013**, *71*, 1022–1028.
- (54) Chen, Y.-C.; Peng, Y.-Y.; Liu, J.-L.; Tong, M.-L. *Inorg. Chem. Commun.* **2019**, *107*, 107449.
- (55) Caravan, P.; Ellison, J. J.; McMurry, T. J.; Lauffer, R. B. *Chem. Rev.* **1999**, *99*, 2293–2352.
- (56) De Stasio, G.; Casalbore, P.; Pallini, R.; Gilbert, B.; Sanita, F.; Ciotti, M. T.; Rosi, G.; Festinesi, A.; Larocca, L. M.; Rinelli, A., et al. *Cancer Res.* **2001**, *61*, 4272–4277.

- 
- (57) Leinweber, G.; Barry, D. P.; Trbovich, M.; Burke, J.; Drindak, N.; Knox, H.; Ballard, R.; Block, R.; Danon, Y.; Severnyak, L. *Nucl. Sci. Eng.* **2006**, *154*, 261–279.
- (58) Raymond, K. N.; Pierre, V. C. *Bioconjug. Chem.* **2005**, *16*, 3–8.
- (59) Carr, D.; Brown, J.; Bydder, G.; Weinmann, H.; Speck, U.; Thomas, D.; Young, I. *Lancet* **1984**, *323*, 484–486.
- (60) Evangelisti, M.; Roubeau, O.; Palacios, E.; Camón, A.; Hooper, T. N.; Brechin, E. K.; Alonso, J. J. *Angew. Chem. Int. Ed.* **2011**, *50*, 6606–6609.
- (61) Lorusso, G.; Palacios, M. A.; Nichol, G. S.; Brechin, E. K.; Roubeau, O.; Evangelisti, M. *Chem. Commun.* **2012**, *48*, 7592–7594.
- (62) Liu, S.-J.; Han, S.-D.; Zhao, J.-P.; Xu, J.; Bu, X.-H. *Coord. Chem. Rev.* **2019**, *394*, 39–52.
- (63) Pecharsky, V. K.; Gschneidner Jr, K. A. *J. Magn. Magn. Mater.* **1999**, *200*, 44–56.
- (64) Hooper, T. N.; Schnack, J.; Piligkos, S.; Evangelisti, M.; Brechin, E. K. *Angew. Chem. Int. Ed.* **2012**, *51*, 4633–4636.
- (65) Guo, F.-S.; Chen, Y.-C.; Liu, J.-L.; Leng, J.-D.; Meng, Z.-S.; Vrabel, P.; Orendáč, M.; Tong, M.-L. *Chem. Commun.* **2012**, *48*, 12219–12221.
- (66) Liu, J.-L.; Chen, Y.-C.; Tong, M.-L. *Chem. Rec.* **2016**, *16*, 825–834.
- (67) Zabala-Lekuona, A.; Seco, J. M.; Colacio, E. *Coord. Chem. Rev.* **2021**, *441*, 213984.
- (68) Lorusso, G.; Sharples, J. W.; Palacios, E.; Roubeau, O.; Brechin, E. K.; Sessoli, R.; Rossin, A.; Tuna, F.; McInnes, E. J.; Collison, D., et al. *Adv. Mater.* **2013**, *25*, 4653–4656.



---

*ARTICLE 7*

*A Gadolinium(III) Complex  
Based on the Thymine  
Nucleobase with Properties  
Suitable for Magnetic  
Resonance Imaging*







Article

# A Gadolinium(III) Complex Based on the Thymine Nucleobase with Properties Suitable for Magnetic Resonance Imaging

Marta Orts-Arroyo <sup>1</sup>, Amadeo Ten-Esteve <sup>2</sup> , Sonia Ginés-Cárdenas <sup>2</sup>, Isabel Castro <sup>1</sup> , Luis Martí-Bonmatí <sup>2,\*</sup> and José Martínez-Lillo <sup>1,\*</sup>

<sup>1</sup> Instituto de Ciencia Molecular (ICMol), Universitat de València, c/Catedrático José Beltrán 2, Paterna, 46980 Valencia, Spain; marta.orts-arroyo@uv.es (M.O.-A.); isabel.castro@uv.es (I.C.)

<sup>2</sup> Radiology Department and Biomedical Imaging Research Group (GIBI230), La Fe University and Polytechnic Hospital and La Fe Health Research Institute, 46026 Valencia, Spain; ten\_ama@gva.es (A.T.-E.); soniagibi230@gmail.com (S.G.-C.)

\* Correspondence: marti\_lui@gva.es (L.M.-B.); f.jose.martinez@uv.es (J.M.-L.); Tel.: +34-9635-44460 (J.M.-L.)

**Abstract:** The paramagnetic gadolinium(III) ion is used as contrast agent in magnetic resonance (MR) imaging to improve the lesion detection and characterization. It generates a signal by changing the relaxivity of protons from associated water molecules and creates a clearer physical distinction between the molecule and the surrounding tissues. New gadolinium-based contrast agents displaying larger relaxivity values and specifically targeted might provide higher resolution and better functional images. We have synthesized the gadolinium(III) complex of formula  $[Gd(thy)_2(H_2O)_6](ClO_4)_3 \cdot 2H_2O$  (**1**) [thy = 5-methyl-1H-pyrimidine-2,4-dione or thymine], which is the first reported compound based on gadolinium and thymine nucleobase. **1** has been characterized through UV-vis, IR, SEM-EDAX, and single-crystal X-ray diffraction techniques, and its magnetic and relaxometric properties have been investigated by means of SQUID magnetometer and MR imaging phantom studies, respectively. On the basis of its high relaxivity values, this gadolinium(III) complex can be considered a suitable candidate for contrast-enhanced magnetic resonance imaging.

**Keywords:** thymine; gadolinium; contrast agent; magnetic resonance; metal complexes; crystal structure; relaxivity



**Citation:** Orts-Arroyo, M.; Ten-Esteve, A.; Ginés-Cárdenas, S.; Castro, I.; Martí-Bonmatí, L.; Martínez-Lillo, J. A Gadolinium(III) Complex Based on the Thymine Nucleobase with Properties Suitable for Magnetic Resonance Imaging. *Int. J. Mol. Sci.* **2021**, *22*, 4586. <https://doi.org/10.3390/ijms22094586>

Academic Editor: Diego Tesouro

Received: 25 March 2021

Accepted: 23 April 2021

Published: 27 April 2021

**Publisher's Note:** MDPI stays neutral with regard to jurisdictional claims in published maps and institutional affiliations.



**Copyright:** © 2021 by the authors. Licensee MDPI, Basel, Switzerland. This article is an open access article distributed under the terms and conditions of the Creative Commons Attribution (CC BY) license (<https://creativecommons.org/licenses/by/4.0/>).

## 1. Introduction

Thymine is one of the four natural nitrogen bases that are precursors and part of the structure of the deoxyribonucleic acid (DNA) macromolecule [1,2]. This pyrimidine base has been widely studied, in part because of the common mutations of DNA caused when adjacent thymines are irradiated by UV light and are dimerized, generating the well-known thymine dimers [2,3]. Furthermore, considerable effort has also been devoted to the rational design of drugs that might selectively inhibit thymine biosynthesis, thereby blocking DNA replication, especially in rapidly dividing malignant cells [2].

In comparison with other natural nucleobases, the coordination chemistry of thymine-based metal complexes has been much less investigated. Most of the thymine-containing complexes have been prepared with the nucleobase in the form of thymine anion, that is, releasing one or two protons of its N-H groups, whereas the reported examples obtained with the thymine molecule acting through its carbonyl groups as a neutral ligand toward the metal are much scarcer [4–7]. In that respect, theoretical studies have been performed on metal clusters to investigate the preferential binding sites of the thymine molecule [8].

There exist some published thymine-based complexes that exhibit singular properties, as, for instance, the Ru<sup>II</sup>-thymine complex  $[Ru(PPh_3)_2(thy)(bpy)]PF_6$  [where PPh<sub>3</sub> = triphenylphosphine and bpy = 2,2'-bipyridine], which is a potent cytotoxic agent with the ability to bind to DNA, inducing apoptotic cell death in human colon carcinoma [6,7]. Thymine has also shown to be a highly specific ligand toward Hg<sup>II</sup> metal ion [9,10]. The

discovery of the linear thymine-Hg<sup>II</sup>-thymine structure, which affords a high stabilization of thymine-thymine pairs in DNA, has led to the designing and development of recent thymine-based sensors [11–13].

Regarding lanthanide complexes, only two structures based on thymine anion have been published so far, namely, the heteropolynuclear complexes of general formula  $[\{Cp^*Rh^{III}(\mu\text{-thym})\}_4\{Ln^{III}(NO_3)_2\}]^+$ , where  $Ln = Dy^{III}$  and  $Er^{III}$ , which form cationic metallacalix[4]arene-type systems [14]. Hence, no crystal structure of gadolinium complex based on thymine has been reported up to date.

As a continuation of our interest in investigating biomolecule-based complexes [15–20], herein we report the synthesis and characterization of a new gadolinium(III) complex of formula  $[Gd(\text{thy})_2(\text{H}_2\text{O})_6](\text{ClO}_4)_3 \cdot 2\text{H}_2\text{O}$  (**1**) [ $\text{thy} = \text{thymine}$ ], which exhibits a linearly disposed thymine-Gd<sup>III</sup>-thymine structure (Figure 1 and Figure S1). **1** displays the first reported crystal structure based on gadolinium and thymine and is a suitable candidate for contrast-enhanced magnetic resonance (MR) imaging applications.

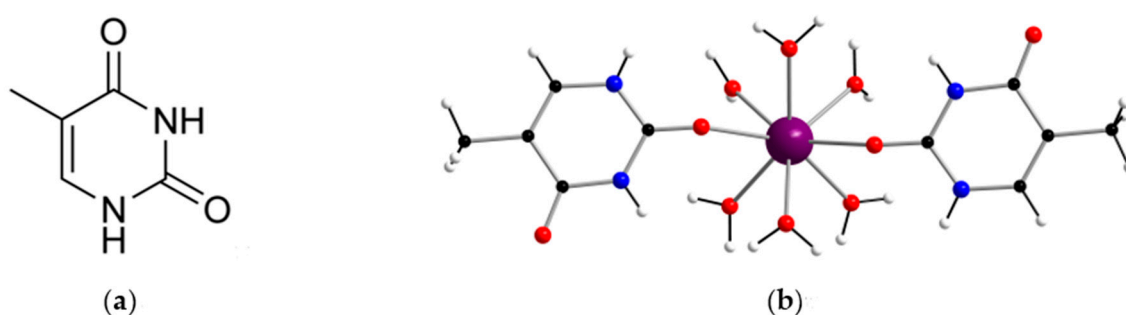


**Figure 1.** (a) Molecular structure of the thymine nucleobase (thy); (b) Mononuclear  $[Gd(\text{thy})_2(\text{H}_2\text{O})_6]^{3+}$  complex in **1**.  $\text{ClO}_4^-$  anions and non-coordinated water molecules have been omitted for clarity. Color code: purple, Gd; red, O; blue, N; black, C; white, H.

## 2. Results and Discussion

### 2.1. Synthetic Procedure

Compound **1** was prepared from a mixture of  $\text{Gd}_2\text{O}_3$  and thymine, which reacted in an aqueous suspension acidulated with perchloric acid, and was stirred at 60 °C for 1 h. The resulting solution was left to evaporate at room temperature for 1 week, thus generating colorless parallelepipeds of **1**. Once synthesized, **1** is air-stable over a period of several days. In order to study its stability further, electronic absorption spectra of **1** were collected both in solid state and in aqueous solution (Figure 2 and Figure S2). Remarkably, the two spectra show the same absorption bands and different ones to that of the free thymine ligand (Figure S2), with this fact indicating the stability of **1** in aqueous solution (Figure 2a). SEM-EDAX analysis gave a molar ratio of 1:3 for the Gd/Cl relation in **1** (Figure 2b).

### 2.2. IR Spectroscopy

The infrared spectra of **1** and free thymine ligand are given in Figure S3. The infrared spectrum of thymine has been studied in detail in previous works [21,22], nevertheless, it has been included here just for comparison. The most interesting feature that is observed are the main vibrational bands associated to the two C=O groups, whose values for the free thymine ligand are 1735 and 1679  $\text{cm}^{-1}$ , respectively [21,22]. For **1**, these vibrational bands are observed at 1747 and 1679  $\text{cm}^{-1}$  (Figure S3), which is consistent with the coordination of the ligand through of only one C=O group [23].

The main vibrational bands associated to perchlorate anion are observed at 1145, 1112, and 1089  $\text{cm}^{-1}$ , which indicate the presence of this anion counterbalancing the positive charges of the cationic  $[Gd(\text{thy})_2(\text{H}_2\text{O})_6]^{3+}$  complex of **1** (Figure S3).

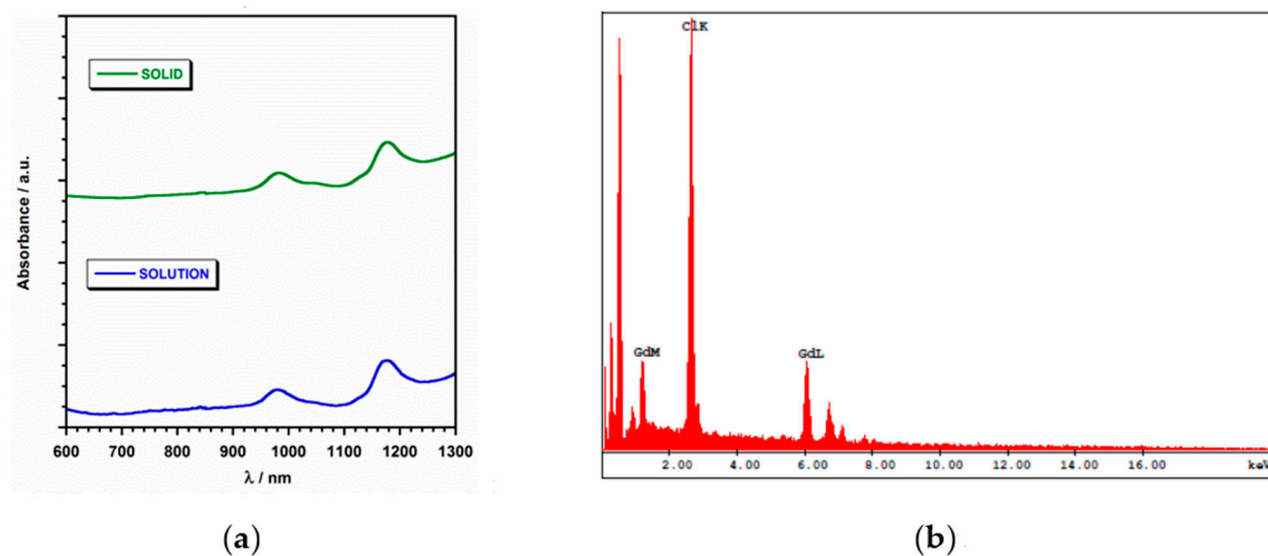


**Figure 2.** (a) Electronic absorption spectra from samples of compound **1** in solid state (top) and in aqueous solution (bottom); (b) SEM-EDAX spectrum for compound **1**.

### 2.3. Description of the Crystal Structure

Crystal data and structure refinement parameters are summarized in Table 1. Compound **1** crystallizes in the monoclinic system with space group  $P2_1/c$ . Its crystal structure is made up of  $[\text{Gd}(\text{thy})_2(\text{H}_2\text{O})_6]^{3+}$  cations,  $\text{ClO}_4^-$  anions, and water molecules of crystallization, which are held together mainly by electrostatic forces and H-bonding interactions. A  $[\text{Gd}(\text{thy})_2(\text{H}_2\text{O})_6]^{3+}$  cation, three  $\text{ClO}_4^-$  anions, and two non-coordinating water molecules are present in the asymmetric unit of **1**.

**Table 1.** Summary of the crystal data and structure refinement parameters for **1**.

Compound	<b>1</b>
CCDC	2009091
Formula	$\text{C}_{10}\text{H}_{28}\text{N}_4\text{O}_{24}\text{Cl}_3\text{Gd}$
$M_r/\text{g mol}^{-1}$	851.96
Crystal system	Monoclinic
Space group	$P2_1/c$
$a/\text{Å}$	13.192 (1)
$b/\text{Å}$	9.901 (1)
$c/\text{Å}$	20.985 (1)
$\alpha/^\circ$	90
$\beta/^\circ$	95.18 (1)
$\gamma/^\circ$	90
$V/\text{Å}^3$	2729.8 (2)
Z	4
$D_c/\text{g cm}^{-3}$	2.073
$\mu (\text{Mo} - \text{K}\alpha)/\text{mm}^{-1}$	2.832
Goodness-of-fit on $F^2$	1.081
$R_1 [I > 2\sigma(I)]/\text{all}$	0.0280/0.0325
$wR_2 [I > 2\sigma(I)]/\text{all}$	0.0703/0.0733

The  $\text{Gd}^{\text{III}}$  ion in **1** is eight-coordinate and bonded to eight oxygen atoms, two oxygen atoms from carbonyl groups of two neutral thymine ligands, and six oxygen atoms of six water molecules (Figure 1). Given the neutral nature of the thymine molecule, coordination through the O(1) and O(3) atoms is expected (Figures S1 and S4). The average value of the Gd-O bond lengths [2.381(1) Å] is somewhat shorter than that of the Gd-O<sub>water</sub> bond lengths [2.390(1) Å] (Table S1). The O-Gd-O bond angles show values covering the

range of 70.24(6)–148.57(7)°. These values are in agreement with those reported for other species with a similar Gd<sup>III</sup> environment [24–26]. In **1**, the thymine molecules are planar and form an angle between them of ca. 7.8(1)° with an intramolecular thymine–thymine separation of ca. 4.08 Å, which corresponds to the O(1)⋯O(3) distance. The C–C, C–N, and C–O bond lengths agree with those found in the literature for the thymine molecule (Table S1) [27].

In the crystal packing of **1**, adjacent [Gd(thy)<sub>2</sub>(H<sub>2</sub>O)<sub>6</sub>]<sup>3+</sup> cations are connected through H-bonding interactions that occur between thymine pairs, linking them into chains [N(3)⋯O(4a) = 2.763(3) Å and O(2)⋯N(10a) = 2.785(3) Å; (a) = x, y – 1, z], which grow along the *b* crystallographic axis (Figure S5). These chains are separated from each other through perchlorate anions, which interact with coordinated water molecules by means of H-bonding interactions involving the following set of atoms: O(3w)⋯O(11b) [2.944(3) Å; (b) = –x + 1, –y + 1, –z + 1], O(4w)⋯O(10b) [2.870(3) Å], O(4w)⋯O(15c) [2.847(3) Å; (c) = –x + 1, y – 1/2, –z + 3/2], and O(5w)⋯O(12) [2.713(3) Å] (Figure 3). The chains based on [Gd(thy)<sub>2</sub>(H<sub>2</sub>O)<sub>6</sub>]<sup>3+</sup> cations are arranged forming a herringbone type structure, generating thymine planes that exhibit an angle of ca. 64(1)° (Figure 3b). The shortest Gd⋯Gd separation is 8.256(1) Å [Gd(1)⋯Gd(1d) distance; (d) = –x, –y + 1, –z + 1]. A supramolecular network is generated by additional H-bonding interactions involving coordinated and non-coordinated water molecules, along with weaker C–H⋯O interactions [the average value of the C⋯O distance being ca. 3.34 Å for C(13)⋯O(16), C(6)⋯O(5d) and C(13)⋯O(11e); (e) = –x + 1, y + 1/2, –z + 3/2], which contribute to stabilizing the crystal structure in **1** (Table 2).

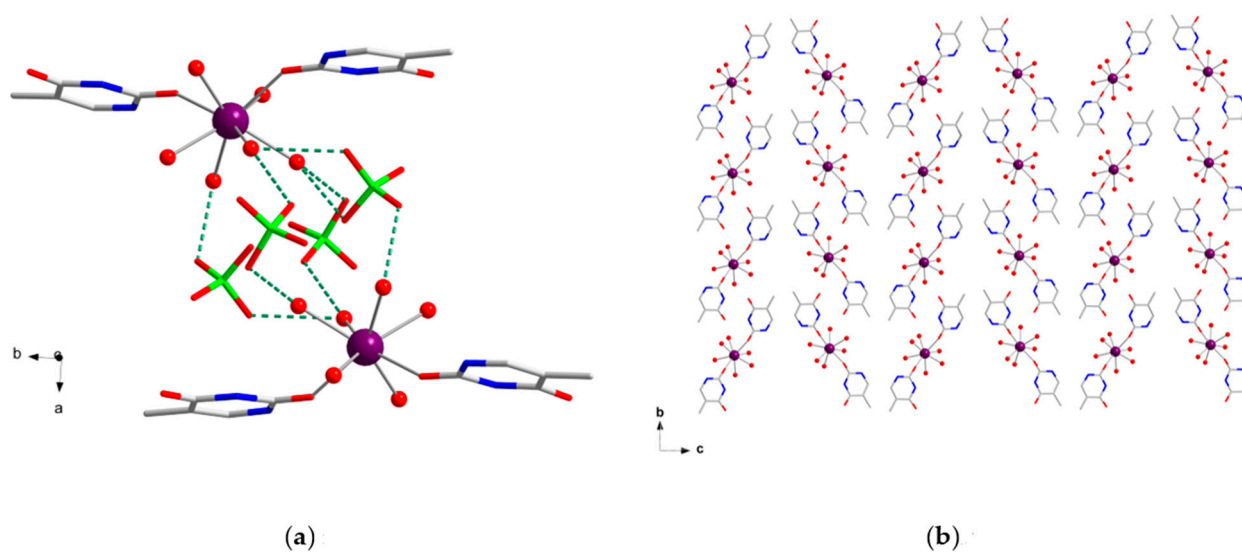


**Figure 3.** (a) View along the crystallographic *c* axis of the H-bonding interactions (green dashed lines) between perchlorate anions (capped sticks model) and [Gd(thy)<sub>2</sub>(H<sub>2</sub>O)<sub>6</sub>]<sup>3+</sup> cations in **1**. For the sake of clarity, H atoms are omitted and only coordinated water molecules are shown. Color code: purple, Gd; green, Cl; red, O; blue, N; grey, C; (b) View along the crystallographic *a* axis of the herringbone type structure of **1**. H atoms, perchlorate anions, and non-coordinating water molecules have been omitted for clarity. Color code: purple, Gd; red, O; blue, N; grey, C.

To further analyze the coordination environment and geometry of the Gd<sup>III</sup> ion in **1**, the SHAPE program was used [28]. In **1**, the single Gd<sup>III</sup> ion exhibits a coordination number (CN) equal to 8. For Gd(1), a value of 0.307 was obtained and associated with a square antiprism (SAPR) geometry, the next and closer computed value being 1.733, which was assigned to a biaugmented trigonal prism (BTTPR) geometry (Table 3). Hence, these calculated values allow us to assign the D<sub>4d</sub> symmetry to the Gd(1) ion in complex **1** (Table 3).

**Table 2.** Selected hydrogen-bonding interactions in **1**<sup>a</sup>.

D-H⋯A	D-H/Å	H⋯A/Å	D⋯A/Å	(DHA) <sup>o</sup>
N(1)-H(1)⋯O(8f)	0.880	2.12(1)	2.982(1)	165.4(1)
N(3)-H(3)⋯O(4a)	0.880	1.89(1)	2.763(1)	175.6(1)
N(10)-H(10)⋯O(2g)	0.880	1.92(1)	2.785(1)	168.7(1)
O(1w)-H(1wA)⋯O(7)	0.951	2.05(1)	2.986(1)	168.4(1)
O(1w)-H(1wB)⋯O(4a)	0.953	1.77(1)	2.677(1)	159.1(1)
O(2w)-H(2wA)⋯O(2g)	0.948	1.75(1)	2.691(1)	169.2(1)
O(3w)-H(3wA)⋯O(11b)	0.953	2.07(1)	2.944(1)	151.0(1)
O(3w)-H(3wB)⋯O(7wf)	0.950	1.76(1)	2.660(1)	156.0(1)
O(4w)-H(4wA)⋯O(10b)	0.951	2.01(1)	2.870(1)	149.4(1)
O(4w)-H(4wB)⋯O(15c)	0.953	1.944(1)	2.847(1)	157.4(1)
O(5w)-H(5wA)⋯O(12)	0.950	1.77(1)	2.713(1)	169.2(1)
O(5w)-H(5wB)⋯O(14)	0.950	1.87(1)	2.810(1)	169.1(1)
O(6w)-H(6wA)⋯O(9h)	0.951	2.27(1)	2.939(1)	126.9(1)
O(6w)-H(6wA)⋯O(7wf)	0.951	2.31(1)	2.986(1)	127.4(1)
O(6w)-H(6wB)⋯O(8w)	0.953	1.75(1)	2.694(1)	171.9(1)
O(7w)-H(7wB)⋯O(8wc)	0.961	1.91(1)	2.896(1)	172.5(1)
O(8w)-H(8wA)⋯O(13)	0.954	1.91(1)	2.855(1)	170.8(1)
O(8w)-H(8wB)⋯O(15e)	0.953	1.92(1)	2.846(1)	163.9(1)

<sup>a</sup> Symmetry codes: (a) =  $x, y - 1, z$ ; (b) =  $-x + 1, -y + 1, -z + 1$ ; (c) =  $-x + 1, y - 1/2, -z + 3/2$ ; (e) =  $-x + 1, y + 1/2, -z + 3/2$ ; (f) =  $x, -y + 3/2, z - 1/2$ ; (g) =  $x, y + 1, z$ ; (h) =  $-x + 1, -y + 2, -z + 1$ .

**Table 3.** Selected values for possible geometries with coordination number (CN) equal to 8 obtained through the SHAPE program and from the structural parameters of complex **1**<sup>a</sup>.

HPY	HBPY	CU	SAPR	TDD	JGBF	JETBPY	BTPR	JSD	TT
23.392	16.322	9.171	0.307	1.913	15.656	28.471	1.733	4.830	10.015

<sup>a</sup> HPY: heptagonal pyramid ( $C_{7v}$ ); HBPY: hexagonal bipyramid ( $D_{6h}$ ); CU: cube ( $O_h$ ); SAPR: square antiprism ( $D_{4d}$ ); TDD: triangular dodecahedron ( $D_{2d}$ ); JGBF: Johnson gyrobifastigium ( $D_{2d}$ ); JETBPY: Johnson elongated triangular bipyramid ( $D_{3h}$ ); BTPR: biaugmented trigonal prism ( $C_{2v}$ ); JSD: snub disphenoid ( $D_{2d}$ ); TT: triakis tetrahedron (Td).

#### 2.4. Analysis of the Hirshfeld Surfaces

Hirshfeld surfaces of the cationic  $[Gd(thy)_2(H_2O)_6]^{3+}$  complex were calculated, and its closer intermolecular interactions were analyzed through the *CrystalExplorer* program [29,30]. These surfaces were mapped taking into account the distance from a point on the surface to the nearest atom outside ( $d_e$ ) and inside ( $d_i$ ) the surface. To overcome limitations related to the size of atoms, a normalized contact distance ( $d_{norm}$ ) was also considered [29,30]. For compound **1**, Hirshfeld surfaces are shown in Figure 4 and Figure S6, where the shorter contacts are displayed using red color [31]. Intermolecular O⋯H contacts between water molecules and between water molecules and carbonyl groups of the thymine molecules are the main interactions detected on the Hirshfeld surface (Figure 4 and Figure S6). The most important O⋯H contacts are those involving H-bonds between non-coordinated and coordinated water molecules, which are approximately 48% of the complete fingerprint plot, whereas the O⋯H interactions involving non-coordinated water molecules and carbonyl groups are highlighted from the full fingerprint as ca. 19% of the plot. Finally, additional N⋯H contacts involving non-coordinated water molecules and N-H groups of the thymine molecules only cover approximately 2% of the fingerprint plot (Figure 4).

#### 2.5. Magnetic Properties

Dc magnetic susceptibility measurements were carried out on a freshly prepared microcrystalline sample of **1** in the 2–300 K temperature range and under an external magnetic field of 0.5 T. The  $\chi_M T$  vs.  $T$  plot ( $\chi_M$  being the molar magnetic susceptibility per  $Gd^{III}$  ion) for compound **1** is given in Figure 5. At room temperature, the  $\chi_M T$  value is ca.  $7.89 \text{ cm}^3 \text{ mol}^{-1} \text{ K}$ , which is very close to that expected for a magnetically isolated  $Gd^{III}$  ion ( $4f^7$  ion with  $g_{Gd} = 2.0$ ,  $S_{Gd} = 7/2$  and  $L_{Gd} = 0$ ), that is,  $7.88 \text{ cm}^3 \text{ mol}^{-1} \text{ K}$  [26,32]. Upon



cooling, the  $\chi_M T$  value approximately follows the Curie law to ca. 25 K with decreasing temperature, before  $\chi_M T$  decreases, reaching a minimum value of ca.  $7.21 \text{ cm}^3 \text{ mol}^{-1} \text{ K}$  at 2 K. The decrease of the  $\chi_M T$  value observed for complex **1** would likely be assignable to intermolecular interactions and/or very small zero-field splitting (ZFS) effects [32].

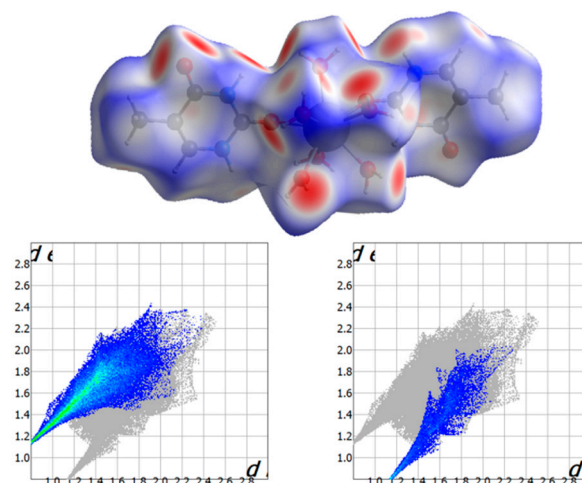


**Figure 4.** (Top) Hirshfeld surface mapped with  $d_{\text{norm}}$  function for **1**; (bottom) Fingerprint plots for **1**; (bottom, left) Intermolecular O...H contacts between non-coordinated and coordinated water molecules are highlighted from the full fingerprint; (bottom, right) Non-coordinated water molecules and thymine carbonyl groups are highlighted from the full fingerprint.

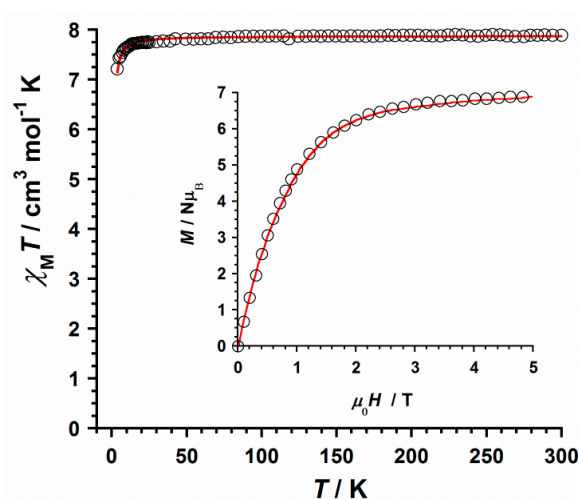


**Figure 5.**  $\chi_M T$  vs.  $T$  plot obtained for compound **1**. The inset shows the field dependence of the molar magnetization ( $M$ ) plot at 2.0 K for **1**. The solid red lines represent the best fit of the experimental data.

To analyze the magnetic behavior and fit the experimental data of the  $\chi_M T$  vs.  $T$  plot for complex **1**, the theoretical expression for the magnetic susceptibility of a single and isotropic  $S_{\text{Gd}} = 7/2$  center was used [ $\chi_M = (N\mu_B^2 g_{\text{Gd}}^2 / 3k_B) S_{\text{Gd}}(S_{\text{Gd}} + 1) / (T - \Theta)$ ] [25]. Due to possible intermolecular interactions that can take place in **1**, a  $\Theta$  parameter was also included in this expression. The best least-squares fit gave the parameters  $g_{\text{Gd}} = 2.008$  (1) and  $\Theta = -0.039$  (1) K with  $R = 1.9 \times 10^{-5}$  for **1** [ $R$  being the agreement factor defined as  $\sum_i [(\chi_M T)_i^{\text{obs}} - (\chi_M T)_i^{\text{calcd}}]^2 / [(\chi_M T)_i^{\text{obs}}]^2$ ].

Field dependence of the molar magnetization ( $M$ ) plot for **1** at 2 K is given in the inset of Figure 5. This plot exhibits a continuous increase of  $M$  with the applied magnetic field, showing a maximum value of  $M$  obtained for **1** (ca.  $6.92 \mu_B$ ) at 5.0 T, which is as expected for a mononuclear  $\text{Gd}^{\text{III}}$  complex [25]. The experimental data of the  $M$  vs.  $H$  plot were

close to the Brillouin curve generated, with values of  $g$  and  $S$  of 2.0 and  $7/2$ , respectively (Figure 5) [32].

### 2.6. MR Imaging Phantom Studies

The relaxometric properties of compound **1** as a potential high-field MR imaging contrast agent were evaluated [33]. Thirteen samples of **1** were prepared in physiological serum with concentrations covering the range of 0.0–3.2 mM and were measured on a clinical MR scanner (Achieva 3T TX, Philips Healthcare, Best, The Netherlands) by using the volumetric head eight channels SENSE coil (Figure 6 and Figure S7).

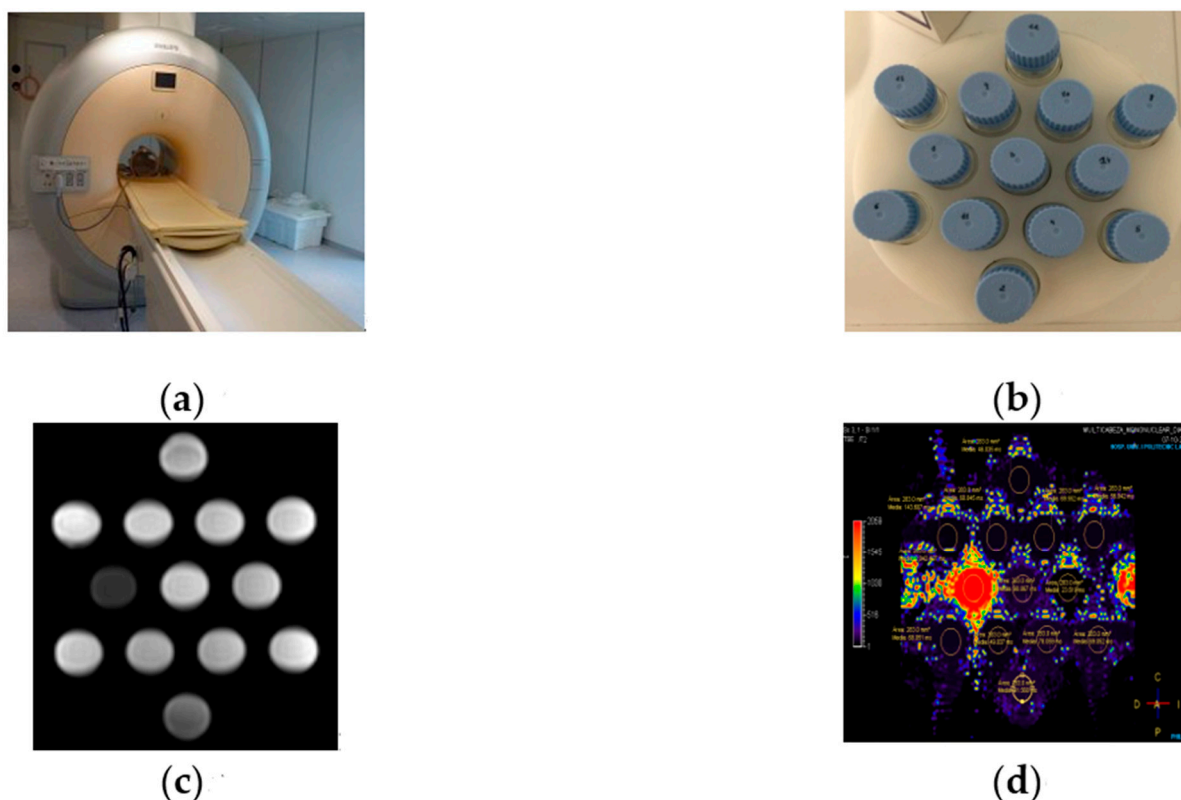


**Figure 6.** (a) MR imaging scanner (Philips Achieva 3T); (b) Samples of **1** prepared in physiological serum with concentrations covering the range of 0.0–3.2 mM; (c) MR images of the tube phantoms of **1**; (d)  $T_2$  parametric map analysis.

The relaxation rate, denoted by  $R$  (and expressed in  $s^{-1}$ ), was obtained for each concentration through the calculation of the corresponding relaxation time  $T$ .  $R_1$  was obtained by calculating the  $T_1$  time from FFE sequences with  $2^\circ$ ,  $5^\circ$ ,  $10^\circ$ ,  $15^\circ$ ,  $25^\circ$ , and  $45^\circ$  flip angles, whereas  $r_2$  and  $r_2^*$  values were obtained after calculating  $T_2$  and  $T_2^*$  relaxation times from TSE and GRE sequences with 32 echo times each,  $TE_1 = 10$  ms,  $\Delta TE = 10$  ms and  $TE_1 = 0.9$  ms,  $\Delta TE = 0.7$  ms, respectively [34]. Thus, the longitudinal relaxivity ( $r_1$ ) of **1** at 3 T was determined to be  $16.1 \text{ mM}^{-1}\text{s}^{-1}$ , whereas the transversal relaxivities  $r_2$  and  $r_2^*$  values were  $13.5$  and  $14.5 \text{ mM}^{-1}\text{s}^{-1}$ , respectively (Figures 7 and 8). These results show relaxivity values for **1** that are much higher than those of commercial MR imaging contrast agents currently employed on 3 T equipment [33], such as Magnevist, Gadovist, Prohance, Multihance, Dotarem, and Omniscan, among others [34], which makes **1** potentially useful. The fact that the  $\text{Gd}^{\text{III}}$  ion in **1** exhibits a higher number of coordinate water molecules than the typical commercial contrast agents would enhance, at least in part, the common relaxivity values reported for these commercial contrast agents [34].

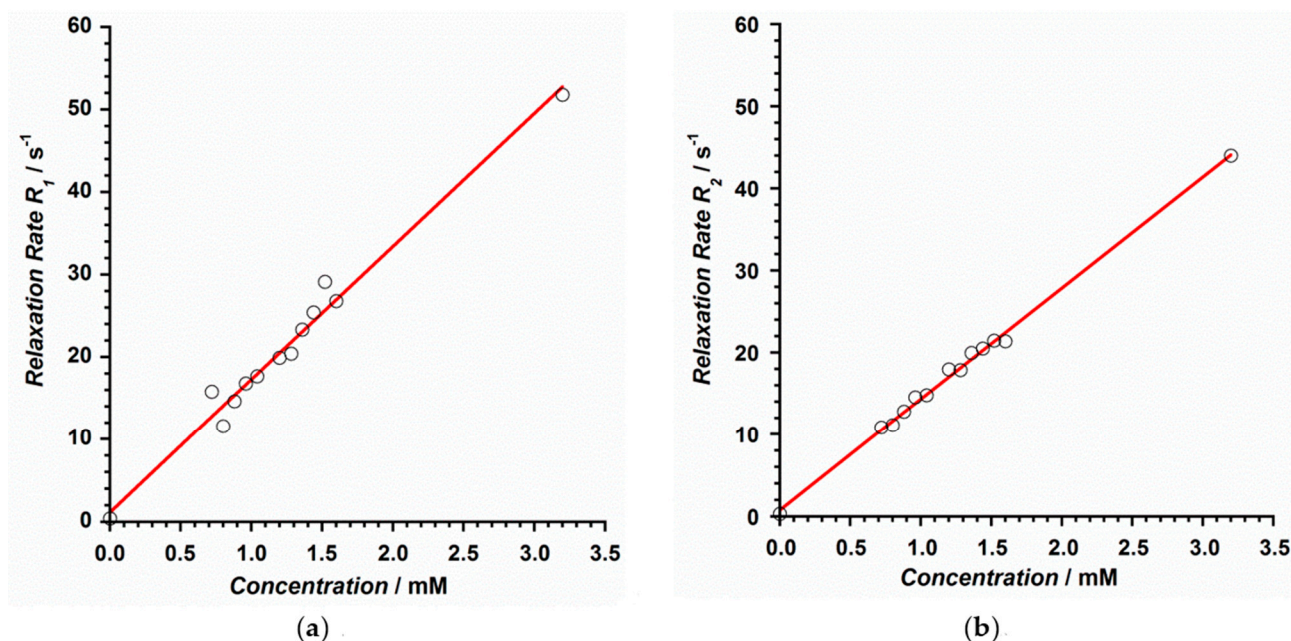


**Figure 7.** Relaxation rate vs. contrast concentration plot obtained for the relaxivities  $r_1$  (a) and  $r_2$  (b) of compound 1. The red line represents the best linear fit of the experimental data.

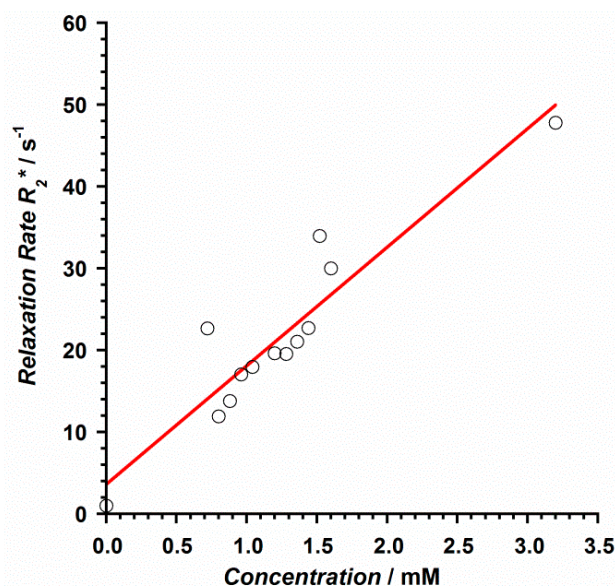


**Figure 8.** Relaxation rate vs. contrast concentration plot obtained for the relaxivity  $r_2^*$  of compound 1. The red line represents the best linear fit of the experimental data.

### 3. Materials and Methods

#### 3.1. Reagents and Instruments

All of the manipulations were performed under aerobic conditions. All the commercial chemicals were used as received. CAUTION: Although no problems were encountered in this work, care should be taken when using the potentially explosive perchlorate anion ( $\text{ClO}_4^-$ ).

Elemental analyses (C, H, N) and X-ray microanalysis were performed by the Central Service for the Support to Experimental Research (SCSIE) at the University of Valencia. Scanning electron microscopy (SEM) images and results were obtained from a Hitachi S-4800 field emission scanning electron microscope (Hitachi Ltd., Tokyo, Japan). The electronic absorption spectra of **1** and thymine were measured at room temperature in



a Jasco V-670 UV-vis-NIR spectrophotometer (Jasco Ltd., Tokyo, Japan) in the range of 600 to 1400 nm. Infrared spectra (IR) of **1** and thymine were recorded with a PerkinElmer Spectrum 65 FT-IR spectrometer (PerkinElmer Inc., Waltham, USA) in the range of 400 to 4000  $\text{cm}^{-1}$ . Variable-temperature, solid-state direct current (DC) magnetic susceptibility data down to 2.0 K were collected on a Quantum Design MPMS-XL SQUID magnetometer (Quantum Design, Inc., San Diego, CA, USA) equipped with a 5 T DC magnet. The experimental magnetic data were corrected for the diamagnetic contributions of the constituent atoms and also for the sample holder. MR data were collected on a Philips Achieva 3T clinical scanner (Philips Healthcare, Best, The Netherlands) with a volumetric head eight channels SENSE coil at La Fe University and Polytechnic Hospital.

### 3.2. Preparation of Compound

#### Synthesis of $[\text{Gd}(\text{thy})_2(\text{H}_2\text{O})_6](\text{ClO}_4)_3 \cdot 2\text{H}_2\text{O}$ (**1**)

A mixture of  $\text{Gd}_2\text{O}_3$  (0.091 g, 0.25 mmol) and thymine (0.063 g, 0.50 mmol) in an aqueous suspension (5 mL) was acidulated with perchloric acid (1.0 mL, 2 M) and was stirred and heated at 60 °C for 1 h. The resulting solution was left to evaporate at room temperature for 1 week. Colorless parallelepipeds were obtained and were suitable for single-crystal X-ray diffraction studies. Yield: ca. 45%. Anal. Calcd. for  $\text{C}_{10}\text{H}_{24}\text{N}_4\text{O}_{22}\text{Cl}_3\text{Gd}$ : C, 14.7; H, 3.0; N, 6.9. Found: C, 14.5; H, 3.0; N, 6.8. SEM-EDAX: a molar ratio of 1:3 for Gd/Cl was found for **1**. IR (KBr pellet/ $\text{cm}^{-1}$ ): peaks were observed at 3399 (br), 3218 (m), 3063 (m), 2928 (m), 2813 (m), 1747 (s), 1679 (vs), 1635 (m), 1483 (w), 1449 (m), 1427 (w), 1383 (m), 1246 (m), 1205 (m), 1145 (vs), 1112 (vs), 1089 (vs), 935 (m), 835 (m), 815 (m), 760 (m), 744 (m), 627 (vs), 560 (m), 477 (m), 432 (m).

### 3.3. X-ray Data Collection and Structure Refinement

X-ray diffraction data from a single crystal of **1** with dimensions  $0.34 \times 0.12 \times 0.05 \text{ mm}^3$  was collected on a Bruker D8 Venture diffractometer (Bruker, Billerica, MA, USA) with graphite-monochromated  $\text{Mo-K}_\alpha$  radiation ( $\lambda = 0.71073 \text{ \AA}$ ). The structures were solved by standard direct methods and subsequently completed by Fourier recycling by using the SHELXTL software packages. The obtained model was refined with version 2018/1 of SHELXL against  $F^2$  on all data by full-matrix least squares [35]. All non-hydrogen atoms were anisotropically refined, whereas the hydrogen atoms of the thymine molecules were set in calculated positions and refined isotropically by using the riding model. The graphical manipulations were performed with the DIAMOND program [36]. The CCDC code for **1** is 2009091.

## 4. Conclusions

In summary, the preparation, crystal structure, magnetic properties, and MR imaging phantom studies of a novel  $\text{Gd}^{\text{III}}$  complex based on the thymine nucleobase, of formula  $[\text{Gd}(\text{thy})_2(\text{H}_2\text{O})_6](\text{ClO}_4)_3 \cdot 2\text{H}_2\text{O}$  (**1**) [thy = thymine], have been reported. **1** displays the first reported crystal structure based on gadolinium and thymine. Furthermore, **1** exhibits high relaxivity values and, therefore, can be considered a suitable candidate for further developments and MR analysis. Given that most of the thymine-containing complexes have been reported with this ligand in the form of thyminate anion, we presented in this work a singular strategy to prepare lanthanide compounds where the thymine molecule acts as a neutral ligand toward the metal ion. Further investigations dealing with the synthesis and characterization of this type of lanthanide complexes are now in progress in our group, incorporating other 4f ions and similar biomolecules.

**Supplementary Materials:** The following are available online at <https://www.mdpi.com/article/10.3390/ijms22094586/s1>, X-ray crystallographic data in CIF format for compound **1**, Figures S1–S7, and Table S1.

**Author Contributions:** L.M.-B. and J.M.-L. conceived the idea and obtained funding for the project. M.O.-A. carried out the synthesis, the UV-vis-NIR measurements, the X-ray data collection, and the calculations through the SHAPE and CrystalExplorer programs. S.G.-C. and A.T.-E. performed the acquisition of the MR images, the phantoms, and the parametric map analysis. A.T.-E., L.M.-B., I.C., and J.M.-L. analyzed the data associated with all the experiments and wrote the manuscript, which all authors discussed and commented on. All authors have read and agreed to the published version of the manuscript.

**Funding:** This research was funded by the VLC-BIOMED Program (2017) of the University of Valencia [Subprogram A “Ayudas para el fomento de acciones preparatorias coordinadas UV-HUP/IIS La Fe”, Project 11-2017-A] and the Spanish Ministry of Science, Innovation and Universities [Project PID2019-109735GB-I00 and CEX2019-000919-M (Excellence Unit “María de Maeztu”)].

**Institutional Review Board Statement:** Not applicable.

**Informed Consent Statement:** Not applicable.

**Data Availability Statement:** The reported data are available on request from the corresponding author.

**Acknowledgments:** The authors thank Nicolás Moliner for assistance in SQUID measurements. M.O.-A. and J.M.-L. thank the Spanish “FPI fellowships” and “Ramón y Cajal” Programmes, respectively.

**Conflicts of Interest:** The authors declare no conflict of interest.

## References

1. Lippert, B.; Sanz Miguel, P.J. The renaissance of metal–pyrimidine nucleobase coordination chemistry. *Acc. Chem. Res.* **2016**, *49*, 1537–1545. [[CrossRef](#)] [[PubMed](#)]
2. Somerville, R.L. *Encyclopedia of Genetics*; Academic Press: San Diego, CA, USA, 2001; pp. 1965–1966.
3. Park, H.J.; Zhang, K.; Ren, Y.; Nadji, S.; Sinha, N.; Taylor, J.-S.; Kang, C.H. Crystal structure of a DNA decamer containing a cis-syn thymine dimer. *Proc. Natl. Acad. Sci. USA* **2002**, *99*, 15965–15970. [[CrossRef](#)]
4. Sakate, M.; Hosoda, H.; Suzuki, T. Crystal structures of bis-[2-(pyridin-2-yl)phenyl- $\kappa^2N,C^1$ ]rhodium(III) complexes containing an acetonitrile or monodentate thymine(1–) ligand. *Acta Cryst.* **2016**, *E72*, 543–547. [[CrossRef](#)] [[PubMed](#)]
5. Vegas, V.G.; Lorca, R.; Latorre, A.; Hassanein, K.; Gómez-García, C.J.; Castillo, O.; Somoza, A.; Zamora, F.; Amo-Ochoa, P. Copper(II)-thymine coordination polymer nanoribbons as potential oligonucleotide nanocarriers. *Angew. Chem. Int. Ed.* **2017**, *56*, 987–991. [[CrossRef](#)] [[PubMed](#)]
6. Correa, R.S.; Freire, V.; Barbosa, M.I.F.; Bezerra, D.P.; Bomfim, L.M.; Moreira, D.R.M.; Soares, M.B.P.; Ellena, J.; Batista, A.A. Ru(II)–thymine complexes: New metallodrug candidates against tumor cells. *New J. Chem.* **2018**, *42*, 6794–6802. [[CrossRef](#)]
7. Silva, S.L.R.; Baliza, I.R.S.; Dias, R.B.; Sales, C.B.S.; Rocha, C.A.G.; Soares, M.B.P.; Correa, R.S.; Batista, A.A.; Bezerra, D.P. Ru(II)-thymine complex causes DNA damage and apoptotic cell death in human colon carcinoma HCT116 cells mediated by JNK/p38/ERK1/2 via a p53-independent signaling. *Sci. Rep.* **2019**, *9*, 11094. [[CrossRef](#)]
8. De, H.; Paul, A.; Datta, A. Theoretical study of Au<sub>4</sub> thymine, Au<sub>20</sub> and Ag<sub>20</sub> uracil and thymine complexes for surface enhanced Raman scattering. *Comput. Theor. Chem.* **2017**, *1111*, 1–13. [[CrossRef](#)]
9. Kondo, J.; Yamada, T.; Hirose, C.; Okamoto, I.; Tanaka, Y.; Ono, A. Crystal structure of metallo DNA duplex containing consecutive Watson-Crick-like T-Hg(II)-T base pairs. *Angew. Chem. Int. Ed.* **2014**, *24*, 2385–2388. [[CrossRef](#)]
10. Yamaguchi, H.; Šebera, J.; Kondo, J.; Oda, S.; Komuro, T.; Kawamura, T.; Dairaku, T.; Kondo, Y.; Okamoto, I.; Ono, A.; et al. The structure of metallo-DNA with consecutive thymine–Hg<sup>II</sup>–thymine base pairs explains positive entropy for the metallo base pair formation. *Nucleic Acids Res.* **2014**, *42*, 4094–4099. [[CrossRef](#)]
11. Kuriyama, M.; Haruta, K.; Dairaku, T.; Kawamura, T.; Kikkawa, S.; Inamoto, K.; Tsukamoto, H.; Kondo, Y.; Torigoe, H.; Okamoto, I.; et al. Hg<sup>2+</sup>-trapping beads: Hg<sup>2+</sup>-specific recognition through thymine–Hg(II)–thymine base pairing. *Chem. Pharm. Bull.* **2014**, *62*, 709–712. [[CrossRef](#)]
12. Li, L.; Wen, Y.; Xu, L.; Xu, Q.; Song, S.; Zuo, X.; Yan, J.; Zhang, W.; Liu, G. Development of mercury (II) ion biosensors based on mercury-specific oligonucleotide probes. *Biosens. Bioelectron.* **2016**, *75*, 433–445. [[CrossRef](#)] [[PubMed](#)]
13. Chun, H.J.; Kim, S.; Han, Y.D.; Kim, D.W.; Kim, K.R.; Kim, H.S.; Kim, J.H.; Yoon, H.C. Water-soluble mercury ion sensing based on the thymine–Hg<sup>2+</sup>–thymine base pair using retroreflective Janus particle as an optical signaling probe. *Biosens. Bioelectron.* **2018**, *104*, 138–144. [[CrossRef](#)] [[PubMed](#)]
14. Kashima, A.; Sakate, M.; Ota, H.; Fuyuhiko, A.; Sunatsukia, Y.; Suzuki, T. Thymine(2–)-bridged cyclic tetranuclear rhodium(III) complexes formed by a template of a sodium, calcium or lanthanoid ion. *Chem. Commun.* **2015**, *51*, 1889–1892. [[CrossRef](#)] [[PubMed](#)]
15. Armentano, D.; Marino, N.; Mastropietro, T.F.; Martínez-Lillo, J.; Cano, J.; Julve, M.; Lloret, F.; De Munno, G. Self-assembly of a chiral carbonate- and cytidine-containing dodecanuclear Copper(II) Complex: A multiarm-supplied globular capsule. *Inorg. Chem.* **2008**, *47*, 10229–10231. [[CrossRef](#)] [[PubMed](#)]

16. Martínez-Lillo, J.; Mastropietro, T.F.; Lappano, R.; Madeo, A.; Alberto, M.E.; Russo, N.; Maggiolini, M.; De Munno, G. Rhenium(IV) compounds inducing apoptosis in cancer cells. *Chem. Commun.* **2011**, *47*, 5283–5285. [[CrossRef](#)]
17. Marino, N.; Armentano, D.; Mastropietro, T.F.; Julve, M.; De Munno, G.; Martínez-Lillo, J. Cubane-Type  $\text{Cu}^{\text{II}}_4$  and  $\text{Mn}^{\text{II}}_2\text{Mn}^{\text{III}}_2$  complexes based on pyridoxine: A versatile ligand for metal assembling. *Inorg. Chem.* **2013**, *52*, 11934–11943. [[CrossRef](#)]
18. Armentano, D.; Barquero, M.A.; Rojas-Dotti, C.; Moliner, N.; De Munno, G.; Brechin, E.K.; Martínez-Lillo, J. Enhancement of intermolecular magnetic exchange through halogen...halogen interactions in bisadeninium rhenium(IV) salts. *Cryst. Growth Des.* **2017**, *17*, 5342–5348. [[CrossRef](#)]
19. Orts-Arroyo, M.; Castro, I.; Lloret, F.; Martínez-Lillo, J. Field-induced slow relaxation of magnetisation in two one-dimensional homometallic dysprosium(III) complexes based on alpha- and beta-amino acids. *Dalton Trans.* **2020**, *49*, 9155–9163. [[CrossRef](#)]
20. Orts-Arroyo, M.; Castro, I.; Martínez-Lillo, J. Detection of Hypoxanthine from inosine and unusual hydrolysis of immunosuppressive drug azathioprine through the formation of a diruthenium(III) system. *Biosensors* **2021**, *11*, 19. [[CrossRef](#)] [[PubMed](#)]
21. Colarusso, P.; Zhang, K.-Q.; Guo, B.; Bernath, P.F. The infrared spectra of uracil, thymine, and adenine in the gas phase. *Chem. Phys. Lett.* **1997**, *269*, 39–48. [[CrossRef](#)]
22. Singh, J.S. FTIR and Raman spectra and fundamental frequencies of biomolecule: 5-Methyluracil (thymine). *J. Mol. Struct.* **2008**, *876*, 127–133. [[CrossRef](#)]
23. Azab, H.A.; Al-Deyab, S.S.; Anwar, Z.M.; El-Gawad, I.I.A.; Kamel, R.M. Comparison of the coordination tendency of amino acids, nucleobases, or mononucleotides toward the monomeric and dimeric lanthanide complexes with biologically important compounds. *J. Chem. Eng. Data* **2011**, *56*, 2613–2625. [[CrossRef](#)]
24. Guillou, O.; Bergerat, P.; Kahn, O.; Bakalbassis, E.; Boubekour, K.; Batail, P.; Guillot, M. Ferromagnetically coupled gadolinium(III)copper(II) molecular material. *Inorg. Chem.* **1992**, *31*, 110–114. [[CrossRef](#)]
25. Cañadillas-Delgado, L.; Fabelo, O.; Cano, J.; Ruiz-Pérez, C. *Magnetic Interactions in Oxo-Carboxylate Bridged Gadolinium(III) Complexes Synthesis, Crystal Structures and Magnetic Properties*; Nova Science Publishers, Inc.: Hauppauge, NY, USA, 2010.
26. Martínez-Lillo, J.; Cañadillas-Delgado, L.; Cano, J.; Lloret, F.; Julve, M.; Faus, J. A heteropentanuclear oxalato-bridged  $[\text{Re}^{\text{IV}}_4\text{Gd}^{\text{III}}]$  complex: Synthesis, crystal structure and magnetic properties. *Chem. Commun.* **2012**, *48*, 9242–9244. [[CrossRef](#)] [[PubMed](#)]
27. Portalone, G.; Bencivenni, L.; Colapietro, M.; Pieretti, A.; Ramondo, F. The Effect of hydrogen bonding on the structures of uracil and some methyl derivatives studied by experiment and theory. *Acta Chem. Scand.* **1999**, *53*, 57–68. [[CrossRef](#)]
28. Llundell, M.; Casanova, D.; Cirera, J.; Alemany, P.; Alvarez, S. *SHAPE 2.1*; Universitat de Barcelona: Barcelona, Spain, 2013.
29. Spackman, M.A.; Jayatilaka, D. Hirshfeld surface analysis. *CrystEngComm* **2009**, *11*, 19–32. [[CrossRef](#)]
30. Turner, M.J.; McKinnon, J.J.; Wolff, S.K.; Grimwood, D.J.; Spackman, P.R.; Jayatilaka, D.; Spackman, M.A. *Crystal Explorer 17*; University of Western Australia: Perth, Australia, 2017.
31. Orts-Arroyo, M.; Castro, I.; Lloret, F.; Martínez-Lillo, J. Molecular self-assembly in a family of oxo-bridged dinuclear ruthenium(IV) systems. *Cryst. Growth Des.* **2020**, *20*, 2044–2056. [[CrossRef](#)]
32. Kahn, O. *Molecular Magnetism*; VCH: New York, NY, USA, 1993.
33. Mousavi, B.; Chauvin, A.-S.; Moriggi, L.; Helm, L. Carbazole as linker for dinuclear gadolinium-based MRI contrast agents. *Eur. J. Inorg. Chem.* **2017**, 5403–5412. [[CrossRef](#)]
34. Rohrer, M.; Bauer, H.; Mintonovitch, J.; Requardt, M.; Weinmann, H.-J. Comparison of magnetic properties of MRI contrast media solutions at different magnetic field strengths. *Investig. Radiol.* **2005**, *40*, 715–724. [[CrossRef](#)] [[PubMed](#)]
35. Bruker Analytical X-ray Instruments. *SHELXL-2018/1*; Bruker Analytical X-ray Instruments: Madison, WI, USA, 2018.
36. Crystal Impact GbR. *DIAMOND 4.5.0*; Crystal Impact GbR: Bonn, Germany, 2018.



---

*ARTICLE 8*

*Field-induced slow relaxation of  
magnetisation in two  
one-dimensional homometallic  
dysprosium(III) complexes based  
on alpha- and beta-amino acids*



Cite this: *Dalton Trans.*, 2020, **49**, 9155

## Field-induced slow relaxation of magnetisation in two one-dimensional homometallic dysprosium(III) complexes based on alpha- and beta-amino acids†

Marta Orts-Arroyo, Isabel Castro,\* Francesc Lloret and José Martínez-Lillo \*

Two one-dimensional dysprosium(III) complexes based on  $\alpha$ -glycine (gly) and  $\beta$ -alanine ( $\beta$ -ala) amino acids, with the formula  $\{[\text{Dy}_2(\text{gly})_6(\text{H}_2\text{O})_4](\text{ClO}_4)_6 \cdot 5\text{H}_2\text{O}\}_n$  (**1**) and  $\{[\text{Dy}_2(\beta\text{-ala})_6(\text{H}_2\text{O})_4](\text{ClO}_4)_6 \cdot \text{H}_2\text{O}\}_n$  (**2**), have been synthesised and characterised structurally and magnetically. Both compounds crystallise in the triclinic system with the space group  $P\bar{1}$ . In **1**, two Dy<sup>III</sup> ions are eight-coordinate and bound to six oxygen atoms from six gly ligands and two oxygen atoms from two water molecules, showing different geometries (bicapped trigonal prism and square antiprism). In **2**, two Dy<sup>III</sup> ions are nine-coordinate and bound to seven oxygen atoms from six  $\beta$ -ala ligands and two oxygen atoms from two water molecules in the same geometry (capped square antiprism). In the crystal packing of both compounds, cationic  $\{[\text{Dy}_2(\text{L})_6(\text{H}_2\text{O})_4]^{6+}\}_n$  [L =  $\alpha$ -glycine (**1**) and  $\beta$ -alanine (**2**)] chains,  $\text{ClO}_4^-$  anions, and water molecules generate a network connected through H-bonding interactions. The study of the magnetic properties of **1** and **2** through dc magnetic susceptibility measurements reveals different magnetic behaviour **1** and **2**. In addition, ac magnetic susceptibility measurements show a field-induced slow relaxation of magnetisation for both compounds, pointing out that the single-molecule magnet (SMM) phenomenon occurs in both **1** and **2**.

Received 25th March 2020,  
Accepted 9th June 2020

DOI: 10.1039/d0dt01126f

rsc.li/dalton

## Introduction

Amino acids (AAs) are currently being used to prepare new technological materials. Natural and synthetic amino acid-based materials, due to their chemical versatility, are being investigated for several applications such as gas storage and separation,<sup>1</sup> proton conduction,<sup>2</sup> catalysis<sup>3</sup> and biomedicine.<sup>4</sup> The nature of the AA residue, its chirality, and its ability for hydrogen bond formation strongly influence the molecular self-assembly of many amino acid-based systems and the macroscopic properties of the final material.<sup>1–4</sup>

On the other hand, Dy<sup>III</sup> coordination chemistry has undergone rapid development in the multidisciplinary research field of molecular magnetism.<sup>5–11</sup> Dy<sup>III</sup> compounds have been widely studied as suitable candidates for obtaining single-molecule magnets (SMMs) due to the high magnetic anisotropy and magnetic moment that this 4f metal ion exhibits.<sup>12–16</sup> Indeed, the records for molecular blocking temperature ( $T_B$ ) and effective energy barrier ( $U_{\text{eff}}$ ) (as high as *ca.* 80 K and *ca.* 1541 cm<sup>-1</sup>, respectively) are currently held by mononuclear Dy<sup>III</sup> complexes. It has been found that the local

symmetries of Dy<sup>III</sup> ions such as  $C_{\infty v}$ ,  $D_{4d}$ ,  $D_{5h}$ ,  $D_{6d}$ , or  $D_{6h}$  can generate better SMMs with larger  $U_{\text{eff}}$  and  $T_B$  values.<sup>8,9,17–19</sup>

SMMs composed of dinuclear  $[\text{Dy}_2^{\text{III}}]$  units are also found to be quite interesting as candidates to achieve high effective energy barriers, besides magnetic anisotropy, because of the possible ferromagnetic exchange interaction that can take place between the involved spin centres,<sup>20</sup> with the intramolecular Dy...Dy distance and the relative orientation of the Dy<sup>III</sup> anisotropy axes being highly investigated parameters.<sup>21,22</sup>

During the last two decades, many examples of SMMs based on dinuclear Dy<sup>III</sup> complexes have been studied from a magnetism point of view.<sup>23–36</sup> Nevertheless, one-dimensional Dy<sup>III</sup> complexes showing slow relaxation of magnetisation have been much less explored.<sup>22,37–42</sup>

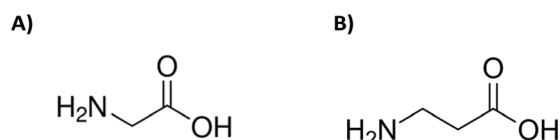
In the literature, there exist only two magnetostructural studies based on homometallic Dy<sup>III</sup> compounds and AAs.<sup>43,44</sup> In the first one, a family of four pentanuclear  $[\text{Dy}_5(\text{OH})_5(\alpha\text{-AA})_4(\text{Ph}_2\text{acac})_6]$  complexes ( $\alpha\text{-AA}$  = D-PhGly, L-Pro, L-Trp, and Ph<sub>2</sub>Gly; Ph<sub>2</sub>acac = dibenzoylmethanide) showing SMM behaviour was reported.<sup>43</sup> The second one deals with a 3D compound of the formula  $\{[\text{Dy}_4(\text{OH})_4(\text{asp})_3(\text{H}_2\text{O})_8](\text{ClO}_4)_2 \cdot 10\text{H}_2\text{O}\}_n$  that was obtained with aspartic acid and that exhibits weak anti-ferromagnetic coupling between the involved Dy<sup>III</sup> ions.<sup>44</sup>

In this context, we have focused our research work on Dy<sup>III</sup> and glycine, the simplest amino acid, and on  $\beta$ -alanine that has the amino group at the  $\beta$ -position from the carboxylate group (Scheme 1).

Instituto de Ciencia Molecular (ICMol), Universitat de València, c/Catedrático José Beltrán 2, 46980 Paterna, Valencia, Spain. E-mail: f.jose.martinez@uv.es

† Electronic supplementary information (ESI) available: Fig. S1–S8 and Tables S1–S5. CCDC 1991872 and 1991873 for **1** and **2**, respectively. For crystallographic data in CIF or other electronic format see DOI: 10.1039/d0dt01126f





**Scheme 1** Structures of the amino acids  $\alpha$ -glycine (A) and  $\beta$ -alanine (B).

Herein, we report the synthesis, crystal structure and magnetic properties of two carboxylato-bridged Dy<sup>III</sup> 1D coordination polymers of the formula  $\{[\text{Dy}_2(\text{gly})_6(\text{H}_2\text{O})_4](\text{ClO}_4)_6 \cdot 5\text{H}_2\text{O}\}_n$  (**1**) and  $\{[\text{Dy}_2(\beta\text{-ala})_6(\text{H}_2\text{O})_4](\text{ClO}_4)_6 \cdot \text{H}_2\text{O}\}_n$  (**2**) [gly =  $\alpha$ -glycine and  $\beta$ -ala =  $\beta$ -alanine]. To the best of our knowledge, no magneto-structural study on one-dimensional homometallic dysprosium(III) complexes based on amino acids has been reported so far.

## Experimental section

### Materials and physical measurements

All reagents were of commercial origin and were used as received. All manipulations were performed under aerobic conditions. **CAUTION!**: although no problems were encountered in this work, care should be taken when using the potentially explosive perchlorate anion ( $\text{ClO}_4^-$ ).

Elemental analyses (C, H, and N) were performed by using an elemental analyzer (CE Instruments CHNS1100) and the molar ratio between the heavier elements was found by means of a Philips XL-30 scanning electron microscope (SEM/EDAX), equipped with an X-ray microanalysis system, in the Central Service for the Support to Experimental Research (SCSIE) at the University of Valencia. Infrared spectra (IR) of complexes **1** and **2** were recorded with a PerkinElmer Spectrum 65 FT-IR spectrometer in the 4000–400  $\text{cm}^{-1}$  region. Variable-temperature and solid-state (dc and ac) magnetic susceptibility data were collected by using a Quantum Design MPMS-XL SQUID magnetometer equipped with a 5 T dc magnet. Experimental magnetic data were corrected for the diamagnetic contributions of both the sample holder and eicosene. The diamagnetic contribution of the involved atoms was corrected by using Pascal's constants.<sup>45</sup>

### Preparation of compounds **1** and **2**

**Compound 1.** A solvothermal reaction of  $\text{Dy}_2\text{O}_3$  (0.072 g, 0.2 mmol) and glycine (0.030 g, 0.4 mmol) was performed in an aqueous suspension (4 mL) acidulated with perchloric acid (1.5 mL, 2 M) at 80 °C for 48 h, followed by a cooling process at 4.5 °C  $\text{h}^{-1}$  to room temperature. Colourless parallelepipeds were obtained and were suitable for single-crystal X-ray diffraction studies. Yield: ca. 70%. Anal. calcd for  $\text{C}_{12}\text{H}_{48}\text{N}_6\text{O}_{45}\text{Cl}_6\text{Dy}_2$  (**1**): C, 9.4; H, 3.2; N, 5.5. Found: C, 8.9; H, 3.0; N, 5.2. SEM (EDAX): a molar ratio of 1 : 3 for Dy/Cl was found for **1**. IR (KBr pellet/ $\text{cm}^{-1}$ ): peaks assigned to the glycine ligand are observed at 3313 (s), 1631 (m), 1603 (m), 1570 (m), 1451 (m), 1145 (w), 1108 (s), 1088 (s), 905 (w), and 627 (s)  $\text{cm}^{-1}$ .

**Compound 2.** A mixture of  $\text{Dy}_2\text{O}_3$  (0.093 g, 0.25 mmol) and  $\beta$ -alanine (0.022 g, 0.25 mmol) in an aqueous suspension (5 mL) acidulated with perchloric acid (1.5 mL, 2 M) was stirred and heated at 60 °C for 1 h. The resulting solution was left to evaporate at room temperature for 2 weeks. Colourless parallelepipeds were obtained and were suitable for single-crystal X-ray diffraction studies. Yield: ca. 60%. Anal. calcd for  $\text{C}_{18}\text{H}_{52}\text{N}_6\text{O}_{41}\text{Cl}_6\text{Dy}_2$  (**2**): C, 14.0; H, 3.4; N, 5.4. Found: C, 13.8; H, 3.2; N, 5.4. SEM (EDAX): a molar ratio of 1 : 3 for Dy/Cl was found for **2**. IR (KBr pellet/ $\text{cm}^{-1}$ ): peaks assigned to the  $\beta$ -alanine ligand are observed at 3369 (s), 1624 (m), 1577 (m), 1457 (m), 1145 (w), 1109 (s), 1090 (s), 963 (w), 940 (w), and 627 (s)  $\text{cm}^{-1}$ .

### X-ray data collection and structure refinement

X-ray diffraction data of single crystals of dimensions 0.13  $\times$  0.13  $\times$  0.06 (**1**) and 0.23  $\times$  0.14  $\times$  0.05  $\text{mm}^3$  (**2**) were collected by using a Bruker D8 Venture diffractometer with a PHOTON II detector and by using monochromatised Mo- $K_\alpha$  radiation ( $\lambda = 0.71073$  Å). Crystal parameters and refinement results of **1** and **2** are summarized in Table 1. The structures were solved by standard direct methods and subsequently completed by Fourier recycling using the SHELXTL<sup>46</sup> software packages and refined by the full-matrix least-square refinements based on  $F^2$  with all observed reflections. The final graphical manipulations were performed with the DIAMOND<sup>47</sup> and CRYSTALMAKER<sup>48</sup> programs. Crystallographic data have been deposited in the Cambridge Structural Data Centre (CCDC) with numbers 1991872 and 1991873 for **1** and **2**, respectively.†

## Results and discussion

### Structure description of **1** and **2**

Single-crystal X-ray analysis reveals that both compounds (**1** and **2**) crystallise in the triclinic system with the centrosymmetric space group  $P\bar{1}$  (Table 1). As shown in Fig. 1 and 2,

**Table 1** Summary of the crystal data and structure refinement parameters for **1** and **2**

Compound	<b>1</b>	<b>2</b>
Formula	$\text{C}_{12}\text{H}_{48}\text{N}_6\text{O}_{45}\text{Cl}_6\text{Dy}_2$	$\text{C}_{18}\text{H}_{52}\text{N}_6\text{O}_{41}\text{Cl}_6\text{Dy}_2$
$M_r$	1534.26	1546.35
Crystal system	Triclinic	Triclinic
Space group	$P\bar{1}$	$P\bar{1}$
$a/\text{Å}$	11.399(1)	9.123(1)
$b/\text{Å}$	13.972(1)	12.741(1)
$c/\text{Å}$	15.469(1)	21.566(1)
$\alpha/^\circ$	96.43(1)	76.28(1)
$\beta/^\circ$	102.60(1)	81.27(1)
$\gamma/^\circ$	106.04(1)	82.23(1)
$V/\text{Å}^3$	2271.5(2)	2394.1(4)
$Z$	2	2
$D_c/\text{g cm}^{-3}$	2.243	2.145
$\mu(\text{Mo-}K_\alpha)/\text{mm}^{-1}$	3.752	3.555
$F(000)$	1512	1528
Goodness-of-fit on $F^2$	1.083	0.982
$R_1 [I > 2\sigma(I)]$ (all data)	0.0213 (0.0344)	0.0230 (0.0507)
$wR_2 [I > 2\sigma(I)]$ (all data)	0.0439 (0.0509)	0.0320 (0.0554)



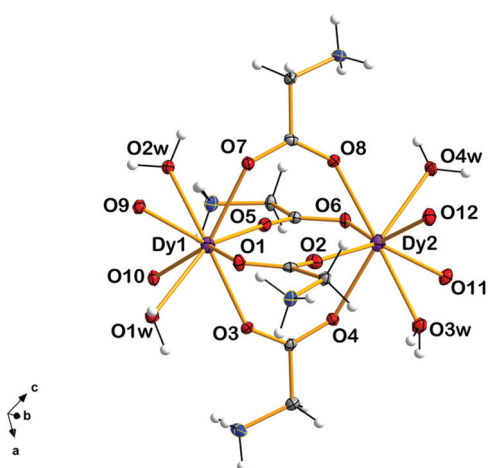


Fig. 1 View of a detailed structure of the dinuclear  $[\text{Dy}_2(\text{gly})_6(\text{H}_2\text{O})_4]^{6+}$  unit in **1**. Perchlorate anions and non-coordinating water molecules have been omitted for clarity. Thermal ellipsoids are depicted at the 50% probability level.

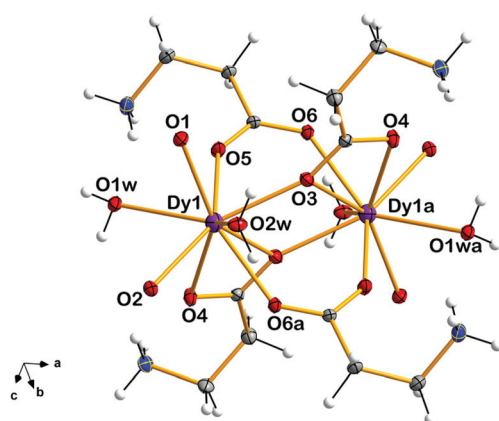


Fig. 2 View of a detailed structure of the dinuclear  $[\text{Dy}_2(\beta\text{-ala})_6(\text{H}_2\text{O})_4]^{6+}$  unit in **2**. Perchlorate anions and non-coordinating water molecules have been omitted for clarity. Thermal ellipsoids are depicted at the 50% probability level.

the crystal structures of both **1** and **2** are mainly described as cationic dinuclear  $[\text{Dy}_2^{\text{III}}]^{6+}$  units that are linked through carboxylate groups from glycine (**1**) and  $\beta$ -alanine (**2**) amino acids, generating one-dimensional  $\{[\text{Dy}_2^{\text{III}}]^{6+}\}_n$  system structures (Fig. 3 and 4), with  $\text{ClO}_4^-$  anions counterbalancing the positive charges.  $\text{H}_2\text{O}$  solvent molecules are present in the crystal lattice of both **1** and **2**. The asymmetric unit in **1** consists of a dinuclear  $[\text{Dy}_2(\text{gly})_6(\text{H}_2\text{O})_4]^{6+}$  entity, six  $\text{ClO}_4^-$  anions, and five non-coordinating water molecules, whereas in **2** two halves of crystallographically independent dinuclear  $[\text{Dy}_2(\beta\text{-ala})_6(\text{H}_2\text{O})_4]^{6+}$  units, six  $\text{ClO}_4^-$  anions, and one non-coordinating water molecule are present in the asymmetric unit.

In **1**, the two  $\text{Dy}^{\text{III}}$  ions of the dinuclear  $[\text{Dy}_2(\text{gly})_6(\text{H}_2\text{O})_4]^{6+}$  unit are connected with each other by four bridging carboxylate groups from four glycine (gly) ligands and are separated by a distance of 4.237(1) Å. Two additional gly ligands link these two  $\text{Dy}^{\text{III}}$  ions to neighbouring dinuclear units, with separations of 5.200(1) Å  $[\text{Dy}(1)\cdots\text{Dy}(1a)]$ ;  $(a) = 1 - x, -y, 1 - z$  and 5.101(1) Å  $[\text{Dy}(2)\cdots\text{Dy}(2b)]$ ;  $(b) = 2 - x, 1 - y, 2 - z$ , thus generating a one-dimensional  $\{[\text{Dy}_2^{\text{III}}]^{6+}\}_n$  coordination polymer (Fig. 3 and S1†).

Each  $\text{Dy}^{\text{III}}$  ion in **1** is eight-coordinate and bound to six oxygen atoms from six carboxylate groups, of their respective gly ligands, and two oxygen atoms of two water molecules (Fig. 1).

The average value of the Dy–O bond lengths [2.347(1) Å] is somewhat shorter than that of the Dy– $\text{O}_{\text{water}}$  bond lengths [2.482(1) Å] (see Table S1†). The coordinated water molecules connect further the dinuclear units of the 1D system through intramolecular H-bonding interactions with  $\text{O}(1w)\cdots\text{O}(2wa)$  and  $\text{O}(3w)\cdots\text{O}(4wb)$  distances of 2.842(2) and 2.774(2) Å, respectively (Table S2†). All the gly ligands are present in the zwitterionic form, and their C–C, C–N, and C–O bond lengths agree with those found in the literature for similar lanthanide-based complexes (Table S1†).<sup>49,50</sup>

In the crystal lattice of **1**, the cationic  $\{[\text{Dy}_2^{\text{III}}]^{6+}\}_n$  chains are quite separated from each other by  $\text{ClO}_4^-$  anions (Fig. 5). Indeed, the shortest interchain Dy $\cdots$ Dy distance is ca. 11.4(1) Å. Nevertheless, adjacent chains are interlinked at long-range

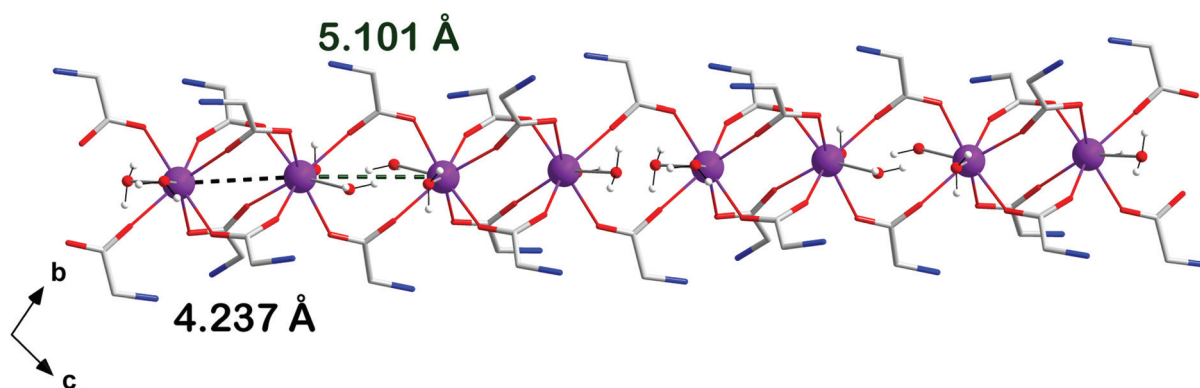


Fig. 3 A fragment of the one-dimensional motif of the homometallic  $\{[\text{Dy}_2(\text{gly})_6(\text{H}_2\text{O})_4](\text{ClO}_4)_6 \cdot 5\text{H}_2\text{O}\}_n$  chain in **1**. Perchlorate anions and non-coordinating water molecules have been omitted for clarity. Colour code: purple, Dy; red, O; blue, N; grey, C; white, H.

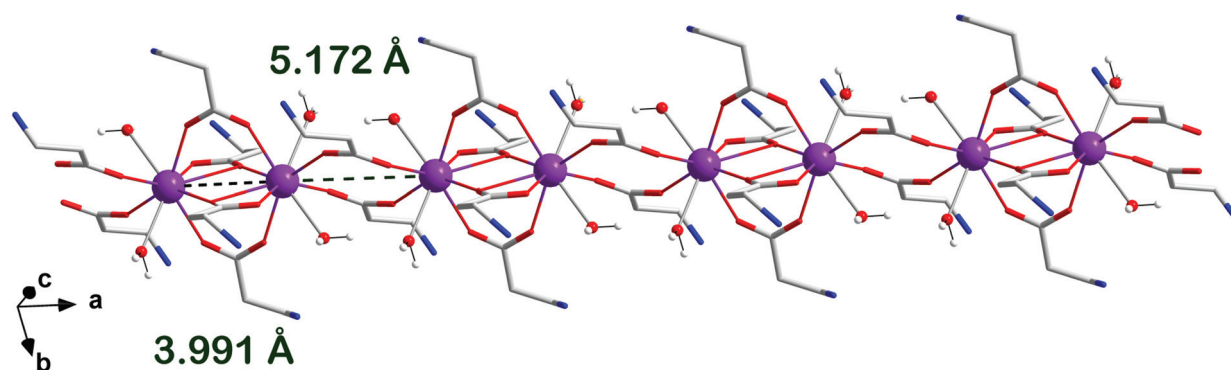


Fig. 4 A fragment of the one-dimensional motif of the homometallic  $\{[Dy_2(\beta\text{-ala})_6(H_2O)_4](ClO_4)_6 \cdot H_2O\}_n$  chain in **2**. Perchlorate anions and non-coordinating water molecules have been omitted for clarity. Colour code: purple, Dy; red, O; blue, N; grey, C; white, H.

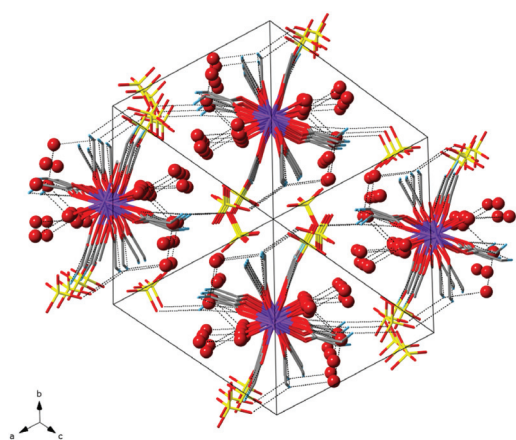


Fig. 5 View along the crystallographic [111] direction of the homometallic  $[Dy_2(\text{gly})_6(H_2O)_4]^{6+}$  chains,  $ClO_4^-$  anions and  $H_2O$  molecules connected by H-bonding interactions (dashed lines) in **1**. Perchlorate anions are depicted as red and yellow capped sticks, and coordinated and non-coordinated water molecules are shown as red spheres.

through hydrogen bonds involving the protonated  $-NH_2$  groups of the gly ligands and  $ClO_4^-$  anions (Table S2†), as previously reported in similar structures.<sup>51–53</sup>

The supramolecular network is supported by additional H-bonding interactions involving coordinated and non-coordinated water molecules, together with weaker C–H...O interactions [the shortest C...O distance is *ca.* 3.12 Å, C(2)...O(31d)], which stabilize the crystal structure in **1** (Table S2†).

In **2**, two  $Dy^{III}$  ions are connected with each other by means of four bridging carboxylate groups from four  $\beta$ -alanine ( $\beta$ -ala) ligands to form the dinuclear  $[Dy_2(\beta\text{-ala})_6(H_2O)_4]^{6+}$  unit. These two  $Dy^{III}$  ions are separated by an average distance of 3.984(1) Å (Fig. 4 and S1†), [the symmetry codes for the Dy(1)...Dy(1a) and Dy(2)...Dy(2b) distances being (a) = 2 – *x*, 1 – *y*, 2 – *z* and (b) = 3 – *x*, 2 – *y*, 1 – *z*, respectively]. Neighbouring dinuclear units are connected through additional  $\beta$ -ala ligands, with separations of 5.172(1) [Dy(1)...Dy(1c); (c) = 1 – *x*, 1 – *y*, 2 – *z*] and 5.182(1) Å [Dy(2)...Dy(2d); (d) = 2 – *x*, 2 – *y*, 1 – *z*], to afford a cationic 1D system that grows along the *a* axis (Fig. 4 and S1†).

Each  $Dy^{III}$  ion in **2** is nine-coordinate and bound to seven oxygen atoms from six carboxylate groups of  $\beta$ -ala ligands and two oxygen atoms of two water molecules (Fig. 2). As in **1**, the average value of the Dy–O bond lengths [2.389(1) Å] is shorter than that of the Dy–O<sub>water</sub> bond lengths [2.505(1) Å] (Table S1†). The two coordinated water molecules additionally link the dinuclear units through intramolecular H-bonding interactions with adjacent coordinated water molecules [O(1w)...O(2wc) and O(3w)...O(4wd) distances of 2.887(3) and 2.943(3) Å, respectively] (Fig. S2 and Table S3†). Remarkably, **2** is the first reported example of a crystal structure containing  $Dy^{III}$  and  $\beta$ -alanine. The  $\beta$ -ala ligands are coordinated in **2** as zwitterionic molecules and the values of the C–C, C–N, and C–O bond lengths agree with those found in the literature for similar systems based on other lanthanide(III) complexes (Table S1†).<sup>54,55</sup>

In the crystal packing of **2**, cationic  $\{[Dy_2^{III}]^{6+}\}_n$  chains and  $ClO_4^-$  anions are arranged in an alternate way (Fig. 6). Together with the non-coordinated water molecules, they are connected through intermolecular H-bonding interactions (Table S3†). The shortest interchain Dy...Dy distance is somewhat shorter than that of compound **1** [11.001(1) Å for the Dy(2)...Dy(1a) distance]. As in **1**, the supramolecular structure in **2** is tied up by means of additional H-bonding interactions (Fig. 6 and Table S3†).

To further analyse the coordination environment and geometry of the  $Dy^{III}$  ions in compounds **1** and **2**, the SHAPE program was used.<sup>56–58</sup> In **1**, the two  $Dy^{III}$  ions show a coordination number (CN) equal to 8 (Fig. S3†). For Dy(1), a value of 0.712 was associated with a bicapped trigonal prism [BCTPR] geometry, whereas a value of 0.882 was assigned to a square antiprism [SAPR] geometry of Dy(2) (Fig. 7), these features suggesting different geometries for Dy(1) and Dy(2). In **2**, the two  $Dy^{III}$  ions exhibit a CN = 9 (Fig. S4†). Similar SHAPE values were computed for these two  $Dy^{III}$  ions (1.091 and 1.186 for Dy(1) and Dy(2), respectively), which were assigned to a capped square antiprism [CSAPR] geometry (Fig. 7), hence indicating the same geometry for the  $Dy^{III}$  ions in the dinuclear  $[Dy_2^{III}]^{6+}$  unit of **2**. Additional crystallographic parameters (Tables S4 and S5†) support these results obtained from SHAPE and, in

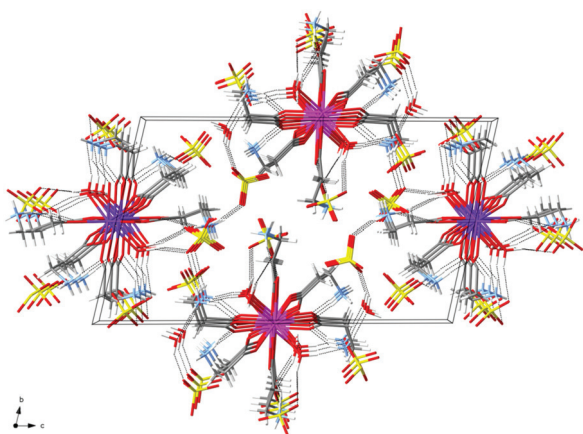


Fig. 6 Perspective view along the crystallographic *a* axis of the homometallic  $[\text{Dy}_2(\beta\text{-ala})_6(\text{H}_2\text{O})_4]^{6+}$  chains and  $\text{ClO}_4^-$  anions (red and yellow capped sticks) connected by H-bonding interactions (dashed lines) in **2**.

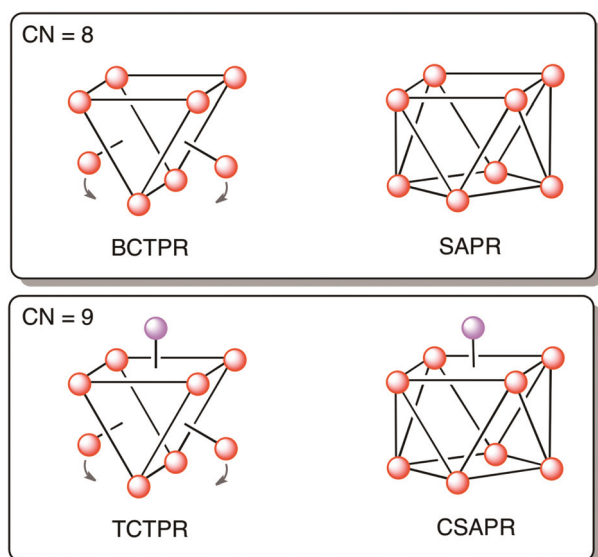


Fig. 7 Schematic of the more common geometries for complexes with coordination number 8: bicapped trigonal prism [BCTPR] and square antiprism [SAPR] (top), and those for complexes with coordination number 9: tricapped trigonal prism [TCTPR] and capped square antiprism [CSAPR] (bottom).

the case of **1**, they allow us to assign the  $C_{2v}$  and  $D_{4d}$  symmetries to the Dy(1) and Dy(2) ions, respectively. In **2**, both Dy<sup>III</sup> ions [Dy(1) and Dy(2)] exhibit  $C_{4v}$  symmetry (Tables S4 and S5<sup>†</sup>). It seems that the diverse synthetic processes would lead to the difference in the coordination environment of the metal ions of **1** and **2**.

### Magnetic properties

**Dc magnetic susceptibility.** Dc magnetic susceptibility measurements were carried out on freshly prepared microcrystalline samples of compounds **1** and **2** in the 2–300 K tempera-

ture range and under an external magnetic field of 0.5 T. Powder XRD results previously confirmed the purity and homogeneity of these bulk samples (Fig. S5<sup>†</sup>). To keep the samples both immobilized and well isolated from the moisture of the air at all moments, the organic compound eicosene was used.

Given that both compounds are structurally formed by dinuclear Dy<sup>III</sup> subunits (see the Structure description section), we have considered this fact in order to study their magnetic properties.

The  $\chi_M T$  versus  $T$  plots ( $\chi_M$  being the molar magnetic susceptibility per two Dy<sup>III</sup> ions) for **1** and **2** are given in Fig. 8 and 9, respectively. For compound **1**, the  $\chi_M T$  value at room temperature is *ca.* 27.8  $\text{cm}^3 \text{mol}^{-1} \text{K}$ , which is somewhat lower than that expected for two magnetically uncoupled Dy<sup>III</sup> ions (28.3  $\text{cm}^3 \text{mol}^{-1} \text{K}$ , with  $^6\text{H}_{15/2}$  ground state,  $J = 15/2$  and  $g = 4/3$ ). Upon cooling, the  $\chi_M T$  value remains approximately constant at *ca.* 90 K, and then it decreases gradually with decreasing temperature, more abruptly at *ca.* 20 K, reaching a

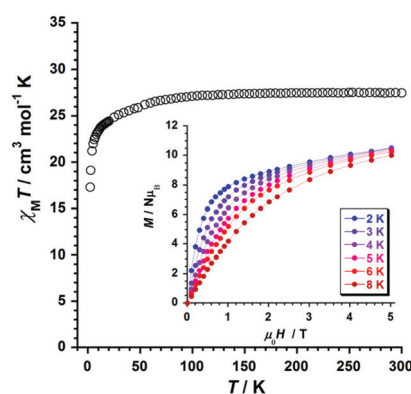


Fig. 8 Thermal variation of the  $\chi_M T$  product obtained for **1**. The inset shows details of the field dependence of the molar magnetisation ( $M$ ) plots at several temperatures (2–8 K) for **1**. The solid lines are a guide for the eye.

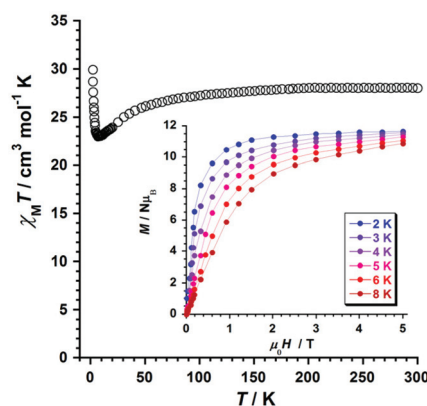


Fig. 9 Thermal variation of the  $\chi_M T$  product obtained for **2**. The inset shows details of the field dependence of the molar magnetisation ( $M$ ) plots at several temperatures (2–8 K) for **2**. The solid lines are a guide for the eye.



minimum value of *ca.* 17.4 cm<sup>3</sup> mol<sup>-1</sup> K at 2 K. For compound 2, the  $\chi_M T$  value at 300 K is *ca.* 28.1 cm<sup>3</sup> mol<sup>-1</sup> K, which is very close to that expected for two magnetically uncoupled Dy<sup>III</sup> ions. The  $\chi_M T$  value decreases very slowly to *ca.* 50 K upon cooling and decreases faster with decreasing temperature to reach a minimum value of 23.0 cm<sup>3</sup> mol<sup>-1</sup> K at *ca.* 7 K, and then it increases to reach a maximum value of 30.0 cm<sup>3</sup> mol<sup>-1</sup> K at 2 K. These features are suggestive of the occurrence of a dominant ferromagnetic exchange between Dy<sup>III</sup> ions at low temperatures in 2, whereas the decrease observed for the  $\chi_M T$  value in 1 would be due to antiferromagnetic interactions and/or the thermal depopulation of the Stark sublevels of  $\pm M_J$  states of the <sup>6</sup>H<sub>15/2</sub> term, as previously reported.<sup>23–36</sup> It is more likely that the low  $\chi_M T$  value at 300 K is due to the high orbital contribution to the magnetic moment that the Dy<sup>III</sup> ions exhibit. The difference between the experimental values of  $\chi_M T$  at room temperature could be due to the different magnetic exchanges in 1 and 2. In any case, these values are consistent with those previously reported from other research groups.<sup>23–36</sup>

The field dependence of the molar magnetisation (*M*) plots for both compounds are given in the insets of Fig. 8 and 9. These *M* versus *H* plots show substantial differences between them, thus evidencing a different magnetic behaviour for 1 and 2 (see insets in Fig. 8 and 9, respectively). While a continuous increase of *M* with the applied magnetic field is observed for 1 (with a maximum value of *ca.* 10.5 μ<sub>B</sub>), compound 2 exhibits a faster increase at a low field of the *M* value reaching a higher maximum value (*ca.* 11.5 μ<sub>B</sub>), as previously observed for two ferromagnetically coupled Dy<sup>III</sup> spins.<sup>20</sup> In any case, these experimental values for 1 and 2 are lower than that expected theoretically to reach the saturation of the two Dy<sup>III</sup> ions (*ca.* 20.0 μ<sub>B</sub>), which is most likely because of a combination of magnetic anisotropy and crystal-field effects that modify the degeneracy of the <sup>6</sup>H<sub>15/2</sub> ground state.<sup>20</sup>

These features observed in both  $\chi_M T$  vs. *T* and *M* vs. *H* plots would suggest the occurrence of antiferromagnetic and ferromagnetic exchanges in the compounds 1 and 2, respectively.

The molecular structures of 1 and 2 are described as cationic  $\{[\text{Dy}_2^{\text{III}}]^{6+}\}_n$  chains, but these chains present alternating intrachain Dy...Dy distances, being shorter in the above-described dinuclear  $[\text{Dy}_2^{\text{III}}]^{6+}$  units [covering the range of 3.984 (1)–4.237 (1) Å] and longer among neighbouring dinuclear  $[\text{Dy}_2^{\text{III}}]^{6+}$  units [varying in the range of 5.101 (1)–5.200 (1) Å]. Having this fact in mind, the different magnetic behaviour observed for these very similar Dy<sup>III</sup> complexes could be explained by comparing the diverse exchange pathways through the carboxylate bridges, the metal coordination environments and the Dy...Dy distances in the dinuclear  $[\text{Dy}_2^{\text{III}}]^{6+}$  units of 1 and 2. While there is just one possible pathway to transmit the magnetic exchange (Dy–O–C–O–Dy with a Dy...Dy separation as short as *ca.* 4.24 Å) in the dinuclear  $[\text{Dy}_2^{\text{III}}]^{6+}$  unit of 1, two pathways, Dy–O–C–O–Dy and Dy–O–Dy (with an even shorter intradinuclear Dy...Dy distance of *ca.* 3.98 Å), occur in 2. In any case, besides these diverse values of the Dy...Dy distances, the relative orientation of the magnetic

anisotropy axes of the involved Dy<sup>III</sup> ions would lead to the different magnetic behaviour observed in 1 and 2.

The fact that  $\chi_M T$  reaches a maximum value of *ca.* 30.0 cm<sup>3</sup> mol<sup>-1</sup> K at 2.0 K for 2, which has been previously reported for ferromagnetically coupled dinuclear Dy<sup>III</sup> complexes,<sup>20,32</sup> supports the consideration that the predominant magnetic behaviour in both compounds is that of the dinuclear  $[\text{Dy}_2^{\text{III}}]^{6+}$  unit rather than that of the whole chain.

**Ac magnetic susceptibility.** Alternating current (ac) magnetic susceptibility measurements were performed on freshly prepared microcrystalline samples of 1 and 2 in the temperature range of 2–7 K and in a 5.0 G ac field oscillating at different frequencies. No out-of-phase ac signals ( $\chi''_M$ ) were observed at *H*<sub>dc</sub> = 0 G, most likely due to the occurrence of Quantum Tunnelling of Magnetisation (QTM) in both compounds. Nevertheless, out-of-phase ac signals were observed at low temperatures in 1 and 2 when an external dc magnetic field (*H*<sub>dc</sub> = 1000 and 2500 G) was applied. These features would indicate that both compounds show field-induced slow relaxation of magnetisation, which is reminiscent of single-molecule magnet (SMM) behaviour.<sup>5,6,10</sup>

The  $\chi'_M$  and  $\chi''_M$  versus  $\nu$  plots for 1 and 2 are given in Fig. 10 and 11 (and also in Fig. S6 and S7<sup>†</sup>), which indicate a quite different relaxation dynamics for both compounds. For compound 1, no  $\chi''_M$  maxima covering the temperature range of 2–8 K are observable when a dc magnetic field of 2500 G is

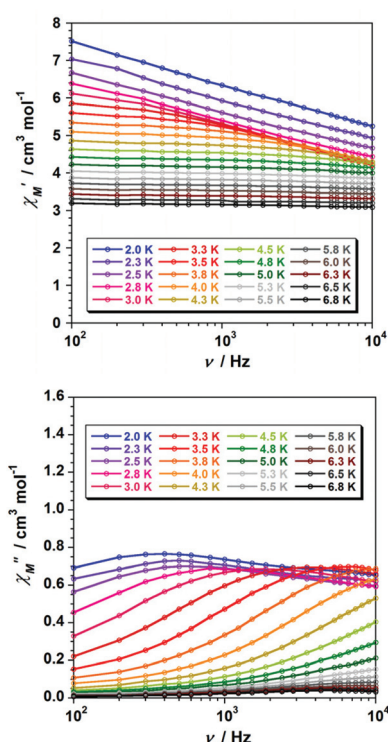


Fig. 10 Frequency dependence of the in-phase (top) and out-of-phase (bottom) ac magnetic susceptibility signals for compound 1. Measurements performed at different temperatures and under a dc field of 1000 G.

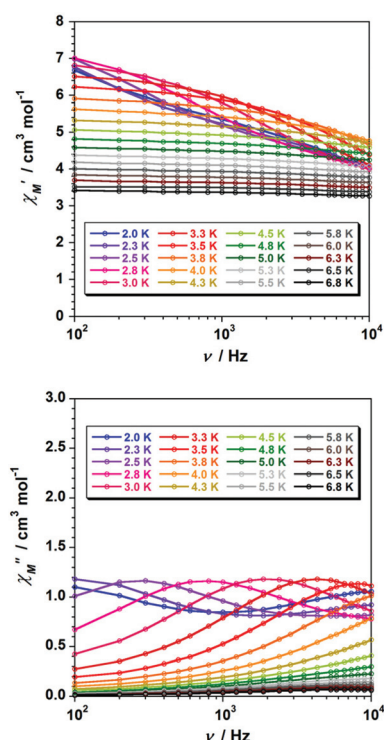


Fig. 11 Frequency dependence of the in-phase (top) and out-of-phase (bottom) ac magnetic susceptibility signals for compound **2**. Measurements performed at different temperatures and under a dc field of 1000 G.

applied (Fig. S6†), whereas  $\chi''_M$  maxima are present when an optimal field of 1000 G is used (Fig. 10). However, the best experimental data for **2** are obtained by applying an external dc field of 2500 G (Fig. S7†).

The  $\ln(\tau)$  versus  $1/T$  curve for **1** shown in Fig. 12 is plotted with the data of the out-of-phase ac signals obtained at  $H_{dc} = 1000$  G. It shows experimental data drawing a straight line (high-temperature region) followed by a curved line (low-temperature region), accounting for the presence of several relaxation mechanisms in **1** (Fig. 12).

The high-temperature region data were fitted to the Arrhenius equation [ $\tau = \tau_0 \exp(U_{eff}/k_B T)$ , where  $\tau_0$  is the pre-exponential factor,  $\tau$  is the relaxation time,  $U_{eff}$  is the barrier to the relaxation of magnetisation and  $k_B$  is the Boltzmann constant], by considering that magnetisation relaxation only involves an Orbach process in this region for **1** (Fig. 12). The values of  $U_{eff}$  and  $\tau_0$  are  $18.5 \text{ cm}^{-1}$  (26.6 K) and  $1.3 \times 10^{-8}$  s, respectively.

$$\tau^{-1} = \tau_0^{-1} \exp(-U_{eff}/k_B T) + AT + CT^n + \tau_{QTM}^{-1} \quad (1)$$

In order to fit the whole curve, several relaxation mechanisms were considered for **1** at low temperatures. In consequence, the whole  $\ln(\tau)$  versus  $1/T$  curve was fitted through eqn (1) in which four mechanisms for the relaxation of magnetisation were considered, namely, Orbach [ $\tau_0^{-1} \exp(-U_{eff}/k_B T)$ ], direct [ $AT$ ], Raman [ $CT^n$ ] and quantum tunnelling (QTM).<sup>10,15</sup>

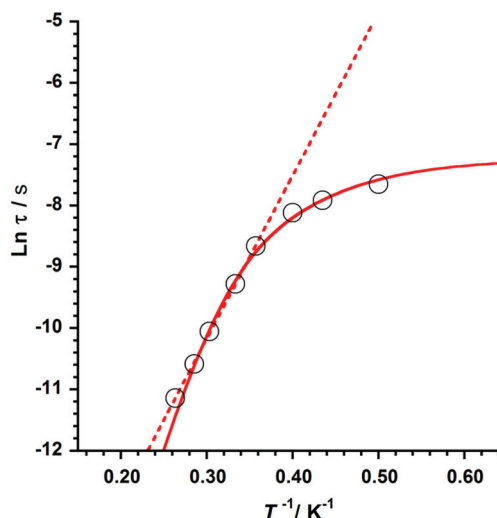


Fig. 12  $\ln(\tau)$  versus  $1/T$  plot for **1**, obtained with out-of-phase ac data at  $H_{dc} = 1000$  G, showing the fit to the Arrhenius law (dashed line) and the fit considering the contribution of Orbach, direct, Raman and QTM mechanisms (solid line).

The least-squares fit of the experimental data of **1** through eqn (1) leads to the following set of parameters:  $U_{eff} = 31.6 \text{ cm}^{-1}$  (45.4 K),  $\tau_0 = 8.7 \times 10^{-10}$  s,  $A = 252.9 \text{ s}^{-1} \text{ K}^{-1}$ ,  $C = 22.2 \text{ s}^{-1} \text{ K}^{-n}$ ,  $n = 5.1$  and QTM =  $6.2 \times 10^{-4}$  s, which are very close to those previously reported for similar  $\text{Dy}^{\text{III}}$  complexes.<sup>23–36</sup>

The  $\ln(\tau)$  versus  $1/T$  curve for **2** obtained with the out-of-phase ac data at  $H_{dc} = 1000$  G is shown in Fig. S8.† In this case, the experimental data drew just a straight line that was fitted to the Arrhenius equation, affording values of  $U_{eff}$  and  $\tau_0$  of  $20.4 \text{ cm}^{-1}$  (29.4 K) and  $4.6 \times 10^{-9}$  s, respectively (Fig. S8†). However, a different magnetic behaviour was reflected in the  $\ln(\tau)$  versus  $1/T$  curve for **2** obtained at  $H_{dc} = 2500$  G (Fig. 13), where the experimental points do exhibit a curved line. As in **1**, these data were fitted through eqn (1), considering four possible mechanisms for the relaxation of magnetisation leading to the following parameters:  $U_{eff} = 43.7 \text{ cm}^{-1}$  (62.9 K),  $\tau_0 = 7.6 \times 10^{-10}$  s,  $A = 538.4 \text{ s}^{-1} \text{ K}^{-1}$ ,  $C = 4.3 \text{ s}^{-1} \text{ K}^{-n}$ ,  $n = 5.9$  and QTM =  $5.9 \times 10^{-5}$  s.

The values of the effective energy barrier ( $U_{eff}$ ) obtained for **1** and **2** are the first ones reported for one-dimensional homometallic  $\text{Dy}^{\text{III}}$  complexes based on amino acids, even though they are very similar to previously reported 1D SMMs based on  $\text{Dy}^{\text{III}}$  metal ions.<sup>42</sup>

In all these cases, the  $U_{eff}$  value calculated for **2** is higher than that of **1**. These results are consistent with the fact that the main magnetic exchange coupling between the  $\text{Dy}^{\text{III}}$  ions of the dinuclear  $[\text{Dy}_2^{\text{III}}]^{6+}$  units is ferromagnetic in **2**. Taking into account the previous works dealing with  $\text{Dy}^{\text{III}}$  complexes, the local symmetry  $D_{4d}$  found in **1** would lead to better SMM properties. Nevertheless, this fact relies on the relative orientation of the magnetic anisotropy axes of all the spin carriers. The local symmetries exhibited in these dinuclear  $\text{Dy}^{\text{III}}$  units are  $C_{2v}$  and  $D_{4d}$  in **1** and only  $C_{4v}$  in **2**, which would make it

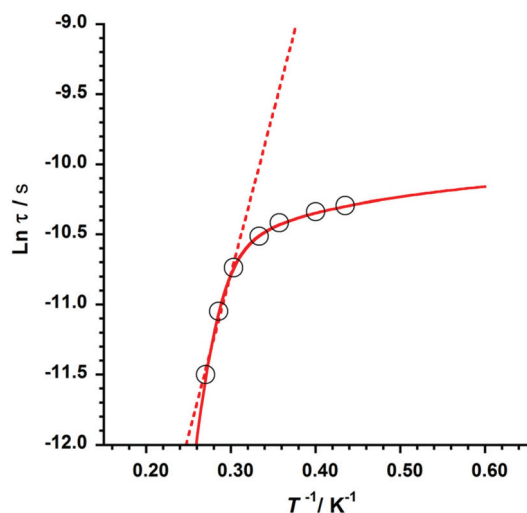


Fig. 13  $\ln(\tau)$  versus  $1/T$  plot for **2**, obtained with out-of-phase ac data at  $H_{dc} = 2500$  G, showing the fit to the Arrhenius law (dashed line) and the fit considering the contribution of Orbach, direct, Raman and QTM mechanisms (solid line).

more feasible to obtain the same orientation in **2** rather than in **1**.<sup>6,32</sup>

The  $\tau_0$  values obtained for both **1** and **2** (ca.  $\sim 10^{-8}$ – $10^{-10}$  s) agree with those in the typical range for single-ion or single-molecule magnets, which also supports our consideration that the predominant magnetic behaviour in both **1** and **2** would be that of single-molecule magnets and not of single-chain magnets.

Finally, the  $n$  values calculated for **1** and **2** are close to 6, and hence they fall into the common range of metal ions with a relaxation involving at least a Raman-like process, as previously reported.<sup>10,17,59,60</sup>

## Conclusions

In summary, the synthesis, crystal structure and magnetic properties of two novel one-dimensional  $\text{Dy}^{\text{III}}$  complexes based on the  $\alpha$ -glycine (gly) and  $\beta$ -alanine ( $\beta$ -ala) amino acids (AAs), with the formula  $\{[\text{Dy}_2(\text{gly})_6(\text{H}_2\text{O})_4](\text{ClO}_4)_6 \cdot 5\text{H}_2\text{O}\}_n$  (**1**) and  $\{[\text{Dy}_2(\beta\text{-ala})_6(\text{H}_2\text{O})_4](\text{ClO}_4)_6 \cdot \text{H}_2\text{O}\}_n$  (**2**), have been reported. Remarkably, **2** is the first reported example of a crystal structure containing  $\text{Dy}^{\text{III}}$  and  $\beta$ -alanine, and both compounds are the first examples of 1D systems based on  $\text{Dy}^{\text{III}}$  and AAs that have been structurally and magnetically characterised. Different symmetries of the  $\text{Dy}^{\text{III}}$  ions, namely,  $C_{2v}$  and  $D_{4d}$  in **1** and  $C_{4v}$  in **2**, have been found in the study of their coordination environment.

The investigation of the magnetic properties of **1** and **2** through dc magnetic susceptibility measurements reveals different magnetic behaviour for both compounds, with **2** showing ferromagnetic behaviour. Ac magnetic susceptibility measurements show field-induced slow relaxation of magnetisation for both **1** and **2**, which indicates that the single-molecule magnet (SMM) phenomenon occurs in these novel one-

dimensional  $\text{Dy}^{\text{III}}$  complexes based on AAs. Further work based on other lanthanide ions and AAs is in progress.

## Conflicts of interest

There are no conflicts to declare.

## Acknowledgements

Financial support from the Spanish Ministry of Science, Innovation and Universities [projects CTQ2016-75068P and MDM-2015-0538 (Excellence Unit “María de Maeztu”)] is gratefully acknowledged. M. O. A. and J. M. L. thank the Spanish “FPI fellowships” and “Ramón y Cajal” Programmes, respectively.

## Notes and references

- M. Mon, R. Bruno, E. Tiburcio, A. Grau-Atienza, A. Sepúlveda-Escribano, E. V. Ramos-Fernandez, A. Fuoco, E. Esposito, M. Monteleone, J. C. Jansen, J. Cano, J. Ferrando-Soria, D. Armentano and E. Pardo, *Chem. Mater.*, 2019, **31**, 5856–5866.
- S. Wang, M. Wahiduzzaman, L. Davis, A. Tissot, W. Shepard, J. Marrot, C. Martineau-Corcus, D. Hamdane, G. Maurin, S. Devautour-Vinot and C. Serre, *Nat. Commun.*, 2018, **9**, 4937.
- A. C. Kathalikkattil, R. Babu, R. K. Roshan, H. Lee, H. Kim, J. Tharun, E. Suresh and D.-W. Park, *J. Mater. Chem. A*, 2015, **3**, 22636–22647.
- S. Begum, Z. Hassan, S. Bräse, C. Wöll and M. Tsotsalass, *Acc. Chem. Res.*, 2019, **52**, 1598–1610.
- D. N. Woodruff, R. E. P. Winpenny and R. A. Layfield, *Chem. Rev.*, 2013, **113**, 5110–5148.
- S. Gómez-Coca, D. Aravena, R. Morales and E. Ruiz, *Coord. Chem. Rev.*, 2015, **289–290**, 379–392.
- S.-S. Liu, L. Xu, S.-D. Jiang, Y.-Q. Zhang, Y.-S. Meng, Z. Wang, B.-W. Wang, W.-X. Zhang, Z. Xi and S. Gao, *Inorg. Chem.*, 2015, **54**, 5162–5168.
- Y.-C. Chen, J.-L. Liu, L. Ungur, J. Liu, Q.-W. Li, L.-F. Wang, Z.-P. Ni, L. F. Chibotaru, X.-M. Chen and M.-L. Tong, *J. Am. Chem. Soc.*, 2016, **138**, 2829–2837.
- J. Liu, Y.-C. Chen, J.-L. Liu, V. Vieru, L. Ungur, J.-H. Jia, L. F. Chibotaru, Y. Lan, W. Wernsdorfer, S. Gao, X.-M. Chen and M.-L. Tong, *J. Am. Chem. Soc.*, 2016, **138**, 5441–5450.
- S. G. McAdams, A.-M. Ariciu, A. K. Kostopoulos, J. P. S. Walsh and F. Tuna, *Coord. Chem. Rev.*, 2017, **346**, 216–239.
- J. Li, S. Gómez-Coca, B. S. Dolinar, L. Yang, F. Yu, M. Kong, Y.-Q. Zhang, Y. Song and K. R. Dunbar, *Inorg. Chem.*, 2019, **58**, 2610–2617.
- N. Ishikawa, M. Sugita, T. Ishikawa, S.-y. Koshihara and Y. Kaizu, *J. Am. Chem. Soc.*, 2003, **125**, 8694–8695.
- R. A. Layfield and M. Murugesu, *Lanthanides and Actinides in Molecular Magnetism*, Wiley-VCH Verlag GmbH & Co. KGaA, 2015.



- 14 S. Biswas, S. Das, J. Acharya, V. Kumar, J. van Leusen, P. Kögerler, J. M. Herrera, E. Colacio and V. Chandrasekhar, *Chem. – Eur. J.*, 2017, **23**, 5154–5170.
- 15 I. Cimatti, X. Yi, R. Sessoli, M. Puget, B. Le Guennic, J. Jung, T. Guizouarn, A. Magnani, K. Bernot and M. Mannini, *Appl. Surf. Sci.*, 2018, **432**, 7–14.
- 16 A. Ullah, J. Cerdá, J. J. Baldoví, S. A. Varganov, J. Aragón and A. Gaita-Ariño, *J. Phys. Chem. Lett.*, 2019, **10**, 7678–7683.
- 17 C. A. P. Goodwin, F. Ortu, D. Reta, N. F. Chilton and D. P. Mills, *Nature*, 2017, **548**, 439–442.
- 18 F.-S. Guo, B. M. Day, Y.-C. Chen, M.-L. Tong, A. Mansikkamäki and R. A. Layfield, *Science*, 2018, **362**, 1400–1403.
- 19 A. B. Canaj, S. Dey, E. Regincós-Martí, C. Wilson, G. Rajaraman and M. Murrie, *Angew. Chem., Int. Ed.*, 2019, **58**, 1–7.
- 20 P.-H. Lin, T. J. Burchell, R. Clérac and M. Murugesu, *Angew. Chem., Int. Ed.*, 2008, **47**, 8848–8851.
- 21 X. Zhang, S. Liu, V. Vieru, N. Xu, C. Gao, B.-W. Wang, W. Shi, L. F. Chibotaru, S. Gao, P. Cheng and A. K. Powell, *Chem. – Eur. J.*, 2018, **24**, 6079–6086.
- 22 G. Huang, G. Fernández-García, I. Badiane, M. Camarra, S. Freslon, O. Guillou, C. Daiguebonne, F. Totti, O. Cador, T. Guizouarn, B. Le Guennic and K. Bernot, *Chem. – Eur. J.*, 2018, **24**, 6983–6991.
- 23 G.-F. Xu, Q.-L. Wang, P. Gamez, Y. Ma, R. Clérac, J. Tang, S.-P. Yan, P. Cheng and D.-Z. Liao, *Chem. Commun.*, 2010, **46**, 1506–1508.
- 24 F. Habib, G. Brunet, V. Vieru, I. Korobkov, L. F. Chibotaru and M. Murugesu, *J. Am. Chem. Soc.*, 2013, **135**(36), 13242–13245.
- 25 L. Zhang, Y.-Q. Zhang, P. Zhang, L. Zhao, M. Guo and J. Tang, *Inorg. Chem.*, 2017, **56**, 7882–7889.
- 26 D. Pinkowicz, M. Ren, L.-M. Zheng, S. Sato, M. Hasegawa, M. Morimoto, M. Irie, B. K. Breedlove, G. Cosquer, K. Katoh and M. Yamashita, *Chem. – Eur. J.*, 2014, **20**, 12502–12513.
- 27 P. Kalita, J. Goura, J. M. Herrera-Martínez, E. Colacio and V. Chandrasekhar, *Eur. J. Inorg. Chem.*, 2019, 212–220.
- 28 B. S. Sran, J. Flores-Gonzalez, V. Montigaud, B. Le Guennic, F. Pointillart, O. Cador and G. Hundal, *Dalton Trans.*, 2019, **48**, 3922–3929.
- 29 X. Ma, B. Chen, Y.-Q. Zhang, J. Yang, Q. Shi, Y. Ma and X. Liu, *Dalton Trans.*, 2019, **48**, 12622–12631.
- 30 S. Biswas, L. Mandal, Y. Shen and M. Yamashita, *Dalton Trans.*, 2019, **48**, 14096–14102.
- 31 G. Huang, X. Yi, F. Gendron, B. Le Guennic, T. Guizouarn, C. Daiguebonne, G. Calvez, Y. Suffren, O. Guillou and K. Bernot, *Dalton Trans.*, 2019, **48**, 16053–16061.
- 32 P. Cen, X. Liu, Y.-Q. Zhang, J. Ferrando-Soria, G. Xie, S. Chen and E. Pardo, *Dalton Trans.*, 2020, **49**, 808–816.
- 33 Y.-J. Wang, D.-F. Wu, J. Gou, Y.-Y. Duan, L. Li, H.-H. Chen, H.-L. Gao and J.-Z. Cui, *Dalton Trans.*, 2020, **49**, 2850–2861.
- 34 F. Habib and M. Murugesu, *Chem. Soc. Rev.*, 2013, **42**, 3278–3288.
- 35 C. Y. Chow, H. Bolvin, V. E. Campbell, R. Guillot, J. W. Kampf, W. Wernsdorfer, F. Gendron, J. Autschbach, V. L. Pecoraro and T. Mallah, *Chem. Sci.*, 2015, **6**, 4148–4159.
- 36 J. Xiong, H.-Y. Ding, Y.-S. Meng, C. Gao, X.-J. Zhang, Z.-S. Meng, Y.-Q. Zhang, W. Shi, B.-W. Wang and S. Gao, *Chem. Sci.*, 2017, **8**, 1288–1294.
- 37 F. Luo, Z.-W. Liao, Y.-M. Song, H.-X. Huang, X.-Z. Tian, G.-M. Sun, Y. Zhu, Z.-Z. Yuan, M.-B. Luo, S.-J. Liu, W.-Y. Xu and X.-F. Feng, *Dalton Trans.*, 2011, **40**, 12651–12655.
- 38 F. Luo, Y.-M. Song, H.-X. Huang, X.-Z. Tian, G.-M. Sun, Y. Zhu and X.-F. Feng, *Aust. J. Chem.*, 2012, **65**, 1436–1442.
- 39 Y. Zhu, F. Luo, Y.-M. Song, H.-X. Huang, G.-M. Sun, X.-Z. Tian, Z.-Z. Yuan, Z.-W. Liao, M.-B. Luo, S.-J. Liu, W.-Y. Xu and X.-F. Feng, *Dalton Trans.*, 2012, **41**, 6749–6755.
- 40 E. Bartolomé, J. Bartolomé, S. Melnic, D. Prodius, S. Shova, A. Arauzo, J. Luzón, F. Luis and C. Turta, *Dalton Trans.*, 2013, **42**, 10153–10171.
- 41 J. Jung, F. Le Natur, O. Cador, F. Pointillart, G. Calvez, C. Daiguebonne, O. Guillou, T. Guizouarn, B. Le Guennic and K. Bernot, *Chem. Commun.*, 2014, **50**, 13346–13348.
- 42 G.-J. Zhou, Y.-S. Ding and Y.-Z. Zheng, *Dalton Trans.*, 2017, **46**, 3100–3104.
- 43 D. T. Thielemanna, A. T. Wagner, Y. Lan, C. E. Ansona, M. T. Gamera, A. K. Powell and P. W. Roesky, *Dalton Trans.*, 2013, **42**, 14794–14800.
- 44 B.-Q. Ma, D.-S. Zhang, S. Gao, T.-Z. Jin, C.-H. Yan and G.-X. Xu, *Angew. Chem., Int. Ed.*, 2000, **39**, 3644–3646.
- 45 G. A. Bain and J. F. Berry, *J. Chem. Educ.*, 2008, **85**, 532–536.
- 46 SHELXTL-2013/4, *Bruker Analytical X-ray Instruments*, Madison, WI, 2013.
- 47 *Diamond 4.5.0, Crystal Impact GbR, CRYSTAL IMPACT*, 2018.
- 48 *CrystalMaker 8.5.1*, CrystalMaker Software Ltd, Oxford, England.
- 49 J. Legendziewicz, E. Huskowska, A. Waśkowska and G. Argay, *Inorg. Chim. Acta*, 1984, **92**, 151–157.
- 50 J. Legendziewicz, E. Huskowska, G. Argay and A. Waśkowska, *J. Less-Common Met.*, 1989, **146**, 33–47.
- 51 J. Martínez-Lillo, N. Dolan and E. K. Brechin, *Dalton Trans.*, 2013, **42**, 12824–12827.
- 52 J. Martínez-Lillo, N. Dolan and E. K. Brechin, *Dalton Trans.*, 2014, **43**, 4408–4414.
- 53 C. Rojas-Dotti, N. Moliner, F. Lloret and J. Martínez-Lillo, *Crystals*, 2019, **9**, 23.
- 54 X. Zheng, L. Jin, S. Lu and Y. Zheng, *Z. Anorg. Allg. Chem.*, 2003, **629**, 2577–2584.
- 55 X.-J. Zheng and L.-P. Jin, *J. Mol. Struct.*, 2003, **655**, 7–15.
- 56 M. Llonell, D. Casanova, J. Cirera, P. Alemany and S. Alvarez, *SHAPE 2.1*, Universitat de Barcelona, Barcelona, Spain, 2013.
- 57 S. Alvarez, P. Alemany, D. Casanova, J. Cirera, M. Llonell and D. Avnir, *Coord. Chem. Rev.*, 2005, **249**, 1693–1708.
- 58 A. Ruiz-Martínez, D. Casanova and S. Alvarez, *Chem. – Eur. J.*, 2008, **14**, 1291–1303.
- 59 C. Rojas-Dotti, A. Sanchis-Perucho, M. Orts-Arroyo, N. Moliner, R. González, F. Lloret and J. Martínez-Lillo, *Magnetochemistry*, 2020, **6**, 20.
- 60 A. Sanchis-Perucho and J. Martínez-Lillo, *Dalton Trans.*, 2019, **48**, 13925–13930.





---



*ARTICLE 9*

*One-Dimensional Gadolinium  
(III) Complexes Based on Alpha  
and Beta-Amino Acids  
Exhibiting Field-Induced Slow  
Relaxation of Magnetization*



Article

# One-Dimensional Gadolinium (III) Complexes Based on Alpha- and Beta-Amino Acids Exhibiting Field-Induced Slow Relaxation of Magnetization

Marta Orts-Arroyo, Adrián Sanchis-Perucho, Nicolas Moliner, Isabel Castro , Francesc Lloret and José Martínez-Lillo \* 

Departament de Química Inorgànica, Instituto de Ciencia Molecular (ICMol), Universitat de València, c/ Catedrático José Beltrán 2, Paterna, 46980 València, Spain; marta.orts-arroyo@uv.es (M.O.-A.); adrian.sanchis@uv.es (A.S.-P.); fernando.moliner@uv.es (N.M.); isabel.castro@uv.es (I.C.); francisco.lloret@uv.es (F.L.)

\* Correspondence: f.jose.martinez@uv.es; Tel.: +34-9635-44460

**Abstract:** Gadolinium (III) complexes exhibiting slow relaxation of magnetization are uncommon and have been much less studied than other compounds based on anisotropic lanthanide (III) ions. We prepared two one-dimensional gadolinium (III) complexes based on  $\alpha$ -glycine (gly) and  $\beta$ -alanine ( $\beta$ -ala) amino acids, with the formula  $\{[\text{Gd}_2(\text{gly})_6(\text{H}_2\text{O})_4](\text{ClO}_4)_6 \cdot 5\text{H}_2\text{O}\}_n$  (**1**) and  $\{[\text{Gd}_2(\beta\text{-ala})_6(\text{H}_2\text{O})_4](\text{ClO}_4)_6 \cdot \text{H}_2\text{O}\}_n$  (**2**), which were magneto-structurally characterized. Compounds **1** and **2** crystallize in the triclinic system (space group  $\bar{P}1$ ). In complex **1**, two Gd (III) ions are eight-coordinate and bound to six oxygen atoms from six gly ligands and two oxygen atoms from two water molecules, the metal ions showing different geometries (bicapped trigonal prism and square antiprism). In complex **2**, two Gd (III) ions are nine-coordinate and bound to seven oxygen atoms from six  $\beta$ -ala ligands and two oxygen atoms from two water molecules in the same geometry (capped square antiprism). Variable-temperature dc magnetic susceptibility measurements performed on microcrystalline samples of **1** and **2** show similar magnetic behavior for both compounds, with antiferromagnetic coupling between the Gd (III) ions connected through carboxylate groups. Ac magnetic susceptibility measurements reveal slow relaxation of magnetization in the presence of an external dc field in both compounds, hence indicating the occurrence of the field-induced single-molecule magnet (SMM) phenomenon in both **1** and **2**.

**Keywords:** amino acids; glycine;  $\beta$ -alanine; gadolinium; metal complexes; crystal structure; magnetic properties; single-molecule magnet



**Citation:** Orts-Arroyo, M.; Sanchis-Perucho, A.; Moliner, N.; Castro, I.; Lloret, F.; Martínez-Lillo, J. One-Dimensional Gadolinium (III) Complexes Based on Alpha- and Beta-Amino Acids Exhibiting Field-Induced Slow Relaxation of Magnetization. *Inorganics* **2022**, *10*, 32. <https://doi.org/10.3390/inorganics10030032>

Academic Editor: Akseli Mansikkamäki

Received: 8 February 2022

Accepted: 28 February 2022

Published: 3 March 2022

**Publisher's Note:** MDPI stays neutral with regard to jurisdictional claims in published maps and institutional affiliations.



**Copyright:** © 2022 by the authors. Licensee MDPI, Basel, Switzerland. This article is an open access article distributed under the terms and conditions of the Creative Commons Attribution (CC BY) license (<https://creativecommons.org/licenses/by/4.0/>).

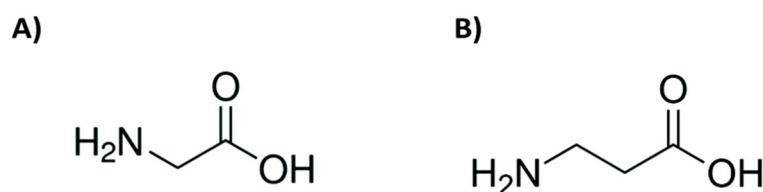
## 1. Introduction

Since the discovery of the mononuclear phthalocyanine-based lanthanide (III) complexes, which exhibit the single-molecule magnet (SMM) phenomenon, in 2003 [1,2], many efforts have focused on the synthesis and development of lanthanide(III)-based complexes in order to study this singular magnetic behavior, which allows SMMs to become promising candidates for potential applications in high-density data storage, quantum computing, molecular refrigeration and spintronics investigations [3–8].

Heterometallic 3d–4f mixed systems, radical bridged compounds, mono- and polynuclear lanthanide (III) complexes containing highly anisotropic 4f ions, mainly Dy (III) and to a lesser extent Tb (III), Ho (III) and Er (III), were investigated during the last two decades in the field of molecular magnetism [9–17]. More recently, mononuclear SMMs, also known as single-ion magnets (SIMs), based on dysprosium metallocenes were reported displaying energy barriers of magnetization reversal exceeding the  $1500\text{ cm}^{-1}$  value and blocking temperatures as high as that of the liquid nitrogen ( $>77\text{ K}$ ), which exemplify the current progress in this research area [18,19].

In comparison with other members of the lanthanides family, the Gd (III) ion has been largely ignored in this type of study. This metal ion is considered magnetically isotropic due to the half-occupied  $4f^7$  electron configuration and the lack of orbital contribution ( $S = 7/2$ ,  $L = 0$ ) with an  $^8S_{7/2}$  ground state and a spherical quadrupole moment. Hence, the number of reported Gd (III) complexes that exhibit slow relaxation of magnetization is quite scarce [20,21]. Nevertheless, in some cases, Gd (III) cations show a very low or negligible value of the zero-field splitting ( $D$ ), which induces the occurrence of ac signals for complexes of this quasi-isotropic  $4f$  metal ion. In this way, when an external magnetic field is applied, the degeneracy between energy levels can be removed and the Quantum Tunnelling of Magnetisation (QTM) can be suppressed, which could result in mixed mechanisms of spin–lattice, spin–phonon and spin–spin relaxations [20]. This fact makes this type of study on both new and old Gd(III) systems very appealing.

Herein, we report the synthesis, crystal structure and magnetic properties of two carboxylate-bridged  $Gd^{III}$  1D coordination polymers of the formula  $\{[Gd_2(\text{gly})_6(\text{H}_2\text{O})_4](\text{ClO}_4)_6 \cdot 5\text{H}_2\text{O}\}_n$  (**1**) and  $\{[Gd_2(\beta\text{-ala})_6(\text{H}_2\text{O})_4](\text{ClO}_4)_6 \cdot \text{H}_2\text{O}\}_n$  (**2**) [ $\text{gly} = \alpha\text{-glycine}$  and  $\beta\text{-ala} = \beta\text{-alanine}$ ]. To the best of our knowledge, no magneto-structural study on homometallic gadolinium (III) complexes based on these amino acids has been reported so far (Scheme 1).



**Scheme 1.** Molecular structure of the amino acids  $\alpha$ -glycine (A) and  $\beta$ -alanine (B).

## 2. Results and Discussion

### 2.1. Synthetic Procedure

Compounds **1** and **2** are prepared from a mixture of  $Gd_2O_3$  and glycine (**1**)/ $\beta$ -alanine (**2**). Both mixtures react in an aqueous solution acidulated with perchloric acid. However, the employed crystallization technique was different. While for preparing **1** the reaction mixture was heated at  $80\text{ }^\circ\text{C}$  for 48 h and then cooled at a rate of  $4.5\text{ }^\circ\text{C/h}$  to room temperature, the reaction mixture that generates compound **2** was heated at  $60\text{ }^\circ\text{C}$  for 1h and the resulting solution was left to evaporate at room temperature for 2 weeks. It is important to mention that, although no problems were encountered in this work, care should be taken when using the potentially explosive perchlorate anion ( $\text{ClO}_4^-$ ), which comes from the perchloric acid.

### 2.2. Description of the Crystal Structures

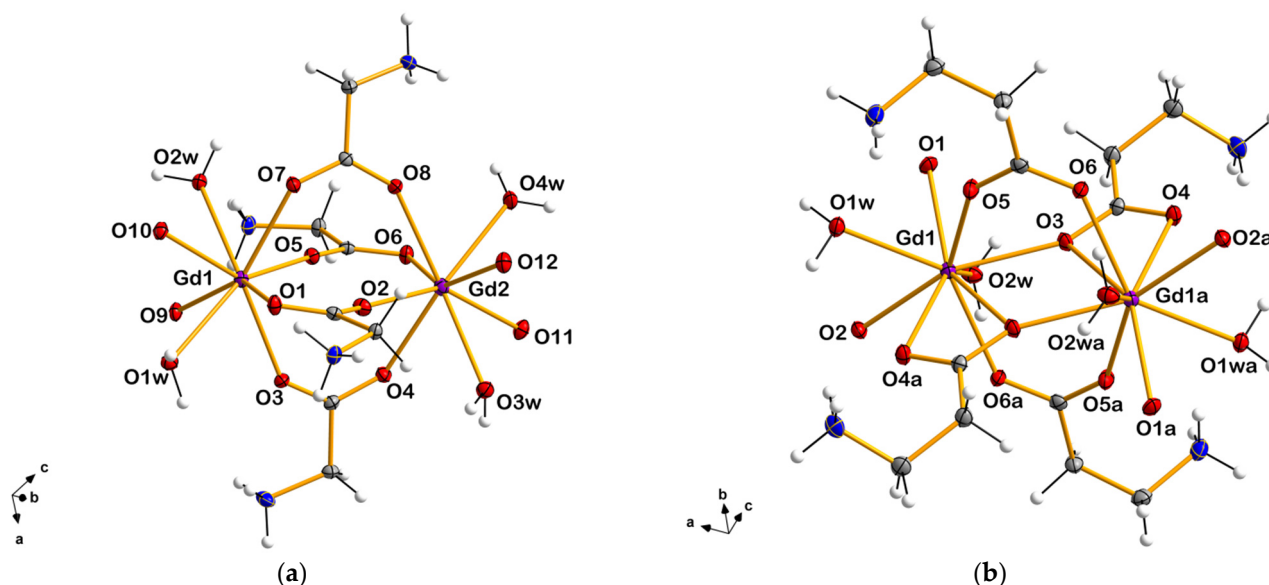
Crystal data and structure refinement parameters for **1** and **2** are summarized in Table 1, where we indicate that both compounds crystallize in the triclinic system with centrosymmetric space group  $P\bar{1}$ . A recent review of the Cambridge Structural Database (CSD) revealed that the crystal structures of **1** and **2** were previously deposited with identifiers UKIKIJ and TEHKUN, respectively. Nevertheless, they were collected at room temperature and were deposited with refinement and resolution levels lower than the ones reported in this work [22,23].

The crystal structures of **1** and **2** are better described as cationic dinuclear  $[Gd^{III}_2]^{6+}$  units which are connected through carboxylate groups from glycine (**1**) and  $\beta$ -alanine (**2**), forming one-dimensional  $\{[Gd^{III}_2]^{6+}\}_n$  systems, the positive charges being counterbalanced by means of  $\text{ClO}_4^-$  anions.  $\text{H}_2\text{O}$  solvent molecules are also present in their crystal structure (Figure 1).

**Table 1.** Summary of the crystal data and structure refinement parameters for **1** and **2**.

Compound	1	2
CIF	2149741	2149742
Formula	C <sub>12</sub> H <sub>48</sub> Cl <sub>6</sub> N <sub>6</sub> O <sub>45</sub> Gd <sub>2</sub>	C <sub>18</sub> H <sub>52</sub> Cl <sub>6</sub> N <sub>6</sub> O <sub>41</sub> Gd <sub>2</sub>
Fw/g mol <sup>-1</sup>	1523.76	1535.85
Temperature/K	120 (2)	120 (2)
Crystal system	Triclinic	Triclinic
Space group	P $\bar{1}$	P $\bar{1}$
<i>a</i> /Å	11.401 (1)	9.172 (1)
<i>b</i> /Å	13.986 (1)	12.733 (1)
<i>c</i> /Å	15.506 (1)	21.558 (1)
$\alpha$ /°	96.47 (1)	76.39 (1)
$\beta$ /°	102.59 (1)	81.26 (1)
$\gamma$ /°	105.99 (1)	82.47 (1)
<i>V</i> /Å <sup>3</sup>	2280.1 (2)	2406.9 (2)
<i>Z</i>	2	2
<i>D<sub>c</sub></i> /g cm <sup>-3</sup>	2.219	2.119
$\mu$ (Mo – K $\alpha$ )/mm <sup>-1</sup>	3.370	3.187
<i>F</i> (000)	1504	1520
Goodness-of-fit on <i>F</i> <sup>2</sup>	1.013	0.989
<i>R</i> <sub>1</sub> [ <i>I</i> > 2 $\sigma$ ( <i>I</i> )]/all data	0.0160/0.0175	0.0274/0.0302
<i>wR</i> <sub>2</sub> [ <i>I</i> > 2 $\sigma$ ( <i>I</i> )]/all data	0.0417/0.0426	0.0741/0.0760

CIF in Supplementary Materials.

**Figure 1.** (a) Detail of the dinuclear [Gd<sub>2</sub>(gly)<sub>6</sub>(H<sub>2</sub>O)<sub>4</sub>]<sup>6+</sup> unit in **1**; (b) Detail of the dinuclear [Gd<sub>2</sub>(β-ala)<sub>6</sub>(H<sub>2</sub>O)<sub>4</sub>]<sup>6+</sup> unit in **2**. In both cases, perchlorate anions and non-coordinating water molecules were omitted for clarity. Thermal ellipsoids are depicted at the 50% probability level.

In complex **1**, two Gd<sup>III</sup> ions of the dinuclear [Gd<sub>2</sub>(gly)<sub>6</sub>(H<sub>2</sub>O)<sub>4</sub>]<sup>6+</sup> unit are linked between them through four bridging carboxylate groups of four glycinate ligands (gly). These two Gd<sup>III</sup> ions are separated by a distance of 4.223(1) Å. Another two glycinate ligands connect these two Gd<sup>III</sup> ions to adjacent dinuclear units with separations of 5.229 (1) Å [Gd (1)⋯Gd (1a); (a) = 2 – *x*, 1 – *y*, 1 – *z*] and 5.135 (1) Å [Gd (2)⋯Gd (2b); (b) = 3 – *x*, 2 – *y*, 2 – *z*], thus generating a 1D {[Gd<sup>III</sup><sub>2</sub>]<sup>6+</sup>}<sub>n</sub> chain (Figure 2). Each Gd<sup>III</sup> ion of the dinuclear [Gd<sub>2</sub>(gly)<sub>6</sub>(H<sub>2</sub>O)<sub>4</sub>]<sup>6+</sup> unit is eight-coordinate and bonded to six oxygen atoms from six glycinate ligands and two oxygen atoms of two water molecules (Figure 1).

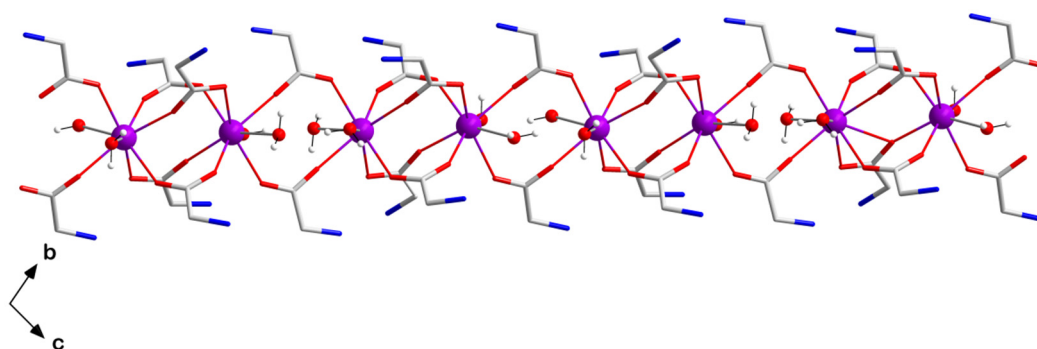


**Figure 2.** View of the one-dimensional motif of the homometallic  $\{[Gd_2(\text{gly})_6(\text{H}_2\text{O})_4](\text{ClO}_4)_6 \cdot 5\text{H}_2\text{O}\}_n$  chain in **1**. Perchlorate anions and non-coordinating water molecules were omitted for clarity. Colour code: violet, Gd; red, O; blue, N; grey, C; white, H.

The Gd–O bond lengths exhibit an average value of 2.419 (1) Å, which is somewhat shorter than that of the Gd–O<sub>w</sub> bond lengths [2.506 (1) Å] [24]. The glycinate ligands are present in their zwitterionic form with C–C, C–N, and C–O bond lengths, which are in agreement with those found in the literature for similar lanthanide-based complexes [25,26].

In the packing of **1**, the cationic  $\{[Gd^{III}_2]^{6+}\}_n$  chains are intercalated by  $\text{ClO}_4^-$  anions. The shortest interchain Gd⋯Gd distance is approximately 11.0(1) Å. The dinuclear  $[Gd_2(\text{gly})_6(\text{H}_2\text{O})_4]^{6+}$  units in the chains of **1** are connected through H-bonding interactions, which involve coordinated water molecules [O (1w)⋯O (2wa) and O (3w)⋯O (4wb) distances of 2.844 (1) and 2.780 (1) Å, respectively]. Further H-bonding interactions generated by protonated  $-\text{NH}_2$  groups of the glycinate ligands and  $\text{ClO}_4^-$  anions link the  $\{[Gd^{III}_2]^{6+}\}_n$  chains in the structure of **1**, as previously reported in the study of other SMMs structures [27–29].

In complex **2**, two  $Gd^{III}$  ions are connected between them through four bridging carboxylate groups from four  $\beta$ -alanine ( $\beta$ -ala) ligands to form the dinuclear  $[Gd_2(\beta\text{-ala})_6(\text{H}_2\text{O})_4]^{6+}$  unit. The two  $Gd^{III}$  ions are distanced from each other by an average separation of ca. 4.008 (1) Å (Figure 1), (the symmetry codes for the Gd (1)⋯Gd (1a) and Gd (2)⋯Gd (2b) distances being (a) =  $-x, 1 - y, -z$  and (b) =  $1 - x, -y, 1 - z$ , respectively). Additional  $\beta$ -ala ligands link adjacent dinuclear units with separations of 5.196 (1) Å [Gd (1)⋯Gd (1c); (c) =  $1 - x, 1 - y, -z$ ] and 5.203 (1) Å [Gd (2)⋯Gd (2d); (d) =  $2 - x, -y, 1 - z$ ], generating a cationic 1D coordination polymer that grows along the crystallographic a-axis (Figure 3).

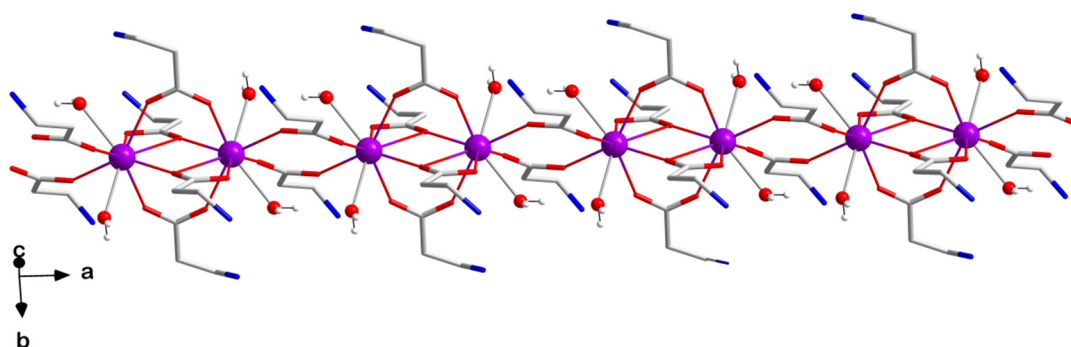


**Figure 3.** View of the one-dimensional motif of the homometallic  $\{[Gd_2(\beta\text{-ala})_6(\text{H}_2\text{O})_4](\text{ClO}_4)_6 \cdot \text{H}_2\text{O}\}_n$  chain in **2**. Perchlorate anions and non-coordinating water molecules were omitted for clarity. Colour code: violet, Gd; red, O; blue, N; grey, C; white, H.

Each  $Gd^{III}$  ion in **2** is nine-coordinate and bonded to seven oxygen atoms from six carboxylate groups of  $\beta$ -ala ligands and two oxygen atoms of two water molecules (Figure 1). The average value of the Gd–O bond lengths [2.388 (1) Å] is shorter than that of the Gd–O<sub>w</sub>

bond lengths [2.522 (1) Å]. The  $\beta$ -ala ligands are coordinated in **2** as zwitterionic molecules and the values of the C–C, C–N, and C–O bond lengths agree with those found in the literature for similar complexes based on other lanthanide (III) ions [26,30].

In the packing of **2**, the cationic  $[\text{Gd}^{\text{III}}_2]^{6+}$  chains and  $\text{ClO}_4^-$  anions are arranged in an alternate way. They are linked through intermolecular H-bonding interactions involving non-coordinated water molecules and protonated  $-\text{NH}_2$  groups of  $\beta$ -ala ligands. The shortest interchain  $\text{Gd}\cdots\text{Gd}$  distance in **2** is approximately 11.0 Å, which is for the  $\text{Gd}(2)\cdots\text{Gd}(1c)$  separation. The supramolecular structure of **2** is generated through additional H-bonding interactions.

### 2.3. Analysis of the Polyhedral Structures

The coordination environment and geometry of the  $\text{Gd}^{\text{III}}$  ions in **1** and **2** were further analyzed through the SHAPE program [31–33]. In **1**, the two  $\text{Gd}^{\text{III}}$  ions show a coordination number equal to eight (Figure 1). The lower computed value for  $\text{Gd}(1)$  was 0.732, which was associated with a bicapped trigonal prism (BCTPR) geometry (Table 2). For  $\text{Gd}(2)$ , however, a value of 0.915 was assigned to a square antiprism (SAPR) geometry (Figure 4 and Table 2). These features would suggest different geometries for the metal centers  $\text{Gd}(1)$  and  $\text{Gd}(2)$  in compound **1** (Figure 4).

**Table 2.** Selected values for possible geometries with coordination number (CN) equal to 8 obtained through the SHAPE program and from structural parameters of complex **1**<sup>a</sup>.

Metal Ion	HBPY	CU	SAPR	TDD	JGBF	JETBPY	BTPR	JSD	TT
Gd(1)	17.116	11.317	1.254	1.763	13.137	27.406	0.732	3.440	11.813
Gd(2)	13.944	9.336	0.915	2.077	12.464	28.179	1.167	3.889	9.984

<sup>a</sup> HBPY: Hexagonal bipyramid ( $D_{6h}$ ); CU: Cube (Oh); SAPR: Square antiprism ( $D_{4d}$ ); TDD: Triangular dodecahedron ( $D_{2d}$ ); JGBF: Johnson gyrobifastigium ( $D_{2d}$ ); JETBPY: Johnson elongated triangular bipyramid ( $D_{3h}$ ); BTPR: Biaugmented trigonal prism ( $C_{2v}$ ); JSD: Snub diphenoid ( $D_{2d}$ ); TT: Triakis tetrahedron (Td).

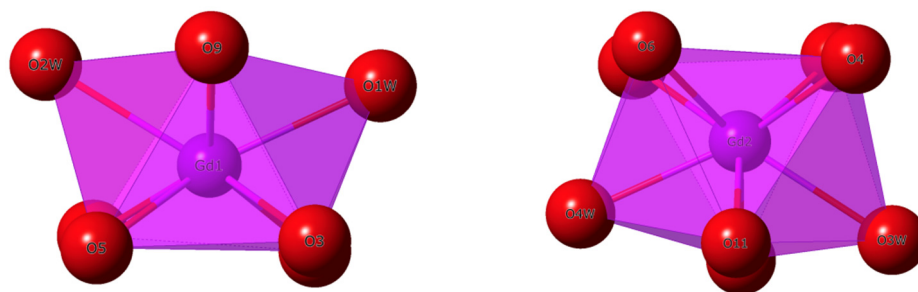


**Figure 4.** Polyhedral view of the coordination sphere around the gadolinium (III) ions of the dinuclear  $[\text{Gd}^{\text{III}}_2]^{6+}$  unit in complex **1** [ $\text{Gd}(1)$ , (left);  $\text{Gd}(2)$  (right)].

Unlike **1**, the two  $\text{Gd}^{\text{III}}$  ions of the dinuclear  $[\text{Gd}^{\text{III}}_2]^{6+}$  unit in compound **2** exhibit a coordination number equal to nine (Figure 1). The lower SHAPE values computed for these two  $\text{Gd}^{\text{III}}$  ions were 1.117 and 1.208 for  $\text{Gd}(1)$  and  $\text{Gd}(2)$ , respectively (Table 3). These calculated values were assigned to a capped square antiprism (CSAPR) geometry (Figure 5), hence indicating the same geometry for the  $\text{Gd}^{\text{III}}$  ions in the dinuclear  $[\text{Gd}^{\text{III}}_2]^{6+}$  unit of **2**.

**Table 3.** Selected values for possible geometries with coordination number (CN) equal to 9 obtained through the SHAPE program and from structural parameters of complex **2**<sup>a</sup>.

Metal Ion	HPY	JTC	JCCU	CSAPR	JTCTPR	TCTPR	JTDIC	HH	MFF
Gd(1)	19.213	15.400	10.340	1.117	2.255	1.543	12.866	10.100	1.368
Gd(2)	18.545	14.843	10.477	1.208	2.134	1.561	13.375	9.502	1.489

<sup>a</sup> HPY: Heptagonal bipyramid ( $D_{7h}$ ); JTC: Johnson triangular cupola ( $C_{3v}$ ); JCCU: Capped cube ( $C_{4v}$ ); CSAPR: Spherical capped square antiprism ( $C_{4v}$ ); JTCTPR: Tricapped trigonal prism ( $D_{3h}$ ); TCTPR: Spherical tricapped trigonal prism ( $D_{3h}$ ); JTDIC: Tridiminished icosahedron ( $C_{3v}$ ); HH: Hula-hoop ( $C_{2v}$ ); MFF: Muffin (Cs).



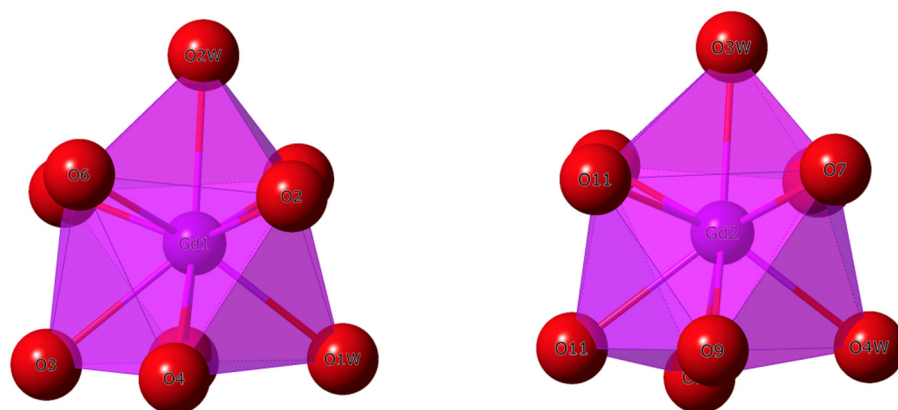


**Figure 5.** Polyhedral view of the coordination sphere around the gadolinium (III) ions of the dinuclear  $[\text{Gd}^{\text{III}}_2]^{6+}$  unit in complex **2** [Gd (1), (left); Gd (2) (right)].

As shown in Tables 2 and 3, these computed values for **1** allow us to assign the  $C_{2v}$  and  $D_{4d}$  symmetries to the Gd (1) and Gd (2) ions, respectively, whereas both  $\text{Gd}^{\text{III}}$  ions (Gd (1) and Gd (2)) exhibit  $C_{4v}$  symmetry in **2**. In any case, they would be approximate symmetries.

#### 2.4. Magnetic Properties

Dc magnetic susceptibility measurements were carried out on microcrystalline samples of **1** and **2** in the 2–300 K temperature range and under an external magnetic field of 0.5 T. In order to keep the samples both immobilized and well isolated from the moisture of the air at all moments, the organic compound eicosene was used. The  $\chi_M T$  versus  $T$  plots ( $\chi_M$  being the molar magnetic susceptibility per two  $\text{Gd}^{\text{III}}$  ions) for compounds **1** and **2** are given in Figure 6. At room temperature, the  $\chi_M T$  values are ca. 15.7 (**1**) and ca. 15.9  $\text{cm}^3 \text{mol}^{-1} \text{K}$  (**2**), which are very close to that expected for two magnetically uncoupled  $\text{Gd}^{\text{III}}$  ions ( $4f^7$  ion with  $g_{\text{Gd}} = 2.0$ ,  $S_{\text{Gd}} = 7/2$  and  $L_{\text{Gd}} = 0$ ) [34]. Upon cooling, the  $\chi_M T$  values approximately follow the Curie law with decreasing temperature to ca. 20 K, before they decrease reaching minimum values of approximately 13.4 (**1**) and 14.0  $\text{cm}^3 \text{mol}^{-1} \text{K}$  (**2**) at 2 K. The decrease in the  $\chi_M T$  value observed for both compounds would likely be assignable to antiferromagnetic interactions and/or small zero-field splitting (ZFS) effects [20,21].

The field dependence of the molar magnetization ( $M$ ) plots for **1** and **2** are given in the respective insets of Figure 6. The  $M$  values display a continuous increase with the applied magnetic field at 2 K. The higher  $M$  value is ca. 14.0  $\mu_B$  for both compounds, which is in agreement with those of similar  $\text{Gd}^{\text{III}}$  compounds containing dinuclear units [35,36].

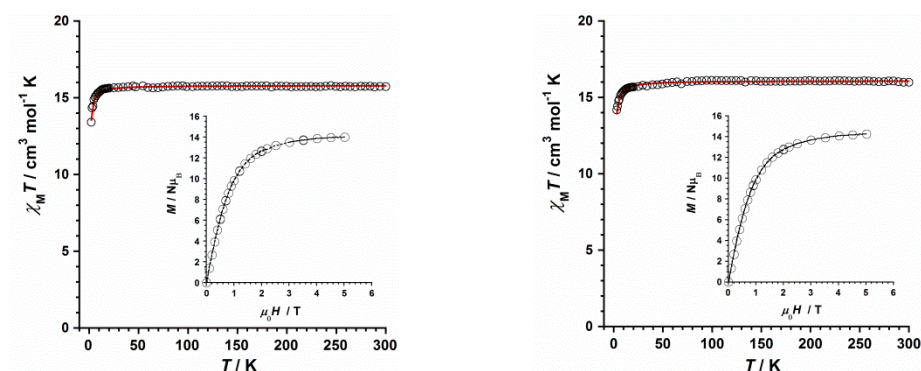


**Figure 6.** Thermal variation of the  $\chi_M T$  product for complexes **1** (left) and **2** (right). The solid red line represents the theoretical fit of the experimental data and the inset shows the  $M$  versus  $H$  plot at 2.0 K.

Taking into account the crystal structures described for **1** and **2**, which are made up of linked dinuclear  $\text{Gd}^{\text{III}}$  units, we considered them as magnetically isolated dinuclear  $\text{Gd}^{\text{III}}$



systems. Thus, we performed the treatment of the experimental data of the  $\chi_M T$  versus  $T$  plots through the isotropic Hamiltonian of Equation (1):

$$\hat{H} = -J\hat{S}_1 \cdot \hat{S}_2 + \mu_B g H \hat{S} \quad (1)$$

The best least-squares fit gave the parameters  $J = -0.042$  (1)  $\text{cm}^{-1}$  and  $g = 2.003$ (1) with  $R = 4.7 \times 10^{-5}$  for **1**, and  $J = -0.030$  (3)  $\text{cm}^{-1}$  and  $g = 2.002$  (1) with  $R = 5.2 \times 10^{-5}$  for **2** [ $R$  being the agreement factor defined as  $\sum_i [(\chi_M T)_i^{\text{obs}} - (\chi_M T)_i^{\text{calcd}}]^2 / [(\chi_M T)_i^{\text{obs}}]^2$ ]. As shown in Figure 6, the calculated curves (solid red lines) reproduce the experimental magnetic data in the whole temperature range quite well. The sign and magnitude of the  $J$  values indicate the presence of weak antiferromagnetic exchanges between the  $\text{Gd}^{\text{III}}$  ions connected through carboxylate bridges of the  $\alpha$ -glycine and  $\beta$ -alanine amino acids in **1** and **2**, respectively. As far as we know, these  $J$  values are the first ones reported for  $\text{Gd}^{\text{III}}$  complexes based on these two amino acids. Nevertheless, they are in agreement with those previously reported for  $\text{Gd}^{\text{III}}$  systems linked through similar carboxylate bridges [36].

Ac magnetic susceptibility measurements were performed on **1** and **2** in the temperature range of 2–25 K and in a 5.0 G ac field oscillating at different frequencies. No out-of-phase ac signals ( $\chi''_M$ ) were observed at  $H_{\text{dc}} = 0$  G, which may be caused by a very fast Quantum Tunnelling of Magnetization (QTM) in **1** and **2**. Nevertheless, out-of-phase ac signals were observed in both compounds when an external dc magnetic field (the optimal field being  $H_{\text{dc}} = 2500$  G) was applied. This applied dc magnetic field suppresses QTM and breaks the Kramer's doublet, leading to the observed slow relaxation [17,20,21]. In this way, both compounds show field-induced slow relaxation of magnetization, which is indicative of single-molecule magnet (SMM) behavior [4,7]. This magnetic relaxation observed for **1** and **2** was studied through both in-phase ( $\chi'_M$ ) and out-of-phase ( $\chi''_M$ ) ac susceptibilities versus frequency ( $\nu/\text{Hz}$ ) plots, which are given in Figures 7 and 8, respectively. The experimental data of the maxima in **2** display higher intensity than those of **1**, even though similar relaxation dynamics could be a priori expected for both compounds.

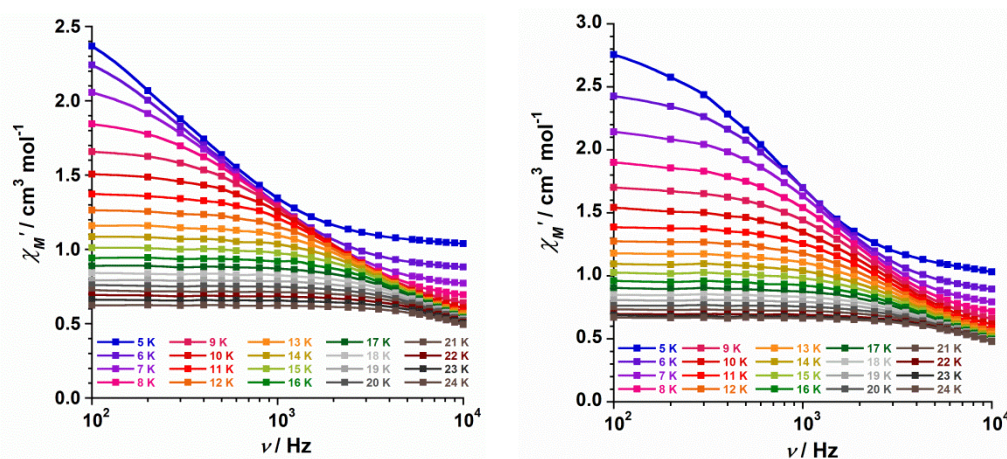


**Figure 7.** Frequency dependence of the in-phase ac susceptibility signals under a dc field of 2500 G for **1** (left) and **2** (right).

The insets in Figure 8 show the  $\ln(\tau)$  versus  $1/T$  curves for **1** and **2**. In both compounds, the experimental data draw a straight line along the ranges of ca. 0.03–0.15 (**1**) and ca. 0.04–0.07  $\text{K}^{-1}$  (**2**) of the high-temperature region of **1** and **2**, which connect with other straight-line behavior in the ranges of ca. 0.20–0.47 (**1**) and ca. 0.09–0.44  $\text{K}^{-1}$  (**2**) of the low-temperature region. In order to fit the experimental data of the  $\ln(\tau)$  versus  $1/T$  plots, several relaxation mechanisms were considered for both compounds [7,9]. Nevertheless, the whole  $\ln(\tau)$  versus  $1/T$  curves were reasonably fitted through two mechanisms for the

relaxation of magnetization, namely, Orbach [ $\tau_0^{-1} \exp(-U_{\text{eff}}/k_B T)$ ] and Raman [ $CT^n$ ], according to Equation (2):

$$\tau^{-1} = \tau_0^{-1} \exp(-U_{\text{eff}}/k_B T) + CT^n \quad (2)$$

The least-squares fit of the experimental data of **1** and **2** through Equation (2) leads to the following set of parameters:  $U_{\text{eff}} = 26.3$  (2)  $\text{cm}^{-1}$ ,  $\tau_0 = 3.1$  (2)  $\times 10^{-6}$  s,  $C = 168$  (5)  $\text{s}^{-1}\text{K}^{-n}$  and  $n = 1.5$  (2) for **1**, and  $U_{\text{eff}} = 7.8$  (2)  $\text{cm}^{-1}$ ,  $\tau_0 = 2.6$  (1)  $\times 10^{-5}$  s,  $C = 2.6$  (2)  $\text{s}^{-1}\text{K}^{-n}$ , and  $n = 3.1$  (2) for **2**. Although these values are the first ones reported for one-dimensional homometallic  $\text{Gd}^{\text{III}}$  complexes based on these amino acids, they are close to those previously reported for similar  $\text{Gd}^{\text{III}}$  complexes [12,13]. The values of the effective energy barrier ( $U_{\text{eff}}$ ) obtained for **1** and **2** are lower than those reported for the derivatives complexes containing  $\text{Dy}^{\text{III}}$  ion [26]. Nevertheless, the  $U_{\text{eff}}$  values reported for **1** and **2** should be carefully considered as they could not correspond to any excited  $\text{Gd}^{\text{III}}$  states and therefore would not be real effective energy barrier values [13,21].

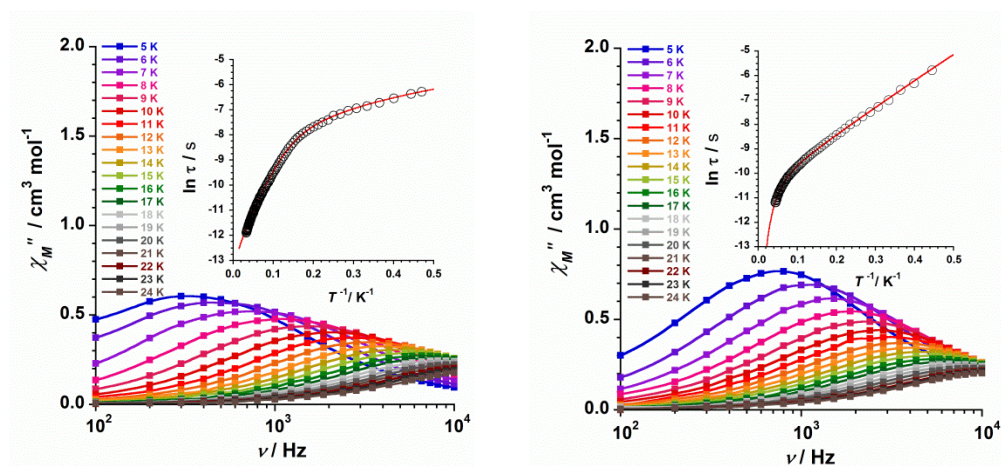


**Figure 8.** Frequency dependence of the out-of-phase ac susceptibility signals under a dc field of 2500 G for **1** (left) and **2** (right). The inset shows the  $\ln(\tau)$  versus  $1/T$  plot with the fit considering the contribution of two mechanisms (Orbach + Raman).

The local symmetries displayed in the dinuclear  $\text{Gd}^{\text{III}}$  units are  $C_{2v}$  and  $D_{4d}$  in **1** and  $C_{4v}$  in **2**. According to previous lanthanide (III) complexes studies, a priori, the local symmetry  $D_{4d}$  found in **1** would lead to better SMM properties [5–7], as observed for its  $U_{\text{eff}}$  value when compared with that of **2**, but this fact relies at last on the relative orientation of the magnetic anisotropy axes of all the spin carriers [26].

The  $\tau_0$  values obtained for **1** and **2**, being approximately  $10^{-6}$ – $10^{-5}$  s, are in agreement with those previously reported for single-ion and single-molecule magnets [13,17], which supports our consideration that the predominant magnetic behavior in both compounds would be that of dinuclear single-molecule magnets, rather than a single-chain magnet.

Finally, according to our results, the relaxation pathway for **1** and **2** should be a combination of different processes, namely, Orbach (at a higher temperature) and Raman (at a lower temperature), both of them involving two phonons. The reported  $n$  value for **1** ( $n \approx 2$ ) would indicate the presence at least of a phonon bottleneck effect, whereas the  $n$  value for **3** ( $n \approx 3$ ) would indicate the contribution of a Raman mechanism, as previously reported [37]. These  $n$  values suggest that only a direct process would not be operative in the relaxation dynamics of **1** and **2**. In any case, further detailed magnetic and theoretical studies performed on different  $\text{Gd}^{\text{III}}$  complexes will be necessary to correctly understand the relaxation dynamics of  $\text{Gd}^{\text{III}}$  SMMs.

### 3. Experimental Section

#### 3.1. Preparation of the Complexes

##### 3.1.1. Synthesis of $\{[\text{Gd}_2(\text{gly})_6(\text{H}_2\text{O})_4](\text{ClO}_4)_6 \cdot 5\text{H}_2\text{O}\}_n$ (**1**)

A solvothermal reaction of  $\text{Gd}_2\text{O}_3$  (0.072 g, 0.20 mmol) and glycine (0.030 g, 0.40 mmol) was performed in an aqueous suspension (2 mL) acidulated with perchloric acid (1.0 mL, 2 M) at 80 °C for 48 h, followed by a cooling process at 4.5 °C/h to room temperature. Colourless parallelepipeds were obtained and were suitable for single-crystal X-ray diffraction studies. Yield: ca. 60%. Anal. Calcd. for  $\text{C}_{12}\text{H}_{48}\text{N}_6\text{O}_{45}\text{Cl}_6\text{Gd}_2$  (**1**): C, 9.5; H, 3.2; N, 5.5. Found: C, 9.9; H, 3.0; N, 5.3. SEM-EDAX: a molar ratio of 1:3 for Gd/Cl was found for **1**. IR (KBr pellet): peaks associated mainly to the glycine ligand and also to the perchlorate anion are observed at 3407 (s), 3080(m), 3006 (m), 2781 (w), 2708 (w), 1628 (vs), 1609 (vs), 1570 (m), 1499 (m), 1466 (m), 1413 (m), 1335 (m), 1144 (vs), 1109 (vs), 1088 (s), 905 (m), 626 (s), 536 (w), 507 (w)  $\text{cm}^{-1}$ .

##### 3.1.2. Synthesis of $\{[\text{Gd}_2(\beta\text{-ala})_6(\text{H}_2\text{O})_4](\text{ClO}_4)_6 \cdot \text{H}_2\text{O}\}_n$ (**2**)

A mixture of  $\text{Gd}_2\text{O}_3$  (0.090 g, 0.25 mmol) and  $\beta$ -alanine (0.022 g, 0.25 mmol) in an aqueous suspension (5 mL) acidulated with perchloric acid (1.0 mL, 2 M) was stirred and heated at 60 °C for 1h. The resulting solution was left to evaporate at room temperature for 2 weeks. Colourless needles were obtained, which were suitable for single-crystal X-ray diffraction. Yield: ca. 55%. Anal. Calcd for  $\text{C}_{18}\text{H}_{52}\text{N}_6\text{O}_{41}\text{Cl}_6\text{Gd}_2$  (**2**): C, 14.1; H, 3.4; N, 5.5. Found: C, 14.0; H, 3.3; N, 5.6. SEM-EDAX: a molar ratio of 1:3 for Gd/Cl was found for **2**. IR (KBr pellet): peaks associated to  $\beta$ -alanine ligand and perchlorate anion are observed at 3396 (s), 1622 (s), 1578 (s), 1460 (s), 1406 (m), 1336 (m), 1312 (w), 1264 (w), 1144 (vs), 1116 (vs), 1090 (s), 958 (m), 941 (w), 641 (m), 627 (s), 590 (w), 520 (w)  $\text{cm}^{-1}$ .

#### 3.2. X-ray Data Collection and Structure Refinement

X-ray diffraction data collection on single crystals of dimensions  $0.18 \times 0.11 \times 0.09$  (**1**) and  $0.18 \times 0.09 \times 0.06$  mm<sup>3</sup> (**2**) were collected on a Bruker D8 Venture diffractometer with PHOTON II detector and by using monochromatised Mo- $\text{K}\alpha$  radiation ( $\lambda = 0.71073$  Å). Crystal parameters and refinement results for **1** and **2** are summarized in Table 1. The structures were solved by standard direct methods and subsequently completed by Fourier recycling using the SHELXTL [38] software packages and refined by the full-matrix least-squares refinements based on  $F^2$  with all observed reflections. The final graphical manipulations were performed with the DIAMOND [39] and CRYSTALMAKER [40] programs. CCDC 2,149,741 and 2,149,742 for **1** and **2**, respectively.

#### 3.3. Physical Measurements

Elemental analyses (C, H, N) were performed in an Elemental Analyzer CE Instrument CHNS1100 and the molar ratio between heavier elements was found by means of a Philips XL-30 scanning electron microscope (SEM-EDAX), equipped with a system of X-ray microanalysis, in the Central Service for the Support to Experimental Research (SCSIE) at the University of Valencia. Infrared spectra (IR) of **1** and **2** were recorded with a PerkinElmer Spectrum 65 FT-IR spectrometer in the 4000–400  $\text{cm}^{-1}$  range. Variable-temperature, solid-state (dc and ac) magnetic susceptibility data were collected on Quantum Design MPMS-XL SQUID and Physical Property Measurement System (PPMS) magnetometers. Experimental magnetic data were corrected for the diamagnetic contributions of both the sample holder and the eicosene. The diamagnetic contribution of the involved atoms was corrected by using Pascal's constants [41].

### 4. Conclusions

In summary, the synthesis, crystal structure and magnetic properties of two one-dimensional  $\text{Gd}^{\text{III}}$  complexes based on the  $\alpha$ -glycine (gly) and  $\beta$ -alanine ( $\beta$ -ala) amino acids, with the formula  $\{[\text{Gd}_2(\text{gly})_6(\text{H}_2\text{O})_4](\text{ClO}_4)_6 \cdot 5\text{H}_2\text{O}\}_n$  (**1**) and  $\{[\text{Gd}_2(\beta\text{-ala})_6(\text{H}_2\text{O})_4](\text{ClO}_4)_6 \cdot \text{H}_2\text{O}\}_n$  (**2**), were reported. Their structures are described as cationic dinuclear  $[\text{Gd}^{\text{III}}_2]^{6+}$  units which

are connected through carboxylate groups from glycine (**1**) and  $\beta$ -alanine (**2**), forming one-dimensional  $\{[\text{Gd}^{\text{III}}_2]^{6+}\}_n$  systems. Different symmetries of the  $\text{Gd}^{\text{III}}$  ions, namely,  $\text{C}_{2v}$  and  $\text{D}_{4d}$  in **1** and  $\text{C}_{4v}$  in **2**, were found in the study of their coordination environment.

The investigation of the magnetic properties of **1** and **2** through dc magnetic susceptibility measurements reveals a similar magnetic behavior, with both compounds exhibiting weak antiferromagnetic exchange couplings between  $\text{Gd}^{\text{III}}$  ions. In addition, ac magnetic susceptibility measurements show field-induced slow relaxation of magnetization for both **1** and **2**, which indicates that the single-molecule magnet (SMM) phenomenon takes place in these novel one-dimensional  $\text{Gd}^{\text{III}}$  complexes.

**Supplementary Materials:** The following supporting information can be downloaded at: <https://www.mdpi.com/article/10.3390/inorganics10030032/s1>, CIF files 2149741 (**1**) and 2149742 (**2**).

**Author Contributions:** Conceptualization, J.M.-L.; funding acquisition, I.C., F.L. and J.M.-L.; methodology, M.O.-A., A.S.-P., N.M., I.C. and J.M.-L.; investigation, M.O.-A., A.S.-P., N.M., F.L. and J.M.-L.; formal analysis, M.O.-A., A.S.-P., N.M., I.C. and J.M.-L.; writing—original draft preparation, J.M.-L.; writing—review and editing, J.M.-L. All authors have read and agreed to the published version of the manuscript.

**Funding:** This research was funded by the Spanish Ministry of Science and Innovation (Grant numbers PID2019-109735GB-I00 and CEX2019-000919-M (Excellence Unit “María de Maeztu”)) and also by the VLC-BIOMED Program of the University of Valencia (Grant number PI-2020-19-DIGABIO).

**Institutional Review Board Statement:** Not applicable.

**Informed Consent Statement:** Not applicable.

**Data Availability Statement:** The raw data that support the findings of this study are available from the corresponding author upon reasonable request.

**Acknowledgments:** The authors M.O.-A. and A.S.-P. thank the Spanish “FPI fellowships” and “FPU fellowships” programs, respectively.

**Conflicts of Interest:** The authors declare no conflict of interest.

## References

1. Ishikawa, N.; Sugita, M.; Ishikawa, T.; Koshihara, S.Y.; Kaizu, Y. Lanthanide double-decker complexes functioning as magnets at the single-molecular level. *J. Am. Chem. Soc.* **2003**, *125*, 8694–8695. [[CrossRef](#)]
2. Ishikawa, N.; Sugita, M.; Ishikawa, T.; Koshihara, S.Y.; Kaizu, Y. Mononuclear Lanthanide Complexes with a Long Magnetization Relaxation Time at High Temperatures: A New Category of Magnets at the Single-Molecular Level. *J. Phys. Chem. B* **2004**, *108*, 11265–11271. [[CrossRef](#)]
3. Habib, F.; Murugesu, M. Lessons learned from dinuclear lanthanide nano-magnets. *Chem. Soc. Rev.* **2013**, *42*, 3278–3288. [[CrossRef](#)]
4. Ferrando-Soria, J.; Vallejo, J.; Castellano, M.; Martínez-Lillo, J.; Pardo, E.; Cano, J.; Castro, I.; Lloret, F.; Ruiz-García, R.; Julve, M. Molecular magnetism, quo vadis? A historical perspective from a coordination chemist viewpoint. *Coord. Chem. Rev.* **2017**, *339*, 17–103. [[CrossRef](#)]
5. Liu, J.-L.; Chen, Y.-C.; Tong, M.-L. Symmetry strategies for high performance lanthanide-based single-molecule magnets. *Chem. Soc. Rev.* **2018**, *47*, 2431–2453. [[CrossRef](#)] [[PubMed](#)]
6. Dey, A.; Kalita, P.; Chandrasekhar, V. Lanthanide(III)-Based Single-Ion Magnets. *ACS Omega* **2018**, *3*, 9462–9475. [[CrossRef](#)] [[PubMed](#)]
7. Zabala-Lekuona, A.; Seco, J.M.; Colacio, E. Single-Molecule Magnets: From Mn12-ac to dysprosium metallocenes, a travel in time. *Coord. Chem. Rev.* **2021**, *441*, 213984. [[CrossRef](#)]
8. Gebrezgiabher, M.; Bayeh, Y.; Gebretsadik, T.; Gebreslassie, G.; Elemo, F.; Thomas, M.; Linert, W. Lanthanide-Based Single-Molecule Magnets Derived from Schiff Base Ligands of Salicylaldehyde Derivatives. *Inorganics* **2020**, *8*, 66. [[CrossRef](#)]
9. McAdams, S.G.; Ariciu, A.-M.; Kostopoulos, A.K.; Walsh, J.P.S.; Tuna, F. Molecular single-ion magnets based on lanthanides and actinides: Design considerations and new advances in the context of quantum technologies. *Coord. Chem. Rev.* **2017**, *346*, 216–239. [[CrossRef](#)]
10. Karotsis, G.; Evangelisti, M.; Dalgarno, S.J.; Brechin, E.K. A Calix[4]arene 3d/4f Magnetic Cooler. *Angew. Chem. Int. Ed.* **2009**, *48*, 9928–9931. [[CrossRef](#)]



11. Ghosh, T.K.; Maity, S.; Mayans, J.; Ghosh, A. Family of Isomeric Cu<sup>II</sup>–Ln<sup>III</sup> (Ln = Gd, Tb, and Dy) Complexes Presenting Field-Induced Slow Relaxation of Magnetization Only for the Members Containing Gd<sup>III</sup>. *Inorg. Chem.* **2020**, *60*, 438–448. [[CrossRef](#)] [[PubMed](#)]
12. Borah, A.; Murugavel, R. Magnetic relaxation in single-ion magnets formed by less-studied lanthanide ions Ce(III), Nd(III), Gd(III), Ho(III), Tm(II/III) and Yb(III). *Coord. Chem. Rev.* **2022**, *453*, 214288. [[CrossRef](#)]
13. Maciel, J.W.D.O.; Lemes, M.A.; Valdo, A.K.; Rabelo, R.; Martins, F.T.; Maia, L.J.Q.; Costa de Santana, R.; Lloret, F.; Julve, M.; Cangussu, D. Europium(III), Terbium(III), and Gadolinium(III) Oxamate-Based Coordination Polymers: Visible Luminescence and Slow Magnetic Relaxation. *Inorg. Chem.* **2021**, *60*, 6176–6190. [[CrossRef](#)] [[PubMed](#)]
14. Rodríguez-Barea, B.; Mayans, J.; Rabelo, R.; Sanchis-Perucho, A.; Moliner, N.; Martínez-Lillo, J.; Julve, M.; Lloret, F.; Ruiz-García, R.; Cano, J. Holmium(III) Single-Ion Magnet for Cryomagnetic Refrigeration Based on an MRI Contrast Agent Derivative. *Inorg. Chem.* **2021**, *60*, 12719–12723. [[CrossRef](#)]
15. Orts-Arroyo, M.; Rabelo, R.; Carrasco-Berlanga, A.; Moliner, N.; Cano, J.; Julve, M.; Lloret, F.; De Munno, G.; Ruiz-García, R.; Mayans, J.; et al. Field-induced slow magnetic relaxation and magnetocaloric effects in an oxalato-bridged gadolinium(III)-based 2D MOF. *Dalton Trans.* **2021**, *50*, 3801–3805. [[CrossRef](#)]
16. Arauzo, A.; Lazarescu, A.; Shova, S.; Bartolomé, E.; Cases, R.; Luzón, J.; Bartolomé, J.; Turta, C. Structural and magnetic properties of some lanthanide (Ln = Eu(III), Gd(III) and Nd(III)) cyanoacetate polymers: Field-induced slow magnetic relaxation in the Gd and Nd substitutions. *Dalton Trans.* **2014**, *43*, 12342–12356. [[CrossRef](#)]
17. Izuogu, D.C.; Yoshida, T.; Zhang, H.; Cosquer, G.; Katoh, K.; Ogata, S.; Hasegawa, M.; Nojiri, H.; Damjanović, M.; Wernsdorfer, W.; et al. Slow Magnetic Relaxation in a Palladium–Gadolinium Complex Induced by Electron Density Donation from the Palladium Ion. *Chem. Eur. J.* **2018**, *24*, 9285–9294. [[CrossRef](#)]
18. Guo, F.-S.; Day, B.M.; Chen, Y.-C.; Tong, M.-L.; Mansikkamäki, A.; Layfield, R.A. Magnetic hysteresis up to 80 kelvin in a dysprosium metallocene single-molecule magnet. *Science* **2018**, *362*, 1400–1403. [[CrossRef](#)]
19. Ullah, A.; Cerdá, J.; Baldoví, J.J.; Varganov, S.A.; Aragón, J.; Gaita-Ariño, A. In Silico Molecular Engineering of Dysprosocenium-Based Complexes to Decouple Spin Energy Levels from Molecular Vibrations. *J. Phys. Chem. Lett.* **2019**, *10*, 7678–7683. [[CrossRef](#)]
20. Chen, Y.-C.; Peng, Y.-Y.; Liu, J.-L.; Tong, M.-L. Field-induced slow magnetic relaxation in a mononuclear Gd(III) complex. *Inorg. Chem. Commun.* **2019**, *107*, 107449. [[CrossRef](#)]
21. Mayans, J.; Escuer, A. Correlating the axial Zero Field Splitting with the slow magnetic relaxation in Gd<sup>III</sup> SIMs. *Chem. Commun.* **2021**, *57*, 721–724. [[CrossRef](#)] [[PubMed](#)]
22. Lu, J.-L.; Liu, B.-P.; Tan, Z.-C.; Zhang, D.-S.; Li, L.; Chen, Y.-D.; Shi, Q. Synthesis, Crystal Structure and Thermochemical Study of [Gd<sub>2</sub>(Gly)<sub>6</sub>(H<sub>2</sub>O)<sub>4</sub>](ClO<sub>4</sub>)<sub>6</sub>(H<sub>2</sub>O)<sub>5</sub>. *Acta Chim. Sin. Chin. Ed.* **2007**, *65*, 2349–2355.
23. Liang, F.-P.; Ma, L.-F.; Huang, S.-W.; Huang, Y.-Q. Synthesis, Crystal Structure and Antibacterial Activity of β-Alanine Complexes with Nd, Gd, Er. *Chin. J. Appl. Chem.* **2004**, *21*, 58–62.
24. Orts-Arroyo, M.; Ten-Esteve, A.; Ginés-Cárdenas, S.; Castro, I.; Martí-Bonmatí, L.; Martínez-Lillo, J. A Gadolinium(III) Complex Based on the Thymine Nucleobase with Properties Suitable for Magnetic Resonance Imaging. *Int. J. Mol. Sci.* **2021**, *22*, 4586. [[CrossRef](#)]
25. Legendziewicz, J.; Huskowska, E.; Waśkowska, A.; Argay, G. Spectroscopy and crystal structure of neodymium coordination compound with glycine: Nd<sub>2</sub>(Gly)<sub>6</sub>·(ClO<sub>4</sub>)<sub>6</sub>·9H<sub>2</sub>O. *Inorg. Chim. Acta* **1984**, *92*, 151–157. [[CrossRef](#)]
26. Orts-Arroyo, M.; Castro, I.; Lloret, F.; Martínez-Lillo, J. Field-induced slow relaxation of magnetisation in two one-dimensional homometallic dysprosium(III) complexes based on alpha- and beta-amino acids. *Dalton Trans.* **2020**, *49*, 9155–9163. [[CrossRef](#)]
27. Martínez-Lillo, J.; Dolan, N.; Brechin, E.K. A cationic and ferromagnetic hexametallc Mn(III) single-molecule magnet based on the salicylamidoxime ligand. *Dalton Trans.* **2013**, *42*, 12824–12827. [[CrossRef](#)]
28. Martínez-Lillo, J.; Dolan, N.; Brechin, E.K. A family of cationic oxime-based hexametallc manganese(III) single-molecule magnets. *Dalton Trans.* **2014**, *43*, 4408–4414. [[CrossRef](#)]
29. Rojas-Dotti, C.; Moliner, N.; Lloret, F.; Martínez-Lillo, J. Ferromagnetic Oxime-Based Manganese(III) Single-Molecule Magnets with Dimethylformamide and Pyridine as Terminal Ligands. *Crystals* **2019**, *9*, 23. [[CrossRef](#)]
30. Jianxue, L.; Ninghai, H.; Chunji, N.; Qingbo, M. The crystal structure of a samarium complex with β-alanine. *J. Alloys Compd.* **1992**, *184*, L1–L3. [[CrossRef](#)]
31. Llunell, M.; Casanova, D.; Cirera, J.; Alemany, P.; Alvarez, S. *SHAPE 2.1*; Universitat de Barcelona: Barcelona, Spain, 2013.
32. Alvarez, S.; Alemany, P.; Casanova, D.; Cirera, J.; Llunell, M.; Avnir, D. Shape maps and polyhedral interconversion paths in transition metal chemistry. *Coord. Chem. Rev.* **2005**, *249*, 1693–1708. [[CrossRef](#)]
33. Ruiz-Martínez, A.; Casanova, D.; Alvarez, S. Polyhedral Structures with an Odd Number of Vertices: Nine-Coordinate Metal Compounds. *Chem. Eur. J.* **2008**, *14*, 1291–1303. [[CrossRef](#)] [[PubMed](#)]
34. Martínez-Lillo, J.; Cañadillas-Delgado, L.; Cano, J.; Lloret, F.; Julve, M.; Faus, J. A heteropentannuclear oxalato-bridged [Re<sup>IV</sup><sub>4</sub>Gd<sup>III</sup>] complex: Synthesis, crystal structure and magnetic properties. *Chem. Commun.* **2012**, *48*, 9242–9244. [[CrossRef](#)]
35. Roy, L.E.; Hughbanks, T. Magnetic Coupling in Dinuclear Gd Complexes. *J. Am. Chem. Soc.* **2006**, *128*, 568–575. [[CrossRef](#)] [[PubMed](#)]
36. Cañadillas-Delgado, L.; Fabelo, O.; Cano, J.; Ruiz-Pérez, C. *Magnetic Interactions in Oxo-Carboxylate Bridged Gadolinium(III) Complexes Synthesis, Crystal Structures and Magnetic Properties*; Nova Science Publishers, Inc.: Hauppauge, NY, USA, 2010.

37. Handzlik, G.; Magott, M.; Arczyński, M.; Sheveleva, A.M.; Tuna, F.; Baran, S.; Pinkowicz, D. Identical anomalous Raman relaxation exponent in a family of single ion magnets: Towards reliable Raman relaxation determination? *Dalton Trans.* **2020**, *49*, 11942–11949. [[CrossRef](#)]
38. *SHELXTL-2013/4, Bruker Analytical X-Ray Instruments*; Sheldrick, G.M. (Ed.) Bruker Analytical X-ray Systems, Inc.: Madison, WI, USA, 2013.
39. *Diamond 4.5.0*; Crystal Impact GbR; Crystal Impact: Bonn, Germany, 2018.
40. *CrystalMaker 8.7.5*; CrystalMaker Software Ltd.: Oxford, UK, 2013.
41. Bain, G.A.; Berry, J.F. Diamagnetic Corrections and Pascal's Constants. *J. Chem. Educ.* **2008**, *85*, 532–536. [[CrossRef](#)]

---

*ARTICLE 10*

*Field-induced slow magnetic  
relaxation and magnetocaloric  
effects in an oxalato-bridged  
gadolinium(III)-based 2D MOF*





Cite this: *Dalton Trans.*, 2021, **50**, 3801Received 10th February 2021,  
Accepted 25th February 2021

DOI: 10.1039/d1dt00462j

rsc.li/dalton

## Field-induced slow magnetic relaxation and magnetocaloric effects in an oxalato-bridged gadolinium(III)-based 2D MOF†

Marta Orts-Arroyo,<sup>a</sup> Renato Rabelo,<sup>a</sup> Ainoa Carrasco-Berlanga,<sup>a</sup> Nicolás Moliner,<sup>a</sup> Joan Cano,<sup>ib</sup> Miguel Julve,<sup>a</sup> Francesc Lloret,<sup>a</sup> Giovanni De Munno,<sup>ib</sup> Rafael Ruiz-García,<sup>a</sup> Júlia Mayans,<sup>ib</sup>\*<sup>a</sup> José Martínez-Lillo<sup>ib</sup>\*<sup>a</sup> and Isabel Castro<sup>ib</sup>\*<sup>a</sup>

The coexistence of field-induced slow magnetic relaxation and moderately large magnetocaloric efficiency in the supra-Kelvin temperature region occurs in the 2D compound  $[\text{Gd}_2^{\text{III}}(\text{ox})_3(\text{H}_2\text{O})_6]_n \cdot 4n\text{H}_2\text{O}$  (**1**), a feature that can be exploited in the proof-of-concept design of a new class of slow-relaxing magnetic materials for cryogenic magnetic refrigeration.

Lanthanide(III) metal-organic frameworks (MOFs) have attracted much attention in the last decade because of their potential technological applications in Quantum Information Processing (QIP) and Cryogenic Magnetic Refrigeration (CMR).<sup>1–6</sup> The high spin ground state and almost-negligible magnetic anisotropy of  $\text{Gd}^{\text{III}}$  ions, combined with an extremely low magnetic ordering temperature due to the weak exchange magnetic interactions, make gadolinium(III)-based MOFs of varying dimensionalities very good candidates as magnetic molecular coolers for CMR.<sup>7–16</sup> Among them, a rare class of  $\text{Gd}^{\text{III}}$  MOFs with field-induced slow magnetic relaxation (SMR), typical of mononuclear gadolinium(III) single-ion magnets (SIMs),<sup>17,18</sup> referred to as  $\text{Gd}^{\text{III}}$  SIM-MOFs, are ideally suited for CMR investigations due to their well-known magnetocaloric (MCE) and spin-lattice relaxation (SLR) effects.<sup>19,20</sup> Hence, large changes in the isothermal magnetic entropy ( $\Delta S_m$ ) and adiabatic temperature ( $\Delta T_{\text{ad}}$ ) are expected to occur when switching off the applied magnetic field in the neighborhood of the magnetization blocking temperature. In terms of not only chemical stability and tunability but also addressing scalability,  $\text{Gd}^{\text{III}}$  SIM-MOFs are superior to their  $\text{Gd}^{\text{III}}$  SIMs analogues, which have been recently investigated both as proto-

types of quantum bits (qubits) for QIP and ultra-low temperature (sub-Kelvin) molecular coolers for CMR.<sup>21</sup>

We are particularly interested in the well-known family of 2D and 3D Ln MOFs prepared by using the simplest dicarboxylic acid, oxalic acid, as a lightweight organic bridging ligand for the design and synthesis of cryogenic magnetic coolers (Table S1, ESI†). Herein, we report our first results along this line concerning the synthesis, structural characterization, and magnetic and magnetothermal properties of a gadolinium(III) sesquioxalate decahydrate of formula  $[\text{Gd}_2^{\text{III}}(\text{ox})_3(\text{H}_2\text{O})_6]_n \cdot 4n\text{H}_2\text{O}$  (**1**). Compound **1** is a rare example of 2D  $\text{Gd}^{\text{III}}$  SIM-MOFs displaying SMR and MCE at the same time, being proposed as a new class of low-temperature (supra-Kelvin) slow-relaxing magnetic refrigerant material.

Colorless plates of **1** suitable for single-crystal X-ray diffraction (XRD) have been obtained in a pure form and good yield (ca. 70%) by slow diffusion of aqueous solutions of oxalic acid ( $\text{H}_2\text{ox}$ ) and  $\text{GdCl}_3 \cdot 6\text{H}_2\text{O}$  (3:2 molar ratio) into an H-shaped tube after several weeks at 50 °C (see the Experimental section and Table S2, ESI†). The crystal structure of **1** is made up of neutral oxalato-bridged gadolinium(III) layers of honeycomb type with a hexagonal net topology ( $6^3\text{-hcb}$ ), together with both coordinated and disordered hydrogen-bonded crystallization water (Fig. 1 and Fig. S1–S3, ESI†), as reported earlier for  $[\text{Gd}_2^{\text{III}}(\text{ox})_3(\text{H}_2\text{O})_6]_n \cdot 2.5n\text{H}_2\text{O}$  (**1'**).<sup>22</sup>

The crystallographically independent gadolinium atom of **1** has a nine-coordinate environment formed by six oxygen atoms from three bis-bidentate oxalato bridging ligands ( $\mu\text{-oxalato-}\kappa^2\text{O},\text{O}':\kappa^2\text{O}',\text{O}''$ ) plus three oxygen atoms from the three coordinated water molecules (Fig. S1†). The spherical-type distorted metal coordination polyhedron is an intermediate between a tricapped trigonal prism (TCTPR) and a mono-capped square antiprism (CSAPR), as supported by the continuous shape measures (CSHM = 0.714 and 0.790, respectively).<sup>23</sup> Interestingly, the asymmetric propeller-like tris (chelate) mononuclear units are chiral, as reported earlier for **1'**,<sup>22</sup> so that the two helical enantiomers, (*M*)- and (*P*)-

<sup>a</sup>Instituto de Ciencia Molecular (ICMol), Universitat de València, c/José Beltrán 2, 46980 Paterna (València), Spain. E-mail: julia.mayans@qi.uv.es, f.jose.martinez@uv.es, isabel.castro@uv.es

<sup>b</sup>Dipartimento di Chimica e Tecnologie Chimiche, Università della Calabria, 87030 Arcavacata di Rende, Cosenza, Italy

† Electronic supplementary information (ESI) available: Synthetic, structural and magnetic data. CCDC 2047766. For ESI and crystallographic data in CIF or other electronic format see DOI: 10.1039/d1dt00462j

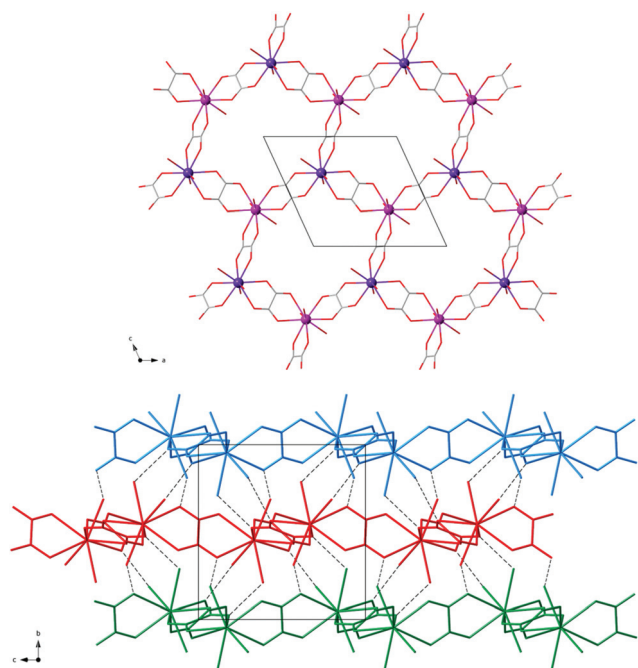


**Fig. 1** Projection views of the neutral oxalato-bridged gadolinium(III) hexagonal layer and the crystal packing of adjacent layers of **1** along the crystallographic *b* (top) and *a* axes (bottom). The two centrosymmetrically related mononuclear units of opposite chiralities are shown as dark and light purple spheres (top), while the adjacent layers are shown in different colors for clarity (bottom). Hydrogen bonds between the coordinated water molecules and the oxalato bridges are shown as dashed lines.

[Gd<sup>III</sup>(ox)<sub>3/2</sub>(H<sub>2</sub>O)<sub>3</sub>], are present in their crystal structures giving rise to achiral  $\mu$ -oxalato- $\kappa^2O,O':\kappa O'',O'''$ -gadolinium(III) layers growing in the *ac* plane (Fig. 1, top).

In the crystal lattice of **1**, the adjacent oxalato-bridged gadolinium(III) hexagonal layers are stacked along the crystallographic *b* axis (Fig. 1, bottom). However, they are not eclipsed but displaced by half a unit cell along the crystallographic *c* axis giving rise to an *-ABA-* sequence (Fig. S3,† left). Overall, this interlayer packing leads to small hexagonal pores along the [011] direction, in which the hydrogen-bonded, coordinated and free water molecules are placed (Fig. S3,† right).

The intralayer voids within the hexagonal rings are occupied by free water molecules that are hydrogen-bonded to each other [Ow...Ow = 2.85 Å] or to the oxalato bridging groups [Ow...O = 3.01 Å] (Fig. S2,† top). The interlayer space is occupied by additional free water molecules that establish moderate hydrogen bonds with the oxalato bridges (Ow...O = 2.75–2.76 Å) and with both the intralayer crystallized (Ow...Ow = 2.67–2.80 Å) and coordinated water molecules (Ow...Ow = 2.68–2.85 Å) (Fig. S2,† bottom). In addition, moderate to weak hydrogen bonds are formed among the coordinated water molecules and the oxalato bridging groups from adjacent layers [Ow...O = 2.68–3.03 Å], thereby leading to a dense packed, hydrogen-bonded multilayer structure (Fig. 1, bottom). Hence, the shortest interlayer metal separation through the hydrogen-bonded coordinated water molecules (Gd...Gd =

6.127 Å) is even shorter than the intralayer metal distances across the oxalato bridges (Gd...Gd = 6.306–6.457 Å).

The static magnetic properties of **1** were measured on frozen matrix water suspensions to prevent partial water loss (see the Experimental section). The  $\chi_M T$  vs. *T* plot shows very small deviations from the Curie law behaviour in the temperature range 2.0–300 K (Fig. S4, ESI†). The small decay of  $\chi_M T$  at low temperatures is likely due to the very weak intralayer anti-ferromagnetic interactions between the Gd<sup>III</sup> ions across the oxalato bridge, as reported earlier for **1'**.<sup>22</sup> The least-squares fit of the magnetic susceptibility data of **1** through an empirical law ( $\chi_M T$  vs.  $T/JS(S+1)$ ) with  $S = 7/2$  obtained from a Monte Carlo simulation on a 2D honeycomb network using a classical spin approach gave  $g = 2.0040(7)$  and  $J = -0.0205(5)$  cm<sup>-1</sup>, where  $g$  is the isotropic Landé factor of the Gd<sup>III</sup> ion and  $J$  is the magnetic coupling parameter (Fig. S4,† inset).<sup>24</sup> The calculated  $-J$  value for **1** is very small but non-negligible, being four-fold higher than that previously reported for **1'** [ $-J = 0.0050(2)$  K].<sup>22</sup> This scenario agrees with the isothermal magnetisation at 2 K that slightly deviates from the Brillouin function for the sum of two isolated octets ( $S = 7/2$ ) reflecting a very weak intralayer antiferromagnetic interaction between the Gd<sup>III</sup> ions (Fig. S5, ESI†). The *M* vs. *H/T* plots in the temperature range of  $T = 2.0$ – $20$  K show superimposable curves, indicating a negligible anisotropy of the Gd<sup>III</sup> ions (Fig. S5,† inset).

When measuring the dynamic magnetic properties of **1** at a fixed frequency of  $\nu = 1000$  Hz under different applied dc magnetic fields ( $H = 0, 0.1$  and  $0.25$  T), a field-induced SMR behaviour was observed (Fig. S6, ESI†). When no bias field is applied, neither  $\chi'_M$  maximum nor  $\chi''_M$  signal were observed. However, when a relatively small dc magnetic field is applied ( $H = 0.1$  T), a shoulder appears in the high-temperature tail of the  $\chi'_M$  vs. *T* plot (Fig. S6,† left), while the  $\chi''_M$  vs. *T* plot shows a distinct maximum at  $T_{\max} = 5.0$  K for  $\nu = 1000$  Hz (Fig. S6,† right). Moreover, upon increasing the magnitude of the dc magnetic field ( $H = 0.25$  T), a distinct  $\chi'_M$  maximum is observed (Fig. S6,† left), while the  $\chi''_M$  maximum increases in intensity and shifts towards higher temperatures, up to  $T_{\max} = 8.0$  K for  $\nu = 1000$  Hz (Fig. S6,† right).

A magnetic field of  $H = 0.25$  T was then selected to scan the  $\chi'_M$  and  $\chi''_M$  vs. temperature response for **1** in the frequency range of  $\nu = 40$ – $10\,000$  Hz (Fig. 2). Under these conditions, a single maximum appears in the  $\chi''_M$  vs. *T* plot, whose intensity decreases continuously upon increasing the frequency of the oscillating ac field of  $\pm 5$  Oe and progressively shifts toward higher blocking temperatures, from  $T_{\max} = 4.0$  up to  $12.0$  K (Fig. 2, bottom).

The values of the magnetic relaxation time ( $\tau$ ) for **1** at  $H = 0.25$  T can be calculated from the joint analysis of the  $\chi'_M$  and  $\chi''_M$  vs. frequency plots through the generalised Debye model (Fig. S7, ESI†), which considers the adiabatic ( $\chi_S$ ) and isothermal ( $\chi_T$ ) magnetic susceptibilities, as well as the exponential factor ( $\alpha$ ), as additional fitting parameters. The corresponding Argand plots at  $H = 0.25$  T in the temperature range 2.5–11.0 K can be perfectly simulated with the calculated values of  $\alpha$ ,  $\chi_S$  and  $\chi_T$  parameters obtained from the general-

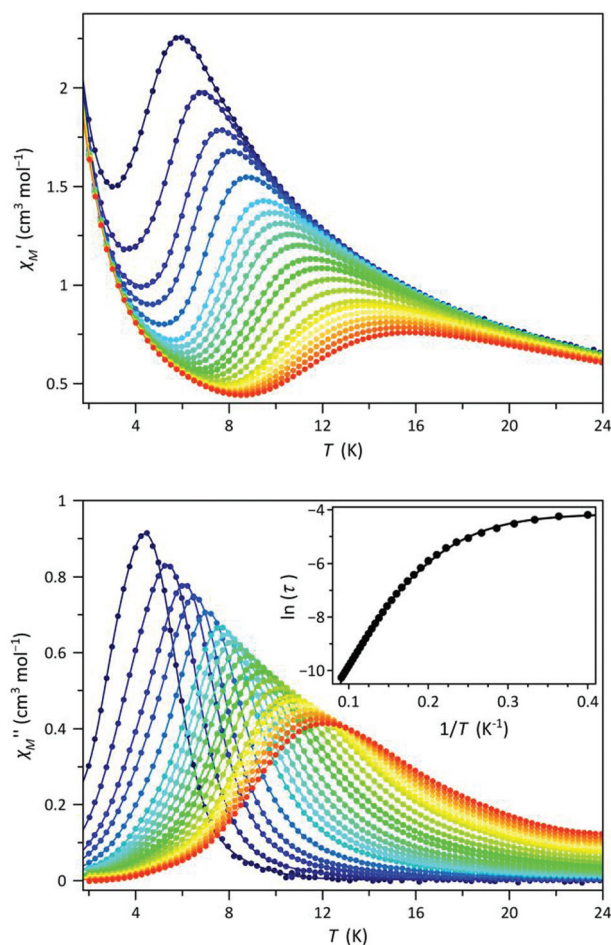


**Fig. 2** Temperature dependence of  $\chi'_M$  (top) and  $\chi''_M$  (bottom) for **1** at an oscillating magnetic field of  $\pm 5$  Oe in the frequency range  $\nu = 40$ – $10\,000$  Hz (blue to red) and  $H = 0.25$  T. The solid lines are only eye-guides. The inset shows the Arrhenius plot in the temperature range 2.5–11 K. The solid line is the best-fit curve (see text).

used Debye model fitting (Fig. S8, ESI†). This fact suggests a single relaxation path in contrast to the double magnetic relaxation process earlier reported for the related dysprosium(III) oxalate decahydrate analogue of formula  $[\text{Dy}_2^{\text{III}}(\text{ox})_3(\text{H}_2\text{O})_6]_n \cdot 4n\text{H}_2\text{O}$ .<sup>25</sup> The calculated relatively low values of the  $\alpha$  parameter ( $\alpha = 0.075$ – $0.195$ ) support a narrow distribution of  $\tau$  in the single magnetic relaxation process.

The calculated  $\tau$  values for **1** at  $H = 0.25$  T are represented in the form of the  $\ln(\tau)$  vs.  $1/T$  (so-called Arrhenius) plot (in agreement with what was done the ordinate scale in the inset of Fig. 2 bottom). The experimental data deviate from the linear Arrhenius law characteristic of a single thermally activated magnetic relaxation process. Instead, they begin to saturate at low temperatures indicating the presence of a temperature-independent magnetic relaxation. The fitting of the Arrhenius plot between 2.5 and 11.0 K is in good agreement with the following equation:

$$\tau^{-1} = \tau_{\text{IK}}^{-1} + CT^n, \quad (1)$$

where the two terms correspond to intraKramers (IK) and Raman relaxation mechanisms, respectively, yielding the best fitting values of  $\tau_{\text{IK}} = 0.0162(6)$  s,  $C = 0.028(3)$   $\text{s}^{-1} \text{K}^{-n}$  and  $n = 5.83(4)$ .

The IK contribution in the low-temperature region ( $T < 3$  K) should be seen as a zero-order term associated with a slower passage between the two components  $m_S = \pm 1/2$  ( $S = 7/2$ ), where the conversion is feasible, and not as a quantum tunneling of the magnetisation (QTM) of the Zeeman-split  $m_S$  levels, which is inconsistent with an isotropic  $\text{Gd}^{\text{III}}$  ion. Remarkably, the calculated  $\tau_{\text{IK}}$  value for **1** at  $H = 0.25$  T is rather high, being comparable with those earlier reported for the QTM regime in mononuclear gadolinium(III)-based polyoxometalates (POMs) which exhibit SMR effects at very low temperatures ( $T_B < 0.1$  K) in the absence of an applied magnetic field ( $\tau_{\text{QTM}} = 0.000015$ – $0.05$  s).<sup>17</sup> On the other hand, the calculated  $n$  value for **1** at  $H = 0.25$  T is slightly lower than that expected for a Kramer ion (accepted  $n = 6$ – $8$ ). However, it is higher than those previously reported for the related example of 3D  $\text{Gd}^{\text{III}}$  SIM-MOFs, namely the gadolinium(III) fumarate heptahydrate of formula  $[\text{Gd}_2^{\text{III}}(\text{fum})_3(\text{H}_2\text{O})_4]_n \cdot 3n\text{H}_2\text{O}$  (**Gd-fum**), which has been recently proposed as a cryogenic magnetic cooler.<sup>19</sup> In this case, the authors argued that the SMR effects are not associated with a magnetic anisotropy energy barrier but with a resonant phonon trapping through a phonon-bottleneck process ( $n = 2.6$  at  $H = 0.1$  T).<sup>20</sup> The two different processes in the relaxation are represented in the different slopes of a log–log plot (Fig. S10†).

The magnetothermal properties of **1** have been investigated by variable-temperature ( $T = 2.0$ – $20$  K, with  $\Delta T = 1$  K) and variable-field ( $H = 0$ – $8$  T, with  $\Delta H = 0.2$  T) magnetisation measurements (see the Experimental section, Fig. S9, ESI†). The magnetic entropy change ( $\Delta S_M$ ) for a selected magnetic field change ( $\Delta H = H - H_0$  with  $H_0 = 0$ ) can then be estimated from the  $M$  vs.  $T$  and  $H$  plots using the Maxwell equation.<sup>26</sup>

The  $-\Delta S_M$  vs.  $T$  and  $H$  plots for **1** increase monotonically upon increasing the magnetic field variation or decreasing the temperature, respectively (Fig. 3). No maximum of  $-\Delta S_M$  was observed at  $T > 2$  K for  $\Delta H < 8$  T. In contrast, the related 2D gadolinium(III) sesquioxalate hydrate of formula  $[\text{Gd}_2^{\text{III}}(\text{ox})_3(\text{H}_2\text{O})_6]_n \cdot 0.6n\text{H}_2\text{O}$  (**1''**) shows a  $-\Delta S_M$  maximum for **1** around 2.75 K for magnetic field changes higher than 7.0 T, even if it remains paramagnetic with no field-induced SMR behaviour above 2 K.<sup>14</sup> The lack of  $-\Delta S_M$  maxima for **1** suggests that the SMR effects do not enable the observation of a large MCE in the pure IK quantum regime of this  $\text{Gd}^{\text{III}}$  SIM-MOF ( $T < 3$  K). In fact, the  $-\Delta S_M$  values (in molar units) of 31.5 (**1**) and 33.1  $\text{J mol}^{-1} \text{K}^{-1}$  (**1''**) at  $T = 2$  K and  $\Delta H = 8$  T are similar, being close to the limiting value for two magnetically isolated, isotropic  $\text{Gd}^{\text{III}}$  ions [ $\Delta S_M = 2R \ln(2S + 1) = 4.16R = 34.6 \text{ J mol}^{-1} \text{K}^{-1}$  with  $S = 7/2$ ].

The MCE efficiency of **1** is among the largest ones yet reported for the related  $\text{Gd}^{\text{III}}$  MOFs proposed as cryogenic magnetic coolers (Table S3, ESI†). Hence, the  $-\Delta S_M$  value (in gravimetric units) of 41.5  $\text{J kg}^{-1} \text{K}^{-1}$  for **1** at  $T = 2$  K and  $\Delta H = 8$  T compares well with those of the more dense 3D  $\text{Gd}^{\text{III}}$  MOFs



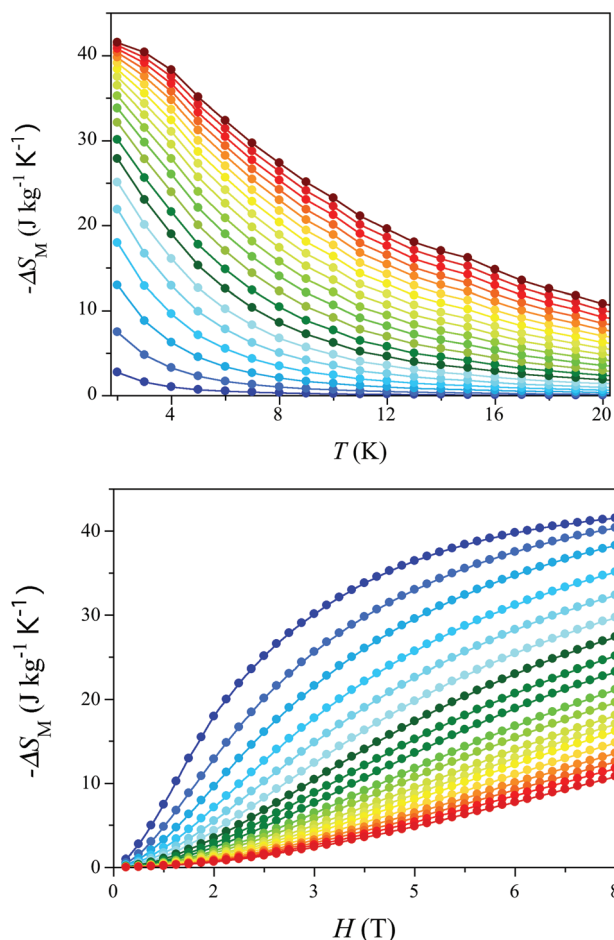


**Fig. 3** Temperature dependence of  $-\Delta S_M$  for **1** in the magnetic field range 0–8 T (blue to red) (top). Field dependence of  $-\Delta S_M$  in the temperature range 2–20 K (blue to red) (bottom). The solid lines are only eye-guides.

reported in the literature ( $-\Delta S_M = 40.6\text{--}60.0 \text{ J kg}^{-1} \text{ K}^{-1}$  at  $T = 2 \text{ K}$  and  $\Delta H = 7 \text{ T}$ ; Table S3,† entries 2, 4–8, 12, and 13).<sup>7–12</sup> This situation conforms with the presence of the lightweight oxalate ligand, which leads to a relatively high percentage mass ratio of magnetic/non-magnetic atoms.<sup>13–16</sup> Moreover, the  $-\Delta S_M$  value of  $21.9 \text{ J kg}^{-1} \text{ K}^{-1}$  for **1** at  $T = 2 \text{ K}$  and  $\Delta H = 2 \text{ T}$  are somewhat higher than that of the aforementioned  $\text{Gd}^{\text{III}}$  SIM-MOF with the heavier fumarate bridging ligand ( $-\Delta S_M = 18.0 \text{ J kg}^{-1} \text{ K}^{-1}$  at  $T = 1 \text{ K}$  and  $\Delta H = 2 \text{ T}$ ).<sup>19</sup> This low magnetic field is sufficiently close to the stronger one that can be achieved with the common permanent magnets used commercially (ranging from 0.5 to 1 T for ceramic magnets and up to 1.4 T for the neodymium ones). This feature is mandatory for the practical applications of 2D gadolinium(III) sesquioxalates as cryogenic magnetic coolers.

In summary, compound **1** constitutes a unique example of  $\text{Gd}^{\text{III}}$  SIM-MOF displaying SMR effects at moderately high blocking temperatures in the presence of a relatively low applied magnetic field. Interestingly, it exhibits moderate to large MCE for relatively low variations in the applied magnetic

field. Both features allow this novel class of field-induced  $\text{Gd}^{\text{III}}$  SIM-MOFs with a dense-packed oxalato-bridged gadolinium(III) hexagonal layer structure to be proposed as candidates as low-temperature molecular magnetic refrigerant materials for CMR. Current efforts are devoted to preparing magnetically diluted samples in order to further investigate the SMR behaviour, as well as the quantum coherence properties in this ordered 2D array of potential qubits for QIP.

## Conflicts of interest

There are no conflicts to declare.

## Acknowledgements

This work was supported by the Spanish MINECO (Project PID2019-109735GB-I00 and Unidad de Excelencia María de Maeztu CEX2019-000919-M) and Generalitat Valenciana (AICO/2020/183). M. O.-A. and R. R. thank the MICIU and the Generalitat Valenciana (GRISOLIA/2017/057) for doctoral grants, respectively. J. M. acknowledges the MINECO for a Juan de la Cierva contract.

## References

- 1 M. J. Graham, J. M. Zdrozny, M. S. Fataftah and D. E. Freedman, *Chem. Mater.*, 2017, **29**, 1885.
- 2 M. Atzori and R. Sessoli, *J. Am. Chem. Soc.*, 2019, **141**, 11339.
- 3 M. R. Wasielewski, M. D. E. Forbes, N. L. Frank, K. Kowalski, G. D. Scholes, J. Yuen-Zhou, M. A. Baldo, D. E. Freedman, R. H. Goldsmith, T. Goodson III, M. L. Kirk, J. K. McCusker, J. P. Ogilvie, D. A. Shultz, S. Stoll and B. Whaley, *Nat. Rev. Chem.*, 2020, **4**, 490.
- 4 M. Evangelisti, *Molecule-based magnetic coolers: measurement, design and application in Molecular Magnets: Physics and Applications*, ed. J. Bartolomé, F. Luis and J. F. Fernández, Springer-Verlag, Heidelberg, 2014, ch. 14, pp. 365.
- 5 Y.-Z. Zheng, G.-J. Zhou, Z. Zheng and R. E. P. Winpenny, *Chem. Soc. Rev.*, 2014, **43**, 1462.
- 6 J.-L. Liu, Y.-C. Chen, F.-S. Guo and M.-L. Tong, *Coord. Chem. Rev.*, 2014, **281**, 26.
- 7 G. Lorusso, M. A. Palacios, G. S. Nichol, E. K. Brechin, R. Sessoli, O. Roubeau and M. Evangelisti, *Chem. Commun.*, 2012, **48**, 7592.
- 8 J.-M. Jia, S.-J. Liu, Y. Cui, S.-D. Han, T.-L. Hu and X.-H. Bu, *Cryst. Growth Des.*, 2013, **13**, 4631.
- 9 R. Sibille, T. Mazet, B. Malaman and M. François, *Chem. – Eur. J.*, 2012, **18**, 12970.
- 10 G. Lorusso, J. W. Sharples, E. Palacios, O. Roubeau, E. K. Brechin, R. Sessoli, A. Rossin, F. Tuna, E. J. L. McInnes, D. Collison and M. Evangelisti, *Adv. Mater.*, 2015, **25**, 4653.

- 11 S. Biswas, A. K. Mondal and S. Konar, *Inorg. Chem.*, 2016, **55**, 2085.
- 12 C. Das, A. Upadhyay, K. U. Ansari, N. Ogiwara, T. Kitao, S. Horike and M. Shanmugam, *Inorg. Chem.*, 2018, **57**, 6584.
- 13 S. Biswas, H. S. Jena, A. Adhikary and S. Konar, *Inorg. Chem.*, 2014, **53**, 3926.
- 14 R. Sibille, E. Didelot, T. Mazet, B. Malaman and M. François, *APL Mater.*, 2014, **2**, 124402.
- 15 M. N. Akhtar, Y.-C. Chen, M. A. AlDamen and M.-L. Tong, *Dalton Trans.*, 2017, **46**, 116.
- 16 S.-D. Han, J.-H. Li, H.-H. Liu and G.-M. Wang, *Dalton Trans.*, 2017, **46**, 10023.
- 17 M.-J. Martínez-Pérez, S. Cardona-Serra, C. Schlegel, F. Moro, P. J. Alonso, H. Primo-García, J. M. Clemente-Juan, M. Evangelisti, A. Gaita-Ariño, J. Sesé, J. van Slageren, E. Coronado and F. Luis, *Phys. Rev. Lett.*, 2012, **108**, 247213.
- 18 M.-J. Martínez-Pérez, O. Montero, M. Evangelisti, F. Luis, J. Sesé, S. Cardona-Serra and E. Coronado, *Adv. Mater.*, 2012, **24**, 4301.
- 19 L. Sedláková, J. Hanko, A. Orendcov, M. Orendác, C. L. Zhou, W. H. Zhu, B. W. Wang, Z. M. Wang and S. Gao, *J. Alloys Compd.*, 2009, **487**, 425.
- 20 M. Orendac, L. Sedlakova, E. Cizmar, A. Orendacova, A. Feher, S. A. Zvyagin, J. Wosnitza, W. H. Zhu, Z. M. Wang and S. Gao, *Phys. Rev. B: Condens. Matter Mater. Phys.*, 2010, **81**, 214410.
- 21 F. Luis and M. Evangelisti, *Struct. Bond.*, 2015, **164**, 431–460.
- 22 L. Cañadillas-Delgado, J. Pasan, O. Fabelo, M. Hernandez-Molina, F. Lloret, M. Julve and C. Ruiz-Perez, *Inorg. Chem.*, 2006, **45**, 10585.
- 23 Electronic Structure Group, *SHAPE (Version 2.1)*, Universitat de Barcelona, 2013.
- 24 J. Cano and Y. Journaux, *Monte Carlo simulations: a tool to analyse magnetic properties in Magnetism: Molecules to Materials V*, ed. J. S. Miller and M. Drillon, Wiley-VCH, Weinheim, 2005, ch. 6, pp. 189.
- 25 S. Zhang, H. Ke, X. Liu, Q. Wei, G. Xie and S. Chen, *Chem. Commun.*, 2015, **51**, 15188.
- 26 L. Tocado, E. Palacios and R. Burriel, *J. Appl. Phys.*, 2009, **105**, 093918.



## *CHAPTER 4*

---

### *Conclusions and Perspectives*





We have established in the general objectives that investigating the Coordination Chemistry and magnetochemistry of different paramagnetic metal ions, by using biomolecules and biocompatible ligands can allow us to develop magnetic molecular compounds in different fields such as Molecular Therapy, which utilise antitumour agents and miscellaneous drugs, or Molecular Bioimaging, which employs MRI contrast agents and radioactive markers. On the other hand, magnetic coordination polymers can be exploited in Molecular Refrigeration via low-temperature magnetic cooling, or in Molecular Sensing through chemical sensors and biosensors.

In this regard, in Chapter 2, we investigated the magnetic properties of mono- and dinuclear complexes of ruthenium(III) based on nucleobases. These systems could also exhibit relevant biological and biochemical properties and, in some cases, the properties of these systems make them potentially appealing for applications in different research areas such as redox catalysis, but further theoretical and experimental studies will be required to fully understand the relaxation dynamics of the very interesting ruthenium(III)-based SIMs.

On the other hand, we have demonstrated that some purine-based ruthenium(III) complexes can be helpful as a first step in the development of sensor devices. The diruthenium systems display such sensitivity, reproducibility and stability that make these compounds viable candidates for detecting the hypoxanthine and other biomolecules. In addition, we have reported for the first time that a dinuclear ruthenium(III) complex based on adenine has been tested toward cancer cell lines, and further studies will be performed to get new insights into its potential chemotherapeutic action.

Apart from that, the initial test of the dinuclear ruthenium(III) complex based on adenine against cancer cell lines inspired us to develop a family of this type

---

of compound. As a result, we continued researching novel ruthenium-based antitumour agents like Runat-BI, which offers an intriguing alternative to current chemotherapy drugs and overcomes many of the drawbacks of the ruthenium(III) complex based on adenine by being *in vitro* more effective against a variety of cancers, having a better toxicity profile and having a multitargeted mechanism of action. Three cancer cell lines derived from colon, stomach, and breast cancers, all of which had rapid proliferation rates, were drastically decreased in viability and migration by Runat-BI. This fact demonstrates the complex efficacy in treating aggressive, highly proliferative tumours that have few therapy alternatives.

On the other hand, analysis of the crystal structure of diruthenium(IV) complexes revealed that they are ideal candidates to be used as building blocks to assemble new supramolecular structures. In addition, by using the correct organic linkers, these compounds might potentially be used in electrical devices, as demonstrated by the study of its redox properties. This later work is still ongoing.

Finally, in Chapter 3, lanthanide-based complexes of different dimensionality were studied, revealing interesting magnetic properties, such as SIM and SMM behaviours in 1D and 2D MOFs (referred to as SIM-MOFs), respectively. They display moderately high blocking temperatures ( $T_B$ ) in the presence of a relatively low applied magnetic field, and moderate to large MCE for relatively low variations in the applied magnetic field.

Our approach in this topic will be to focus on homoleptic oxalato-bridged 2D and 3D Ln SIM-MOFs built on the well-known family of lanthanide(III) sesquioxalate hydrates that experience blocking of the magnetisation in the presence of an applied magnetic field (Figure 4.1). In both situations, activating the magnetic field below the  $T_B$  would cause each of the Ln<sup>III</sup> ions that constitute the network

nodes to function as an individual magnet. We may suggest them as novel candidates for low-temperature, slow-relaxing molecular magnetic refrigerant materials thanks to all of their structural, magnetic, and magnetothermal features. The preparation of thin films of these 2D and 3D Gd SIM-MOFs is another current focus for research into the SIM and MCE when used in actual devices.

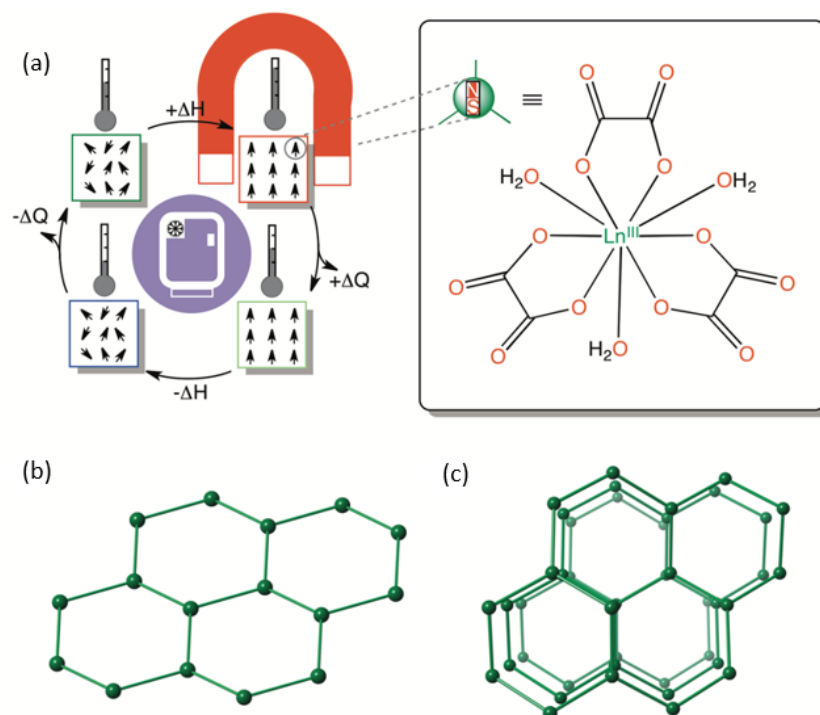


Figure 4.1: (a) Illustration of the MCE upon on-off switching of the applied magnetic field in field-induced Ln SMM-MOFs based on the family of lanthanide(III) sesquioxalates hydrates with 2D hexagonal layer (b) or 3D mixed hexagonal/decahedral net (c) structures. The boxed structure shows the tris(oxalate)lanthanide(III)-triaqua mononuclear building units acting as tris(bidentate) molecular tectons.

On the other hand, lanthanide-based complexes, with their diverse magnetic and optical properties and extensive coordination chemistry, provide limitless opportunities for the development of molecular imaging and theranostic agents. It is necessary to develop certain contrast agents that change relaxivity after break-

---

ing certain bonds, that are sensitive to the presence of particular ions, metabolites and so on. As mentioned in the introduction, the currently used contrast agents have limited effectiveness and are not entirely appropriate for the new scanner devices operating at 3 T or more magnetic fields. The primary issue with using heavy metal ions for medicinal purposes, such as the gadolinium(III) ion, is the considerable toxicity of their “free” (aqua-ion) form. Gadolinium(III) must thus be contained in a complex with high stability for therapeutic usage and, even more crucially, it must exhibit long-term resistance to a transmetallation/transchelation loss of the gadolinium(III) ion.

Due to the fact that trivalent gadolinium prefers a coordination number of 9 in current commercial contrast agents, this leaves one accessible coordination site open for an inner sphere water molecule, enabling it to relax more quickly and provide contrast. Therefore, increasing the the number of molecules the complex can enhance the relaxivity of the contrast agents. The range of techniques and concepts needed to build more stable gadolinium-based contrast agents (GBCAs) must be developed by coordination chemists with creativity.

Much effort has been put into designing more efficient contrast agents. However, the design has been primarily focused on modifying the structural motifs of commercial contrast agents such as Gd-DOTA and Gd-DTPA. Perhaps, the most effective of these methods has been the rigidification of the ligand backbone with the addition of a cyclohexyl motif. These ligands just aren't inert enough, which is a crucial component that precludes them from producing the subsequent generation of GBCAs. As a consequence, many of the advancements have been focused on acyclic ligands.

The high relaxivity values of the 0D gadolinium(III) compound based on the thymine nucleobase, presented in this Thesis work, make this complex a potential

candidate for further MRI research. This is due to both the inherent gadolinium properties as a contrast agent as well as the use of biomolecules as ligands in their preparation, which adds new properties that can be combined with the intrinsic ones, to generate a “new era” of more versatile contrast agents. This can be extended to new compounds that present multiproperties by incorporating different biomolecules, such as antibiotics, vitamins, etc.



---

*APPENDIX A:*  
*Supporting Information Chapter*

*2*





# Supporting Information

**Ferromagnetic coupling and single-ion magnet phenomenon in mononuclear ruthenium(III) complexes based on guanine nucleobase**

Marta Orts-Arroyo, Nicolas Moliner, Francesc Lloret and José  
Martínez-Lillo



## Supplementary Materials

# Ferromagnetic coupling and single-ion magnet phenomenon in mononuclear ruthenium(III) complexes based on guanine nucleobase

Marta Orts-Arroyo,<sup>1</sup> Nicolás Moliner,<sup>1</sup> Francesc Lloret<sup>1</sup> and José Martínez-Lillo<sup>1,\*</sup>

<sup>1</sup>Instituto de Ciencia Molecular (ICMol)/Departament de Química Inorgànica, Universitat de València, c/Catedrático José Beltrán 2, Paterna, 46980, València, Spain; marta.orts-arroyo@uv.es (M.O.-A.); fernando.moliner@uv.es (N.M.); francisco.lloret@uv.es (F.L.)

\* Correspondence: f.jose.martinez@uv.es; Tel.: +34-9635-44460

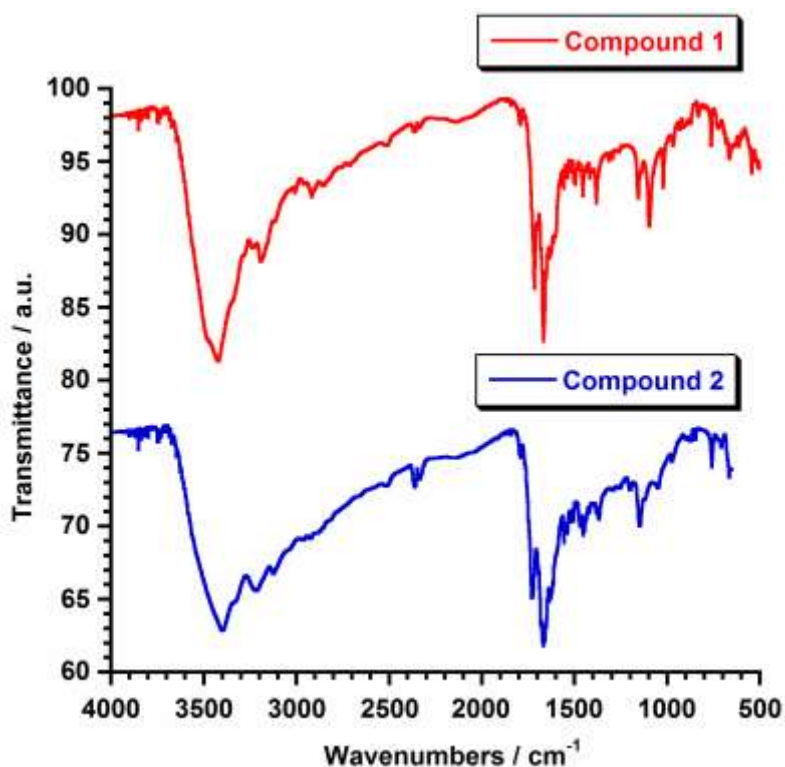


Figure S1. FT-IR spectra for compound 1 (red) and compound 2 (blue).



# Supporting Information

**A novel adenine-based diruthenium(III) complex:  
Synthesis, crystal structure, electrochemical prop-  
erties and evaluation of the anticancer activity**

Marta Orts-Arroyo, Fernanda Gutiérrez, Anabel Gil-Tebar, Mainer Ibarrola-Villava, Elena Jiménez-Martí, Adriana Silvestre-Llora, Isabel Castro, Gloria Ribas, José Martínez-Lillo



## checkCIF/PLATON report

You have not supplied any structure factors. As a result the full set of tests cannot be run.

THIS REPORT IS FOR GUIDANCE ONLY. IF USED AS PART OF A REVIEW PROCEDURE FOR PUBLICATION, IT SHOULD NOT REPLACE THE EXPERTISE OF AN EXPERIENCED CRYSTALLOGRAPHIC REFEREE.

No syntax errors found.      CIF dictionary      Interpreting this report

### Datablock: compound\_1

---

Bond precision:    C-C = 0.0135 A                      Wavelength=0.71073

Cell:                      a=6.9610(8)              b=19.042(2)              c=9.1971(9)  
                                    alpha=90              beta=101.195(4)              gamma=90

Temperature:              296 K

	Calculated	Reported
Volume	1195.9(2)	1195.9(2)
Space group	P 21/n	P 21/n
Hall group	-P 2yn	-P 2yn
Moiety formula	C10 H12 Cl6 N10 Ru2, 2(Cl), 2(O)	C10 H12 Cl6 N10 Ru2, 2(Cl), 2(O)
Sum formula	C10 H12 Cl8 N10 O2 Ru2	C10 H12 Cl8 N10 O2 Ru2
Mr	790.04	790.04
Dx, g cm-3	2.194	2.194
Z	2	2
Mu (mm-1)	2.189	2.189
F000	764.0	764.0
F000'	761.45	
h,k,lmax	9,26,12	9,26,12
Nref	3412	3158
Tmin,Tmax	0.854,0.968	0.624,0.768
Tmin'	0.705	

Correction method= # Reported T Limits: Tmin=0.624 Tmax=0.768  
AbsCorr = MULTI-SCAN

Data completeness= 0.926                      Theta(max)= 29.765

R(reflections)= 0.0589( 2712)              wR2(reflections)= 0.1780( 3158)

S = 1.175                      Npar= 145

---

The following ALERTS were generated. Each ALERT has the format

**test-name\_ALERT\_alert-type\_alert-level.**

Click on the hyperlinks for more details of the test.



### Alert level B

PLAT306\_ALERT\_2\_B Isolated Oxygen Atom (H-atoms Missing ?) ..... OlW Check



### Alert level C

PLAT230\_ALERT\_2\_C Hirshfeld Test Diff for N6 --C6 . 5.4 s.u.  
PLAT230\_ALERT\_2\_C Hirshfeld Test Diff for N7 --C5 . 6.7 s.u.  
PLAT230\_ALERT\_2\_C Hirshfeld Test Diff for C4 --C5 . 5.3 s.u.  
PLAT242\_ALERT\_2\_C Low 'MainMol' Ueq as Compared to Neighbors of Rul Check  
PLAT242\_ALERT\_2\_C Low 'MainMol' Ueq as Compared to Neighbors of N1 Check  
PLAT342\_ALERT\_3\_C Low Bond Precision on C-C Bonds ..... 0.0135 Ang.



### Alert level G

PLAT002\_ALERT\_2\_G Number of Distance or Angle Restraints on AtSite 3 Note  
PLAT003\_ALERT\_2\_G Number of Uiso or Uij Restrained non-H Atoms ... 4 Report  
PLAT007\_ALERT\_5\_G Number of Unrefined Donor-H Atoms ..... 4 Report  
PLAT012\_ALERT\_1\_G N.O.K. \_shelx\_res\_checksum Found in CIF ..... Please Check  
PLAT172\_ALERT\_4\_G The CIF-Embedded .res File Contains DFIX Records 2 Report  
PLAT186\_ALERT\_4\_G The CIF-Embedded .res File Contains ISOR Records 2 Report  
PLAT232\_ALERT\_2\_G Hirshfeld Test Diff (M-X) Rul --Cl3 . 7.7 s.u.  
PLAT232\_ALERT\_2\_G Hirshfeld Test Diff (M-X) Rul --Cl3\_a . 9.6 s.u.  
PLAT431\_ALERT\_2\_G Short Inter HL..A Contact Cl4 ..OlW . 3.13 Ang.  
x,y,z = 1\_555 Check  
PLAT434\_ALERT\_2\_G Short Inter HL..HL Contact Cl3 ..Cl3 3.37 Ang.  
-x,2-y,2-z = 3\_577 Check  
PLAT860\_ALERT\_3\_G Number of Least-Squares Restraints ..... 26 Note  
PLAT883\_ALERT\_1\_G No Info/Value for \_atom\_sites\_solution\_primary . Please Do !  
PLAT965\_ALERT\_2\_G The SHELXL WEIGHT Optimisation has not Converged Please Check

0 **ALERT level A** = Most likely a serious problem - resolve or explain  
1 **ALERT level B** = A potentially serious problem, consider carefully  
6 **ALERT level C** = Check. Ensure it is not caused by an omission or oversight  
13 **ALERT level G** = General information/check it is not something unexpected

2 ALERT type 1 CIF construction/syntax error, inconsistent or missing data  
13 ALERT type 2 Indicator that the structure model may be wrong or deficient  
2 ALERT type 3 Indicator that the structure quality may be low  
2 ALERT type 4 Improvement, methodology, query or suggestion  
1 ALERT type 5 Informative message, check



It is advisable to attempt to resolve as many as possible of the alerts in all categories. Often the minor alerts point to easily fixed oversights, errors and omissions in your CIF or refinement strategy, so attention to these fine details can be worthwhile. In order to resolve some of the more serious problems it may be necessary to carry out additional measurements or structure refinements. However, the purpose of your study may justify the reported deviations and the more serious of these should normally be commented upon in the discussion or experimental section of a paper or in the "special\_details" fields of the CIF. checkCIF was carefully designed to identify outliers and unusual parameters, but every test has its limitations and alerts that are not important in a particular case may appear. Conversely, the absence of alerts does not guarantee there are no aspects of the results needing attention. It is up to the individual to critically assess their own results and, if necessary, seek expert advice.

### **Publication of your CIF in IUCr journals**

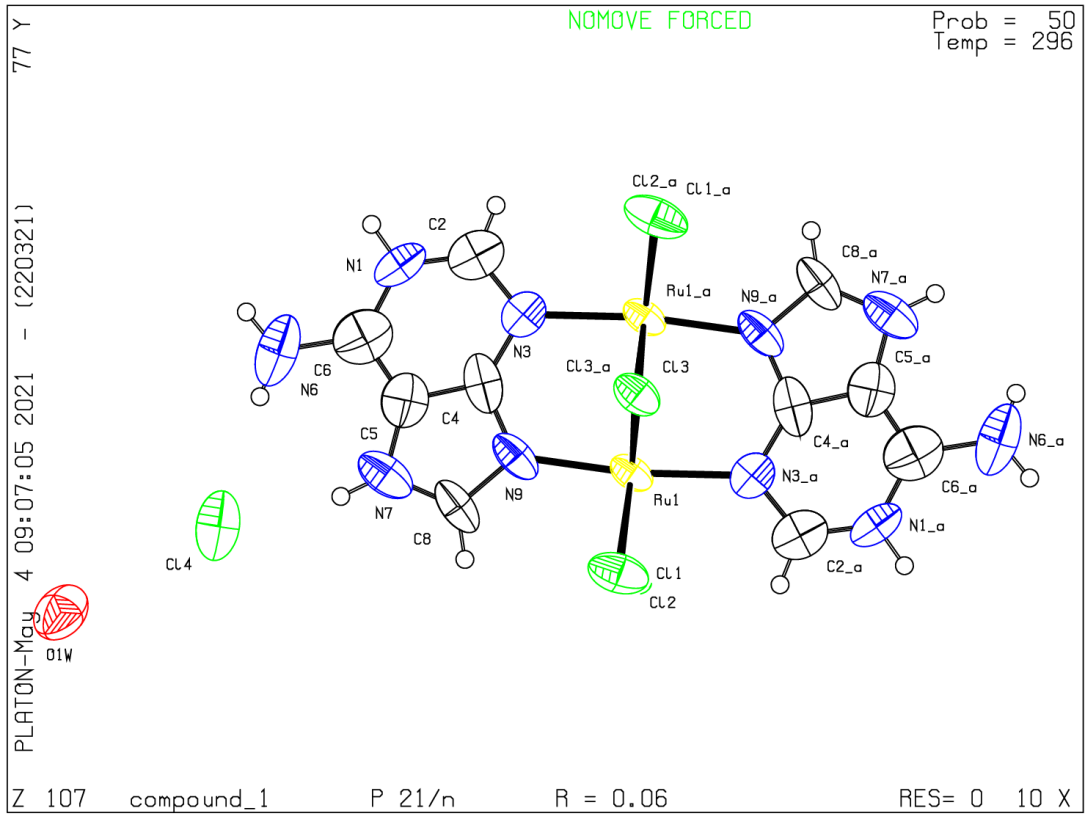
A basic structural check has been run on your CIF. These basic checks will be run on all CIFs submitted for publication in IUCr journals (*Acta Crystallographica*, *Journal of Applied Crystallography*, *Journal of Synchrotron Radiation*); however, if you intend to submit to *Acta Crystallographica Section C* or *E* or *IUCrData*, you should make sure that full publication checks are run on the final version of your CIF prior to submission.

### **Publication of your CIF in other journals**

Please refer to the *Notes for Authors* of the relevant journal for any special instructions relating to CIF submission.

---

**PLATON version of 22/03/2021; check.def file version of 19/03/2021**



# Supporting Information

**RUNAT-BI: a ruthenium(III) complex as a selective antitumoral drug candidate against highly aggressive cancer cell lines**

Marta Albanell-Fernández, Sara S. Oltra, Marta Orts-Arroyo, Maider Ibarrola-Villava, Fany Carrasco, Elena Jiménez-Martí, Andrés Cervantes, Isabel Castro, José Martínez-Lillo, Gloria Ribas



## Supplementary Materials

### **RUNAT-BI: a ruthenium(III) complex as a selective antitumoral drug candidate against highly aggressive cancer cell lines**

Marta Albanell-Fernández<sup>1,†</sup>, Sara S. Oltra<sup>1,†</sup>, Marta Orts-Arroyo<sup>2</sup>, Maider Ibarrola-Villava<sup>1,3</sup>, Fany Carrasco<sup>1,3</sup>, Elena Jiménez-Martí<sup>1,3,4</sup>, Andrés Cervantes<sup>1,3</sup>, Isabel Castro<sup>2</sup>, José Martínez-Lillo<sup>2,\*</sup>, Gloria Ribas<sup>1,3,\*</sup>

<sup>1</sup>Biomedical Research Institute INCLIVA, Hospital Clínico Universitario Valencia, University of Valencia, Spain

<sup>2</sup>Instituto de Ciencia Molecular (ICMol)/Departament de Química Inorgànica, University of Valencia, Spain

<sup>3</sup>Center for Biomedical Network Research on Cancer (CIBERONC)

<sup>4</sup>Departament de Bioquímica i Biología Molecular, Facultat de Medicina, University of Valencia, Spain

\*Correspondence: [gribasdespuig@gmail.com](mailto:gribasdespuig@gmail.com) and [f.jose.martinez@uv.es](mailto:f.jose.martinez@uv.es); Tel.: +34-9635-44460

<b>Table of contents</b>	<b>page</b>
<b>Figure S1</b> .....	<b>2</b>
<b>Figure S2</b> .....	<b>3</b>
<b>Table S1</b> .....	<b>4</b>
<b>Table S2</b> .....	<b>4</b>
<b>Table S3</b> .....	<b>5</b>
<b>Table S4</b> .....	<b>5</b>
<b>Figure S3</b> .....	<b>6</b>
<b>Figure S4</b> .....	<b>7</b>
<b>Figure S5</b> .....	<b>8</b>

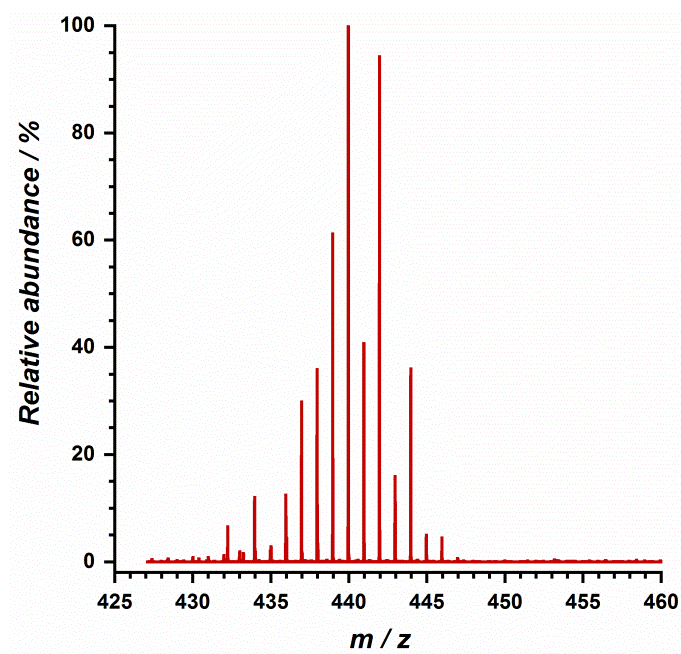


**Figure S1.** Electrospray ionization mass spectrum (ESI-MS) for Runat-BI showing the isotopic distribution for the  $[\text{RuCl}_2(\text{H}_2\text{biim})_2]^+$  cation with  $m/z$ : 439.97 (100%).

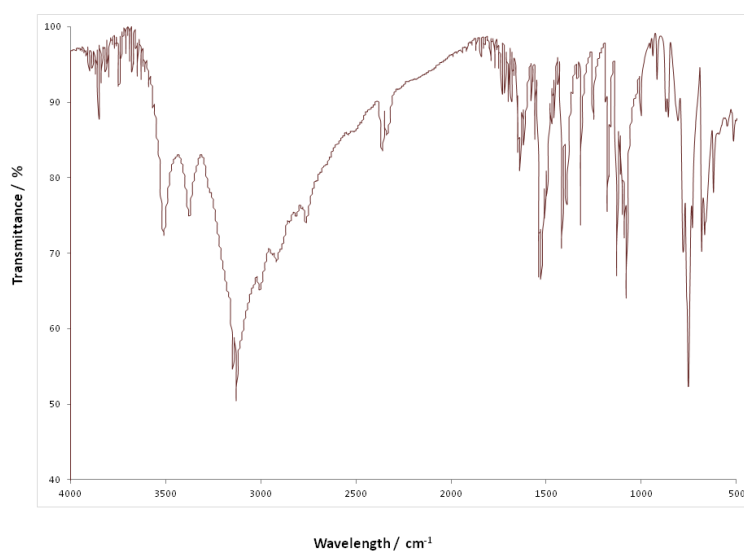
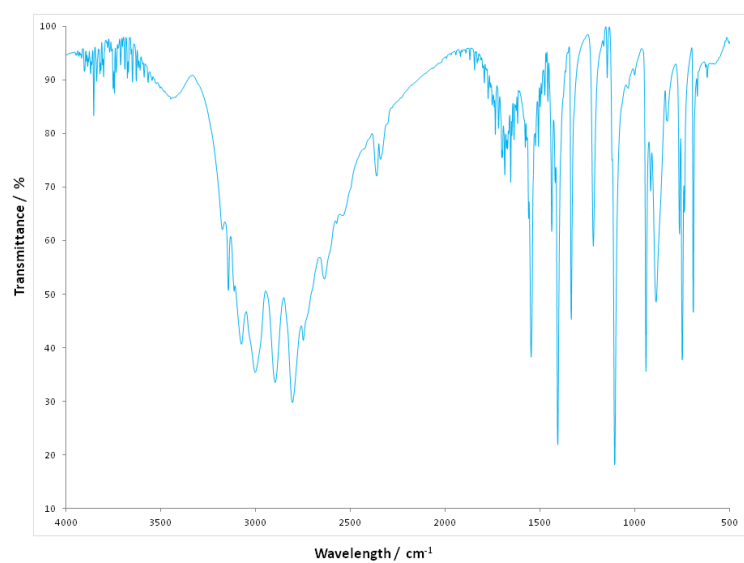


**Figure S2.** FT-IR spectra for 2,2'-biimidazole (H<sub>2</sub>biim, top) and Runat-BI (*cis*-[RuCl<sub>2</sub>(H<sub>2</sub>biim)<sub>2</sub>]Cl)<sub>2</sub>·4H<sub>2</sub>O, bottom).

**Table S1.** Crystal data and structure refinement for Runat-BI.

Compound	Runat-BI
Formula	C <sub>12</sub> H <sub>12</sub> N <sub>8</sub> O <sub>2</sub> Cl <sub>3</sub> Ru
<i>M<sub>r</sub></i> /g mol <sup>-1</sup>	507.72
Crystal system	monoclinic
Space group	<i>P</i> 2 <sub>1</sub>
<i>a</i> /Å	13.457(1)
<i>b</i> /Å	11.317(1)
<i>c</i> /Å	13.749(1)
$\alpha$ /°	90
$\beta$ /°	115.6(1)
$\gamma$ /°	90
<i>V</i> / Å <sup>3</sup>	1888.14(1)
<i>Z</i>	4
<i>D<sub>c</sub></i> /g cm <sup>-3</sup>	1.785
$\mu$ (Mo-K $\alpha$ )/mm <sup>-1</sup>	1.279
<i>F</i> (000)	1004
Goodness-of-fit on <i>F</i> <sup>2</sup>	1.073
<i>R</i> <sub>1</sub> [ <i>I</i> > 2 $\sigma$ ( <i>I</i> )]	0.0423
<i>wR</i> <sub>2</sub> [ <i>I</i> > 2 $\sigma$ ( <i>I</i> )]	0.1301

**Table S2.** Selected bond lengths (Å) and angles (°) for Runat-BI.

Bond lengths		Bond lengths	
Ru1-Cl5	2.362	Ru2-Cl3	2.362
Ru1-Cl6	2.340	Ru2-Cl4	2.340
Ru1-N1	2.050	Ru2-N9	2.050
Ru1-N2	2.075	Ru2-N10	2.075
Ru1-N5	2.055	Ru2-N14	2.055
Ru1-N6	2.069	Ru2-N14	2.069
Angles		Angles	
Cl5-Ru1-Cl6	92.97	Cl3-Ru2-Cl4	96.19
Cl5-Ru1-N1	90.48	Cl3-Ru2-N9	85.84
Cl5-Ru1-N2	91.72	Cl3-Ru2-N10	170.85
Cl5-Ru1-N5	169.60	Cl3-Ru2-N13	94.13
Cl5-Ru1-N6	92.48	Cl3-Ru2-N14	118.65
Cl6-Ru1-N1	176.00	Cl4-Ru2-N9	169.60
Cl6-Ru1-N2	92.75	Cl4-Ru2-N10	92.96
Cl6-Ru1-N5	92.21	Cl4-Ru2-N13	88.98
Cl6-Ru1-N6	90.66	Cl4-Ru2-N14	92.12



**Table S3.** Cell line characteristics and culture conditions.

Cell line	Cancer type	Cancer Subtype	Receptor expression	Tumor type	Culture medium	Conditions	Supplements
HCC1500	BC	Luminal A	ER,PR	IDC	RPMI	5%CO <sub>2</sub> 37 °C	1% L-glu 10% FBS
HCC1937	BC	Basal	EGP2	IDC	RPMI	5%CO <sub>2</sub> 37 °C	1% L-glu 10% FBS
MDA-MB-231	BC	Basal	EGFR, TGF-β	Carcinoma	RPMI	5%CO <sub>2</sub> 37 °C	1% L-glu 10% FBS
MCF-7	BC	Luminal A	ER,IGFBP	IDC	RPMI	5%CO <sub>2</sub> 37 °C	1% L-glu 10% FBS
BT474	BC	Luminal B	ER, PR, HER2	IDC	DMEM	5%CO <sub>2</sub> 37 °C	1% L-glu 10% FBS
HCC1806	BC	Basal	EGP2	Carcinoma	RPMI	5%CO <sub>2</sub> 37 °C	1% L-glu 10% FBS
AGS	Gastric cancer	-	-	Adenocarcinoma	DMEM	5%CO <sub>2</sub> 37 °C	1% L-glu 10% FBS
HCT116	Colon cancer	-	-	Carcinoma	DMEM	5%CO <sub>2</sub> 37 °C	1% L-glu 10% FBS
MCF10A	*Mammary epithelial	-	-		DMEM/ F-12	5%CO <sub>2</sub> 37 °C	1% L-glu 10% FBS

BC: Breast cancer; EGFR: Epidermal growth factor receptor; EGP2: Epithelial glycoprotein 2; ER: estrogen receptor; FBS: fetal bovine serum; HER2: hormonal estrogen receptor 2; IDC: Invasive ductal carcinoma; IGFBP: Insulin growth factor binding protein; L-glu: L-glutamine; PR: progesterone receptor; RPMI: RPMI 1640 medium; TGF-β / α: transforming growth factor β / α. \*MCF10A is non-tumorigenic human mammary epithelial cells.

**Table S4.** IC<sub>50</sub> in μM of the nine cancer cell lines studied after 48 h and 72 h of Runat-BI treatment and Cisplatin. The R square indicates the goodness of fit. IC<sub>50</sub>: half maximal inhibitory concentration.

Cell line	IC <sub>50</sub> (μM) 48h	R (48h)	IC <sub>50</sub> (μM) 72h	R (72h)	IC <sub>50</sub> (μM) Cisplatin
MCF-7	269.00	0.008946	49.43	-0.1836	100.36
HCC1937	94.23	0.401200	65.81	0.4829	133.50
MDA-MB-231	107.40	0.822000	48.89	0.7822	43.15
BT474	68.78	0.794400	32.63	0.8595	1140.20
HCC1806	24.55	0.970300	27.62	0.8830	9.29
HCC1500	76.03	0.127000	192.3	0.3431	97.28
HCT116	22.43	0.918100	15.54	0.8630	14.45
AGS	43.53	0.746200	29.57	0.6740	13.37

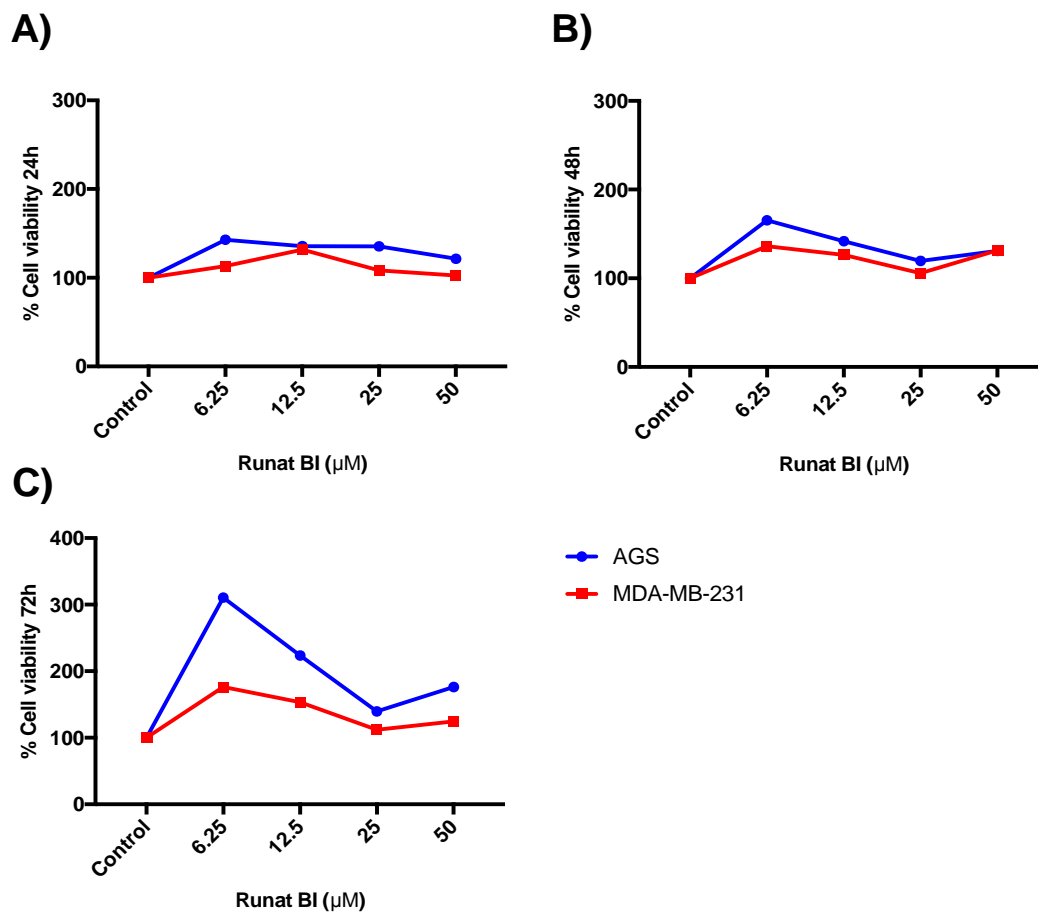


**Figure S3.** Percentage of viability for AGS and MDA-MB-231 cell lines treated with isomer 1 of Runat-BI at 24, 48 and 72 h. The gastric cancer cell line AGS and the BC cell line MDA-MB-231 were treated with isomer 1 of Runat-BI (from 0 to 50  $\mu\text{M}$ ) for 24 h (A); 48 h (B) and 72 h (C). Cell proliferation was determined with the MTT assay. Dots indicate the mean of two independent experiments.

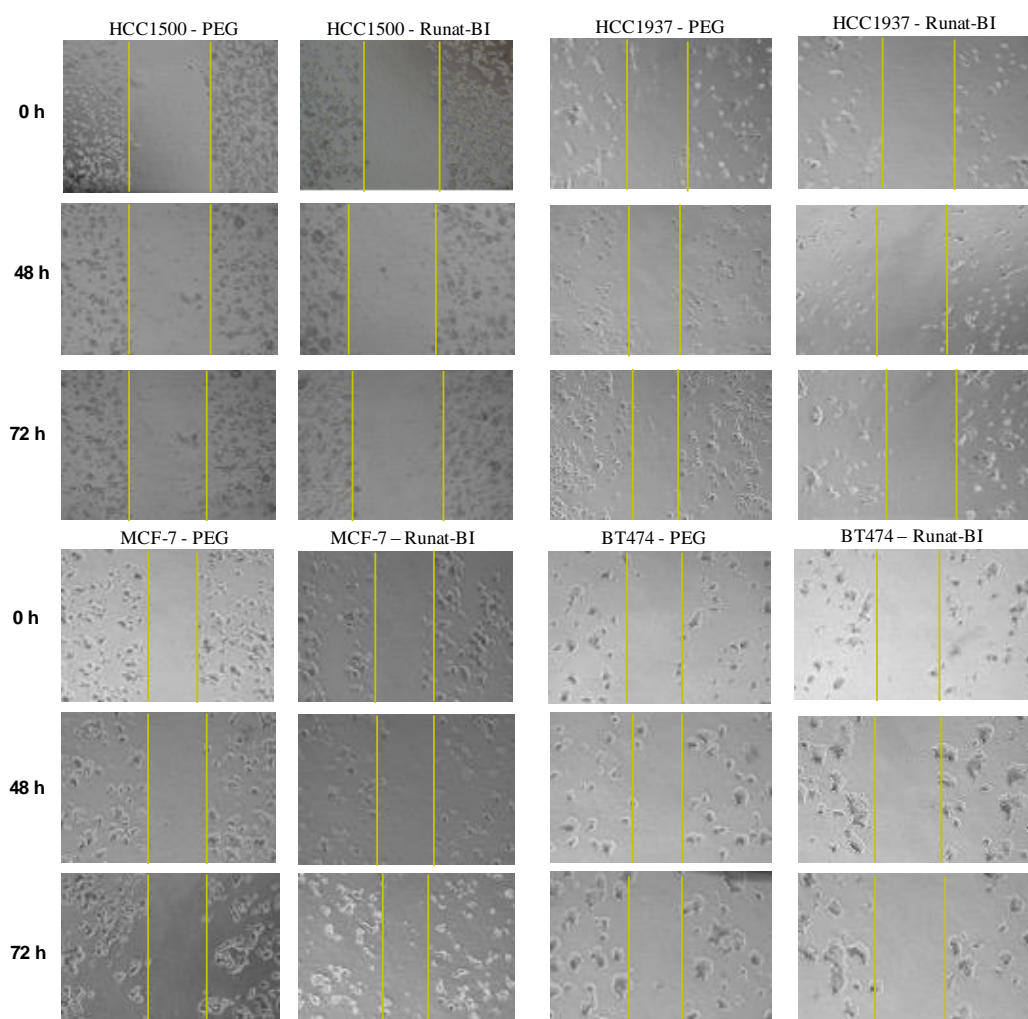


**Figure S4.** Effect of Runat-BI treatment in cell migration. Cell migration in HCC1500, HCC1937, MCF-7 and BT-474 cell lines was measured with the "wound-healing" assay after treatment with Runat-BI (21  $\mu$ M) or control/PEG for 48 and 72 h. Images of cell migration at 0, 48 and 72 h after Runat-BI (21  $\mu$ M) treatment or PEG (control). Three separate experiments were performed and the most representative results are presented (5x amplification).

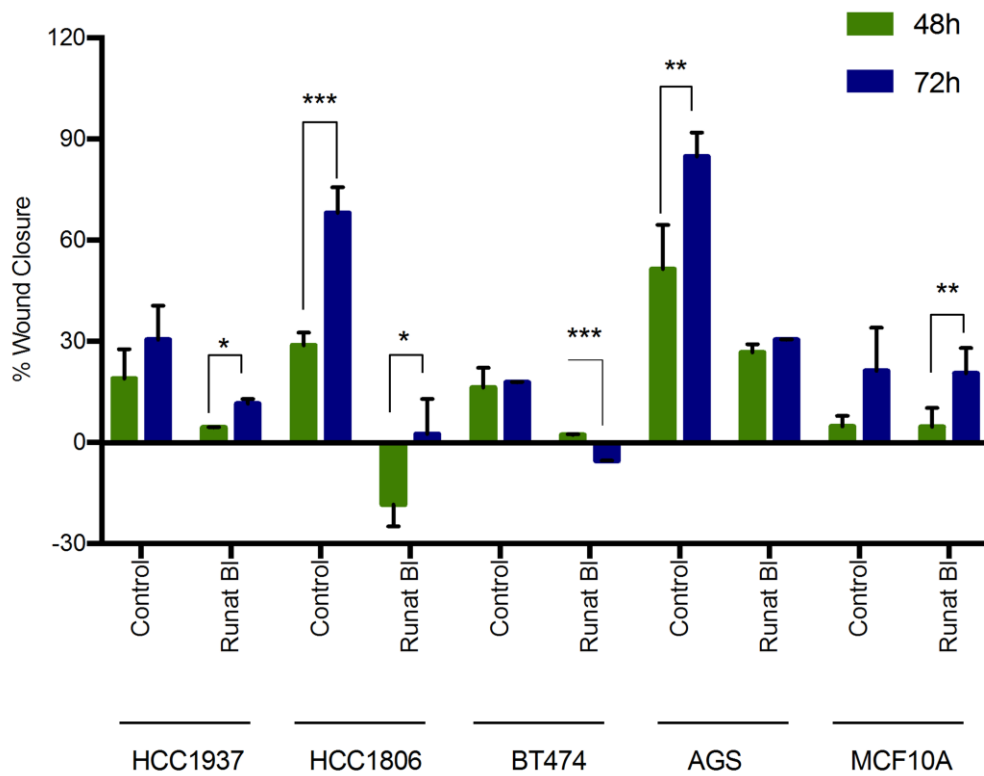


**Figure S5.** Comparison of percentage of wound closure of cell lines treated with Runat-BI (21 μM) and control/PEG for 48 h (green) and 72 h (blue). Columns express the mean ±SD of the percentage of closure in three independent experiments by cell line. \*P ≤ 0.1, \*\*P ≤ 0.05, \*\*\*P ≤ 0.01 statistically significant.

# Supporting Information

## Molecular Self-Assembly in a Family of Oxo-Bridged Dinuclear Ruthenium(IV) Systems

Marta Orts-Arroyo, Isabel Castro, Francesc Lloret, and José  
Martínez-Lillo



# Molecular Self-Assembly in a Family of Oxo-Bridged Dinuclear Ruthenium(IV) Systems

Marta Orts-Arroyo, Isabel Castro,\* Francesc Lloret, and José Martínez-Lillo\*

Instituto de Ciencia Molecular (ICMol), Universitat de València, c/ Catedrático José Beltrán 2, 46980, Paterna, València, Spain

<b>Table of contents</b>	<b>page</b>
<b>Figure S1</b> .....	<b>2</b>
<b>Figure S2</b> .....	<b>3</b>
<b>Figure S3</b> .....	<b>3</b>
<b>Table S1</b> .....	<b>4</b>
<b>Table S2</b> .....	<b>4</b>
<b>Table S3</b> .....	<b>4</b>
<b>Table S4</b> .....	<b>5</b>
<b>Table S5</b> .....	<b>5</b>
<b>Table S6</b> .....	<b>5</b>
<b>Figure S4</b> .....	<b>6</b>
<b>Figure S5</b> .....	<b>6</b>
<b>Figure S6</b> .....	<b>7</b>
<b>Figure S7</b> .....	<b>8</b>
<b>Figure S8</b> .....	<b>8</b>
<b>Figure S9</b> .....	<b>9</b>
<b>Figure S10</b> .....	<b>10</b>
<b>Table S7</b> .....	<b>11</b>
<b>Table S8</b> .....	<b>11</b>
<b>Figure S11</b> .....	<b>12</b>
<b>Figure S12</b> .....	<b>12</b>

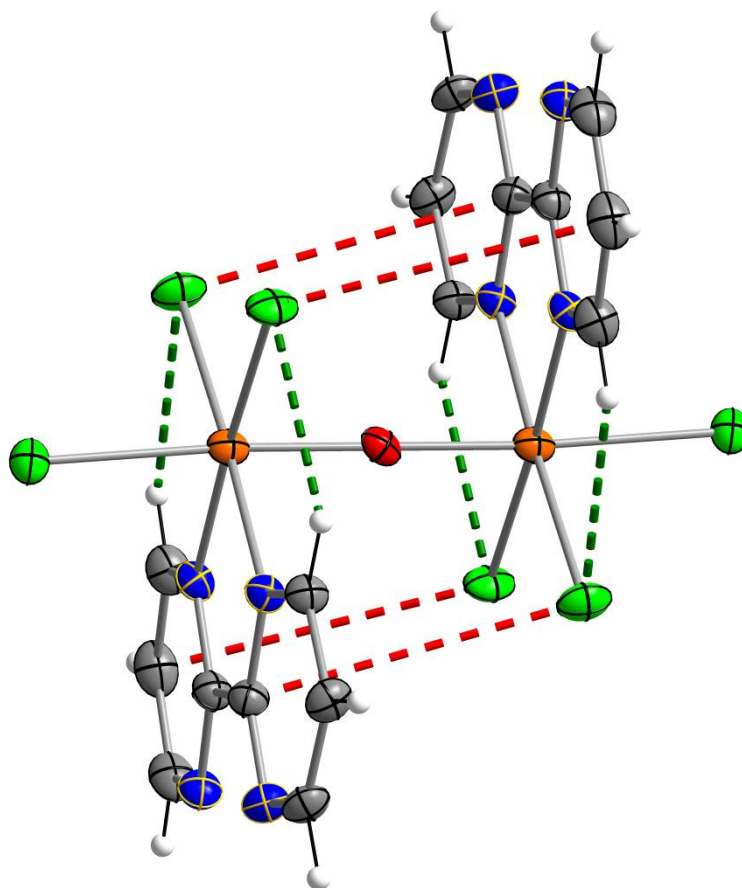


**Figure S1.** Detail of the intramolecular Cl $\cdots\pi$  (dashed red lines) and Cl $\cdots$ H-C (dashed green lines) interactions that occur in the dinuclear  $[\{\text{RuCl}_3(\text{bpym})\}_2(\mu\text{-O})]$  complex of **6**. Thermal ellipsoids are depicted at the 50% probability level. Crystallization water molecules have been omitted for clarity. Color code: orange, Ru; green, Cl; red, O; blue, N; grey, C; white, H.



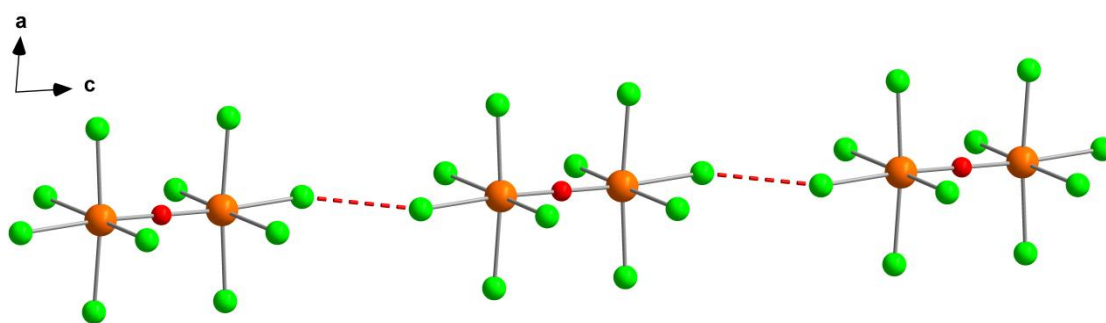


**Figure S2.** Detail of the one-dimensional motif generated by intermolecular Cl...Cl contacts (dashed red lines) between neighboring  $[\{\text{RuCl}_5\}_2(\mu\text{-O})]^{4-}$  complexes in the crystal of **1**. Color code: orange, Ru; green, Cl; red, O.

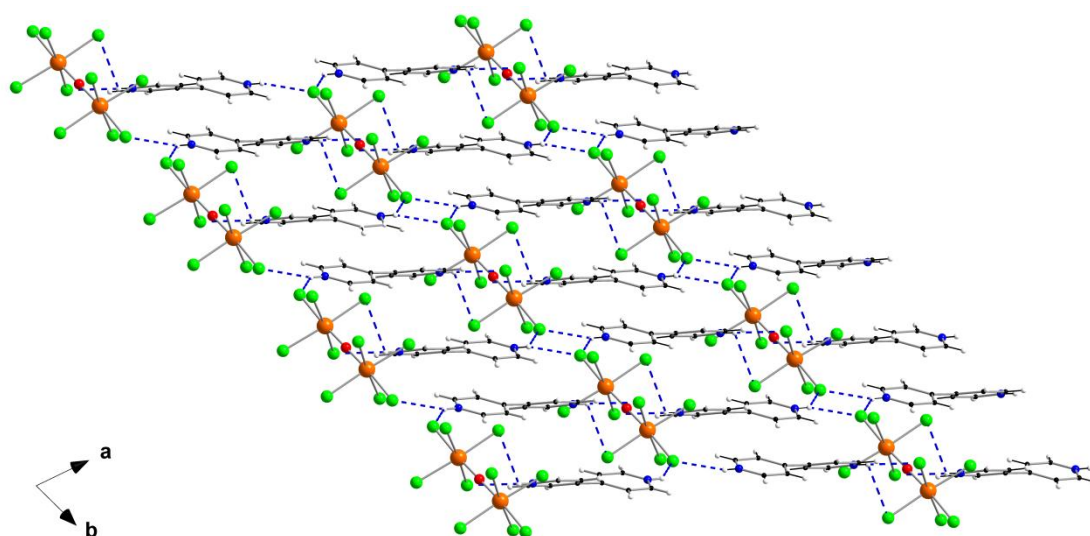


**Figure S3.** Perspective view along the  $c$ -axis direction of the two-dimensional motif formed by means of bifurcated three-centered hydrogen bonds (dashed blue lines) between  $(\text{H}_2\text{bpy})^{2+}$  cations and  $[\{\text{RuCl}_5\}_2(\mu\text{-O})]^{4-}$  anions in the crystal of **1**. Color code: orange, Ru; green, Cl; red, O; blue, N; black, C; white, H.

**Table S1. Values of the C-H...Cl interactions in compound 1.**

C-H...Cl	C-H/Å	H...Cl/Å	C...Cl/Å	(CHCl)/°
C(1)-H(1C)...Cl(3b)	0.930	2.95(1)	3.579(1)	125.9
C(1)-H(1C)...Cl(3d)	0.930	2.90(1)	3.393(1)	114.7
C(4)-H(4A)...Cl(4f)	0.930	2.91(1)	3.477(1)	121.0
C(5)-H(5A)...Cl(2g)	0.930	2.84(1)	3.700(1)	155.2
C(5)-H(5A)...Cl(4f)	0.930	2.79(1)	3.419(1)	126.2
C(8)-H(8A)...Cl(4e)	0.930	2.55(1)	3.468(1)	168.1
C(8)-H(8A)...Cl(5e)	0.930	2.93(1)	3.458(1)	117.5
C(9)-H(9A)...Cl(1c)	0.930	2.89(1)	3.791(1)	163.1
C(9)-H(9A)...Cl(2c)	0.930	2.81(1)	3.425(1)	124.5
C(10)-H(10A)...Cl(1f)	0.930	2.84(1)	3.334(1)	114.6

<sup>a</sup>Symmetry codes: (b) = -x+1, -y, -z+1; (c) = x+1, y, z; (d) = x, y-1, z; (e) = -x+2, -y, -z+1;

(f) = -x+2, -y, -z.

**Table S2. Values of the C-H...Cl interactions in compound 2.**

C-H...Cl	C-H/Å	H...Cl/Å	C...Cl/Å	(CHCl)/°
C(18)-H(18A)...Cl(4)	0.950	2.81(1)	3.578(1)	138.7
C(20)-H(20A)...Cl(1)	0.950	2.81(1)	3.727(1)	163.3
C(30)-H(30A)...Cl(5d)	0.950	2.82(1)	3.672(1)	149.7
C(32)-H(32A)...Cl(8)	0.950	2.95(1)	3.610(1)	127.8

<sup>a</sup>Symmetry codes: (d) = -x+1, -y, -z+1.

**Table S3. Values of the C-H...Cl interactions in compound 3.**

C-H...Cl	C-H/Å	H...Cl/Å	C...Cl/Å	(CHCl)/°
C(20)-H(20)...Cl(2a)	0.950	2.72(1)	3.666(1)	178.2
C(22)-H(22)...Cl(3a)	0.950	2.85(1)	3.664(1)	144.5
C(2)-H(2A)...Cl(2b)	0.980	2.95(1)	3.848(1)	152.6
C(4)-H(4)...Cl(1b)	0.950	2.57(1)	3.331(1)	137.5
C(16)-H(16)...Cl(4d)	0.950	2.96(1)	3.514(1)	118.7
C(26)-H(26)...Cl(3e)	0.950	2.78(1)	3.631(1)	150.0

<sup>a</sup>Symmetry codes: (a) = -x+1, -y+2, -z+1; (b) = x, -y+3/2, z+1/2; (d) = x+1, -y+3/2, z+1/2; (e) = -x+1, y-1/2, -z+3/2.

**Table S4. Values of the C-H...Cl interactions in compound 4.**

C-H...Cl	C-H/Å	H...Cl/Å	C...Cl/Å	(CHCl)/°
C(1)-H(1)...Cl(1a)	0.950	2.75(1)	3.228(1)	112.0
C(3)-H(3A)...Cl(1b)	0.980	2.94(1)	3.869(1)	158.3
C(3)-H(3A)...Cl(3b)	0.980	2.80(1)	3.411(1)	121.1
C(5)-H(5)...Cl(3a)	0.950	2.69(1)	3.393(1)	131.5
C(21)-H(21)...Cl(1b)	0.950	2.94(1)	3.881(1)	172.5
C(23)-H(23)...Cl(2b)	0.950	2.84(1)	3.602(1)	137.6
C(27)-H(27)...Cl(2)	0.950	2.98(1)	3.867(1)	155.7

<sup>a</sup>Symmetry codes: (a) = -x+1, -y, -z+1, (b) = x, -y-1/2, z+1/2.

**Table S5. Values of the C-H...Cl interactions in compound 5.**

C-H...Cl	C-H/Å	H...Cl/Å	C...Cl/Å	(CHCl)/°
C(7)-H(7)...Cl(4c)	0.950	2.99(1)	3.815(1)	146.5
C(17)-H(17)...Cl(1b)	0.950	2.68(1)	3.598(1)	162.9

<sup>a</sup>Symmetry codes: (b) = -x+1, -y+2, -z, (c) = x, y-1, z.

**Table S6. Values of the C-H...Cl interactions in compound 6.**

C-H...Cl	C-H/Å	H...Cl/Å	C...Cl/Å	(CHCl)/°
C(1)-H(1B)...Cl(2)	0.950	2.79(1)	3.380(1)	121.0
C(1)-H(1B)...O(2wd)	0.950	2.56(1)	3.363(1)	143.1
C(2)-H(2A)...Cl(1g)	0.950	2.89(1)	3.832(1)	174.1
C(3)-H(3B)...Cl(1d)	0.950	2.89(1)	3.717(1)	146.8
C(6)-H(6A)...Cl(3)	0.950	2.73(1)	3.332(1)	122.3
C(6)-H(6A)...Cl(3b)	0.950	2.77(1)	3.584(1)	144.7

<sup>a</sup>Symmetry codes: (b) = -x, -y+1, -z+2; (d) = -x+2, -y+1, -z+1; (g) = x+1, y, z.

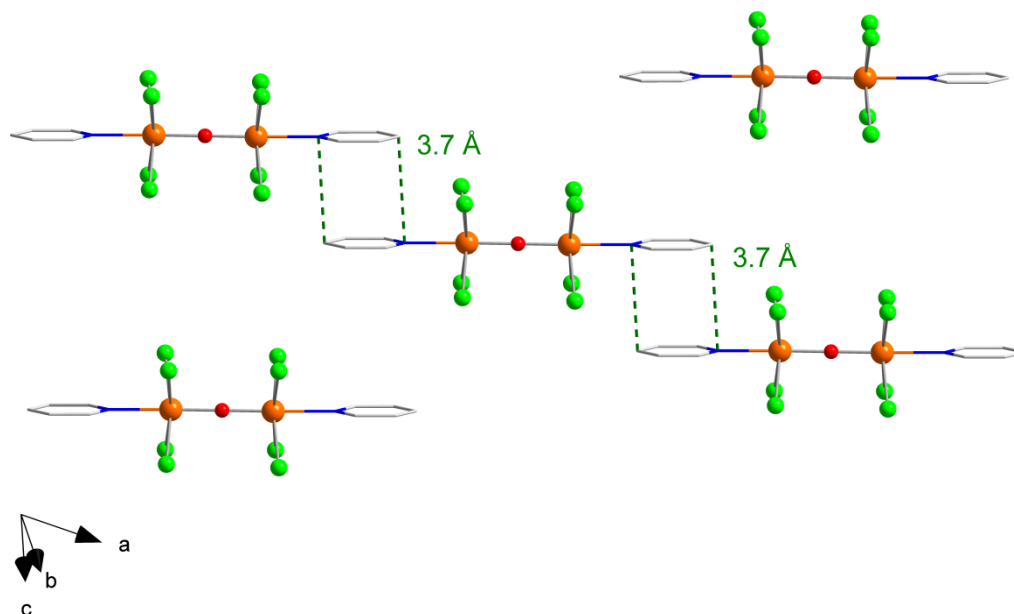


**Figure S4.** Detail of the face-to-face stacked  $\pi\cdots\pi$  interactions [centroid-centroid distance of *ca.* 3.7 Å] between pyridine rings of  $[\{\text{RuCl}_4(\text{py})\}_2(\mu\text{-O})]^{4-}$  anions in the crystal of **5**. Color code: orange, Ru; green, Cl; red, O; blue, N; white, C.

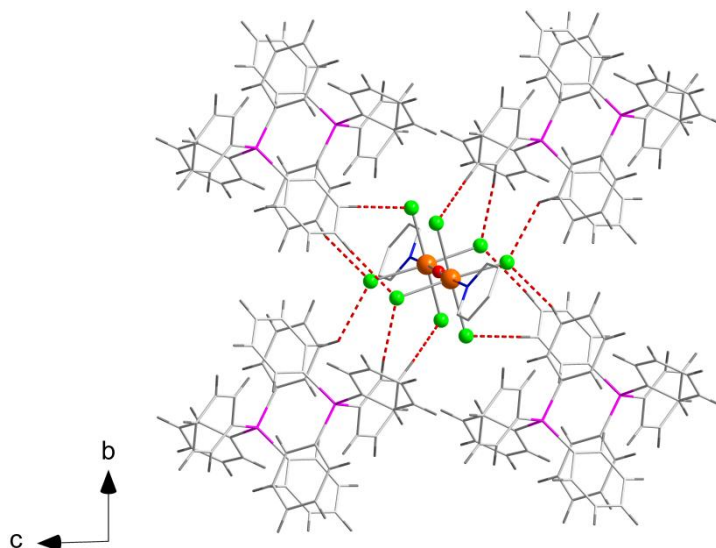


**Figure S5.** View along the *a* axis of the C-H $\cdots$ Cl interactions between  $\text{PPh}_4^+$  cations and one  $[\{\text{RuCl}_4(\text{py})\}_2(\mu\text{-O})]^{4-}$  anion in the crystal of **5**. Color code: orange, Ru; green, Cl; P, pink; red, O; blue, N; white, C; grey, H.

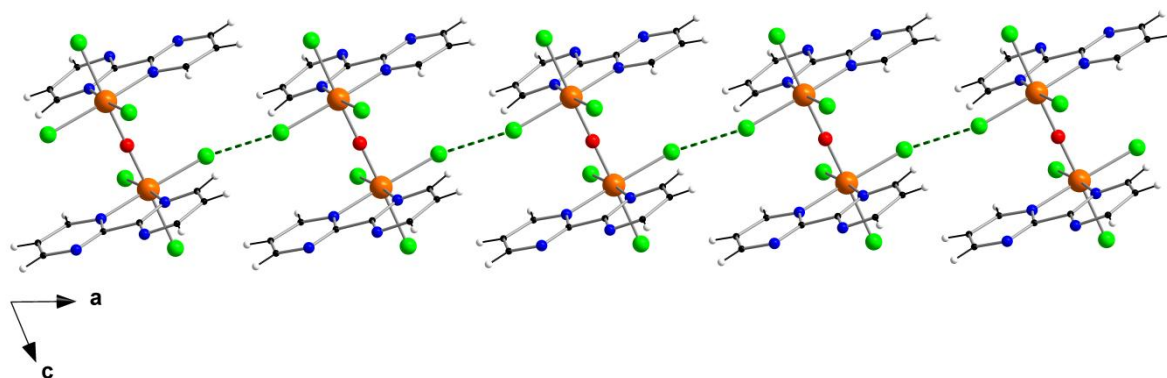


**Figure S6.** Detail of the one-dimensional motif generated through intermolecular Cl...Cl interactions (dashed green lines) between neighboring  $[\{\text{RuCl}_3(\text{bpy})\}_2(\mu\text{-O})]$  complexes in the crystal of **6**. Crystallization water molecules have been omitted for clarity. Color code: orange, Ru; green, Cl; red, O; blue, N; black, C; white, H.

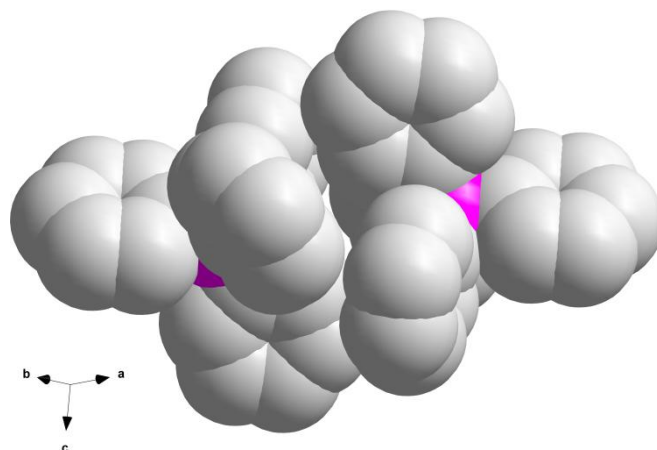


**Figure S7.** Sextuple phenyl embrace (SPE) supramolecular conformation of the  $\text{PPh}_4^+$  cations (space-filling model) in **2**. H atoms have been omitted for clarity. Color code: P, pink; grey, C. [Symmetry code: (b) =  $-x+1, -y-1, -z+1$ ].

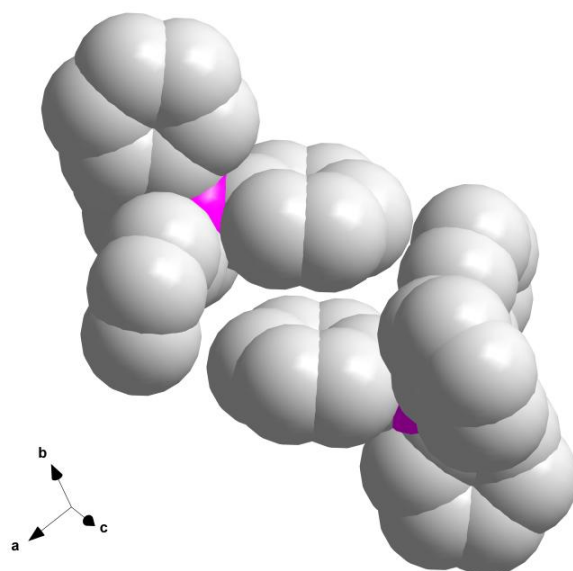


**Figure S8.** Quadruple phenyl embrace (QPPE) motif of the  $\text{PPh}_4^+$  cations (space-filling model) in **2**. H atoms have been omitted for clarity. Color code: P, pink; grey, C. [Symmetry code: (c) =  $-x+1, -y, -z$ ].

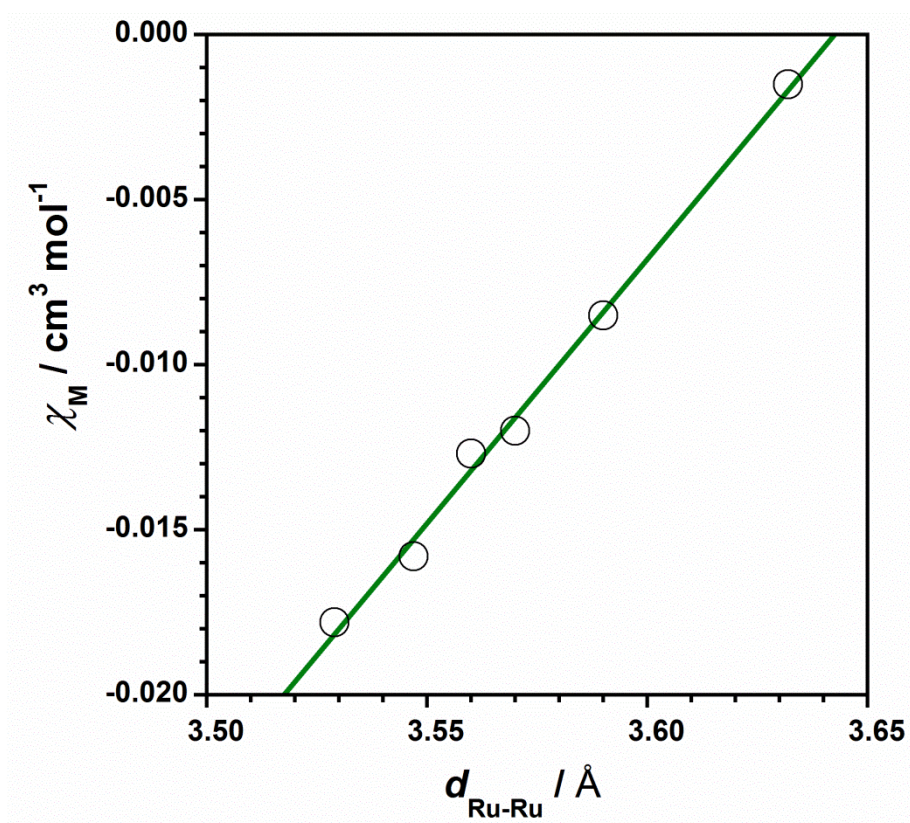


**Figure S9.** Plot of the molar magnetic susceptibility ( $\chi_{\text{M}}$ ) *versus* the intramolecular Ru-Ru distance for **1-6**. The solid line represents the best-fit of the experimental data.

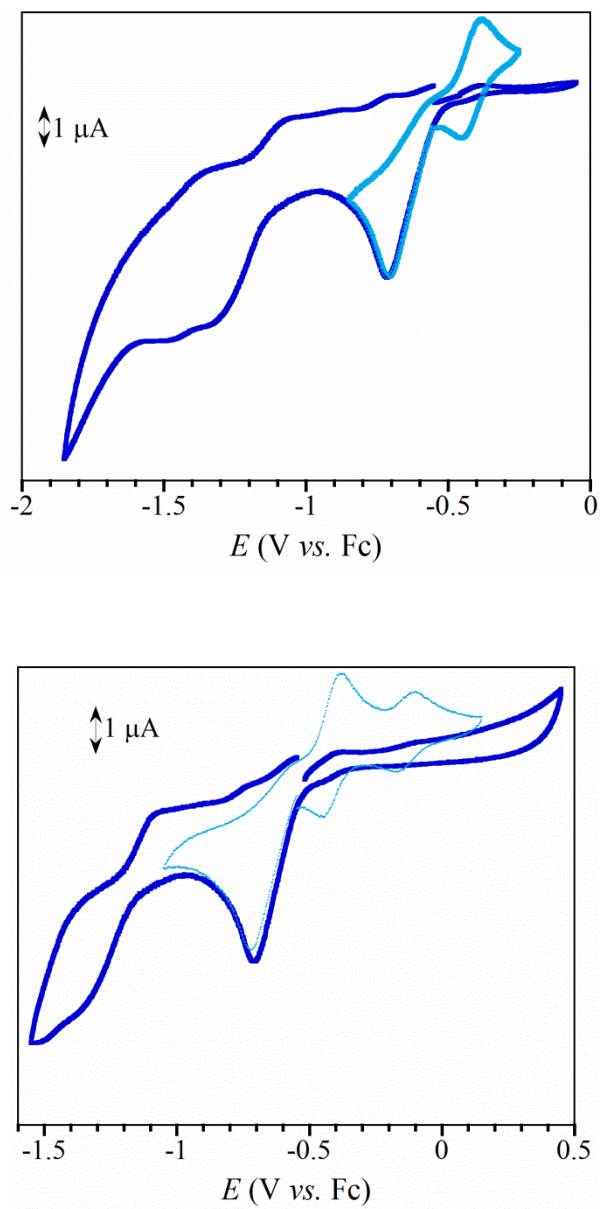


**Figure S10.** Cyclic voltammograms of **2** (top) and **3** (bottom) in dry dmf (0.1 M  $\text{NBu}_4\text{PF}_6$ ) at 25 °C and  $200 \text{ mV s}^{-1}$ . The pale blue curves show the cyclic voltammograms of the oxidation waves when the potential is scanned through the first reversible reduction waves.



**Table S7. Electrochemical potential data for 2-6<sup>a,b</sup>**

	<b>2<sup>i</sup></b>	<b>3<sup>i</sup></b>	<b>4<sup>i</sup></b>	<b>5<sup>i</sup></b>	<b>6</b>
$E_1 (\Delta E_1)$	-0.75	-0.77	-0.77	-0.80	-0.61 (-92)
$E_2 (\Delta E_2)$	-1.34	-1.60	-1.59	-1.68	-0.78 (-97)
$E_3 (\Delta E_3)$	-	-	-	-	-1.05 (-138)
$E_4 (\Delta E_4)$	-	-	-	-	-1.26 (-144)
$E_5 (\Delta E_5)$	-	-	-	-	+0.17 (-75)

<sup>a</sup>Formal potentials are defined as the half-wave potentials for reversible waves or as the cathodic potentials for the irreversible (i) reduction waves (in V).  $\Delta E_n$  are the values of the peak-to-peak separations (in mV).

<sup>b</sup>In dry DMF and at room temperature (0.1M NBu<sub>4</sub>PF<sub>6</sub>).

---

**Table S8. Experimental absorption spectroscopic data for 2-6<sup>a,b</sup>**

$\lambda_n/\text{nm}$ ( $\epsilon \cdot 10^{-5}/\text{M}^{-1}\text{cm}^{-1}$ )	<b>2</b>	<b>3</b>	<b>4</b>	<b>5</b>	<b>6</b>
$\lambda_1 (\epsilon_1)$	398 (2.69)	399 (2.35)	399 (2.31)	437 (1.31)	358 (1.67)
$\lambda_2 (\epsilon_2)$	493 (0.86)	495 (0.76)	495 (0.75)	501 (0.76)	397 (2.84)
$\lambda_3 (\epsilon_3)$	-	-	-	-	498 (1.84)

<sup>a</sup> In dry DMF and at room temperature.

<sup>b</sup>Values of the absorption maxima. The extinction coefficient values are given in parenthesis.

---

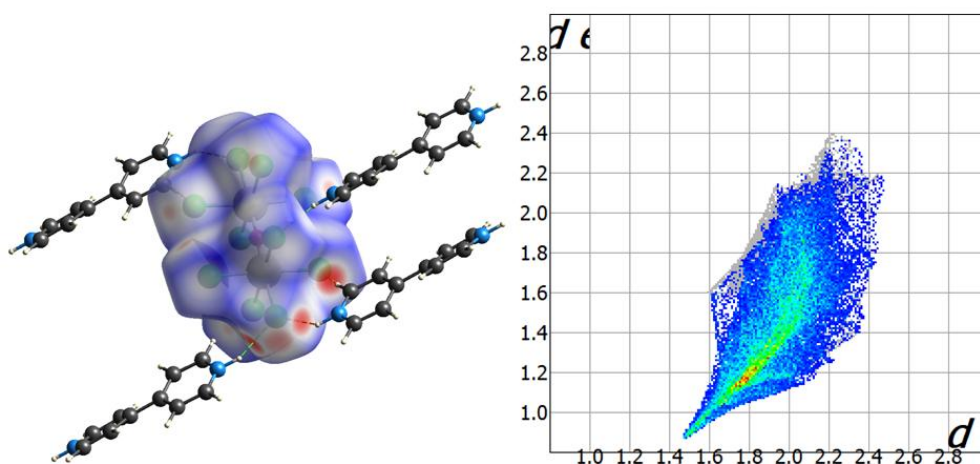


**Figure S11.** Hirshfeld surface mapped with  $d_{\text{norm}}$  function (left) and fingerprint plot (right) for compound **1**. Intermolecular Cl $\cdots$ H contacts are approximately the 90% of the complete fingerprint.

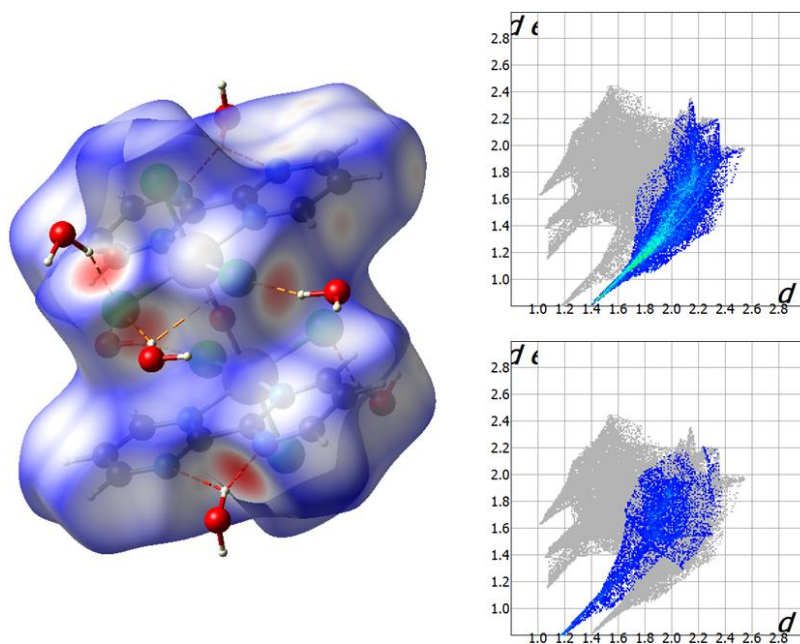


**Figure S12.** Hirshfeld surface mapped with  $d_{\text{norm}}$  function (left) and fingerprint plots (right) for compound **6**. Intermolecular Cl $\cdots$ H (right, top) and N $\cdots$ H (right, bottom) contacts are highlighted from the full fingerprint.

---

*APPENDIX B:*  
*Supporting Information Chapter*

*3*



# Supporting Information

## **A Gadolinium(III) Complex Based on the Thymine Nucleobase with Properties Suitable for Magnetic Resonance Imaging**

Marta Orts-Arroyo, Amadeo Ten-Esteve, Sonia Ginés-Cárdenas,  
Isabel Castro, Luis Martí-Bonmatí and José Martínez-Lillo



## Supplementary Information

### A gadolinium(III) complex based on the thymine nucleobase with properties suitable for magnetic resonance imaging

Marta Orts-Arroyo,<sup>a</sup> Amadeo Ten-Esteve,<sup>b</sup> Sonia Ginés-Cárdenas,<sup>b</sup> Isabel Castro,<sup>a</sup> Luis Martí-Bonmatí<sup>b,\*</sup> and José Martínez-Lillo<sup>a,\*</sup>

<sup>a</sup> *Instituto de Ciencia Molecular (ICMol), c/ Catedrático de Física, 2, 46980, Paterna, València, Spain. E-mail: f.jose.martinez@uv.es.*

<sup>b</sup> *Radiology and Biomedical Imaging Research Group (GIBI2<sup>30</sup>), La Fe University and Polytechnic Hospital and La Fe Health Research Institute, Valencia, Spain. E-mail: marti\_lui@gva.es.*

Table of contents	page
Figure S1.....	2
Figure S2.....	2
Figure S3.....	3
Figure S4.....	4
Table S1.....	5
Figure S5.....	6
Figure S6.....	6
Figure S7.....	7

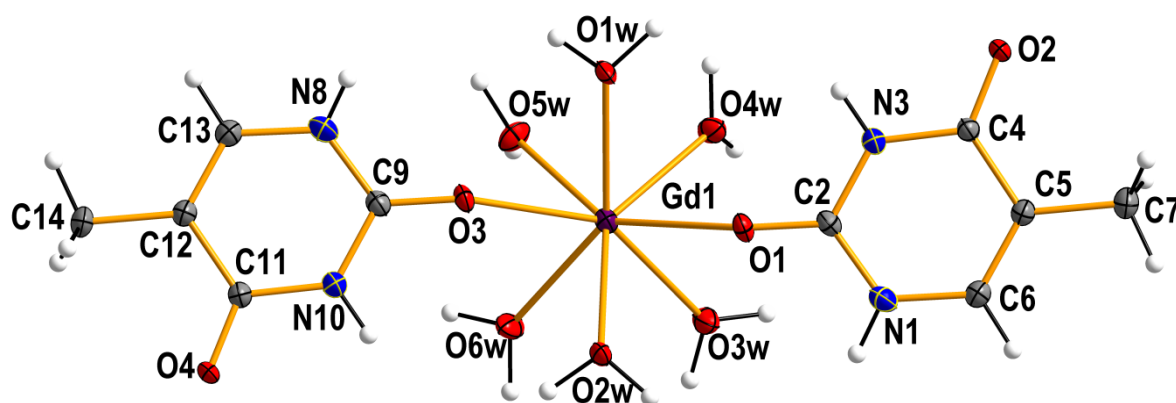


**Figure S1.** Perspective view of the cationic  $[\text{Gd}(\text{thy})_2(\text{H}_2\text{O})_6]^{3+}$  complex showing the atom numbering scheme in **1**. Thermal ellipsoids are drawn at 50% probability level. Perchlorate anions and non-coordinated water molecules have been omitted for clarity.

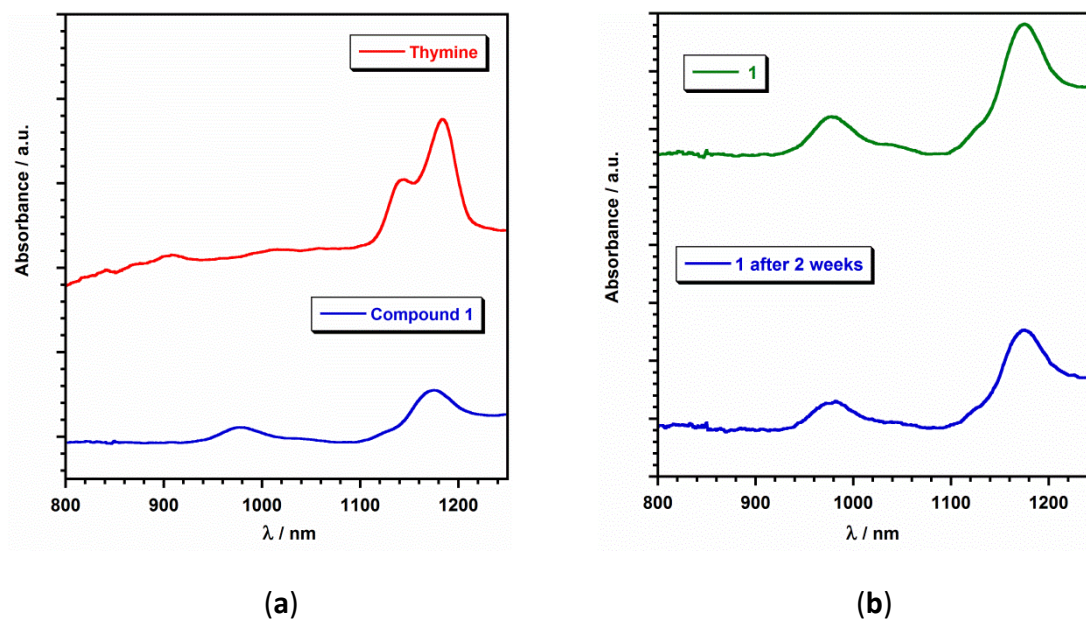


**Figure S2.** (a) Electronic absorption spectra from samples of thymine (red) and compound **1** (blue) in solid state (range: 800-1250 nm); (b) electronic absorption spectra from a sample of compound **1** (green) and the same sample after 2 weeks (blue) (range: 800-1250 nm).



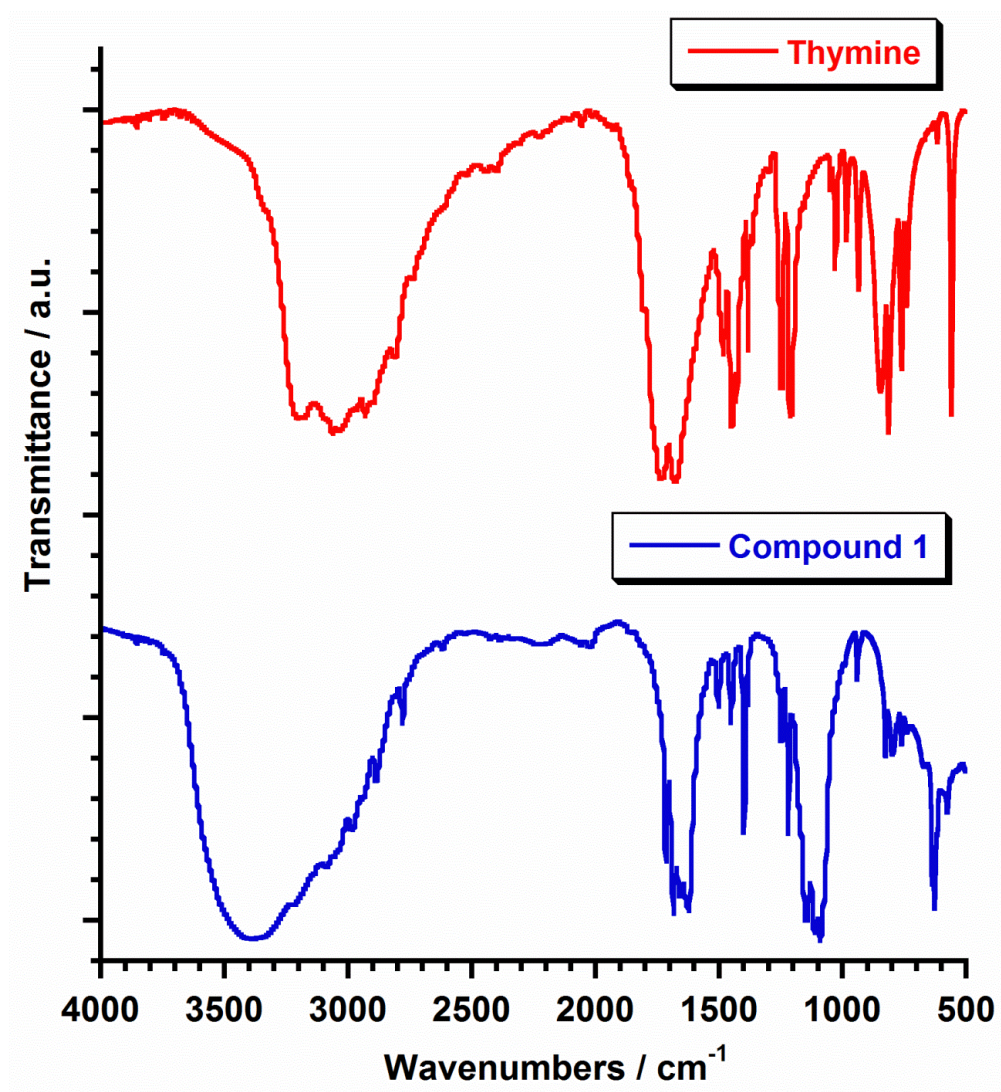


**Figure S3.** FT-IR spectra for thymine (red) and compound **1** (blue).

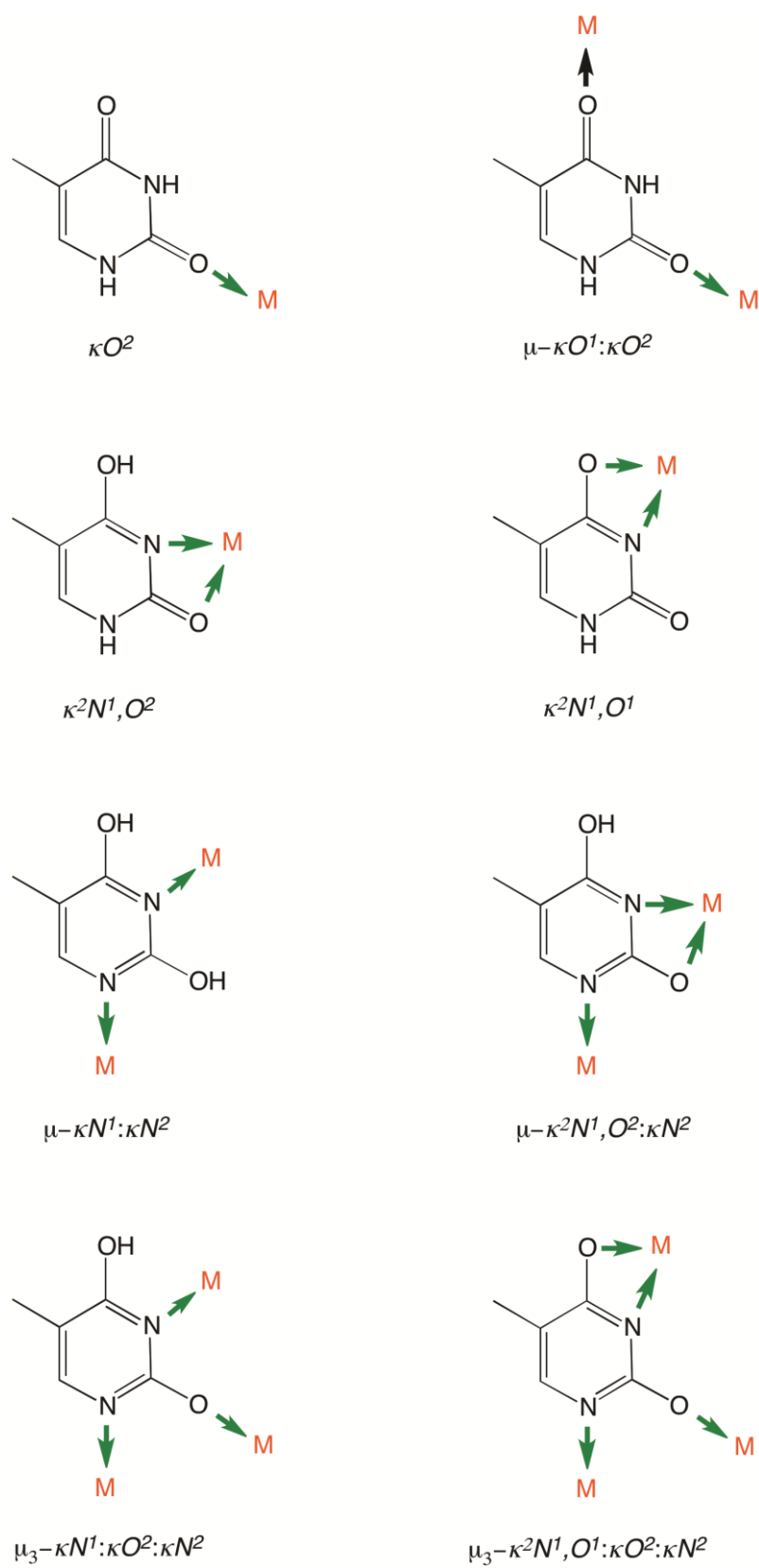


**Figure S4.** Selected coordination modes for the thymine ligand.

**Table S1.** Selected bond lengths (Å) for compound **1**.

Compound	<b>1</b>
Gd(1)-O(1)	2.385(2)
Gd(1)-O(3)	2.377(2)
Gd(1)-O(1w)	2.402(2)
Gd(1)-O(2w)	2.386(2)
Gd(1)-O(3w)	2.371(2)
Gd(1)-O(4w)	2.401(2)
Gd(1)-O(5w)	2.403(2)
Gd(1)-O(6w)	2.379(2)
C(4)-C(5)	1.441(3)
C(5)-C(6)	1.353(3)
C(5)-C(7)	1.499(3)
C(11)-C(12)	1.438(3)
C(12)-C(13)	1.350(3)
C(12)-C(14)	1.495(3)
C(2)-N(1)	1.352(3)
C(6)-N(1)	1.375(3)
C(2)-N(3)	1.357(3)
C(4)-N(3)	1.379(3)
C(9)-N(8)	1.348(3)
C(13)-N(8)	1.380(3)
C(9)-N(10)	1.358(3)
C(11)-N(10)	1.382(3)
C(2)-O(1)	1.245(3)
C(4)-O(2)	1.241(3)
C(9)-O(3)	1.245(3)
C(11)-O(4)	1.240(3)

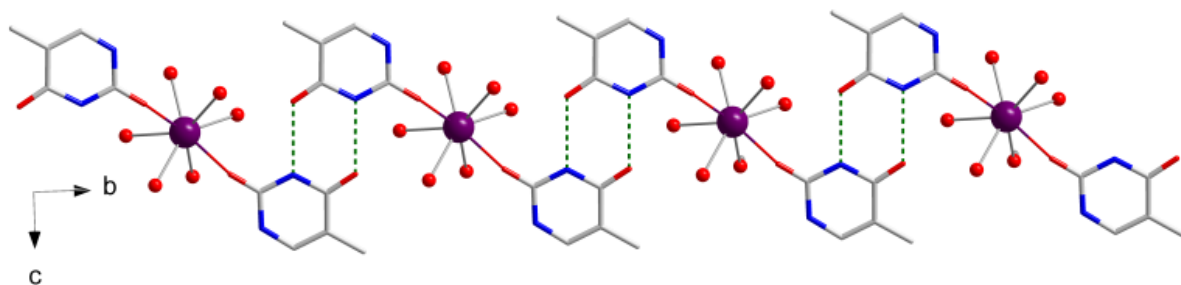


**Figure S5.** View of a fragment of the crystal packing of **1** showing the 1D motif generated by H-bonded thymine ligands (green dashed lines) of adjacent  $[\text{Gd}(\text{thy})_2(\text{H}_2\text{O})_6]^{3+}$  cations. H atoms, perchlorate anions and non-coordinating water molecules have been omitted for clarity. Color code: purple, Gd; red, O; blue, N; grey, C.

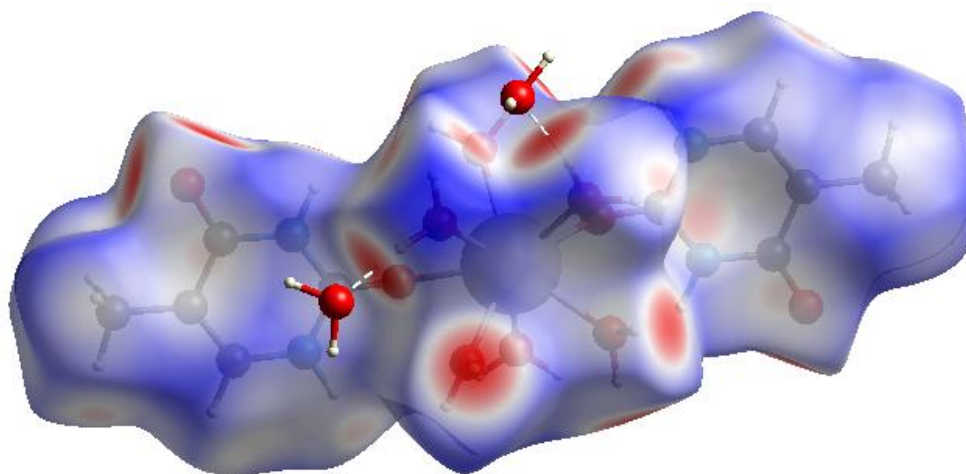
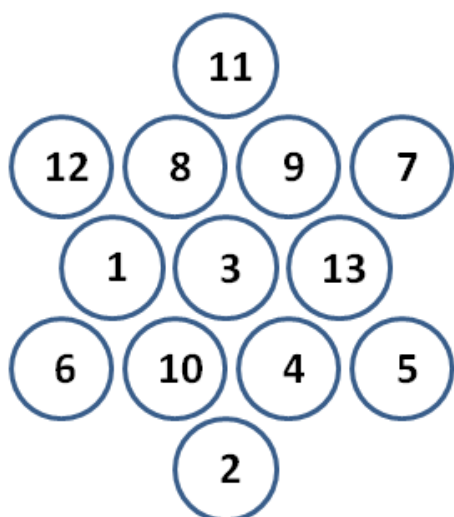


**Figure S6.** Hirshfeld surface mapped with  $d_{\text{norm}}$  function, showing the shorter intermolecular  $\text{O}\cdots\text{H}$  contacts (dashed lines) between non-coordinated and coordinated water molecules for **1**.



(a)

#	Concentration /mM
1	0.00
2	0.72
3	0.80
4	0.88
5	0.96
6	1.04
7	1.20
8	1.28
9	1.36
10	1.44
11	1.52
12	1.60
13	3.20

(b)

**Figure S7.** (a) Schematic of the placement of the 13 samples of **1** studied in the volumetric head 8 channels SENSE MR imaging coil; (b) Concentration in mM of the 13 samples of **1** prepared in physiological serum.



# Supporting Information

**Field-induced slow relaxation of magnetisation in  
two one-dimensional homometallic dysprosium(III)  
complexes based on alpha- and beta-amino acids**

Marta Orts-Arroyo, Isabel Castro, Francesc Lloret and José Martínez-  
Lillo





## Electronic Supplementary Information (ESI)

### Field-induced slow relaxation of magnetisation in two one-dimensional homometallic dysprosium(III) complexes based on alpha- and beta-amino acids

Marta Orts-Arroyo, Isabel Castro,<sup>\*</sup> Francesc Lloret and José Martín <sup>-Lillo\*</sup>

*Instituto de Ciencia Molecular (ICMol), c/ Catedrático*

*2, 46980, Paterna, València, Spain.*

*E-mail: f.jose.martinez@uv.es.*

Table of contents	page
Figure S1.....	2
Figure S2.....	3
Table S1.....	4
Table S2.....	5
Table S3.....	6
Figure S3.....	7
Figure S4.....	7
Table S4.....	8
Table S5.....	8
Figure S5.....	9
Figure S6.....	10
Figure S7.....	11
Figure S8.....	12

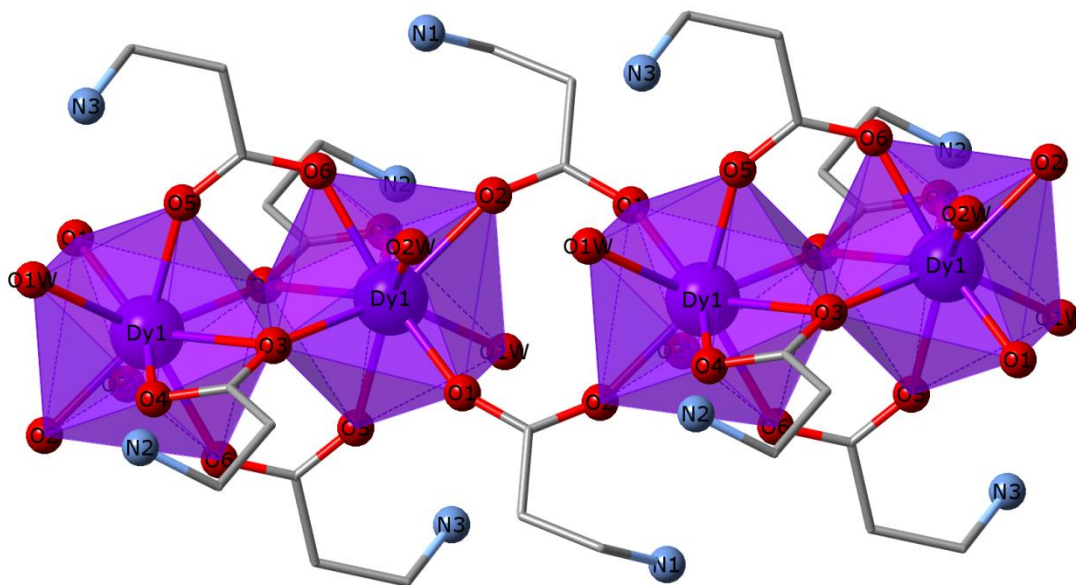
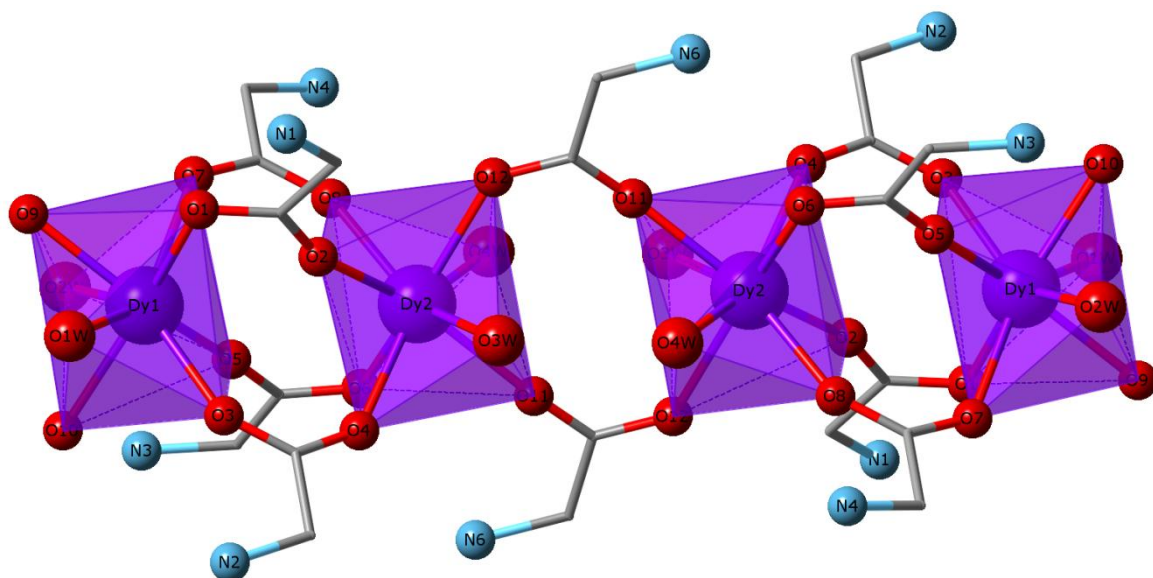


**Figure S1.** View of neighbouring dinuclear  $[\text{Dy}^{\text{III}}_2]^{6+}$  units connected through additional carboxylate groups from glycine (**1**, top) and  $\beta$ -alanine (**2**, bottom) amino acids that generate a cationic 1D system.

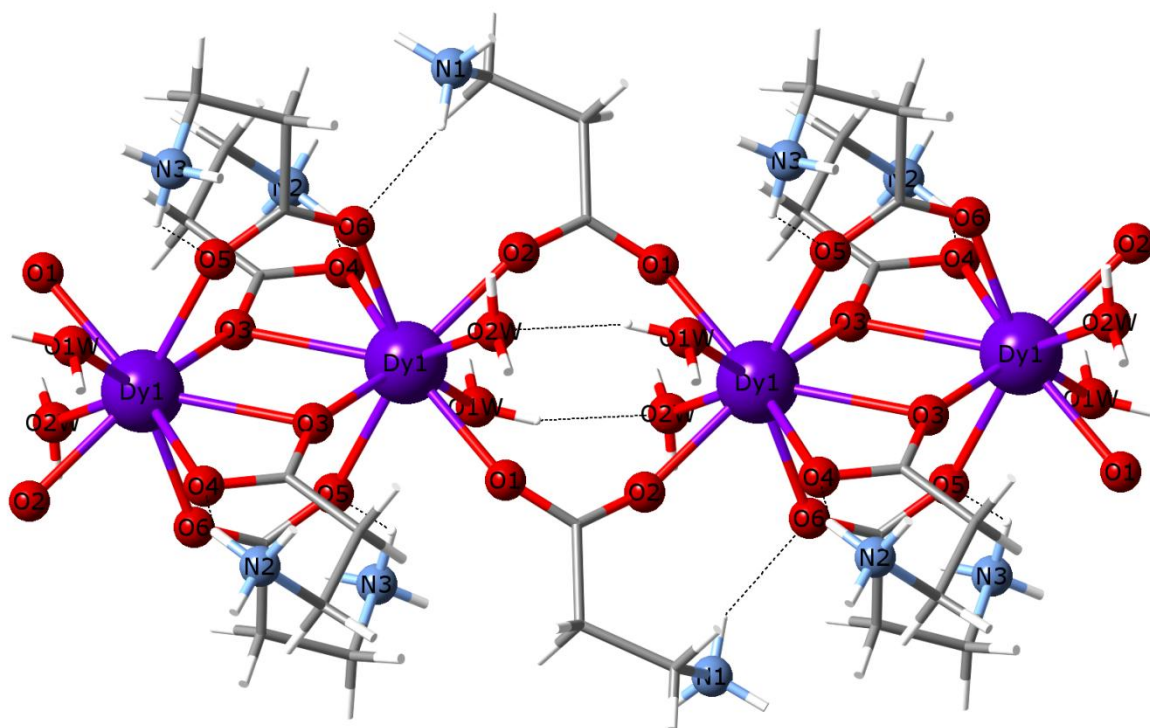


**Figure S2.** Detail of intramolecular H-bonding interactions between coordinated water molecules and also between O atoms of carboxylate and protonated  $\text{-NH}_2$  groups, which connect further the neighbouring dinuclear  $[\text{Dy}^{\text{III}}_2]^{6+}$  units in **2**.

**Table S1. Selected bond lengths (Å) for compounds 1 and 2.**

Compound	1	2
Dy(1)-O(1)	2.470(2)	2.286(2)
Dy(1)-O(2)	2.882(2)	2.327(2)
Dy(1)-O(3)	2.337(2)	2.317(2)
Dy(1)-O(4)		2.455(2)
Dy(1)-O(5)	2.291(2)	2.363(2)
Dy(1)-O(6)		2.387(2)
Dy(1)-O(7)	2.369(2)	
Dy(1)-O(9)	2.285(2)	
Dy(1)-O(1w)	2.495(2)	2.516(2)
Dy(1)-O(2w)	2.537(2)	2.524(2)
Dy(2)-O(3w)	2.501(2)	2.487(2)
Dy(2)-O(4w)	2.395(2)	2.493(2)
Dy(2)-O(2)	2.281(2)	
Dy(2)-O(4)	2.336(2)	
Dy(2)-O(6)	2.398(2)	
Dy(2)-O(7)		2.312(2)
Dy(2)-O(8)	2.358(2)	2.322(2)
Dy(2)-O(9)		2.361(2)
Dy(2)-O(11)	2.319(2)	2.294(2)
C(1)-C(2)	1.506(3)	1.515(3)
C(5)-C(6)	1.509(3)	1.515(3)
C(11)-C(12)	1.517(3)	1.516(4)
C(3)-N(1)		1.495(3)
C(4)-N(2)	1.489(3)	
C(6)-N(2)		1.499(3)
C(6)-N(3)	1.485(3)	
C(1)-O(1)	1.255(3)	1.257(3)
C(1)-O(2)	1.257(3)	1.259(3)

**Table S2. Hydrogen-Bonding Interactions in 1<sup>a</sup>.**

D-H...A	D-H/Å	H...A/Å	D...A/Å	(DHA) <sup>o</sup>
N(1)-H(1A)...O(13c)	0.910	2.08(1)	2.944(1)	158.1(1)
N(1)-H(1A)...O(31d)	0.910	2.45(1)	2.980(1)	117.5(1)
N(1)-H(1B)...O(30e)	0.910	2.32(1)	2.954(1)	126.6(1)
N(1)-H(1C)...O(16c)	0.910	2.56(1)	3.022(1)	112.2(1)
N(1)-H(1C)...O(20)	0.910	2.28(1)	3.014(1)	137.3(1)
N(2)-H(2A)...O(21)	0.910	2.09(1)	2.933(1)	152.7(1)
N(2)-H(2A)...O(33a)	0.910	2.56(1)	3.014(1)	111.5(1)
N(2)-H(2B)...O(9w)	0.910	1.94(1)	2.841(1)	172.7(1)
N(3)-H(3A)...O(22f)	0.910	2.10(1)	2.936(1)	152.4(1)
N(3)-H(3C)...O(24)	0.910	2.14(1)	2.929(1)	144.9(1)
N(4)-H(4A)...O(5w)	0.910	2.03(1)	2.866(1)	152.9(1)
N(4)-H(4B)...O(6wb)	0.910	1.95(1)	2.847(1)	166.6(1)
N(4)-H(4C)...O(30)	0.910	2.05(1)	2.891(1)	154.2(1)
N(5)-H(5A)...O(31d)	0.910	2.53(1)	2.995(1)	112.3(1)
N(5)-H(5B)...O(27g)	0.910	2.13(1)	2.986(1)	157.1(1)
N(6)-H(6A)...O(25)	0.910	2.30(1)	2.843(1)	118.4(1)
N(6)-H(6B)...O(6)	0.910	2.01(1)	2.914(1)	174.6(1)
N(6)-H(6C)...O(8w)	0.910	1.87(1)	2.771(1)	168.8(1)
O(1w)-H(1wA)...O(9w)	0.900	1.87(1)	2.734(1)	159.4(1)
O(2w)-H(2wA)...O(1wa)	0.898	1.95(1)	2.842(1)	175.1(1)
O(2w)-H(2wB)...O(17h)	0.891	2.28(1)	2.912(1)	127.4(1)
O(3w)-H(3wA)...O(7w)	0.900	1.89(1)	2.765(1)	165.2(1)
O(3w)-H(3wB)...O(19)	0.898	1.98(1)	2.855(1)	166.3(1)
O(4w)-H(4wA)...O(5w)	0.899	1.89(1)	2.783(1)	173.2(1)
O(4w)-H(4wB)...O(3wb)	0.902	1.89(1)	2.774(1)	167.3(1)
O(5w)-H(5wB)...O(28)	0.923	2.01(1)	2.914(1)	165.5(1)
O(7w)-H(7wA)...O(28e)	0.901	2.03(1)	2.881(1)	157.2(1)
O(7w)-H(7wB)...O(6w)	0.885	2.00(1)	2.876(1)	170.3(1)
O(8w)-H(8wA)...O(7w)	0.930	1.87(1)	2.779(1)	166.5(1)
O(9w)-H(9wA)...O(16)	0.860	1.99(1)	2.841(1)	168.5(1)
O(9w)-H(9wB)...O(20)	0.923	1.94(1)	2.843(1)	164.5(1)

<sup>a</sup>Symmetry codes: (a) = -x+1, -y, -z+1; (b) = -x+2, -y+1, -z+1; (c) = -x+2, -y, -z+1; (d) = -x+1, -y, -z+2; (e) = x+1, y, z; (f) = -x+1, -y+1, -z+1; (g) = x, y-1, z; (h) = x-1, y, z.

**Table S3. Hydrogen-Bonding Interactions in 2<sup>a</sup>.**

D-H...A	D-H/Å	H...A/Å	D...A/Å	(DHA) <sup>o</sup>
N(1)-H(01A)...O(20)	0.910	2.03(1)	2.854(1)	150.5(1)
N(1)-H(01B)...O(2)	0.910	2.25(1)	2.858(1)	123.5(1)
N(1)-H(01B)...O(6f)	0.910	2.11(1)	2.943(1)	151.3(1)
N(1)-H(01C)...O(14g)	0.910	2.42(1)	2.959(1)	118.0(1)
N(2)-H(02A)...O(32h)	0.910	2.05(1)	2.944(1)	168.7(1)
N(2)-H(02B)...O(4)	0.910	2.15(1)	2.818(1)	129.3(1)
N(2)-H(02C)...O(35)	0.910	2.33(1)	2.902(1)	120.7(1)
N(3)-H(03A)...O(5)	0.910	2.17(1)	2.762(1)	122.0(1)
N(3)-H(03C)...O(14g)	0.910	2.44(1)	3.023(1)	122.6(1)
N(3)-H(03C)...O(15g)	0.910	2.05(1)	2.954(1)	170.8(1)
N(4)-H(04B)...O(10f)	0.910	2.03(1)	2.885(1)	156.1(1)
N(5)-H(05A)...O(9)	0.910	2.05(1)	2.738(1)	131.0(1)
N(5)-H(05B)...O(5we)	0.910	1.95(1)	2.858(1)	172.1(1)
N(5)-H(05C)...O(28d)	0.910	2.18(1)	2.948(1)	142.0(1)
N(6)-H(06A)...O(34i)	0.910	2.26(1)	2.941(1)	131.7(1)
N(6)-H(06B)...O(26e)	0.910	2.23(1)	2.997(1)	142.1(1)
N(6)-H(06C)...O(12)	0.910	2.17(1)	2.829(1)	128.8(1)
N(6)-H(06C)...O(33e)	0.910	2.15(1)	2.952(1)	147.2(1)
O(1w)-H(1wA)...O(25c)	0.893	2.14(1)	2.989(1)	159.8(1)
O(1w)-H(1wB)...O(25c)	0.890	2.06(1)	2.887(1)	154.0(1)
O(2w)-H(2wA)...O(28)	0.926	1.96(1)	2.861(1)	164.3(1)
O(2w)-H(2wB)...O(14e)	0.902	2.58(1)	2.584(1)	127.4(1)
O(2w)-H(2wB)...O(16e)	0.902	2.15(1)	3.022(1)	162.8(1)
O(3w)-H(3wA)...O(35)	0.889	2.06(1)	2.927(1)	163.9(1)
O(3w)-H(3wB)...O(23e)	0.921	1.87(1)	2.778(1)	167.7(1)
O(4w)-H(4wA)...O(3wd)	0.883	2.19(1)	2.943(1)	142.5(1)
O(4w)-H(4wA)...O(8)	0.883	2.29(1)	3.030(1)	141.5(1)
O(4w)-H(4wB)...O(33d)	0.888	2.03(1)	2.889(1)	162.8(1)

<sup>a</sup>Symmetry codes: (c) = -x+1, -y+1, -z+2; (d) = -x+2, -y+2, -z+1; (e) = x+1, y, z; (f) = x-1, y, z; (g) = -x, -y+1, -z+2; (h) = -x+2, -y+1, -z+1; (i) = -x+3, -y+1, -z+1.

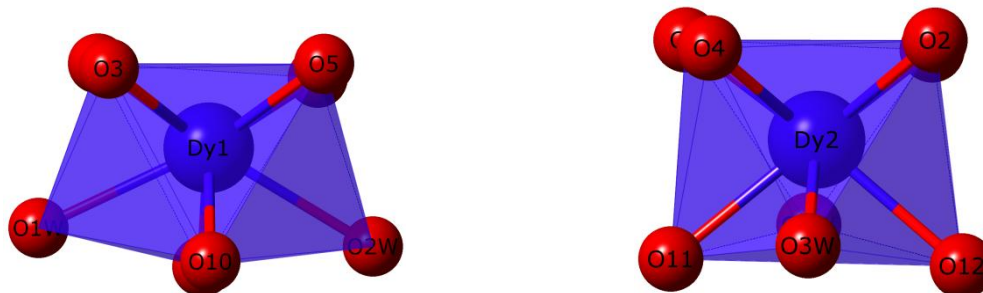


**Figure S3.** Perspective view of the environment of the dysprosium atoms of the dinuclear  $[\text{Dy}^{\text{III}}_2]^{6+}$  unit in compound **1** [Dy(1), left; Dy(2), right].

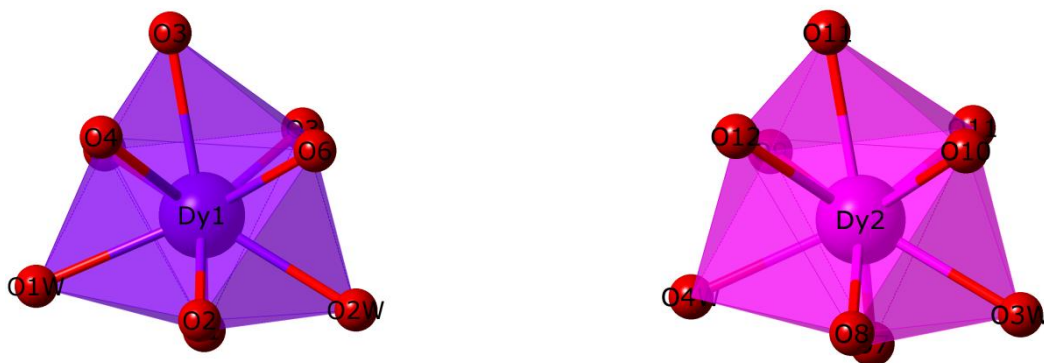


**Figure S4.** Perspective view of the environment of the dysprosium atoms of the dinuclear  $[\text{Dy}^{\text{III}}_2]^{6+}$  units in compound **2** [Dy(1), left; Dy(2), right].

**Table S4. Selected Structural Data for 1<sup>a</sup>**

	Dy(1)	Dy(2)
$S(\text{SAPR})^b$	1.207	0.882
$S(\text{BCTPR})^c$	0.712	1.170
$\text{M}-\text{O}^d$ (Å)	2.470	2.398
$\text{M}-\text{O}^e$ (Å)	2.324	2.334
$\text{M}-\text{O}_w^f$ (Å)	2.516	2.448
$\text{O}-\text{M}-\text{O}^g$ (°)	123.67	122.35
$\Delta^h$ (Å)	0.01	0.01
$\delta^g$ (°)	170.26	164.95
$\delta^{h'}$ (°)	18.27	20.66
$\tau^i$ (°)	2.54	5.70
$\tau^{i'}$ (°)	42.95	49.50
$v/h^k$	1.089	1.059
$v/h^l$	0.997	1.039

<sup>a</sup> Selected structural data for the two crystallographically independent dysprosium atoms (Dy1 and Dy2) for compound 1. <sup>b</sup> Value of the SHAPE parameter relative to the ideal spherical version of the square antiprismatic (SAPR) polyhedron. <sup>c</sup> Value of the SHAPE parameter relative to the ideal spherical version of the bicapped trigonal prismatic (BCTPR) polyhedron. <sup>d</sup> Value of the long metal-oxygen bond length from the carboxylate group. <sup>e</sup> Average value of the short metal-oxygen bond lengths from the carboxylate groups. <sup>f</sup> Average value of the metal-oxygen bond lengths from the coordinated water molecules. <sup>g</sup> Value of the metal-oxygen bond angles from the capping oxygen atoms. <sup>h</sup> Value of the metal deviation from the mean plane formed by the capping oxygen atoms. <sup>g</sup> Value of the dihedral angle between the two opposite triangular faces of the BCTPR. <sup>h'</sup> Value of the dihedral angle between the two adjacent triangular prismatic faces of the basal square face of the SAPR. <sup>i</sup> Value of the trigonal twist angle between the two opposite basal triangular faces of the BCTPR. <sup>i'</sup> Value of the tetragonal twist angle between the two opposite basal square faces of the SAPR. <sup>k</sup> Values of the compression (or elongation) parameter of the lateral rectangular faces of the BCTPR. <sup>l</sup> Values of the compression (or elongation) parameter of the lateral triangular faces of the SAPR.

**Table S5. Selected Structural Data for 2<sup>a</sup>**

	Dy(1)	Dy(2)
$S(\text{CSAPR})^b$	1.091	1.186
$S(\text{TCTPR})^c$	1.530	1.541
$\text{M}-\text{O}^d$ (Å)	2.597	2.550
$\text{M}-\text{O}^e$ (Å)	2.356	2.360
$\text{M}-\text{O}_w^f$ (Å)	2.520	2.490
$\text{O}-\text{M}-\text{O}^g$ (°)	103.0/125.2/130.8	104.9/124.8/126.6
$\Delta^h$ (Å)	0.140	0.112
$\delta^g$ (°)	169.12	170.82
$\delta^{h'}$ (°)	19.06	22.28
$\tau^i$ (°)	6.20	5.02
$\tau^{i'}$ (°)	44.44	42.975
$v/h^k$	1.12	1.08
$v/h^l$	0.98	0.99

<sup>a</sup> Selected structural data for the two crystallographically independent dysprosium atoms (Dy1 and Dy2) for compound 2. <sup>b</sup> Value of the SHAPE parameter relative to the ideal spherical version of the capped square antiprismatic (CSAPR) polyhedron. <sup>c</sup> Value of the SHAPE parameter relative to the ideal spherical version of the tricapped trigonal prismatic (TCTPR) polyhedron. <sup>d</sup> Value of the long metal-oxygen bond length from the carboxylate group. <sup>e</sup> Average value of the short metal-oxygen bond lengths from the carboxylate groups. <sup>f</sup> Average value of the metal-oxygen bond lengths from the coordinated water molecules. <sup>g</sup> Values of the metal-oxygen bond angles from the three capping oxygen atoms of the TCTPR. <sup>h</sup> Value of the metal deviation from the mean plane formed by the three capping oxygen atoms of the TCTPR. <sup>g</sup> Value of the dihedral angle between the two opposite triangular faces of the TCTPR. <sup>h'</sup> Value of the dihedral angle between the two adjacent triangular prismatic faces of the basal square face of the CSAPR. <sup>i</sup> Value of the trigonal twist angle between the two opposite basal triangular faces of the TCTPR. <sup>i'</sup> Value of the tetragonal twist angle between the two opposite basal square faces of the CSAPR. <sup>k</sup> Values of the compression (or elongation) parameter of the lateral rectangular faces of the TCTPR. <sup>l</sup> Values of the compression (or elongation) parameter of the lateral triangular faces of the CSAPR.



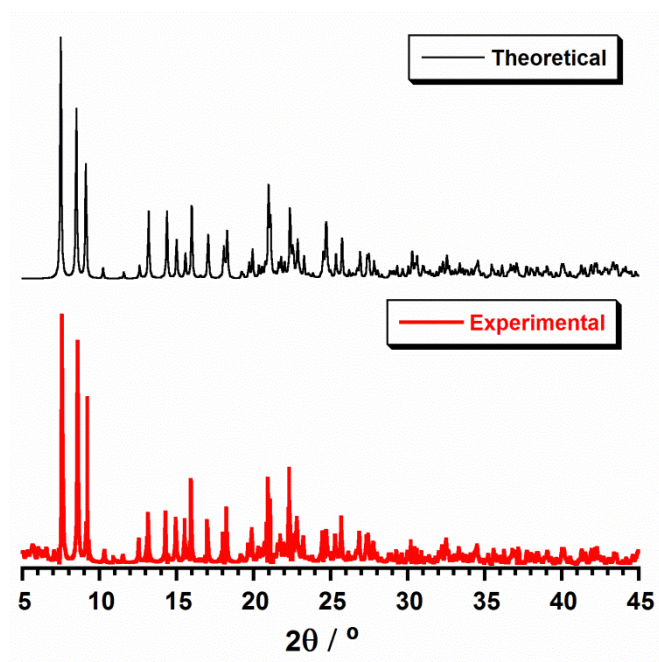
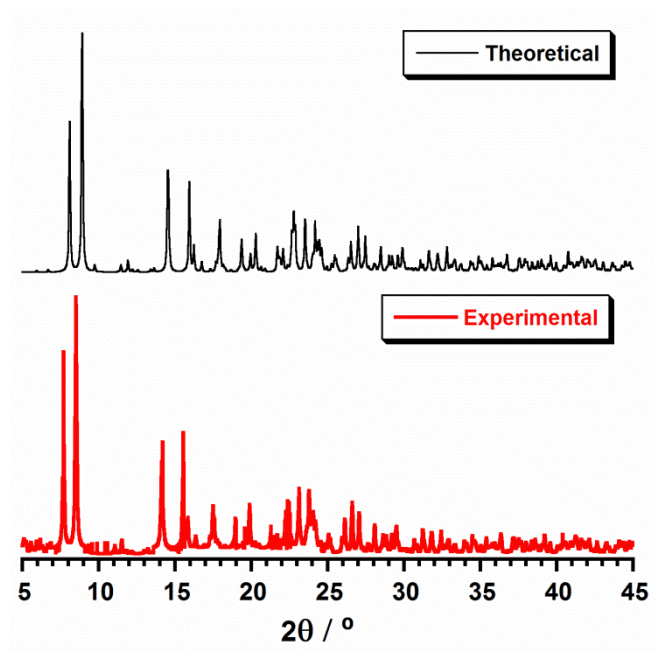


**Figure S5.** Plots of the theoretical and experimental XRD patterns profile ( $2\theta/^\circ$ ) in the range 5-45° for compounds **1** (top) and **2** (bottom).

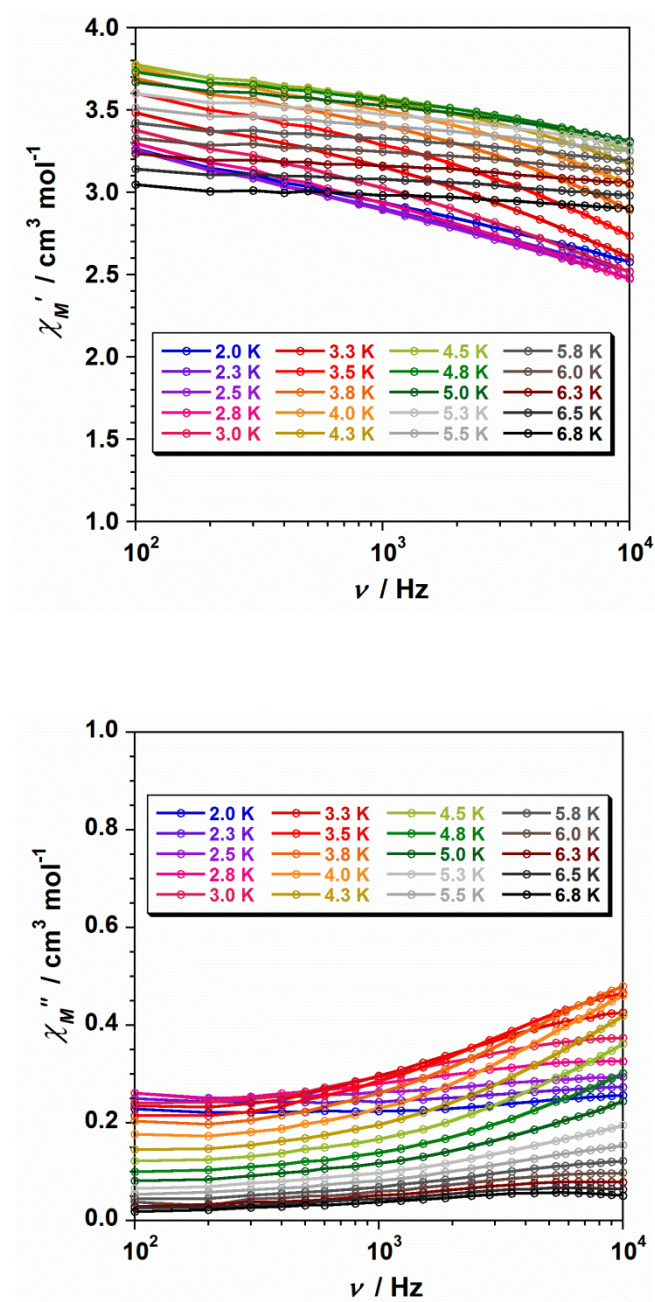


**Figure S6.** Frequency dependence of the in-phase (top) and out-of-phase (bottom) *ac* magnetic susceptibility signals for compound **1** under a dc field of 2500 G.

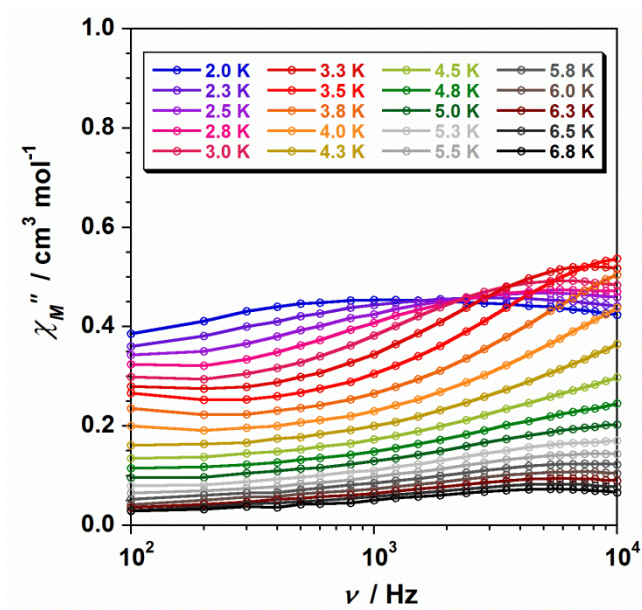
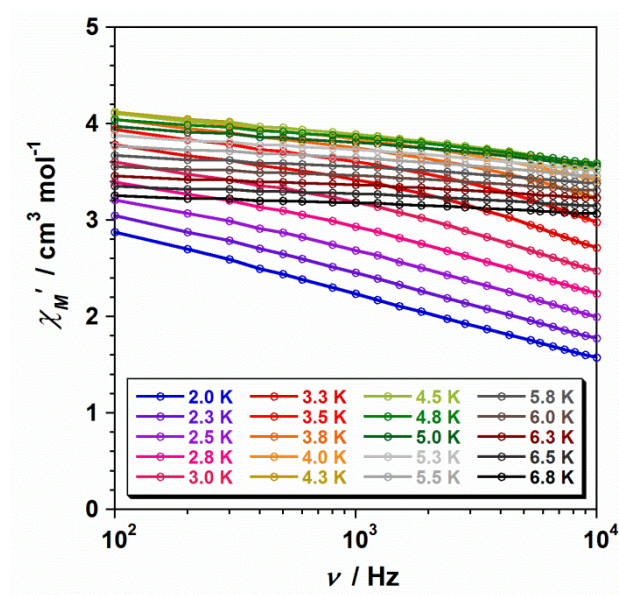


**Figure S7.** Frequency dependence of the in-phase (top) and out-of-phase (bottom)  $ac$  magnetic susceptibility signals for compound **2** under a dc field of 2500 G.

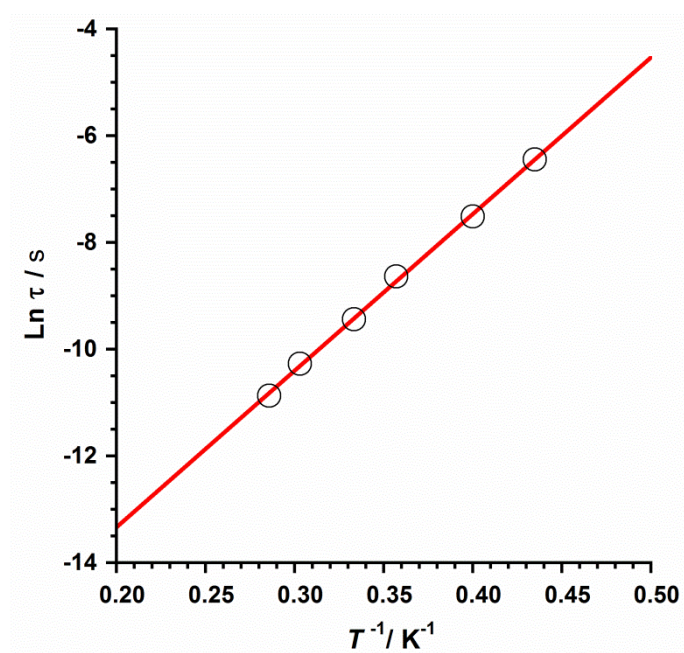


**Figure S8.**  $\ln(\tau)$  versus  $1/T$  plot for **2**, obtained with out-of-phase ac data at  $H_{\text{dc}} = 1000$  G, showing the fit to the Arrhenius law (solid line).

# Supporting Information

## Field-induced slow magnetic relaxation and magnetocaloric effects in an oxalato-bridged gadolinium(III) -based 2D MOF

Marta Orts-Arroyo, Renato Rabelo, Ainoa Carrasco-Berlanga, Nicolás Moliner, Joan Cano, Miguel Julve, Francesc Lloret, Giovanni De Munno, Rafael Ruiz-García, Júlia Mayans, José Martínez-Lillo and Isabel Castro





**Field-induced slow magnetic relaxation and  
magnetocaloric effects in an oxalato-bridged  
gadolinium(III)-based 2D MOF**

Marta Orts-Arroyo, Renato Rabelo, Ainoa Carrasco-Berlanga, Nicolás  
Moliner, Joan Cano, Miguel Julve, Francesc Lloret, Giovanni De Munno,  
Rafael Ruiz-García, Júlia Mayans,\* José Martínez-Lillo\* and Isabel  
Castro\*

## Experimental

### Materials

Oxalic acid (H<sub>2</sub>ox) and gadolinium(III) chloride hexahydrate were of reagent grade and they were used as received.

### Synthetic procedures

**[Gd<sup>III</sup><sub>2</sub>(ox)<sub>3</sub>(H<sub>2</sub>O)<sub>6</sub>]<sub>n</sub>·4nH<sub>2</sub>O (1).** Aqueous concentrated solutions (0.5 mL) of H<sub>2</sub>ox (0.068 g, 0.75 mmol) and GdCl<sub>3</sub>·6H<sub>2</sub>O (0.190 g, 0.5 mmol) were placed at the bottom of each of the two arms of an H-shaped tube and then it was completely filled with water and closed with parafilm. Colorless prisms of **1** were obtained after several weeks of slow diffusion at 50 °C within a thermostated oven. Yield: 0.130 g (68.5%). Anal. calcd (*M*<sub>w</sub> = 758.7 g mol<sup>-1</sup>): C, 9.50; H, 2.66%. Found: C, 9.55; H, 2.61%. IR (KBr, cm<sup>-1</sup>):  $\nu$  = 3421s (br) (O–H from H<sub>2</sub>O), 1671s and 1317m (C=O from ox).

### Physical techniques

Elemental analyses (C, H) were performed by the Servei Central de Suport a la Investigació Experimental de la Universitat de València. FT-IR spectra were recorded on a Nicolet-5700 spectrophotometer as KBr pellets.

### Magnetic measurements

Direct current (*dc*) and alternating current (*ac*) magnetic measurements were performed on frozen matrix water suspensions of **1** to prevent for partial water loss upon vacuum, with a Quantum Design SQUID (Superconducting Quantum Interference Device) magnetometer and a Quantum Design Physical Property



Measurement System (PPMS). The magnetic susceptibility data were corrected for the diamagnetism of the constituent atoms and the sample holder.

### **Crystallographic data collection and refinement**

X-ray diffraction data of a single crystal of **1** were collected on a Bruker D8 Venture diffractometer with PHOTON II detector by using monochromatized Mo- $K\alpha$  radiation ( $\lambda = 0.71073 \text{ \AA}$ ). The structure was solved by standard direct methods and subsequently completed by Fourier recycling by using the SHELXTL software packages. The obtained models were refined with version 2013/4 of SHELXL against  $F^2$  on all data by full-matrix least squares.<sup>1</sup> A face absorption correction has been done by using empirical/numerical methods (Fig. S11). All non-hydrogen atoms were refined anisotropically. Hydrogen atoms from the coordinated water molecules were set on geometrical positions and refined with a riding model, while those from the crystallisation water molecules were neither found nor fixed. The oxygen atoms from the crystallisation water molecules were disordered. A half occupation factor was assigned within each of the two O4Aw/O4Bw and O5Aw/O5Bw pairs. Due to the disorder of the crystallisation water molecules, their connectivity through hydrogen bonding interactions is very difficult to establish. Yet a possible model is given in Fig. S2 which takes into account reasonable values for the intermolecular hydrogen bonding distances and angles. The graphical manipulations were performed with the CRYSTAL MAKER program.<sup>2</sup>

Crystallographic data (excluding structure factors) for **1** (Table S1) have been deposited with the Cambridge Crystallographic Data Centre as supplementary publication number CCDC-2047766. Copies of the data can be obtained free of

---

<sup>1</sup> SHELXTL-2013/4, Bruker Analytical X-ray Instruments; Bruker: Madison, WI, USA, 2013.

<sup>2</sup> CrystalMaker, CrystalMaker Software, Bicester, England, 2015

charge on application to CCDC, 12 Union Road, Cambridge CB21EZ, UK (fax: (+44) 1223–336–033; e-mail: [deposit@ccdc.cam.ac.uk](mailto:deposit@ccdc.cam.ac.uk)).

**Table S2.** Summary of crystallographic data for **1**

Formula	C <sub>3</sub> H <sub>10</sub> GdO <sub>1</sub>
<i>M</i> (g mol <sup>-1</sup> )	379.36
Crystal system	Monoclinic
Space group	<i>P</i> 2 <sub>1</sub> / <i>c</i>
<i>a</i> (Å)	11.0564(5)
<i>b</i> (Å)	9.5549(4)
<i>c</i> (Å)	10.0477(4)
$\alpha$ (°)	90
$\beta$ (°)	114.5420(10)
$\gamma$ (°)	90
<i>V</i> (Å <sup>3</sup> )	965.57(7)
<i>Z</i>	4
$\rho_{\text{calc}}$ (g cm <sup>-3</sup> )	2.610
$\mu$ (mm <sup>-1</sup> )	6.917
<i>T</i> (K)	150(2)
Reflect. collcd.	2172
Reflect. obs. [ <i>I</i> > 2σ( <i>I</i> )]	2041
Data/Restraints/Parameters	2172/6/179
<i>R</i> <sub>1</sub> <sup>a</sup> [ <i>I</i> > 2σ( <i>I</i> )]	0.0209
<i>wR</i> <sub>2</sub> <sup>b</sup> [ <i>I</i> > 2σ( <i>I</i> )]	0.0463
<i>S</i> <sup>c</sup>	1.157

<sup>a</sup>  $R_1 = \sum(|F_o| - |F_c|) / \sum |F_o|$ . <sup>b</sup>  $wR_2 = [\sum w(F_o^2 - F_c^2)^2 / \sum w(F_o^2)^2]^{1/2}$ . <sup>c</sup>  $S = [\sum w(|F_o| - |F_c|)^2 / (N_o - N_p)]^{1/2}$ .

**Table S3.** Selected structural, magnetic, and magnetocaloric data for homo- and heteroleptic Gd<sup>III</sup> MOFs with light organic mono- and/or dicarboxylate linkers proposed as cryogenic molecular magnetic coolers.

Entry	Compound <sup>a</sup>	nD <sup>b</sup>	T <sup>c</sup> (K)	ΔH <sup>d</sup> (T)	-ΔS <sub>M</sub> <sup>e</sup> (J K <sup>-1</sup> K <sup>-1</sup> )	ΔT <sub>ad</sub> <sup>f</sup> (K)	ρ <sup>g</sup> (g cm <sup>-3</sup> )	θ <sup>h</sup> (K)	T <sub>N</sub> <sup>i</sup> (K)	Ref.	
1	Gd <sub>2</sub> (fum) <sub>3</sub> (H <sub>2</sub> O) <sub>4</sub> ·3H <sub>2</sub> O	3D	1.0	2	18.0	7.5	2.52	-7.6	0.2	19	
			1.3	5	20.7						
2	Gd(form)(ac) <sub>2</sub> (H <sub>2</sub> O) <sub>2</sub>	1D	0.9	2	37.1		2.40			7	
			1.8	7	45.9						
3	Gd <sub>2</sub> (abdc) <sub>2</sub> (dmf) <sub>4</sub>	3D	1.8	7	29.0		1.42	-0.18		7	
4	Gd <sub>2</sub> (ida) <sub>3</sub> ·2H <sub>2</sub> O	3D	2.0	2	22.5		2.48		-0.90		8
			2.0	4	34.9						
			2.0	7	40.6						
			1.9	2	25.7						
			1.9	3	33.3						
5	Gd(form)(bdc)	3D	2.25	5	42.4						9
			2.25	7	46.0						
			2.25	9	47.0						
			1.1	2	43.7						
			2.0	7	55.9						
6	Gd(form) <sub>3</sub>	3D	1.1	2	43.7	22.5	3.86	-0.30	0.8	10	
			2.0	7	55.9						
			2.0	3	35.5						
7	Gd <sub>2</sub> (OH) <sub>2</sub> O(CO <sub>3</sub> ) <sub>2</sub> (form) <sub>2</sub> (sq)(H <sub>2</sub> O) <sub>2</sub>	3D	2.0	3	35.5		3.37	-1.64		11	
			2.0	7	60.0						
			3.0	9	64.0						
8	Gd <sub>2</sub> (ox) <sub>2</sub> (sq)(H <sub>2</sub> O) <sub>4</sub>	3D	3.0	2	25.0		2.90	-0.18		13	
			3.0	7	44.0						
9	Gd <sub>2</sub> (ox) <sub>3</sub> ·6.6H <sub>2</sub> O	2D	2.0	1	11.0		3.00	-0.75		14	
			2.0	2	25.3						
			2.0	3	34.4						
			2.0	5	43.0						
			2.0	7	46.6						
10	(H <sub>4</sub> edte)Gd <sub>2</sub> (ox) <sub>4</sub> (H <sub>2</sub> O)	3D	2.0	1	9.9		2.30	-0.09		15	
			2.0	3	27.2						
			2.0	9	35.9						
11	Gd(ox)(H <sub>2</sub> PO <sub>3</sub> )(H <sub>2</sub> O) <sub>2</sub>	2D	2.0	3	35.4		2.88	-0.22		16	
			2.0	7	46.6						
12	Gd <sub>2</sub> (ox)(fum) <sub>2</sub> (H <sub>2</sub> O) <sub>4</sub> ·4H <sub>2</sub> O	3D	3.0	3	31.0			+0.03		12	
			3.0	5	38.4						
			3.0	7	41.6						
13	Gd <sub>2</sub> (ox)(fum) <sub>2</sub>		3.0	3	33.7			-0.28		12	
			3.0	5	47.2						
			3.0	7	52.5						
14	Gd <sub>2</sub> (ox) <sub>3</sub> ·10H <sub>2</sub> O (I)	2D	2.0	1	10.2		2.61	-0.27		This work	
			2.0	2	21.9						
			2.0	3	29.1						
			2.0	4	33.8						
			2.0	5	37.0						
			2.0	6	39.1						
			2.0	7	40.6						
			2.0	8	41.5						

<sup>a</sup> Ligand abbreviations: fum = fumarate; ac = acetate; abdc = 2-amino-1,4-benzenedicarboxylate; ida = iminodiacetate; bdc = 1,4-benzenedicarboxylate; form = formate; sq = squarate; ox = oxalate; H<sub>4</sub>edte = *N,N,N',N'*-tetrakis(2-hydroxy-ethyl)ethylenediamine; fum = fumarate.  
<sup>b</sup> Structural dimensionality. <sup>c</sup> Value of the temperature. <sup>d</sup> Value of the magnetic field change. <sup>e</sup> Value of the maximum magnetic entropy change (in gravimetric units) estimated from indirect variable-field magnetization or heat capacity measurements. <sup>f</sup> Value of the adiabatic temperature change estimated from direct or indirect or indirect heat capacity measurements. <sup>g</sup> Value of the calculated crystal density. <sup>h</sup> Value of the Weiss temperature obtained from the fitting of the magnetic susceptibility data to the Curie-Weiss law. <sup>i</sup> Value of the Néel temperature for the long-range antiferromagnetic order.

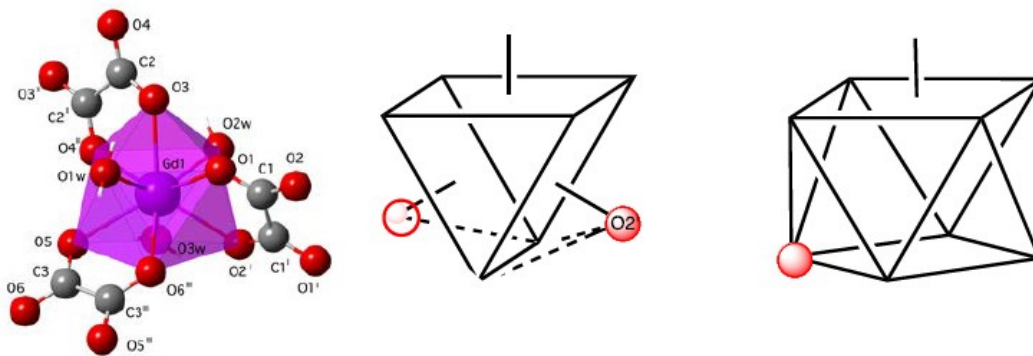


**Fig. S1.** Coordination environment around each crystallographically independent Gd(III) ion for **1** with the atom numbering scheme [symmetry code: IV = 1-x, -y, 1-z]. The two alternative ideal tricapped trigonal prism (TCTPR) and monocapped square antiprism (CSAPR) polyhedra are shown for comparison. The grey arrows represent the simple pathway for the structural transformation between each other.

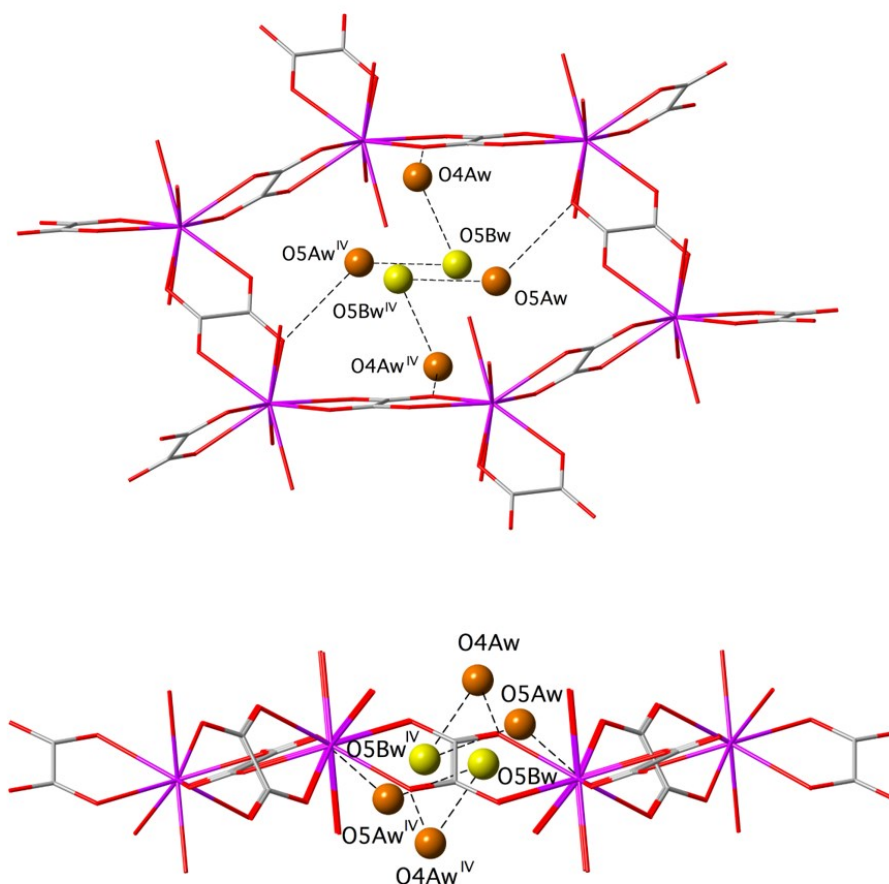


**Fig. S2** Top and front views of the hexagonal ring of the neutral oxalato-bridged gadolinium(III) hexagonal layer of **1** with the atom numbering scheme showing the hydrogen-bonded crystallization water molecules occupying the intra- and interlayer spaces. The two sets of disordered crystallisation water molecules with half-occupancy factors are represented by yellow and orange spheres. Hydrogen bonds are shown as dashed lines.

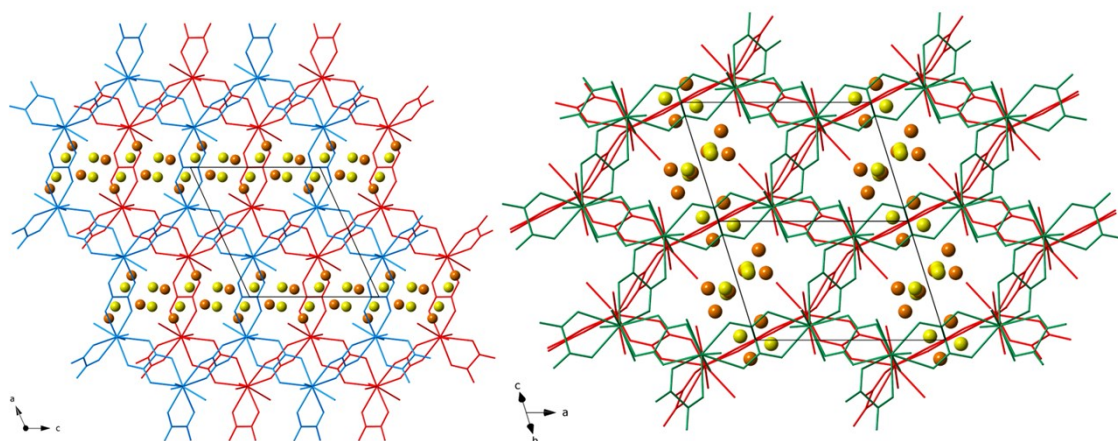


**Fig. S3** Projection views of the crystal packing of **1** along the [010] (left) and [011] (right) directions. The two sets of disordered crystallization water molecules with half-occupancy factors are represented by yellow and orange spheres.

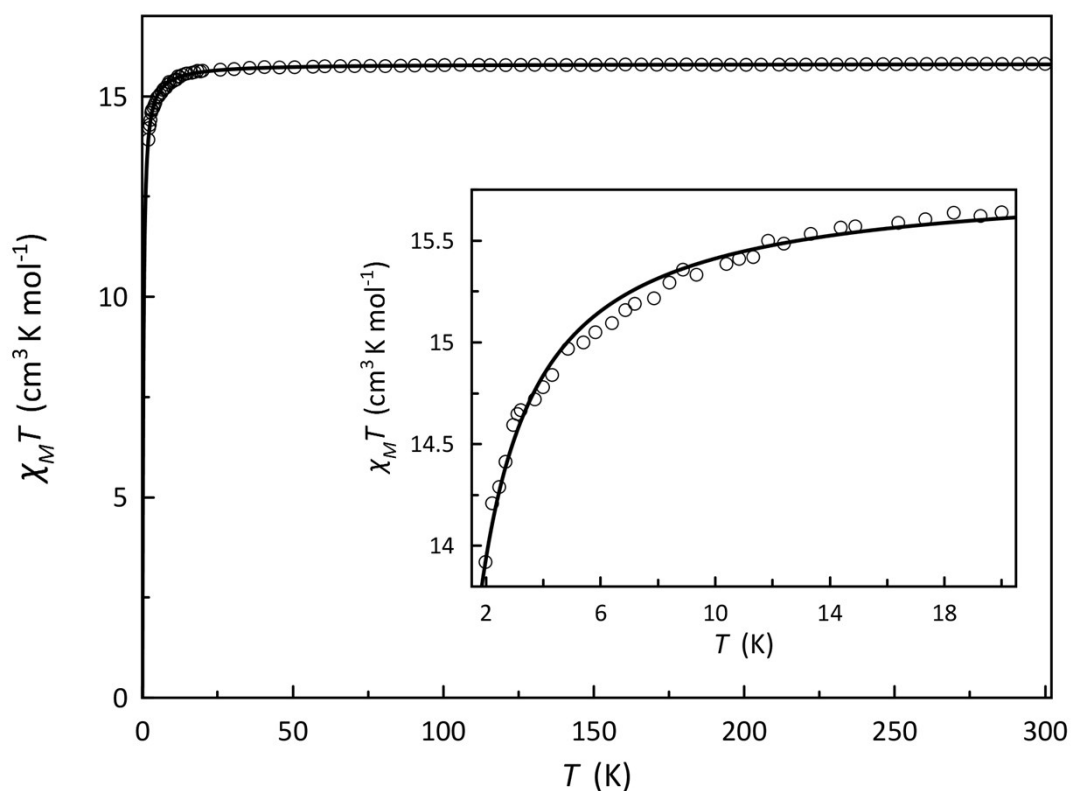


**Fig. S4.** Temperature dependence of  $\chi_M T$  for **1** under applied *dc* magnetic fields of  $H = 0.025$  ( $T \leq 20$  K) and 5 T ( $T > 20$  K). Solid line is the best-fit curve through the Monte Carlo simulations (see text).

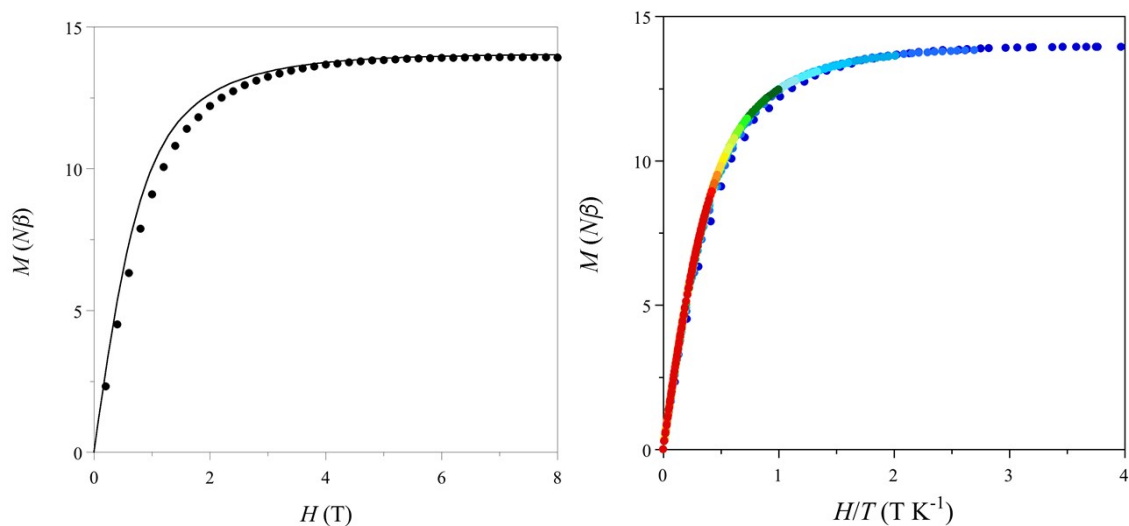


**Fig. S5.** Magnetisation curve (left) at  $T = 2$  K and reduced magnetisation curves (right) in the temperature range of  $T = 2$ – $20$  K (blue to red) for **1**. Solid line is the simulated curve through the Brillouin function (see text).

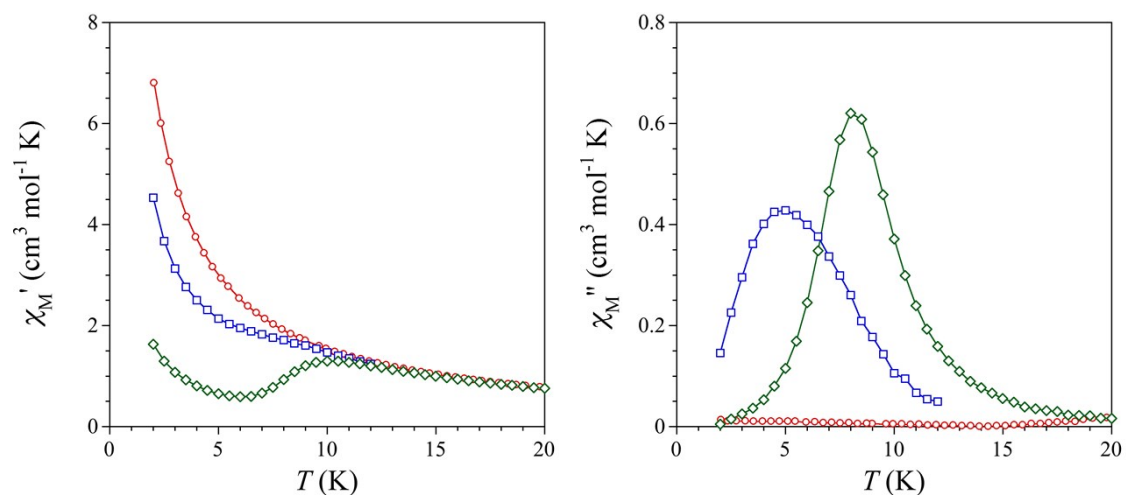


**Fig. S6** Temperature dependence of  $\chi_M'$  (left) and  $\chi_M''$  (right) for **1** at  $\nu = 1000$  Hz of the  $\pm 4$  Oe oscillating field and under an applied static magnetic field of  $H = 0$  (○),  $0.1$  (◐), and  $0.25$  T (◑). Solid lines are only eye-guides.



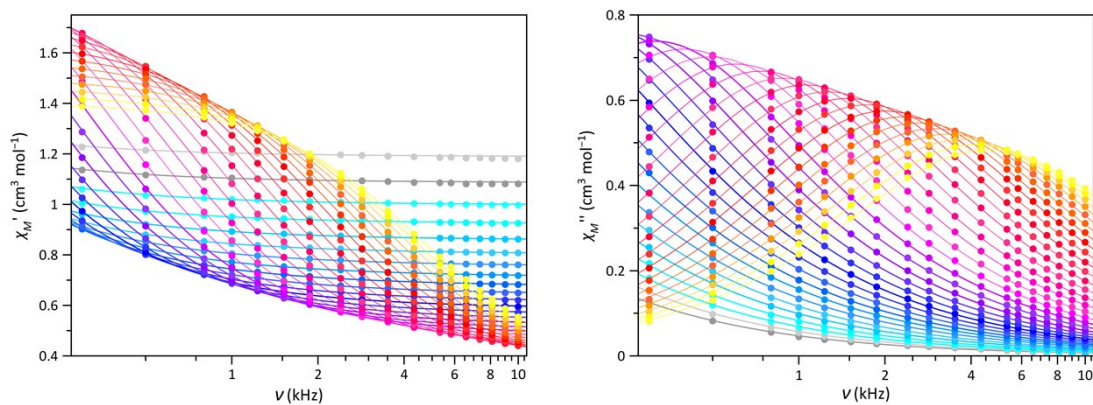


**Fig. S7** Frequency dependence of  $\chi_M'$  and  $\chi_M''$  of **1** in the temperature range of  $T = 2.5$ – $11.0$  K (gray to yellow) at  $H = 0.25$  T. Solid lines are the best-fit curves through the generalised Debye model (see text).

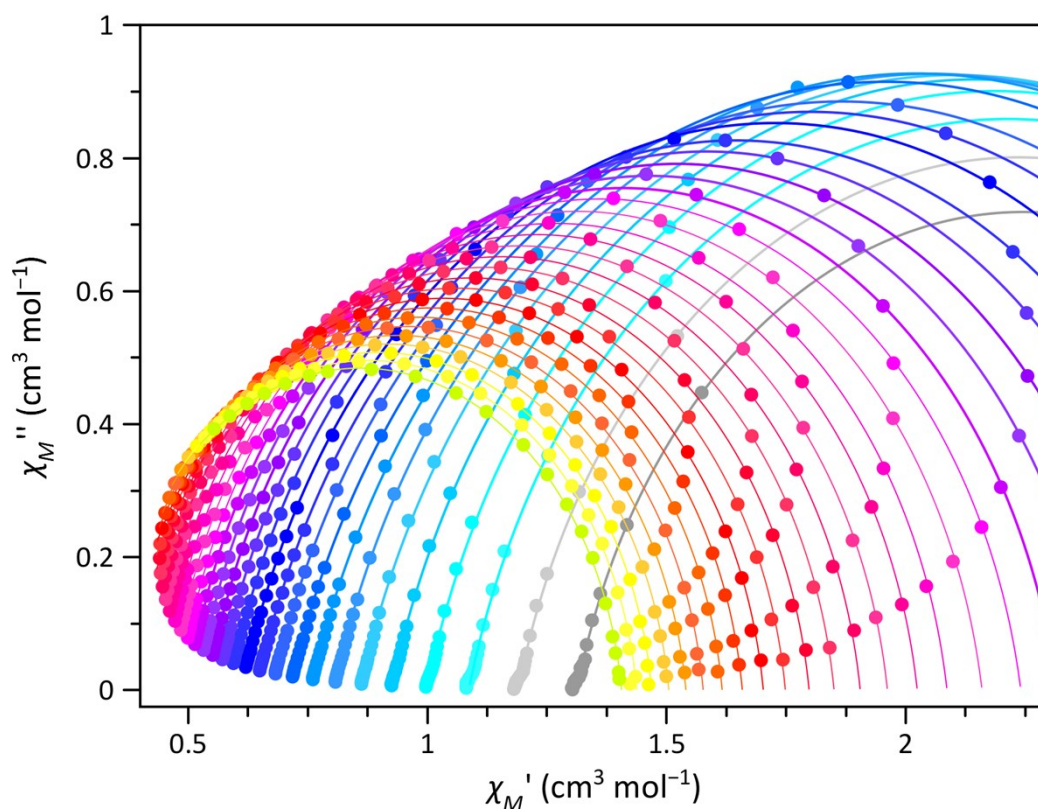


**Fig. S8** Argand plots of **1** in the temperature range of  $T = 2.5$ – $11.0$  K (grey to yellow) at  $H = 0.25$  T. The solid lines are the simulated curves through the generalised Debye model (see text).

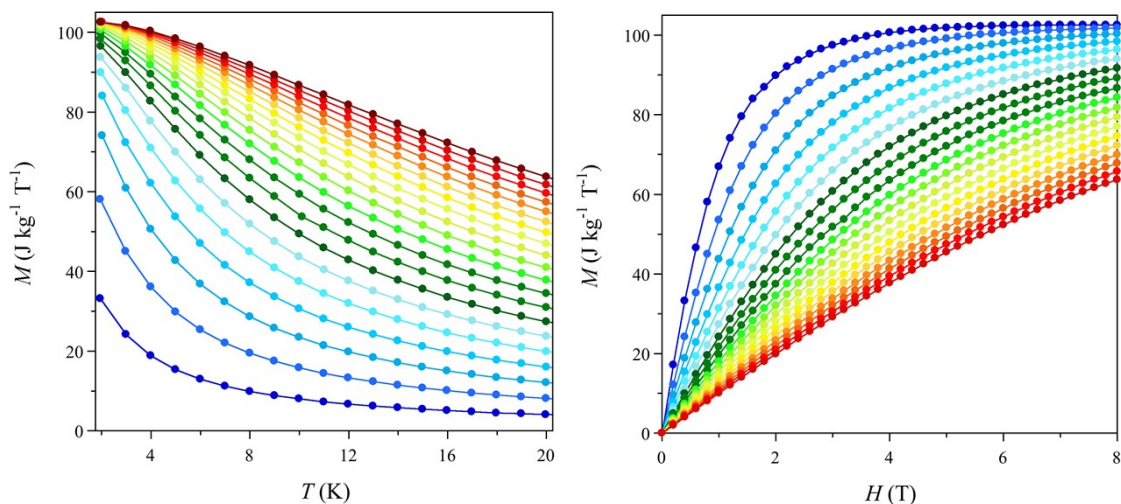


**Fig. S9** Temperature (left) and field dependence (right) of  $M$  for **1** in the magnetic field and temperature ranges of  $H = 0\text{--}8$  T and  $T = 2\text{--}20$  K (blue to red), respectively.

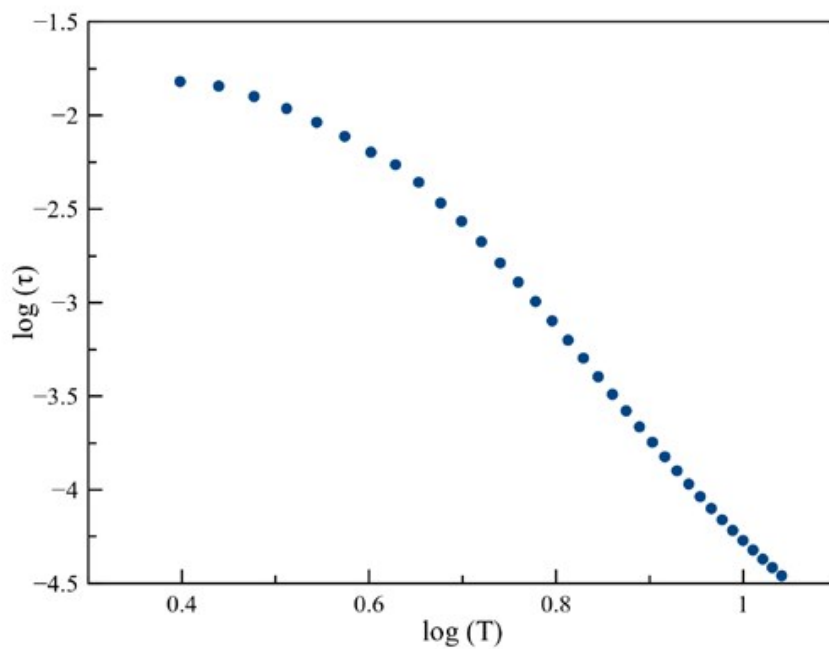


**Fig. S10.** Temperature dependence of the relaxation time of compound **1** represented in a log-log plot. In the representation is evident the two different slopes regime corresponding to the Raman and IK contributions (see text).



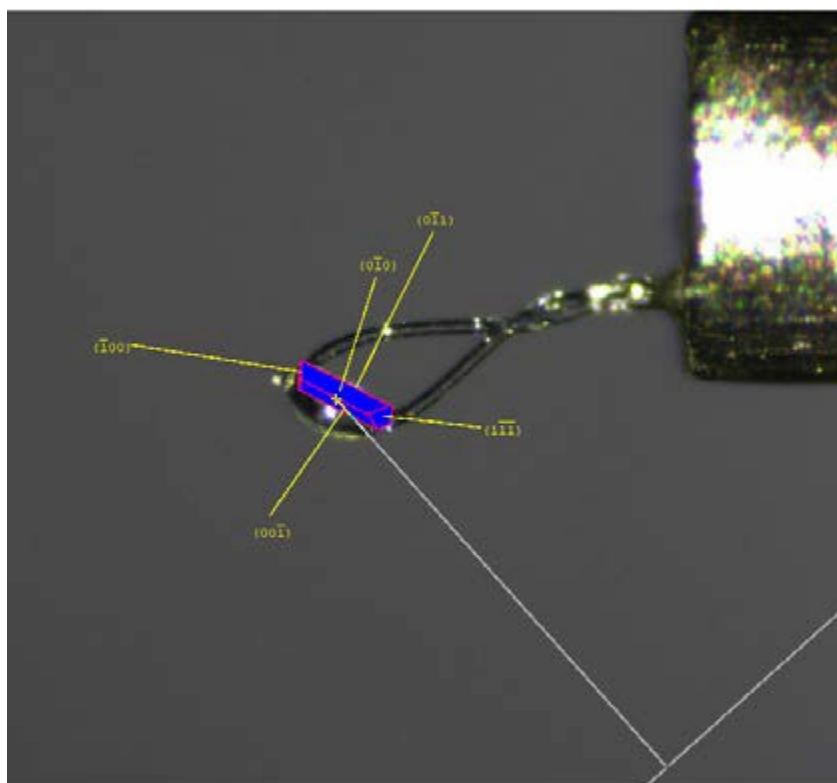


**Fig. S11.** Face indexing of a crystal of 1, mounted on a goniometer head and indicating the crystallographic planes (dimensions: 0.21 x 0.07 x 0.04 mm<sup>3</sup>).





